Report on Pool Boiling Experiment Prototype Model Flown on STS-47 (PBE-IA)

Herman Merte, Jr.
Ho Sung Lee
Robert B. Keller

NASA Contract NAS 3 - 25812
Report No. UM-MEAM-94-09
June 1994

Conducted under:

National Aeronautics and Space Administration
Lewis Research Center
Cleveland, Ohio

ensm

UMR1270

Table of Contents

List of Figures

List of Tables Page #

List of Appendices Page #

1. INTRODUCTION

1.1 General Background

Nucleate boiling is an important mode of heat transfer in that relatively small temperature differences can provide large rates of heat transfer, which can result in significant economic and other benefits associated with the smaller heat transfer areas necessary to accomplish a given function.

A limitation in the development of more compact power sources using nuclear energy lies in the ability to remove the large heat generation rates possible from the reactor core in a manner that is consistent, reliable and predictable. Nucleate boiling would be a candidate for such an application were the fundamental mechanisms that govern the process sufficiently well understood. Additional important applications of nucleate boiling exist, such as steam generation in conventional power plants, distillation processes in petroleum and other chemical plants, and the boiling of refrigerants in cooling coils, in which the motion of the bulk liquid is generally imposed externally. This is termed forced convection boiling, and the liquid motion moves the vapor formed away from the heated surface so that the vapor may be utilized and/or further processed and the nucleate boiling process can continue.

Other applications exist in which externally forced flow is absent, where buoyancy provides the major mechanism for vapor removal from the vicinity of the heating surface, and is generally designated pool boiling. Even in circumstances where forced convection exists to some extent, the forces associated with flow acting on the vapor bubbles may be sufficiently small that buoyancy or body forces will continue to be responsible for the vapor removal process. It should then be possible to describe the behavior, in terms of the basic governing mechanisms, by the pool boiling process. Devices in which pool boiling occurs are two-phase closed thermosyphons, reboilers, and heat pipes, whether gravity assisted or not. Potentially significant applications exist in the cooling of microelectronic circuitry and the internal cooling of gas turbine blades. The latter would involve pool boiling under high gravity fields, and its successful application would permit higher operating temperatures with attendant higher efficiencies, and would also eliminate the need for the development of exotic ceramic materials with the difficulties of thermal stresses and reliability. Another important and as yet poorly understood area incorporated in the mechanism of pool boiling is the breakdown of film boiling into the transition boiling regime. This is of concern in the loss-of-coolant accident in nuclear power plants, and is encompassed in the reflooding and fuel element rewetting processes. A good understanding of this rewetting process in microgravity or in the absence of buoyancy would improve its application with buoyancy.

The effective and enhanced applications of both nucleate pool and forced convection boiling requires a sound understanding of the mechanisms governing the processes. The vapor removal from the vicinity of the heater surface, as understood to this point, occurs primarily by buoyancy in the case of pool boiling and bulk liquid inertia in the case with forced convection. Although the variation of both gravity and forced flow are known to influence the overall heat transfer processes, other forces or potentials are acting as well, and the relative significances of these are as yet poorly understood.

Requirements for the proper functioning of equipment and personnel in the space environment of reduced gravity and vacuum, as will be necessary in space station modules and space power generation, energy dissipation, the storage, transfer, control and conditioning of fluids (including cryogenic liquids), and liquid-vapor separation.

The temperature control in certain locations where internal heat generation takes place as a result of dissipation, as from friction or joulian heating, electronic equipment, or as a consequence of a nuclear or chemical heat source, may require that this energy be transported to other locations of the facility or stored locally for later transport and elimination. The use of the phase changes of vaporization and condensation to transport energy have the advantage of accommodating large variations in heat loads with relatively small temperature gradients and changes in temperature levels, along with the economical use of pumping power. Energy storage might be advantageous for intermittent processes or for processes where momentary surges could not be accommodated by a steady transfer of mass to a remote location, and also could take advantage of the latent heat associated with phase changes.

A distinction must be made between pool boiling and flow boiling when considering applications in the space environment of microgravity, since these two processes may arise in quite different specific technical applications. Pool boiling, for example, would be important for the short term cooling of high power electronic and other devices, and for the long term space storage of cryogens. Flow boiling, on the other hand, occurs in applications where liquid flow is imposed externally, such as in Rankine cycle vapor generation or in thermal energy management using pumped latent heat transport.

Certain effects which can be neglected at normal earth gravity, such as surface tension and vapor momentum, can become quite significant at microgravity conditions. Momentum imparted to the liquid by the vapor bubble during growth tends to draw the vapor bubble away from the surface, depending on the rate of growth, which in turn is governed by the temperature distribution of the liquid. Thermophoretic forces, arising from the variation of the liquid-vapor surface tension with temperature, on the other hand, tend to move the vapor bubble toward the region of higher temperature. The bubble motion will be governed by which of these two effects prevail. In addition, thermophoretic forces acting at the liquid-vapor interface of vapor bubbles in contact with a heated surface could act to bring cooler liquid to the heater surface, delaying or inhibiting the onset of dryout, or promoting and enhancing the rewetting of the heater surface.

1.2 Objectives of Study

The research as originally proposed was intended to seek to improve the understanding of the fundamental mechanisms that constitute nucleate pool boiling. The vehicle for accomplishing this is an investigation, including experiments conducted in microgravity and coupled with appropriate analyses, of the heat transfer and vapor bubble dynamics associated with nucleation, bubble growth/collapse and subsequent motion, considering the interrelations between buoyancy, momentum and surface tension which will govern the motion of the vapor and surrounding liquid, as a function of the heating rate at the heat transfer surface and the temperature level and distribution in the bulk liquid.

As will become clear when the results obtained to date are examined below, a more accurate representation would have been a proposal for a general study of pool boiling in microgravity. The circumstances under which nucleate boiling and what is generally termed, to this point, film boiling takes place with pool boiling in microgravity is as yet unclear. Both of these processes were observed, sometimes simultaneously, in the work to be presented here.

An adequate understanding of the mechanisms in any process implies that its behavior can be predicted in terms of the governing parameters. The behavior here would include the conditions for the onset of boiling, the dynamics of the vapor bubbles, including both the number density of active nucleating sites and the frequency of formation, and the associated heat transfer. Although a considerable amount of research has been conducted on nucleate boiling over the years, and has been useful with respect to application to various technologies on earth, the ability to predict its behavior is as yet very limited, owing to the involvement and interactions of the many parameters. To this now should be added also the limitations in predicting the onset of dryout or rewetting, whether in earth gravity or microgravity.

For the basic study proposed and conducted, with results presented here, it was deemed essential to establish a well-defined "bench mark" which could withstand future interrogations. The availability of a long period of quiescence prior to the onset of each test, as a result of the microgravity environment, means that the initial state at the onset of heating and at the onset of boiling (nucleation) will be well-defined. This is not possible in a gravity field. The availability of relatively long test periods permit the combination of low heat flux and subcooling that require more time for the inception of boiling than is available in a drop tower, and also permit the observing of long-term vapor dynamic behavior following the transient bubble growth.

The components which constitute the nucleate boiling process-nucleation, growth, motion, collapse (if subcooled) of the vapor bubbles - are common to both pool and flow boiling. The study here focuses on the fundamental mechanisms of pool boiling only, under microgravity conditions. This eliminates the complications associated with having an external flow field superimposed on that generated by growing/collapsing vapor bubbles. In addition, this eliminates the possibility of having other effects masked by an external flow field similar to that produced by buoyancy.

In the experiments as conducted, a pool of liquid, initially at a precisely defined pressure and temperature, is subjected to a step imposed heat flux from a semi-transparent thin-film heater forming part of one wall of the container such that boiling is initiated and maintained for a defined period of time at a constant pressure level. Transient measurements of the heater surface and fluid temperatures near the surface are made, noting in particular the conditions at the onset of boiling, along with motion photography of the boiling process in two simultaneous views, from beneath the heating surface and from the side. The conduct of the experiment and the data acquisitions are completely automated and self-contained. A total of nine tests were conducted at three levels of heat flux and three levels of subcooling.

The results presented here were obtained with what is termed the Prototype Version of the experimental facility. Following the successful development work conducted during the ground-based activity under NASA Grant NAG3-663, which included reduced gravity testing in the evacuated 5 second drop tower at the NASA Lewis Research Center, the results of which were reported in Ervin and Merte (1991), Ervin et al (1992), and Lee and Merte (1993), approval was given for a space experiment. An Engineering Model was developed by the NASA Lewis Research Center for testing the feasibility of incorporating the experimental concepts described in the Science Requirements Document by Merte (1989) into the space available in a Get-Away-Special (GAS). Following the successful demonstration of the operation of the Engineering Model, the construction of a Prototype Version was undertaken. This proved to operate so successfully with full testing in earth gravity that when an opportunity for an unexpected early GAS flight came to light a request was made to fly the Prototype Version. This was justified primarily as an opportunity to further test the heretofore untried engineering concepts in the facility, and to confirm the camera timings which could not be determined in the drop tower testing. The successful acquisition of any experimental measurements was thus viewed to be a bonus. The results obtained later with the Flight Version of the experimental apparatus will be the subject of a future report, and will include comparisons with the results presented here.

1.3 Basic Mechanisms of Pool Boiling

As stated above, consideration of any externally imposed flow field on the boiling process, termed as forced convection boiling, is explicitly excluded here in order to:

(a) Eliminate an additional complicating variable from an already complex process at the outset. Pool boiling is the limiting case of forced convection boiling as the imposed velocity is reduced to zero.

(b) Minimize the possibility that certain weak effects would be overshadowed by the kinetic energy associated with the imposed bulk liquid flow. The supposedly weak effects were considered to consist primarily of thermophoretic and molecular momentum forces.

1.3.1 Nucleate Boiling

Nucleate boiling may be characterized as:

(i) A liquid-vapor phase change occurs with the formation of discrete bubbles at individual sites.

(ii) The energy transfer rates are large with small temperature difference driving potentials.

(iii) The process is inherently transient, although quasi cyclic repetitions are possible with vapor removal mechanisms such as buoyancy acting.

Before a nucleate pool boiling system can attain the steady periodic behavior normally observed in a gravity field, where buoyancy is the predominant vapor removal mechanism, the process must pass through a transient phase referred to as the nucleation, initiation or onset of nucleate boiling. Before understanding the cyclic nature of nucleate boiling, one must first understand the elements of the initial transient process.

To provide a perspective of the relationship between the study conducted here and the overall processes which constitute pool boiling, a qualitative physical description of the sequence of events which occur is presented, beginning with the transient heating of a liquid at a solid-liquid interface

a. Conduction

With an initially static liquid the heat transfer process can be described by conduction alone until buoyancy, thermophorysis or other forces set the liquid in motion. The rate of temperature rise and the temperature distributions in this early interval depend on the nature of the heat source and the dynamic interactions with the system. The common idealizations taken as limits in analyses are step changes in either temperature or heat flux at the solid-liquid heater interface. The degree and extent to which the liquid becomes superheated above its saturation temperature in a given time depends on whether and by how much the bulk liquid is subcooled. This temperature distribution will be modified by the onset of natural convection or by other disturbances.

b. Onset of Natural convection

Natural convection is driven by buoyancy, and its onset is described in terms of a stability in which the enervating disturbances are always present. Reducing the buoyancy by reducing the body forces such as to microgravity delays the onset of the convection and reduces the resulting convection velocities. Both of these serve to increase the temperature levels in the liquid adjacent to the heating surface for a given heating time, regardless of whether the bulk liquid is initially saturated or subcooled. The liquid temperature levels and distributions adjacent to the heater surface are thus influenced by buoyancy, and in turn can influence the next two elements of nucleate boiling: the nucleation and bubble growth rates.

c. Nucleation

Vaporization can take place only at an existing liquid-vapor interface, which then constitutes the growth phase of nucleate boiling. If an interface does not exist it must be formed. The formation of a vapor nucleus is called nucleation, and is classified either homogeneous or heterogeneous, depending on the presence of other components or species in the vicinity of the nucleation. The circumstances under which nucleation takes place on a heated solid surface depends on:

(i) The Heater Surface Microgeometry. This can provide the crevices and intergranular defects which serve as pre-existing interfaces. The temperature levels required to activate these pre-existing nuclei have been modeled in terms of thermodynamic equilibrium at curved liquid-vapor interfaces. Assuming that the pre-existing interface has the form of a hemisphere of the size of the surface defect, the liquid superheat required for subsequent bubble growth can be related to cavity size. The smaller is the cavity, the larger is the heater surface superheat required for the onset of nucleate boiling, and the larger will be the bulk liquid temperatures at the onset of the next element of the boiling process.

(ii) The Solid-Fluid properties. This governs not only the temperature distributions in both the heater and fluids, related by their respective thermal properties, but also the surface energy relationships between the solid-liquid-vapor, often expressed in terms of a contact angle or wettability.

(iii) The Liquid Temperature Distribution. This includes the solid-liquid interface temperature, since this is one spatial limit of the liquid temperature. As discussed under "b" above, the onset of natural convection governs the subsequent temperature distributions, as does also the initial imposed heat flux. Once nucleation has occurred, the following bubble growth rates will be governed by the bulk liquid temperature distribution at this time.

d. Vapor Bubble Growth/Collapse

Vapor bubble growth requires that the liquid at the liquid-vapor interface be superheated with respect to the saturation temperature corresponding to the interfacial liquid pressure. The rate of vapor formation, and hence bubble growth, depends on this superheat and on the liquid temperature gradient at the interface, and thus on the liquid temperature distribution at the onset of bubble growth. The interfacial liquid superheat governs the internal vapor bubble pressure, which acts to move the bulk liquid away from the vicinity of the heater surface. In the dynamics of the growth process this pressure is balanced in a complex manner by the liquid inertia, liquid viscosity, buoyancy, and surface tensions. If the bulk liquid is subcooled, the pressure difference can reverse with the subsequent collapse of the vapor bubble. The various forces acting in the bubble growth/collapse can be summarized:

(i) Internal Bubble Pressure. This is governed by the liquid temperature distribution, which in turn is influence by buoyancy.

(ii) Liquid Momentum. This is sometimes referred to as bulk liquid inertia.

(iii) Buoyancy. The pressure differences associated with the liquid-vapor density differences in a body force field act in addition to those natural convection effects which influence the liquid temperature distribution.

(iv) Surface Tension. This includes both that occurring at the liquid-vapor interface and at the liquid-solid-vapor interline.

(v) Viscosity. This refers primarily to the liquid viscosity acting in the vicinity of the solid surface, but could include the viscous normal shear at the liquid-vapor interface away from the solid surface in circumstances where the radial growth rate is very large. Vapor viscosity could also be a factor during the very early periods when surface rates of vapor formation are large.

Since the liquid-vapor interface is deformable, the interfacial shape during growth will be governed by the net balance of the dynamic forces acting at each point on the interface, and the interface will not necessarily be spherical or hemispherical, as has been assumed in the absence of capabilities for dealing with flexible interfaces.

e. Departure

The subsequent motion of the vapor bubble depends on the net effect of the forces listed in "d" above, plus a phenomena associated with simultaneous evaporation and condensation across a vapor bubble, referred to as a molecular momentum effect. This is related to the molecular kinetic energy necessary for vapor molecules to escape or to be retained at a liquid-vapor interface. With thermodynamic equilibrium the net rate of evaporation and condensation is zero, but the normal nucleate boiling process is highly non-equilibrium. The net resulting molecular momentum forces are generally unobservable in the presence of the overwhelming body and other forces which usually exist. The bulk liquid momentum induced by the rapid bubble growth can act to assist in the removal of the bubble from the heater surface. In microgravity, of course, buoyancy effects are reduced significantly.

f. Motion Following Departure

If the circumstances of the forces acting on the vapor bubble are such that departure takes place, the subsequent motion depends on the following:

(i) Buoyancy

(ii) Initial velocity upon departure. This velocity induces momentum in the bulk liquid, which must be considered, and can tend to accelerate the vapor bubble if collapse takes place, or will decelerate the bubble if it grows.

(iii) Degree and distribution of liquid superheat and/or subcooling. The bulk liquid temperature distribution can act via the liquid-vapor surface tension or Marangoni-induced effects, via the bulk liquid momentum effects associated with growth or collapse, together with liquid viscosity, and via the molecular momentum effects. In microgravity conditions, only buoyancy will be changed, except for its more indirect influence on the bulk liquid temperature distribution.

1.3.2 Dryout (Film Boiling in Earth Gravity)

Nucleate boiling can take place only in circumstances where the liquid substantially wets the heater surface. This entails two implications. First, the liquid itself must be inherently wetting on the heater surface. As observed and discussed by Merte (1967), it is well known, for example, that mercury is generally non-wetting except for materials with which it forms amalgams. For the operation of mercury power generation plants it was necessary to add traces of Magnesium and Titanium to the mercury to promote wetting and nucleate boiling in the boiler tubes. The second implication is that the vapor generation rate and hence the heat flux level is not sufficiently high to reach the critical heat flux, sometimes referred to as the first boiling crisis, the nucleate boiling maximum heat flux, or the burnout heat flux. A specific heater surface temperature is generally related to this heat flux, and if the heater surface temperature exceeds this level a decrease in the heat transfer rate takes place, hence the term maximum heat flux. This decrease takes place because of a progressive increase in the dryout of the surface until the liquid is no longer in contact with the heater surface. This condition is then referred to as film boiling, since in the buoyancy of earth gravity it takes on the form of a thin vapor film in contact with the heater, and departure of the vapor from the vicinity occurs in various ways depending on the heater surface configuration and orientation relative to gravity. The minimum heater surface temperature at which film boiling can be sustained at its corresponding heat flux is referred to as the minimum film boiling heat flux, the Leidenfrost point, or the second boiling crisis.

The so-called transition boiling region between the first and second boiling crises can be considered as a spatially averaged combination of nucleate boiling and film boiling, in which the fractional proportion of film boiling or dryout changes from 0 to 1 over this domain. This perspective neglects the contributions of dry areas under individual bubbles at the individual nucleation sites. In the present work, the use of the transparent heater surface permits the direct viewing and assessment of the relative proportions of the dry areas on the heater surface. The processes of the first and second boiling crises, including the transition boiling regime between, can be generically designated by a single term as dryout or wetting, depending on the direction in which this inherently transient or dynamic process is taking place. It appears that the circumstances of operation in the transition region taking place during pool boiling in microgravity are considerably less well-defined than in earth gravity, and could be the subject of further studies.

2. EXPERIMENTAL CONCEPTS AND PARAMETERS

The basic study conducted here is intended to assist in extending the understanding of the mechanisms of nucleate pool boiling. Because of the complexity associated with the conduct of research in a microgravity environment it is essential to establish a well defined "bench mark" which will not require repeating. The availability of a reasonably long period of quiescence prior to the onset of each test means that the initial state at the onset of heating and at the onset of boiling (nucleation) will be well-defined. The availability of relatively long test periods for each run, with a maximum value of 2 minutes selected as representing a compromise, permits the combinations of low heat flux and subcooling that require more than the 5 seconds previously available in a drop tower for the inception of boiling, and also permits the observing of long-term vapor dynamic behavior following the transient bubble growth. Although the experiment as conducted is quite specific and well defined, it is also exploratory in nature, and has the potential for relatively fast turn-around with follow-on experiments.

The elements of nucleate boiling for which research conducted under microgravity would advance the basic understanding are stated in brief here:

(i) Nucleation or onset of boiling. Indications are that both heater surface temperature and temperature distribution in the liquid are necessary to describe nucleation, in addition to the character of the heater surface itself.

(ii) The dynamic growth of a vapor bubble in the vicinity of the heater surface. This includes the shape as well as motion of the liquid-vapor interface as growth is taking place. These are influenced by the liquid temperature distribution at the initiation of growth.

(iii) The subsequent behavior of the vapor bubble. This includes the motion, whether departure takes place or not, and the associated heat transfer.

Each of the specific features of the experiment were selected so as to provide data which will be consistent with and maximize the objectives of improving the basic understanding embodied in these elements. The features include:

2.1 Geometry and Configuration

(a) Pool boiling. This eliminates the complications associated with having an external flow field superimposed on that generated by a growing/collapsing vapor bubble.

(b) Large flat heater surface. A flat surface avoids poorly defined local surface tension effects associated with curved interfaces, and with a transparent substrate can permit viewing from beneath the heater surface. A size as large as possible consistent with other constraints is desirable in order to minimize edge effects, and to permit a reasonable degree of axial symmetry of the vapor bubble as it grows to a quasi-steady condition. Additional considerations associated with large flat heater surfaces are:

   (i) With heating from curved surfaces, different liquid flow patterns will occur during bubble growth depending on whether the liquid is on the convex or concave side.

   (ii) With flat surfaces, which may also be approximations of curved surfaces, the orientation with respect to the body force vector will affect the flow behavior, down to some (as yet) unknown body force level.

   (iii) The fluid motion with large surfaces will differ depending on whether the surface is heated uniformly or locally.

One further facet of vapor bubble nucleation and growth as influenced by surface tension and related to geometry can be mentioned here. The superheat that the liquid acquires in the boundary layer adjacent to the heater surface can be considerable, prior to nucleation. It is thus possible for the vapor formed initially to completely envelope the heater surface. With certain configurations such as small wires or cylinders it is possible that subsequent surface tension effects will maintain a stable "pseudo" film boiling process only because of the particular geometry used. It is expected that even if film boiling becomes suppressed to nucleate boiling on a small wire or cylinder, thermophoretic and surface tension effects and the resulting heat transfer will be quite different than with flat surfaces. Observations made by Weinzierl and Straub (1982) that pool nucleate boiling is uninfluenced by changes from earth gravity to microgravity are believed to be a result of the large surface tension effects associated with the fine wire used, so that buoyancy is relatively unimportant.

(c) Transparent heater surface. This permits the observation of the detailed behavior of the boiling process from beneath the heating surface, including rewetting of the heater surface and possibly the microlayer behavior, without distortions due to intervening liquid-vapor interfaces. This also permits viewing of the behavior of the liquid-vapor interfaces simultaneously from the side and from under the heater surface, providing details of behavior otherwise not observable.

(d) Thin-film heater. Using the technique of a thin gold film as a simultaneous heater and resistance thermometer provides a well-defined heat flux and temperature at a precise location, as well as a transparent heater surface.

2.2 Fluid

The fluid to be boiled must be non-conducting. The fluid is in direct contact with the electrical resistance heat source, and a conducting fluid such as water would quickly destroy the thin film surface. For energy conservation in the conduct of the experiment and convenience in comparing results with ground tests it is desirable that the fluid have a boiling point in the vicinity of earth ambient temperatures at near atmospheric pressures. It is further desirable that the fluid used initially have wetting characteristics with the heater surface such that the contact angle is relatively small, in order to evaluate fluids expected to be early candidates for space use, such as cryogenic liquids. The fluorocarbon R-113 meets these requirements, and its properties are well established.

2.3 Controlled Variables:

(a) Pressure. This defines the liquid saturation temperature, and maintaining it constant keeps the temperature at the liquid-vapor interface constant at the saturation level during the transient process. The pressure level also defines the initial liquid subcooling.

(b) Initial uniform temperature in the bulk liquid. This permits the precise calculation of the temperature distribution in the liquid at the onset of boiling, in the absence of buoyancy.

(c) Step change in a uniform heat flux. This permits the ready computation of the temperature distribution in the liquid at the point of nucleation. A constant imposed heat flux provides a well-defined temperature gradient in the liquid at the heat transfer surface. Additionally, it is possible to construct all other desired functional behaviors in heat flux from combinations of step changes.

(d) Length of test. Each individual test should be as long as possible consistent with compromises arising between the size of the test vessel, heater surface size and heat flux, so that a reasonably quasi-static condition can be attained when the early dynamic growth transients are completed. Additionally, certain liquid temperature distributions at the time of nucleation will only be possible with low levels of heat flux, which will require relatively long test periods to achieve nucleation. Independent control of the initial liquid subcooling and imposed heat flux permit the independent variation of the transient temperature distribution in the liquid.

2.4 <u>Measured Parameters</u>:

(a) Bulk liquid temperature distribution. This is necessary to assure the uniformity of the initial temperatures.

(b) Transient temperature of the thin film heater surface. During the non-boiling phase, this serves as an indication of the presence/absence of natural convection effects. During the boiling phase this provides a means for computing the net mean heat flux to the boiling fluid. It also provides a measure of the effectiveness of the boiling heat transfer process.

(c) Local system acceleration. This is necessary to assess the presence/absence of uncontrolled acceleration forces acting on the experimental vessel.

(d) Precision current/voltage drops across the thin film electrical heater. This permits computation of the heater resistance and hence temperature, as well as the heat flux.

(e) Photography. This enables the determination of the time interval between the onset of heating and boiling, along with the transient growth of the vapor bubble and its subsequent motion, as a function of the initial liquid temperature distribution, governed by the heat flux and initial liquid subcooling.

The specific technical requirements for the experiment, taken from the Science Requirements Document, are listed in Appendix A.

The vapor-pressure equation and coefficients used for the R-113 are given in Appendix B. The commercial R-113 was purified and degassed by distillation, filtering, and freezing under a vacuum on stainless steel fins cooled to liquid nitrogen temperatures. The apparatus used is shown schematically in Figure 2.1. The distillation was repeated, and followed by measurement of the vapor-pressure under equilibrium conditions. The R-113 was deemed to be adequately degassed when the measured vapor-pressure corresponded to that given by the equation in Appendix B to within ± 0.025 psia for temperatures measured to within a calibrated accuracy of ± 0.1°F in the laboratory.

The Resistance — Temperature relationship for the heater surface was determined by calibration over the anticipated temperature operating range prior to installation in the experiment test vessel. Prior experience had demonstrated that a linear relationship was entirely adequate. Although maximum laboratory absolute measurement uncertainties of ± 1°F (± 0.6°C) in the mean heater surface temperatures were attained, these were increased to ± 3°F (± 1.7°C) for the space experiments. However, instrumentation equipment sensitivities were requested to detect changes in heater surface temperatures of ± 1°F (± 0.6°C), if not the absolute uncertainty. To reduce the uncertainties, a single point calibration was conducted prior to each test run of the test matrix, using the prevailing equilibrium system temperature as an anchor point of the linear calibration curve.

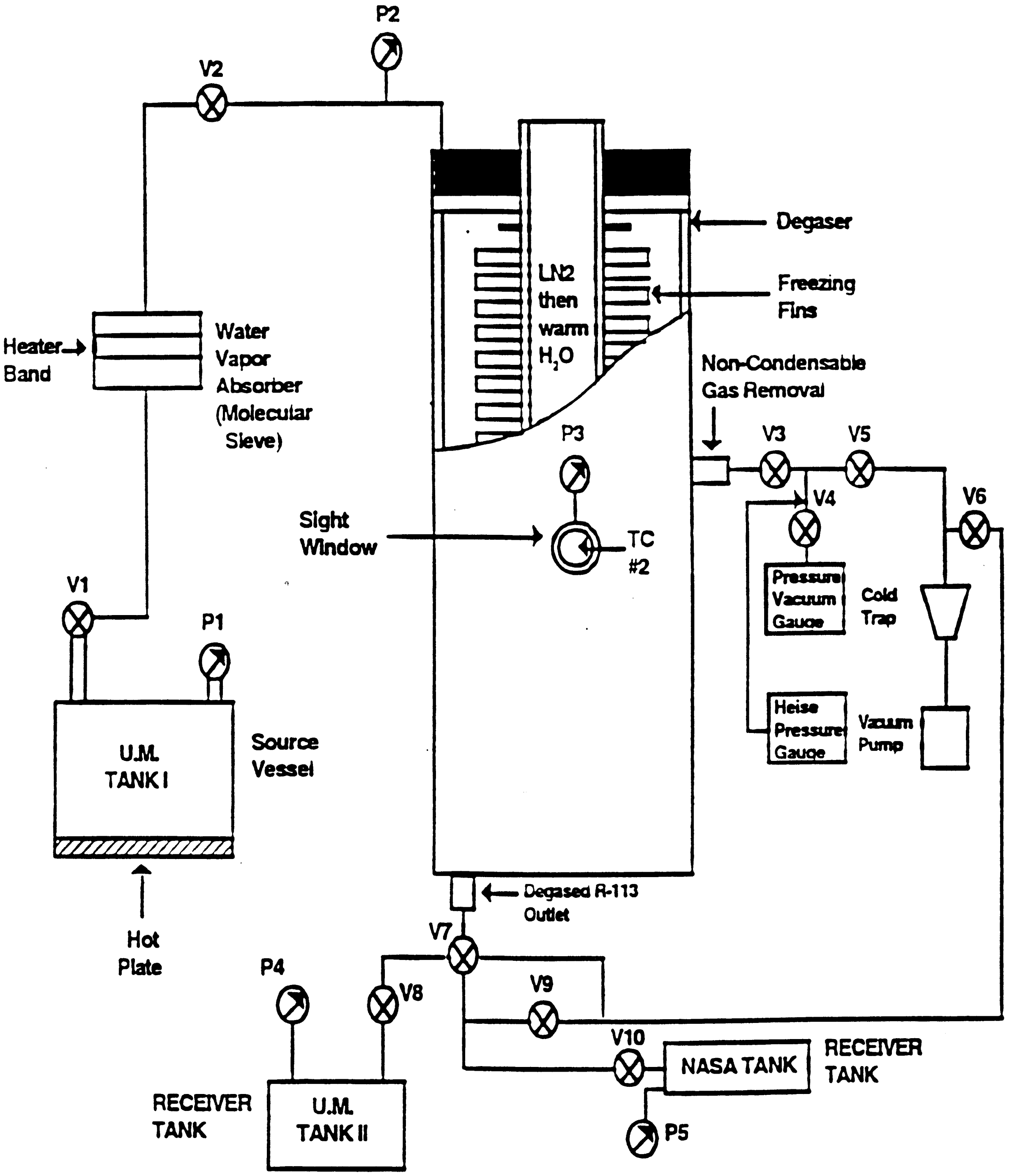

Figure 2.1 R-113 Degassing Unit Schematic.

3. HARDWARE DESCRIPTION

3.1 Heater Surface

A sketch of the transparent gold film heater is shown in Figure 3.1. Two separate heaters are mounted on each surface, identified as the primary and back up heaters, and configured so that should the primary heater fail the backup heater is automatically activated for the next test run of the matrix. A nominal film thickness of 400 Angstroms in the central heater section of size 0.75" × 1.50" (19.1 mm × 38.1 mm) corresponds to a nominal resistance of 3.8 ohms, and provides the desired transparency for viewing the boiling process from beneath. Power to the heater is provided by Silver-Zinc batteries, and the voltage is controlled, with the voltage drops across the potential taps and the calibrated shunt resistor (for the current measurement) stored in the data acquisition system.

The instantaneous heat flux input and the mean heater surface temperature are computed from the voltage drop across the potential tap and the current.

Calibration of both the primary and backup heaters took place prior to installation in the test vessel over temperature ranges of 66°F to 152°F. The electrical resistance — temperature follows a linear relationship within ± 1°F, well within the precision tolerances specified.

A slope — intercept equation of the form

$$\overline{T} = A + B \times \overline{R} \tag{1}$$

is used to compute the mean heater surface temperature $\overline{T}$ from the mean resistance $\overline{R}$ measured. The original values of A and B are given in Table I below.

Table I. Original Prior Flight Calibration
Coefficients for PBE-1A on STS-47.
Measurements made 2/13/92.

	Primary	Backup
A (°F)	-1306.46	-1375.72
B (°F/ohm)	402.065	404.876

The coefficient B is the slope, while A is the intercept at R = O. A single-point calibration is conducted just prior to each Run of the test matrix, using the bulk liquid temperature measured with a calibrated thermister in the immediate vicinity of the heater surface, 1 mm away. This is used to modify the coefficient A for each Run, using the original prior value of B, which was found to change relatively little with a suitably aged heater surface. The surface will be calibrated again over the temperature range, and a new value of B obtained. However, the single-point calibration significantly reduces the effects of unlikely large changes in B taking place over a period of time.

3.2 Test Vessel

A schematic of the test vessel is shown in Figure 3.2, together with the hardware concepts necessary to provide a constant pressure during each Run and an initially uniform fluid temperature. Although the stirrer was intended to be activated only between the various runs of the matrix in order to promote the uniformity of temperature of the fluid, it was also activated toward the end of several runs so as to observe its influence on the vapor bubbles and, in some cases, on the heat transfer.

Figure 3.3 shows the locations of the various sensors used to determine the behavior of the boiling process. PRHV and PRHI are the primary heater voltage taps and current readings, while BRHV and BRHI are the respective values for the back up heater, when used. TM01—TM03 and TM07—TM09 are thermistors above the primary and back up heaters to measure the respective fluid temperatures, at locations 1 mm, 5 mm, and 10 mm above the center of each heater. The thermister beads have a maximum diameter of 0.6 mm, and are stated by the manufacturer as having a time constant of 23 msec when plunged into water. The respective locations of TM04—TM05—TM06 are given in Figure 3.4 as A, B and C, and are provided to check the uniformity of fluid temperatures prior to the beginning of each Run.

Thermistors TM12 and TM11 are cemented to the quartz substrate on the side opposite the gold film, at the center of the primary and back up heaters, respectively, while TM13 is in the canister air space very near the quartz substrate backside.

Figure 3.5 gives the relative locations of the internal components of the test vessel, including the viewing and lighting windows. The lighting is diffused internally for maximum clarity. The maximum internal dimensions of the R-113 chamber are also given, as 14.48 cm diameter by 11.5 cm long, which implies that the maximum diameter of a vapor bubble that can be accommodated without pressing on the heater surface is about 12 cm.

Figures 3.6 and 3.7 present the side and front views of the entire system components within the GAS canister, with the optical path followed to the 16 mm camera, which has a 400 ft. film capacity. This gives a total of approximately 18,000 frames, which must be budgeted among the various Runs.

3.3 Accelerometer System

A space Acceleration Measurement System (SAMS) type traxial accelerometer head is included in the payload, shown in Fig. 3.7. This provides acceleration data in the direct vicinity of the test chamber. The use of an internal accelerometer also eliminates the need to correlate experiment data with a remote acceleration measurement system. Three Sunstrand QA2000-030 accelerometers are used. The manufacturer resolution specification for this model is 1 micro-g, and the accuracy is given as ±100 micro-g, found by using the root sum of squares of the various stabilities (thermal, shock and time).

The correlation between the accelerometer outputs and the local and vehicle coordinates are given in Figs. 3.8 and 3.9. The upper right view in Fig. 3.9 is taken through the heater surface, viewed from left to right in the right side of Fig. 3.5, while the upper left view is taken from the side, viewed from the bottom side of Fig. 3.5.

3.4 Optical System

The views in the upper part of Fig. 3.9 are obtained by combining the images, as illustrated in Fig. 3.6. Also within the camera field of view are LED timing lights for synchronization with the Data Acquisition Unit, seen in Fig. 3.9. The binary code for time is given in Fig. 3.10.

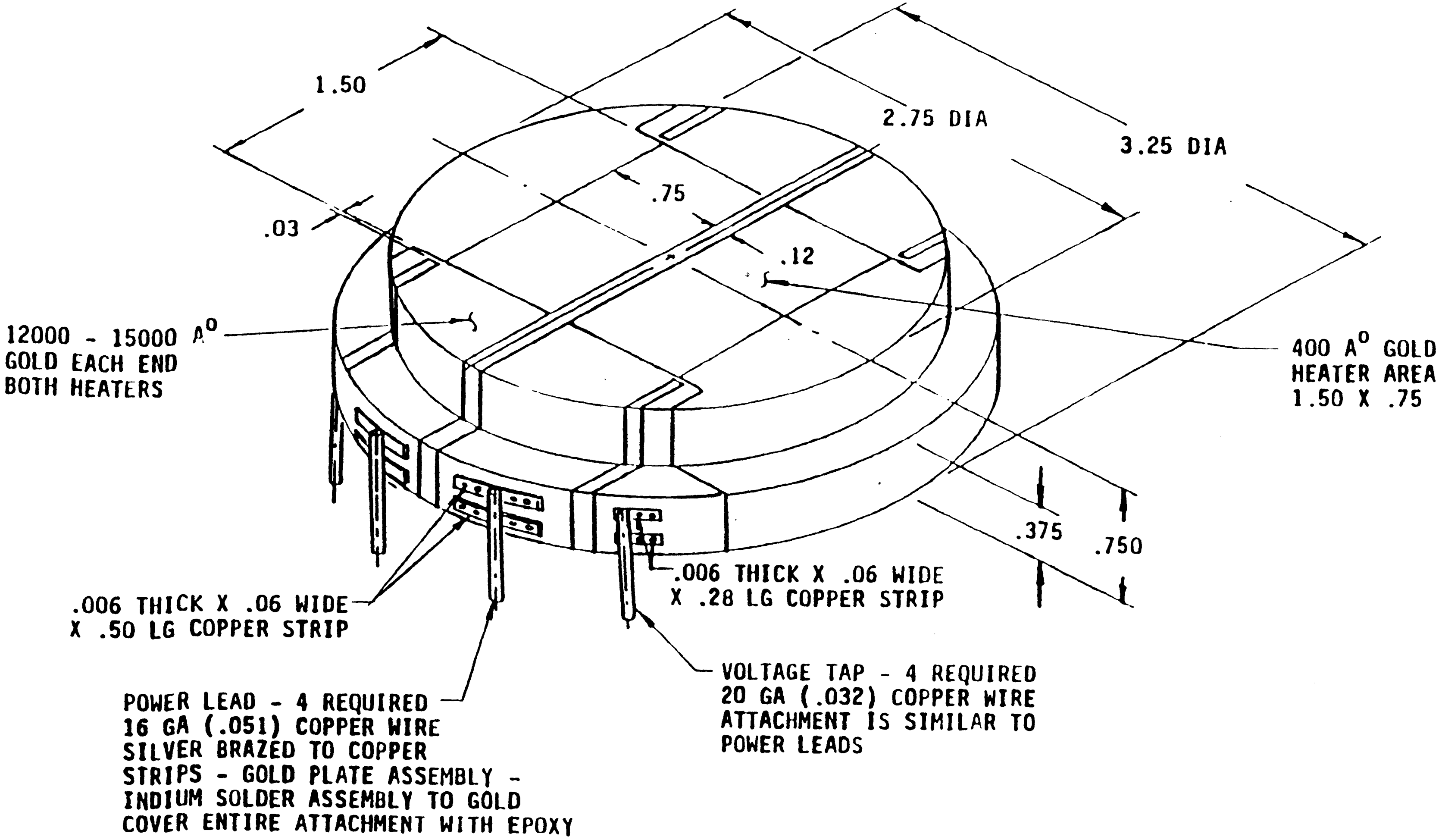

Figure 3.1. Transparent gold film heater/resistance thermometer on quartz substrate.
PBE-IA. STS-47.

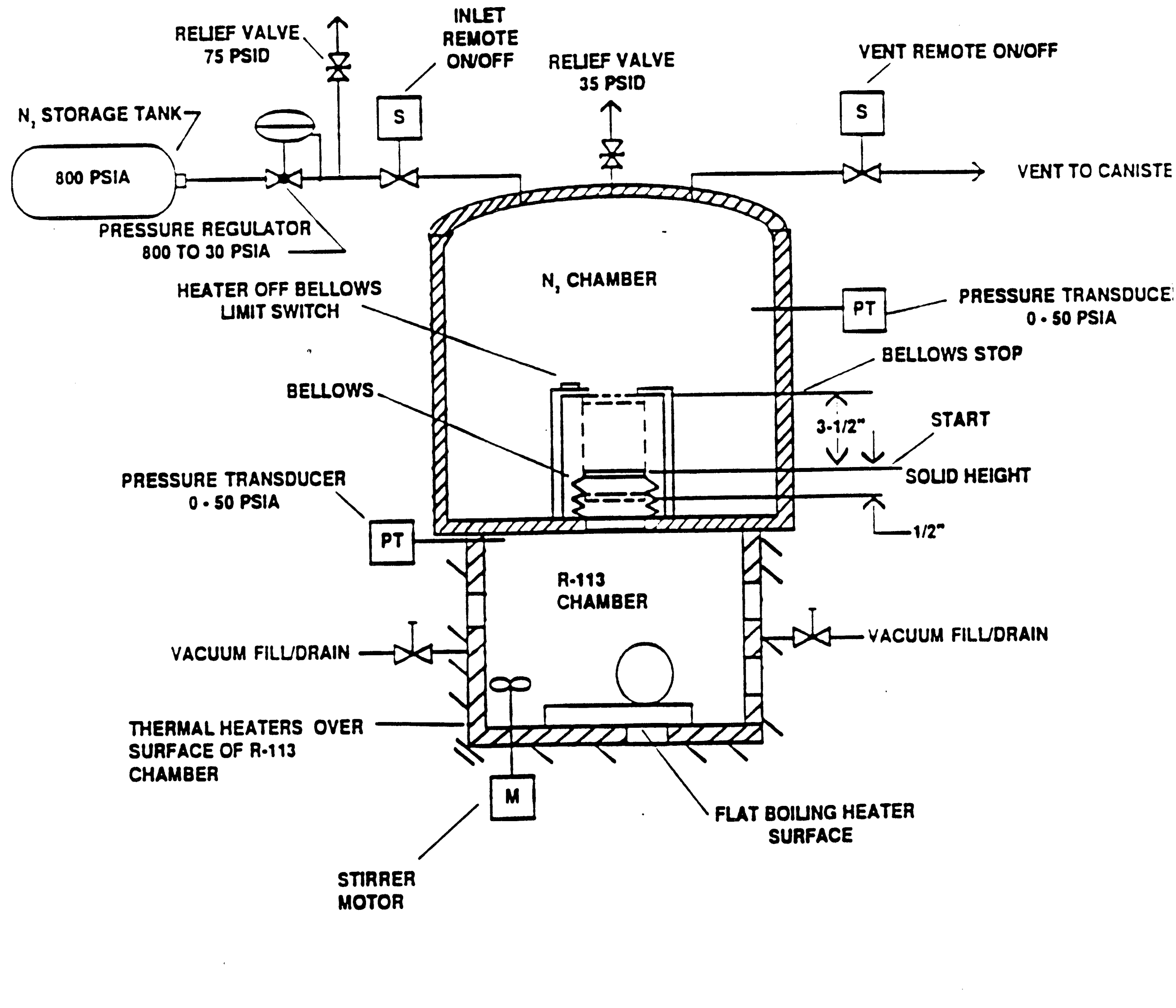

Figure 3.2. Schematic of Test Vessel with concepts to provide constant pressure and initially uniform fluid temperature.

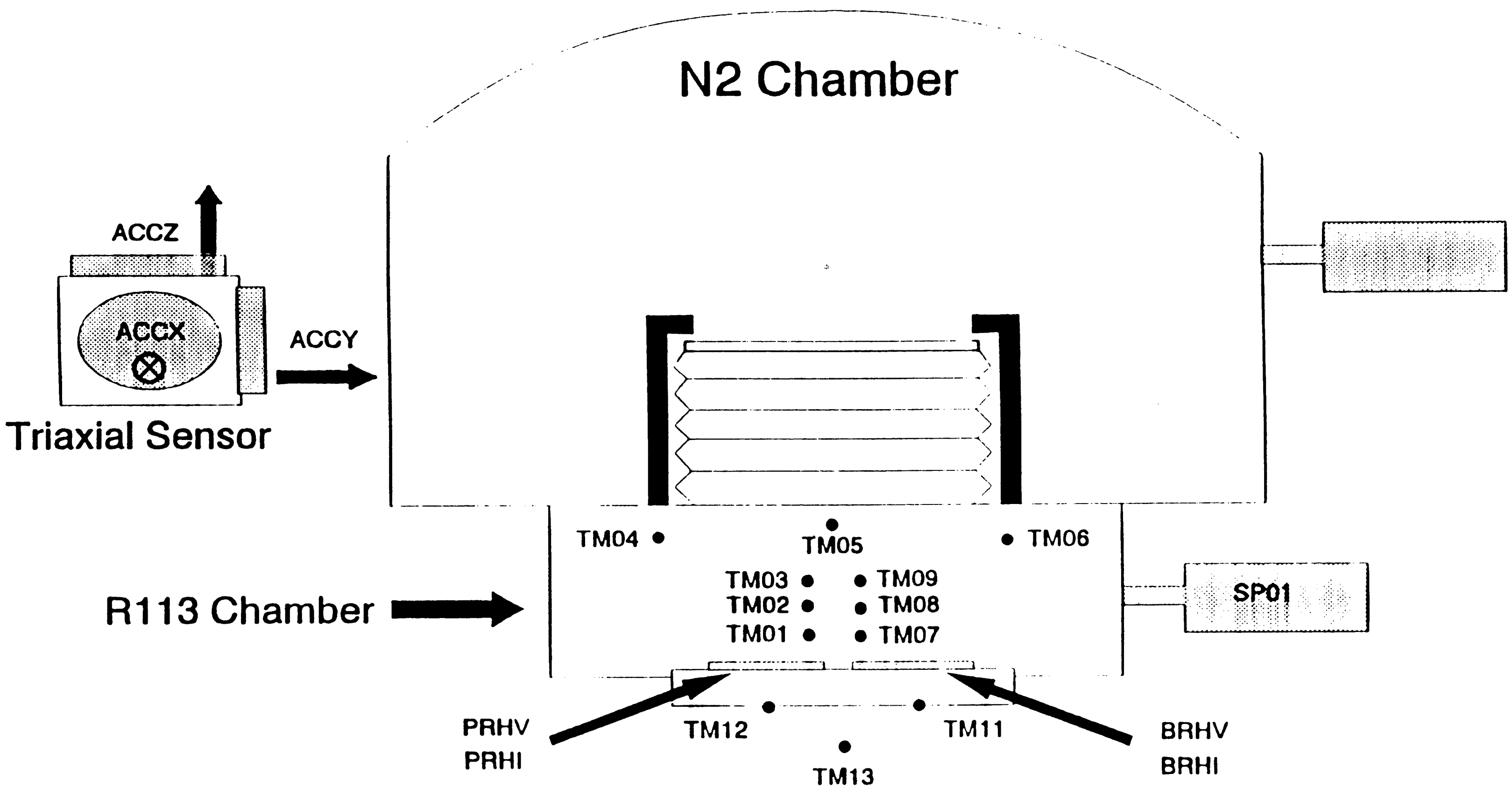

Figure 3.3. Location of Sensors for Scientific Analysis.

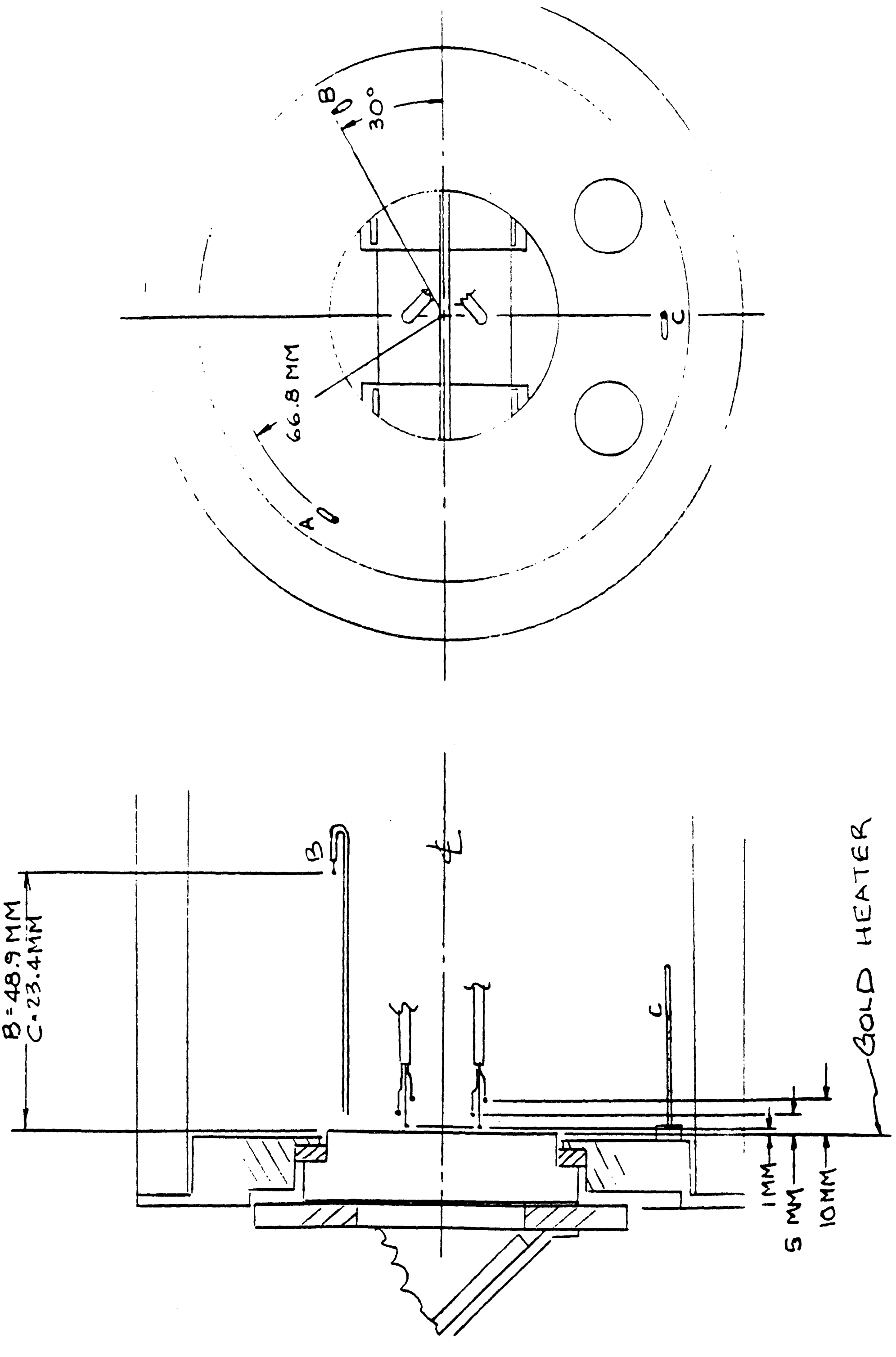

Figure 3.4. Locations of R-113 fluid thermistors in test vessel.

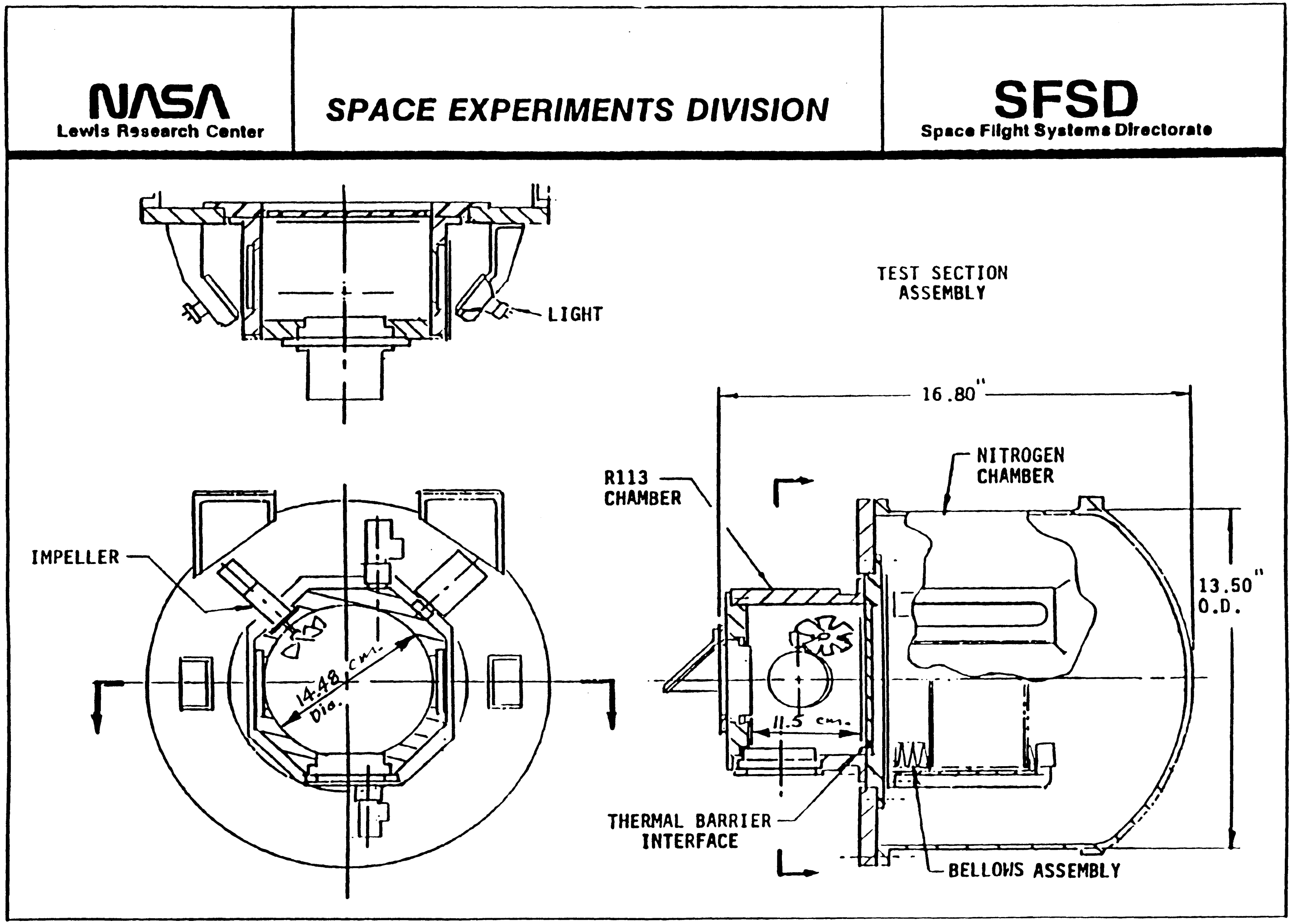

Figure 3.5. Test vessel. Relative locations of internal components, lights and viewing windows.

NASA
Lewis Research Center

SPACE EXPERIMENTS DIVISION

SFSD
Space Flight Systems Directorate

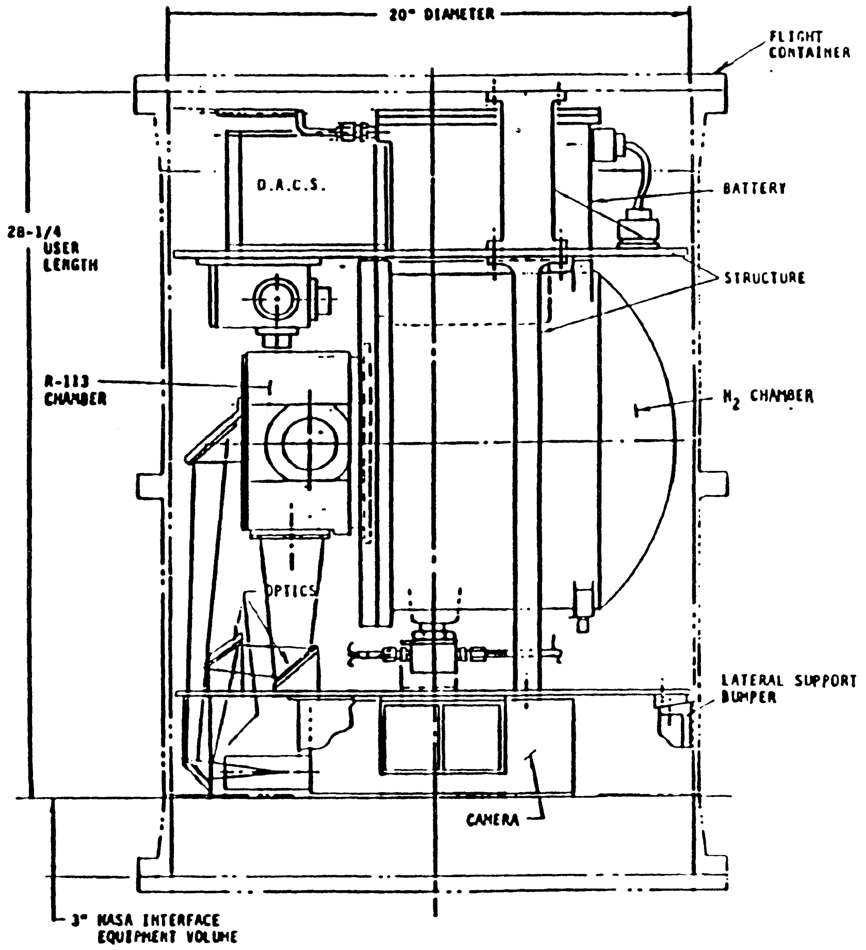

Figure 3.6. PBE components in GAS canister. Side view.

NASA
Lewis Research Center

SPACE EXPERIMENTS DIVISION

SFSD
Space Flight Systems Directorate

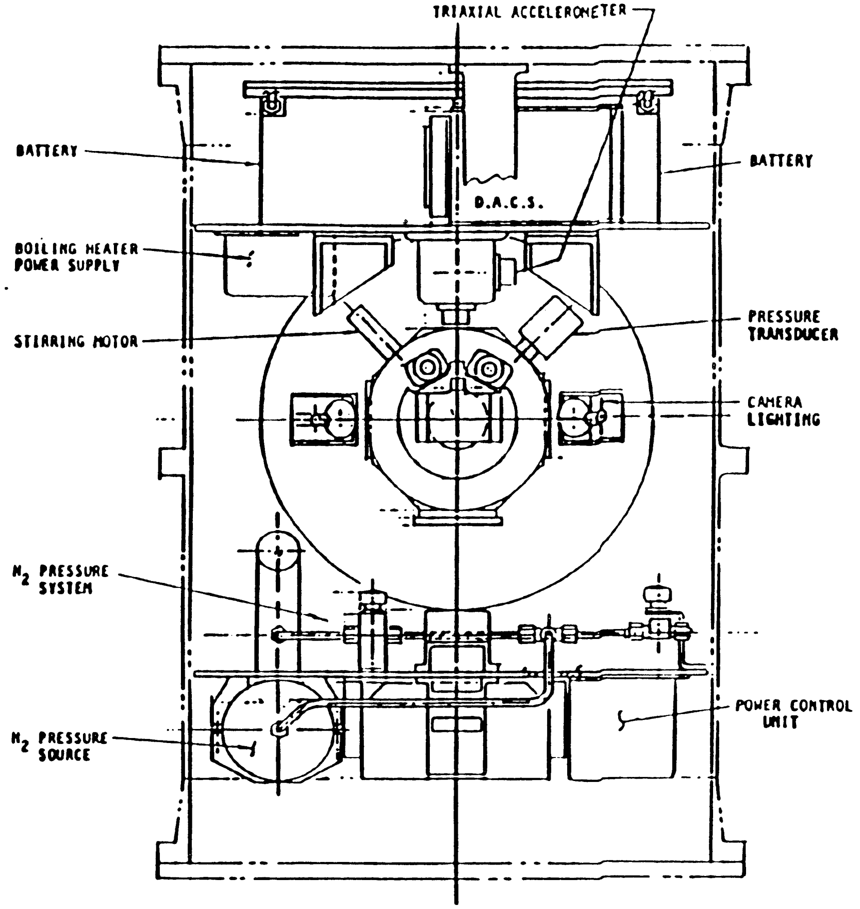

Figure 3.7. PBE components in GAS canister. Front view.

PBE/STS AXIS TRANSLATION

SED-PBE-DOC-028

PBE	STS	SAMS
+Y	+X	+Y
+Z	+Y	-X
+X	+Z	+Z

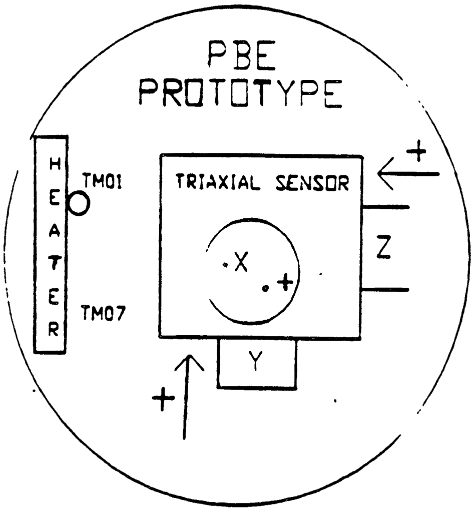

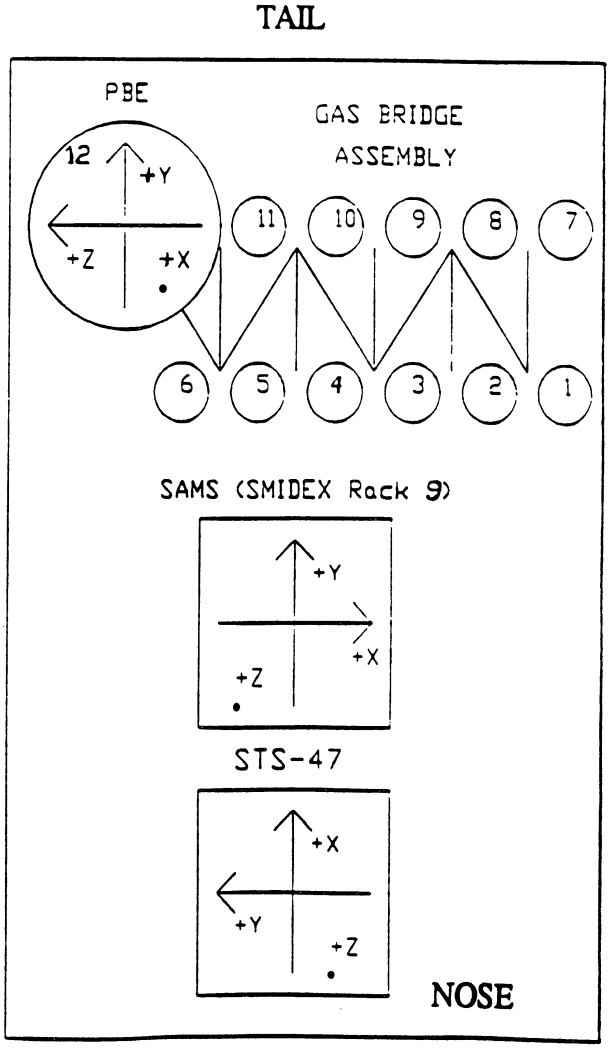

+Z signal indicates that acceleration
is in direction indicated above.
e.g., - this decreases buoyancy moving
vapor bubble <u>away</u> from heater,
or would move the vapor bubble
<u>toward</u> heater.

Figure 3.8. Correlation between PBE-1A accelerometer and SAMS and STS-47 units.

Acceleration coordinate for the space experiment

Example

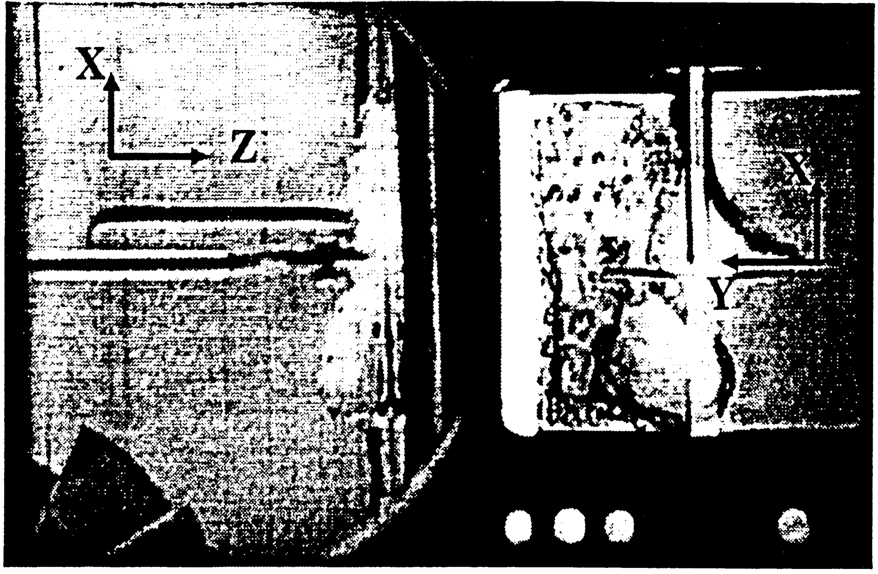

* The above figure shows both side view in left hand side and bottom view in right hand side.

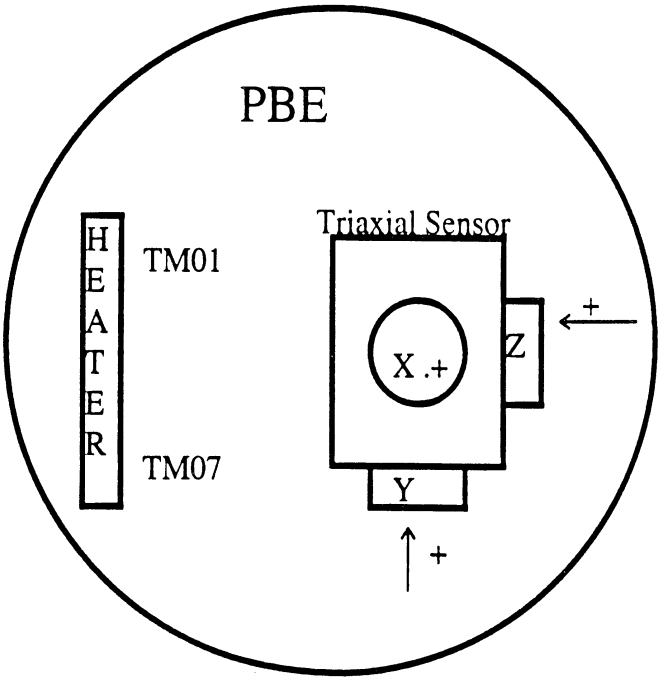

Figure 3.9. Correlation between PBE-1A accelerometer and photographic view on STS-47. Primary heater in use on left side.

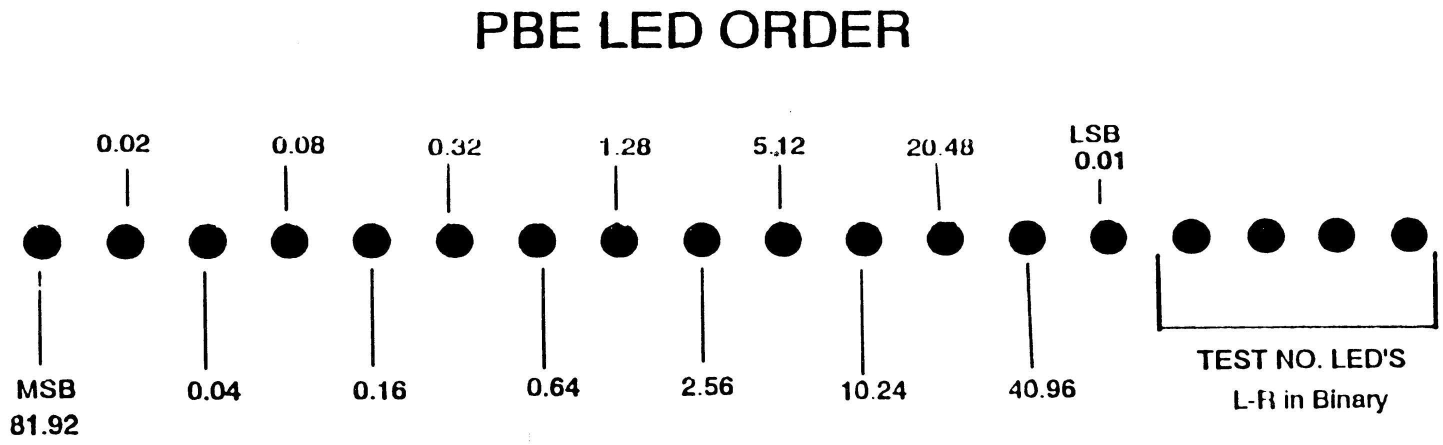

THE LED's COUNT IN BINARY FROM LEFT TO RIGHT, EXCEPT THAT THE LEAST AND MOST SIGNIFICANT BITS HAVE BEEN SWAPPED.

NUMBERS INDICATED WITH EACH LED ARE IN SECONDS. JUST ADD UP THE LIT LED'S TO GET THE TOTAL TIME.

Figure 3.10. Scheme for LED timing lights in camera field of view.

4. TEST MATRIX

The test matrix followed for the PBE-IA on the STS-47 is given as Table II below. The nominal levels of heat flux input (in w/cm^2) and the initial bulk liquid subcooling (in °F) are given for each Test Run, followed by the timing sequences used. The test is initiated with the heater power at 10 seconds. The camera is operated at the maximum speed of 100 pps in the time domain when nucleation is expected to occur in microgravity, based on the prior drop tower testing and extrapolations. Only for Run No. 5 was the nucleation process not captured with the camera speed of 100 pps. Nucleation occurred at 26.15 seconds, and the camera returned to 10 pps at 25 seconds.

Both pre flight and post flight ground tests were conducted conforming to the test matrix with the heater surface in the inverted position, at $a/g = -1$, in order to confirm that the system operated reproducibly following the space flight. A post flight ground test was also conducted at $a/g = +1$ in order to provide normal gravity boiling data, if possible, with which to compare the microgravity boiling behavior. Results of these tests at $a/g = -1$ and $a/g = +1$ are included in this report.

TEST POINT	HEAT FLUX	SUBCOOLING (°F)	HEATER POWER ON/OFF (SEC)	10 FPS ON/OFF (SEC)	100 FPS ON/OFF (SEC)	STIRRER START (SEC)	REPRESS. START (SEC)	TOTAL TEST TIME (SEC)
1	8	20 ± 2	10-70	15-80	10-15	65-	-	80
2	4	20 ± 2	10-100	10-15 25-130	15-25	-	-	130
3	2	20 ± 2	10-120	20-30 50-130	30-50	110-	-	130
4	8	5 ± 1	10-55	15-65	10-15	50-	-	65
5	4	5 ± 1	10-100	10-15 25-105	15-25	-	-	105
6	2	5 ± 1	10-105	20-30 50-115	30-50	-	-	115
7	8	0.5 ± 0.4	10-40	15-55	10-15	-	45-	55
8	4	0.5 ± 0.4	10-70	10-15 25-80	15-25	65-	-	80
9	2	0.5 ± 0.4	10-115	10-30 50-125	30-50	105-	-	125

Table II. Test matrix for PBE-1A on STS-47. (Prototype Hardware).

5. EXPERIMENTAL RESULTS

5.1 Measured Parameters

5.1.1 Internal to Test Vessel

Table III gives the parameters as measured for each of the Runs during the pre- and post- flight tests at $a/g = -1$ and $a/g = +1$, and during the STS-47 Space Flight. These are identified in each Run No. by the date conducted and the orientation. Following this are the nominal and actual levels of input heat flux, followed by the nominal and actual initial bulk liquid subcooling. The initial bulk liquid temperature is virtually constant, and the subcooling is changed by varying the system pressure, which changes the saturation temperature, as indicated in the succeeding columns of Table III. T_w^*, T_{sup}^* and t^* are the mean heater surface temperature, the mean heater surface superheat, and the time from the onset of heating that nucleation or the onset of boiling takes place, respectively.

a/g -1 experiment based on date 4/28/92
a/g 0 experiment based on date 9/11/92 STS-47
a/g -1 experiment based on date 12/22/92
a/g+1 experiment based on data 11/4/92

Run#	Date of Experiment	Flight system	Gravit a/g	Heat Flux, W/cm^ Nom.	Actual	Subcool,oF Nom.o	Actual o	Tbulk oC	Sys.Press psi	Tsat oC	T*wall oC	T*sup oC	t* time sec	100pps On-Off	Remark
1	4/28/92	Prototype	-1	8.00	6.70	20	21.00	49.44	22.26	61:11	93	31.89	1.20	0 -- 5	
	9/11/92	Prototype	0	8.00	7.00	20	18.50	49.44	21.61	59.72	95	35.28	1.58	0 -- 5	
	12/22/92	Prototype	-1	8.00	6.22	20	19.94	49.42	22.19	60.50	77	16.50	0.54	0 -- 5	
	11/4/92	Prototype	1	8.00	7.02	20	20.02	48.31	21.45	59.43	93	33.57	2.10	0 -- 5	
2	4/28/92	Prototype	-1	4.00	3.65	20	19.80	49.00	21.98	60.00	81	21.00	2.68	5 --15	
	9/11/92	Prototype	0	4.00	3.60	20	21.50	49.17	22.40	61.11	110	48.89	12.38	5 --15	
	12/22/92	Prototype	-1	4.00	3.37	20	19.92	49.28	22.09	60.35	100	39.65	8.50	5 --15	
	11/4/92	Prototype	1	4.00	3.56	20.00	20.00	48.14	21.33	59.25	101	41.75	51.20	5 --15	
3	4/28/92	Prototype	-1	2.00	1.78	20	21.00	49.44	22.40	61.11	89	27.89	23.40	20 -- 40	
	9/11/92	Prototype	0	2.00	1.80	20	19.70	49.06	21.93	60.00	95	35.00	31.39	20 -- 40	
	12/22/92	Prototype	-1	2.00	1.80	20	20.28	49.56	22.38	60.83	102	41.17	90.00	20 -- 40	
	11/4/92	Prototype	1	2.00	1.81	20	19.95	48.49	21.54	59.57				20 -- 40	No Nucleation
4	4/28/92	Prototype	-1	8.00	6.50	5	5.30	49.00	16.95	51.94	91	39.06	1.10	0 -- 5	
	9/11/92	Prototype	0	8.00	7.00	5	4.80	49.00	16.80	51.67	91	39.33	1.34	0 -- 5	
	12/22/92	Prototype	-1	8.00	6.30	5	4.22	49.08	16.71	51.43	75	23.57	0.50	0 -- 5	
	11/4/92	Prototype	1	8.00	7.05	5	5.05	47.81	16.25	50.62	94	43.38	1.90	0 -- 5	
5	4/28/92	Prototype	-1	4.00	3.40	5	5.40	49.22	17.00	52.22	102	49.78	8.70	5 --15	
	9/11/92	Prototype	0	4.00	3.60	5	5.00	48.89	16.80	51.67	120	68.33	16.15	5 --15	
	12/22/92	Prototype	-1	4.00	3.38	5	4.93	49.04	16.90	51.78	109	57.22	12.70	5 --15	
	11/4/92	Prototype	1	4.00	3.54	5	4.98	47.92	16.29	50.69				5 --15	No Nucleation

Table III. PBE-IA. Parameters measured at a/g = -1 and a/g = +1 in Pre flight and Post flight tests, and during STS-47 Space Flight.

Page 2 of 2

Run#	Date of Experiment	Flight system	Gravit a/g	Heat Flux, W/cm^		Subcool,oF		Tbulk oC	Sys.Press psi	Tsat oC	T*wall oC	T*sup oC	t* time sec	100pps On-Off	
				Nom.	Actual	Nom.o	Actual o								
6	4/28/92	Prototype	-1	2.00	1.76	5	4.70	49.06	16.80	51.67	87	35.33	34.30	20 -- 40	
	9/11/92	Prototype	0	2.00	1.82	5	5.00	49.17	16.90	51.94	98	46.06	37.47	20 -- 40	
	12/22/92	Prototype	-1	2.00	1.77	5	4.95	49.25	17.02	52.00				20 -- 40	No Nucleation
	11/4/92	Prototype	1	2.00	1.81	5	5.01	48.04	16.37	50.82				20 -- 40	No Nucleation
7	4/28/92	Prototype	-1	8.00	6.70	0.50	1.20	48.78	15.50	49.44	93	43.56	1.18	0 -- 5	
	9/11/92	Prototype	0	8.00	7.00	0.50	1.00	48.89	15.50	49.44	94	44.56	1.36	0 -- 5	
	12/22/92	Prototype	-1	8.00	6.42	0.50	4.92	48.79	16.76	51.52	86	34.48	1.00	0 -- 5	
	11/4/92	Prototype	1	8.00	7.06	0.50	4.74	47.51	16.00	50.14	91	40.86	1.90	0 -- 5	
8	4/28/92	Prototype	-1	4.00	3.50	0.50	1.40	48.67	15.50	49.44	101	51.56	9.30	5 --15	
	9/11/92	Prototype	0	4.00	3.50	0.50	0.70	49.06	15.50	49.44	106	56.56	10.63	5 --15	
	12/22/92	Prototype	-1	4.00	3.42	0.50	0.45	49.09	15.61	49.34	111	61.66	14.50	5 --15	
	11/4/92	Prototype	1	4.00	3.55	0.50	0.56	47.42	14.78	47.73				5 --15	No Nucleation
9	4/28/92	Prototype	-1	2.00	1.80	0.50	1.00	48.72	15.40	49.28	99	49.72	65.90	20 -- 40	
	9/11/92	Prototype	0	2.00	1.80	0.50	0.40	49.22	15.50	49.44	100	50.56	41.48	20 -- 40	
	12/22/92	Prototype	-1	2.00	1.76	0.50	0.41	49.05	15.58	49.28	89	39.72	27.00	20 -- 40	
	11/4/92	Prototype	1	2.00	1.81	0.50	1.23	47.49	15.00	48.17				20 -- 40	No Nucleation

Table III. Continued.

5.1.2 Accelerometer

Table IV lists a summary of the relatively larger acceleration excursions measured during each of the Runs in the PBE-IA of the STS-47 Flight. The accelerometer units here are given as micro-g's, and the heating for each Run begins at 10 seconds. The larger excursions are indicated in bold type in Table IV, and no consistent observable effects were noted at these times either in the vapor bubble boiling behavior from the motion picture films, or in the heat transfer behavior as might be reflected in the heater surface temperature measurements. The interface motions during boiling are reasonable intense, and the relatively large surface tensions are believed to mask influences of these residual acceleration levels.

The accelerometer measurements from which the data in Table IV were extracted are plotted as functions of time for each Run, and are given in Appendix C. The units are given here as milli-g's, and each major ordinate division corresponds to 50 micro-g's.

RUN #	Time, sec	Plots	Max Value			Uncertainty (Noise)	Comments
			x	y	z	2.40E+01	
1		no	50	52	50	2.40E+01	
2		no	76	77	50	2.40E+01	
3		no	51	77	50	2.40E+01	
4		no	101	77	75	2.40E+01	
5	98.3	yes	**179**	52	**348**	2.40E+01	
5	98.9	yes	51	**103**	50	2.40E+01	
6	89.9	yes	51	52	**273**	2.40E+01	
6	90.3	yes	51	**258**	50	2.40E+01	
6	90.2	yes	**254**	52	50	2.40E+01	
7		no	76	77	75	2.40E+01	
8	4.9	yes	**306**	52	75	2.40E+01	
8	5.2	yes	51	**103**	75	2.40E+01	
9	48.2	yes	51	**103**	50	2.40E+01	
9	60.4	yes	**281**	52	75	2.40E+01	

Notes: (1) Accelerometer units are given as micro-g's.
(2) Heating in each run begins at t = 10 sec.

Table IV. Summary of relatively larger acceleration excursions during PBE-IA in STS-47 Flight.

5.2 Thermal Results

5.2.1 Canister Ambient

Fig. 5.1 presents the output of a thermistor mounted on one of the structural members of the PBE-IA, following liftoff of the STS-47. The disturbances initiated by the onset of each of the nine (9) Runs in the test matrix is clearly discernible. The general increase in temperature during and following the tests is a consequence of heating the R-113 to its nominal 120°F (48.9°C) operating temperature level.

5.2.2 Test Matrix Runs

The experimental thermal data for each of the nine (9) Runs of PBE-IA conducted in the microgravity of space on the STS-47 are plotted in Figs. 5.2 - 5.10. Each Run includes five (5) Figures subdivided as a-e, to be described below, with the same format followed for each Run. Figures 5.2 (a-e) are for Run No. 1, and follow the sequences given in Table II with the experimental parameters listed in Table III.

Figure 5.2a includes the measured mean heater surface temperature and the heat transfer coefficient computed from a one-dimensional finite difference procedure in the quartz substrate, using the measured surface temperature as a boundary condition. Cubic splines are fitted through successive data points to provide interpolation between the measured points. The procedure is described by Merte (1992). During the conduction phase of heating the heat transfer coefficient is defined in terms of the difference between the heater surface temperature and the initial temperature. This permits a comparison with the well-known analytical solution of conduction in two semi-infinite solids with a step input in heat flux at the plane between the two solids. This is shown by the labeled dotted curves in Fig. 5.2a. Once motion takes place in the fluid, comparison with the analytic conduction solution is no longer appropriate. However, it is included in all such plots in order to provide a reference. It becomes obvious that deviations from the one-dimensional behavior takes place because of the finite lateral heater dimensions. This issue will be addressed below. Once nucleation takes place the heat transfer coefficient is appropriately defined in terms of the difference between the measured heater surface temperature and the liquid saturation temperature.

Figure 5.2b shows the temporal variation of the input heat flux to the thin gold film. The change noted is a consequence of the increase in resistance of the gold film as it is heated, with the imposed voltage being controlled to remain essentially constant. This variation is relatively small, and it was not deemed worthwhile to control the power input to remain constant.

The measured system pressure is plotted in Fig. 5.2c, along with the heat flux to the fluid as computed from the measured power input and the heat flux to the substrate, computed in turn from the measured heater surface temperature. This parameter makes it possible to determine when steady-state conditions are reached, since the heat flux to the fluid becomes equal to the heat flux input to the film heater. This condition is almost attained in Run Nos. 2, 3, 6 and 9.

The measured mean heater surface temperature is included in both Figs. 5.2d and 5.2e in order to provide temporal reference marks for the various temperatures measured. The center plot in Fig. 5.2d gives the fluid temperatures above the active primary heater at distances of 1 mm, 5 mm and 10 mm above the heater surface. The lower plot in Fig. 5.2d gives the bulk liquid temperatures at the various distances indicated above the heater surfaces, around the perimeter as given in Fig. 3.4. The center plot in Fig. 5.2e shows the changes in liquid temperature at 1 mm, 5 mm, and 10 mm above the center of the backup heater, and thus gives an indication of the effects of lateral motions of the vapor bubble. In the lower part of Fig. 5.2e, TM11 measures the quartz surface temperature centered under the backup heater, while TM12 measures the quartz surface temperature under the center of the primary heater. TM13 measures the air space temperature slightly removed from the center of the underside of the quartz substrate. If necessary, it permits estimating the heat loss from the back side of the quartz substrate.

The figures corresponding to Run Nos. 2 - 9 follow the same pattern described above.

5.3 Test Matrix Representative Photographic Views

Twelve (12) selected representative frames from the 400 ft. 16 mm motion film are presented for each Run in Figs. 5.11 - 5.19, along with the frame number, counted from frame 100 at the onset of heating, and with the time from the onset of heating, at 10 seconds. Filming took place at either 10 or 100 pps, as indicated in the matrix given in Table II. The images were obtained by projecting the film on a large screen, picking it up with a video camera, and using a frame grabber and digitizer for storage on laser discs. The times shown may differ slightly from the frame number because the camera speed may vary, as when changing framing speed. The LED's seen in the bottom of each image provide synchronization with the thermal data, following the time format given in Fig. 3.10.

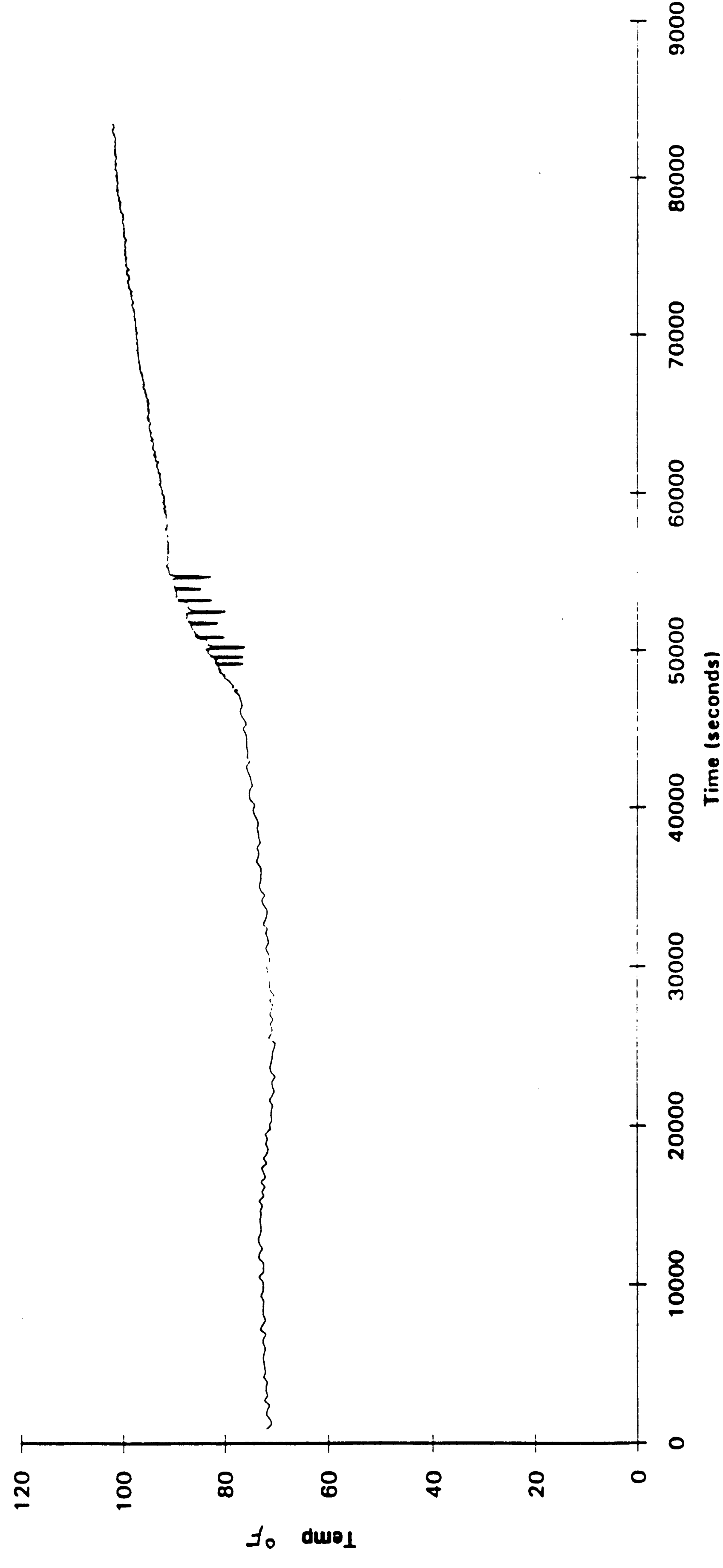

Figure 5.1. PBE-IA structure temperature in GAS canister.

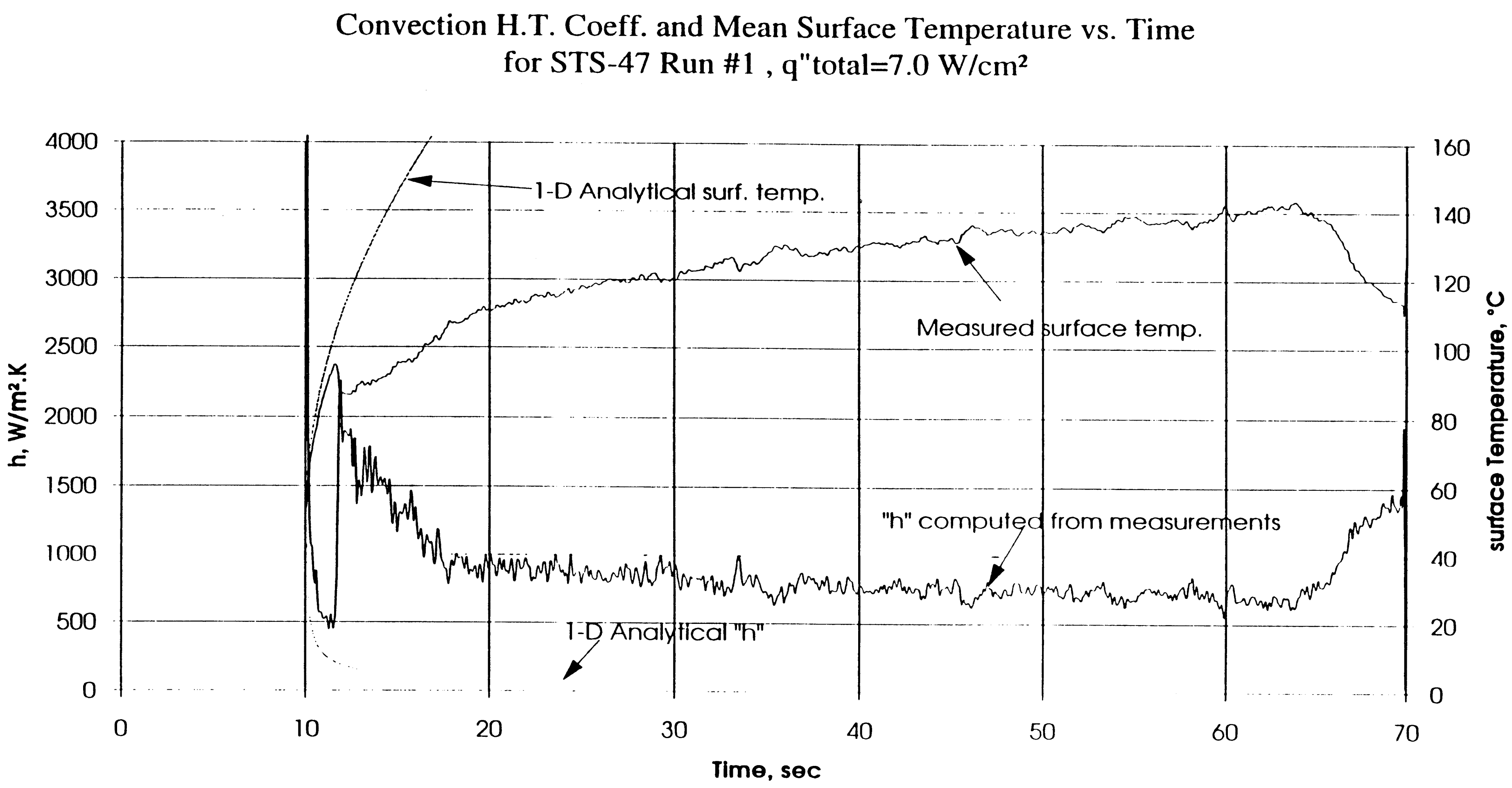

Figure 5.2a. Run No. 1 PBE-IA. STS-47. Mean heater surface temperature and derived heat transfer coefficient.

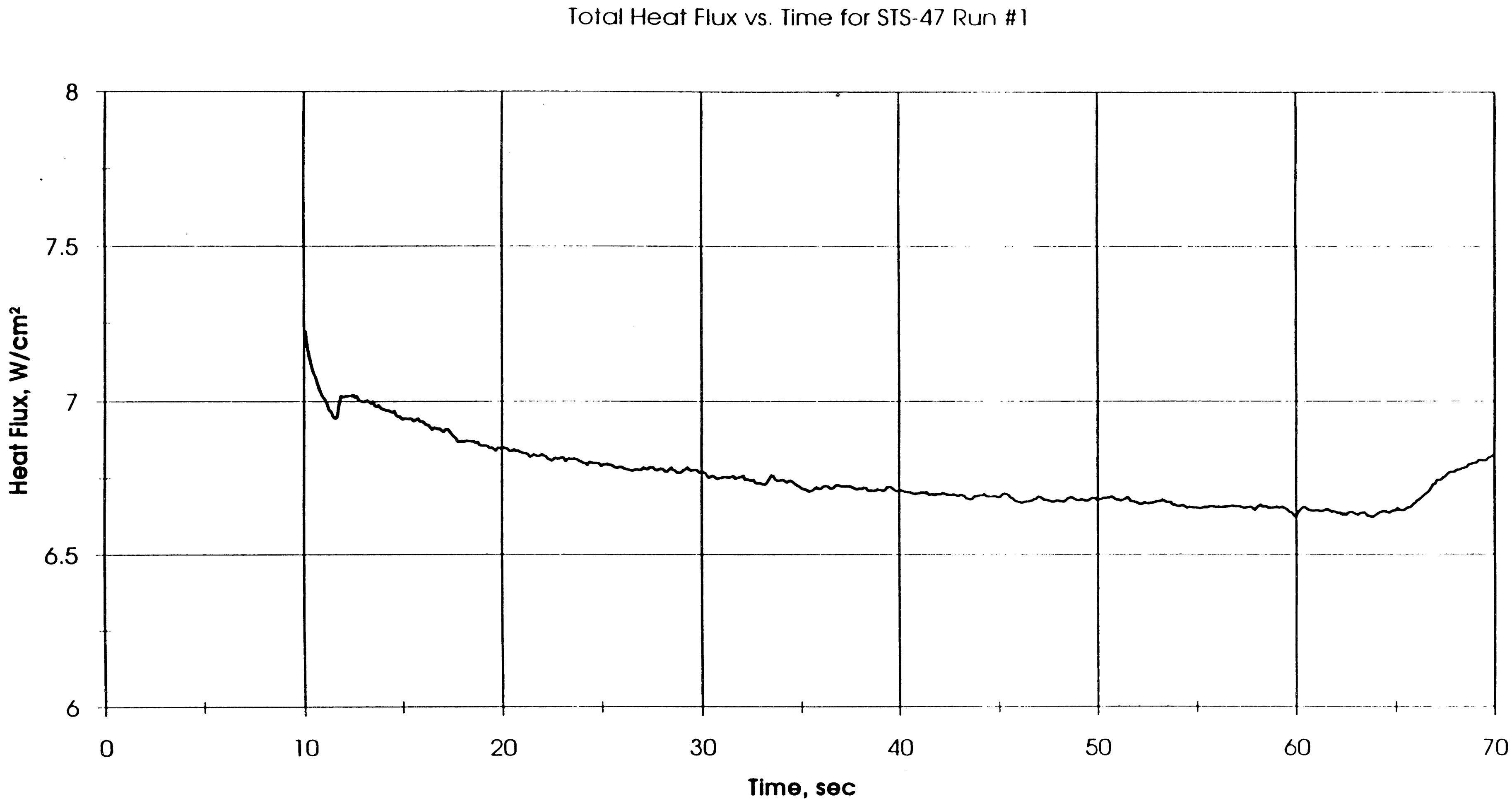

Figure 5.2b. Run No. 1. PBE-IA. STS-47. Heat flux input.

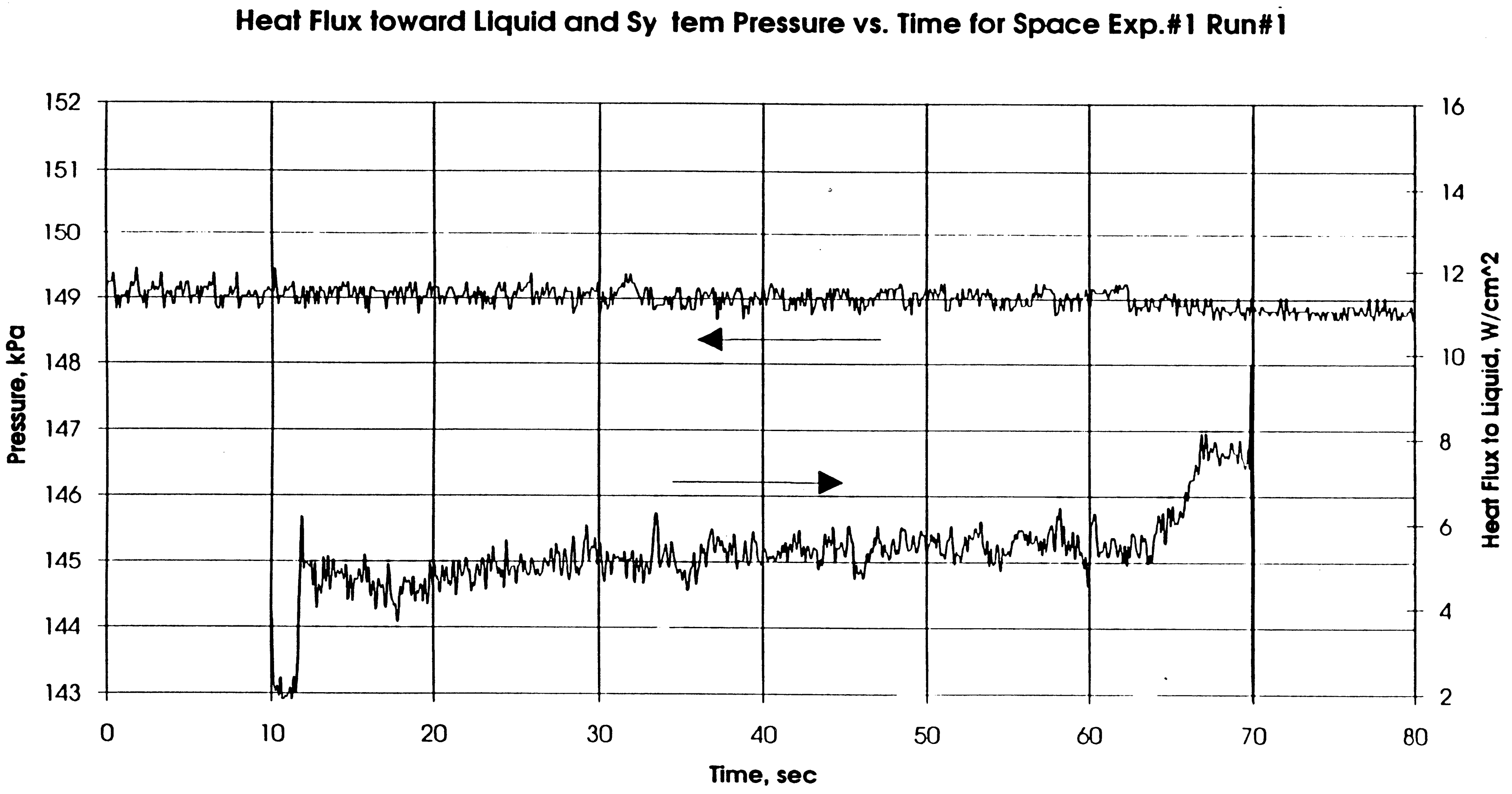

Figure 5.2c. Run No. 1. PBE-IA. STS-47. System pressure and fluid side heat flux.

A. Mean Heater Surface Temperature

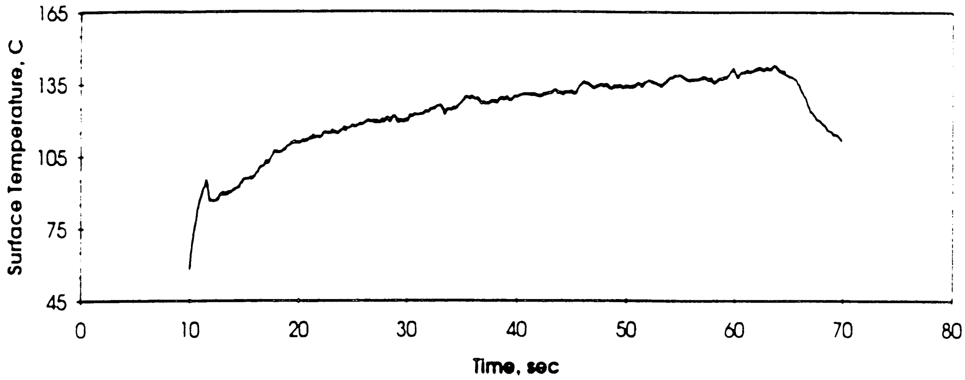

B. Local Fluid Temperatures

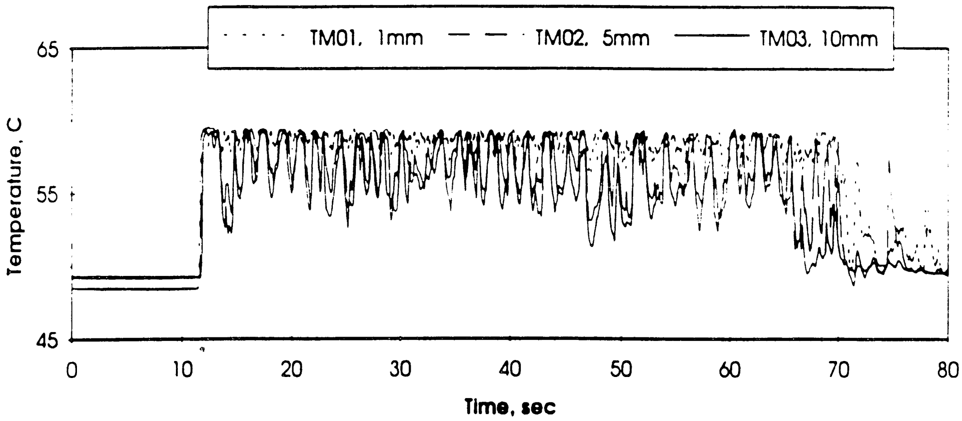

C. Far Field Bulk Temperatures

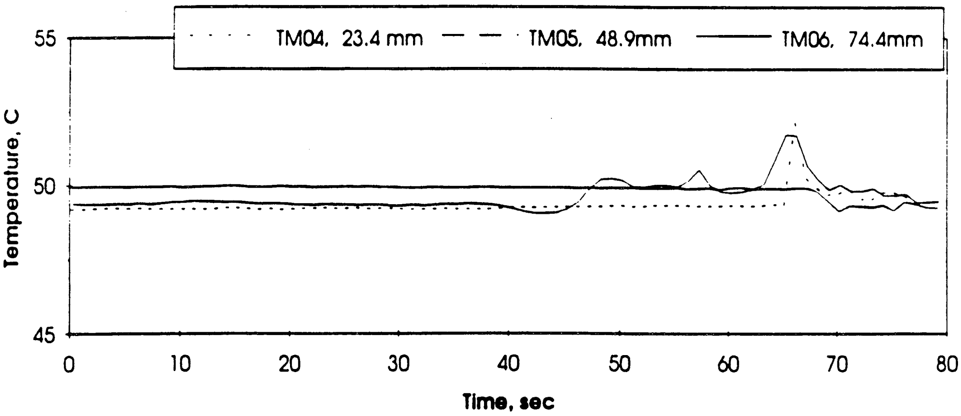

STS 47 - RUN#1

HEAT FLUX	SUBCOOLING (F)	HEATER POWER ON/OFF	100 FPS ON/OFF	STIRRER START	REPRESS START	TOTAL TEST TIME
8	20 ± 2	10-70 sec.	10-15 sec.	65 sec.	----------	80 sec.

Figure 5.2d. Run No. 1. PBE-IA. STS-47. Fluid temperatures near primary heater and far field bulk.

A. Mean Heater Surface Temperature

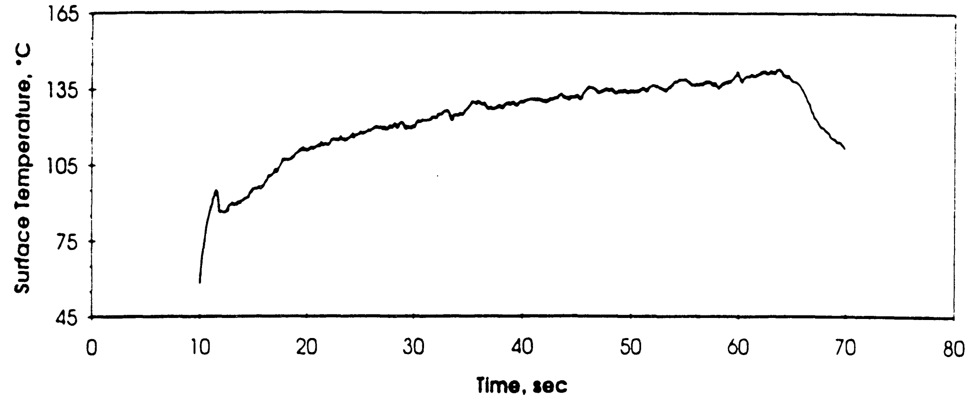

D.

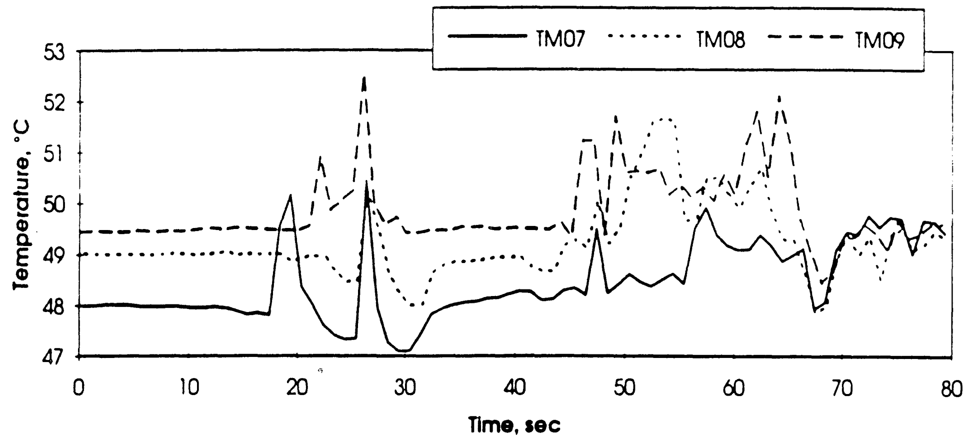

E.

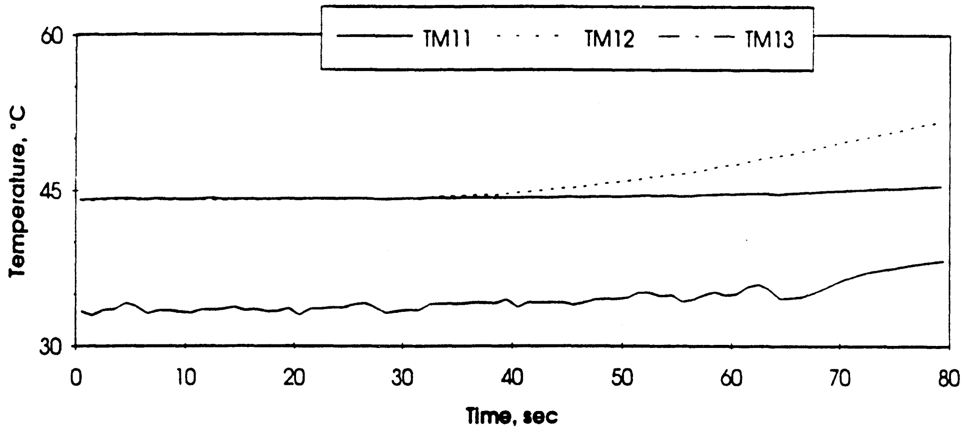

STS 47 - RUN #1

HEAT FLUX	SUBCOOLING (F)	HEATER POWER ON/OFF	100 FPS ON/OFF	STIRRER START	REPRESS START	TOTAL TEST TIME
8	20 ± 2	10-70 sec.	10-15 sec.	65 sec.	----------	80 sec.

Figure 5.2e. Run No. 1. PBE-IA. STS-47. Fluid temperatures near back up heater. Quartz substrate underside and ambient vicinity temperatures.

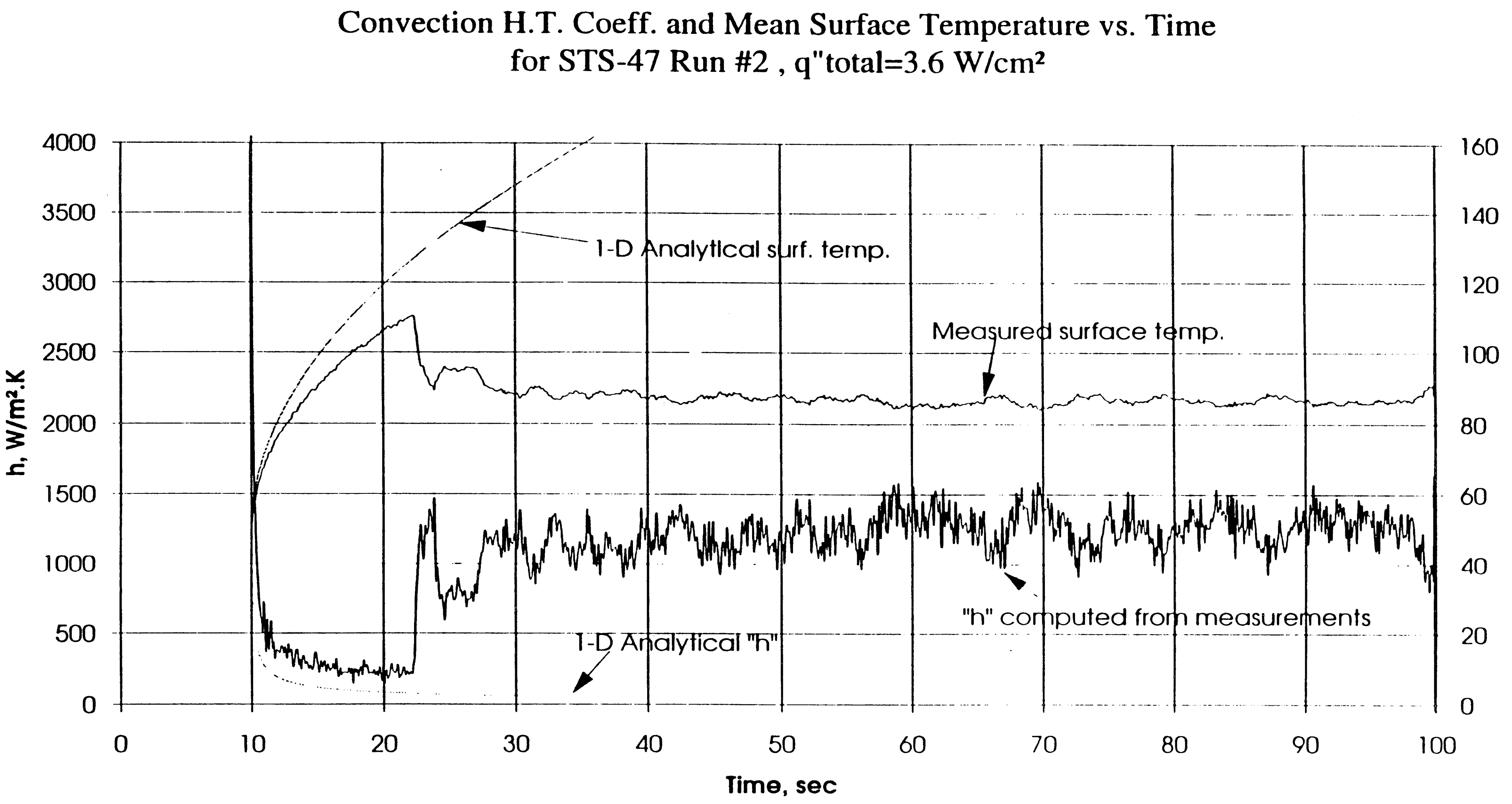
Convection H.T. Coeff. and Mean Surface Temperature vs. Time
for STS-47 Run #2 , q"total=3.6 W/cm²

Figure 5.3a. Run No. 2. PBE-IA. STS-47. Mean heater surface temperature and derived heat transfer coefficient.

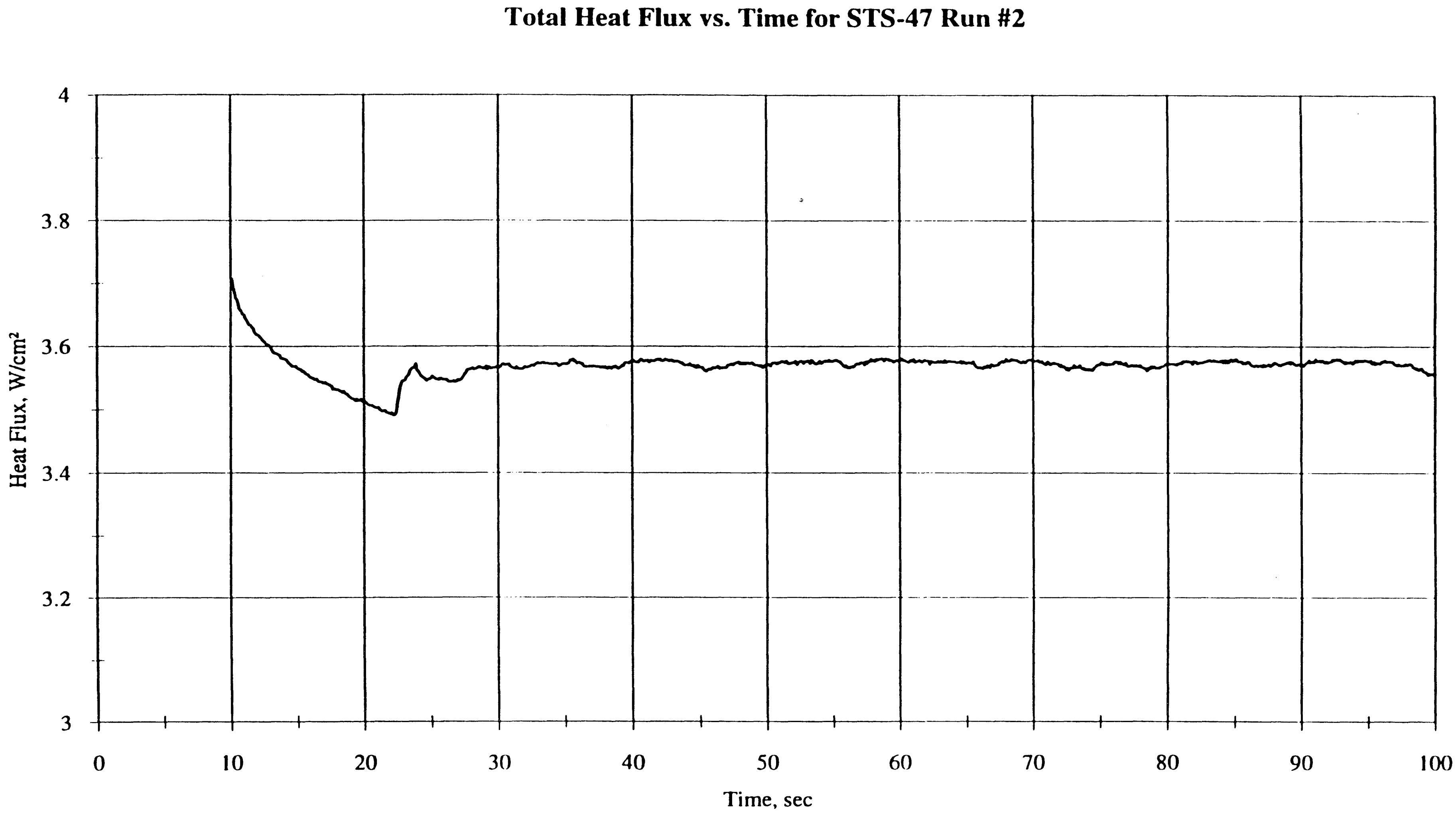

Figure 5.3b. Run No. 2. PBE-IA. STS-47. Heat flux input.

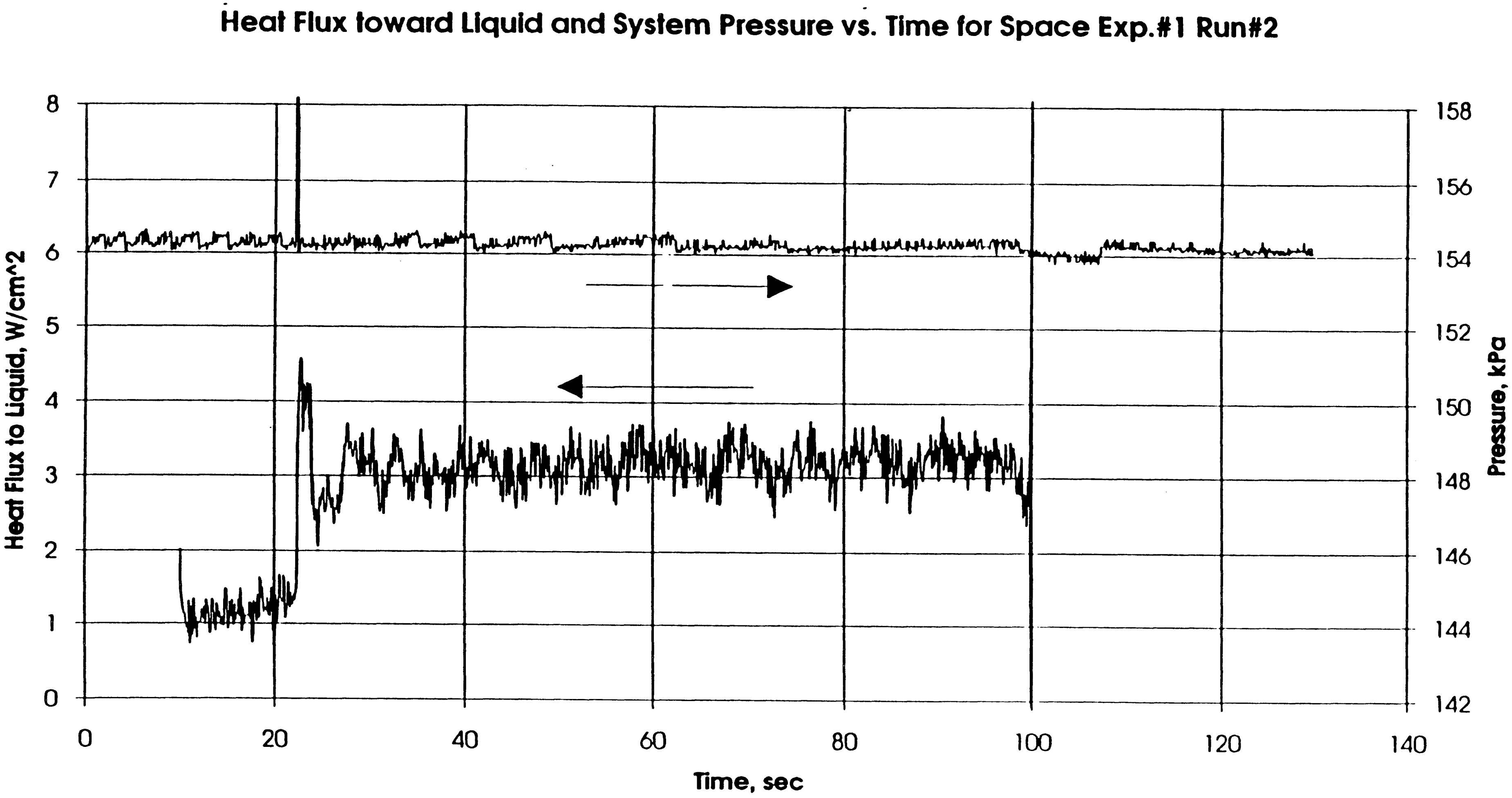

Figure 5.3c. Run No. 2. PBE-IA. STS-47. System pressure and fluid side heat flux.

A. Mean Heater Surface Temperature

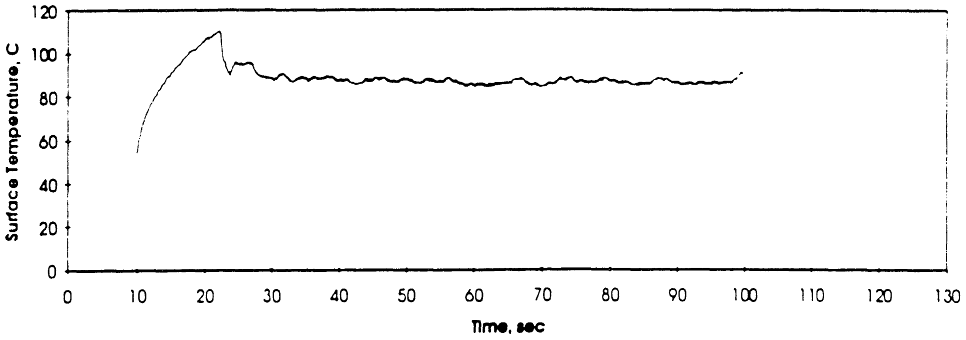

B. Local Fluid Temperatures

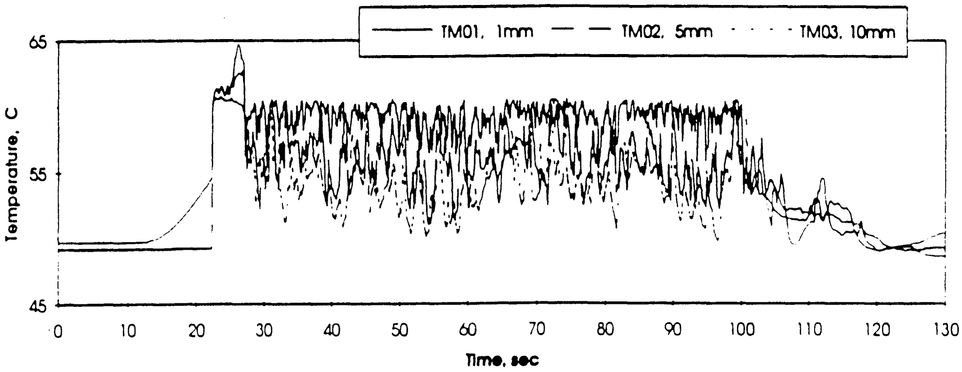

C. Far Field Bulk Temperatures

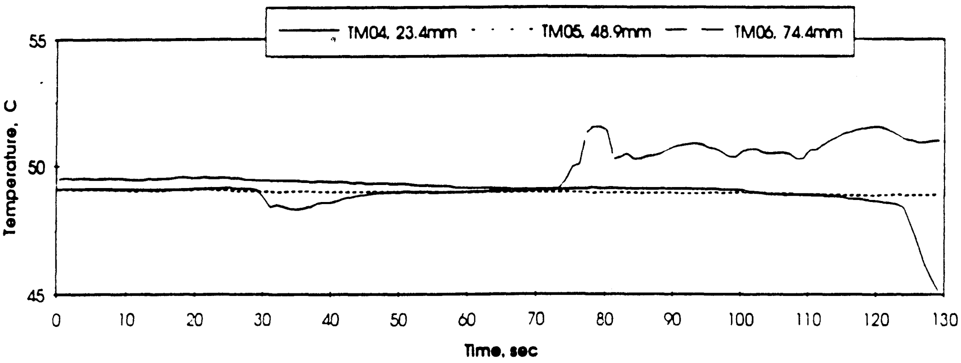

STS 47 - RUN#2

HEAT FLUX	SUBCOOLING (F)	HEATER POWER ON/OFF	100 FPS ON/OFF	STIRRER START	REPRESS START	TOTAL TEST TIME
4	20 ± 2	10-100 sec.	15-25 sec.	-----	----------	130 sec.

Figure 5.3d. Run No. 2. PBE-IA. STS-47. Fluid temperatures near primary heater and far field bulk.

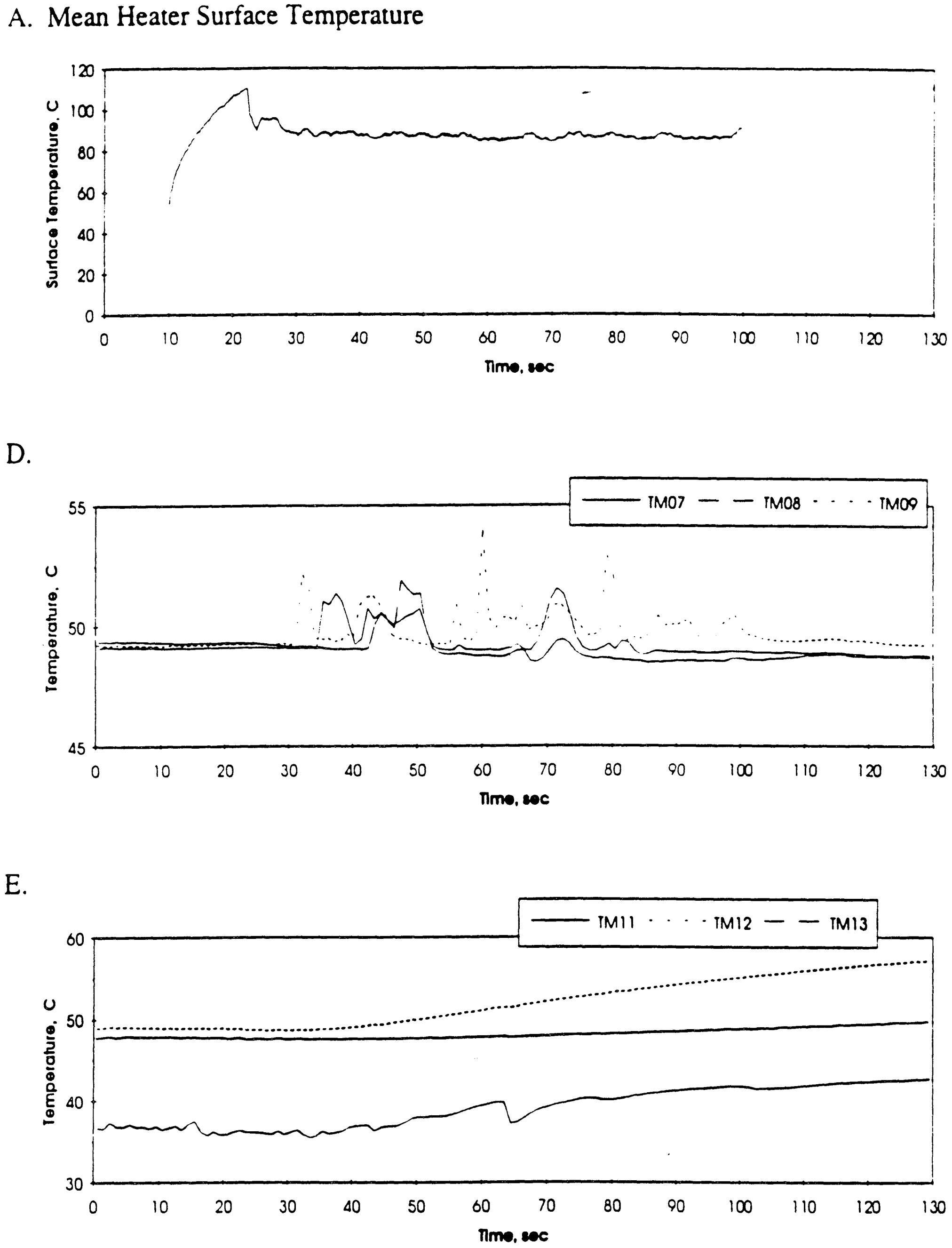

STS 47 - RUN #2

HEAT FLUX	**SUBCOOLING (F)**	**HEATER POWER ON/OFF**	**100 FPS ON/OFF**	**STIRRER START**	**REPRESS START**	**TOTAL TEST TIME**
4	20 ± 2	10-100 sec.	15-25 sec.	-------	----------	130 sec.

Figure 5.3e. Run No. 2. PBE-IA. STS-47. Fluid temperatures near back up heater. Quartz substrate underside and ambient vicinity temperatures.

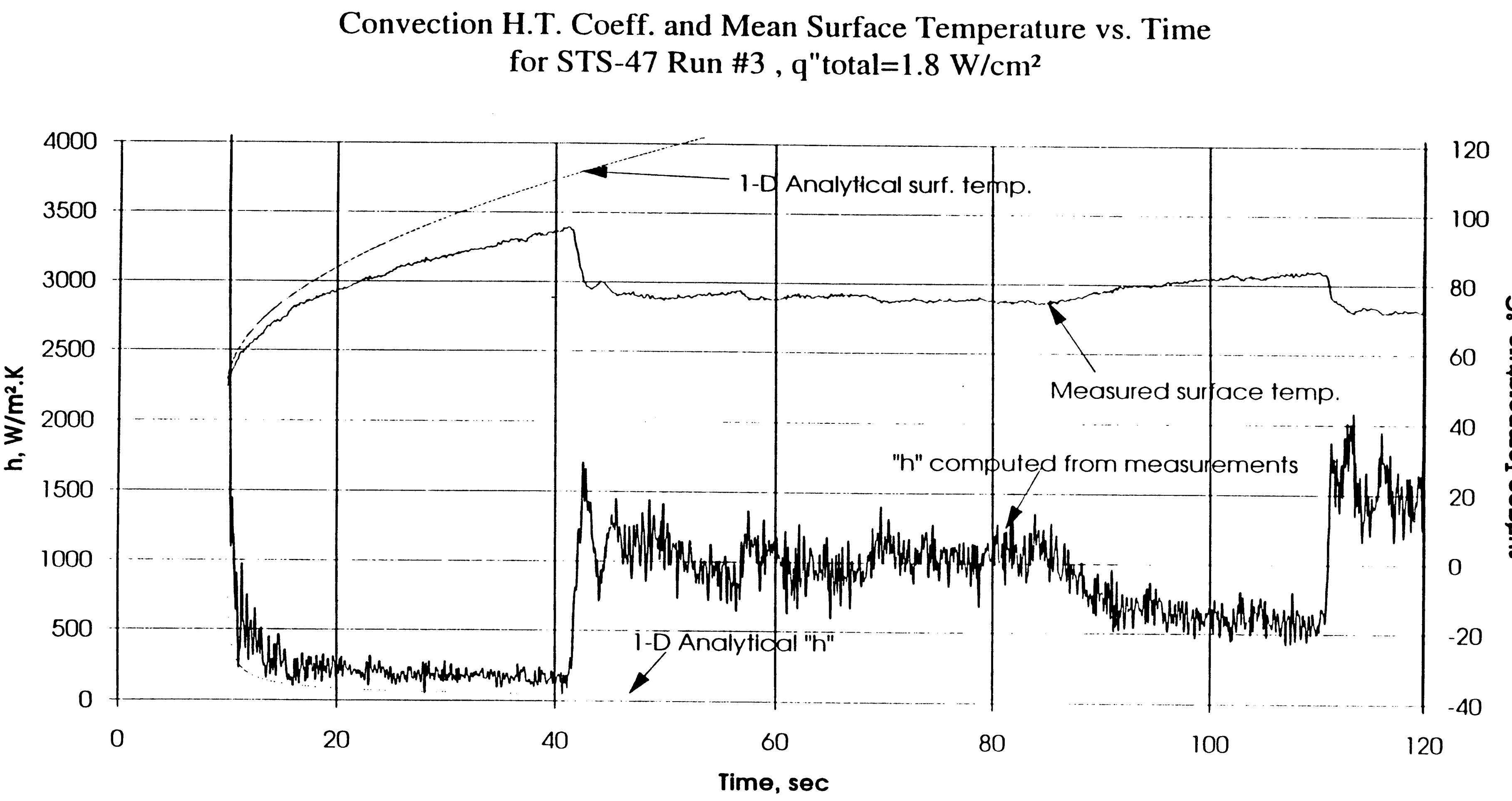

Convection H.T. Coeff. and Mean Surface Temperature vs. Time
for STS-47 Run #3 , q"total=1.8 W/cm²

Figure 5.4a. Run No. 3. PBE-IA. STS-47. Mean heater surface temperature and derived heat transfer coefficient.

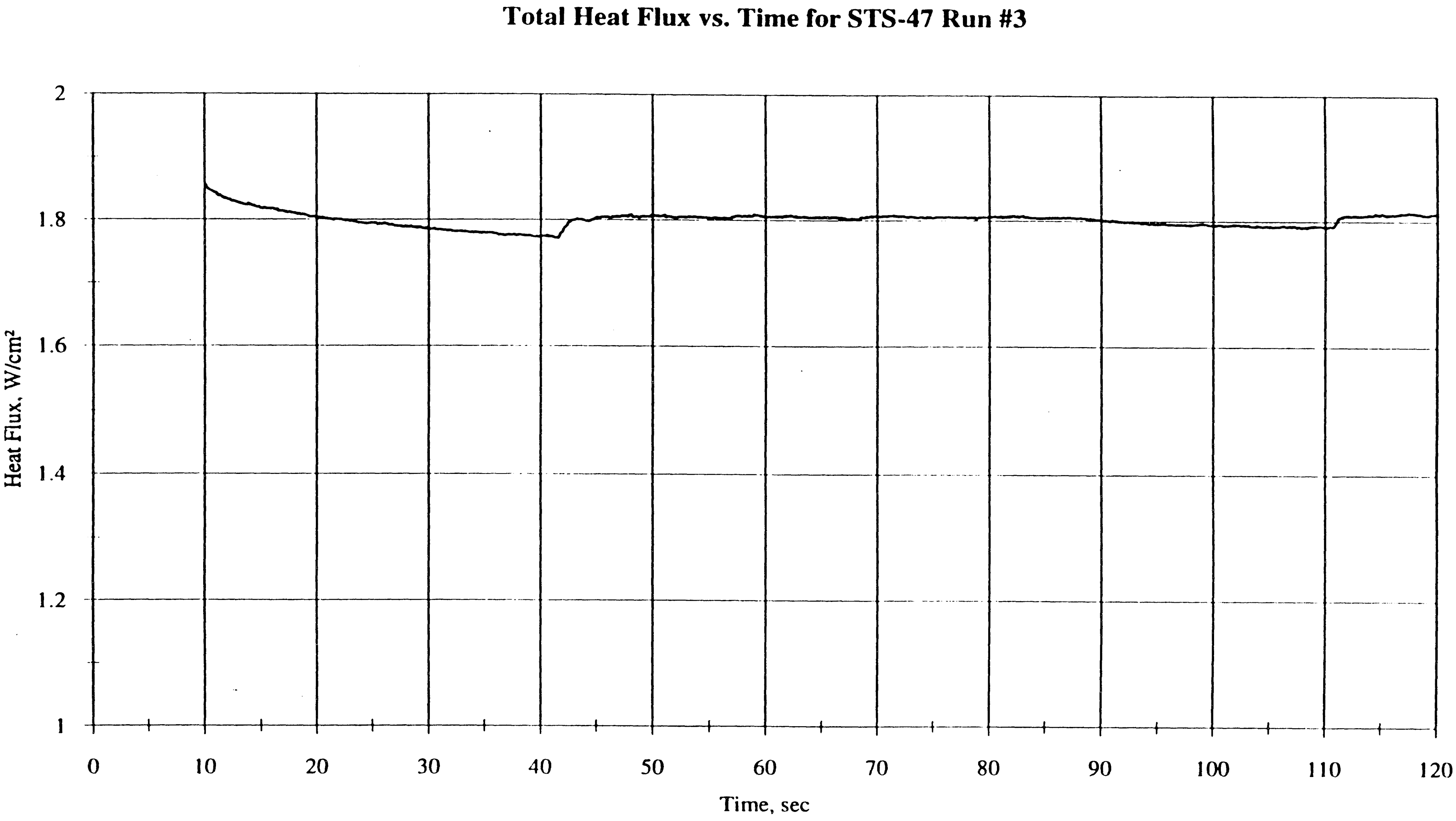

Figure 5.4b. Run No. 3. PBE-IA. STS-47. Heat flux input.

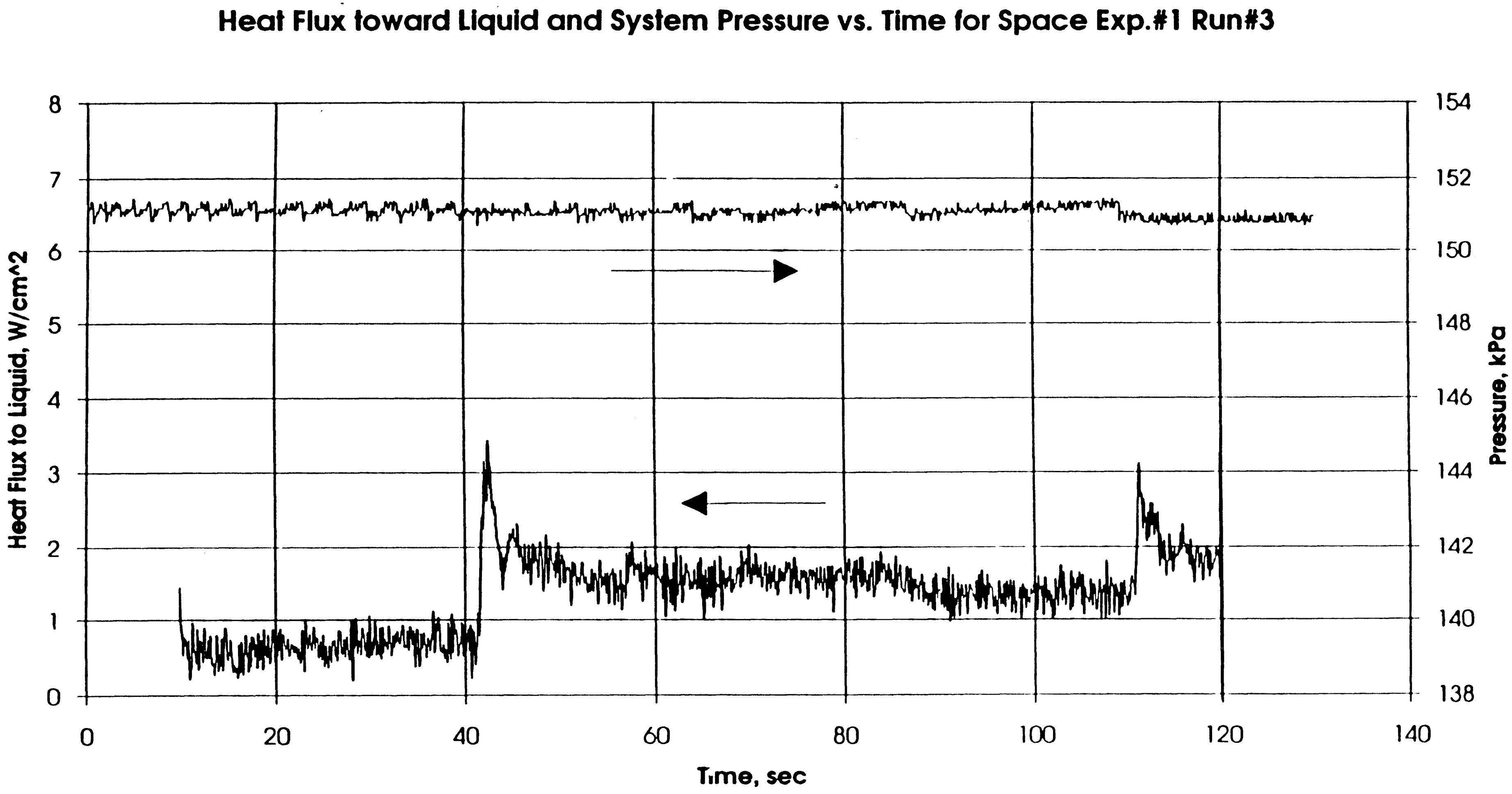

Heat Flux toward Liquid and System Pressure vs. Time for Space Exp.#1 Run#3

Figure 5.4c. Run No. 3. PBE-IA. STS-47. System pressure and fluid side heat flux.

A. Mean Heater Surface Temperature

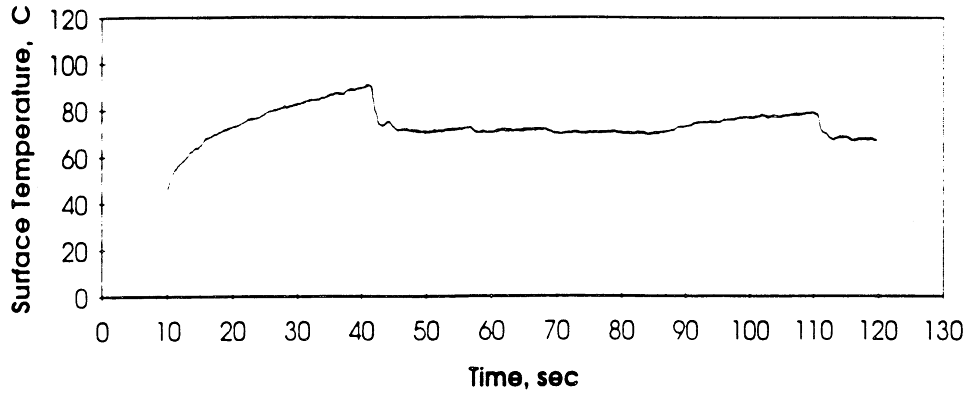

B. Local Fluid Temperatures

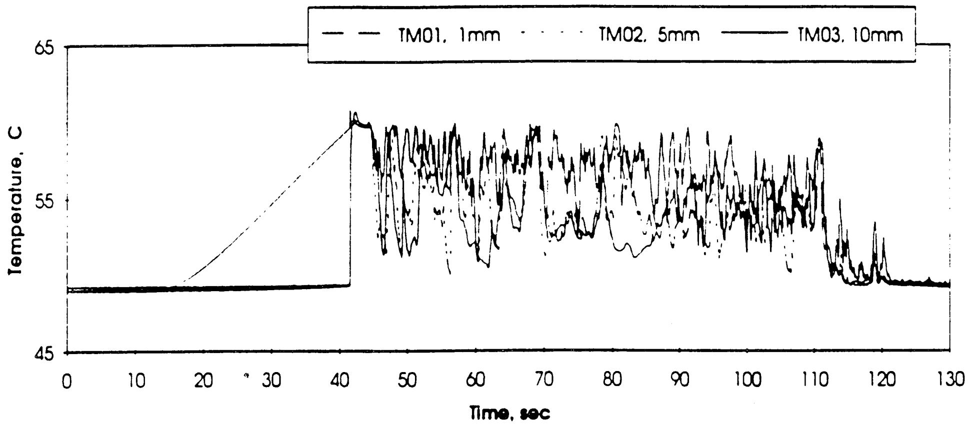

C. Far Field Bulk Temperatures

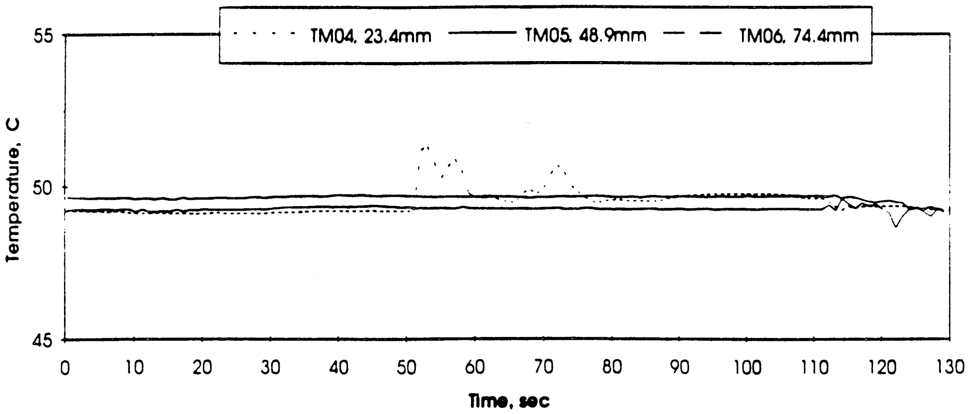

STS 47 - RUN#3

HEAT FLUX	**SUBCOOLING (F)**	**HEATER POWER ON/OFF**	**100 FPS ON/OFF**	**STIRRER START**	**REPRESS START**	**TOTAL TEST TIME**
2	20 ± 2	10-120 sec.	30-50 sec.	110 sec.	----------	130 sec.

Figure 5.4d. Run No. 3. PBE-IA. STS-47. Fluid temperatures near primary heater and far field bulk.

A. Mean Heater Surface Temperature

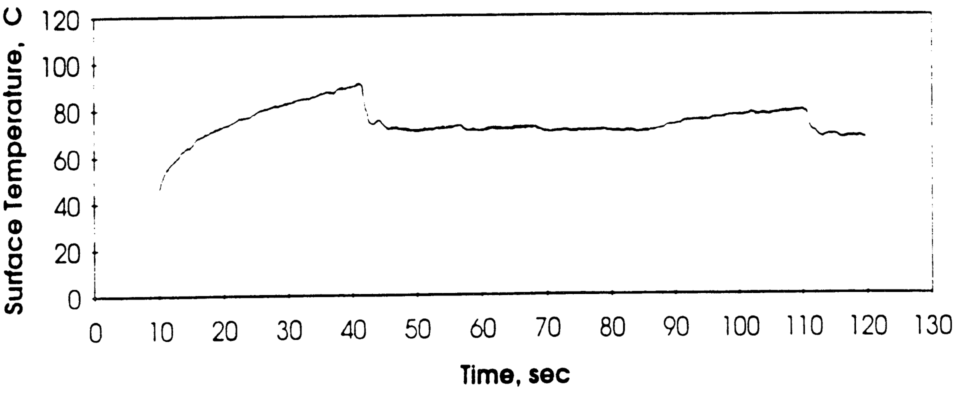

D.

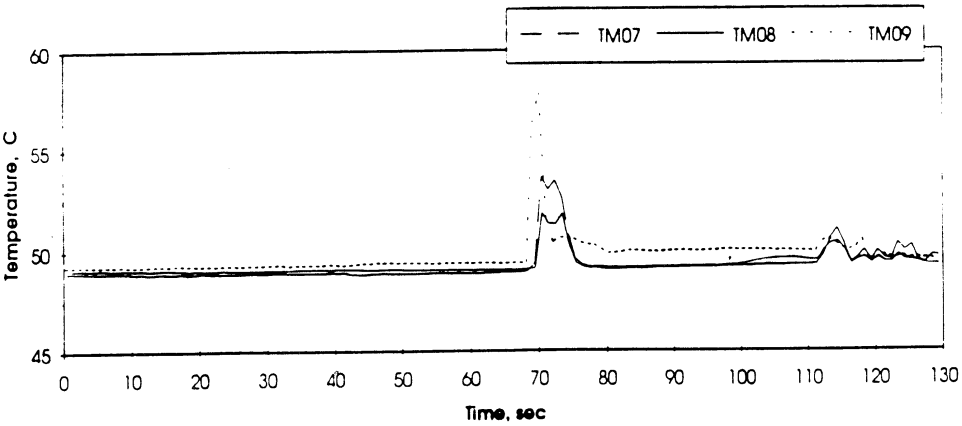

E.

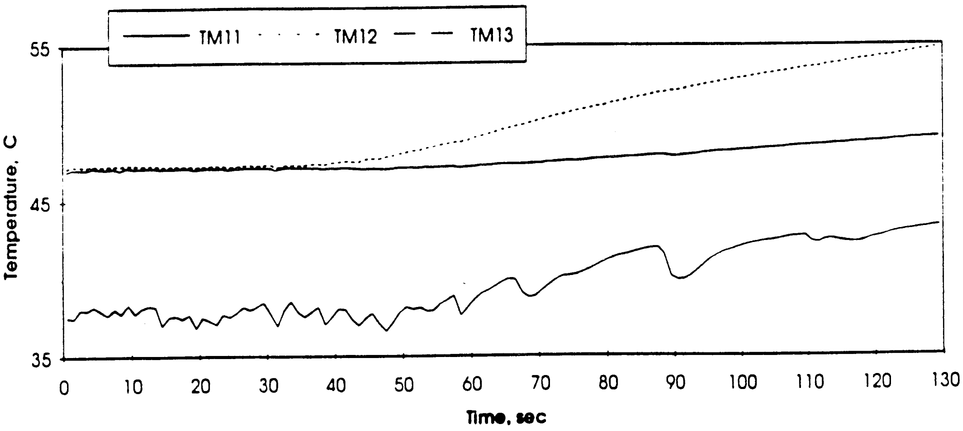

STS 47 - RUN #3

HEAT FLUX	SUBCOOLING (F)	HEATER POWER ON/OFF	100 FPS ON/OFF	STIRRER START	REPRESS START	TOTAL TEST TIME
2	20 ± 2	10-120 sec.	30-50 sec.	110 sec.	----------	130 sec.

Figure 5.4e. Run No. 3. PBE-IA. STS-47. Fluid temperatures near back up heater. Quartz substrate underside and ambient vicinity temperatures.

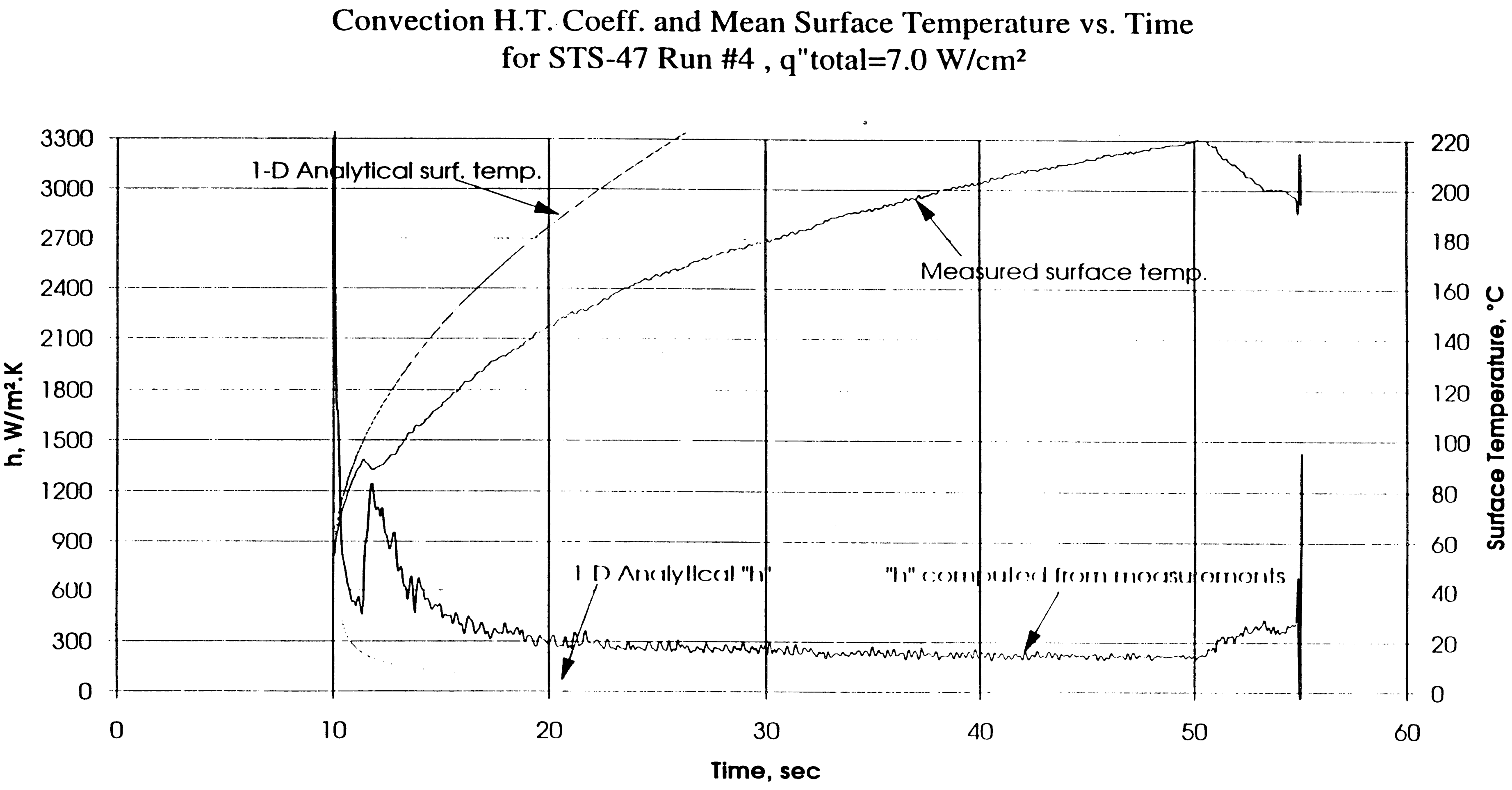

Figure 5.5a. Run No. 4. PBE-IA. STS-47. Mean heater surface temperature and derived heat transfer coefficient.

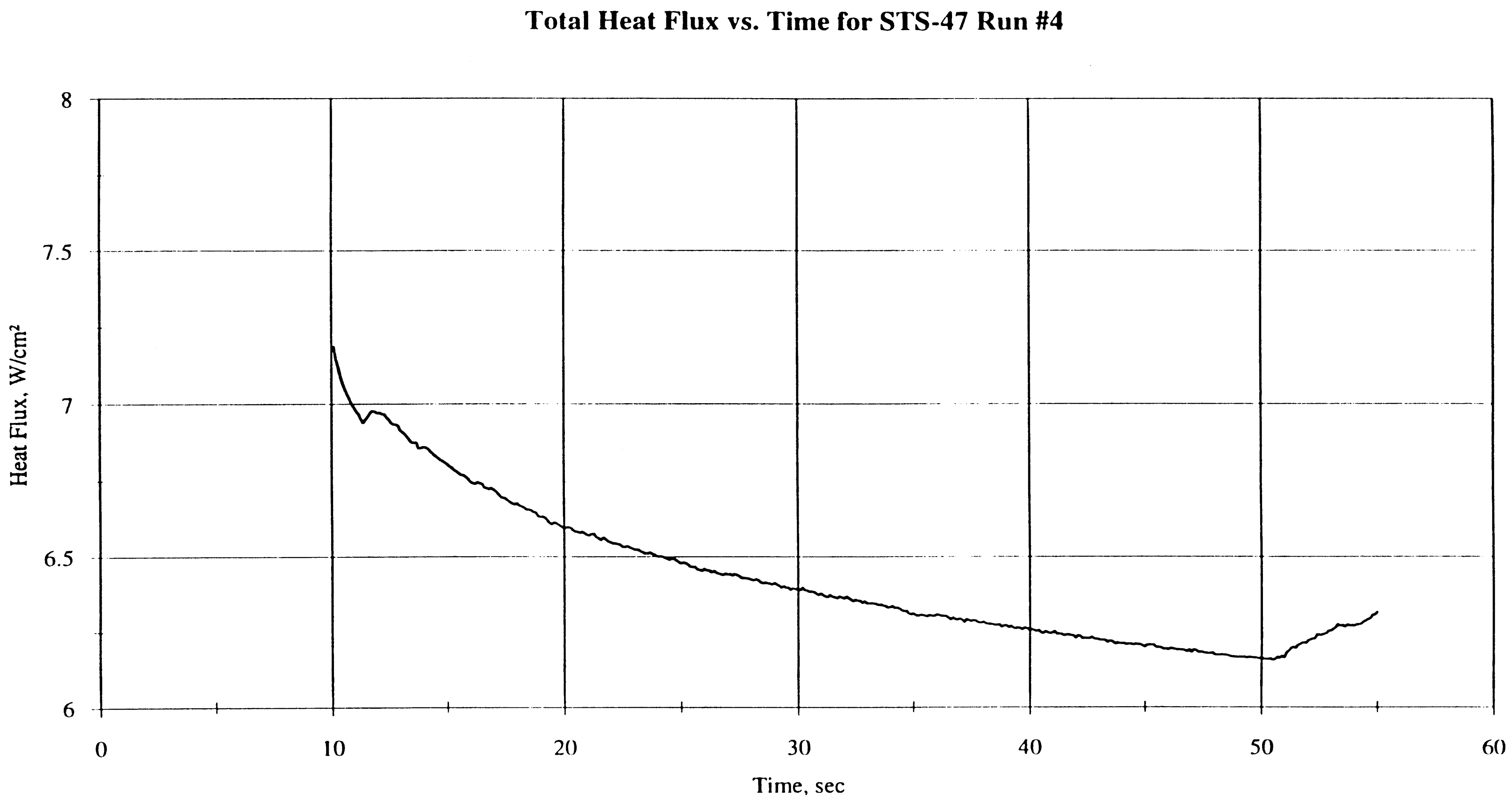

Figure 5.5b. Run No. 4. PBE-IA. STS-47. Heat flux input.

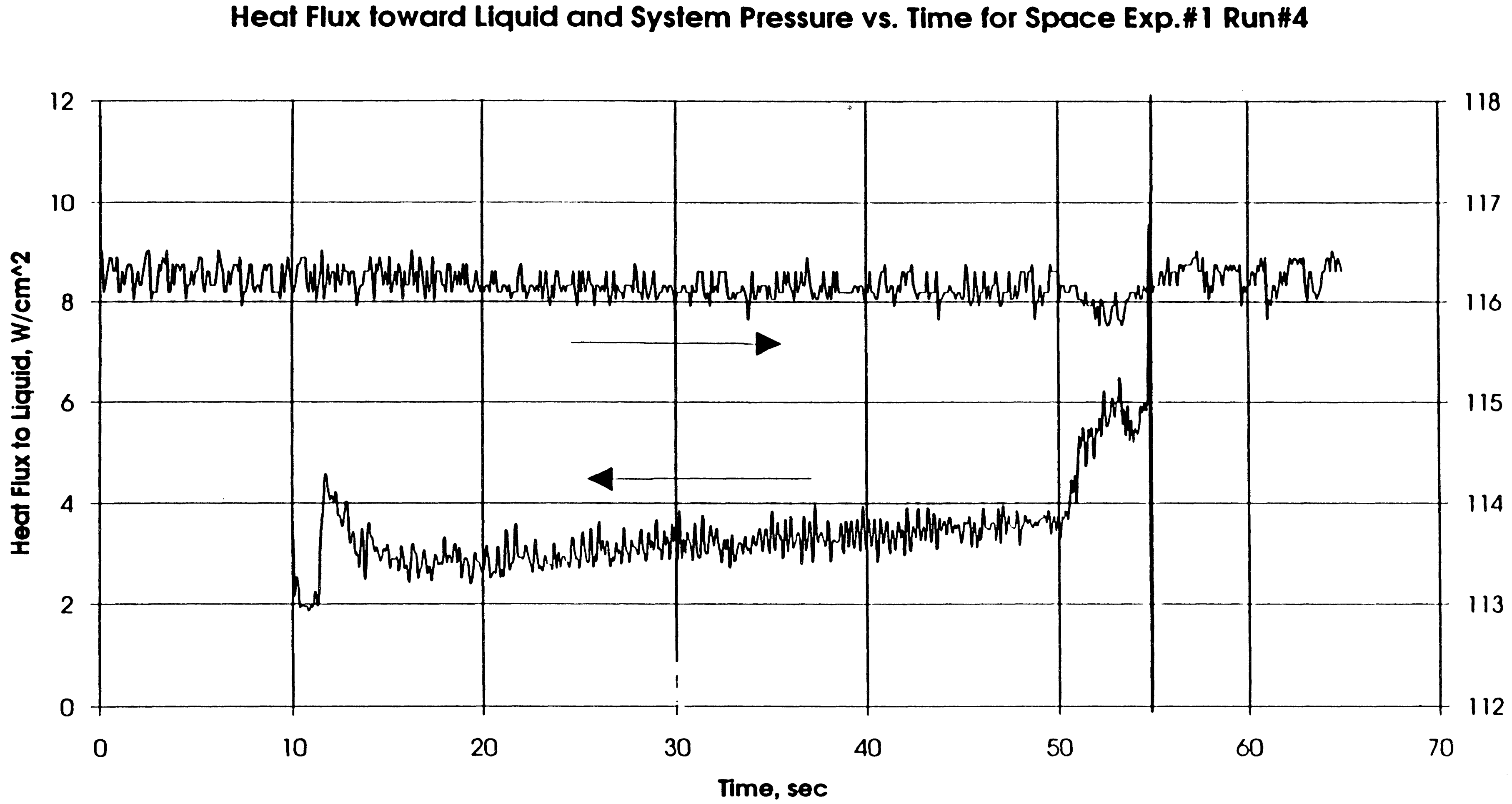

Figure 5.5c. Run No. 4. PBE-IA. STS-47. System pressure and fluid side heat flux.

A. Mean Heater Surface Temperature

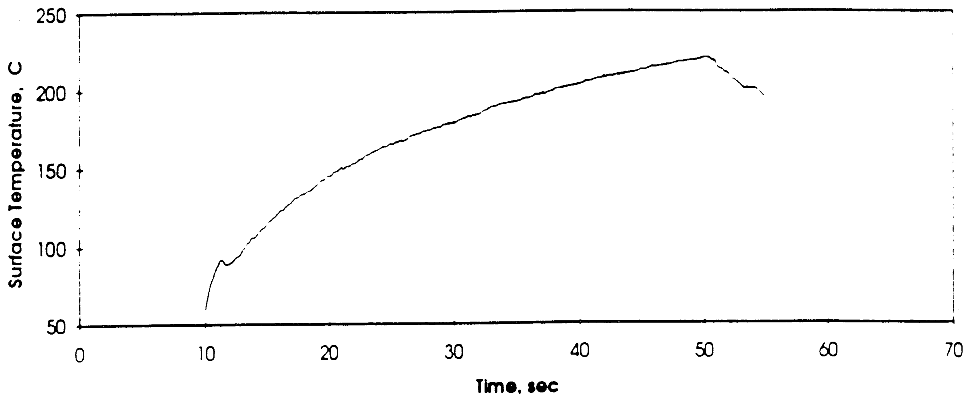

B. Local Fluid Temperatures

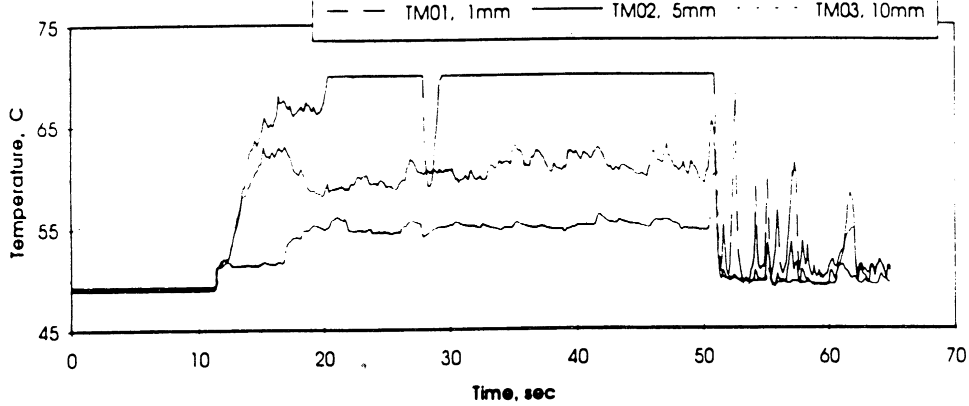

C. Far Field Bulk Temperatures

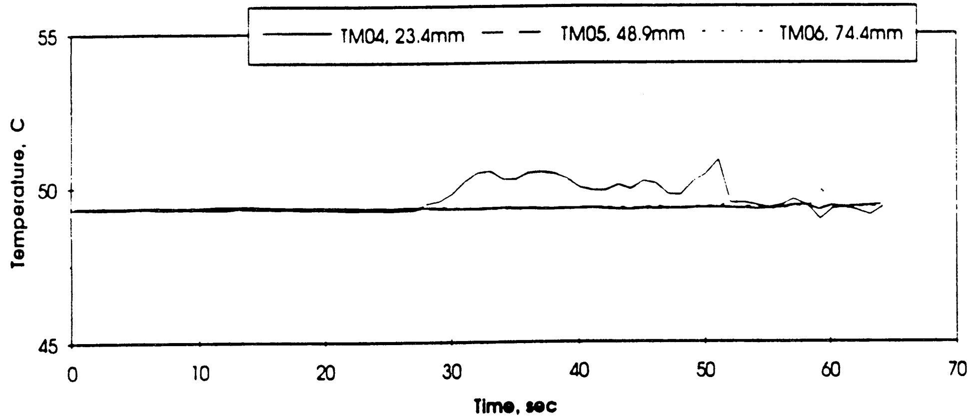

STS 47 - RUN#4

HEAT FLUX	SUBCOOLING (F)	HEATER POWER ON/OFF	100 FPS ON/OFF	STIRRER START	REPRESS START	TOTAL TEST TIME
8	05 ± 1	10-55 sec.	10-15 sec.	50 sec.	----------	65 sec.

Figure 5.5d. Run No. 4. PBE-IA. STS-47. Fluid temperatures near primary heater and far field bulk.

A. Mean Heater Surface Temperature

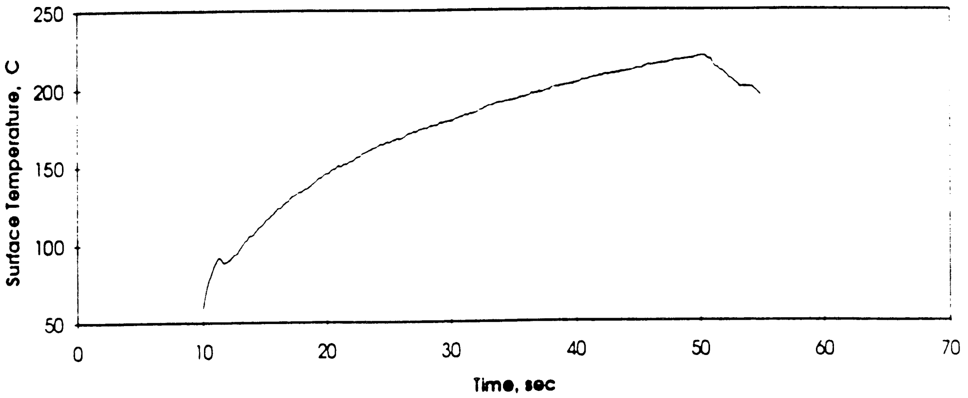

D.

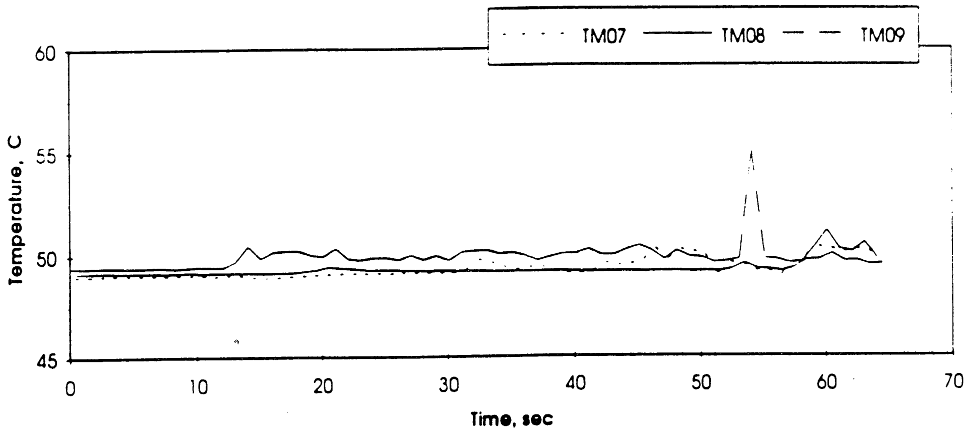

E.

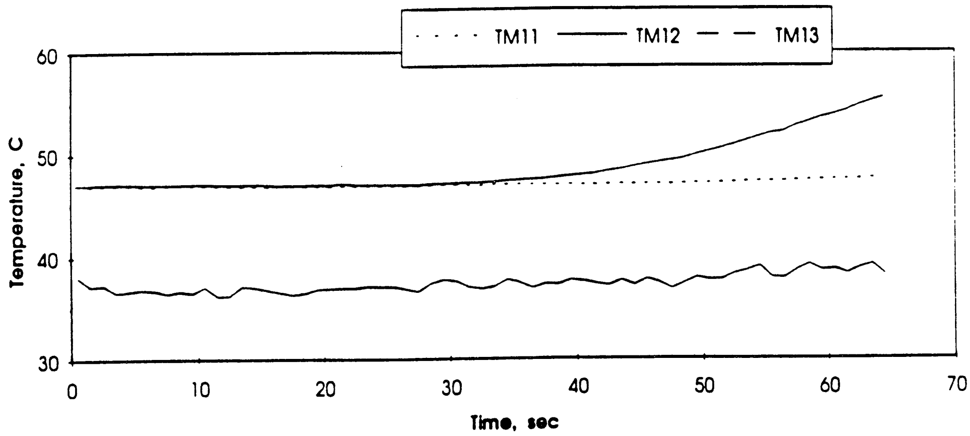

STS 47 - RUN #4

HEAT FLUX	**SUBCOOLING (F)**	**HEATER POWER ON/OFF**	**100 FPS ON/OFF**	**STIRRER START**	**REPRESS START**	**TOTAL TEST TIME**
8	5 ± 1	10-55 sec.	10-15 sec.	50 sec.	----------	65 sec.

Figure 5.5e. Run No. 4. PBE-IA. STS-47. Fluid temperatures near back up heater. Quartz substrate underside and ambient vicinity temperatures.

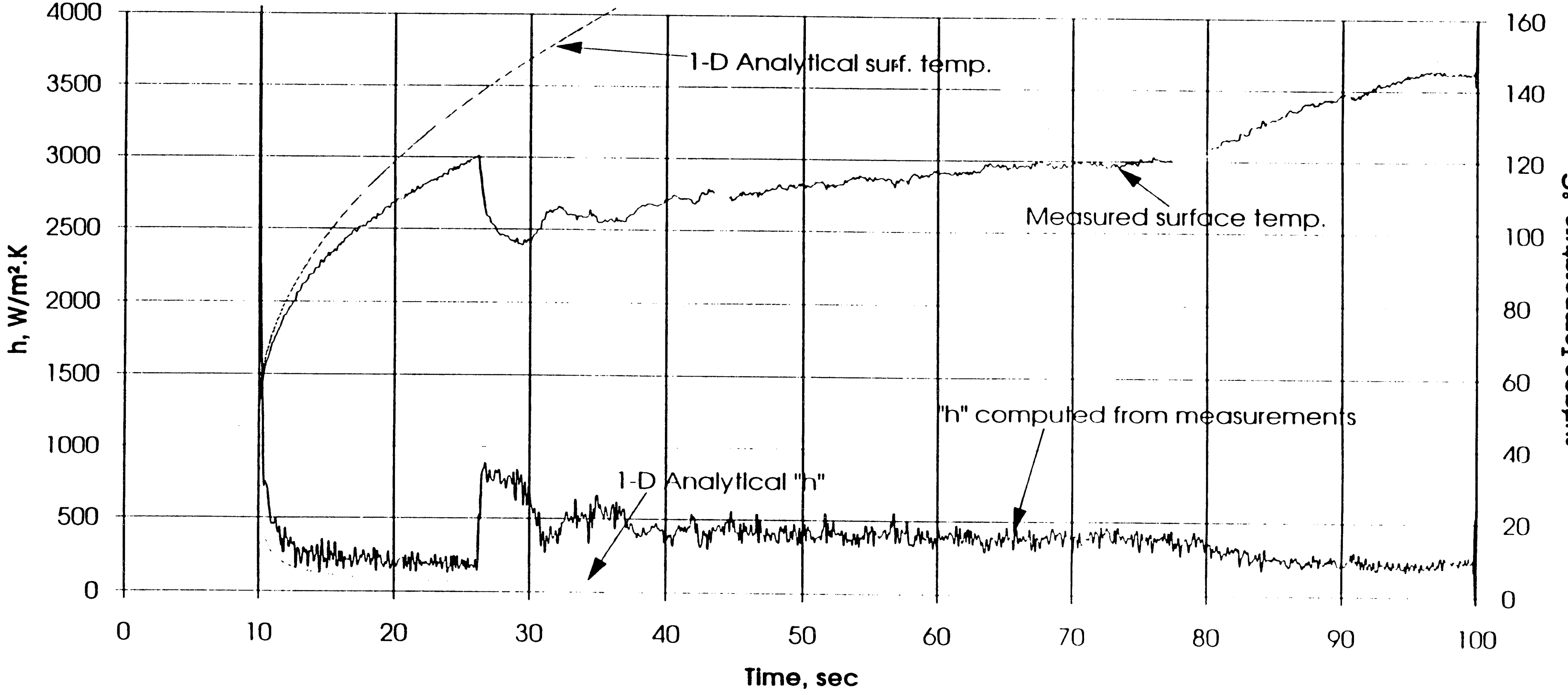

Convection H.T. Coeff. and Mean Surface Temperature vs. Time
for STS-47 Run #5 , q"total=3.6 W/cm²

Figure 5.6a. Run No. 5. PBE-IA. STS-47. Mean heater surface temperature and derived heat transfer coefficient.

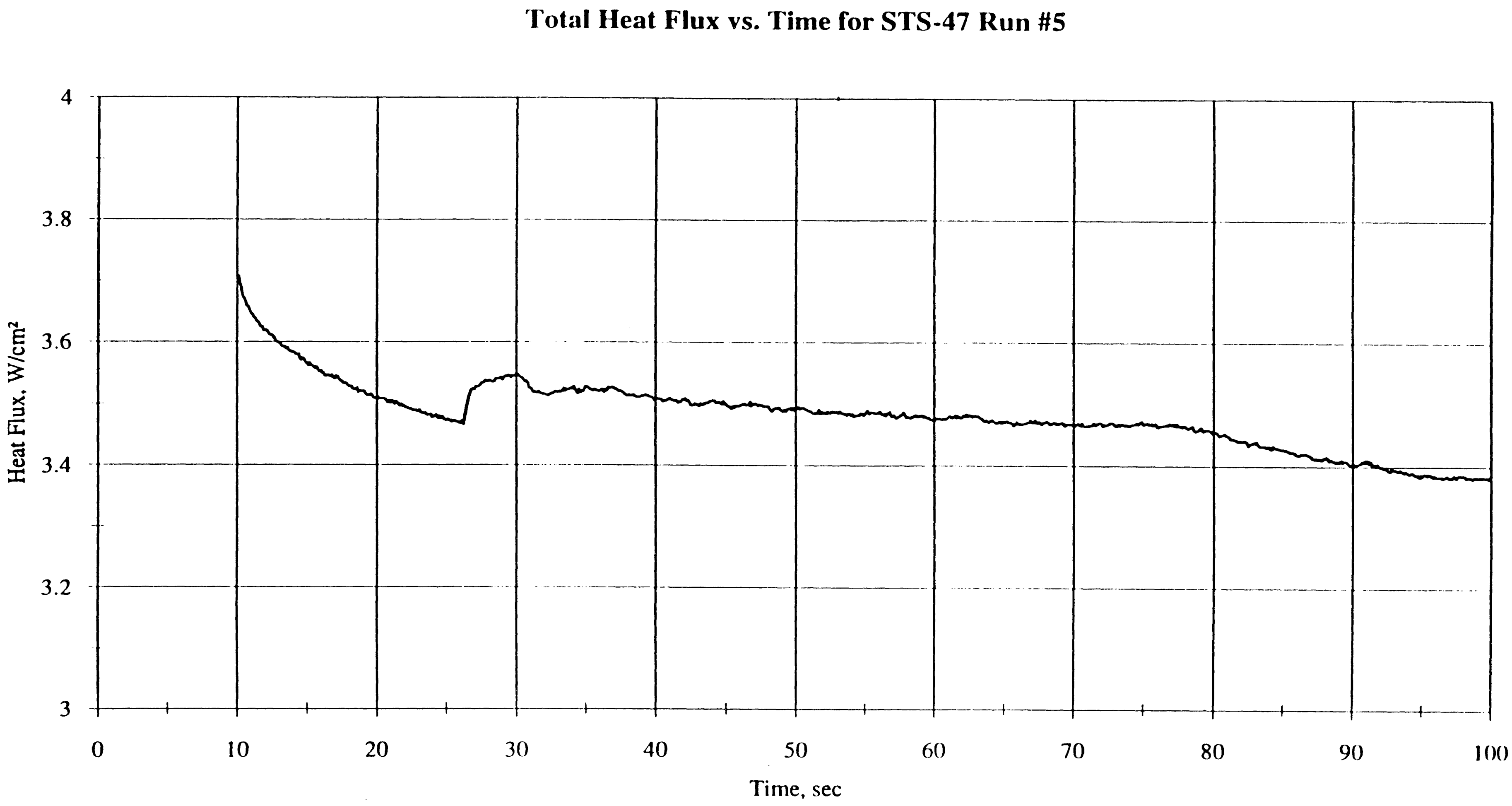

Figure 5.6b. Run No. 5. PBE-IA. STS-47. Heat flux input.

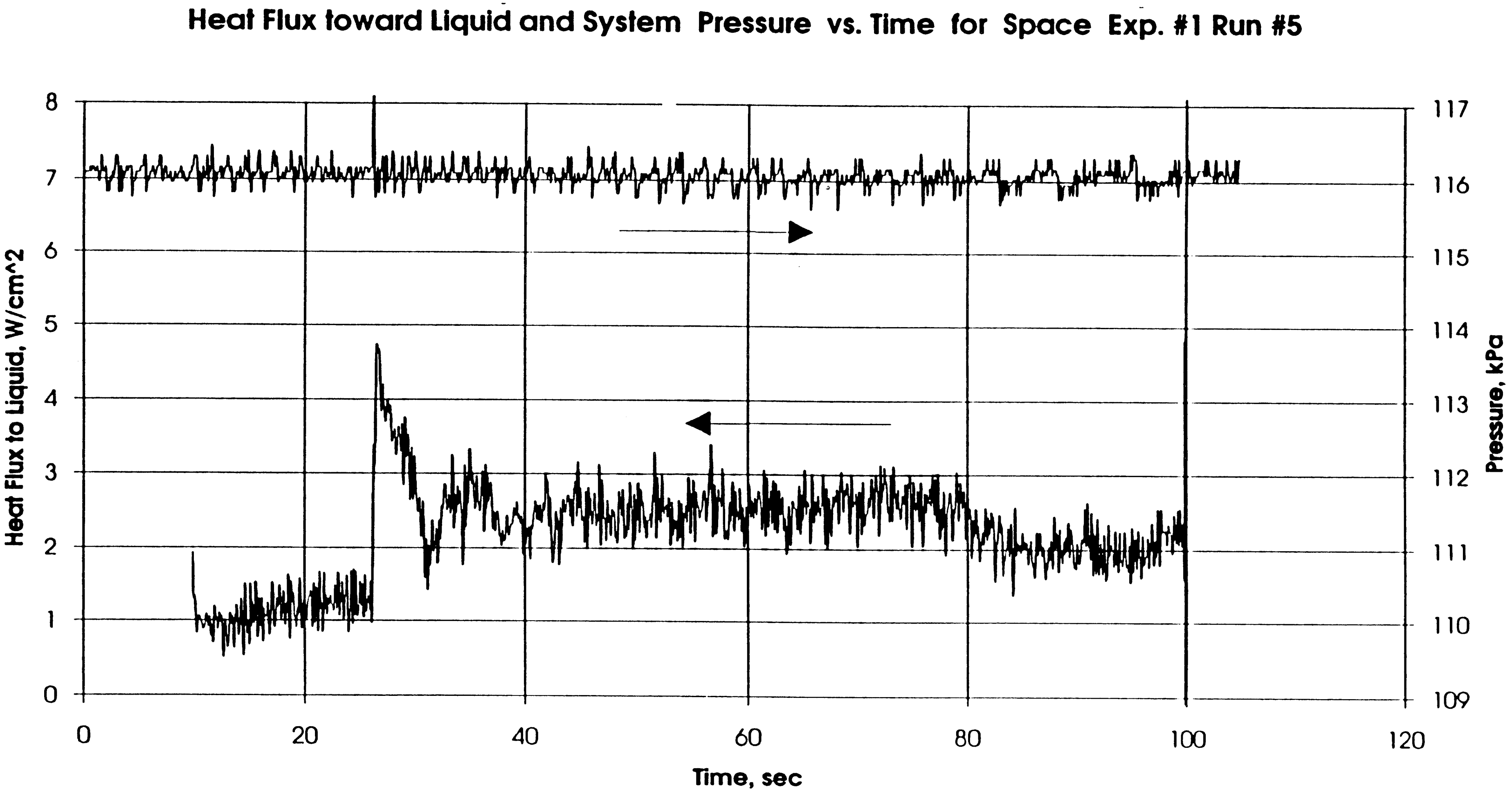

Figure 5.6c. Run No. 5. PBE-IA. STS-47. STS-47. System pressure and fluid side heat flux.

A. Mean Heater Surface Temperature

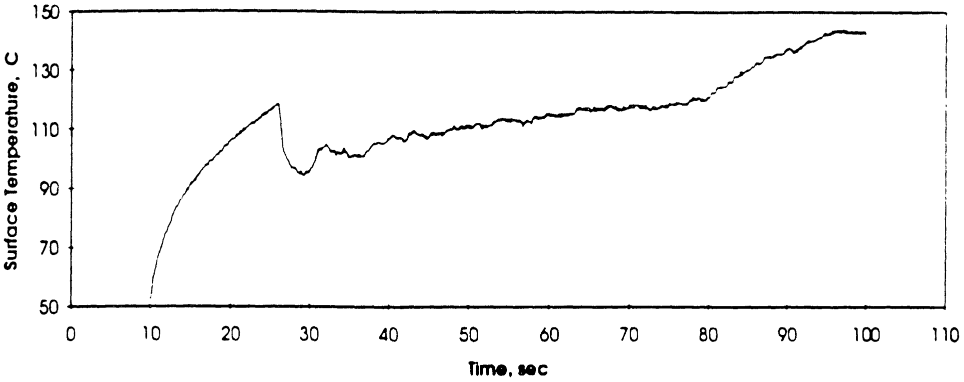

B. Local Fluid Temperatures

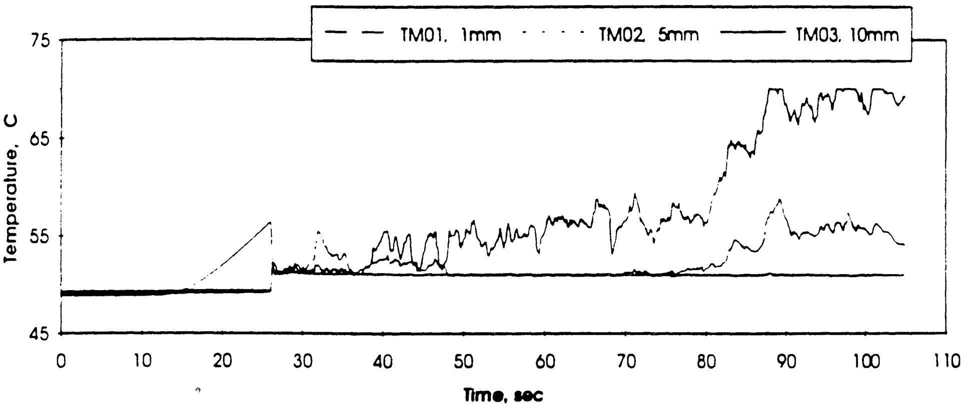

C. Far Field Bulk Temperatures

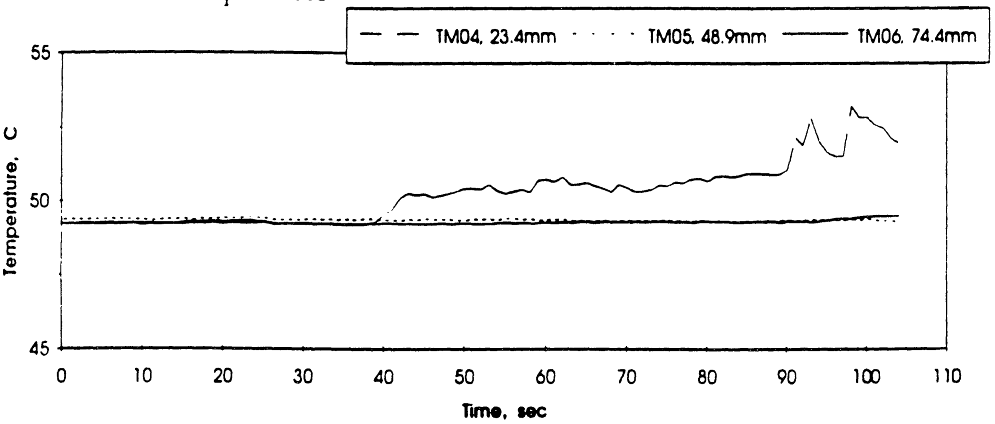

STS 47 - RUN#5

HEAT FLUX	SUBCOOLING (F)	HEATER POWER ON/OFF	100 FPS ON/OFF	STIRRER START	REPRESS START	TOTAL TEST TIME
4	5 ± 1	10-100 sec.	15-25 sec.	--------	----------	105 sec.

Figure 5.6d. Run No. 5. PBE-IA. STS-47. Fluid temperatures near primary heater and far field bulk.

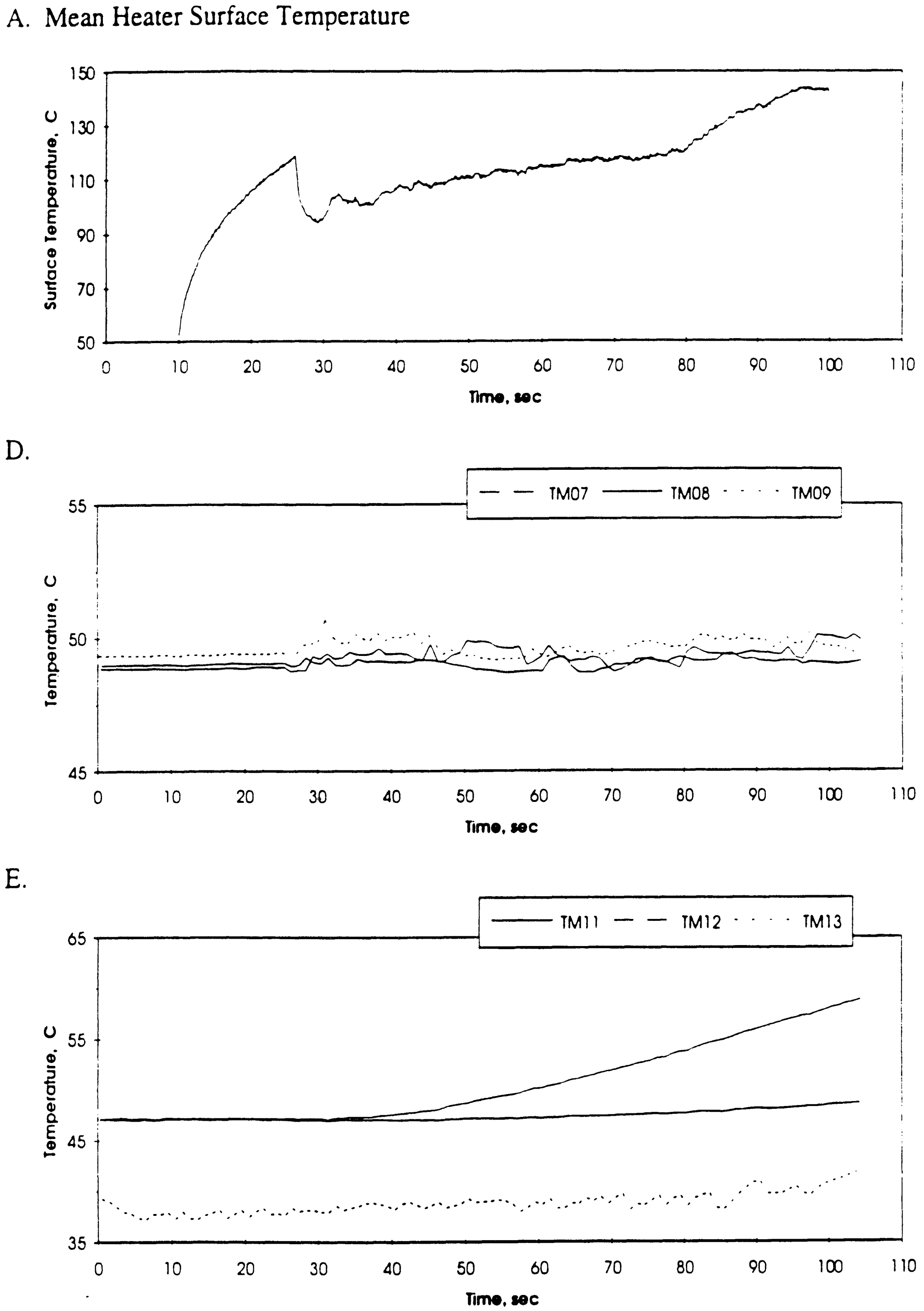

STS 47 - RUN #5

HEAT FLUX	**SUBCOOLING (F)**	**HEATER POWER ON/OFF**	**100 FPS ON/OFF**	**STIRRER START**	**REPRESS START**	**TOTAL TEST TIME**
4	5 ± 1	10-100 sec.	15-25 sec.	--------	----------	105 sec.

Figure 5.6e. Run No. 5. PBE-IA. STS-47. Fluid temperatures near back up heater. Quartz substrate underside and ambient vicinity temperatures.

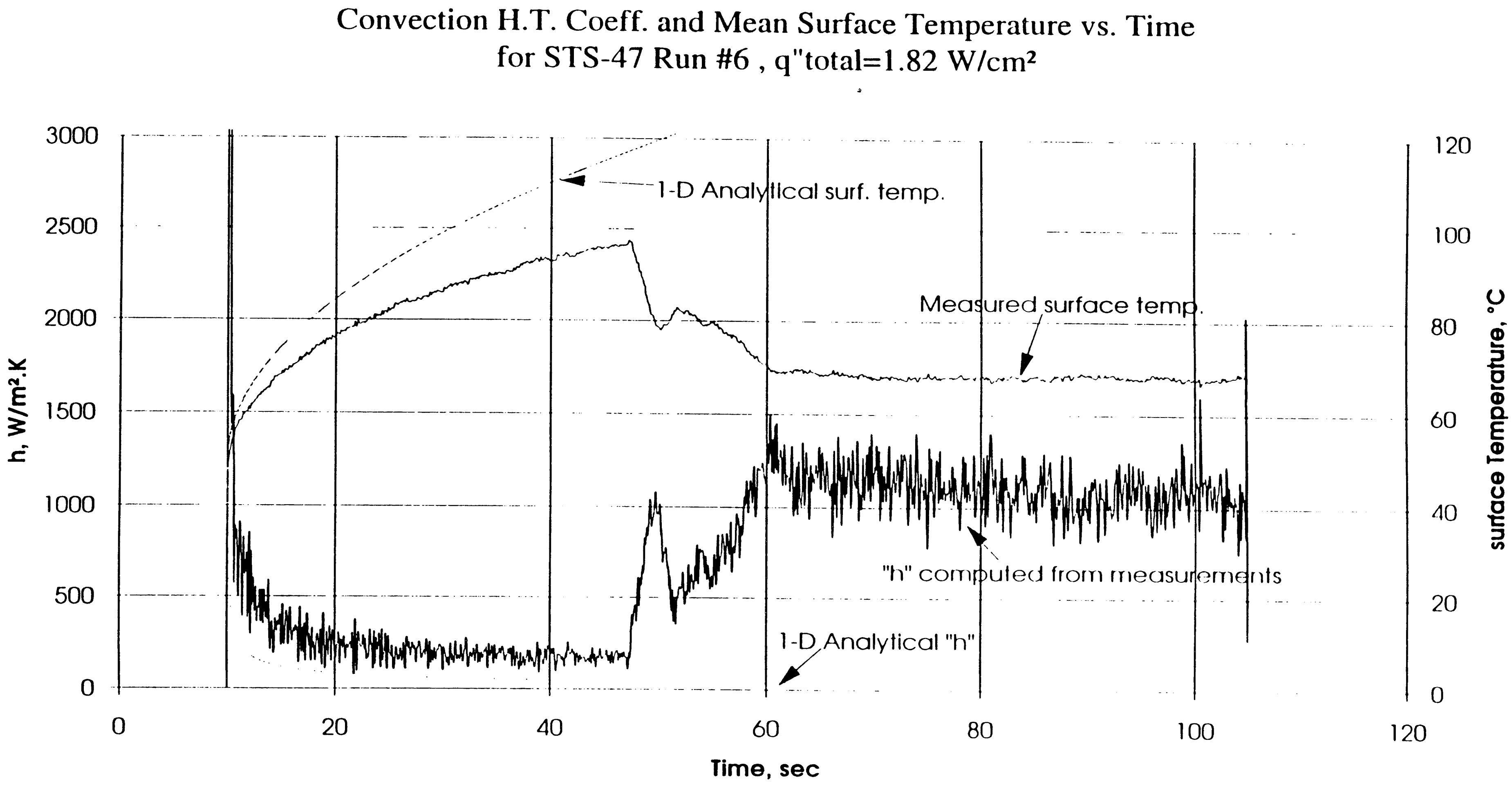

Figure 5.7a. Run No. 6. PBE-IA. STS-47. Mean heater surface temperature and derived heat transfer coefficient.

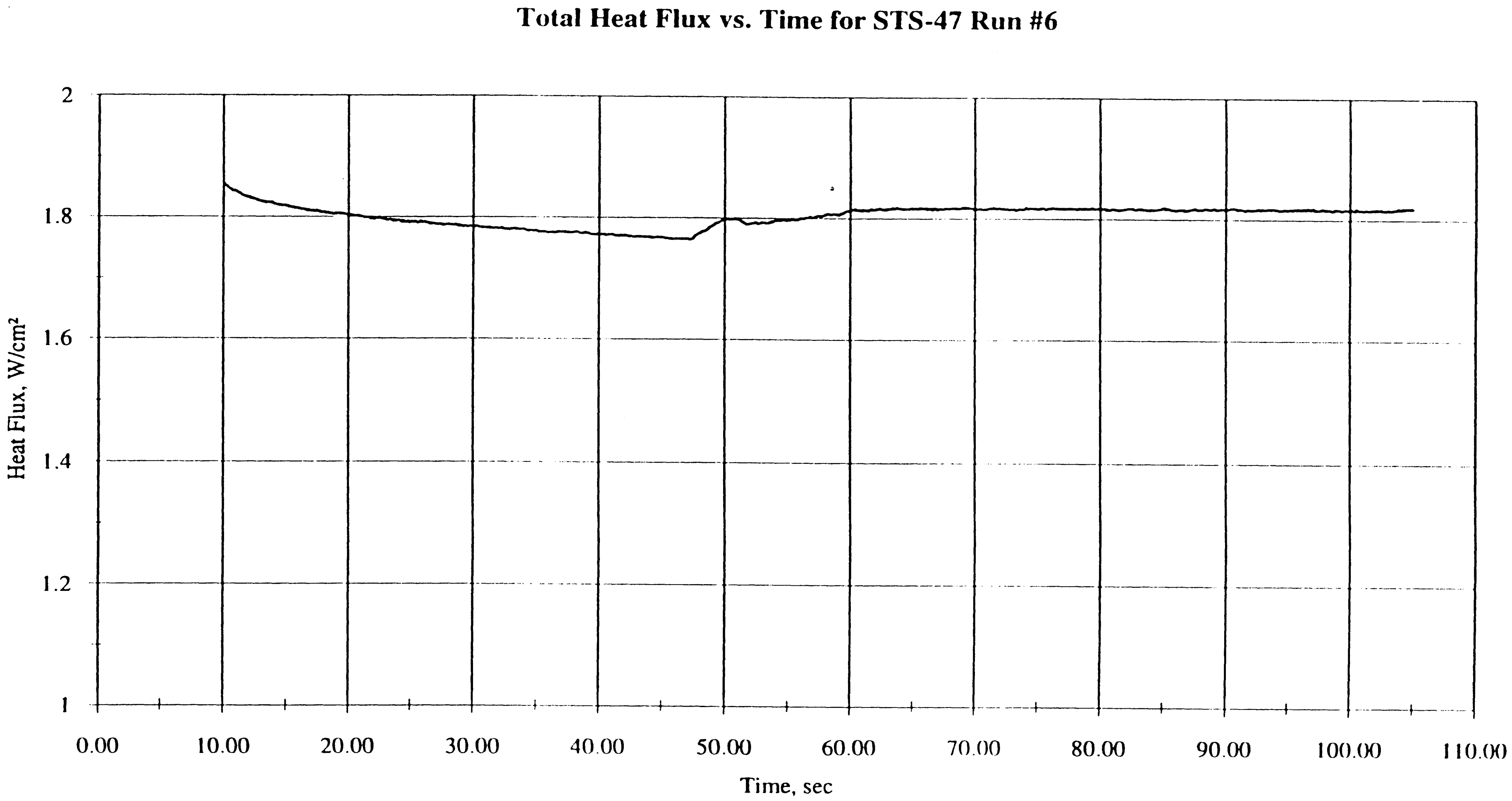

Figure 5.7b. Run No. 6. PBE-IA. STS-47. Heat flux input.

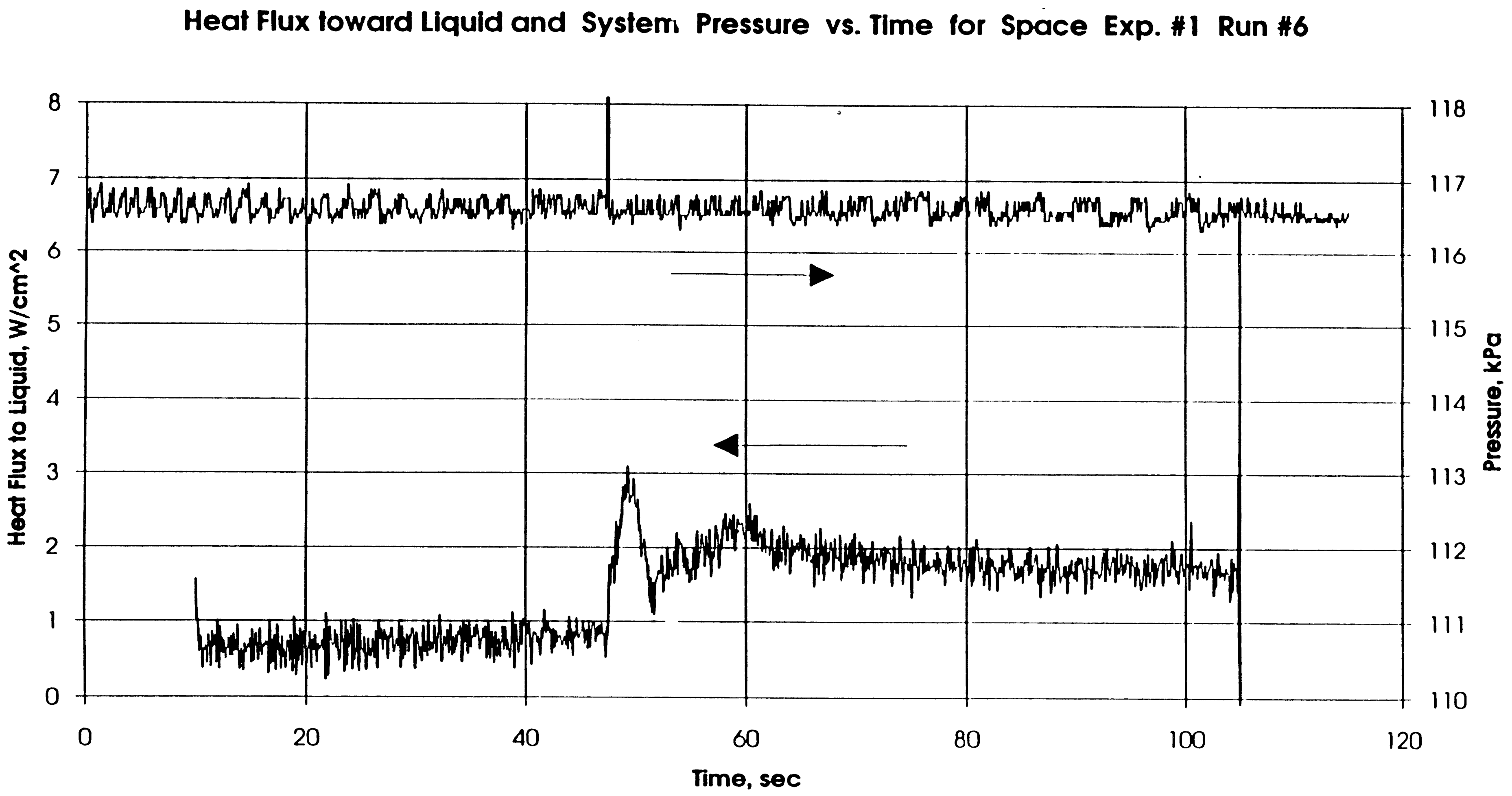

Figure 5.7c. Run No. 6. PBE-IA. STS-47. System pressure and fluid side heat flux.

A. Mean Heater Surface Temperature

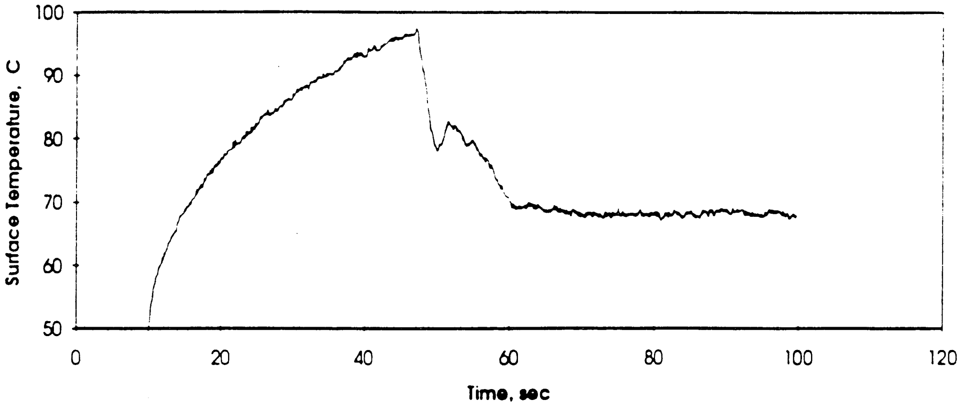

B. Local Fluid Temperatures

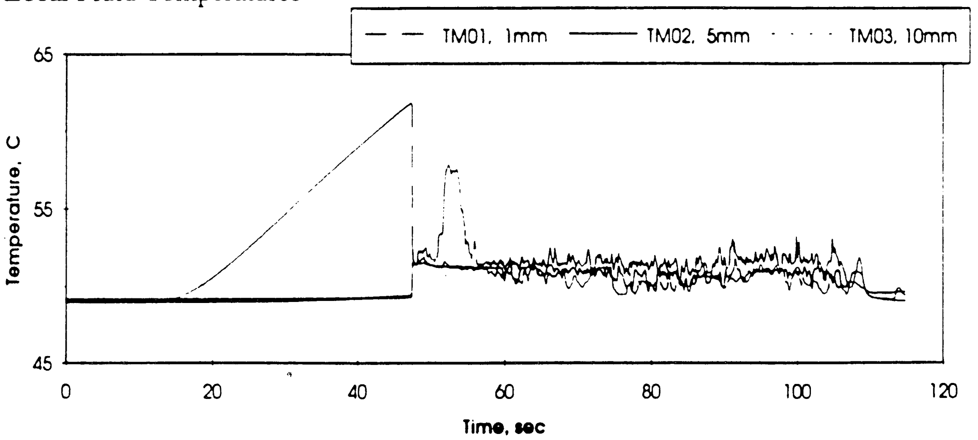

C. Far Field Bulk Temperatures

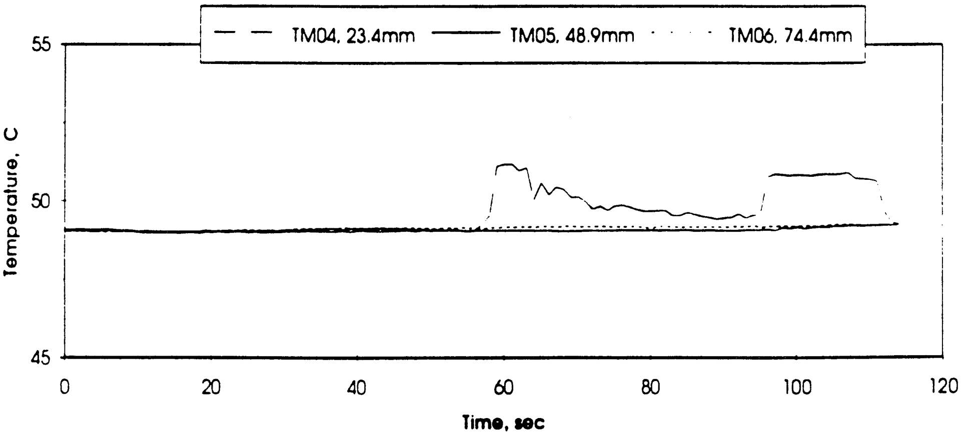

STS 47 - RUN#6

HEAT FLUX	SUBCOOLING (F)	HEATER POWER ON/OFF	100 FPS ON/OFF	STIRRER START	REPRESS START	TOTAL TEST TIME
2	5 ± 1	10-105 sec.	30-50 sec.	--------	----------	115 sec.

Figure 5.7d. Run No. 6. PBE-IA. STS-47. Fluid temperatures near primary heater and far field bulk.

A. Mean Heater Surface Temperature

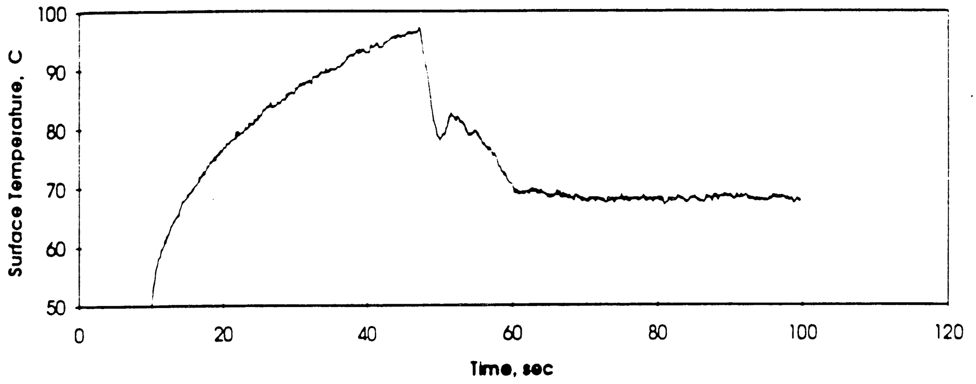

D.

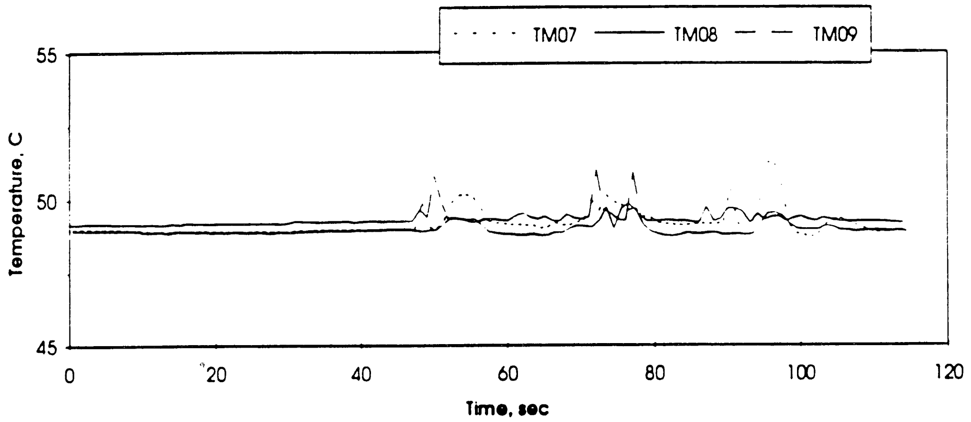

E.

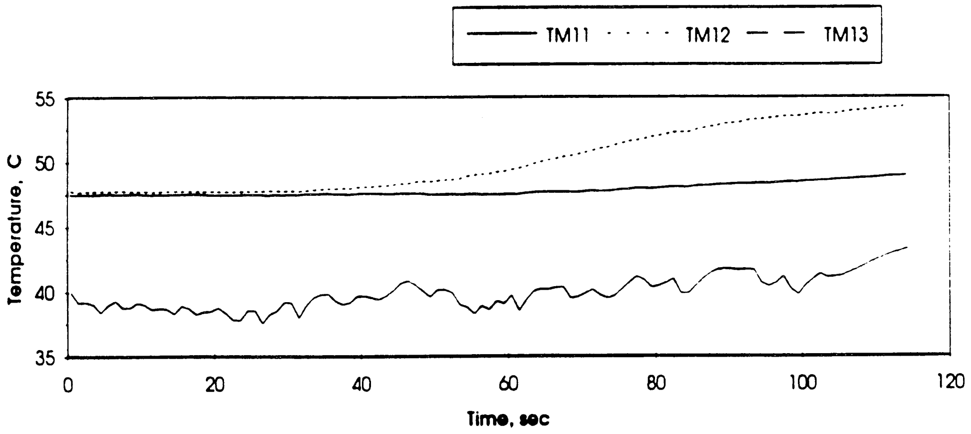

STS 47 - RUN #6

HEAT FLUX	SUBCOOLING (F)	HEATER POWER ON/OFF	100 FPS ON/OFF	STIRRER START	REPRESS START	TOTAL TEST TIME
2	5 ± 1	10-105 sec.	30-50 sec.	--------	----------	115 sec.

Figure 5.7e. Run No. 6. PBE-IA. STS-47. Fluid temperatures near back up heater. Quartz substrate underside and ambient vicinity temperatures.

Convection H.T. Coeff. and Mean Surface Temperature vs. Time
for STS-47 Run #7 , q"total=7.0 W/cm²

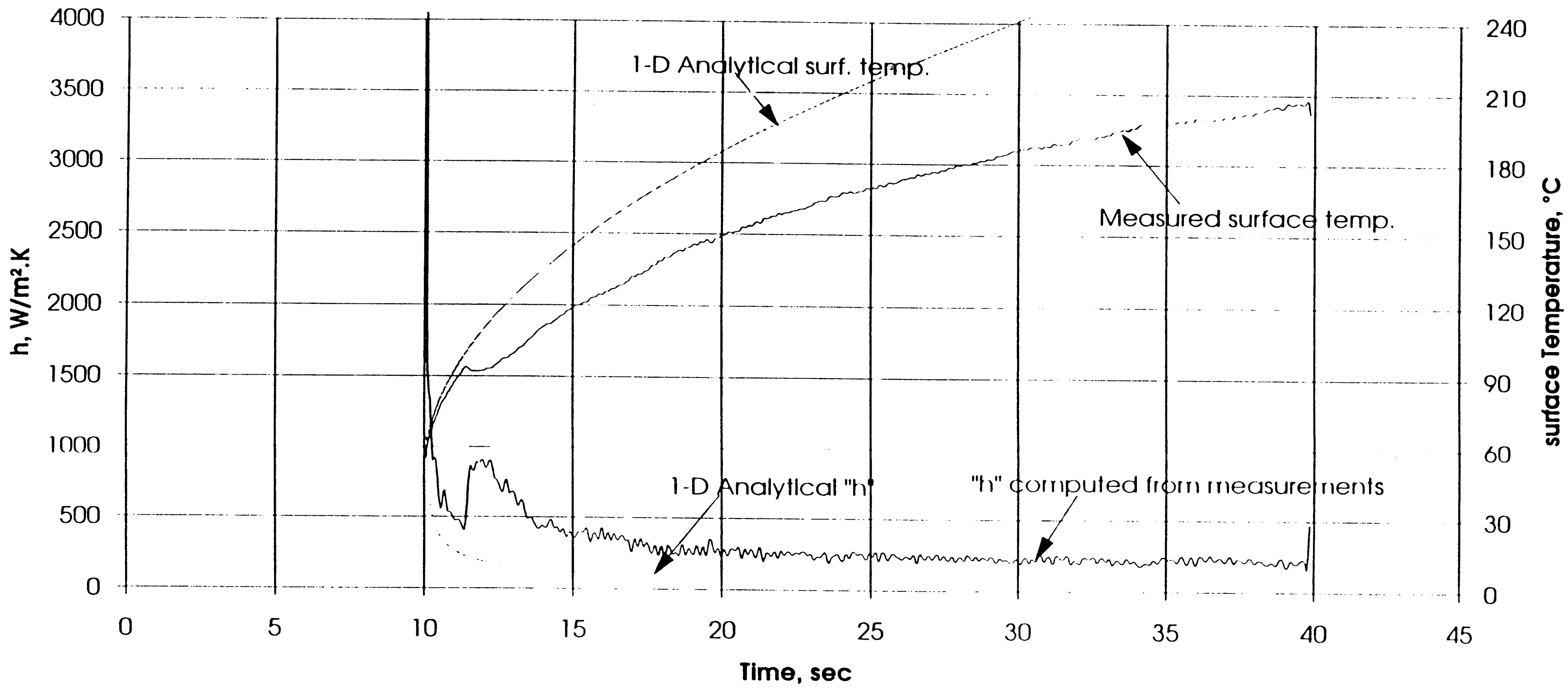

Figure 5.8a. Run No. 7. PBE-IA. STS-47. Mean heater surface temperature and derived heat transfer coefficient.

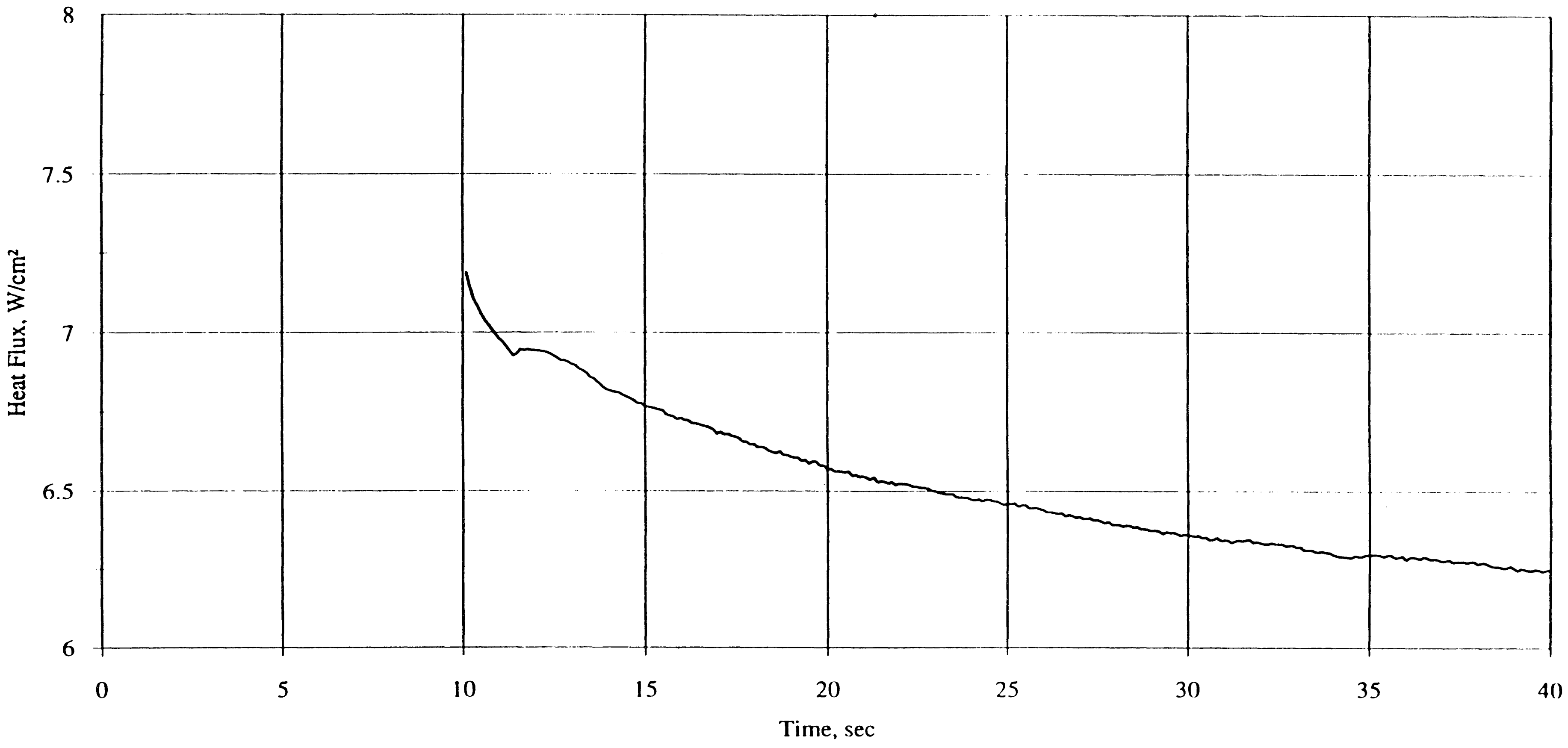

Total Heat Flux vs. Time for STS-47 Run #7

Figure 5.8b. Run No. 7. PBE-IA. STS-47. Heat flux input.

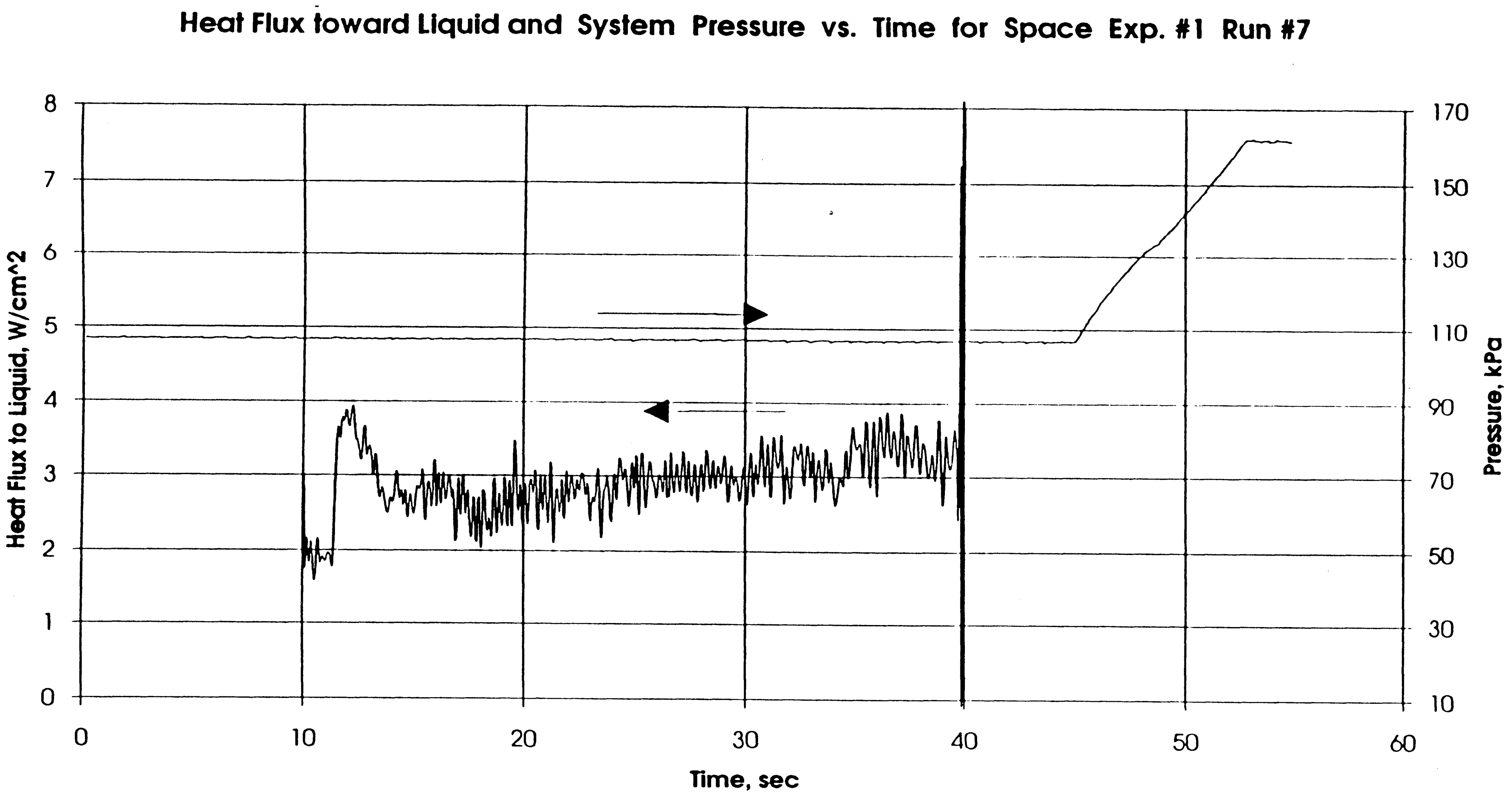

Figure 5.8c. Run No. 7. PBE-IA. STS-47. System pressure and fluid side heat flux.

A. Mean Heater Surface Temperature

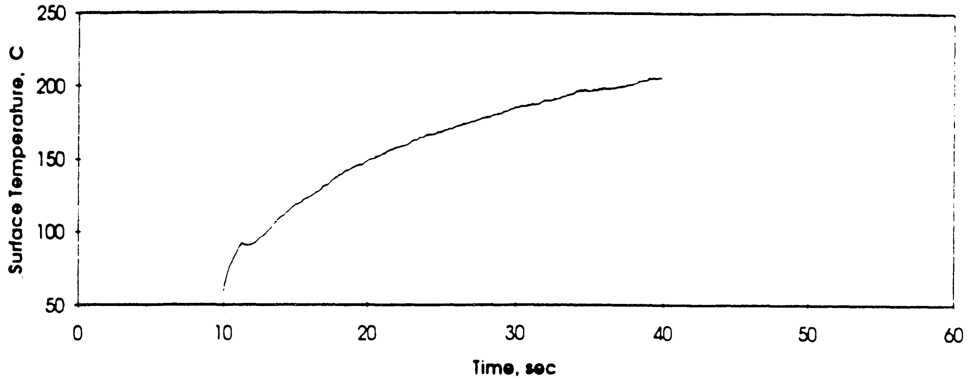

B. Local Fluid Temperatures

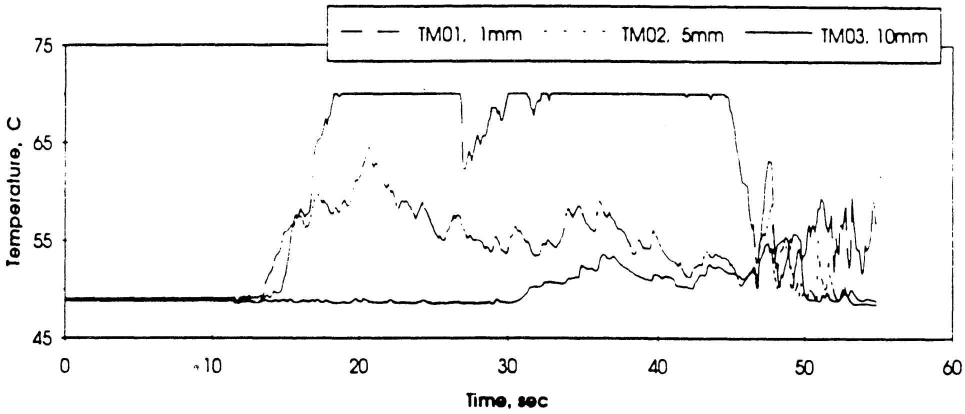

C. Far Field Bulk Temperatures

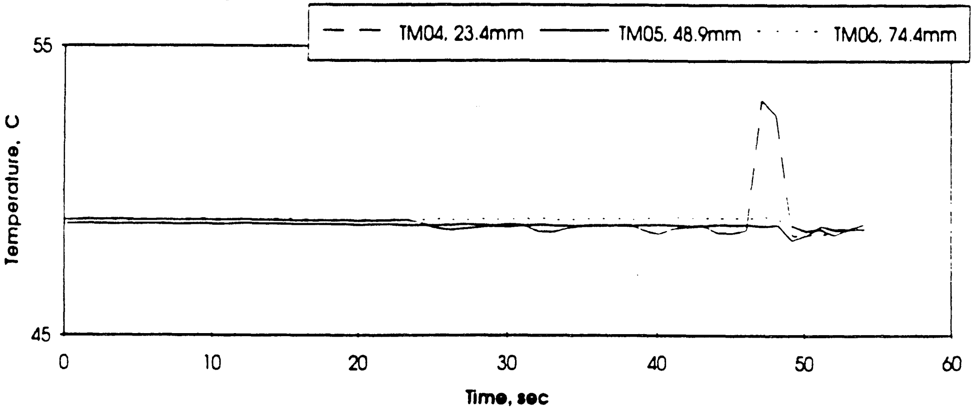

STS 47 - RUN#7

HEAT FLUX	SUBCOOLING (F)	HEATER POWER ON/OFF	100 FPS ON/OFF	STIRRER START	REPRESS START	TOTAL TEST TIME
8	.5 ± .4	10-40 sec.	10-15 sec.	--------	45 sec.	55 sec.

Figure 5.8d. Run No. 7. PBE-IA. STS-47. Fluid temperatures near primary heater and far field bulk.

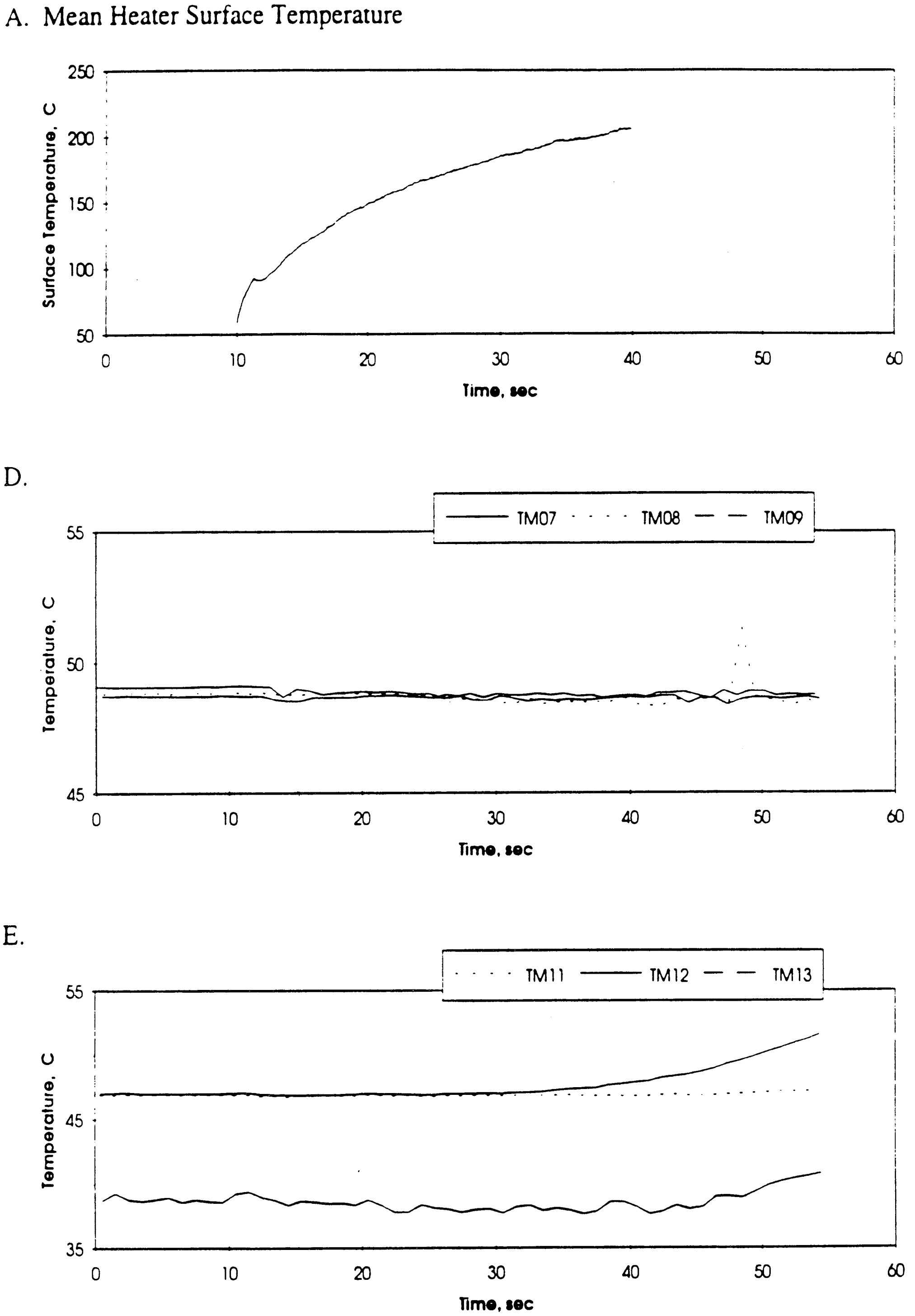

STS 47 - **Run #7**

Heat Flux	**Subcooling (F)**	**Heater Power On/Off**	**100 FPS On/Off**	**Stirrer Start**	**Repress Start**	**Total Test Time**
8	.5 ± .4	10-40 sec.	10-15 sec.	--------	45 sec.	55 sec.

Figure 5.8e. Run No. 7. PBE-IA. STS-47. Fluid temperatures near back up heater. Quartz substrate underside and ambient vicinity temperatures.

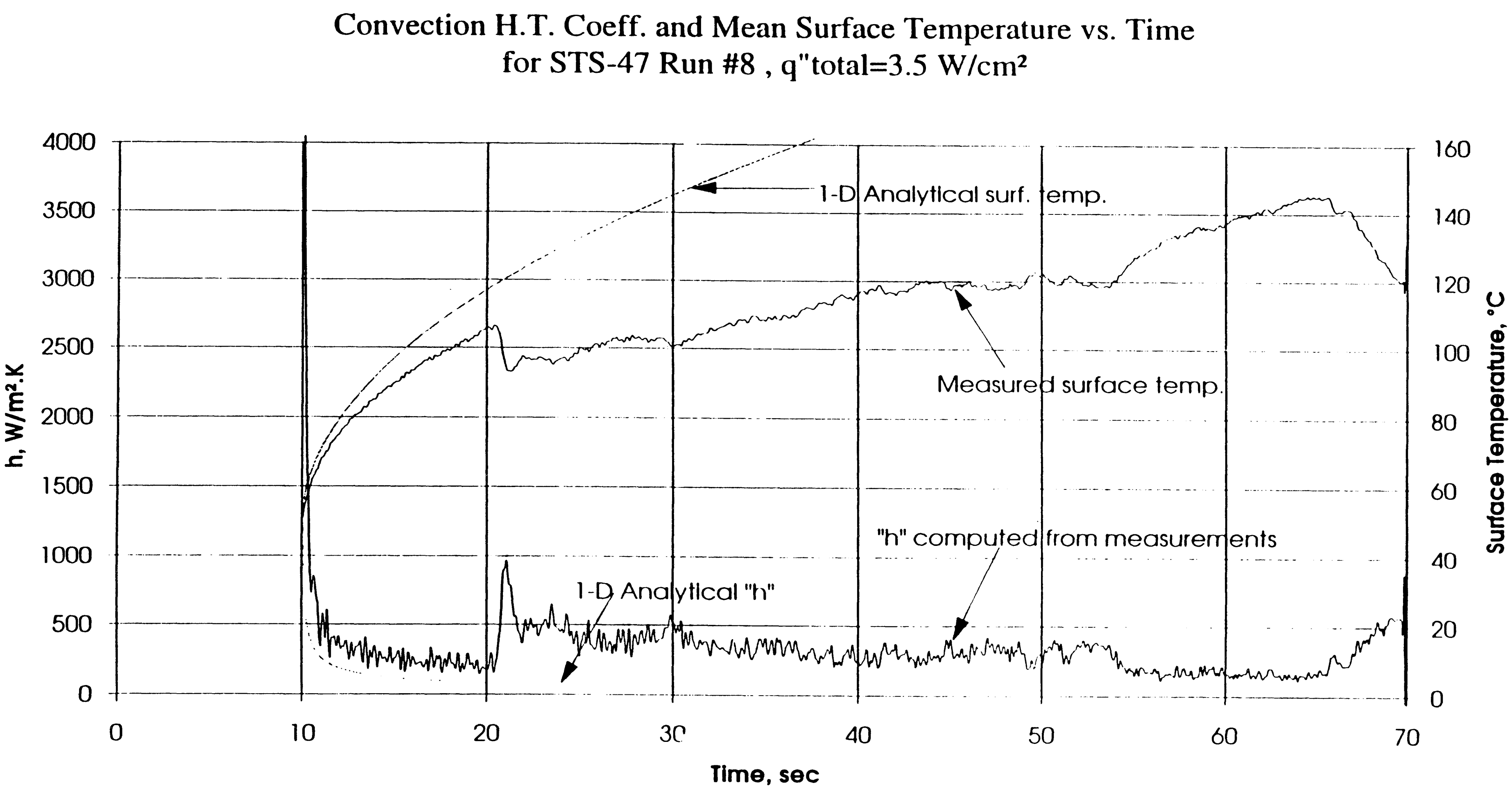

Convection H.T. Coeff. and Mean Surface Temperature vs. Time
for STS-47 Run #8 , q"total=3.5 W/cm²

Figure 5.9a. Run No. 8. PBE-IA. STS-47. Mean heater surface temperature and derived heat transfer coefficient.

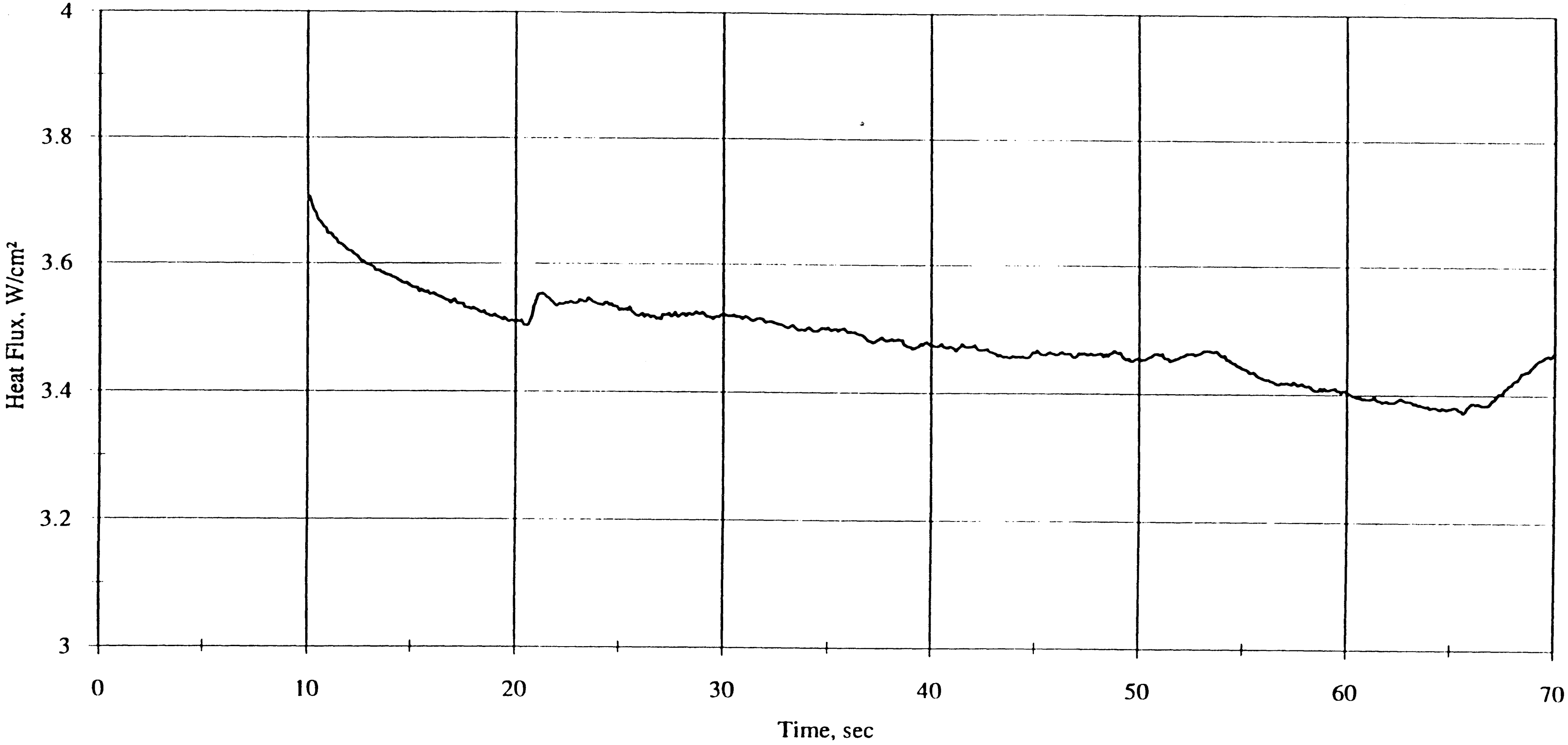
Total Heat Flux vs. Time for STS-47 Run #8

Figure 5.9b. Run No. 8. PBE-IA. STS-47. Heat flux input.

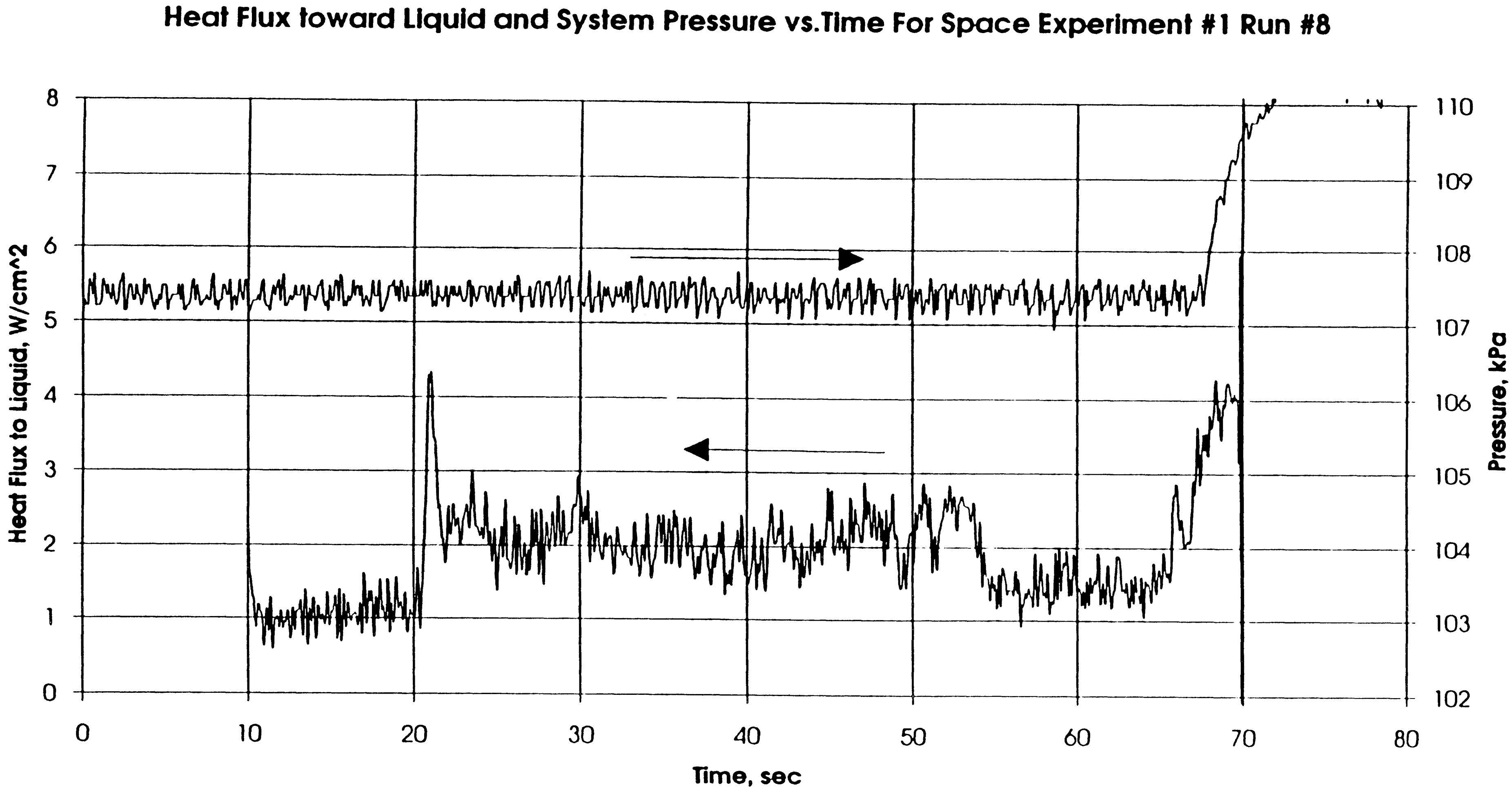

Figure 5.9c. Run No. 8. PBE-IA. STS-47. System pressure and fluid side heat flux.

A. Mean Heater Surface Temperature

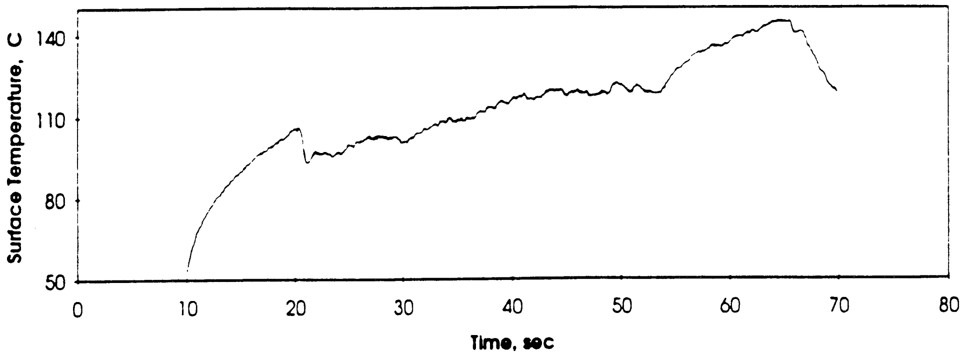

B. Local Fluid Temperatures

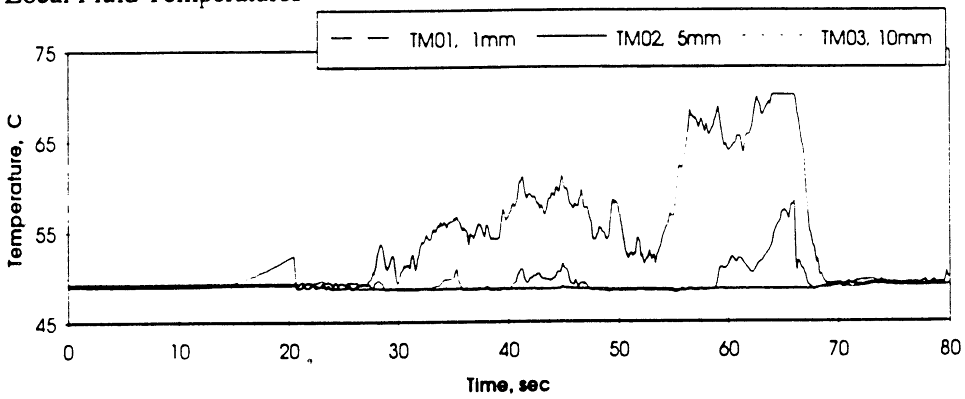

C. Far Field Bulk Temperatures

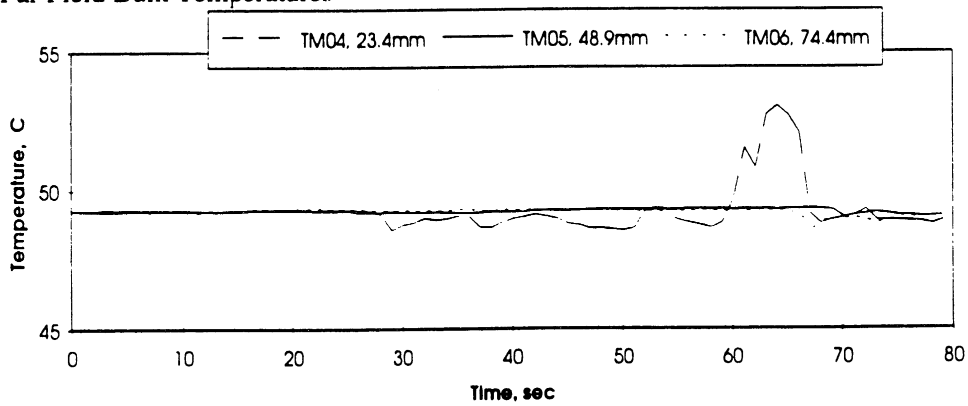

STS 47 - RUN#8

HEAT FLUX	**SUBCOOLING (F)**	**HEATER POWER ON/OFF**	**100 FPS ON/OFF**	**STIRRER START**	**REPRESS START**	**TOTAL TEST TIME**
4	.5 ± .4	10-70 sec.	15-25 sec.	65 sec.	--------	80 sec.

Figure 5.9d. Run No. 8. PBE-IA. STS-47. Fluid temperatures near primary heater and far field bulk.

A. Mean Heater Surface Temperature

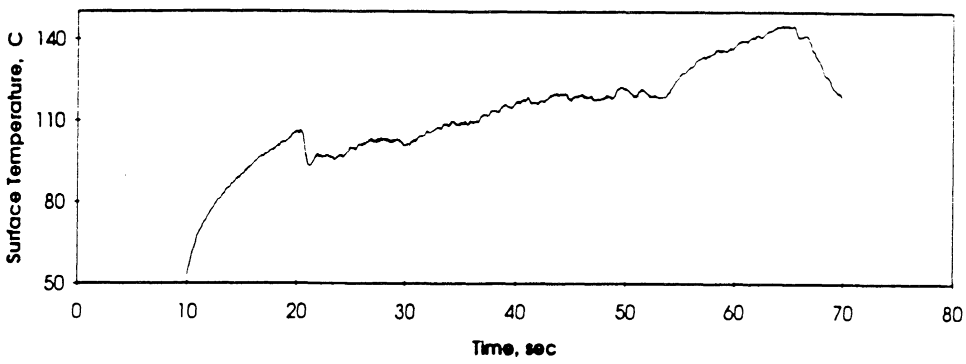

D.

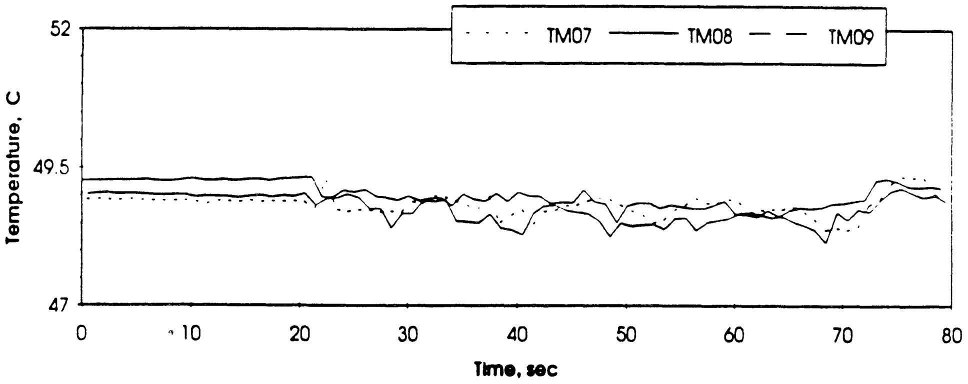

E.

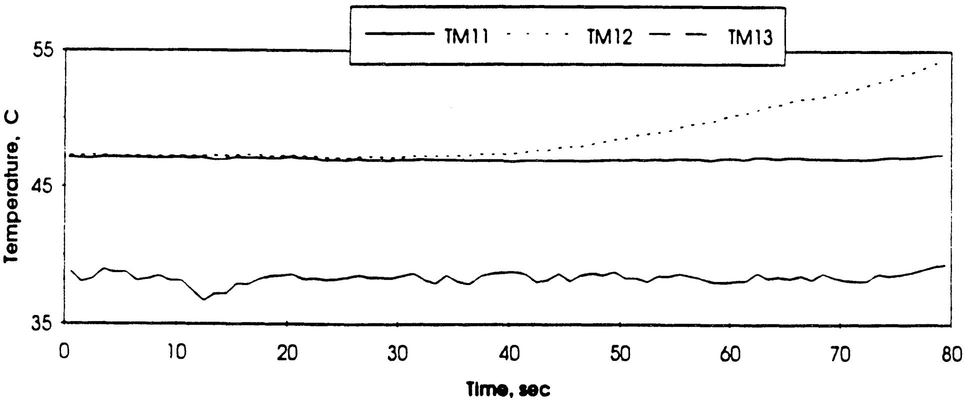

STS 47 - RUN #8

HEAT FLUX	SUBCOOLING (F)	HEATER POWER ON/OFF	100 FPS ON/OFF	STIRRER START	REPRESS START	TOTAL TEST TIME
4	.5 ± .4	10-70 sec.	15-25 sec.	65 sec.	--------	80 sec.

Figure 5.9e. Run No. 8. PBE-IA. STS-47. Fluid temperatures near back up heater. Quartz substrate underside and ambient vicinity temperatures.

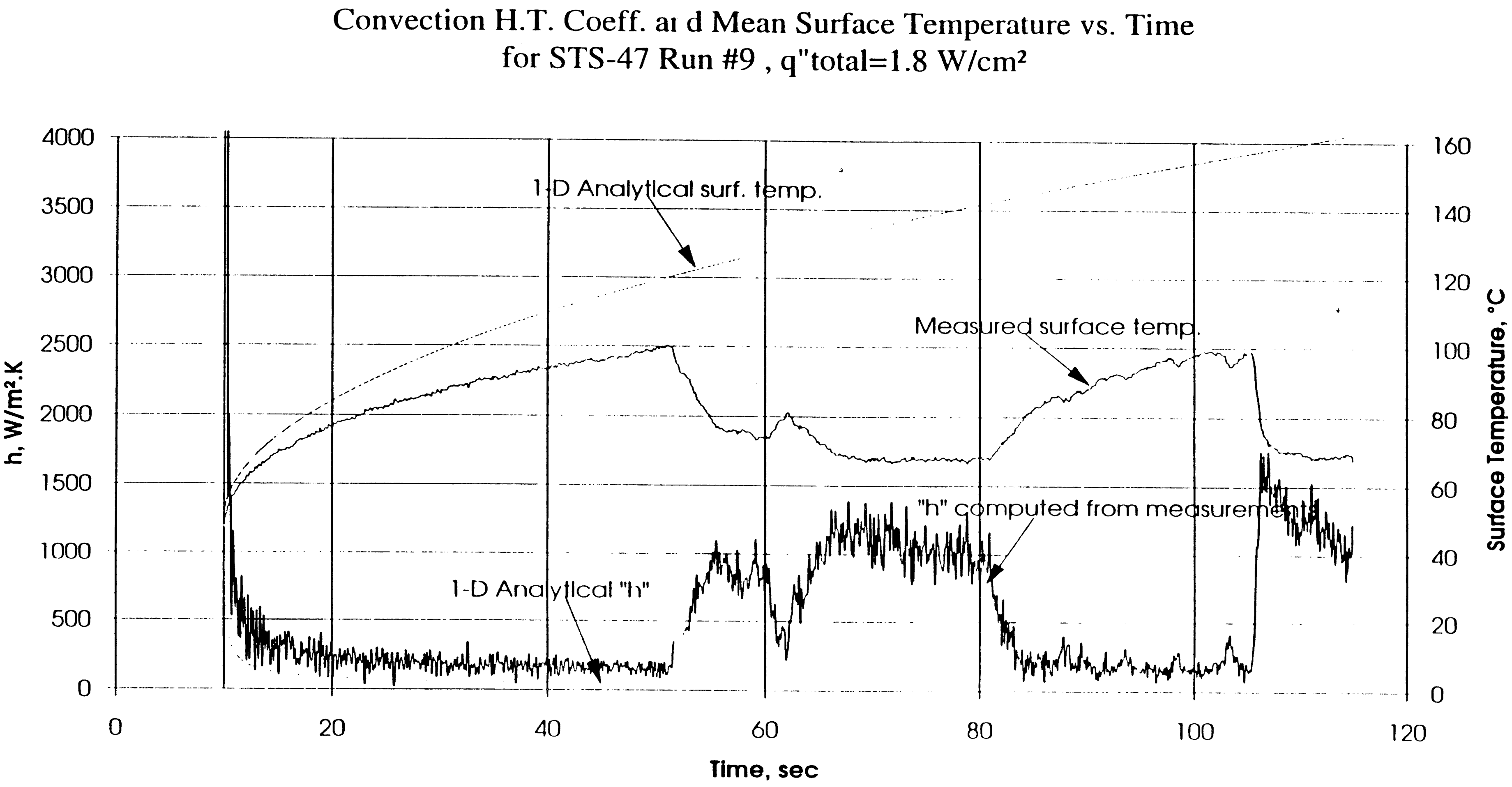
Convection H.T. Coeff. and Mean Surface Temperature vs. Time
for STS-47 Run #9 , q"total=1.8 W/cm²

Figure 5.10a. Run No. 9. PBE-IA. STS-47. Mean heater surface temperature and derived heat transfer coefficient.

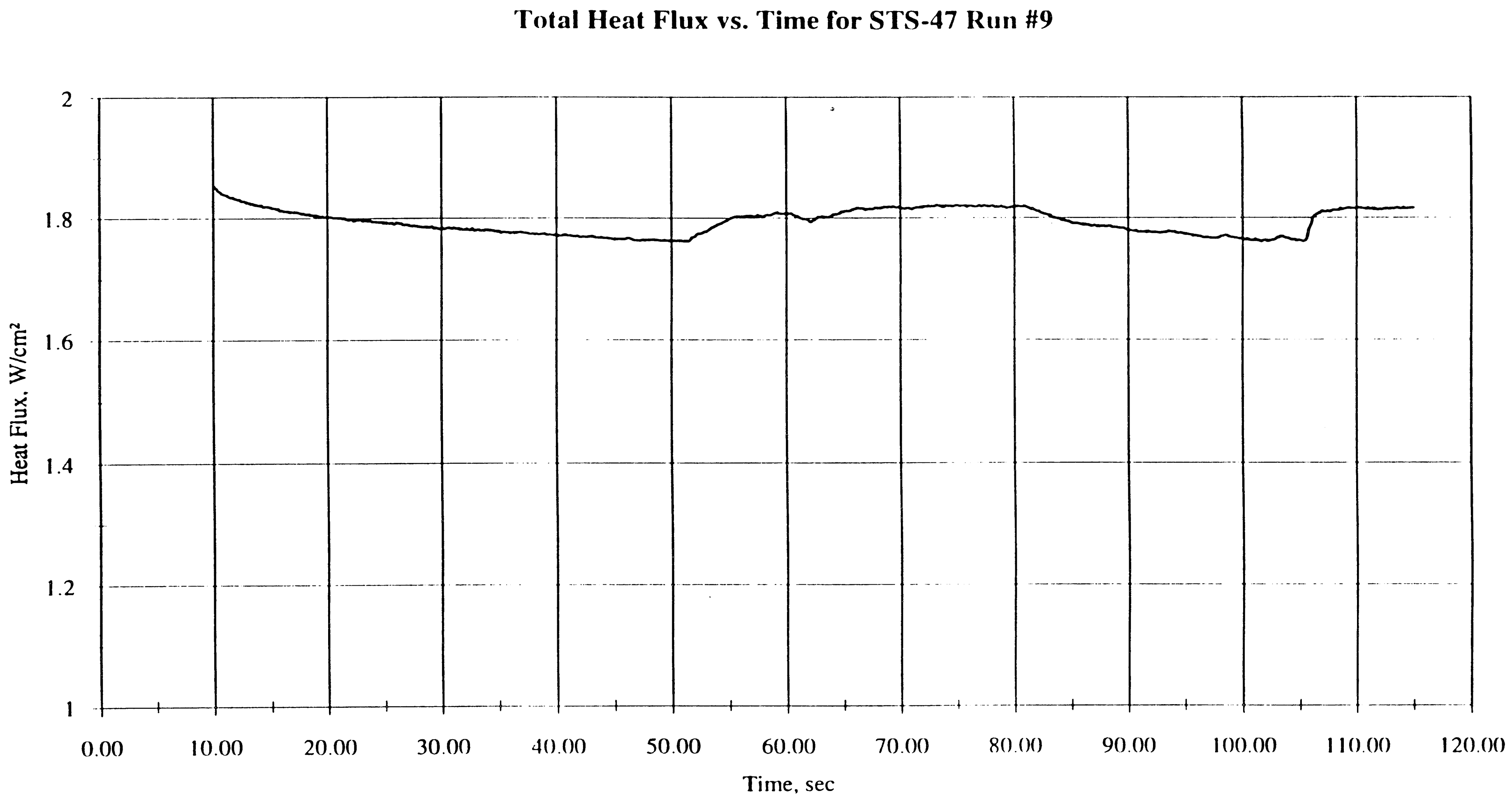

Figure 5.10b. Run No. 9. PBE-IA. STS-47. Heat flux input.

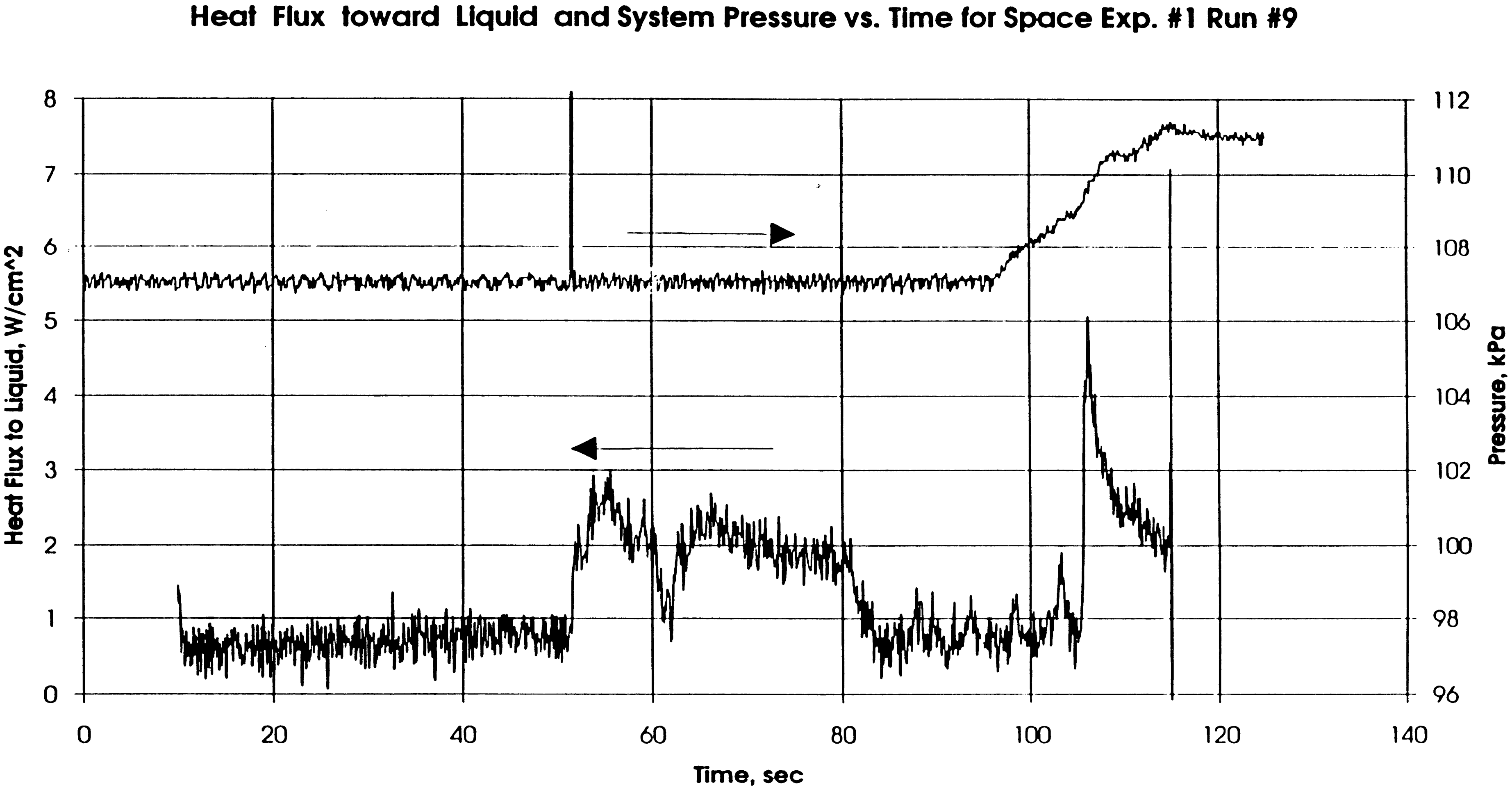

Figure 5.10c. Run No. 9. PBE-IA. STS-47. System pressure and fluid side heat flux.

A. Mean Heater Surface Temperature

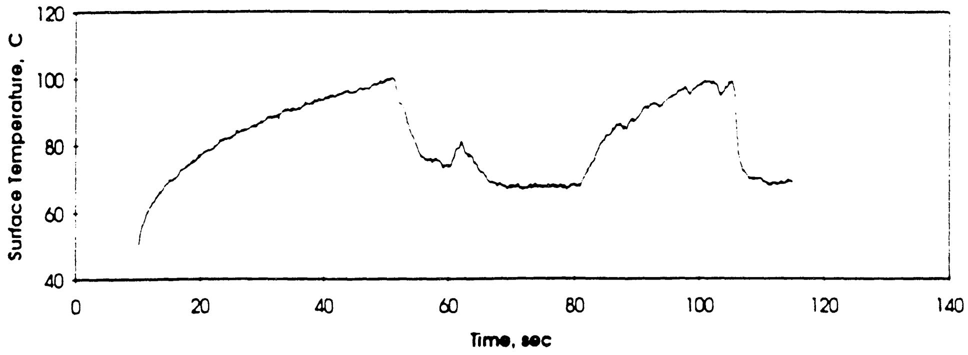

B. Local Fluid Temperatures

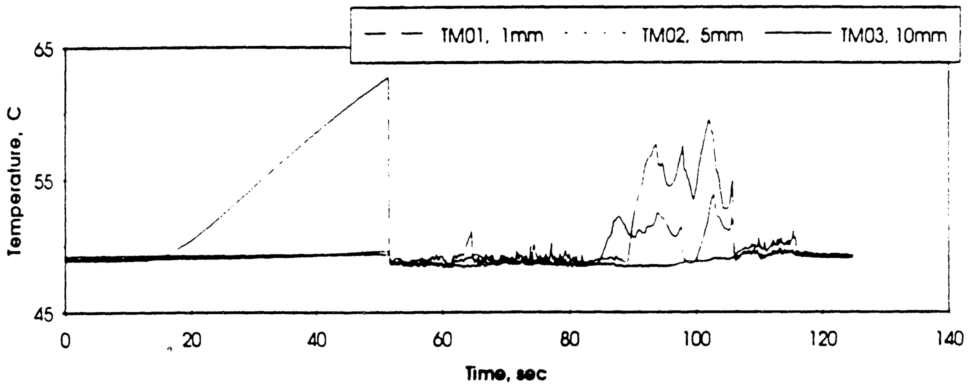

C. Far Field Bulk Temperatures

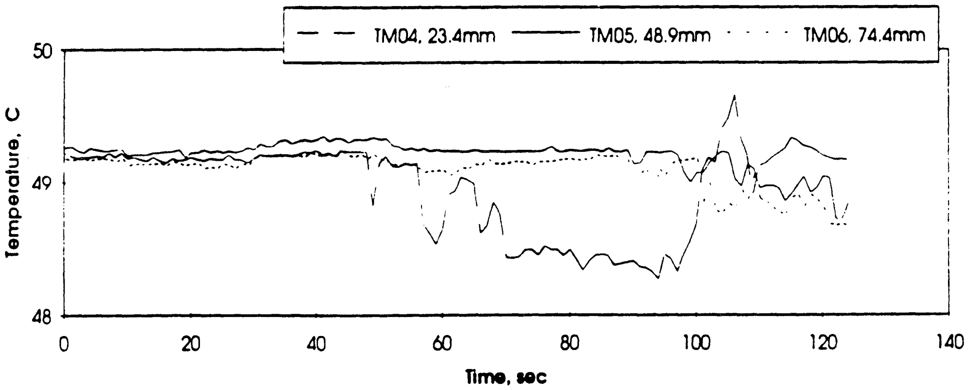

STS 47 - RUN#9

HEAT FLUX	SUBCOOLING (F)	HEATER POWER ON/OFF	100 FPS ON/OFF	STIRRER START	REPRESS START	TOTAL TEST TIME
2	.5 ± .4	10-115 sec.	30-50 sec.	105 sec.	--------	125 sec.

Figure 5.10d. Run No. 9. PBE-IA. STS-47. Fluid temperatures near primary heater and far field bulk.

A. Mean Heater Surface Temperature

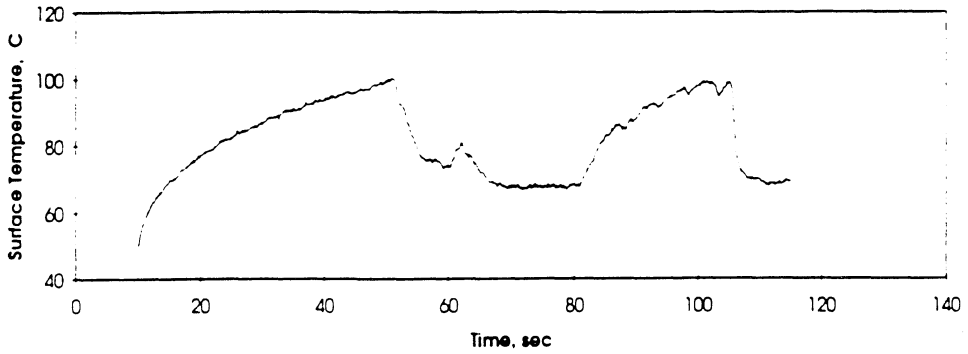

D.

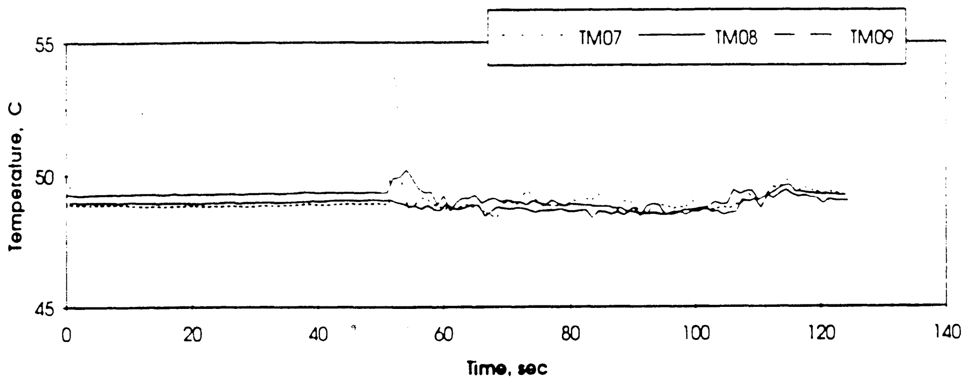

E.

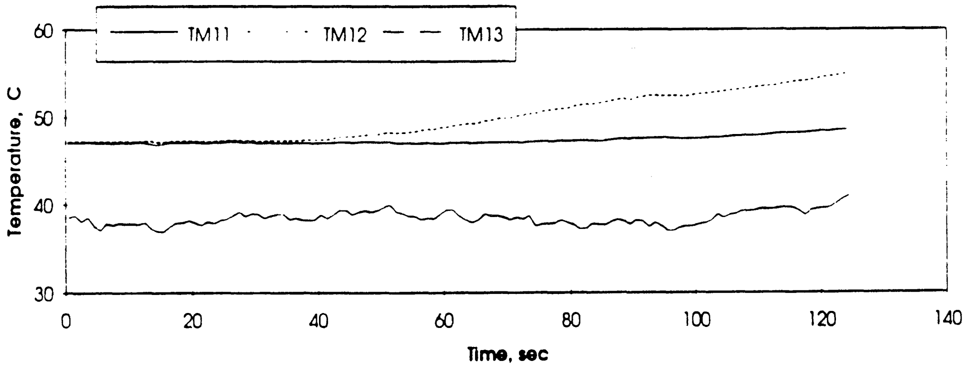

STS 47 - RUN #9

HEAT FLUX	SUBCOOLING (F)	HEATER POWER ON/OFF	100 FPS ON/OFF	STIRRER START	REPRESS START	TOTAL TEST TIME
2	.5 ± .4	10-115 sec.	30-50 sec.	105 sec.	--------	125 sec.

Figure 5.10e. Run No. 9. PBE-IA. STS-47. Fluid temperatures near back up heater. Quartz substrate underside and ambient vicinity temperatures.

STS-47 Run #1

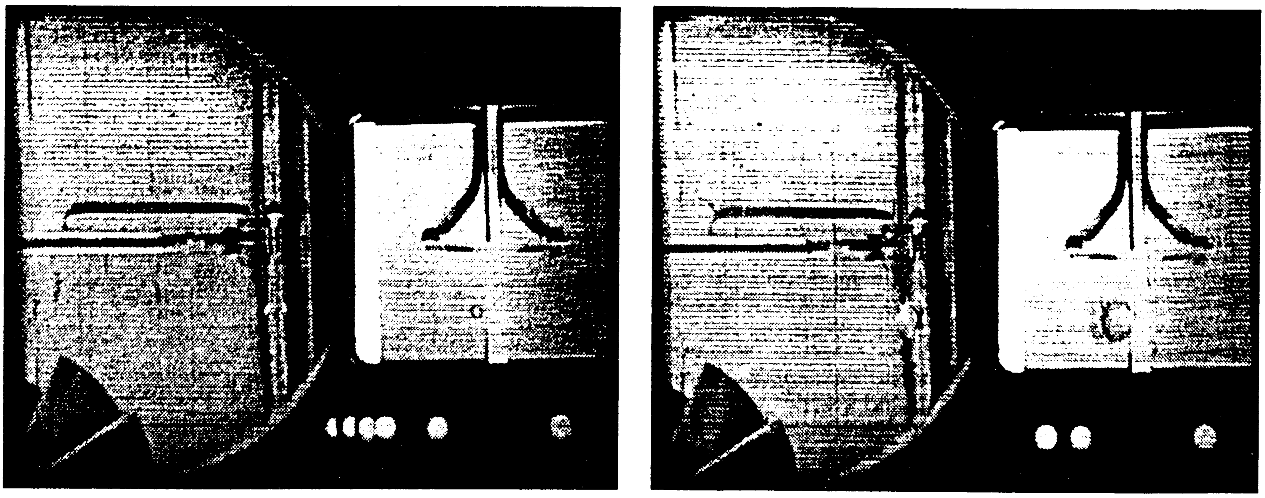

Frame#0158 time=11.58 sec. Frame#0161 time=11.60 sec.

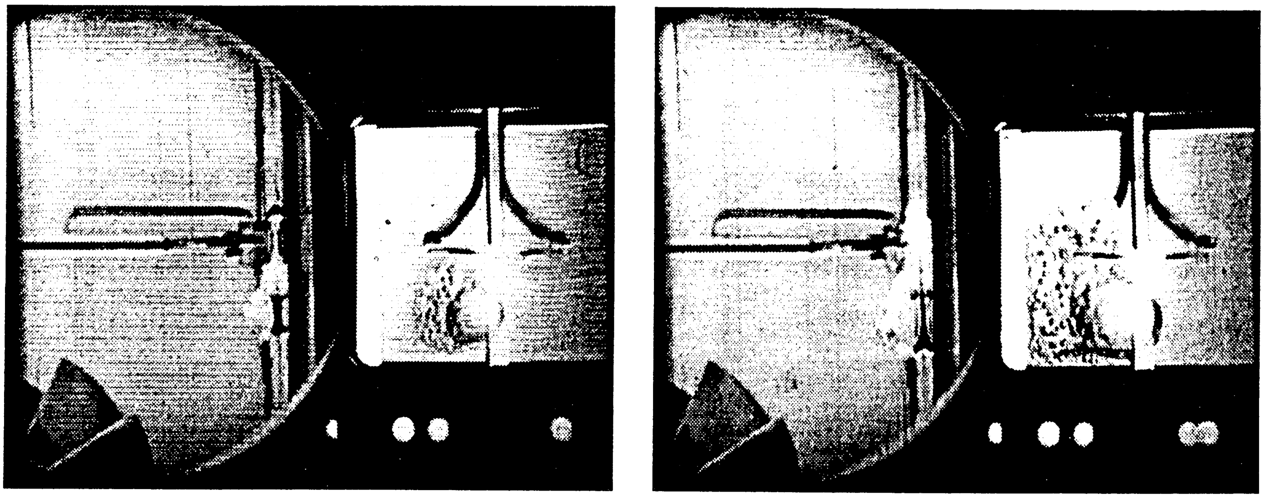

Frame#0163 time=11.62 sec. Frame#0166 time=11.65 sec.

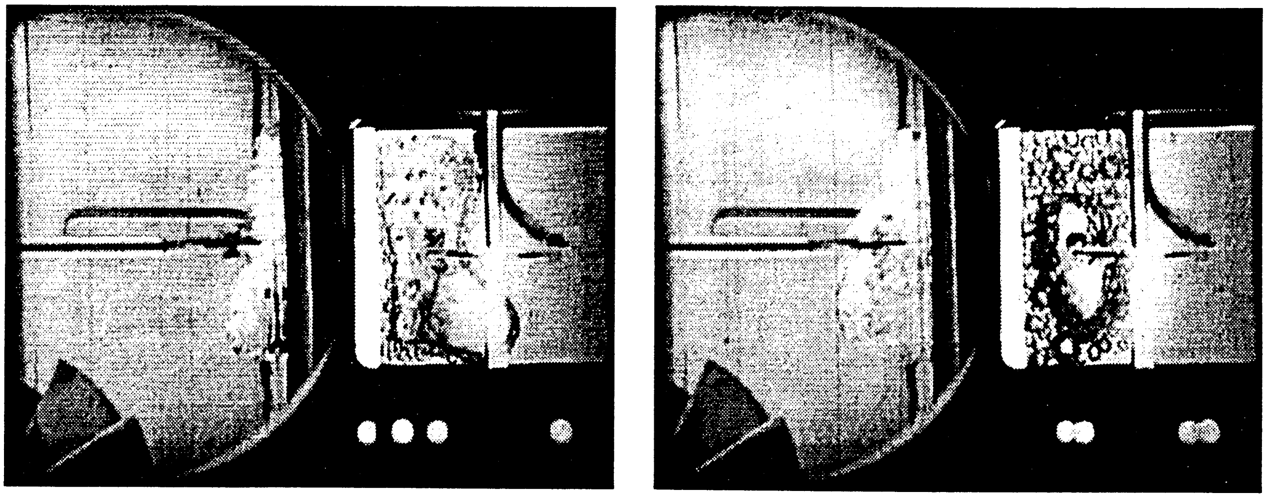

Frame#0169 time=11.68 sec. Frame#0194 time=11.93 sec.

Figure 5.11. Run No. 1. PBE-IA. STS-47. Selected Photographic Images.

STS-47 Run #1

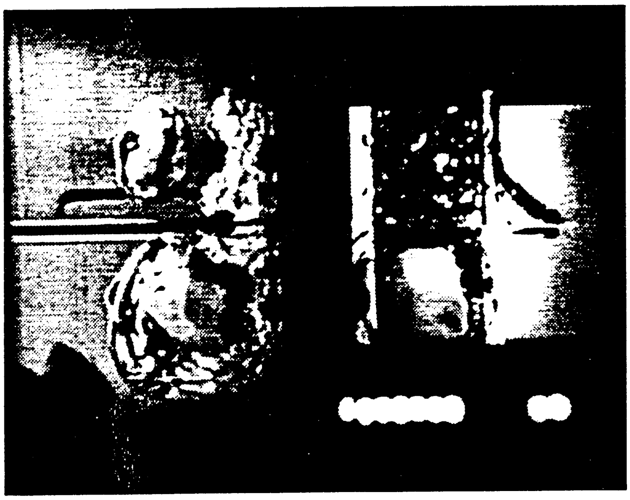

Frame#0511 time=15.09 sec.

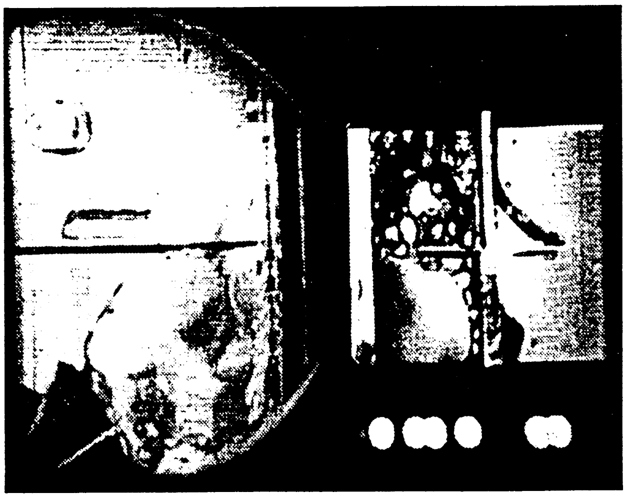

Frame#0000 time=17.20 sec.

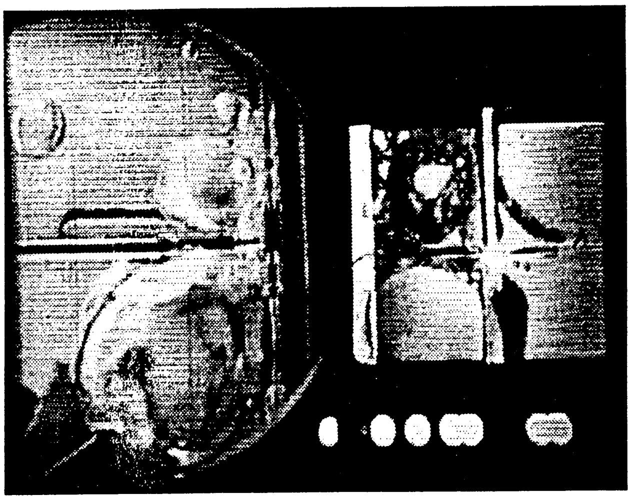

Frame#0013 time=18.50 sec.

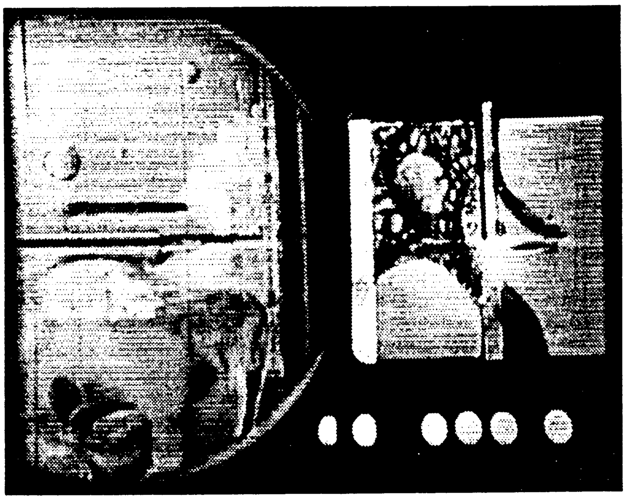

Frame#0742 time=36.98 sec.

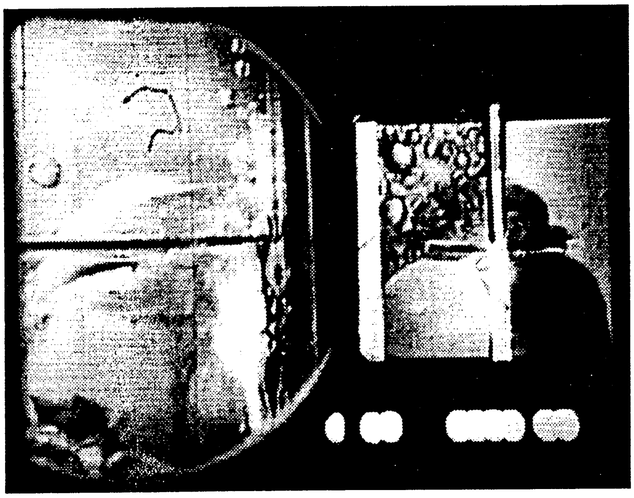

Frame#0859 time=48.67 sec.

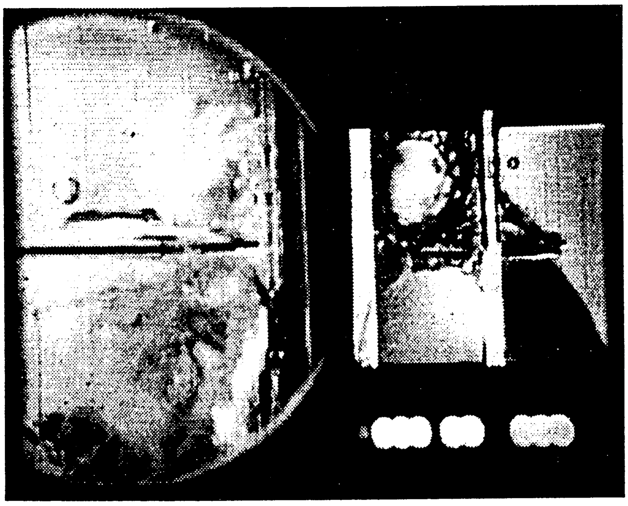

Frame#0970 time=59.77 sec.

Figure 5.11. Continued.

STS-47 Run #2

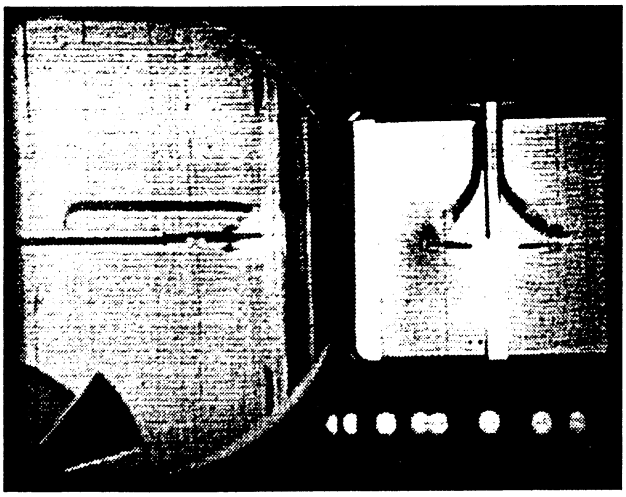
Frame#0783 time=22.38 sec.

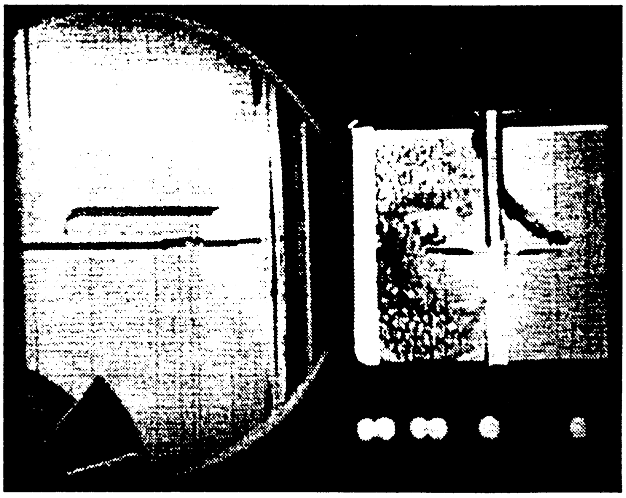
Frame#0784 time=22.39 sec.

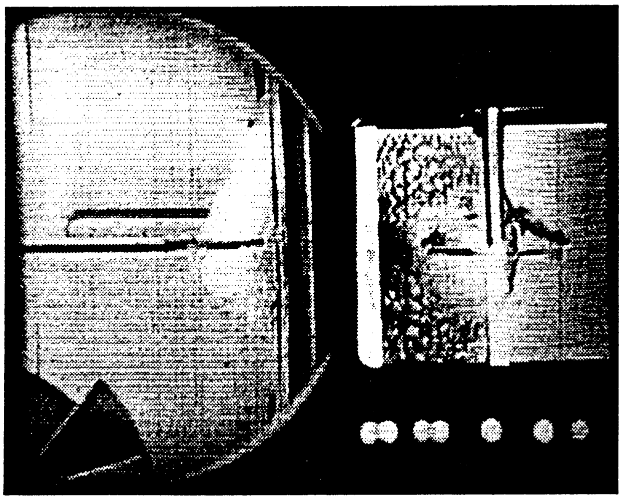
Frame#0785 time=22.40 sec.

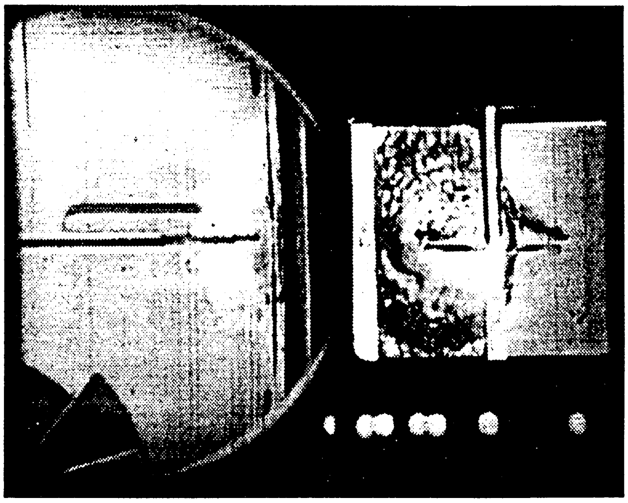
Frame#0786 time=22.41 sec.

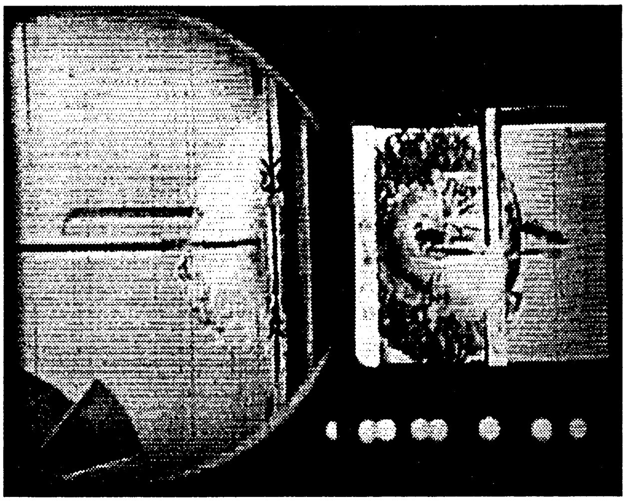
Frame#0787 time=22.42 sec.

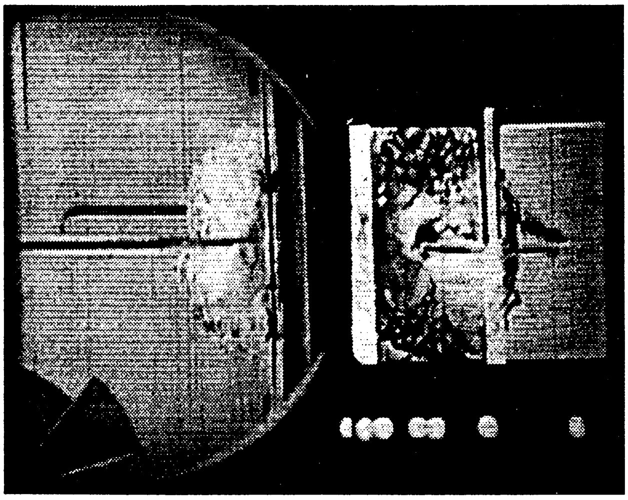
Frame#0788 time=22.43 sec.

Figure 5.12. Run No. 2. PBE-IA. STS-47. Selected Photographic Images.

STS-47 Run #2

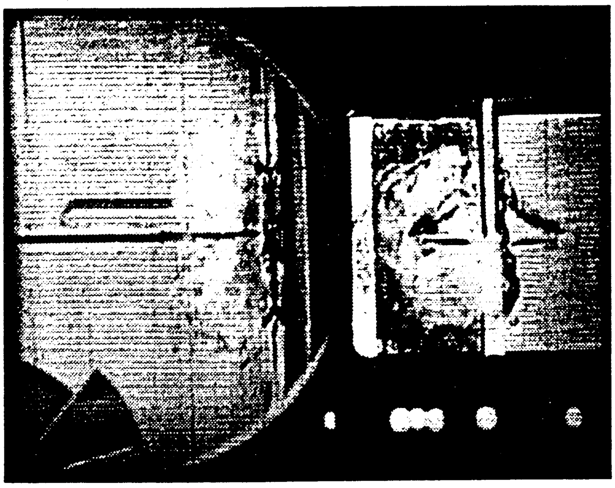
Frame#0795 time=22.50 sec.

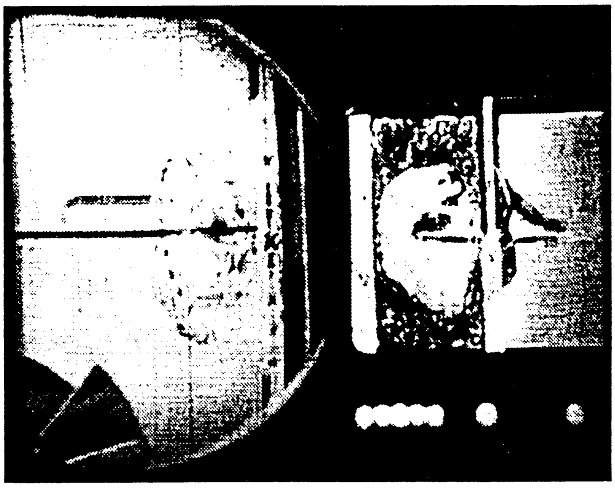
Frame#0817 time=22.72 sec.

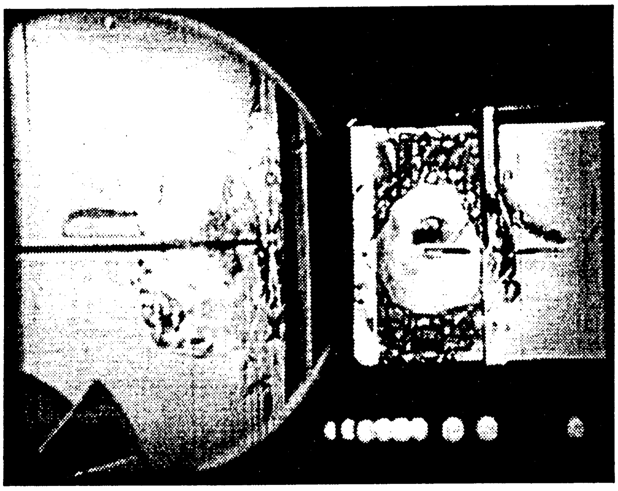
Frame#0952 time=24.06 sec.

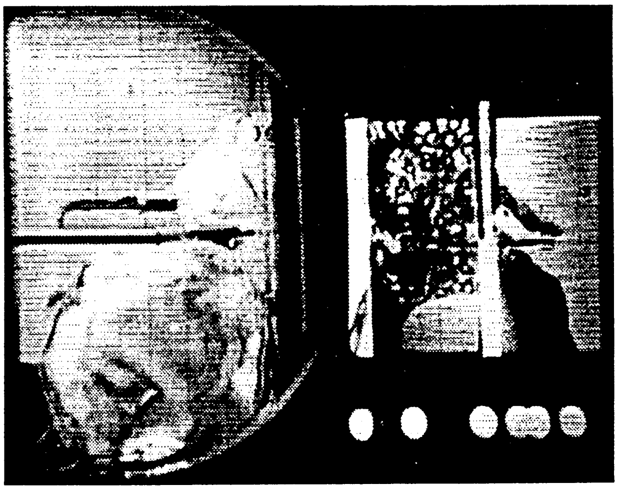
Frame#0385 time=61.93 sec.

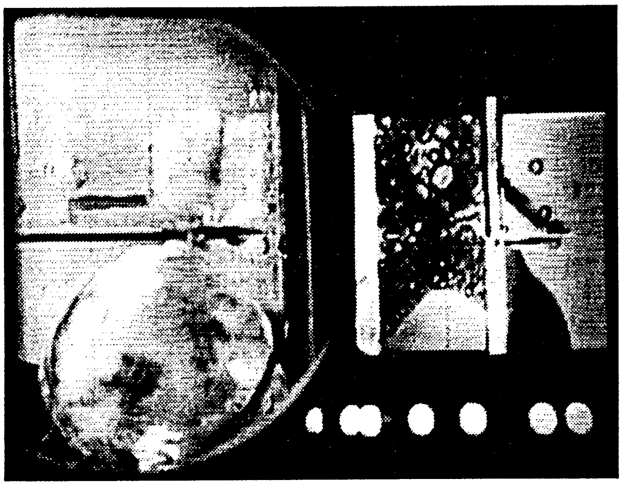
Frame#0744 time=97.81 sec.

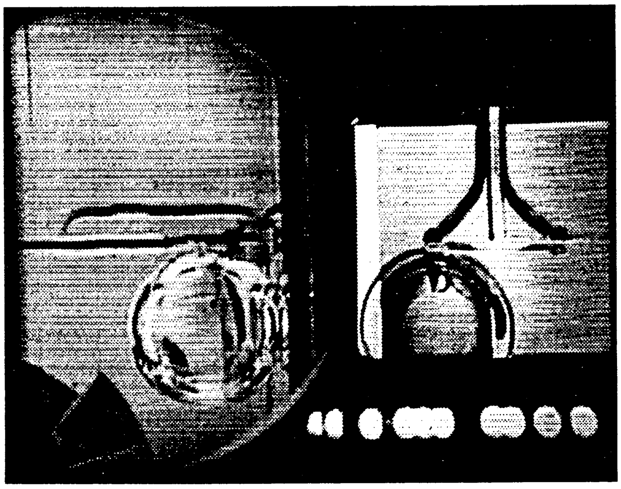
Frame#1016 time=124.99 sec.

Figure 5.12. Continued.

STS-47 Run #3

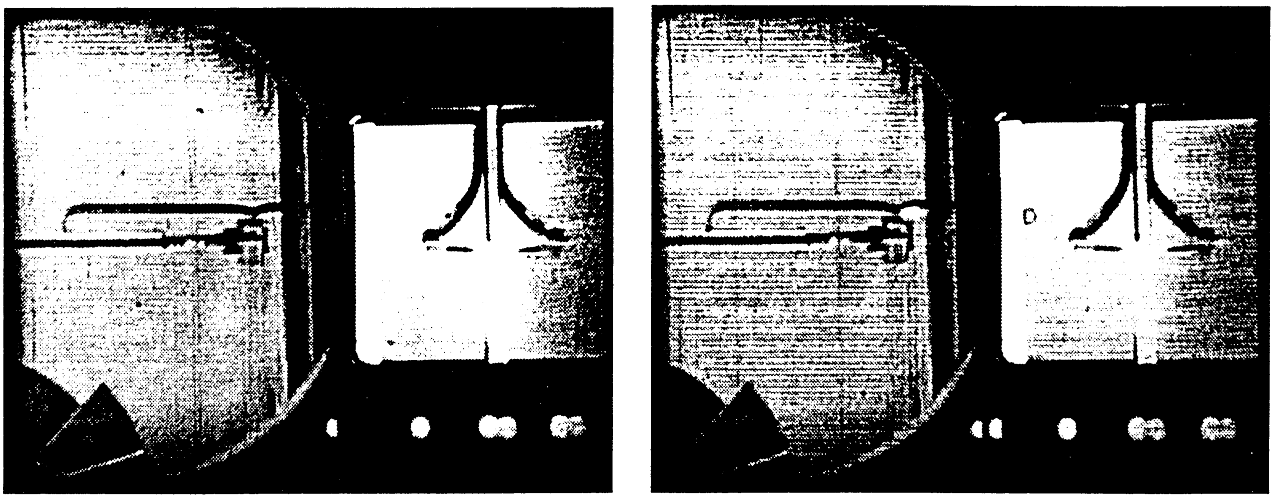

Frame#1233 time=41.39 sec. Frame#1236 time=41.42 sec.

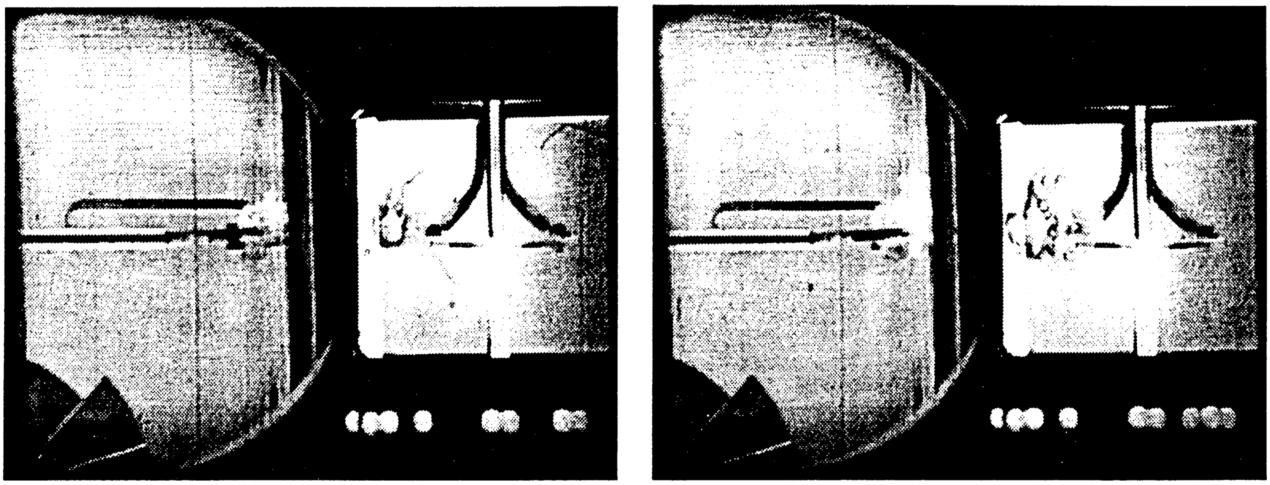

Frame#1258 time=41.64 sec. Frame#1259 time=41.65 sec.

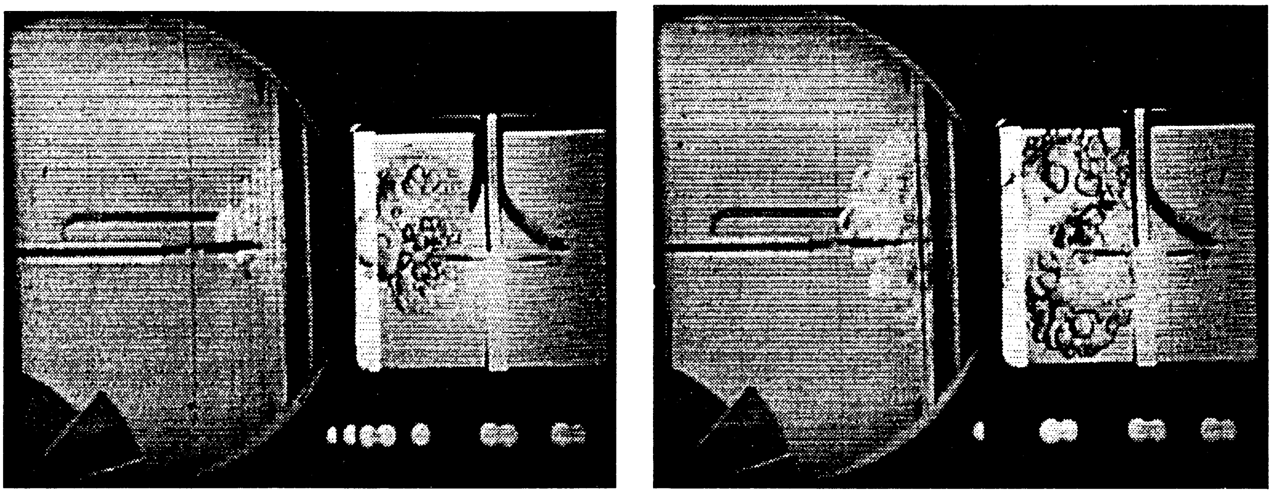

Frame#1260 time=41.66 sec. Frame#1264 time=41.70 sec.

Figure 5.13. Run No. 3. PBE-IA. STS-47. Selected Photographic Images.

STS-47 Run #3

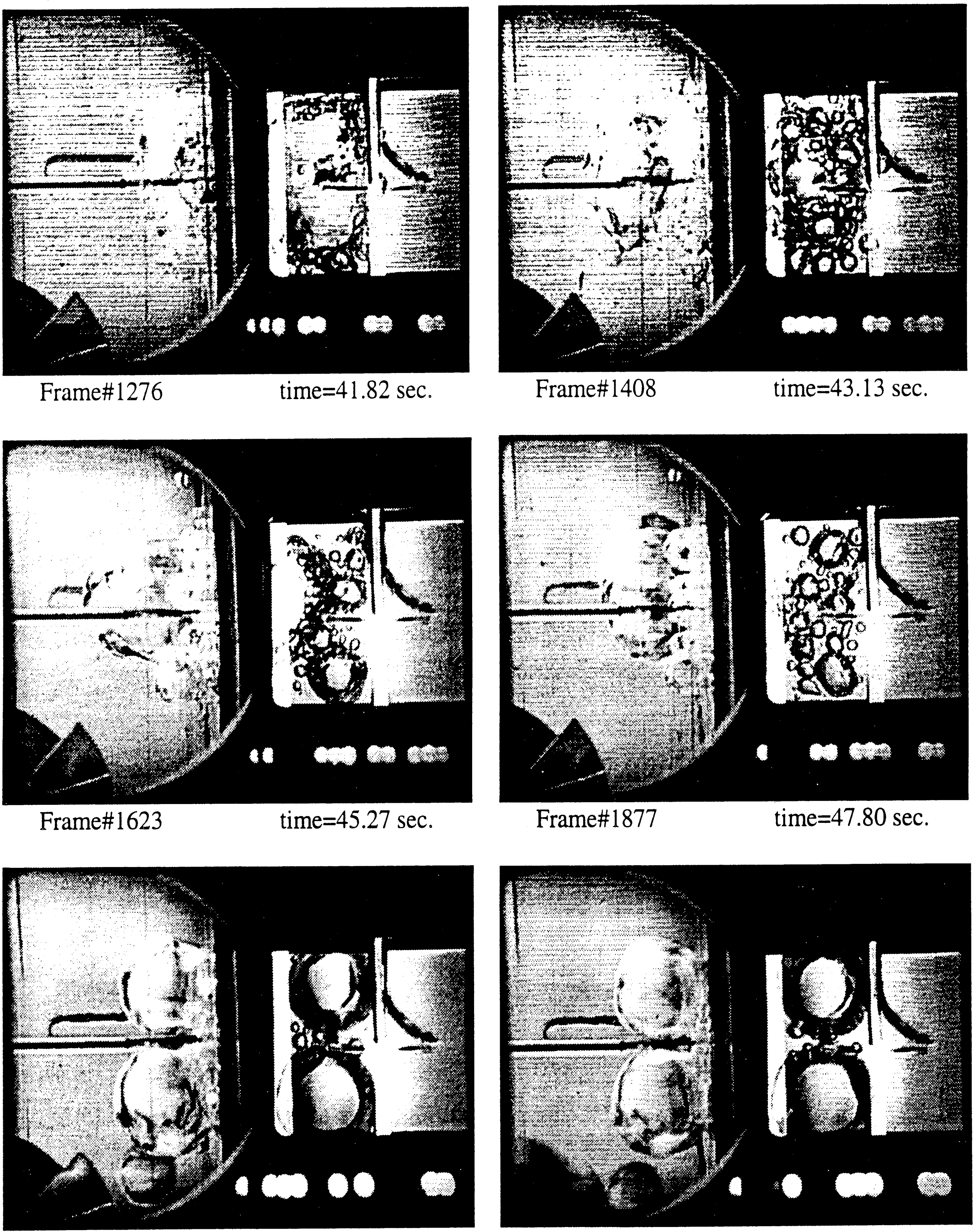

Frame#1276 time=41.82 sec.

Frame#1408 time=43.13 sec.

Frame#1623 time=45.27 sec.

Frame#1877 time=47.80 sec.

Frame#2603 time=98.60 sec.

Frame#2717 time=110.00 sec.

Figure 5.13. Continued.

STS-47 Run #4

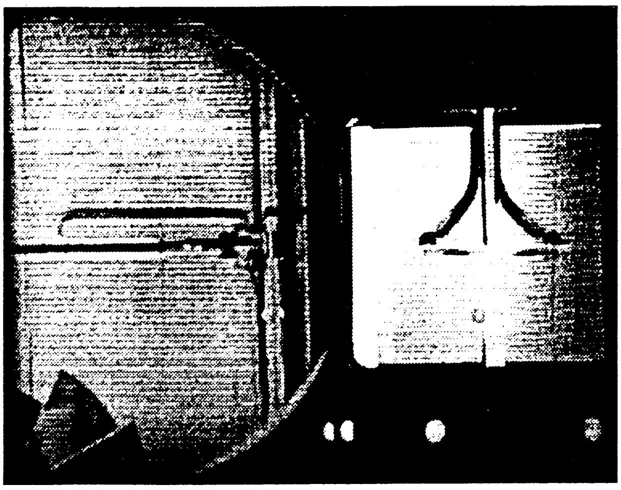
Frame#0134 time=11.34 sec.

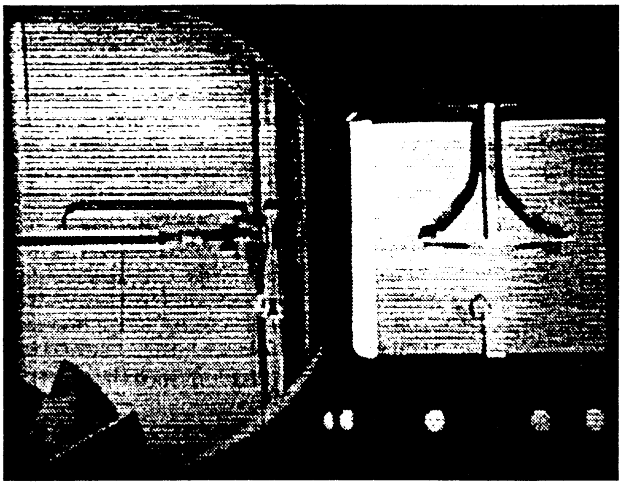
Frame#0135 time=11.35 sec.

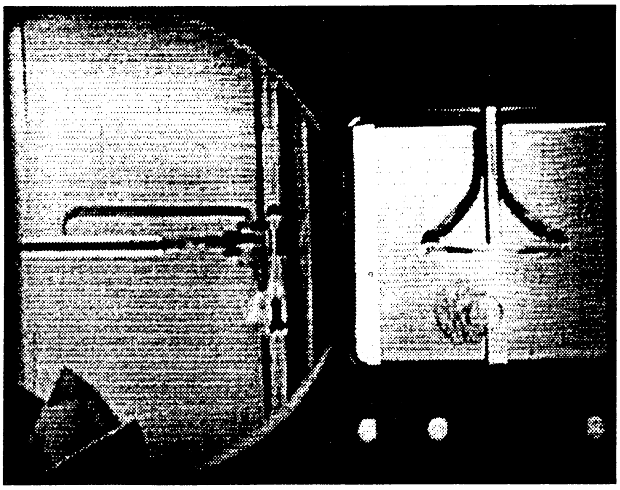
Frame#0136 time=11.36 sec.

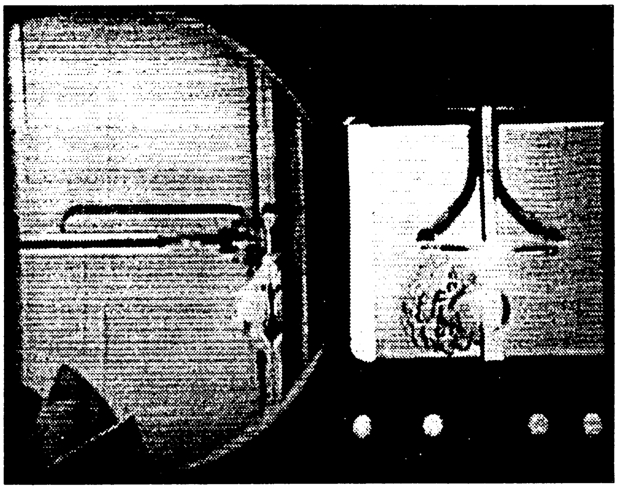
Frame#0137 time=11.37 sec.

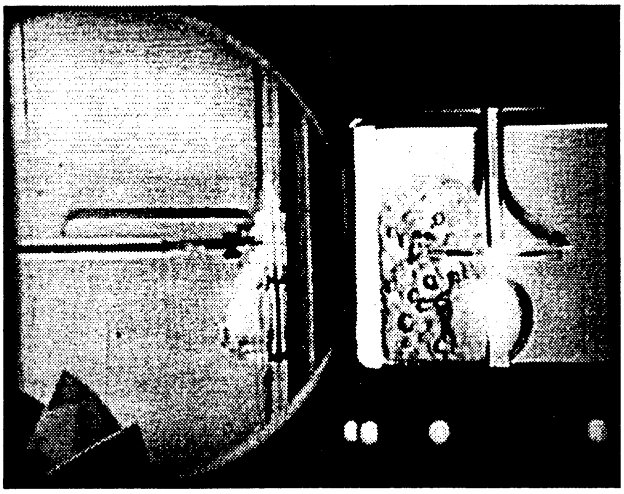
Frame#0140 time=11.40 sec.

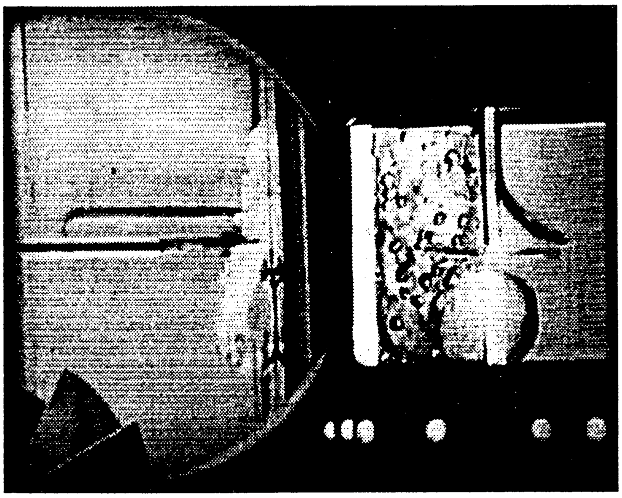
Frame#0143 time=11.43 sec.

Figure 5.14. Run No. 4. PBE-IA. STS-47. Selected Photographic Images.

STS-47 Run #4

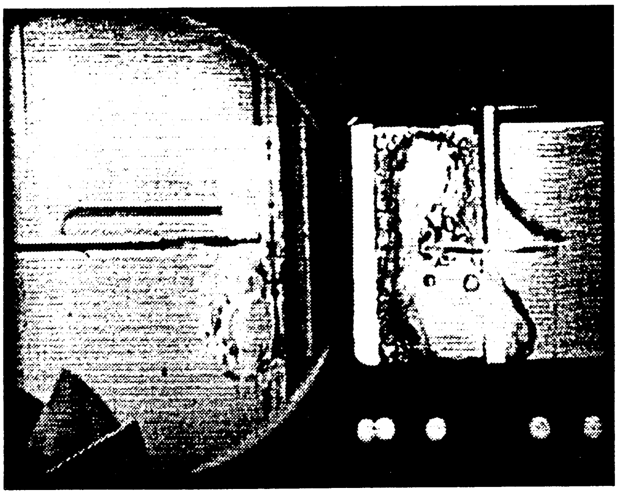

Frame#0153 time=11.53 sec.

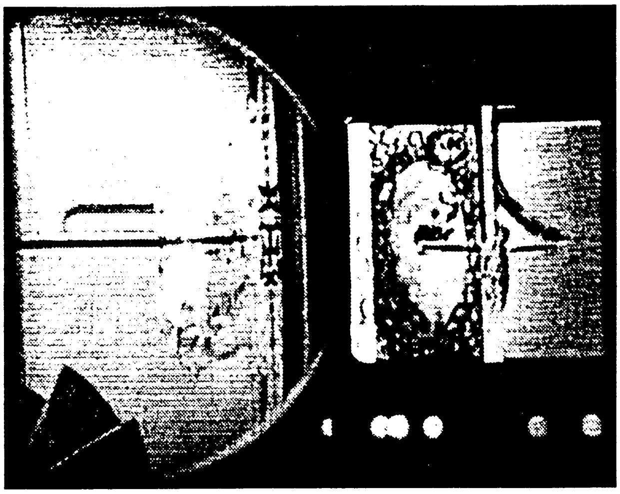

Frame#0179 time=11.79 sec.

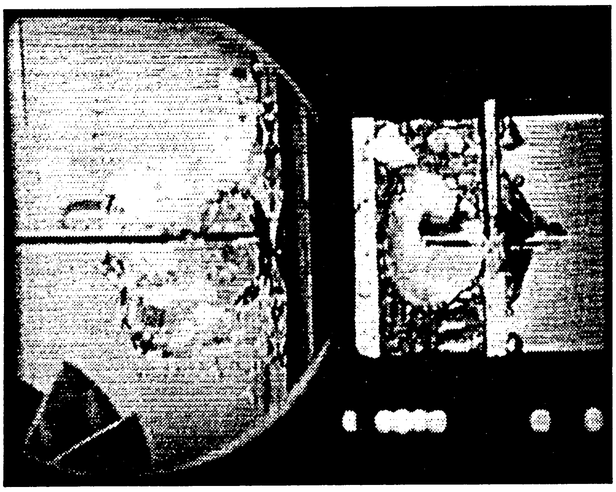

Frame#0245 time=12.45 sec.

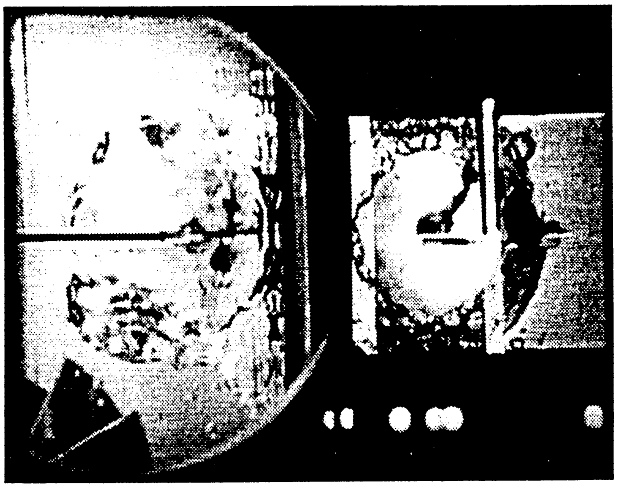

Frame#0423 time=14.22 sec.

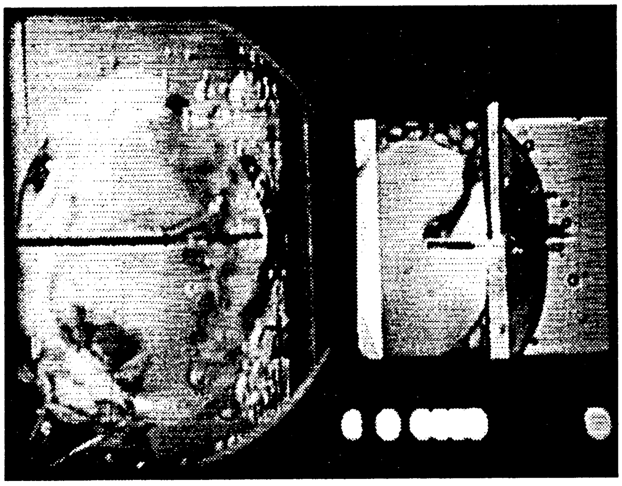

Frame#0567 time=19.82 sec.

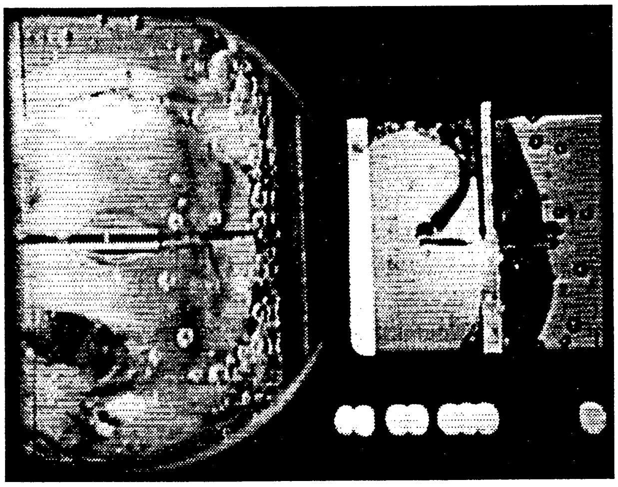

Frame#0092 time=29.00 sec.

Figure 5.14. Continued.

STS-47 Run #5

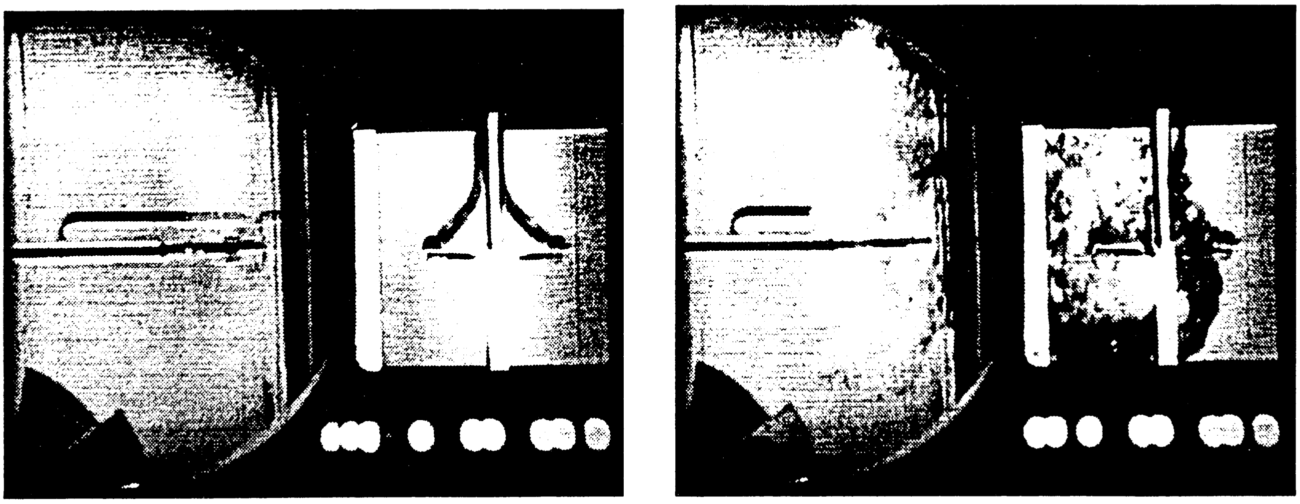

Frame#2098 time=26.15 sec. Frame#2099 time=26.25 sec.

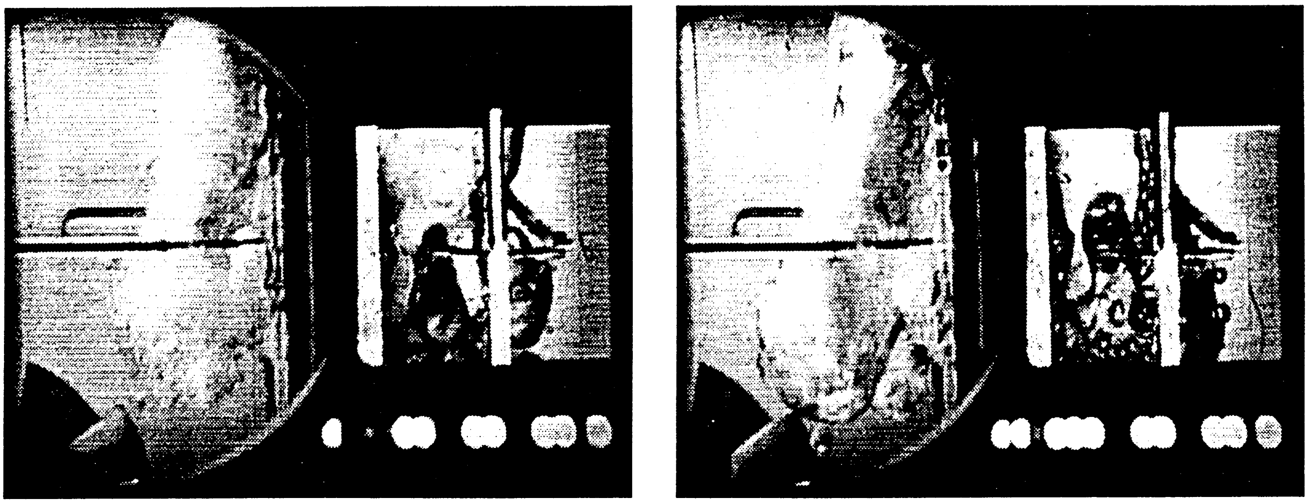

Frame#2100 time=26.35 sec. Frame#2102 time=26.55 sec.

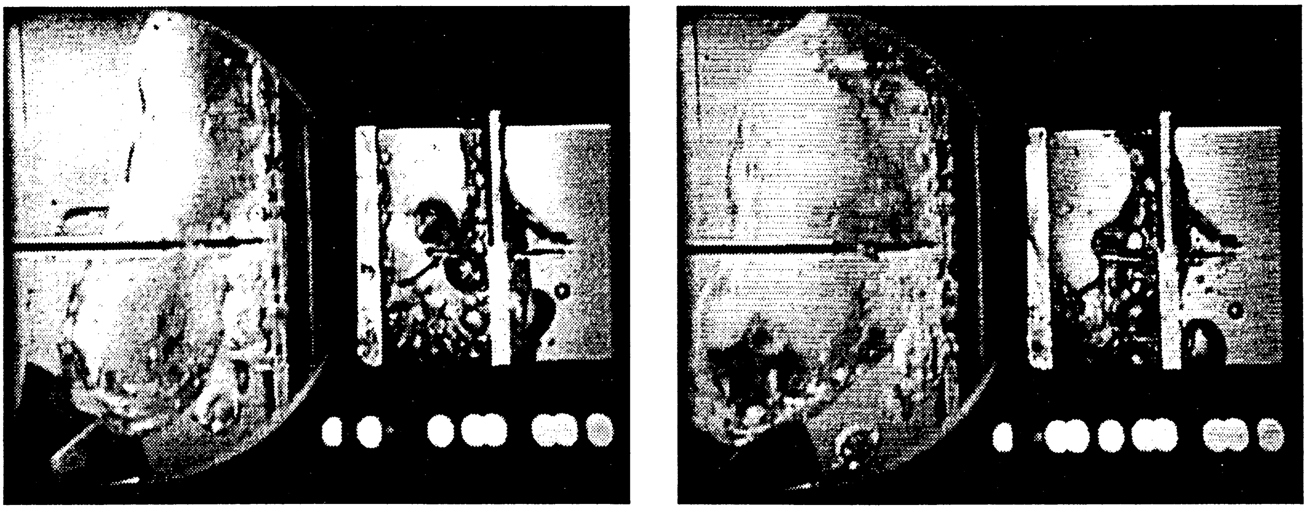

Frame#2104 time=26.75 sec. Frame#2108 time=27.15 sec.

Figure 5.15. Run No. 5. PBE-IA. STS-47. Selected Photographic Images.

STS-47 Run #5


Frame#2111 time=27.45 sec. Frame#2119 time=28.25 sec.

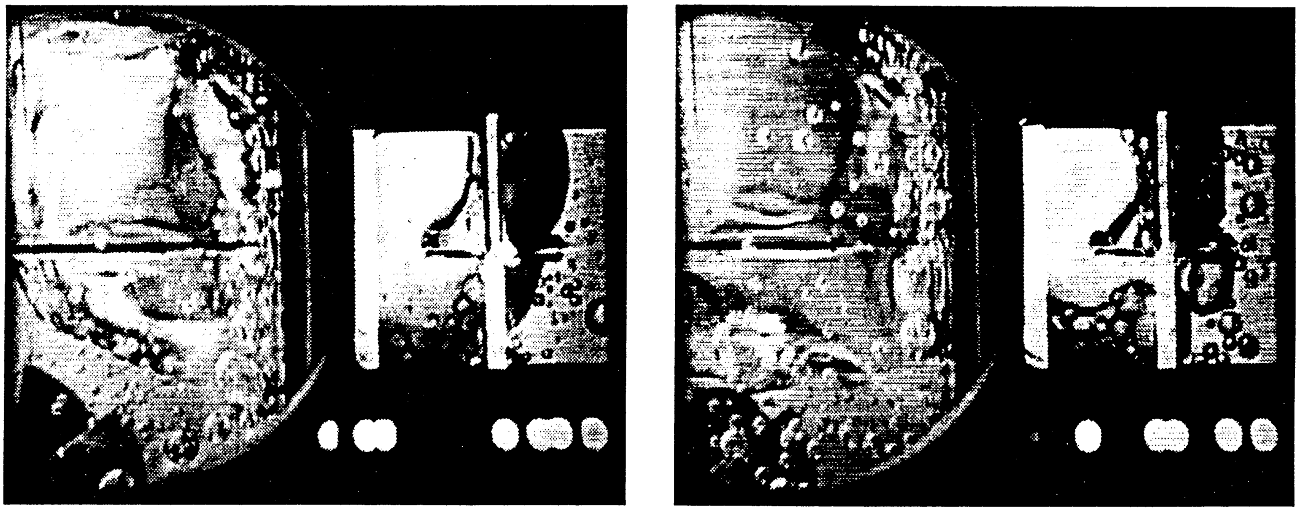
Frame#2144 time=30.75 sec. Frame#2250 time=41.36 sec.

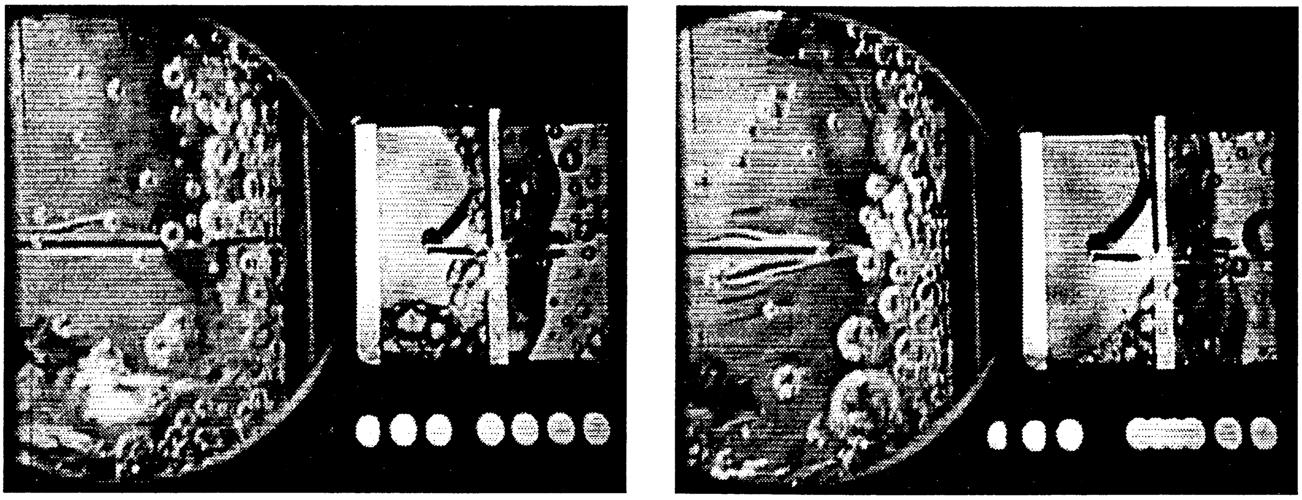
Frame#2465 time=62.88 sec. Frame#2708 time=86.22 sec.

Figure 5.15. Continued.

STS-47 Run #6

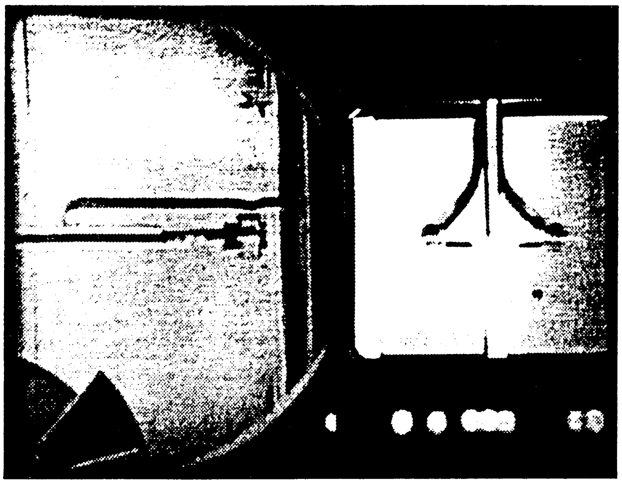

Frame#1843 time=47.46 sec.

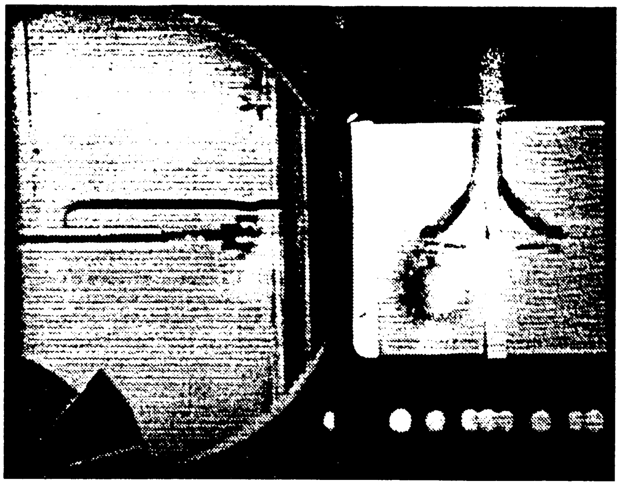

Frame#1844 time=47.47 sec.

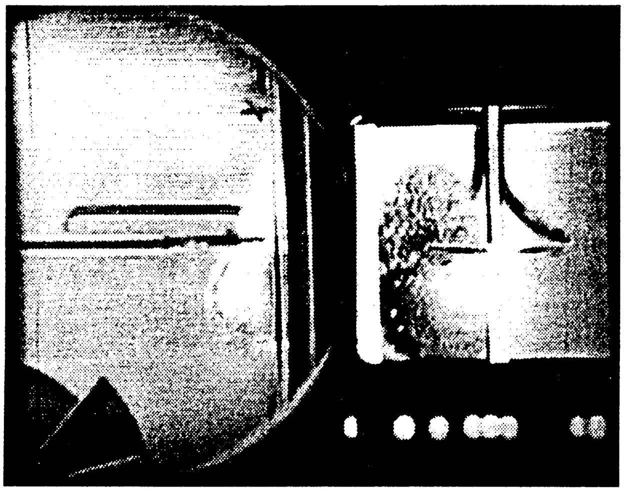

Frame#1845 time=47.48 sec.

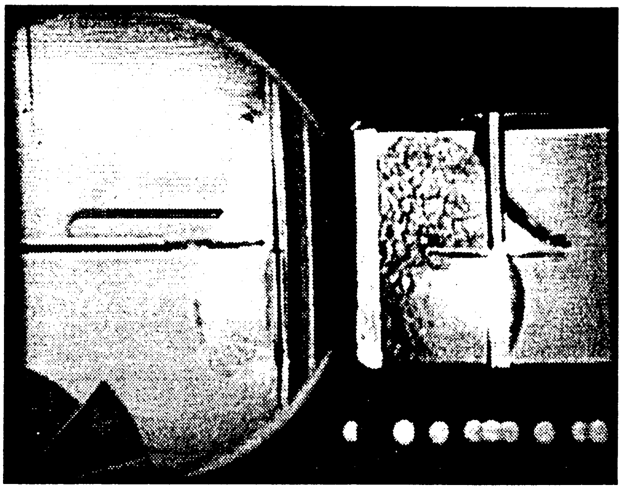

Frame#1846 time=47.49 sec.

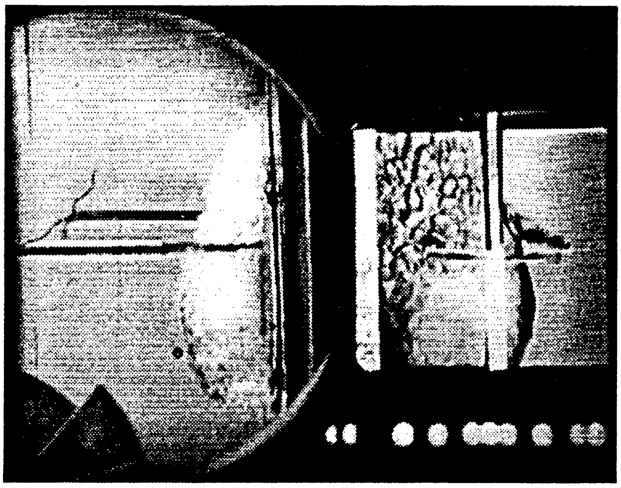

Frame#1848 time=47.51 sec.

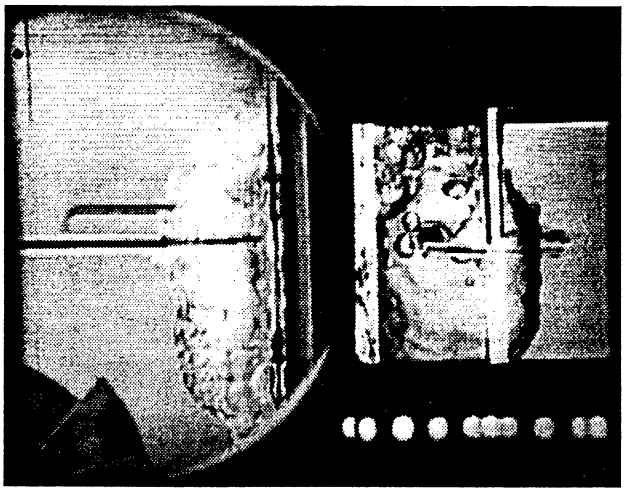

Frame#1854 time=47.57 sec.

Figure 5.16. Run No. 6. PBE-IA. STS-47. Selected Photographic Images.

STS-47 Run #6

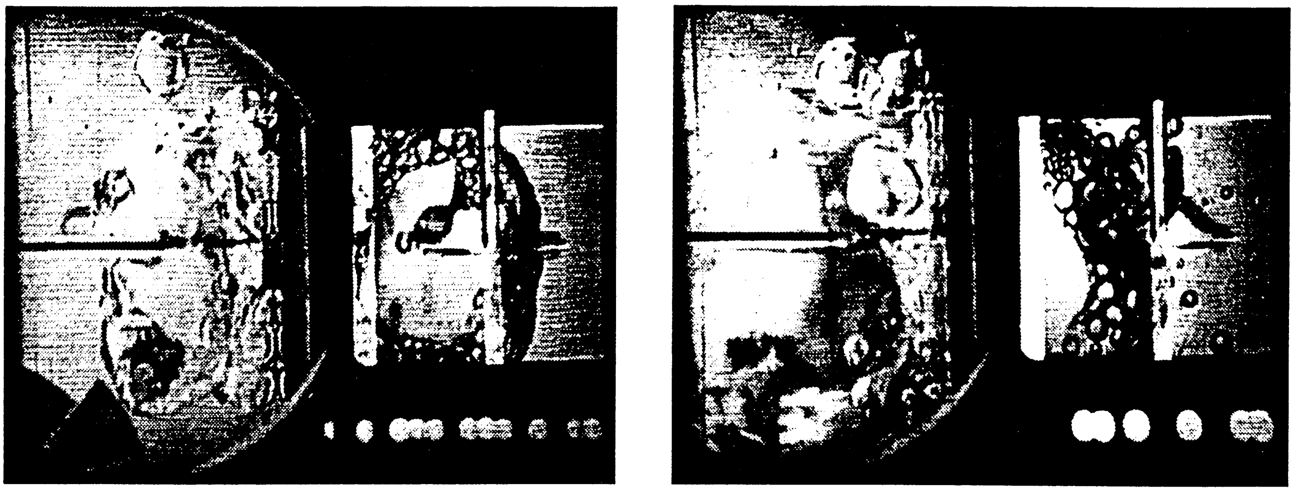
Frame#1916 time=48.19 sec.
Frame#2195 time=58.00 sec.

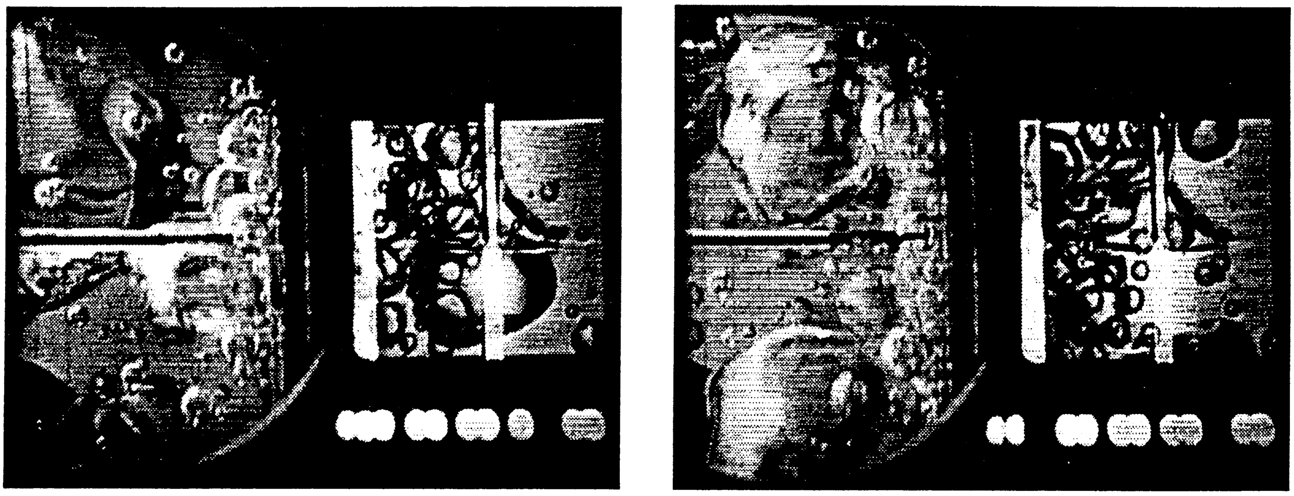
Frame#2300 time=68.52 sec.
Frame#2416 time=80.14 sec.

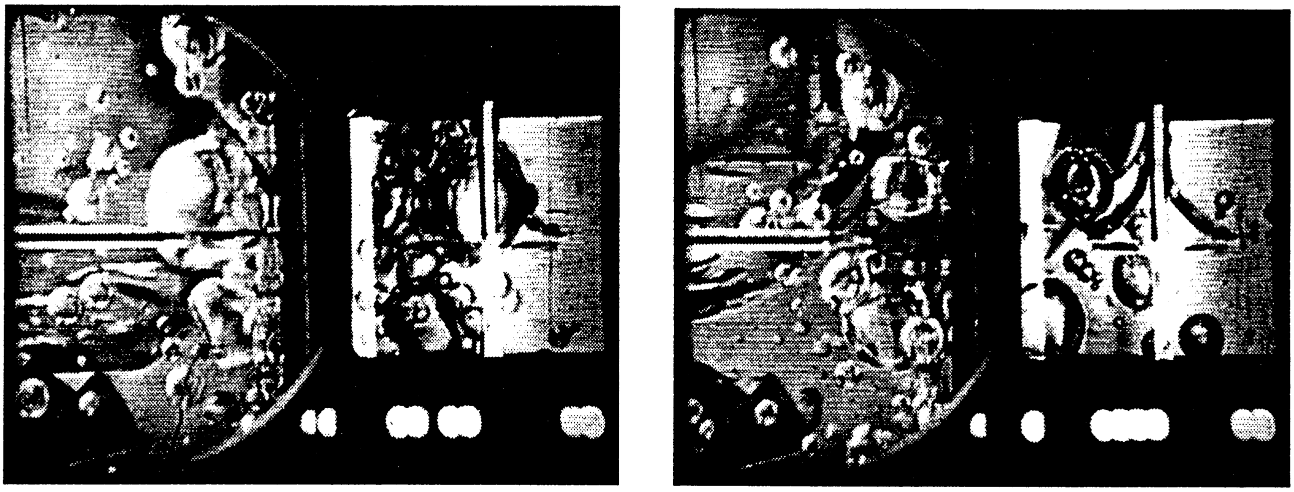
Frame#2620 time=100.58 sec.
Frame#2726 time=111.20 sec.

Figure 5.16. Continued.

STS-47 Run #7

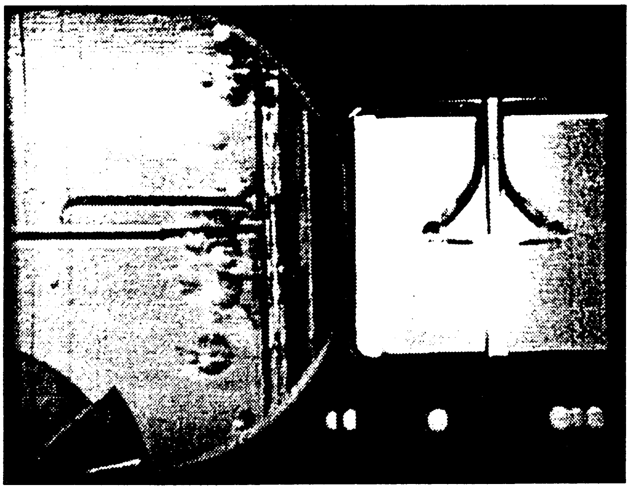

Frame#0164 time=11.34 sec.

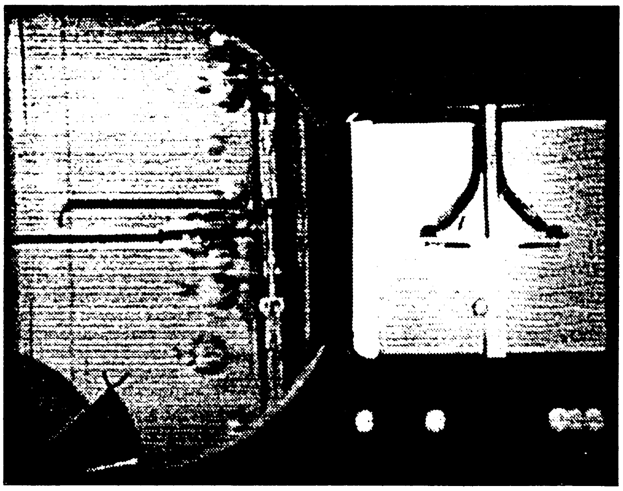

Frame#0166 time=11.36 sec.

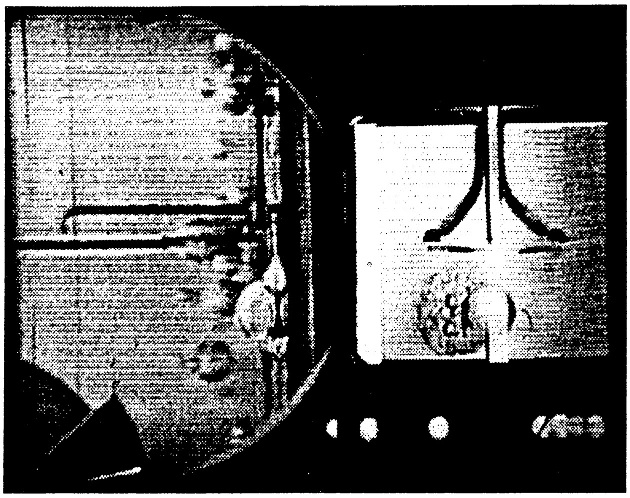

Frame#0169 time=11.39 sec.

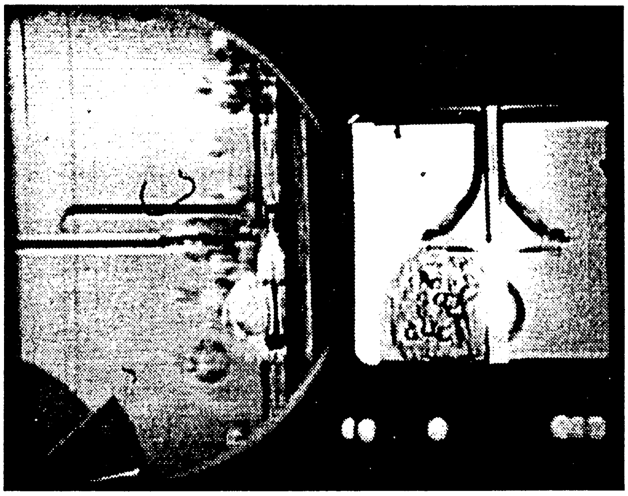

Frame#0170 time=11.40 sec.

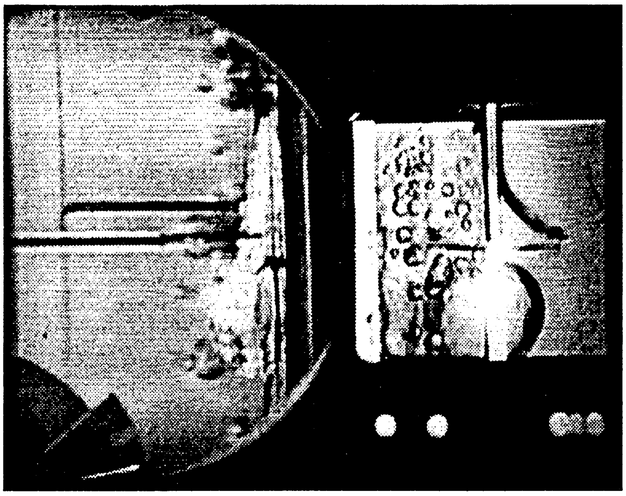

Frame#0174 time=11.44 sec.

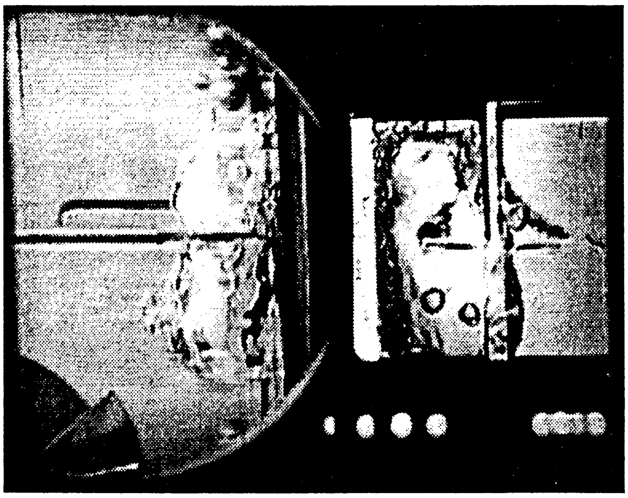

Frame#0201 time=11.71 sec.

Figure 5.17. Run No. 7. PBE-IA. STS-47. Selected Photographic Images.

STS-47 Run #7

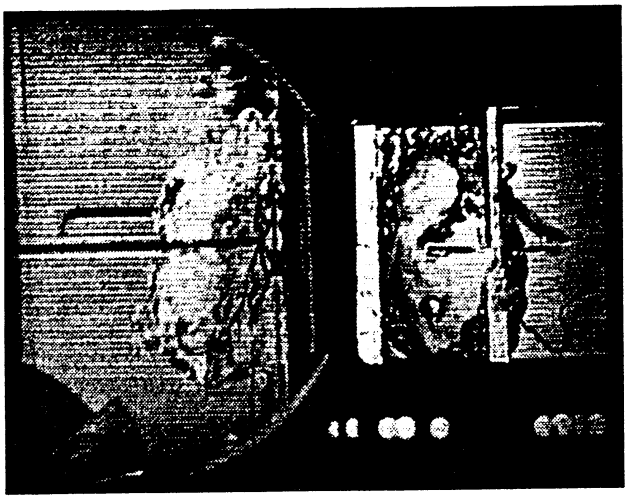
Frame#0213 time=11.83 sec.

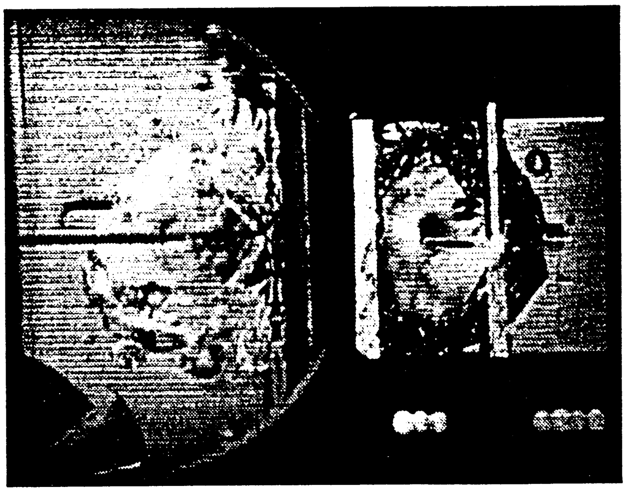
Frame#0256 time=12.24 sec.

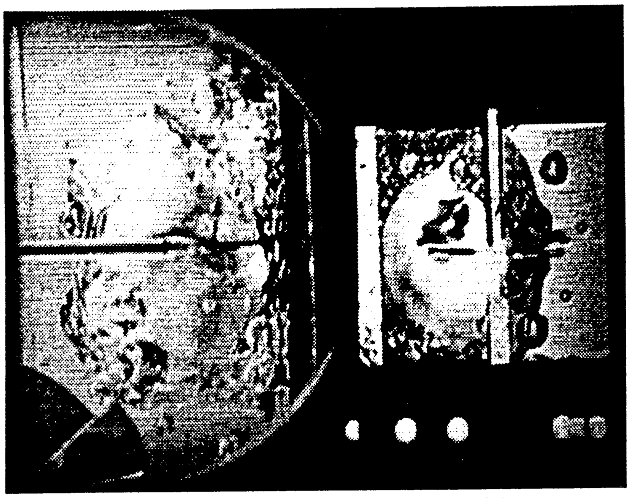
Frame#0323 time=12.92 sec.

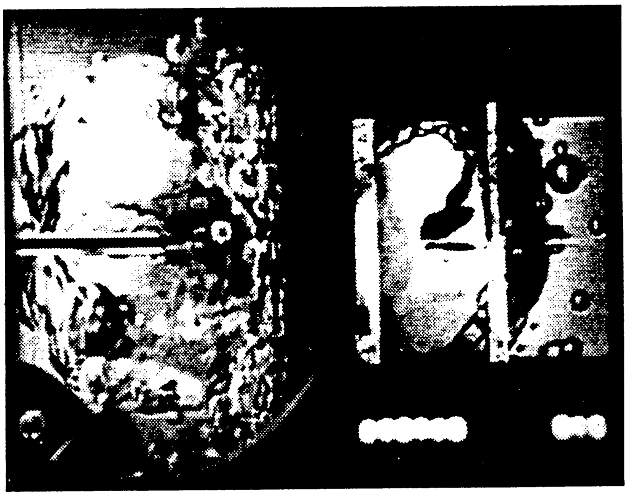
Frame#0536 time=15.04 sec.

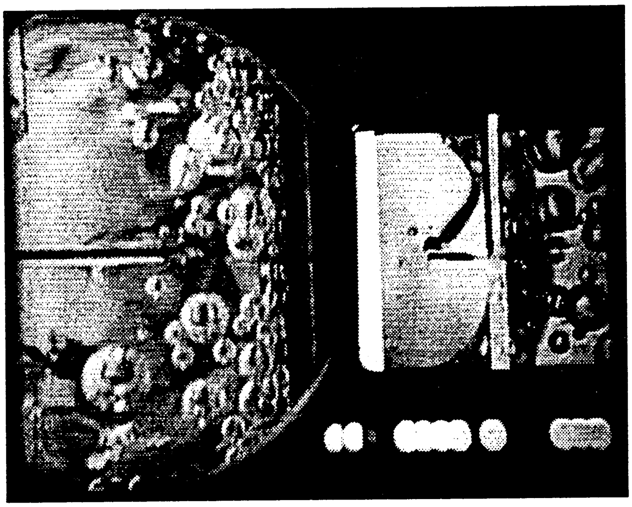
Frame#0650 time=25.10 sec.

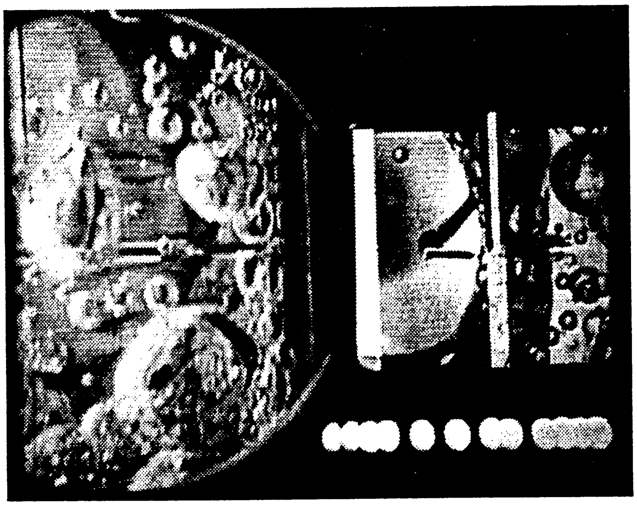
Frame#0841 time=44.23 sec.

Figure 5.17. Continued.

STS-47 Run #8

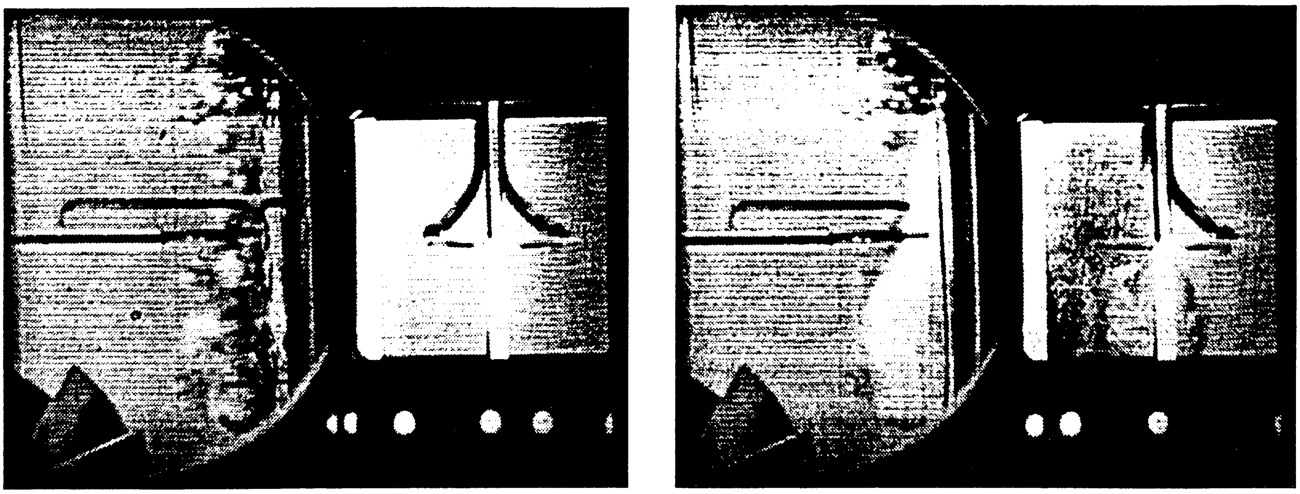

Frame#0611 time=20.63 sec. Frame#0612 time=20.64 sec.

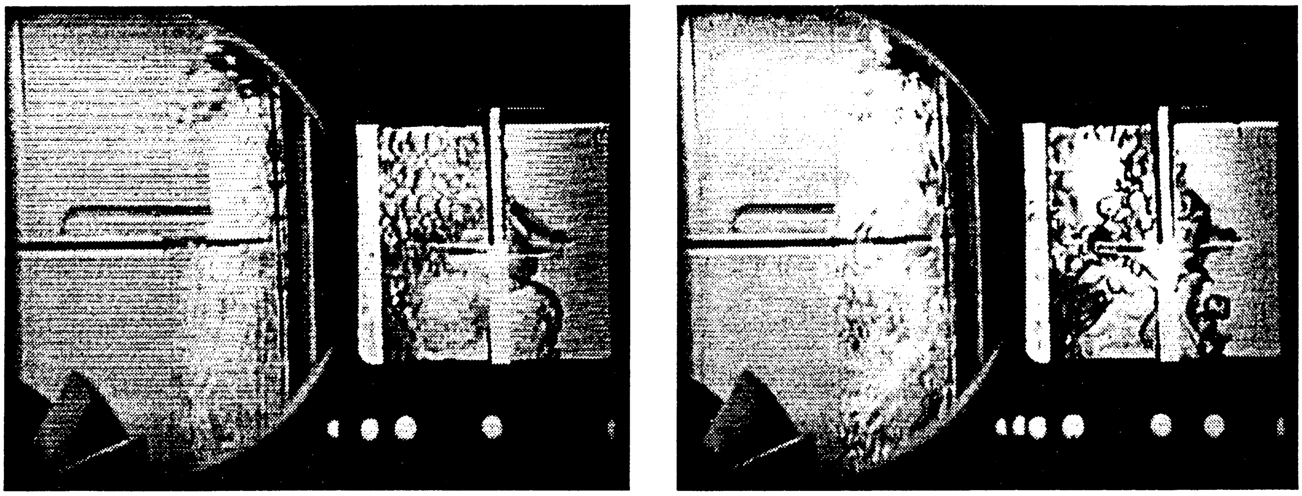

Frame#0614 time=20.66 sec. Frame#0619 time=20.71 sec.

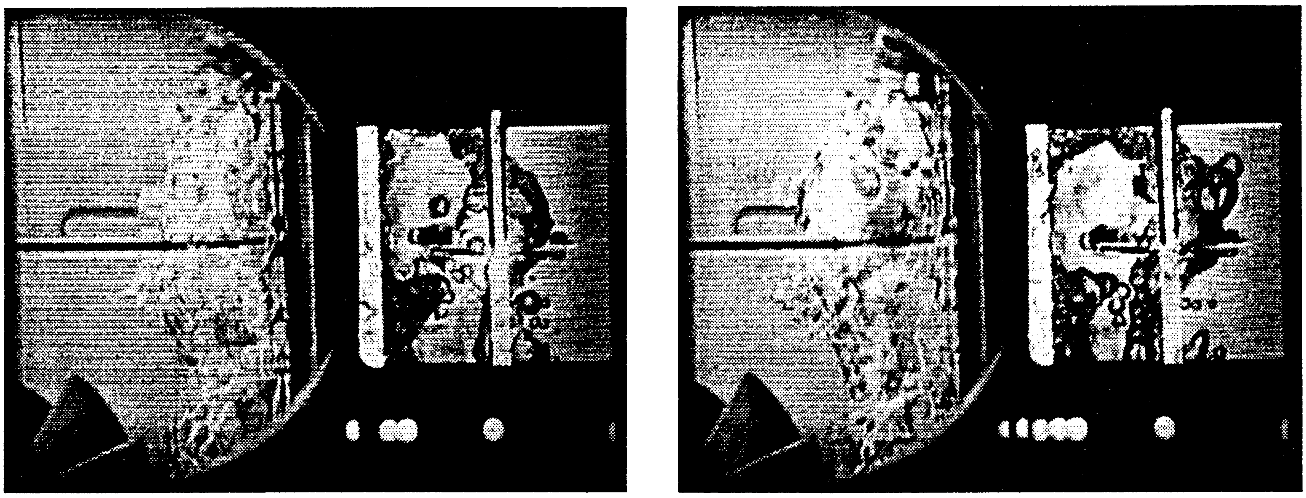

Frame#0624 time=20.76 sec. Frame#0634 time=20.86 sec.

Figure 5.18. Run No. 8. PBE-IA. STS-47. Selected Photographic Images.

STS-47 Run #8

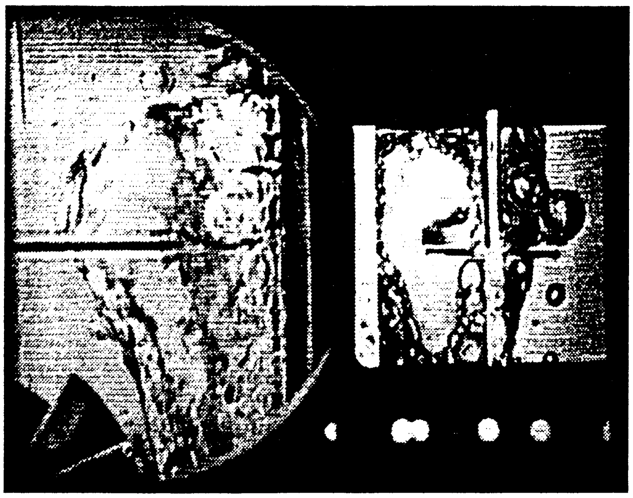

Frame#0671 time=21.22 sec.

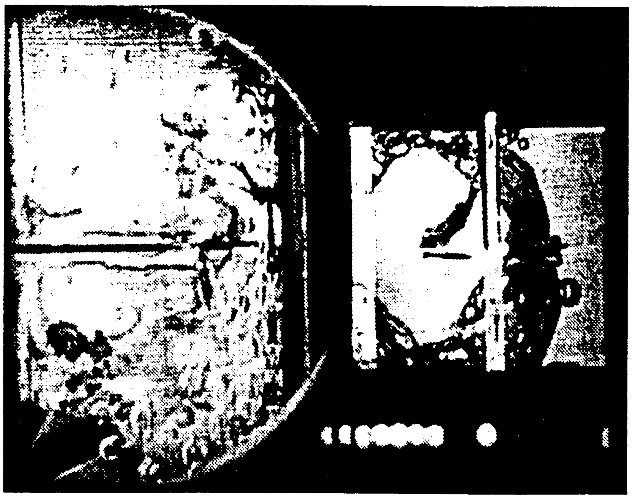

Frame#0827 time=22.78 sec.

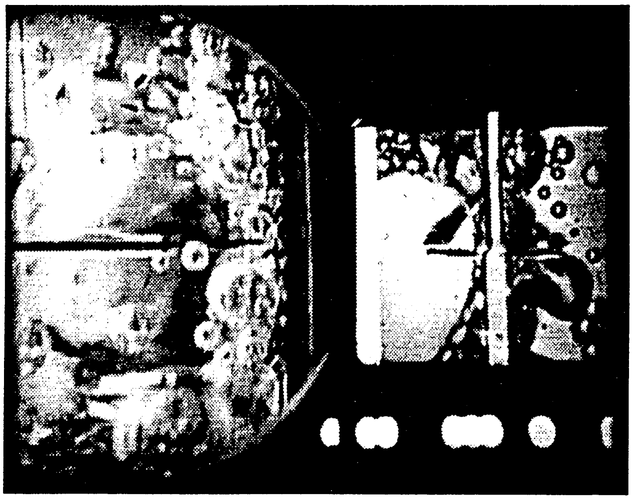

Frame#1099 time=28.19 sec.

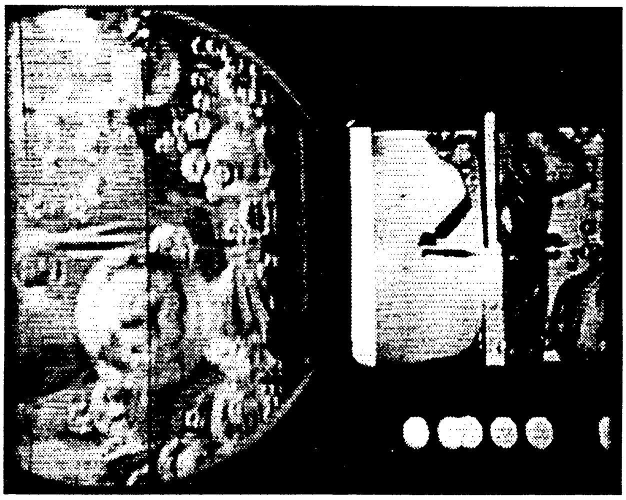

Frame#1205 time=38.81 sec.

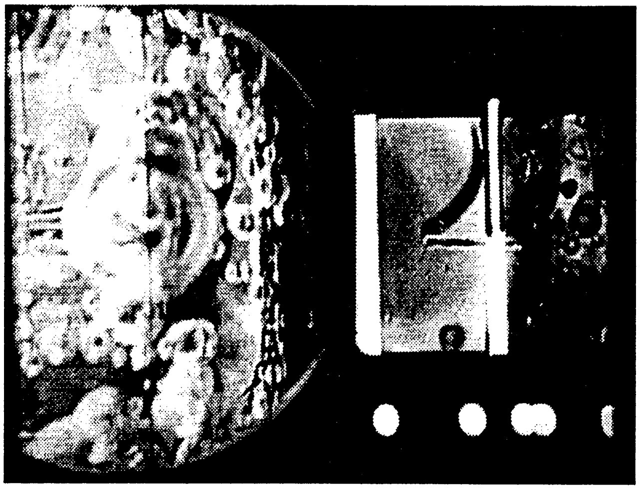

Frame#1379 time=56.27 sec.

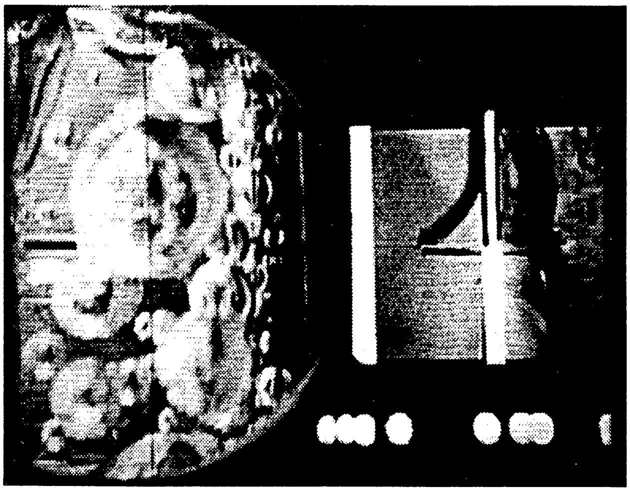

Frame#1433 time=61.67 sec.

Figure 5.18. Continued.

STS-47 Run #9

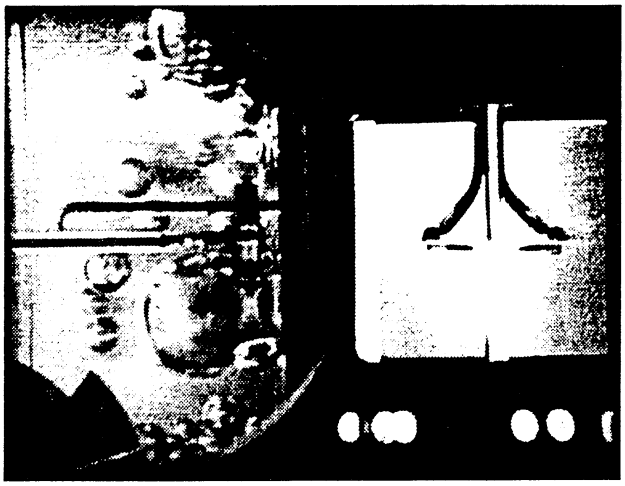

Frame#2229 time=51.48 sec.

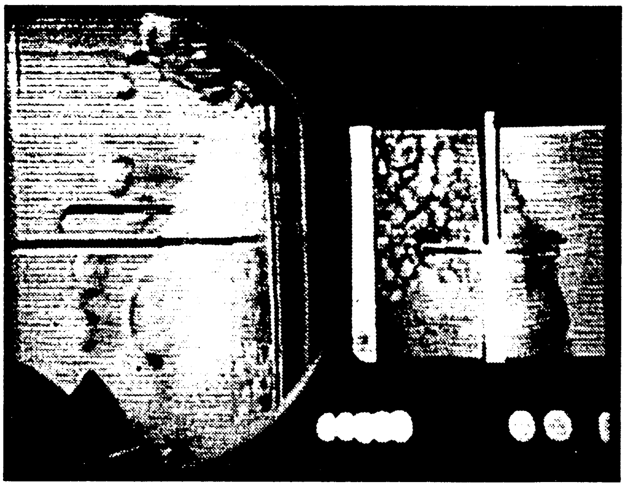

Frame#2230 time=51.58 sec.

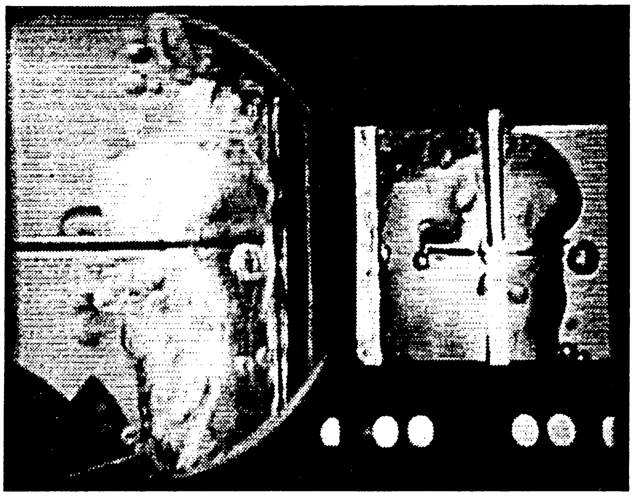

Frame#2232 time=51.78 sec.

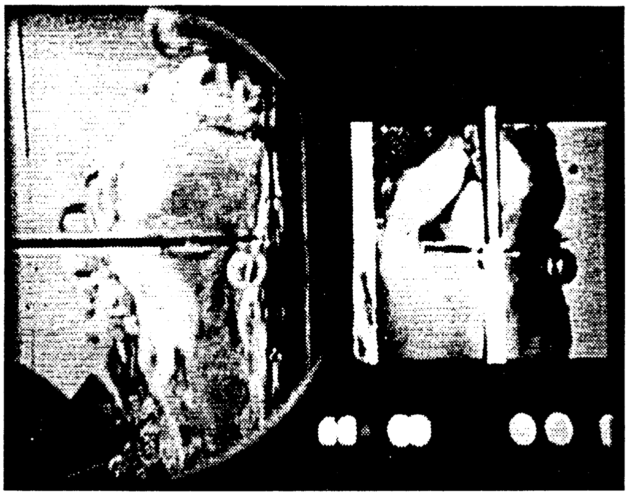

Frame#2234 time=51.98 sec.

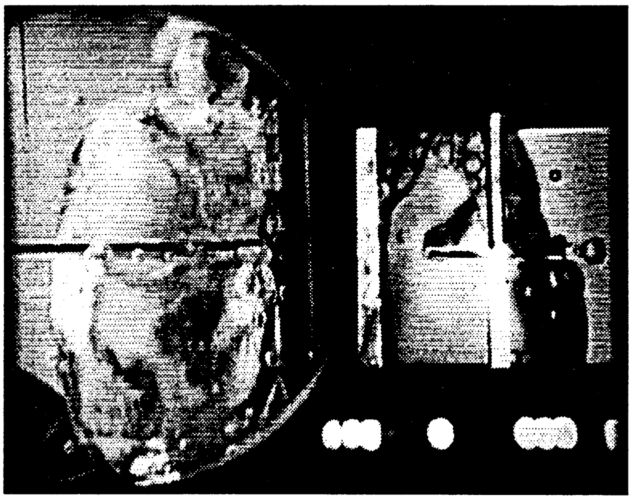

Frame#2238 time=52.39 sec.

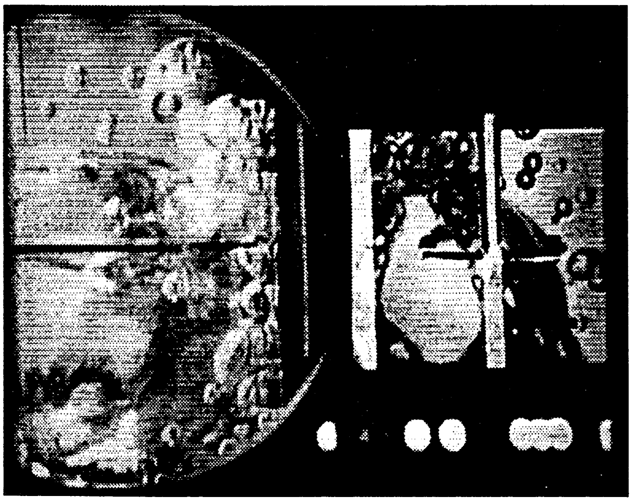

Frame#2256 time=54.19 sec.

Figure 5.19. Run No. 9. PBE-IA. STS-47. Selected Photographic Images.

STS-47 Run #9

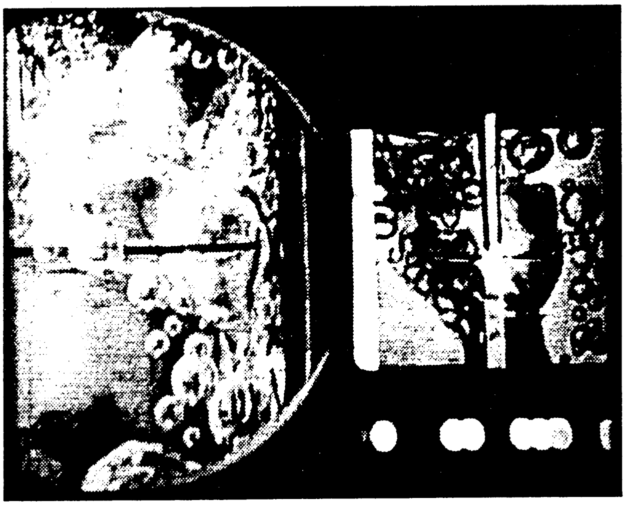

Frame#2302 time=58.81 sec.

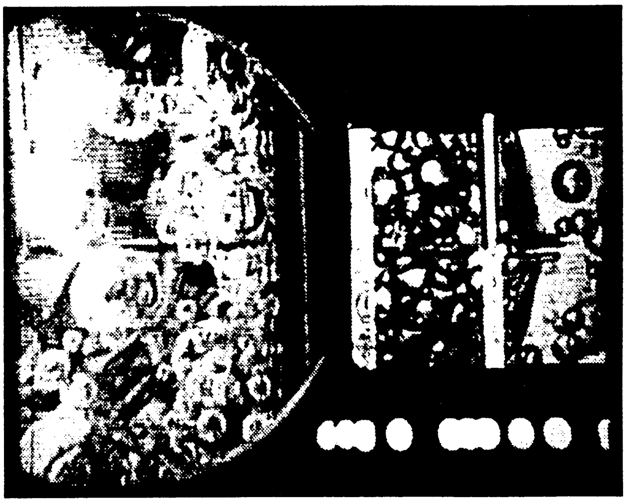

Frame#2407 time=69.34 sec.

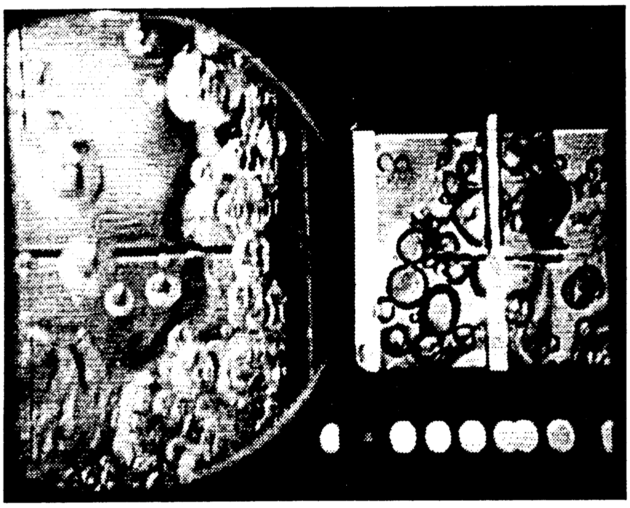

Frame#2495 time=78.18 sec.

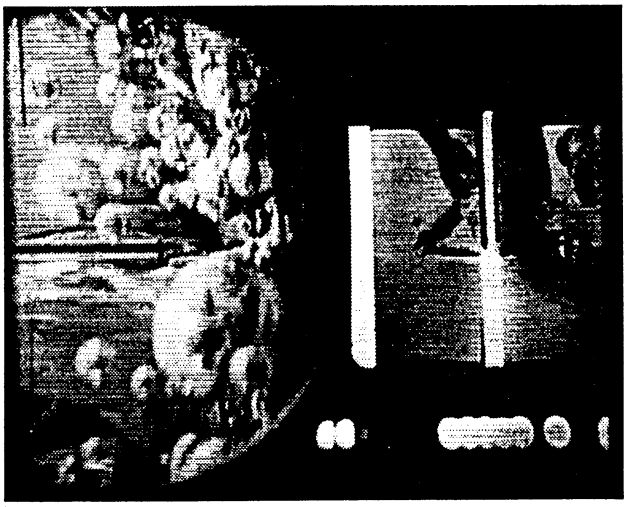

Frame#2607 time=89.42 sec.

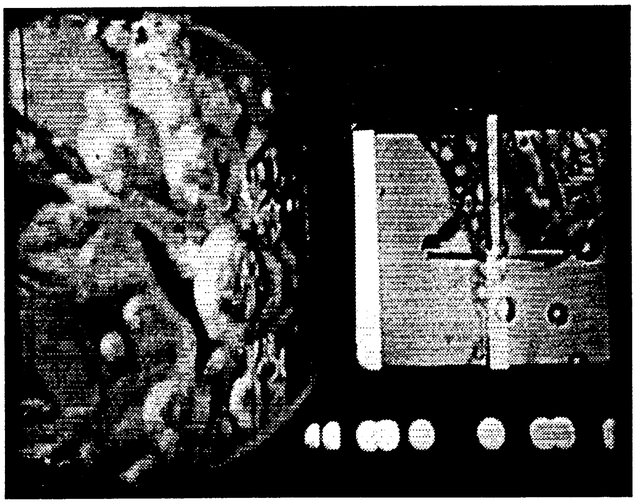

Frame#2743 time=103.07 sec.

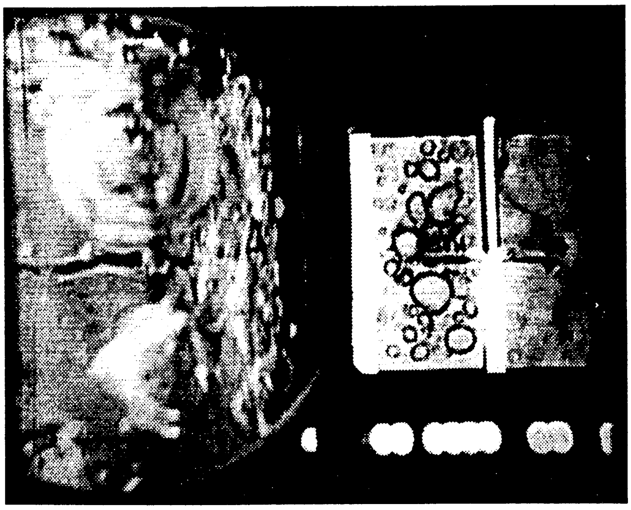

Frame#2828 time=111.63 sec.

Figure 5.19. Continued.

6. DISCUSSION

6.1 Conduction Effects

In the absence of buoyancy and forced convection, heat transfer in fluids takes place by pure stationary conduction, as in solids. This was confirmed for relatively short periods in microgravity, in solids and in fluids before nucleation takes place, by the measurements of Ervin and Merte (1991), also appearing in Ervin et al (1992). In this case the physical processes of conduction conformed closely to the analytical solution for two semi-infinite solids, initially at a uniform temperature, with a uniform step in a plane heat source at the interface.

6.1.1 Conduction in Substrate

The analytic solution of the interface temperature between the two semi-infinite solids, which corresponds to the gold film heater surface temperature in the physical system, is plotted as the 1-D Analytical Surface temperature for reference purposes for each of the Runs of the matrix in Figs. 2.2a - 5.10a.

The discrepancy between the analytical and the measured values increases for the lower level of heat fluxes, for which longer periods of conduction heat transfer in both the solid and fluid domains take place before nucleation occurs. This discrepancy is attributed to three-dimensional conduction effects during this period, primarily in the quartz substrate domain, which has a larger thermal diffusivity, $a = k/\rho c = 8.34 \times 10^{-7} m^2/s$, compared to $a = 5.24 \times 10^{-8} m^2/s$ for R-113. Comparisons of the short 5.1 second drop-tower ground based testing were excellent with the one-dimensional solutions. In this case the quartz substrate was less massive than that in the PBE, and the single heater surface on the substrate was located symmetrically. To confirm that three-dimensional effects were operating in the PBE a 3 - D finite element model was developed for the particular geometry of the PBE. It was computationally intensive, requiring about 10 hours on a 486 base machine, and the results are presented here for demonstration purposes.

Fig. 6-1 shows the measured mean heater surface temperature for Run No. 3 of the PBE-IA on STS-47 from Fig. 5.4a. Also shown are the measured underside surface quartz temperatures under the center of each of the heaters from Fig. 5.4e, with the active heater side measurement being TM11, the larger increase of the two, as anticipated. Also indicated are the 1 - D analytical heater surface predictions from the semi-infinite solid solution, and the 3 - D predictions of both the heater surface and the quartz undersides using the finite element solution procedure with the heat flux input up to the nucleation point, followed by an imposed uniform surface temperature, which approximates quite well the measured value following nucleation. It is noted that the 3 - D computation closely approximates the measured surface temperatures up to the nucleation point. The measured temperature rise occurring at 85 seconds was not incorporated into the 3 - D finite element model. Nevertheless, it is noted that the measured quartz underside temperatures follow the computed changes. The difference of 2°C between the measured and computed quartz underside temperatures is a consequence of taking the initial quartz temperature to be uniform at the initial bulk liquid temperature, in the computational process. An initial difference of 2°C across the quartz existed as a result of the heat transfer from the quartz to the surroundings, which were about 10°C cooler than the quartz surface. This had little effect on net heat losses from the heater surface itself because of the low thermal conductivity of the quartz.

Fig. 6.2 is an isometric plot of the 3 - D temperature distribution in the quartz substrate computed by the 3 - D finite element model, at the onset of nucleation at 40 seconds on Fig. 6.1. This shows clearly the conduction taking place as departures from the 1 - D semi-infinite solid model. The potential influence that 3 - D conduction effects might have on the computation of the heat transfer coefficient to the fluid will be considered in the next section. The upper part of Fig. 6.2 is a central section showing the 2 - D temperature distribution in the R-113 after 30 seconds of heating, and demonstrates that the extent of the penetration of the temperature disturbance is quite small.

Fig. 6.3 presents an isometric plot of the 3 - D temperature distribution in the quartz substrate at 90 seconds in Fig. 6.1, using a constant mean surface temperature of 75°C as measured, following nucleation at 40 seconds. The 2 - D central section temperature distribution in the R-113 is also given at the top, but has no physical significance, since boiling has begun at 40 seconds.

6.1.2 Conduction in Fluid

Fig. 6.4 shows the measured mean heater surface temperatures as fitted from the measurements of heater current and voltage at 10 Hz. Also repeated from Fig. 6.1 are the 1 - D and 3 - D computed heater surface temperatures prior to nucleation. The heat transfer coefficients to the fluid are computed from the measurements with the 1 - D finite difference procedure for the case where a polynomial fit is used between each of the measurement points for interpolation purposes, and results in the oscillations observed. The 3 - D finite element computation of the heat transfer coefficient during the conduction phase up to nucleation provides a reasonable fit to the heat transfer coefficients computed by the finite difference method when some visual filtering is applied. Once nucleation occurred the 3 - D finite element model used a constant imposed temperature, which approximates the measurements out to about 85 seconds when dry-out begins. The heat transfer coefficient computed from the 3 - D finite element model during the 40 second to 85 second interval follows the smoothed version of that computed from measurements with the 1 - D finite difference model. This is a consequence of the relatively low thermal diffusivity of the quartz, which means that the penetration depth of the disturbances taking place at the surface with these frequency levels are not influenced by three dimensional effects.

In order to determine the effect that filtering of the measured mean heater surface temperature would have on the heat transfer coefficient computed with the 1 - D finite difference model, two different degrees of filtering techniques were applied, presented in Figures 6.5 and 6.6 for the same Run No. 3 of PBE-IA on STS-47. Fig. 6.5 presents the mean heater surface temperature and computed heat transfer coefficient taking three (3) successive heater surface temperatures at 100 ms intervals averaged to provide the temperature at the middle point on the time scale. This procedure was advanced for each 100 ms data point. The smoothing obtained is noted by comparison with Fig. 6.4.

Fig. 6.6 is similar to Fig. 6.5, except the averaging process was conducted over five (5) successive measurements, advancing also in 100 ms steps. Excessive filtering is to be avoided, since it is possible that a real transient might be eliminated. The results presented in Figs. 5.2 - 5.10 were obtained without the use of any filtering. Future data reduction will take place using the 3 point averaging technique. However, a polynomial fit for interpolation between data points is necessary in both cases.

One further assessment of the procedures followed in the numerical computation of the heat transfer coefficient from the measured mean heater surface temperatures is necessary. In carrying these computations out it is assumed that the heat flux input to the heater surface is constant, at some interpreted mean value. That this is not the case can be noted by examining Figs. 5.2b - 5.10b.

A detailed examination of the effect of taking a constant heat flux was conducted for PBE-IA Run No. 3, using the 3-D finite element model developed here. In one case a curve is fitted to the measured variation in the input heat flux, while in the other case the input heat flux is taken to be constant. The results are given in Fig. 6.7, and it is noted that any discernible discrepancy occurs only in the immediate vicinity of the nucleation point, where the largest temperature change occurs, with the maximum variation in the input heat flux. At this point the peak computed heat transfer coefficient is reduced from [illegible]00 to 1600 w/m^{2}K. Actual two dimensional variations over the heat transfer surface make such distinctions between the mean input heat fluxes difficult to justify. Furthermore, the 3 - D element computational time required for the constant heat flux is two (2) hours for a 2 minute test run with 0.5 sec. time steps, compared to six (6) hours with a variable input heat flux. As a result, a constant mean input heat flux is used here throughout.

6.2 Nucleation

Fig. 6.8 is a plot of the nucleation delay times obtained in the early ground based testing, including the tests conducted in the 5.1 second NASA-Lewis drop tower, for a particular heater surface designated as Q5. Nucleation delay time is defined as the interval between the onset of heating and the moment when the first vapor bubble appears. For a given input heat flux a distinct relationship exists between the nucleation delay time and the heater surface superheat and liquid temperature distribution at the onset of boiling. The latter quantities govern the character of the early bubble dynamics and the spread of the boiling across the heater surface. Such processes are described in detail in Ervin and Merte (1991), Ervin et al (1992), and Lee and Merte (1993). Based on these ground tests an optimum correlation was developed, as shown in Fig. 6.8, in order to estimate the delay times expected in the flight experiment. A number of the drop tower data were neglected in this process, marked by asterisks, because the heater surface superheats at nucleation, plotted in Fig. 6.10, appeared unusually high. All nucleation delay times measured with the PBE-IA are plotted in Fig. 6.9 together with the identical correlation from Fig. 6.8. The comparison with the flight data is quite good.

Fig. 6.10 is a plot of the mean heater surface superheats at nucleation for the same tests plotted in Fig. 6.8. It was not possible to conduct these tests in the drop tower with the lower levels of input heat flux, since nucleation did not take place in the 5.1 second drop tower test. An intermediate heat flux level was introduced, and it is noted that the heater surface superheat on nucleation at $a/g \approx 0$ appears as a maximum at the heat flux levels between the highest and lowest values, even with different subcooling levels. Fig. 6.11 is the corresponding data obtained from all the PBE-IA tests conducted, including pre- and post- flight. It is noted that a corresponding peak exists in the mean heater surface superheat on nucleation between the high and low levels of heat flux, and is particularly high in microgravity. In addition, for the most part, as the subcooling level increases the heater surface superheat on nucleation is smaller. This is quite opposite to what intuition would provide. No explanations for the above behaviors appear reasonable, as yet, unless the nucleation becomes a function more of the absolute temperature rather than the superheat. The heat flux levels selected for these experiments vary by factors of two, in order to cover the widest range possible with the limited testing available. A proposal has been submitted for further flights to include heat flux input levels of 0.5, 1.0 and 2.0 w/cm^2 with the same subcooling as in Fig. 6.11, and subcoolings up to 22°C with the same heat flux input levels as in Fig. 6.11, so that the explanation mentioned above about the role of the absolute temperature on nucleation rather than the superheat could be explored further. In addition, the role of the liquid temperature gradient at the heater surface interface at nucleation, along with bulk liquid subcooling, is being examined. It was demonstrated by Ervin and Merte (1991) that nucleation of R-113 can occur at heater surface superheat levels on the order of 4°C if a sufficiently rapid heater surface temperature increase can be instituted. In this latter case, approximations to step changes in heater surface temperatures were being attempted. On the other hand, as reported by Iida et al (1993), high rates of heating for ethyl alcohol at atmospheric pressure by a small (0.1 mm × 0.25 mm) platinum film 20 Angstroms thick on quartz, to 10^7°C/s, produced nucleation at the theoretical homogeneous nucleation point of 129°C superheat. In this case the liquid subcooling was 53°C, and the formation of the vapor bubbles was described as "Caviarwise bubble generation".

6.3 Bubble Dynamics

Based on both observations and measurements conducted in earth gravity at $a/g = +1$, $a/g = -1$, and in the 5.1 second NASA-Lewis drop tower, once nucleation occurred the propagation of the boiling across the heater surface and the bubble growths could be classified into one of six categories, termed as follows:

A. Advancement of interface by irregular protuberances.
B. Growth of mushroom-like bubble with spreading along heater surface.
C. Orderly growth of bubble with a "smooth" interface.
D. Orderly growth followed by onset of interface instabilities.
E. Energetic growth of bubble with unstable interface.
F. Slow motion of bubbles toward region of higher temperature.

The circumstances under which these took place with R-113 are given in detail in Ervin and Merte (1991) and in Ervin et al (1992), and will be summarized here:

A took place only at $a/g = +1$ with $q''_T \geq 7$ w/cm^2.
B occurred only at $a/g = +1$ with $2 \leq q''_T < 7$ w/cm^2.
C took place at $a/g = -1$ with high levels of heat flux $q''_T \geq 7$ w/cm^2.
D was observed with $a/g = -1$ with $q''_T < 7$ w/cm^{2}and $a/g \cong 10^{-5}$, also with $q''_T < 7$ w/cm^2. However, the lowest heat flux level possible in the drop tower was $q''_T \cong 6$ w/cm^2.

E was observed only with $a/g \cong 10^{-5}$ and gave rise to the explosive growth with protuberances appearing over the entire liquid-vapor interface. The lowest heat flux possible was $q''_T \cong 6$ w/cm^2.

F occurred at $a/g = -1$ and $a/g \cong 10^{-5}$ with $q''_T > 7$ w/cm^2. The motion is attributed to thermocapillary effects.

Although the initial bulk liquid subcooling was expected to play a part in these categories, its effect is not yet clear.

From examination of the photographs from the PBE-IA on the STS-47, with samples given in Figs. 5.11 - 5.19, all boiling propagations are in either categories D or E, depending on the combination of heat flux and subcooling. The difference between these two categories lies in whether the bubble growth and/or propagation takes place relatively slowly or dynamically (explosively).

The maximum camera speed of 100 pps in the PBE-IA was not capable of following the dynamic cases of category E. It is estimated that a framing rate greater than 3000 pps would have been necessary. Another manifestation of the distinction between categories D and E lies in the absence or presence of measured pressure spikes in connection with nucleation. The rate of data acquisition for the system pressure was limited to 10 Hz (100 ms between readings), and the peak pressure can occur at any time between these measurements. Such pressure spikes can be noted in Fig. 5.3c for Run No. 2, in Fig. 5.6c for Run No. 5, in Fig. 5.7c for Run No. 6, and in Fig. 5.10c for Run No. 9. The pressure control system was not capable of responding to this nucleation spike, nor was it intended to.

From the films, Category D takes place with the highest heat flux and for all subcoolings, in Run Nos. 1, 4, 7, and in Run 3, with the lowest heat flux and the largest subcooling. All other Run Nos. 2, 5, 6, 8, 9 result in very energetic or explosive initial vapor bubble growths, Category E, which include all Runs at the medium heat flux $q''_T \cong 4$ w/cm^2 for all subcoolings, and at the low heat flux $q''_T \cong 2$ w/cm^2 for low or zero subcooling.

The behavior in Run Nos. 2, 5, 8, with $q''_T \cong 4$ w/cm^2 is related to the high heater superheat at nucleation demonstrated in Fig. 6.11, relative to that for the other heat flux levels. It is also noted in Fig. 6.11 that the nucleation heater surface superheat for the lowest heat flux and highest subcooling, Run No. 3, is about the same as in Run No. 1, which also was in Category D. The energy content in the superheated boundary layer thus is not as high as in the other Runs, in microgravity.

It is believed that the dynamic growths taking place in certain cases can result in vapor bubble departures from the heat transfer surface due to the momentum imparted to the liquid, causing rewetting of the heater surface and sustaining the nucleate boiling process. Such a departure appeared to take place here only in Run No. 2. The initial growths in both Run Nos. 6 and 9 were quite dynamic, with dryout but not momentum produced bubble departure, and followed by a relatively slow rewetting process. The heater surface never did dry out completely in Run No. 3, and is believed to be due to the low heat flux together with the large subcooling. All three cases with the lowest heat flux level, Run Nos. 3, 6, 9 appear to produce a sustained steady-state nucleate boiling in microgravity, for all levels of subcooling.

This is set forth in Table V, which summarizes the mean heat transfer coefficients obtained with PBE-IA, both at $a/g = +1$ and in the STS-47 Space Flight. Dry out occurred in all Runs at $a/g = -1$ because of buoyancy effects. It is noted in Table V that nucleate boiling takes place at $a/g = +1$ only for the highest levels of heat flux, in Run Nos. 1, 4, 7, and also in Run No. 2, for the medium heat flux level but with the highest level of subcooling. Even here, subcooling appears to be playing an anomalous role in pool boiling. The heat transfer coefficient is the largest at $h = 2500$ w/m^{2}K with the largest subcooling, in Run 1, while those for Runs 4 and 7 are slightly lower but identical at $h = 2300$ w/m^{2}K. The measured mean natural convection non-boiling heat transfer coefficients are on the same order as predicted by the correlation, as indicated. The maximum discrepancies are on the order of the generally accepted levels of ± 25%.

The decreases in heater surface temperatures., accompanied by increases in the heat transfer coefficients, as noted:

in Fig. 5.2a for Run No. 1 at 65 seconds,
in Fig. 5.4a for Run No. 3 at 110 seconds,
in Fig. 5.5a for Run No. 4 at 50 seconds,
in Fig. 5.9a for Run No. 8 at 65 seconds,
in Fig. 5.10a for Run No. 9 at 105 seconds,

are a result of activating the stirrer motor before the test is completed. This can be confirmed from the test matrix given in Table II.

However, on examining certain Runs it is noted that distinct increases in surface temperature take place, accompanied by decreases in the heat transfer coefficient:

in Fig. 5.4a for Run No. 3 at 85 seconds,
in Fig. 5.6a for Run No. 5 at about 80 seconds,
in Fig. 5.9 for Run No. 8 at about 55 seconds,
in Fig. 5.10a for Run No. 9 at about 80 seconds.

Run No.	q" w/cm^2 Approx.	ΔT_{sub} °C Approx.	$\bar{h}$ w/m^{2}K a/g = + 1 Post Flight 11/4/92	$\bar{h}$ w/m^{2}K a/g ≅ 10^{-5} STS-47
1	7.0	10.7	2500 Nucleate Boiling	700 Dry Out
2	3.6	11.5	1300 Nucleate Boiling	1250** Steady State + Oscillating
3	1.8	11.0	450 (350)* Non-Boiling Convection	1100 → 600 Steady State → Dry Out
4	7.0	2.7	2300 Nucleate Boiling	200 Dry Out
5	3.6	2.8	550 (430)* Non-Boiling Convection	400 → 200 Increased Dry Out
6	1.8	2.8	550 (350)* Non-Boiling Convection	1150 Steady State + Oscillating (Rewet)
7	7.0	0.6	2300 Nucleate Boiling	200 Dry Out
8	3.5	0.4	600 (400)* Non-Boiling Convection	300 → 200 Increased Dry Out
9	1.8	0.2	500 (350)* Non-Boiling Convection	1100 → 200** Steady State + Dry Out & Rewet

Computed from natural convection correlation: $Nu = 0.15 \times Ra^{1/3}$

Table V. PBE-IA. Comparison of measured mean heat transfer coefficients between a/g = +1 and STS-47 Space Flight.

Looking at the photographs in Fig. 5.13 for Run No. 3, with the lowest heat flux and highest subcooling, it may be noted that the dryout area begins to increase over the surface, without any significant amount of nucleate boiling taking place over the wetted portion of the heat transfer surface. It is possible that the subcooling inhibits the nucleation process in the vicinity of the meniscus, so that the agitation of the liquid-vapor interface by the absorbing of these small bubbles is reduced sufficiently that the rewetting of the heat transfer surface by the meniscus becomes inhibited, promoting the dryout process.

For the other Run Nos. 5, 8, 9, it is believed that the distinct increases in surface temperature are due to the vapor bubble growing sufficiently large so that it becomes pressed against the heater surface. It can be seen in Fig. 3.5 that the largest size vapor bubble that can be accommodated in the test vessel before contact is made with the walls is about 12 cm in diameter. If all the heat transfer to the fluid produces vapor, as would take place with a saturated liquid, the size of the vapor bubble in a microgravity environment can be calculated as approximating a sphere. The resulting vapor bubble radius is plotted in Fig. 6.12 as a function of time for the 3 nominal levels of heat flux used. For $q''_T \cong 2$ w/cm^2 a radius of 6 cm is reached at about 85 seconds, which agrees approximately with the behavior of Run No. 9; For $q''_T \cong 4$ w/cm^2 the time is about 55 seconds, which agrees with Run No. 8. Run No. 5 at $q''_T \cong 4$ w/cm^2 has a time of 80 seconds, which is larger than the estimated 55 seconds, because of the nominal subcooling of the liquid which reduces the bubble growth rate as a result of condensation.

6.4 Heat Transfer to Fluid

As described previously, the mean fluid heat transfer coefficients computed from the measured mean heater surface temperatures are plotted in Figs. 5.2a - 5.10a for each of the respective Runs of the matrix. A definite relationship exists between the transient mean heater surface temperature and the heat transfer coefficient. These serve to indicate, qualitatively at present, the modes of heat transfer between the heater surface and fluid: conduction to the liquid; nucleate boiling; conduction to the vapor phase (termed dryout); and combinations of the three forgoing mechanisms based on the fractional part of the heater surface over which each is acting. For the time being the conduction heat transfer mode to the liquid will be neglected in the interest of simplicity. For the heat flux levels used to date, nucleation and its propagation across the heater surface take place early in the process, so that the major part of the heat transfer surface is either covered by vapor or influenced by the nucleate boiling phenomenon itself. For future cases where the heat flux levels are sufficiently low such that relatively smaller portions of the heater surface are influenced by the presence of either nucleating sites or significant amounts of vapor, the heat transfer to the stagnant liquid regions then will be incorporated.

From the photographic data taken through the transparent heating surface from the underside, it is possible to discern quite distinctly those portions of the heater surface on which dryout has taken place. Examples are abundant in Figs. 5.11 - 5.19. It is observed that under some circumstances this is a time varying phenomena, and is related in some fashion to both the transient mean heater surface temperature and heat transfer coefficient. If measurements of the time varying fractional area of the heat transfer surface in contact with vapor, which will be termed the fractional dryout area, can be made with sufficient temporal detail, it is felt that the possibility exists for quantifying the contributions to the total heat transfer of the different modes of heat transfer taking place. Since only mean heater surface temperatures and heat transfer coefficients are measurable at present, only spatial mean parameters can be determined: local measurements in the future would permit determination of these parameters on a spatially local basis.

In order to provide an efficient means for quantifying the time varying fractional dry portion of the heater area from the 16 mm films, an optical processing system has been set up in which the 16 mm film is projected on a screen with a motion picture projector; the motion is stopped at the desired frame; the time noted; the image picked up with a video camera, which can then be stored on a VCR and/or immediately digitized with a frame grabber for greater resolution; the digitized data is stored on an optical disc for later processing.

The following will demonstrate how the measurements of the fractional dry portion of the heater area and the spatial mean heater surface temperatures $\overline{T}_w$ and heat transfer coefficients $\bar{h}_T$ may be related. Fig. 6.13 is a representation, from the underside, of the heater surface on which boiling is taking place in microgravity, and may be considered to be typical of, for example, Fig. 5.12 — Frame #0952 and Fig. 5.13 — Frame #2603, reproduced from digitized 16 mm frames from the STS-47 Flight of the PBE-IA, Run Nos. 2 and 3, respectively, and are runs with the largest subcooling used. The dry portions of the heater surface are readily discernible in both cases, as is the nucleate boiling taking place over the remainder of the surface in Frame 0952 of Fig. 5.12. These bubbles are then "absorbed" by the larger overlaying vapor bubble due to the action of the surface tension. In Frame 2603 of Fig. 5.13, on the other hand, with the lower heat flux, part of the domain between the dry portion appears to be inactive in this frame. In reality, nucleate boiling is also occurring in these domains, but with a significantly smaller frequency and nucleation site density. It should be kept in mind that the pool boiling process in microgravity is inherently transient, because of the changing local subcooling and changing size of the overlaying vapor bubble, and consequently the nature of the local and average boiling processes will be changing as well.

Fig. 6.14 is a simplified representation of Fig. 6.13, and illustrates how the mean heater surface temperatures and heat transfer coefficients are defined for the dry and nucleate boiling areas as $\overline{T}_D$, $\bar{h}_D$ and $\overline{T}_B$, $\bar{h}_B$, respectively. The following additional definitions are made:

$$A_T = A_D + A_B \qquad (2)$$

$$1 = \frac{A_D}{A_T} + \frac{A_B}{A_T} = F_D + F_B \qquad (3)$$

where F_D and F_B are the fractional dry and nucleate boiling areas of the heater surface, respectively.

$$q''_T = q_T/A_T \qquad (4)$$

$$\overline{T}_w = F_D \times \overline{T}_D + F_B \times \overline{T}_B \qquad (5)$$

The overall mean heat transfer coefficient:

$$\bar{h}_T = q''_T/(\overline{T}_w - T_{sat}) = q''_T/\Delta\overline{T}_w \qquad (6)$$

$$q_T = q_D + q_B \qquad (7)$$

$$q''_T = \frac{q_T}{A_T} = \frac{q_D}{A_T} + \frac{q_B}{A_T} = \frac{A_D}{A_T} \times q''_D + \frac{A_B}{A_T} \times q''_B = F_D \times q''_D + F_B \times q''_B \qquad (8)$$

The mean heat transfer coefficient on the dry portion of the heater surface is:

$$\bar{h}_D = q''_D/(\overline{T}_D - T_{sat}) = q''_D/\overline{\Delta T}_D \qquad (9)$$

The mean heat transfer coefficient on the nucleate boiling portion of the heater surface is:

$$\bar{h}_B = q''_B/(\overline{T}_B - T_{sat}) = q''_B/\overline{\Delta T}_B \qquad (10)$$

From Equations (6), (8) - (10):

$$q''_T = \bar{h}_T \times \overline{\Delta T}_w = F_D \times \bar{h}_D \times \overline{\Delta T}_D + F_B \times \bar{h}_B \times \overline{\Delta T}_B \qquad (11)$$

From Equation (11):

$$\bar{h}_T = F_D \times \bar{h}_D \times \frac{\overline{\Delta T}_D}{\overline{\Delta T}_w} + F_B \times \bar{h}_B \times \frac{\overline{\Delta T}_B}{\overline{\Delta T}_w} \tag{12}$$

If, as an approximation, $\bar{h}_B$ can be considered constant for a given heat flux input and bulk liquid subcooling, and also if $\bar{h}_B >> \bar{h}_D$ and $\overline{\Delta T}_B/\overline{\Delta T}_w \approx 1$, then from Equation (12):

$$\bar{h}_B = \frac{\bar{h}_B}{F_B} = \frac{\bar{h}_T}{(1 - F_D)} \tag{13}$$

Both $\bar{h}_T$ and F_D are independently measurable quantities, and the supposition as to the constancy of $\bar{h}_B$ thus can be tested. Should this prove to be the case, then the total heat transfer rate could be approximated, from Equations (4), (6) and (13) as:

$$q_T = A_T \times (1 - F_D) \times \bar{h}_B \times \overline{\Delta T}_w \tag{14}$$

The heat transfer coefficient $\bar{h}_B$ defined by Equation (13) could be viewed, in these circumstances, as a microgravity nucleate pool boiling heat transfer coefficient. The assumptions made in its development are summarized:

(a) $\bar{h}_B \approx$ constant

(b) $\bar{h}_B >> \bar{h}$

(c) $\overline{\Delta T}_B / \overline{\Delta T}_w \approx 1$

An additional assumption was implied:

(d) $F_B \neq \approx 0$

This last condition is related to the fact that F_D is measured, and in Equation (13) the measured $\bar{h}_T$ is divided by $F_B = 1 - F_D$. If F_D is close to unity, then F_B is close to zero, and the relative uncertainty can become quite large. The limit to which F_D can approach unity for these calculations is as yet unknown; as will be shown below, measurements up to $F_D = 0.95$ have been made.

Upon examining the transient mean heater surface temperatures and mean heat transfer coefficients of the PBE-IA on STS-47 microgravity flight, in Figs. 5.2a - 5.10a, photographic candidates were selected from the nine test points of the matrix for detailed measurements of the dry spot areas in order to compute a microgravity boiling heat transfer coefficient. These are tabulated in Table VI, together with the current status. In the early stages of such computations the individual frames were digitized, individual prints of each made, and the dry spot areas measured by hand with a planimeter - an admittedly laborious process. However, it was desired to explore the feasibility of the process, and to examine the results so obtained before investing further resources. In addition to an external optical drive with storage capacities of 600 MB/cartridge, software for computing the manually defined dry spot area has been obtained to bypass the manual area measurements. Estimates of the time required to digitize and measure the dry spot fractional area for each frame have been made, and require approximately 10 minutes per frame, which includes the time required to identify the time from the LEDs on each frame. This is necessary in order to synchronize these measurements as closely as possible with the mean heater surface temperature measurements. Of the total of about 18,000 frames in the 400 foot roll of 16 mm film exposed in the experiments, the times selected in Table VI correspond to about 2400 frames. As indicated in Table VI, about one-fourth of this has been completed, with 1800 remaining.

Computational results will first be presented for PBE-IA Run No. 9, since examination of Fig. 5.2a shows both heater surface rewetting and dryout taking place in the same Run, not associated with the initial transients of nucleation. The effects of heater surface rewetting and dryout beginning at about 62 seconds and 82 seconds, respectively, are noted. In these domains the 16 mm film is running at 10 pps. It was discovered that defining the dry-out portion of the heater surface requires a certain element of human interpretation since the automatic measurements based on a defined gray scale in conjunction with the processing software available tended to produce much larger fractional dry areas than was deemed reasonable. Nucleating sites produce light shaded areas similar to dry areas, but make significant contribution to the heat transfer, and must be discounted in the area evaluation.

Fig. 6.15a shows the measured heater surface fractional dry area and the mean surface temperature for the time interval of 61.5 to 67.5 seconds in Fig. 5.2a. The temperature changes in Fig. 6.15a do not appear as extensive as in Fig. 5.2a because of the considerably expanded time scale. It is noted that the heater surface temperature decreases as the fractional dry area decreases. Fig. 6.15b is a plot of the measured heater surface fractional wet area, obtained from Fig. 6.15a, and the mean heat transfer coefficient

Run No.	Times Selected	Status
1.	Nucleation → 20 Seconds	
2.	20 Sec. → 30 Sec.	
	65 Sec. → 75 Sec.	
	95 Sec. → 100 Sec.	
3.	42 Sec. → 50 Sec.	Completed
	55 Sec. → 60 Sec.	
	83.5 Sec. → 90 Sec.	Completed
4.	Nucleation → 20 Sec.	
5.	Nucleation → 35 Sec.	
	70 Sec. → 90 Sec.	
6.	Nucleation → 65 Sec.	
	50 Sec. → 58 Sec.	Completed
7.	Nucleation → 15 Sec.	
8.	Nucleation → 35 Sec.	
	50 Sec. → 60 Sec.	
9.	Nucleation → 70 Sec.	
	61 Sec. → 69 Sec.	Completed
	80 Sec. → 90 Sec.	
	80.5 Sec. → 85.5 Sec.	Completed

Table VI. PBE-IA on STS-47. Candidates for heater surface dry spot area measurements and computation of microgravity nucleate pool boiling heat transfer coefficients.

replotted from Fig. 5.2a. If the assumption that $\bar{h}_B \approx$ constant, made above, is valid, then the two quantities plotted in Fig. 6.15b should vary in a similar manner, according to Equation (13) above. As can be seen, this appears to be the case. $\bar{h}_B$ can be computed from the data of Fig. 6.15b, and is obtained by dividing the mean heat transfer coefficient by the fractional wet area. This is plotted in Figure 6.15c, together with the measured mean heat transfer coefficient and wet ratio from Figure 6.15b. For convenience eight (8) photographic images showing the rewetting process are included here as Fig. 6.15d. the microgravity boiling heat transfer coefficient in Fig. 6.15c is noted to be approximately constant during the period from 62 seconds onward, with a value of about $h \cong 1250$ w/m^2K. It is also to be noted that the mean heat transfer coefficient converges toward the nucleate boiling heat transfer coefficient as the heater fractional wet area approaches unity, as it must since one is derived from the other. In this connection it should be pointed out that the seemingly large variations in the boiling heat transfer coefficient occur only when the heater fractional wet area is quite small, and is a result of inherent uncertainties in both the mean heat transfer coefficient and the measured fractional dry area. This uncertainty is amplified when dividing the measured mean heat transfer coefficient by the fractional wet area, which is obtained by subtracting the fractional dry area from unity. There is a further contribution to the uncertainty because of the uncertainty of 0.1 second in time in the measurement of the dry area when the camera speed is 10 pps. It is also possible that the boiling heat transfer coefficient is a function of the fractional dry area, but the determination of this must await more accurate local measurements of heater surface temperature.

Figure 6.16a is a plot corresponding to Fig. 6.15a, except for the time interval of 80.5 to 85.5 seconds in Run No. 9, while Figs. 6.16b and 6.16c correspond to Figs. 6.15b and 6.15c for this same time interval. The difference in the boiling heat transfer coefficient between Figs. 6.15c and 6.16c is that the heater fractional wet area is increasing in Fig. 6.15c, while it is decreasing in Fig. 6.16c. In spite of this, the boiling heat transfer coefficients have mean values of approximately 1250 w/m^2K and 1200 w/m^2K, respectively. These are surprisingly close values, within 4%, when the various total uncertainties involved are acknowledged. Fig. 6.16d shows eight (8) images of the dryout process taking place in this same interval.

Figs. 6.17 (a-d) - 6.19 (a-d) present the results of measurements and calculations in the same format as Figs. 6.15 (a-d) and 6.16 (a-d), for two parts of Run No. 3 and one part of Run No. 6, respectively. Figs. 6.17 (a-d) show the oscillatory behavior following the initial dryout associated with nucleation, while Figs. 6.18 (a-d) follow the dryout related to possible effects of subcooling on nucleation in the vicinity of the meniscus, as discussed earlier. The nucleate boiling heat transfer coefficient decreases slightly to $\bar{h} \cong 900$ w/m^{2}K in Fig. 6.18c, whereas it is larger, $\bar{h}_B \cong 1200$ w/m^{2}K earlier in the same Run No. 3, during the rewetting process shown in Fig. 6.17c. It should be noted that both Run No. 3 and Run No. 9, included in Figs. 6.17 (a-d) - 6.18 (a-d) and Figs. 6.15 (a-d) - 6.16 (a-d), respectively, have the same low level of heat flux, with the former having the large degree of subcooling.

The results for Run No. 6, also with the lowest level of heat flux but with a moderate subcooling level, are given in Figs. 6.19 (a-d), also for the rewetting phase following the initial dryout resulting from nucleation. It is seen in Fig. 6.19c that the nucleate boiling heat transfer coefficient remains constant at a level of $\bar{h}_B \cong 1000$ w/m^{2}K even though the wet ratio varies from 40% to 80%.

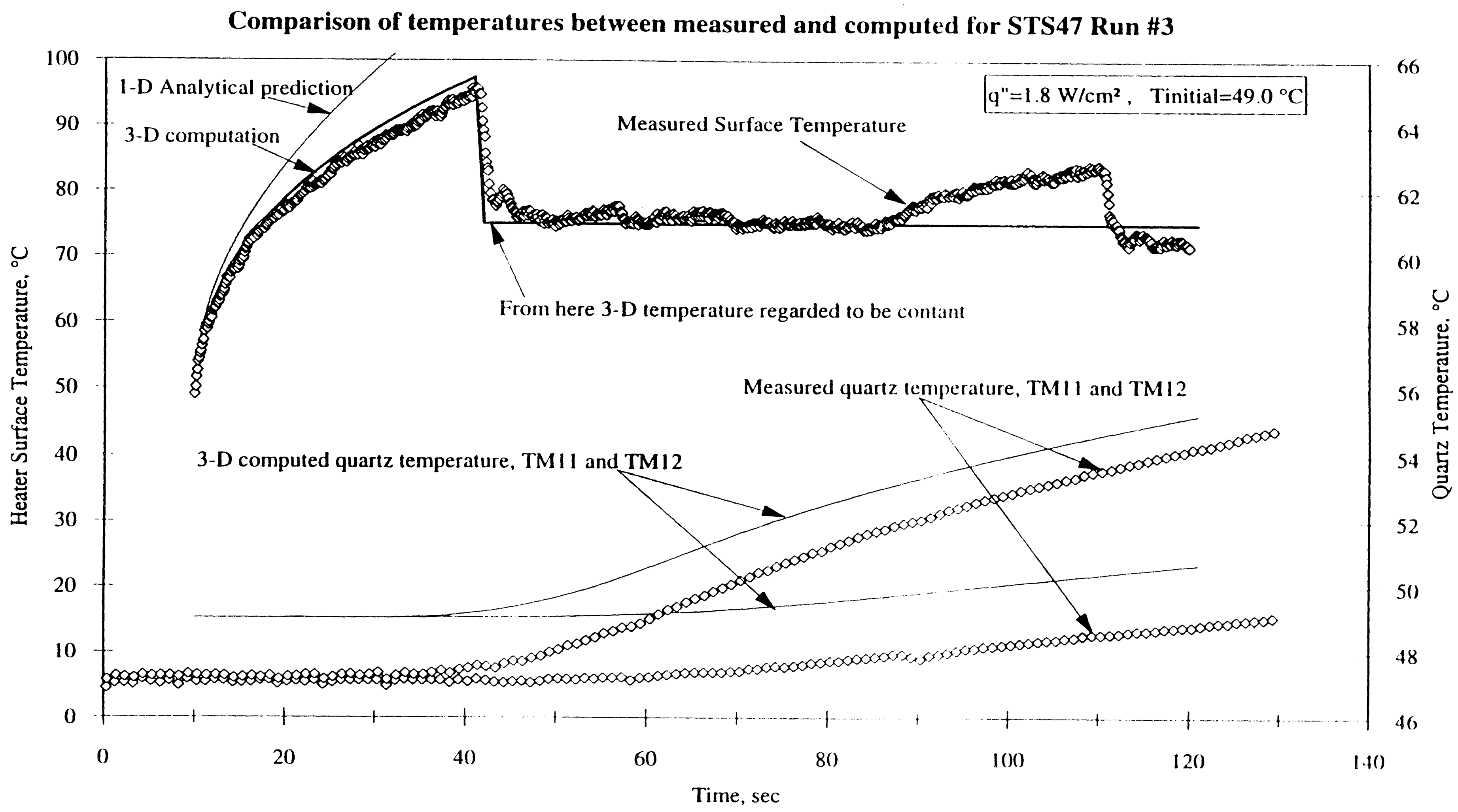

Figure 6.1 Comparison of 1 - D and 3 - D predicted temperatures with measurements. PBE-IA on STS-47. Run No. 3. $q_T'' = 1.8$ w/cm^2, $\Delta T_{sub} = 10.9$°C.

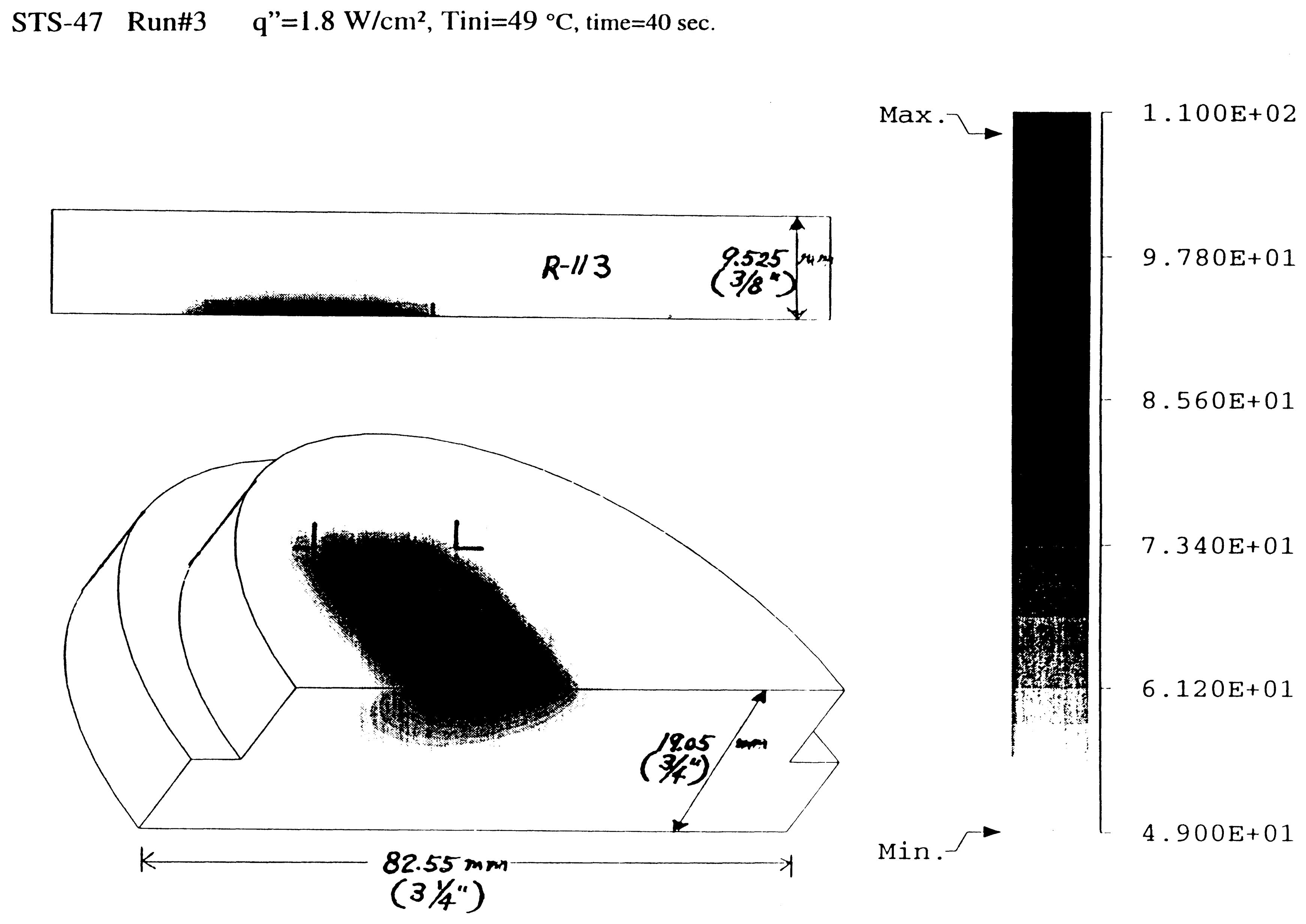

Figure 6.2. PBE-IA on STS-47. Run No. 3. Isometric plot of 3-D temperature distribution in quartz substrate at 40 seconds.

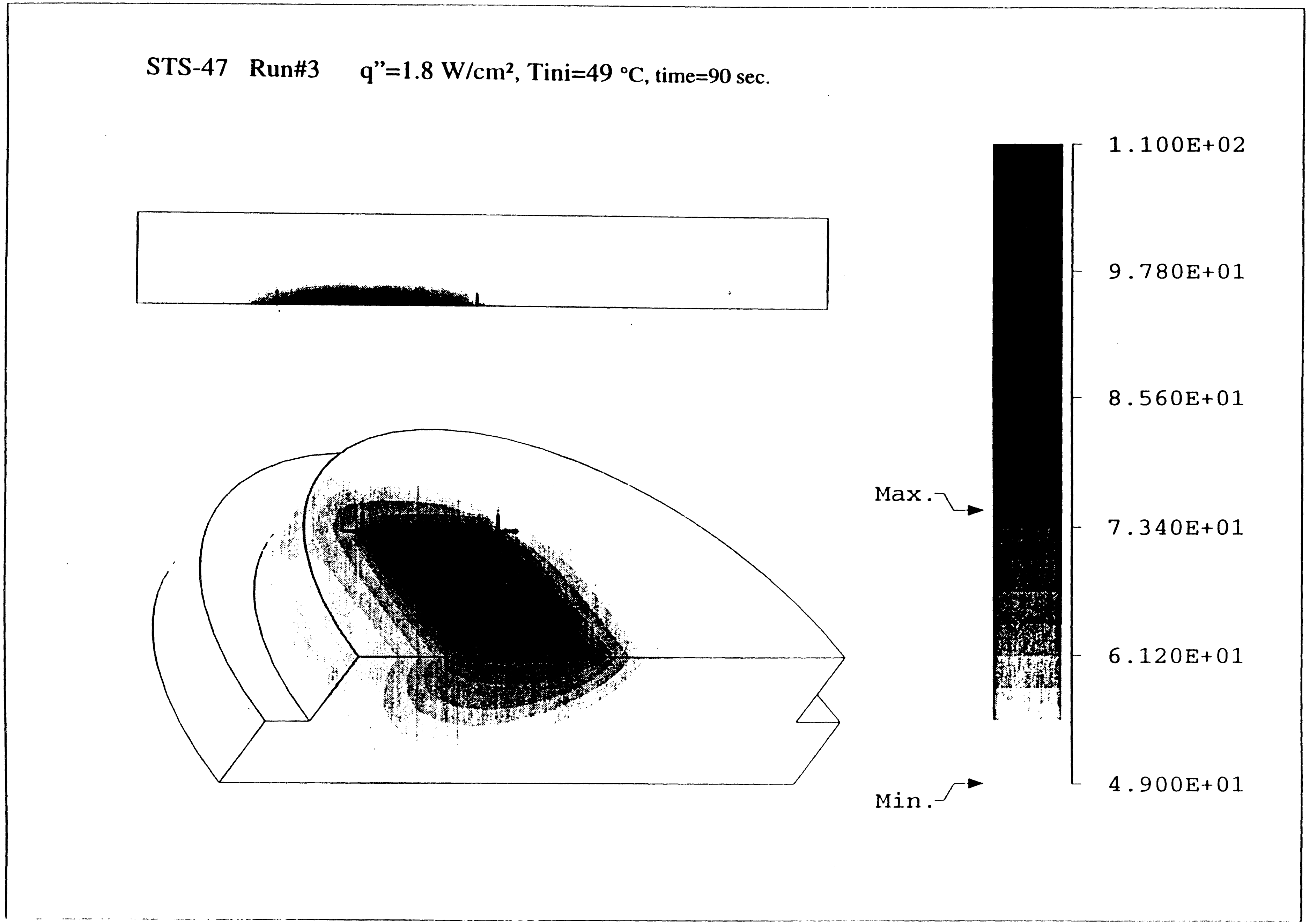

Figure 6.3. PBE-IA on STS-47. Run No. 3. Isometric plot of 3-D temperature

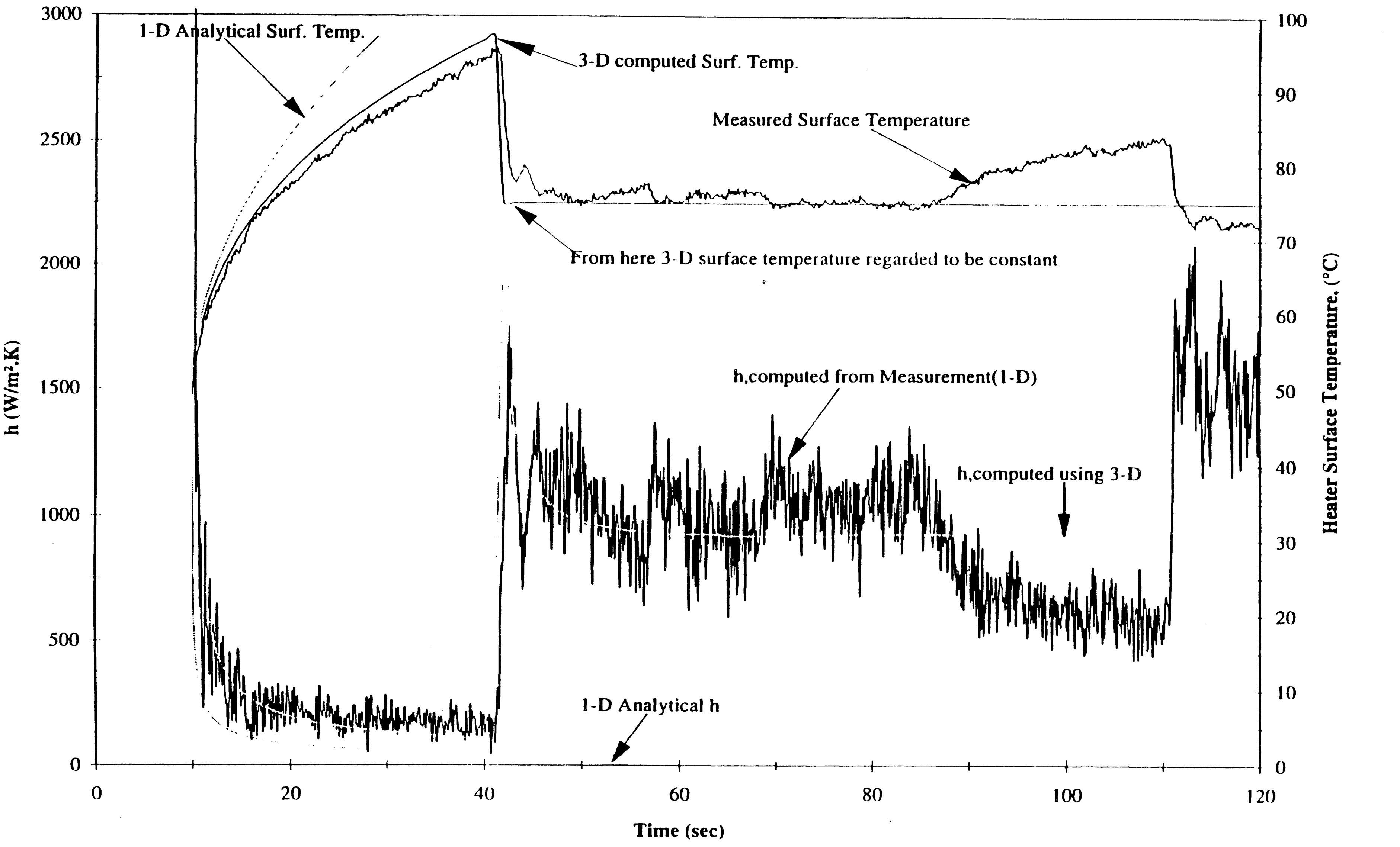

Figure 6.4. PBE-IA on STS-47. Run No. 3. Comparison of fluid heat transfer coefficients computed from measured mean heater surface temperatures using 1-D finite difference and 3 - D finite element models.

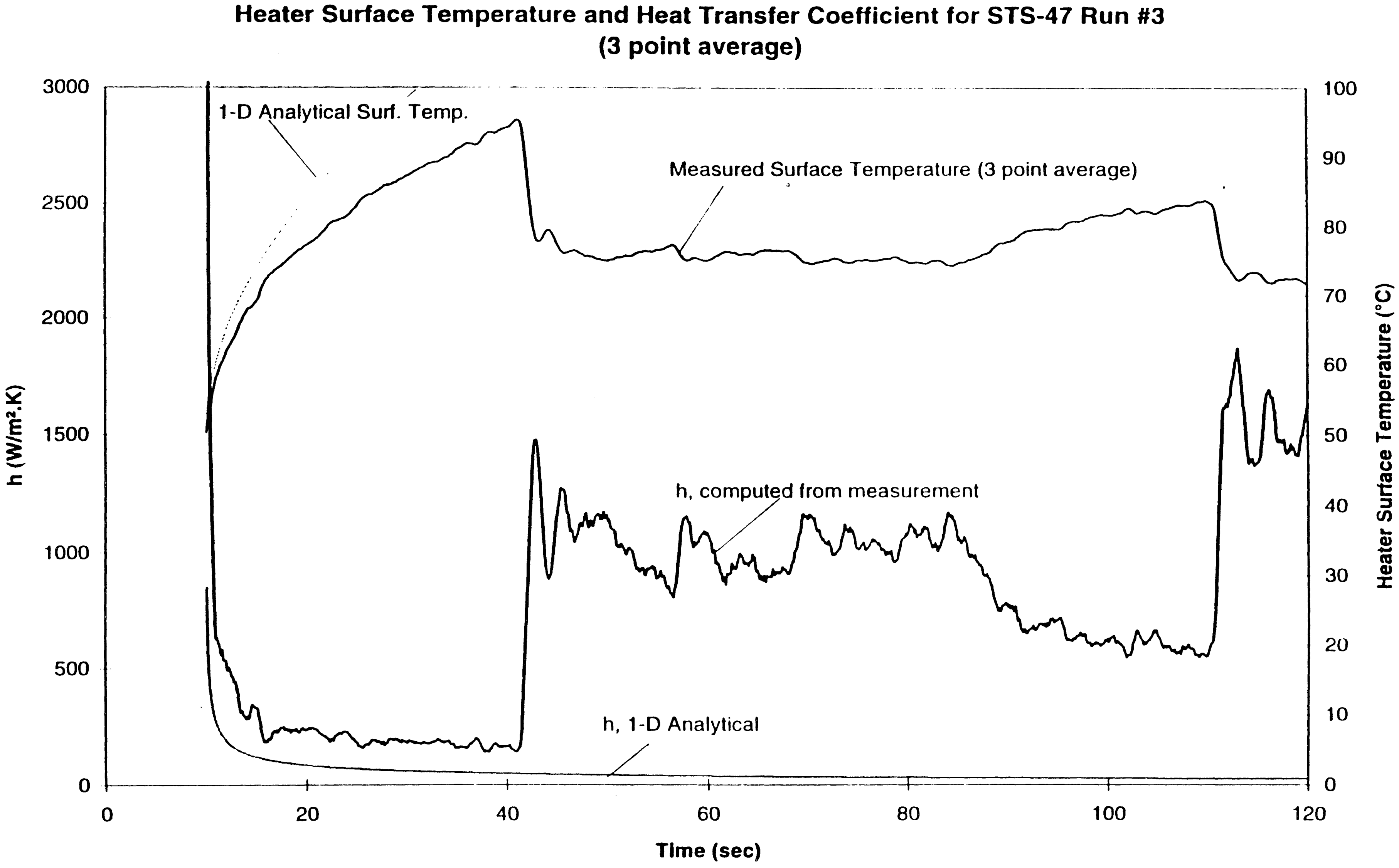

Figure 6.5. PBE-IA on STS-47. Measured heater surface temperature filtered by averaging three (3) consecutive measurement points sequentially.

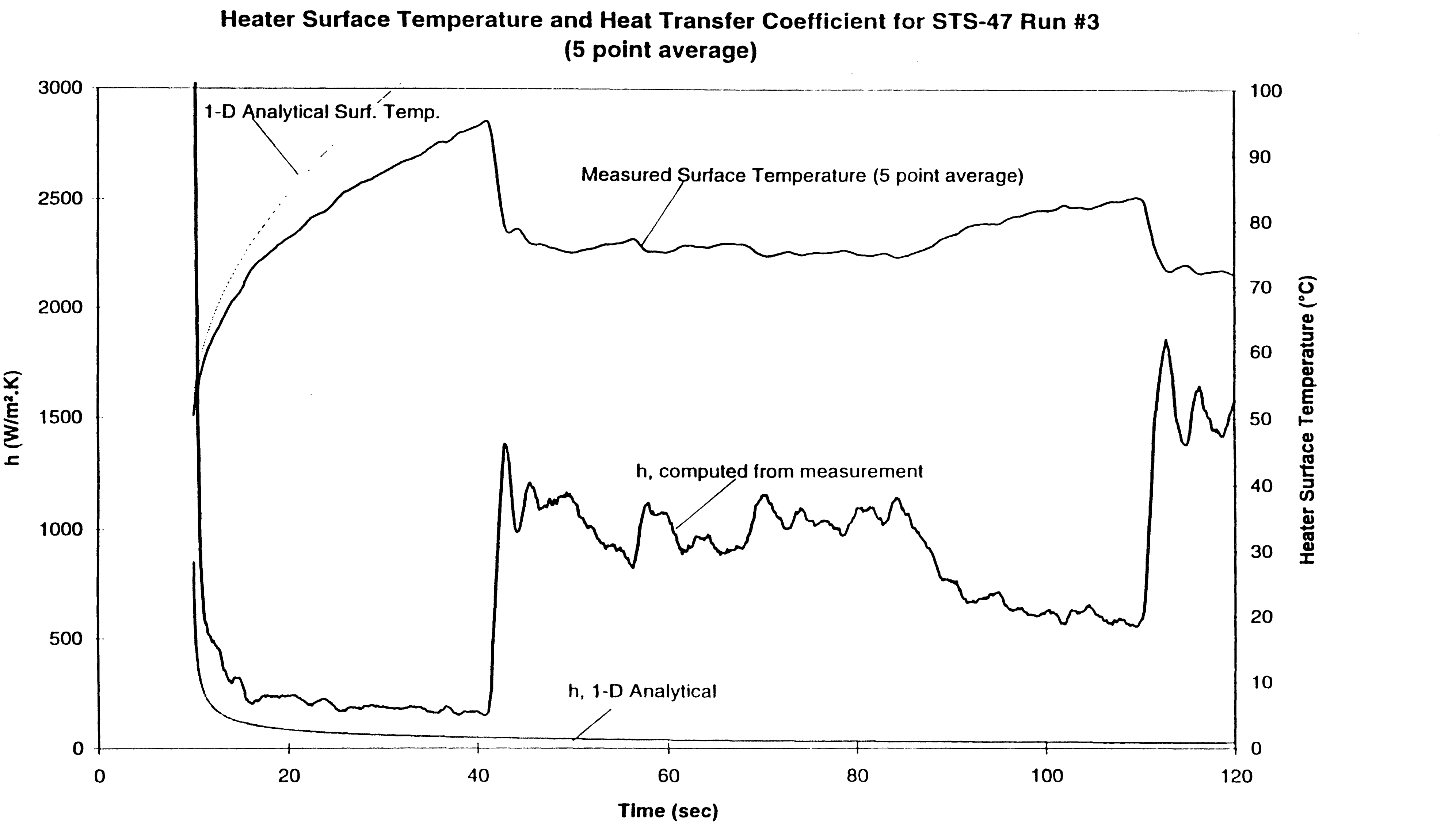

Figure 6.6. PBE-IA on STS-47. Run No. 3. Measured heater surface temperature filtered by averaging five (5) consecutive measurement points sequentially.

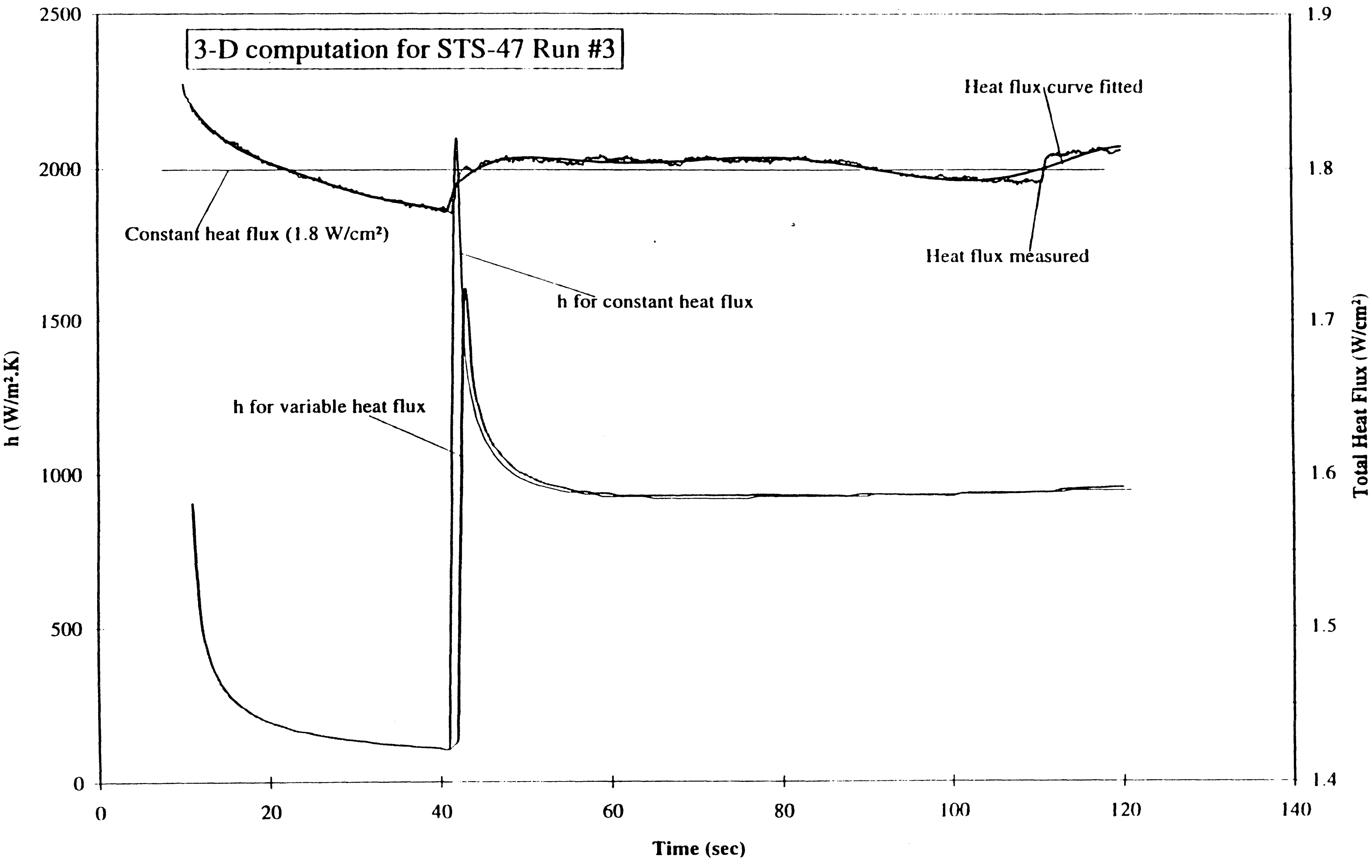

Figure 6.7. PBE-IA on STS-47. Run No. 3. Comparison of the fluid heat transfer coefficients obtained by taking the input heat flux as constant or variable.

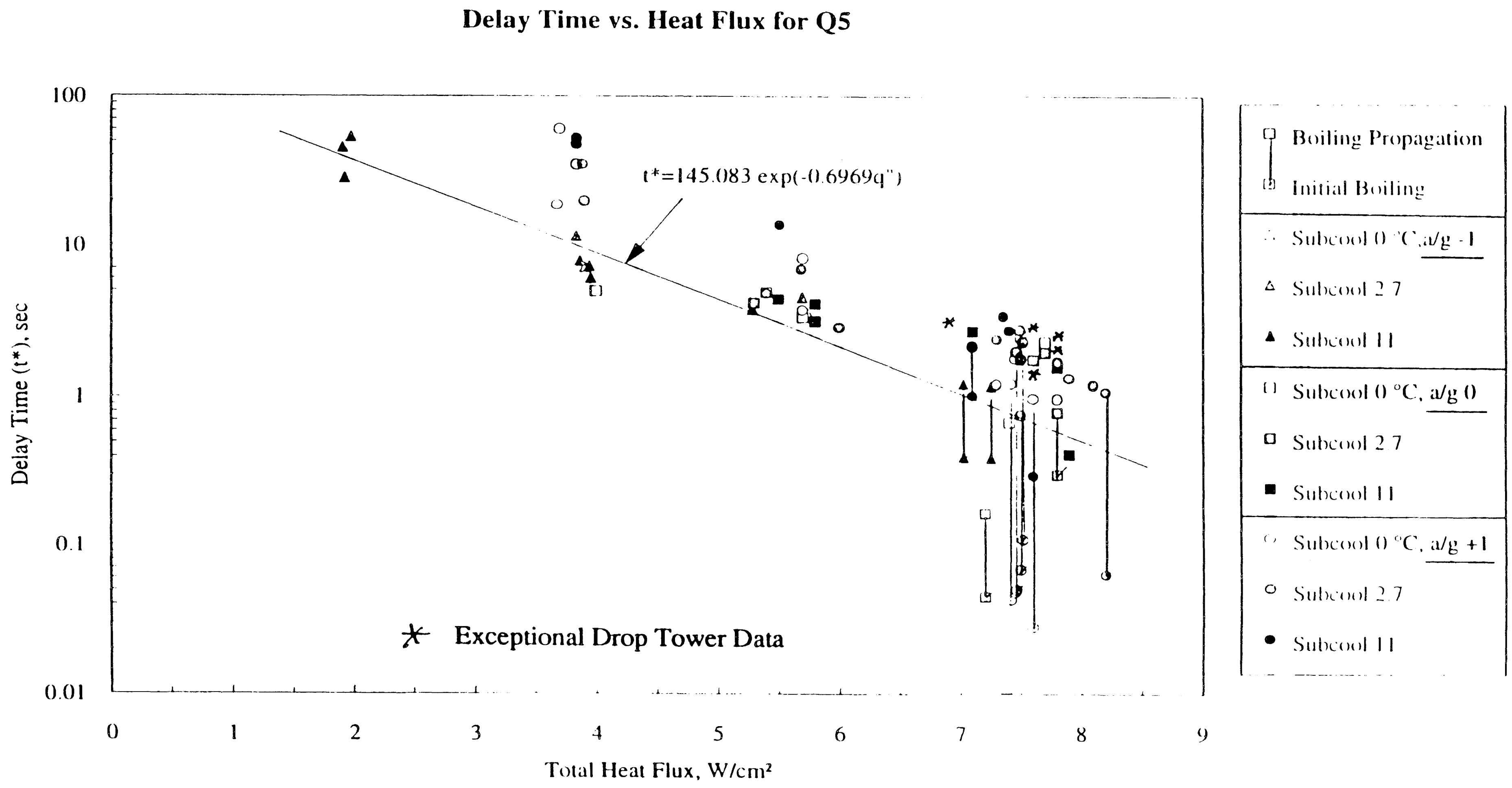

Figure 6.8. Nucleation delay correlation developed during ground based and 5.1 second drop tower testing.

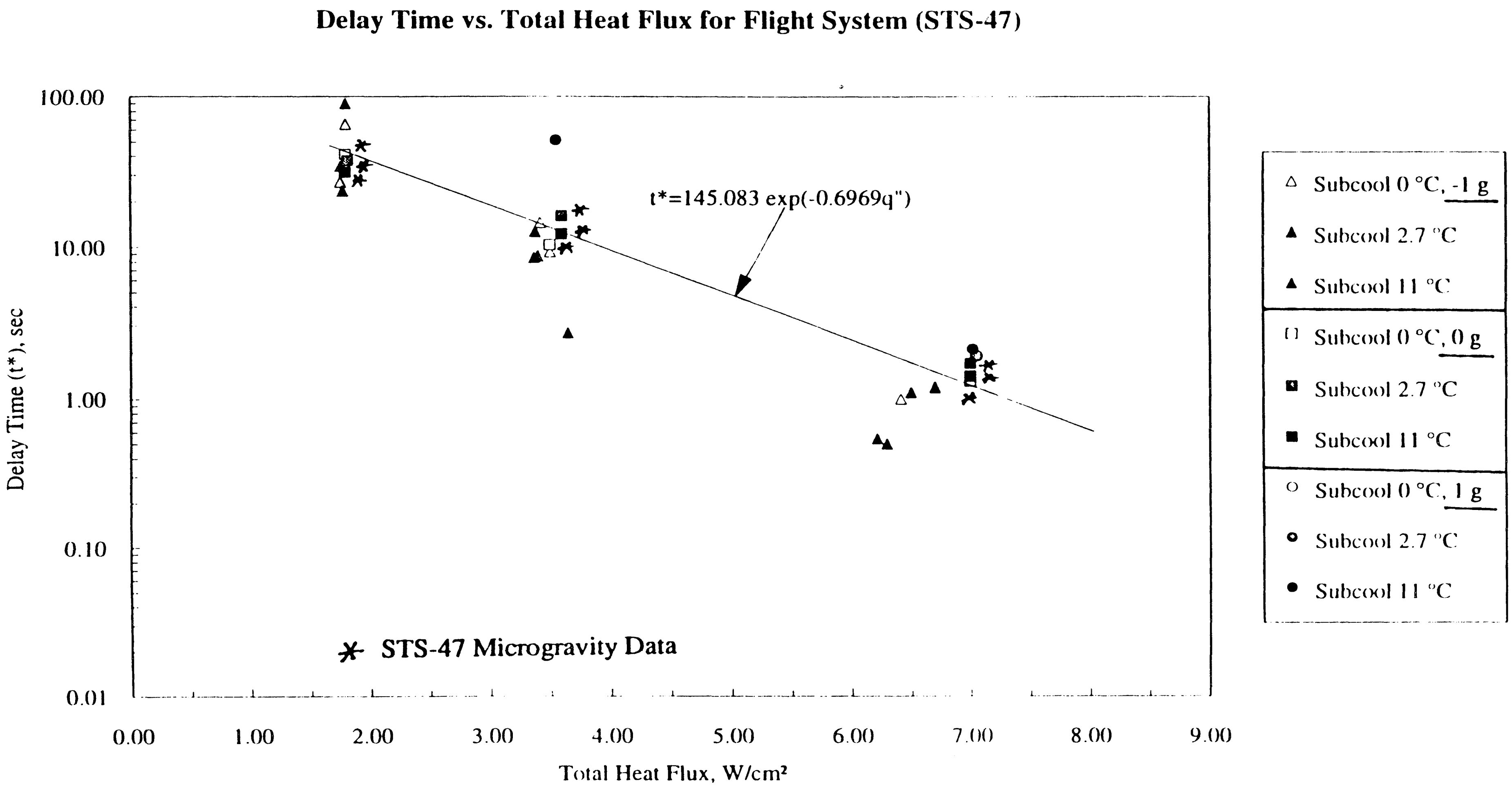

Figure 6.9. Comparison between nucleation delay times of PBE-IA prior to, during, and following STS-47 Flight with ground based and 5.1 second drop tower

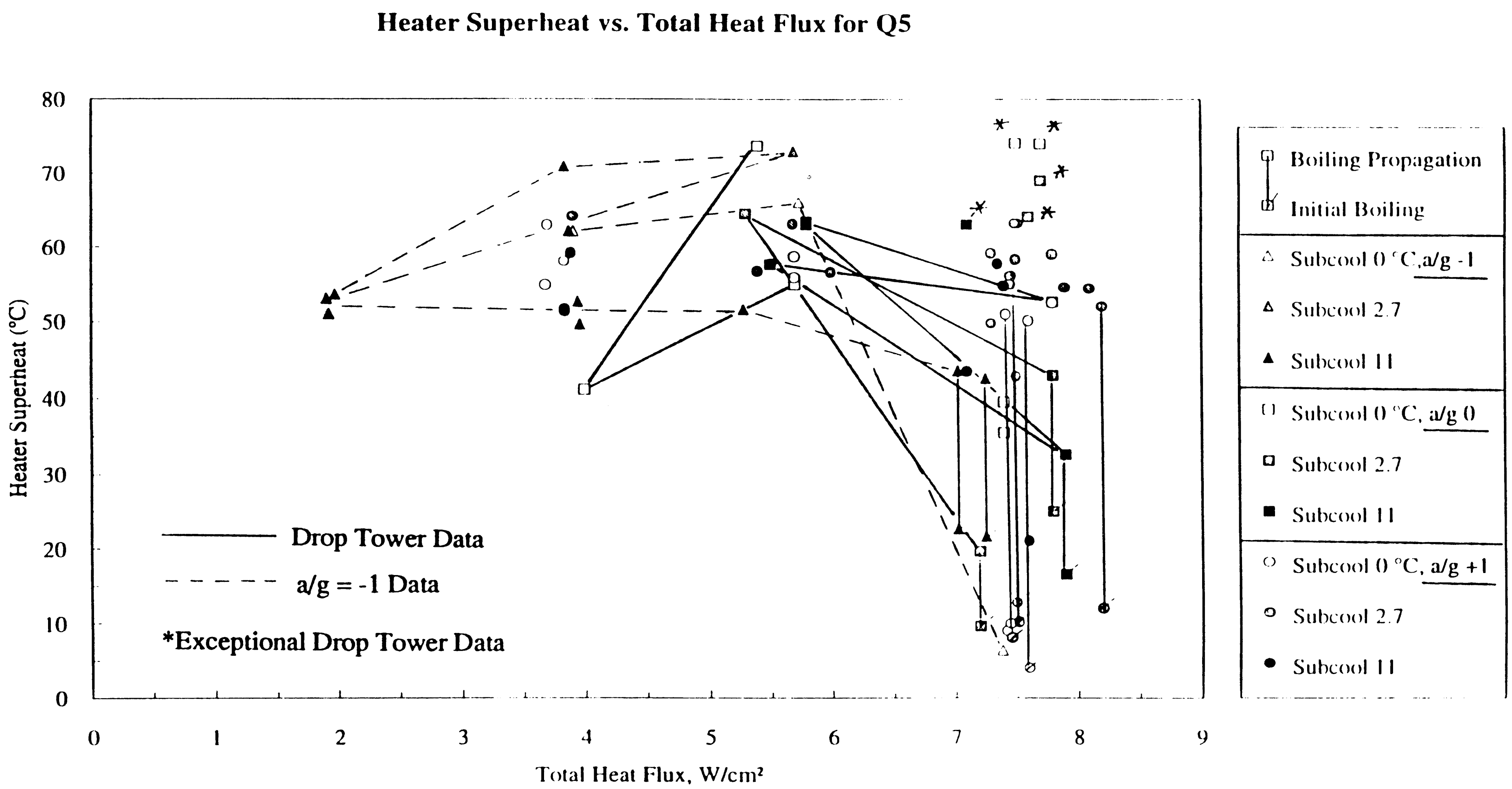

Figure 6.10. Heater surface nucleation superheat during ground based and 5.1 second drop tower testing.

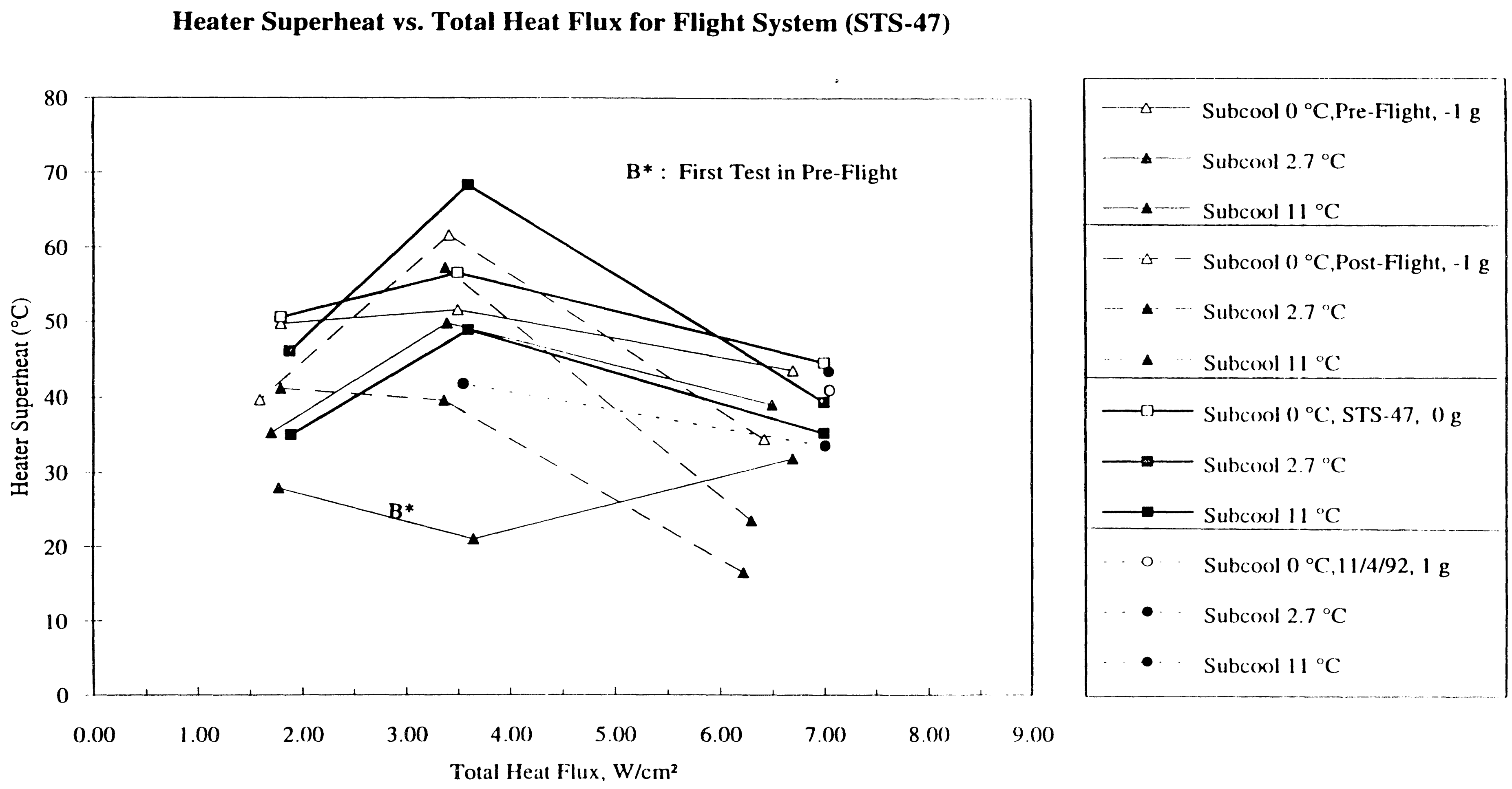

Figure 6.11. Heater surface nucleation superheat of PBE-IA prior to, during, and

Bubble Growth Prediction

Assuming that all energy applied consumed in forming a vapor bubble

$$A\cdot q = hfg\cdot\frac{d}{dt}\left(\frac{4}{3}\cdot\pi\cdot R^3\cdot\rho\right)$$

Fluid : R-113

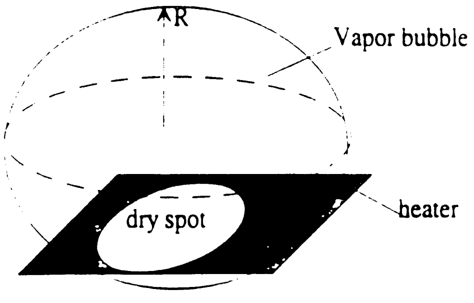

$T := 60$ $A := 7.277\cdot 10^{-4}$

$hfg := hr(T)$ $\rho v := \rho vr(T)$

$t := 1..100$

$$R(q,t) := \left(\frac{3\cdot A\cdot q\cdot 10000}{4\cdot\pi\cdot hfg\cdot\rho v}\cdot t\right)^{\frac{1}{3}}$$

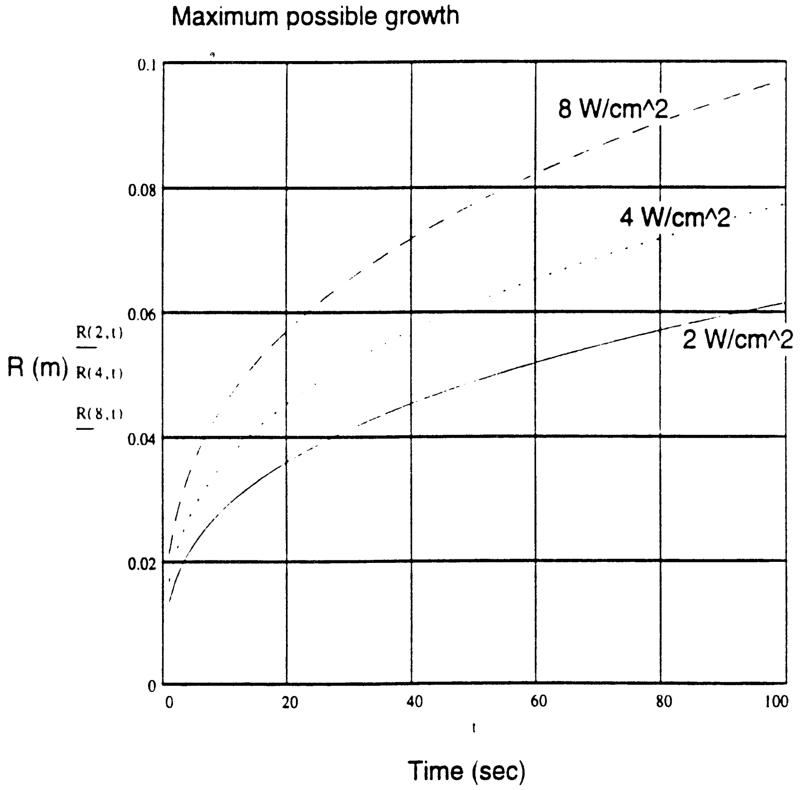

Figure 6.12. Prediction of spherical vapor bubble growth in saturated R-113, corresponding to PBE-IA Run Nos. 7-9.

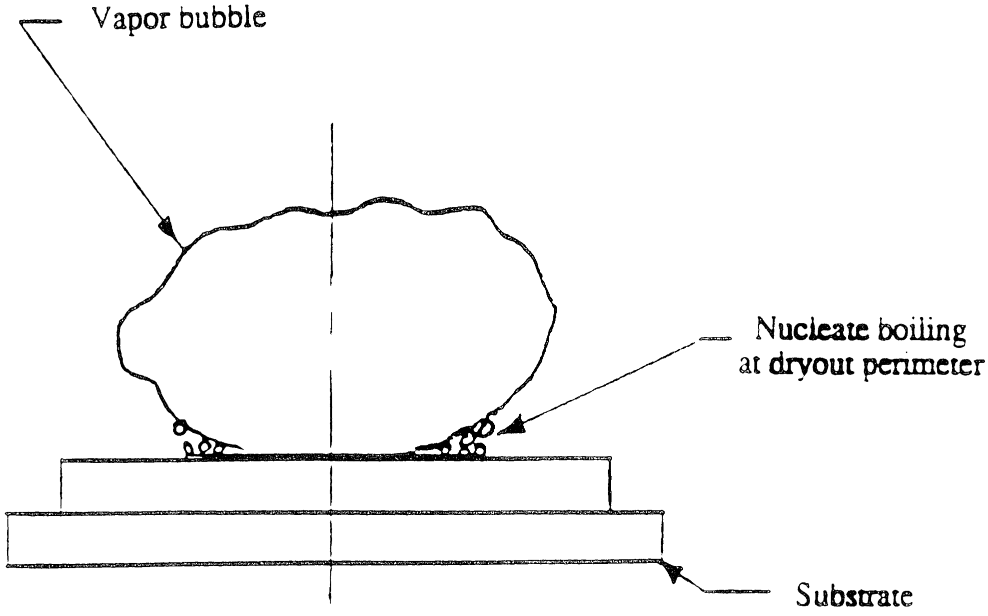

Side View

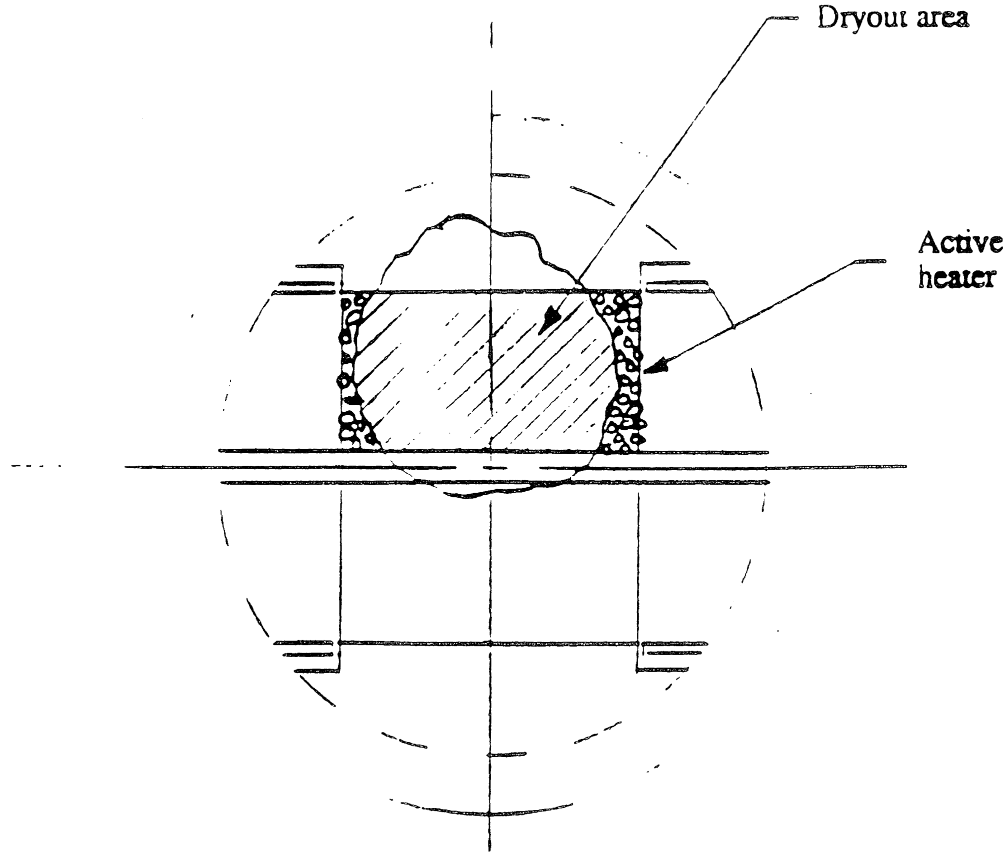

Figure 6.13. Schematic representation of boiling observed on heater surface in microgravity, from PBE-IA on STS 47.

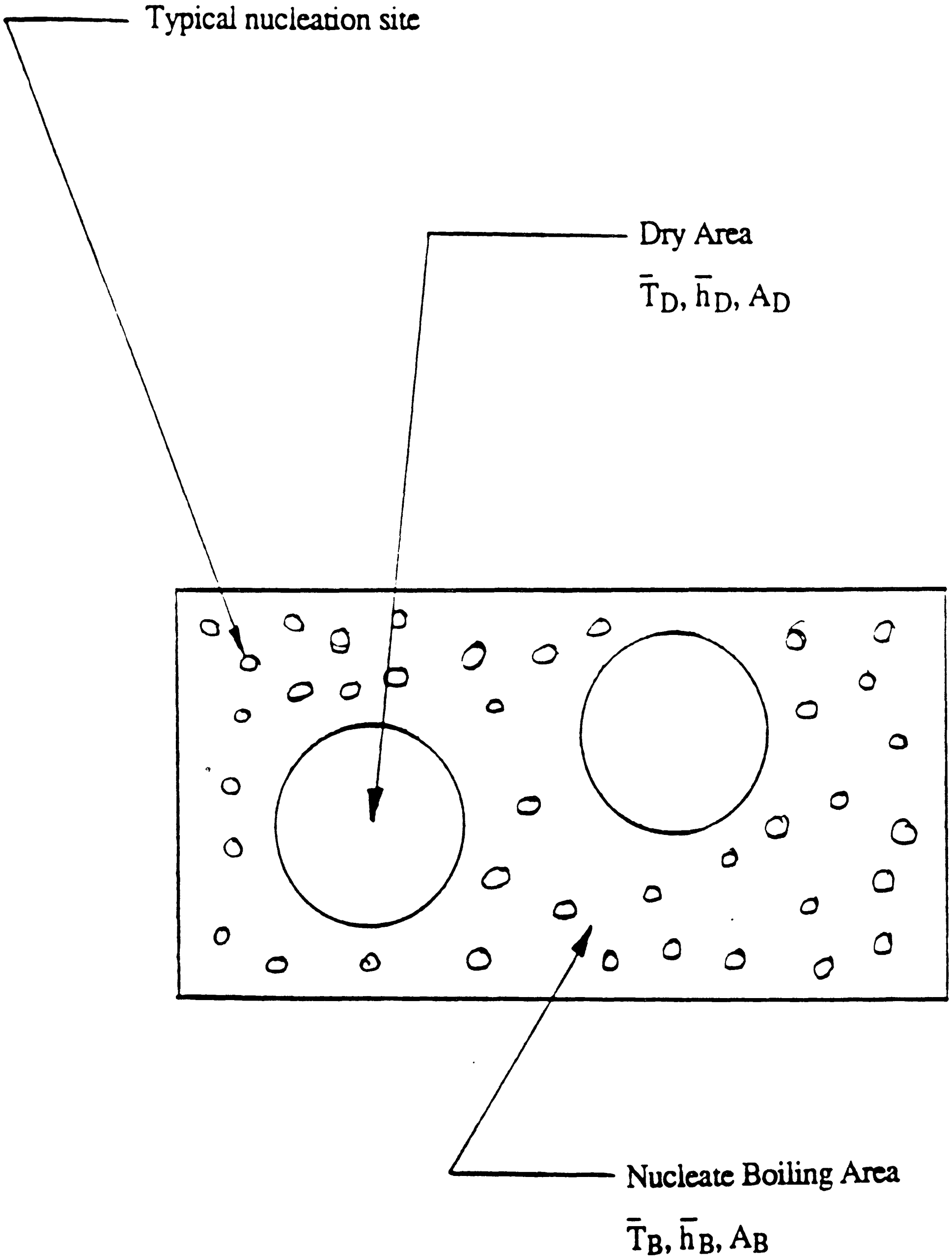

Figure 6.14. Heater surface representation from underside with defined terms.

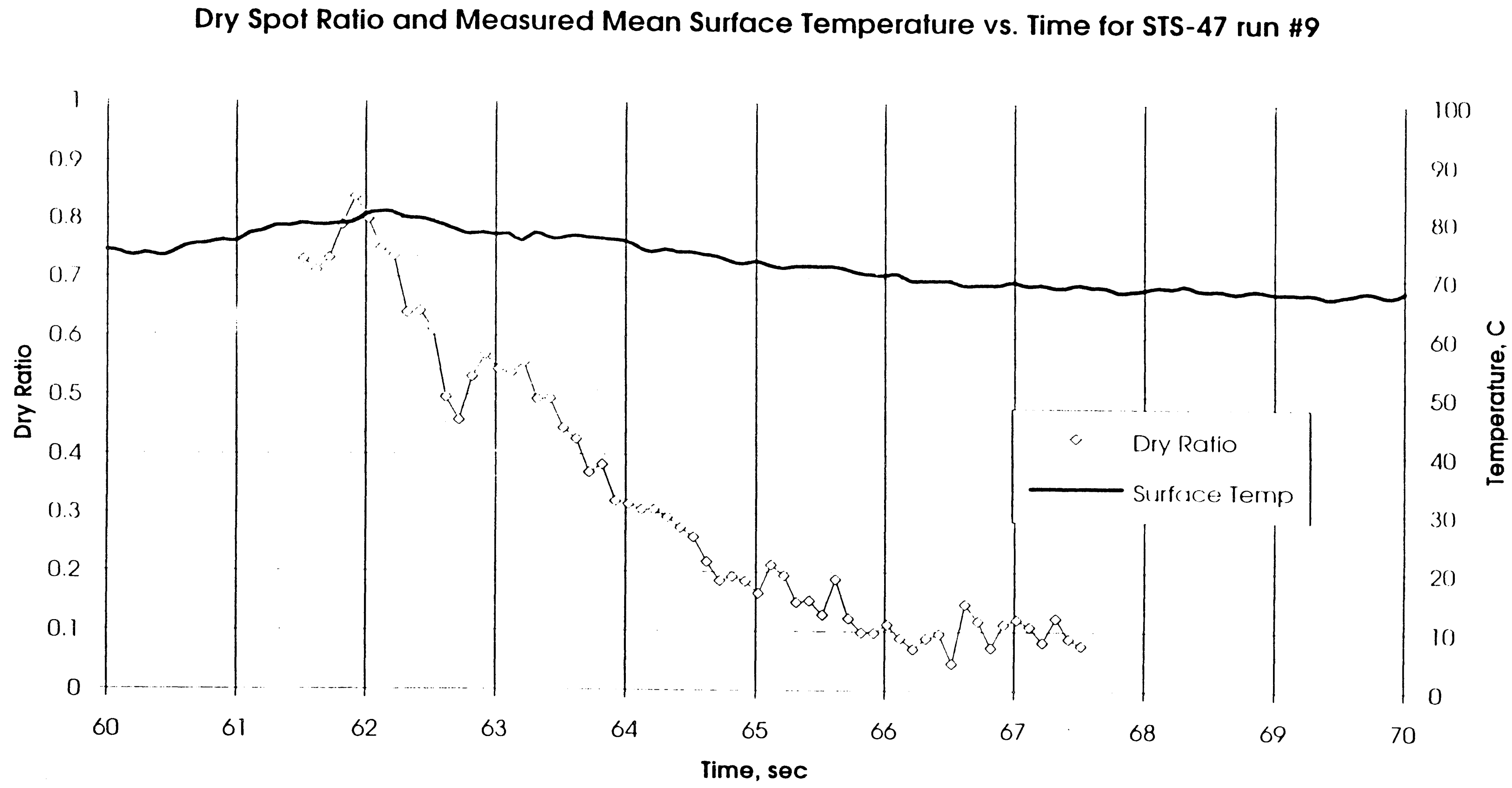

Dry Spot Ratio and Measured Mean Surface Temperature vs. Time for STS-47 run #9

Figure 6.15a. PBE-IA on STS-47. Run No. 9. Transient measured mean heater surface temperature and fractional dry area. Time interval: 61.5-67.5 seconds.

]

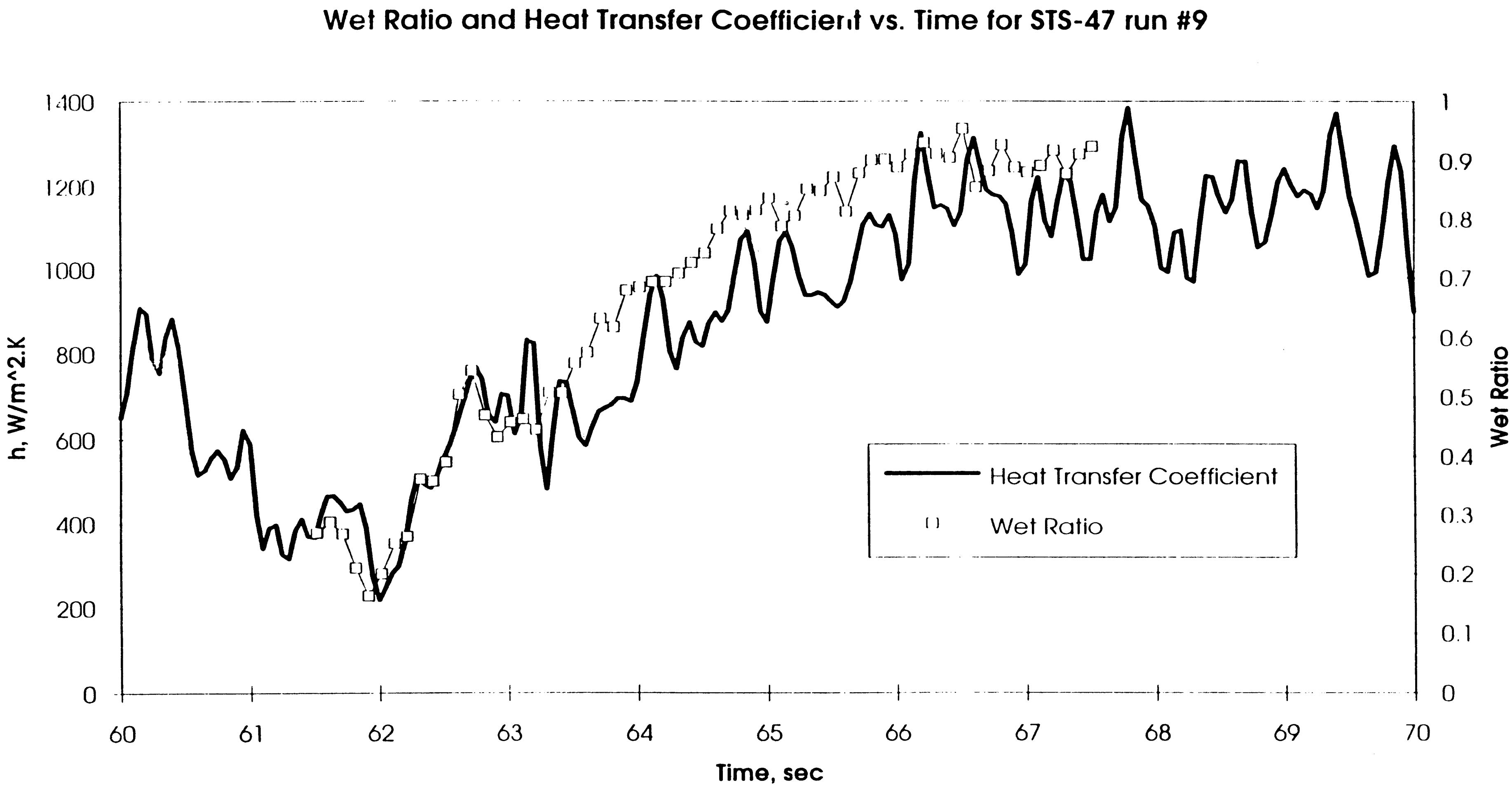

Figure 6.15b. PBE-IA on STS-47. Run No. 9. Relation between measured mean heat transfer coefficient and heater fractional wet area. Time interval: 61.5-67.5 seconds.

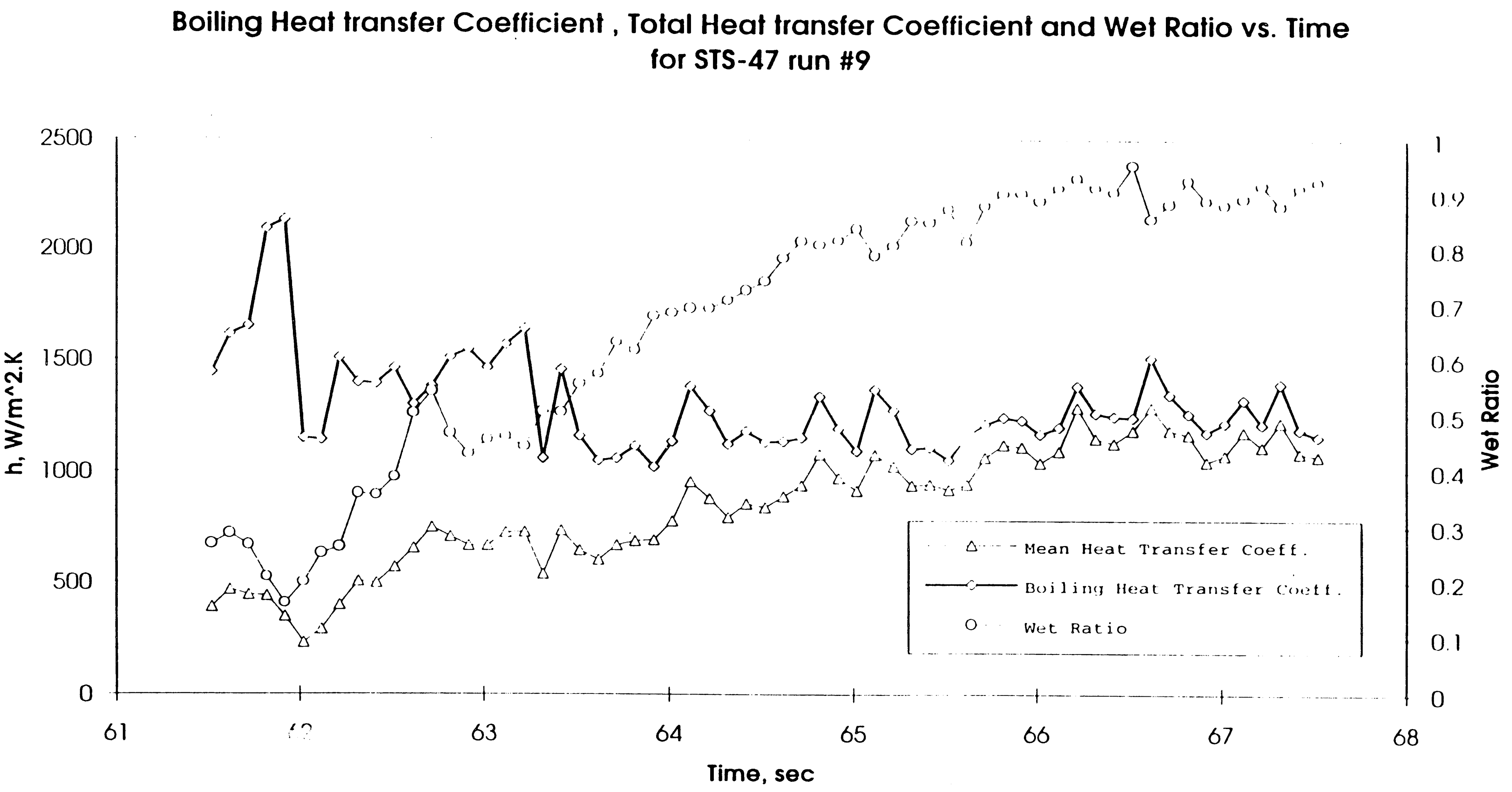

Figure 6.15c. PBE-IA on STS-47. Run No. 9. Relations between the measured mean heat transfer coefficient, measured heater fractional wet area, and derived nucleate boiling heat transfer coefficient. Time interval: 61.5-67.5 seconds.

STS-47 Run # 9 (S1)

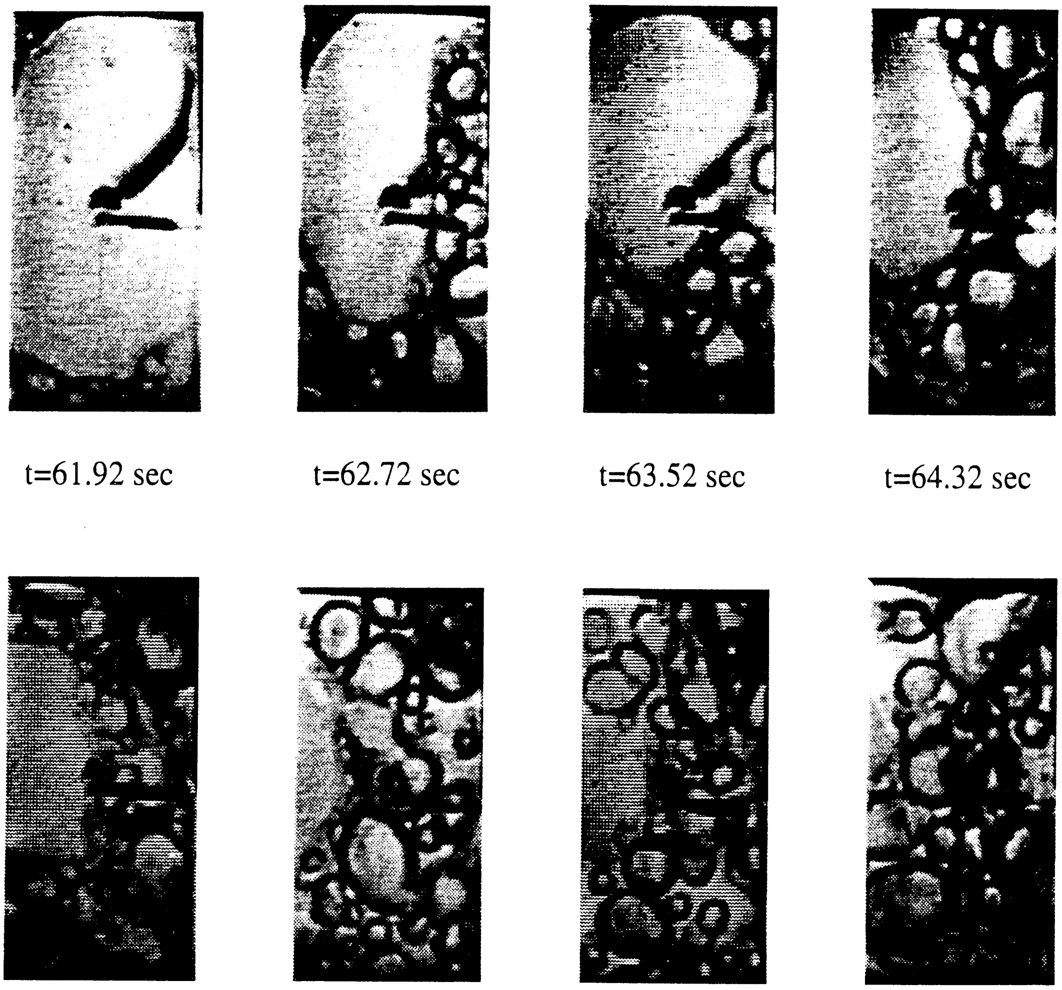

t=61.92 sec t=62.72 sec t=63.52 sec t=64.32 sec

t=65.13 sec t=65.93 sec t=66.73 sec t=67.54 sec

Figure 6.15d. PBE-IA on STS-47. Run No. 9. Sample images showing rewetting. Time interval: 61.5 - 67.5 seconds.

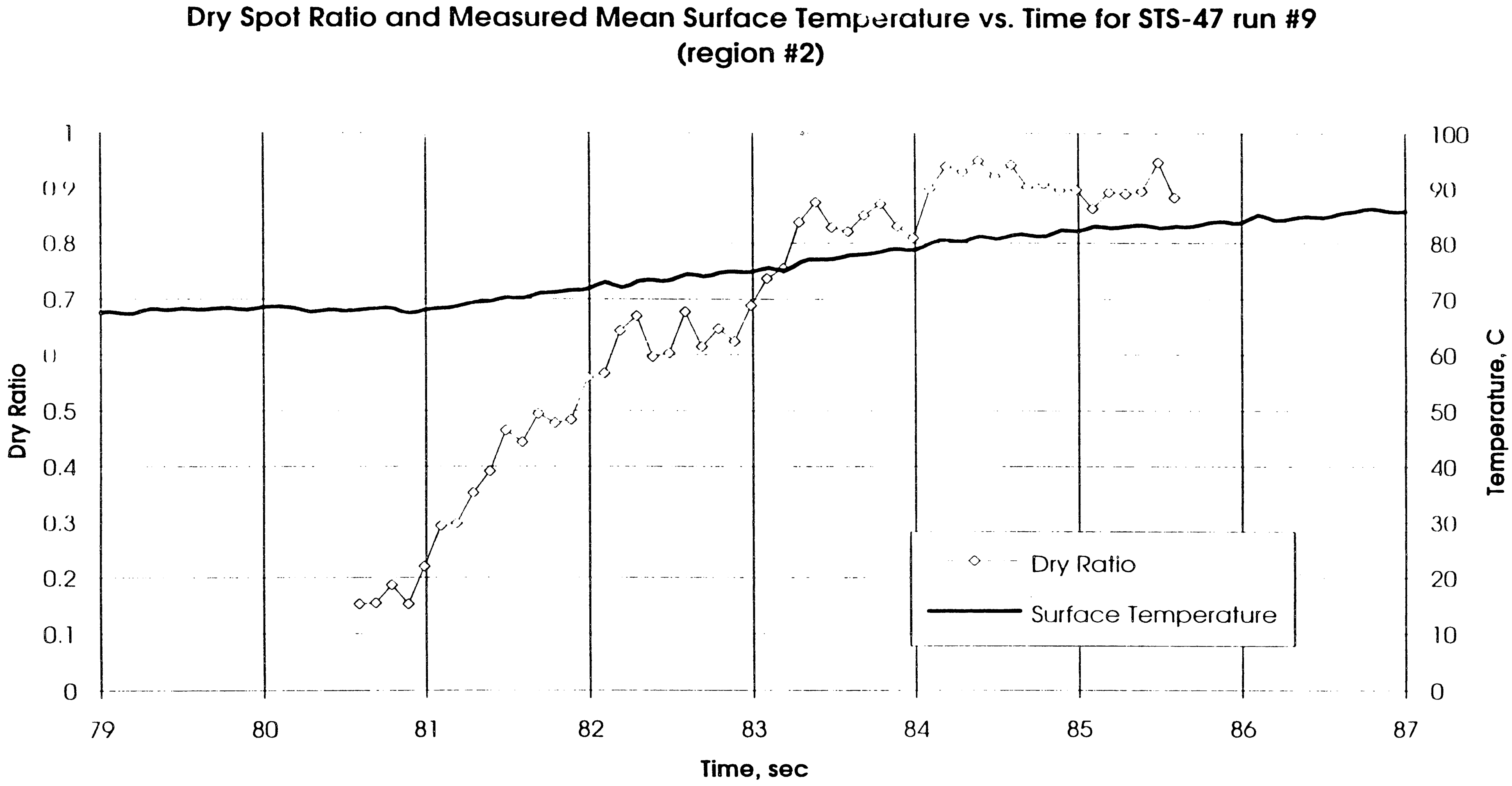

Figure 6.16a. PBE-IA on STS-47. Run No. 9. Transient measured mean heater surface temperature and fractional dry area. Time interval: 80.5-85.5 seconds.

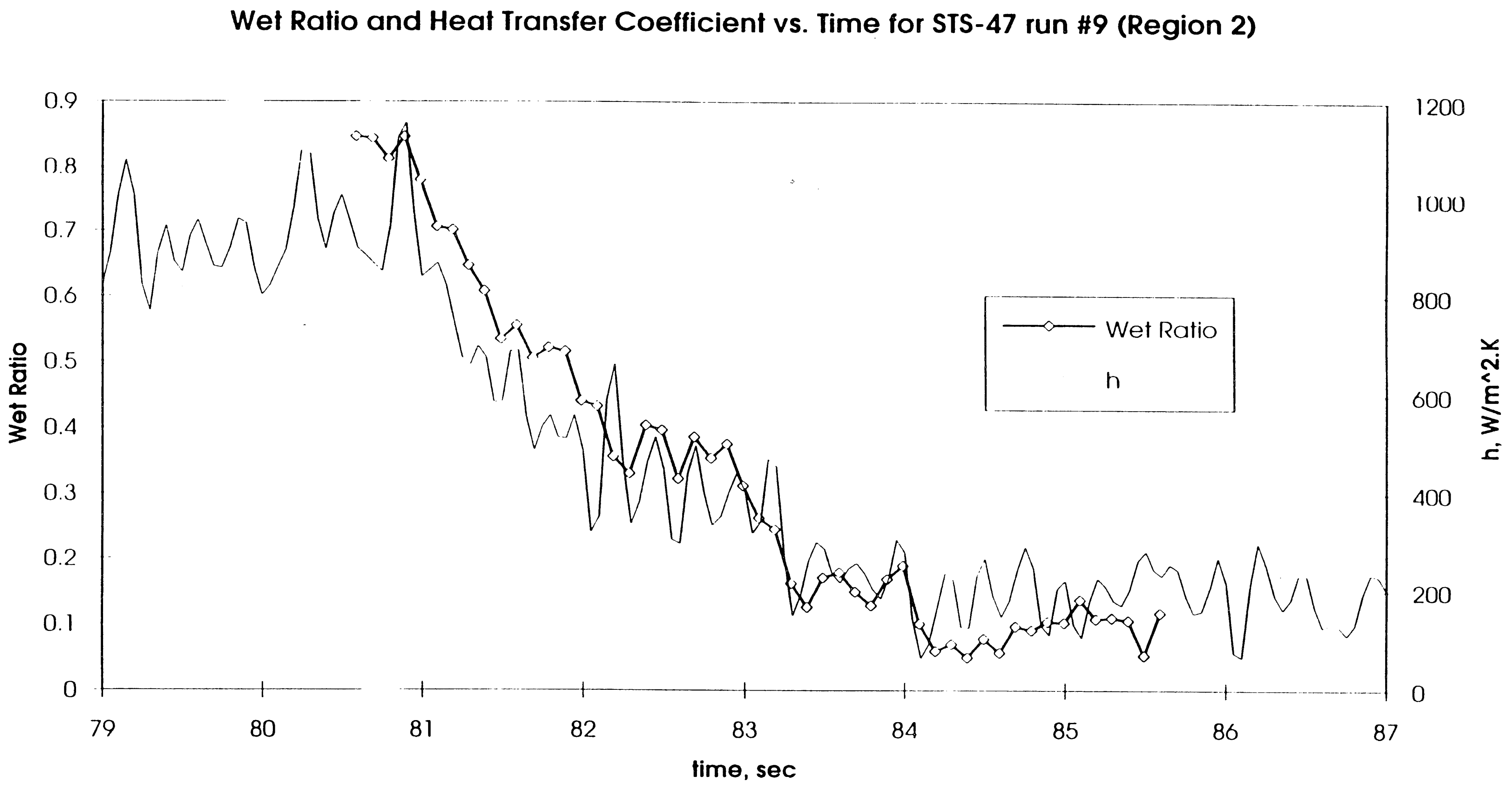

Figure 6.16b. PBE-IA on STS-47. Run No. 9. Relation between measured heat transfer coefficient and heater fractional wet area. Time interval: 80.5-85.5 seconds.

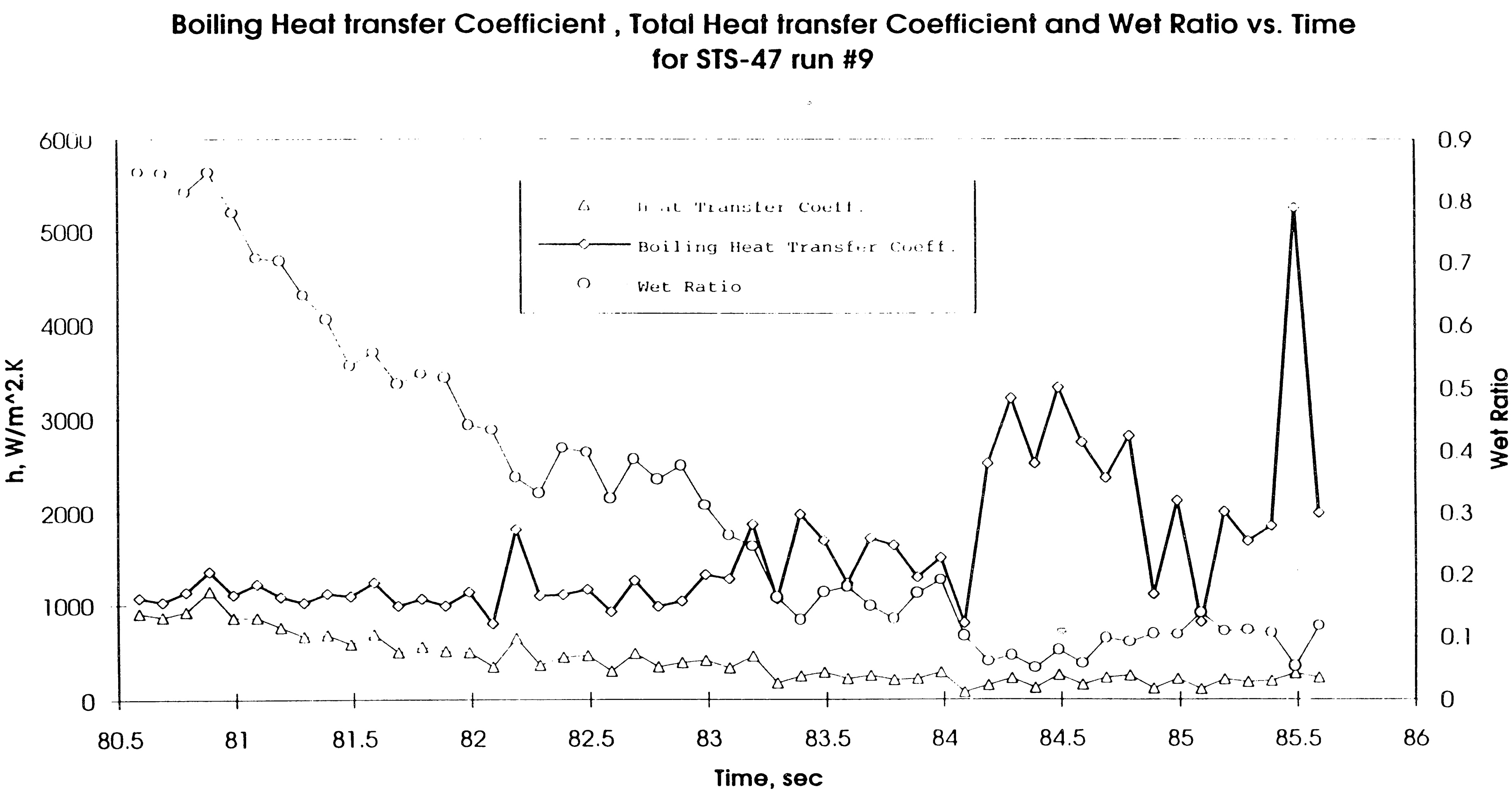

Figure 6.16c. PBE-IA on STS-47. Run No. 9. Relations between the measured mean heat transfer coefficient, measured heater fractional wet area, and derived nucleate boiling heat transfer coefficient. Time interval: 80.5-85.5 seconds

STS-47 Run #9 (S2)

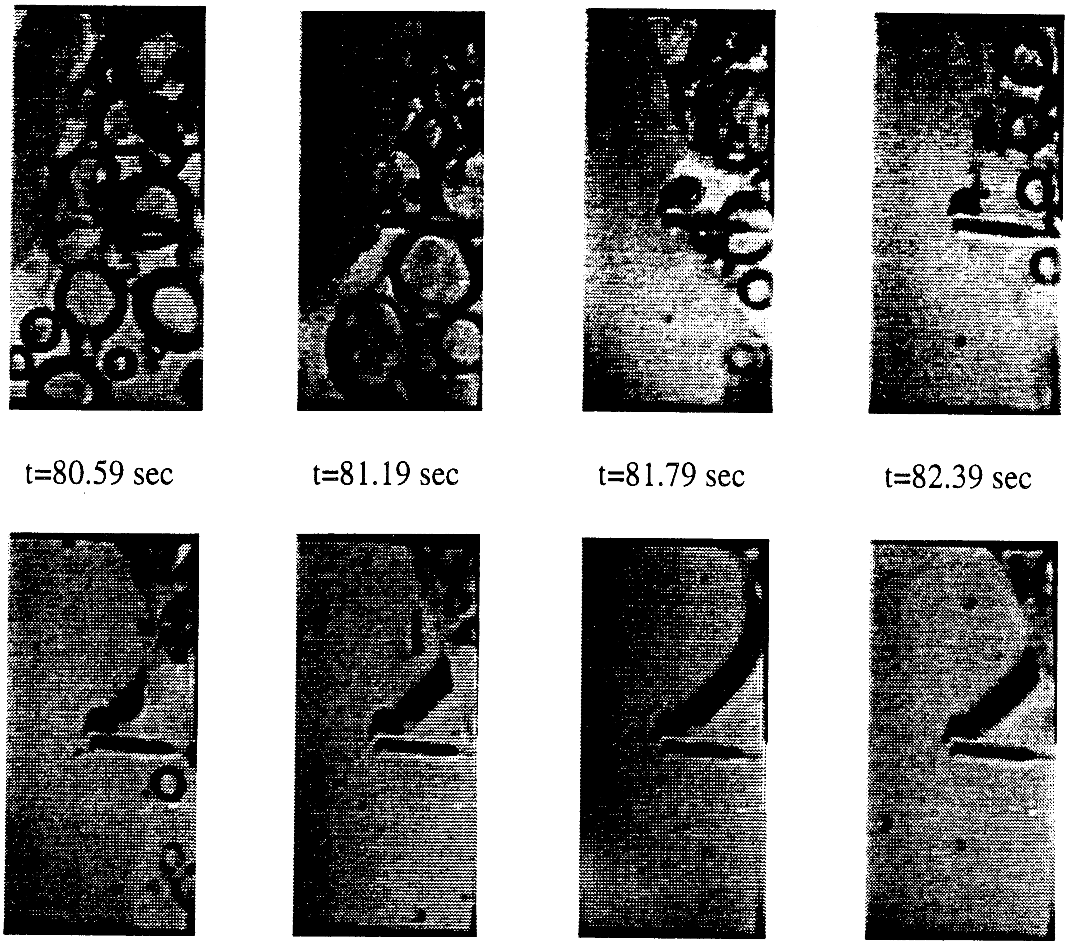

t=80.59 sec

t=81.19 sec

t=81.79 sec

t=82.39 sec

t=82.99 sec

t=83.59 sec

t=84.19 sec

t=84.79 sec

Figure 6.16d. PBE-IA on STS-47. Run No. 9. Sample images showing dryout. Time interval: 80.5 - 85.5 seconds.

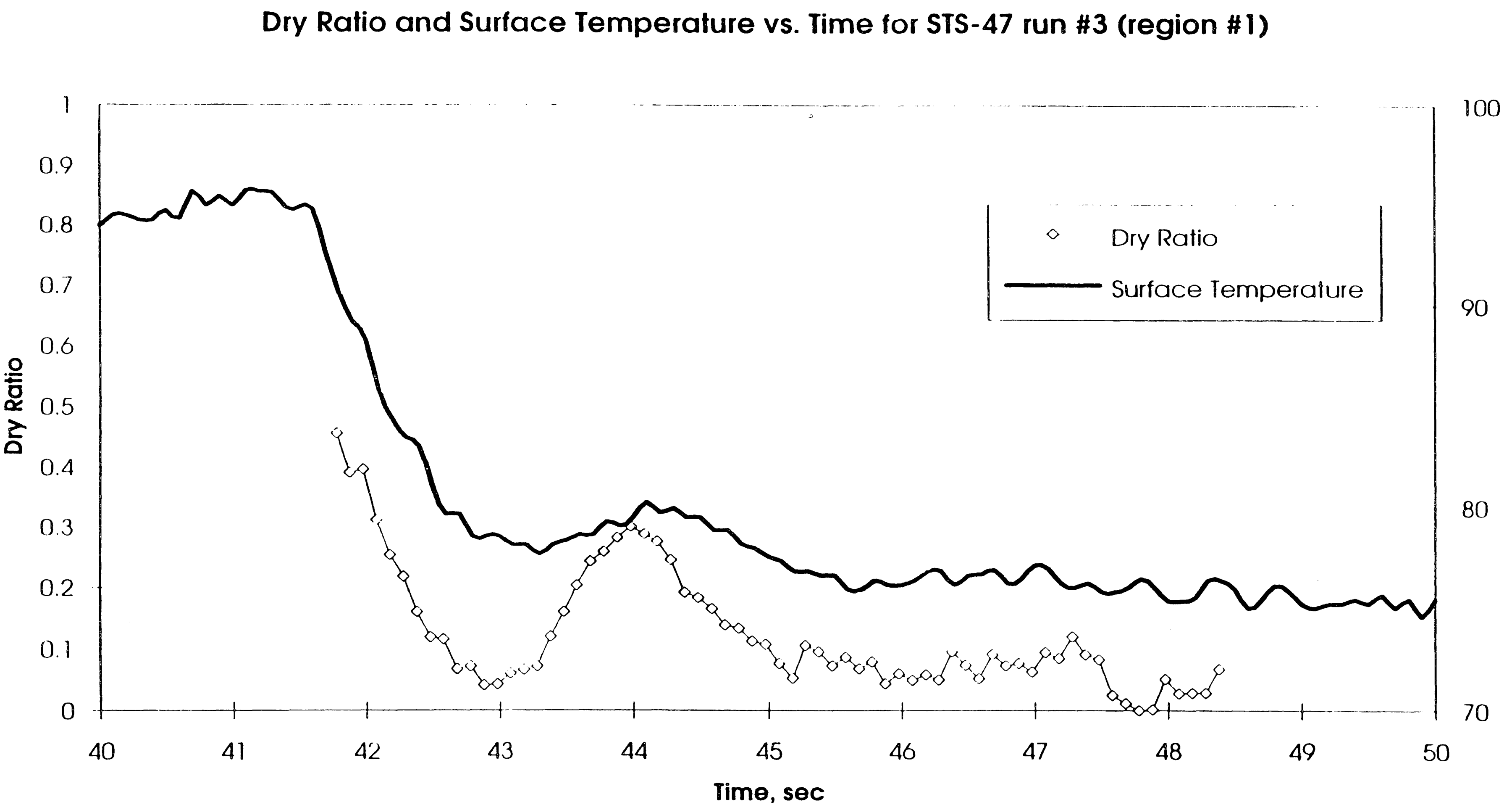

Figure 6.17a. PBE-IA on STS-47. Run No. 3. Transient measured heater surface temperature and fractional dry area. Time interval: 42-50 seconds.

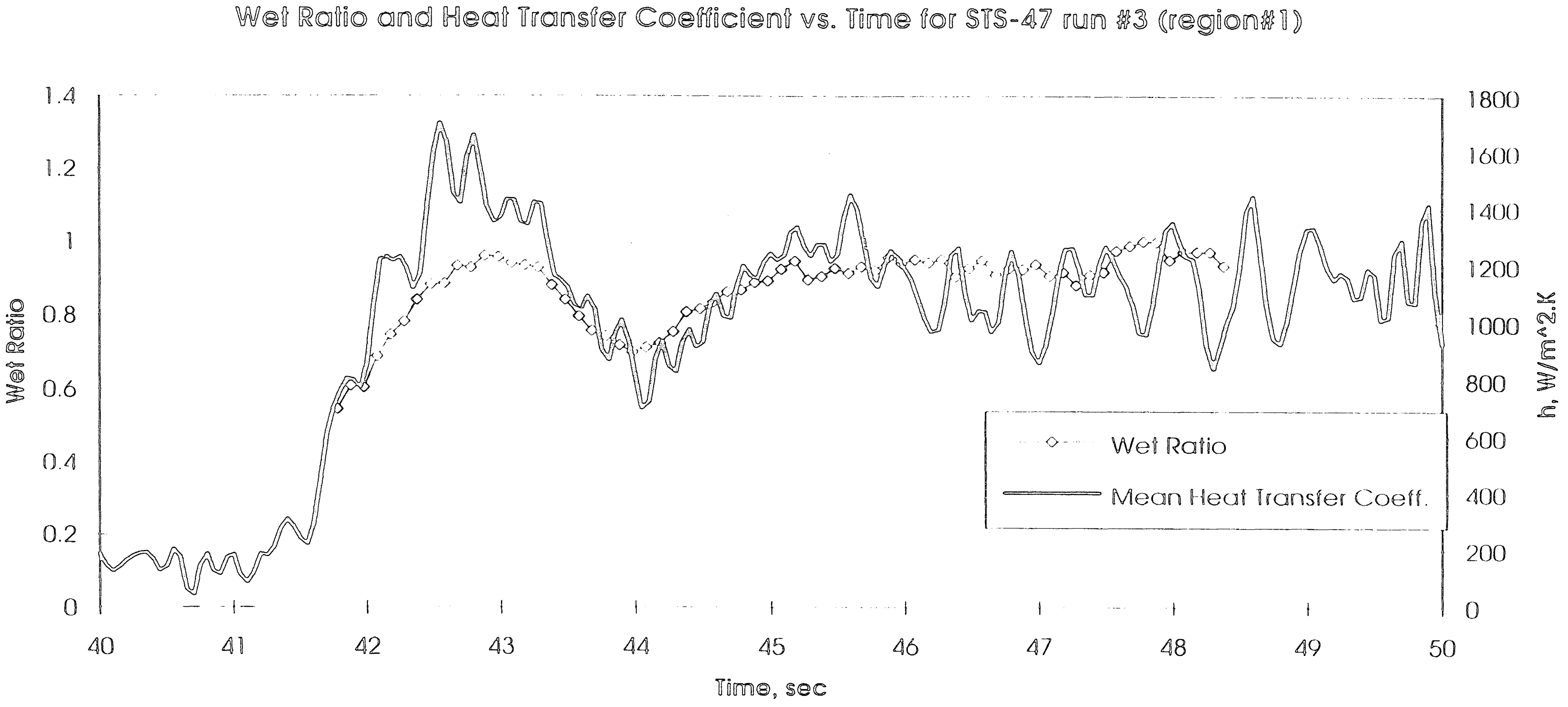

Figure 6.17b. PBE-IA on STS-47. Run No. 3. Relation between measured mean heat transfer coefficient and heater fractional wet area. Time interval: 42-50 seconds.

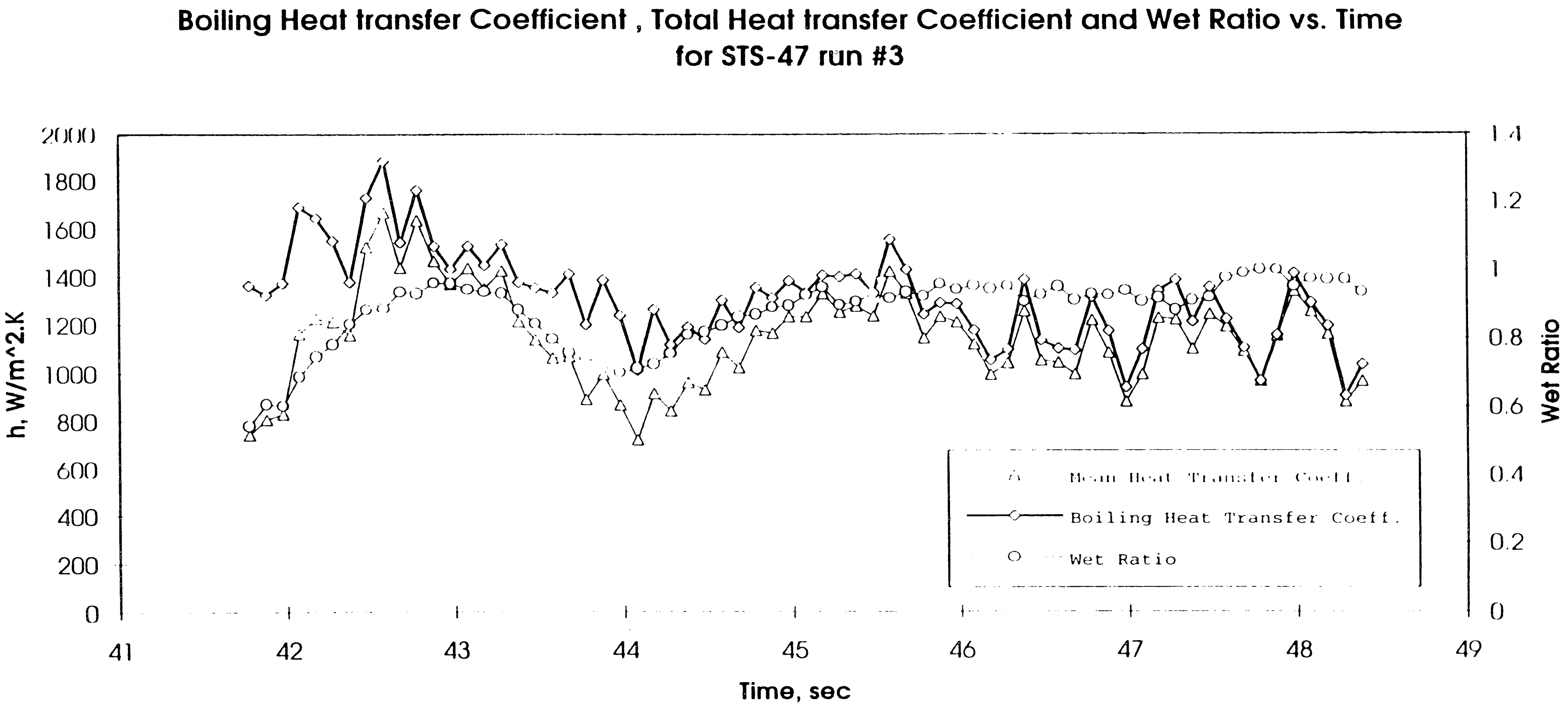

Figure 6.17c. PBE-IA on STS-47. Run No. 3. Relations between the measured mean heat transfer coefficient, measured heater fractional wet area, and derived nucleate boiling heat transfer coefficient. Time interval: 42-50 seconds.

STS-47 Run # 3

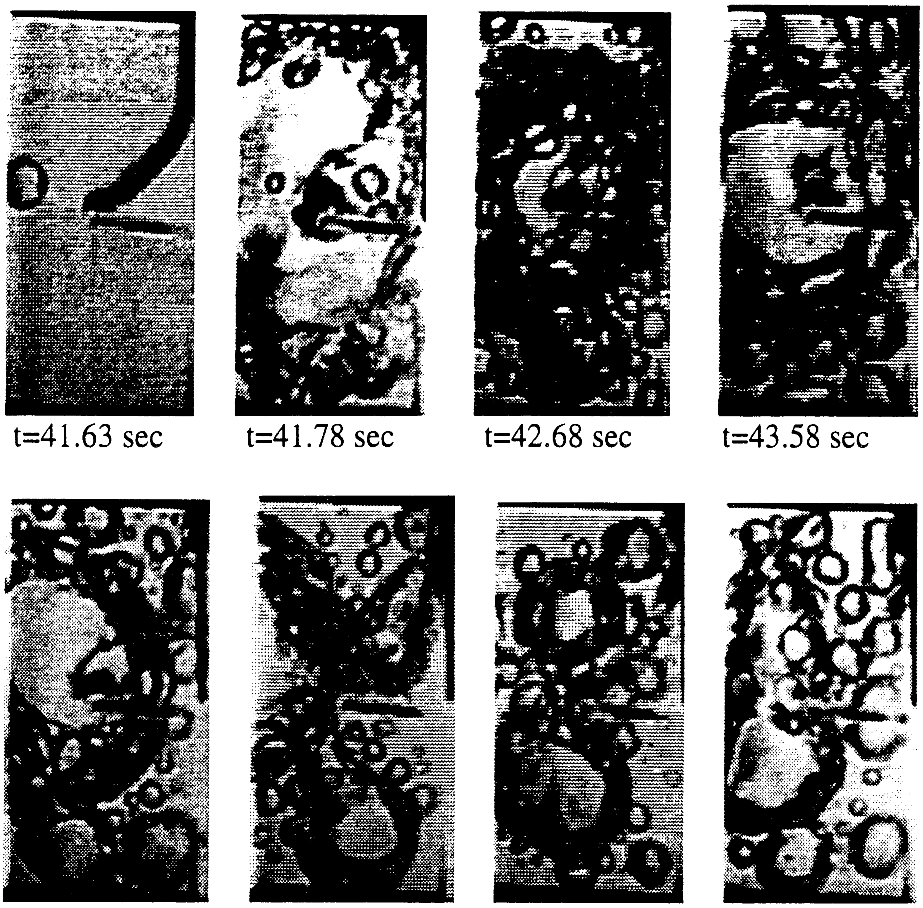

t=41.63 sec t=41.78 sec t=42.68 sec t=43.58 sec

t=44.48 sec t=45.38 sec t=46.28 sec t=47.18 sec

Figure 6.17d. PBE-IA on STS-47. Run No. 3. Sample images showing rewetting oscillations. Time interval: 42 - 50 seconds.

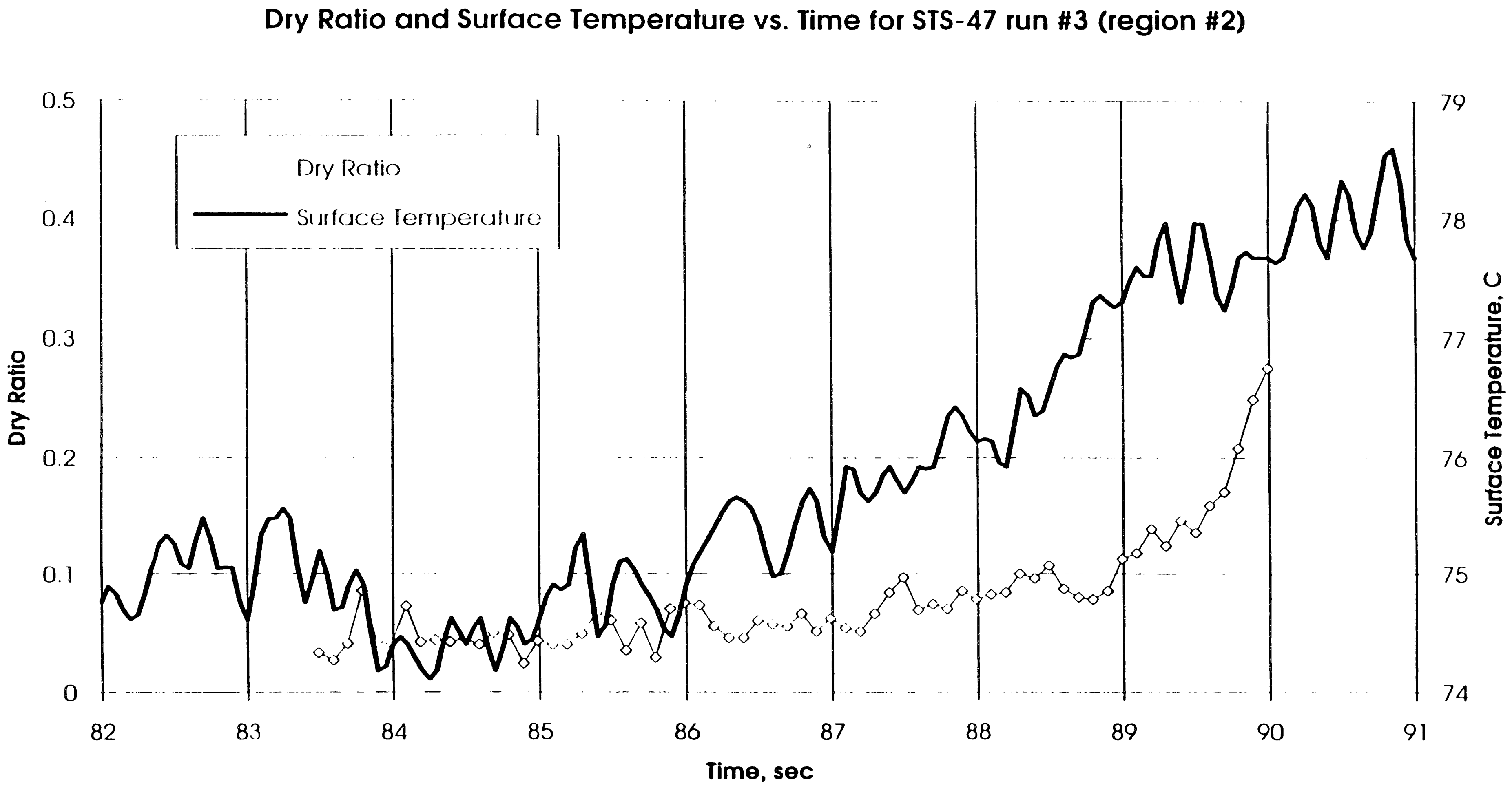

Figure 6.18a. PBE-IA on STS-47. Run No. 3. Transient measured heater surface temperature and fractional dry area. Time interval: 83.5-90 seconds.

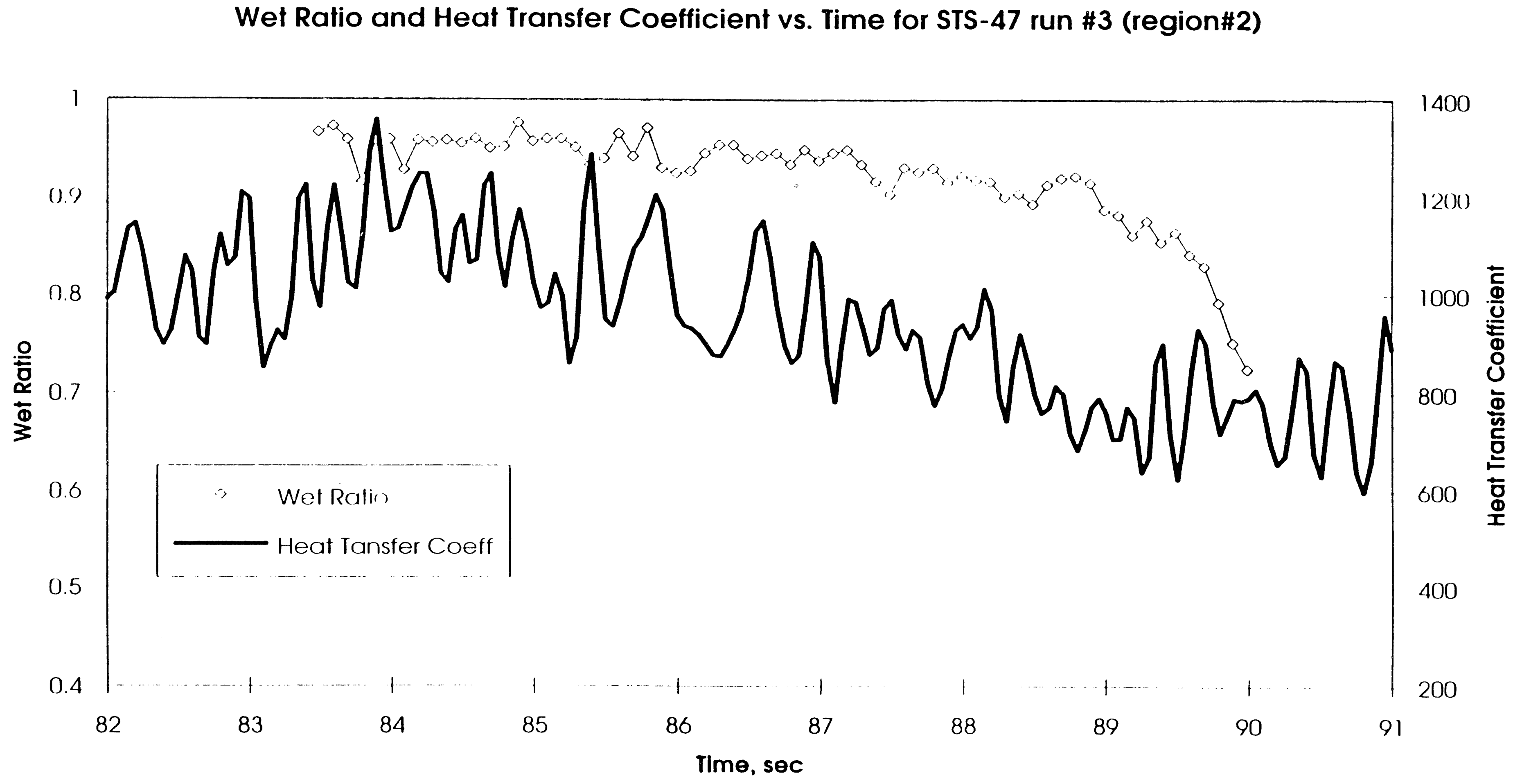

Figure 6.18b. PBE-IA on STS-47. Run No. 3. Relation between measured mean heat transfer coefficient and heater fractional wet area. Time interval: 83.5-90 seconds.

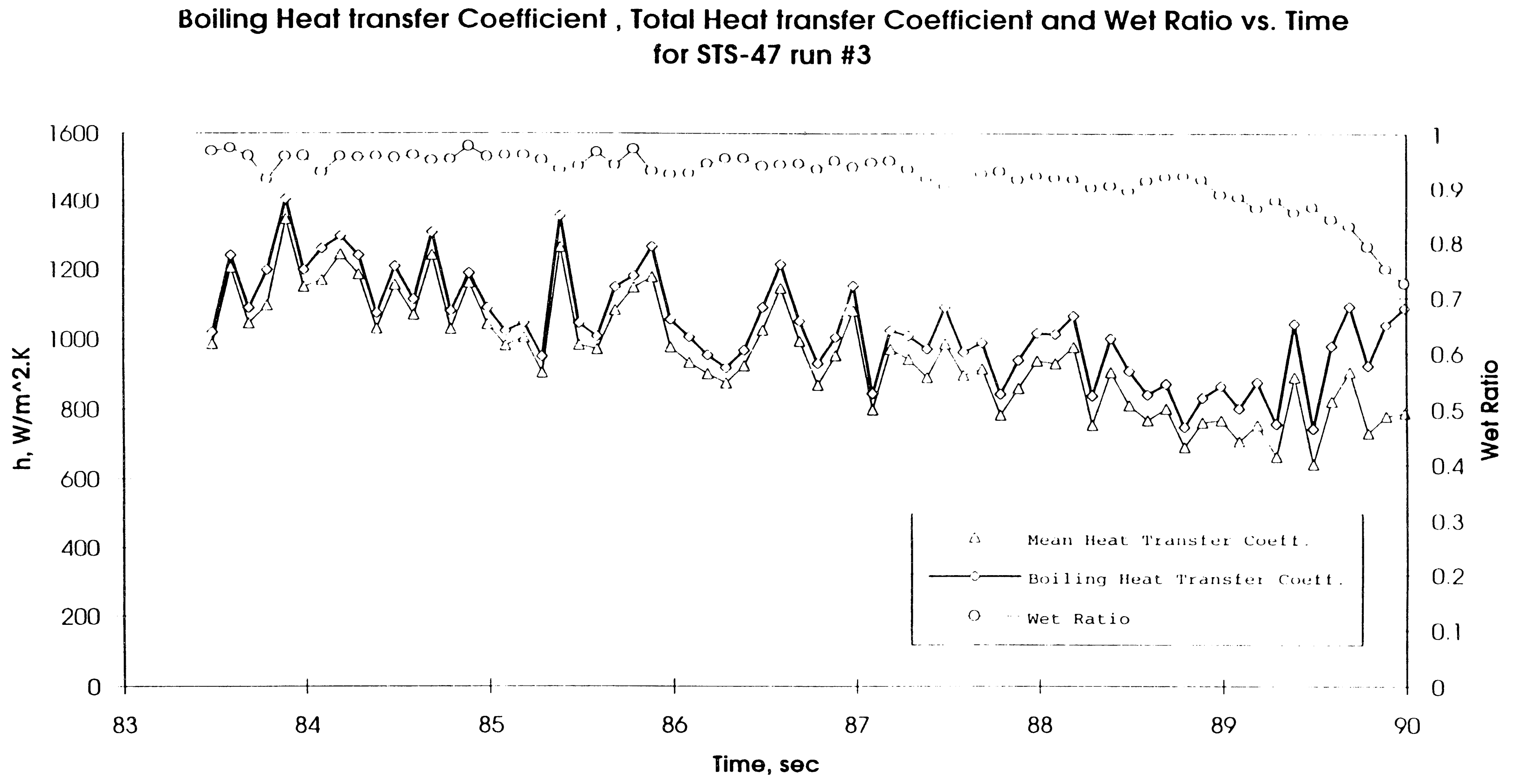

Figure 6.18c. PBE-IA on STS-47. Run No. 3. Relations between the measured mean heat transfer coefficient, measured hater fractional wet area, and derived nucleate boiling heat transfer coefficient. Time interval: 83.5-90 seconds.

STS-47 Run #3

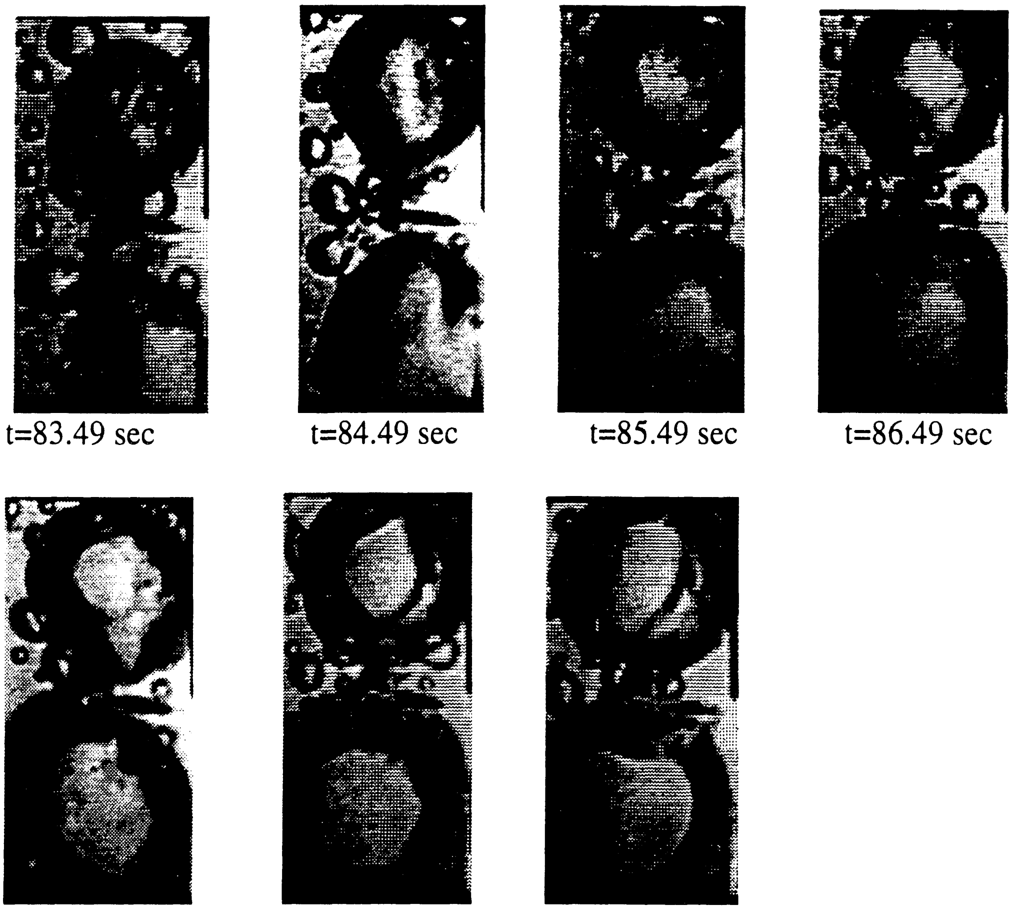

t=83.49 sec
t=84.49 sec
t=85.49 sec
t=86.49 sec

t=87.49 sec
t=88.49 sec
t=89.49 sec

Figure 6.18d. PBE-IA on STS-47. Run No. 3. Sample images showing gradual dryout. Time interval: 83.5 - 90 seconds.

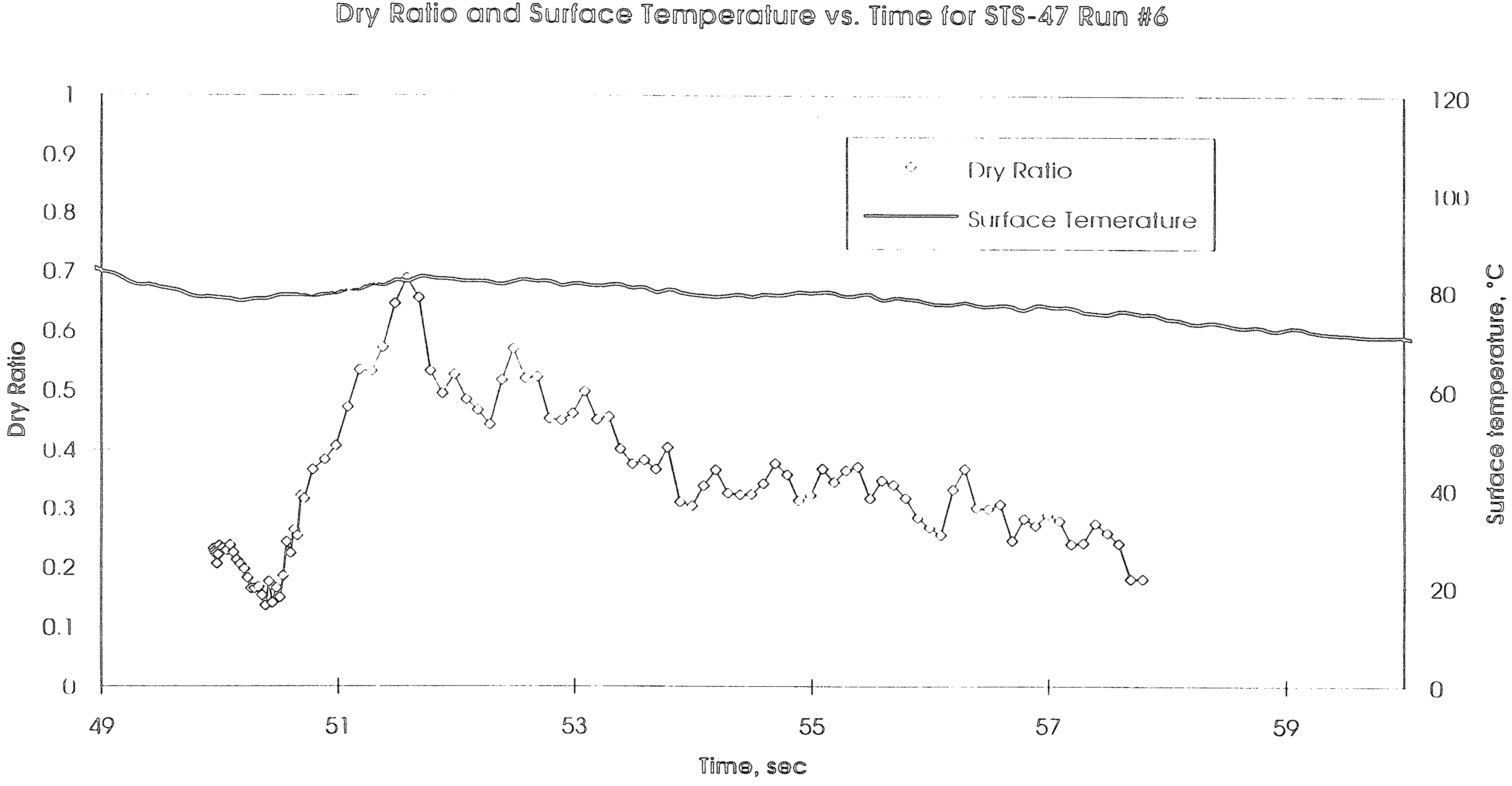

Figure 6.19a. PBE-IA on STS-47. Run No. 6. Transient measured heater surface temperature and fractional dry area. Time interval: 50-58 seconds.

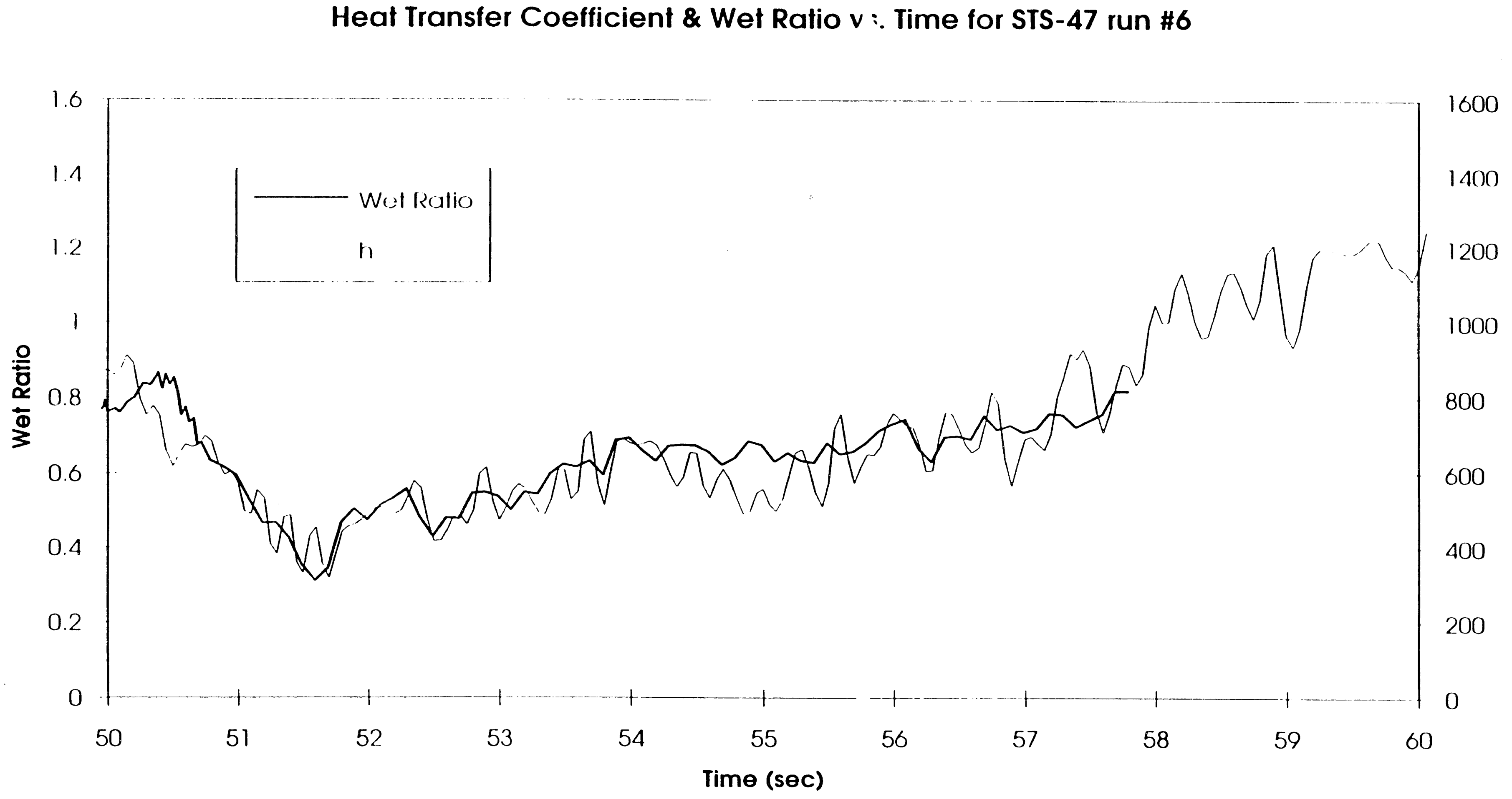

Figure 6.19b. PBE-IA on STS-47. Run No. 6. Relation between measured mean heat transfer coefficient and heater fractional wet area. Time interval: 50-58 seconds.

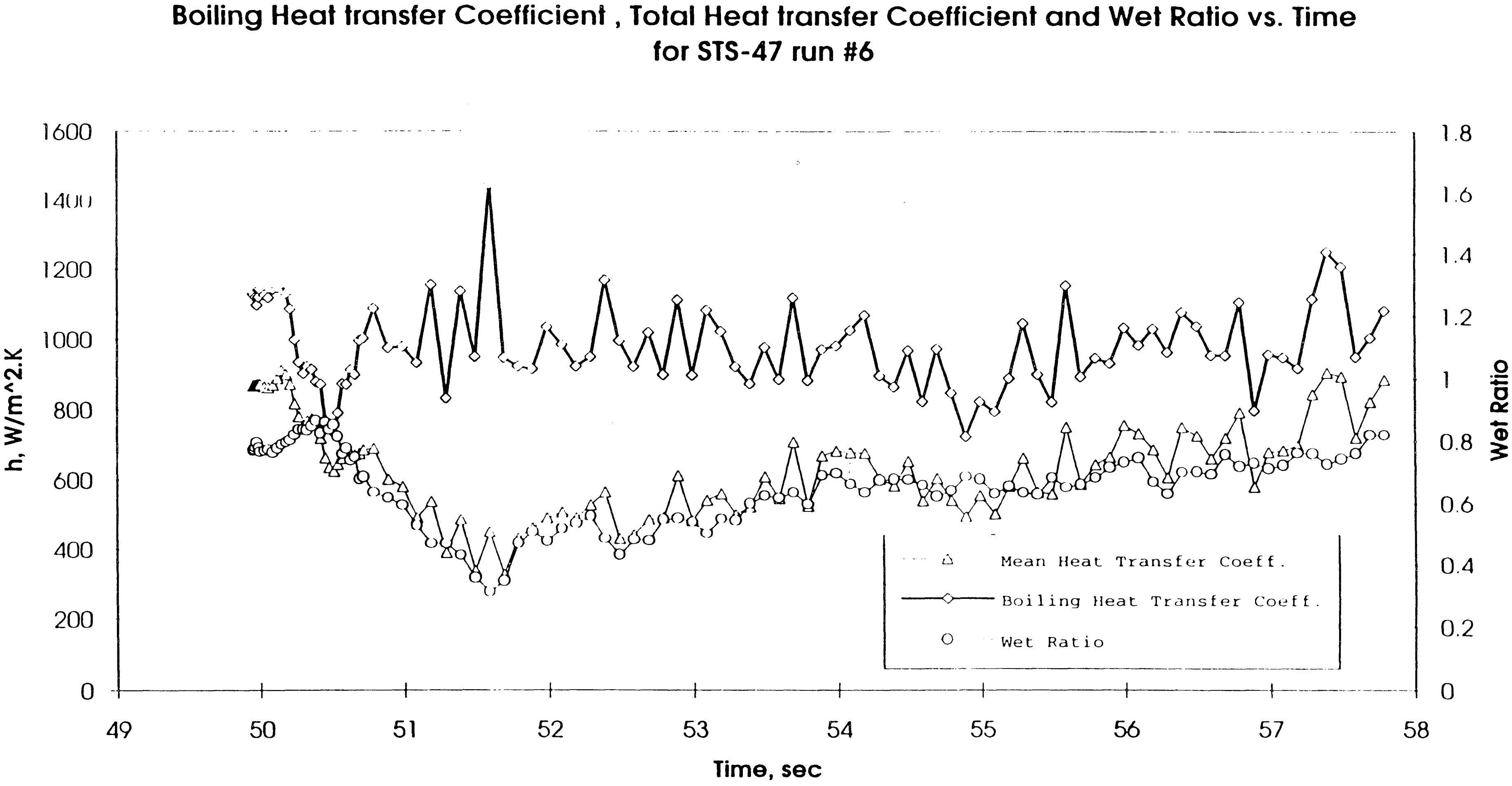

Figure 6.19c. PBE-IA on STS-47. Run No. 6. Relations between the measured mean heat transfer coefficient, measured heater fractional wet area, and derived nucleate boiling heat transfer coefficient. Time interval: 50-58 seconds.

STS-47 Run # 6

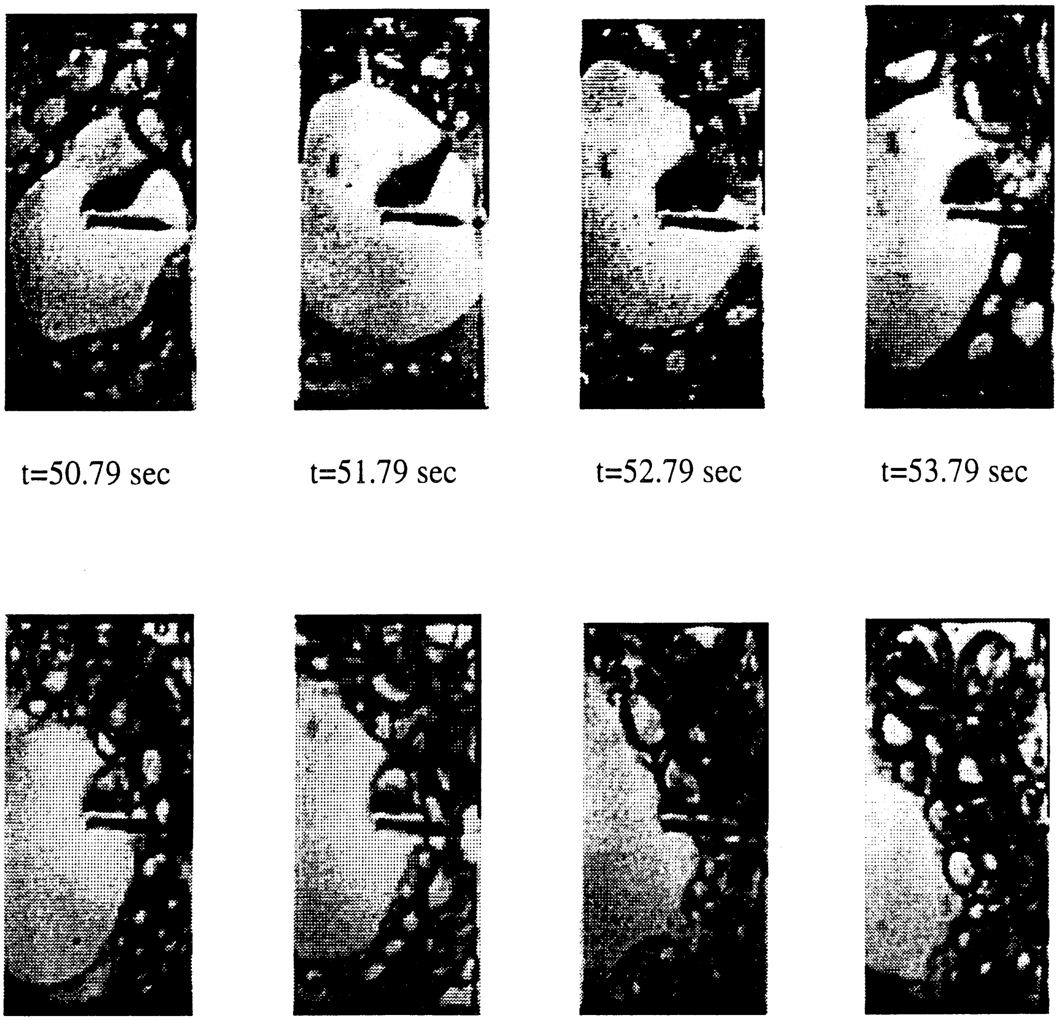

t=50.79 sec t=51.79 sec t=52.79 sec t=53.79 sec

t=54.79 sec t=55.79 sec t=56.79 sec t=57.79 sec

Figure 6.19d. PBE-IA on STS-47. Run No. 6. Sample images of increase in wetting. Time interval: 50 - 58 seconds.

7. CONCLUSIONS

When considered historically over a sufficiently long period of time, the study of a subject as complex as nucleate boiling can be viewed as a continuing evolutionary process. The understanding of the various elements which constitute nucleate boiling has been enhanced considerably as a result of improvements in measurement capabilities, and the use of microgravity is another step in this direction.

Two additional experiments, already completed and similar to that described herein, one with different hardware (identified as PBE-IB) and the other with the identical hardware of the present work (identified as PBE-IC) will hopefully serve to settle uncertainties about the reproducibility and repeatability of nucleate boiling in microgravity, respectively.

With the completion of one phase of this study of pool boiling in microgravity, represented by the current work, questions might be posed as to what has been learned and discovered, and what remains:

(a) It appears that long term steady-state nucleate boiling can take place on a flat heater surface in microgravity with a wetting liquid, but only under quite special conditions of heat flux and subcooling, the boundaries of which are as yet unknown.

(b) Related to (a) above, surface tension has an important role in producing dryout and/or rewetting on a heated surface. The circumstances describing this remain to be explored further.

(c) Two new and interesting heretofore unobserved phenomena have been disclosed in the current work:

    (i) The effect of the heating rate on the heater surface superheat at which nucleation takes place, with the complicating influence of bulk liquid subcooling. It seems that the heater surface superheat at nucleation goes through a maximum as the imposed heat flux is reduced in microgravity. Furthermore, increasing the bulk liquid subcooling reduces the heater superheat at nucleation in microgravity, all other conditions being held constant.

(ii) An extremely dynamic and unusual initial vapor bubble growth has been observed under certain conditions in microgravity, which appears to be associated with an instability problem, producing an unusual interfacial behavior.

(d) A microgravity nucleate boiling heat transfer coefficient has been determined, which to this point appears to take on an almost constant value.

References

Ervin, J.S. and Merte, H., Jr., (1991), "A Fundamental Study of Nucleate Pool Boiling under Microgravity," Report No. UM-MEAM-91-08, Department of Mechanical Engineering and Applied Mechanics, University of Michigan, Ann Arbor, MI., Final Report on NASA Grant NAG3-663.

Ervin, J.S., Merte, H., Keller, R.B., Kirk, K., (1992), "Transient Pool Boiling in Microgravity". Int. J. Heat Mass Transfer, Vol. 35, pp. 659-674.

Iida, Y. Okuyama, K., Sakurai, K., (1993), "Peculiar Bubble Generation on a Film Heater Submerged in Ethyl Alcohol and Imposed a High Heating Rate over 10^7 k/s," Tech. Note, Int. J. Heat Mass Transfer, 36, No. 10, pp. 2699-2701.

Lee, Ho Sung and Merte, H., Jr., (1993), "Vapor Bubble Dynamics in Microgravity," Report No. UM-MEAM-93-10, Department of Mechanical Engineering and Applied Mechanics, University of Michigan, Ann Arbor, MI., Pool Boiling Experiment Report on NASA Contract NAS3-25812.

Mastroianni, M.J., Stahl, R.F., and Sheldon, P.N., (1978), "Physical and Thermodynamic Properties of 1, 1, 2 - Trifluorotrichloroethane (R-113)," J. of Chemical and Engineering Data, 23, 2, pp. 113-118.

Merte, Herman, Jr., (1967), "Liquid Metal Boiling in Agravic Fields," in Investigation of Liquid Metal Boiling Heat Transfer, Air Force Aero Propulsion Lab., Wright-Patterson AFB, OH, AFAPL-TR-66-85, Jan. 1967.

Merte, Herman, Jr., (1989), "Study of Nucleate Pool Boiling under Microgravity," Science Requirements Document to NASA.

Merte, Herman Jr., (1992), "Pool Boiling Experiment," Report No. UM-MEAM-91-19, Department of Mechanical Engineering and Applied Mechanics, University of Michigan, Ann Arbor, Michigan, status Report for period 2/1/91 - 9/30/91 to NASA Lewis Research Center on Contract NAS3-25812.

Weinzierl, A., and Straub, J., (1982), "Nucleate Pool Boiling in Microgravity Environment," Proceedings of the 7th International Heat Transfer Conference, September 6-10, 1982, Munich.

Appendix A

Specific Technical Requirements

Parameter	Requirement
Test Fluid	Fluorocarbon R-113
Heating Surfaces	19.05 mm x 38.1 mm (3/4" x 1-1/2" Gold on Quartz ($7.25\ \text{cm}^2$) Nominal thickness corresponding to a resistance of 3.8 ± 0.2 ohms (Approximately 400 Angstroms), uniform to ± 5% desired.
Test Heat Flux	2 watts/cm^2 14.5 watts 4 watts/cm^2 29.0 watts 8 watts/cm^2 58.0 watts
Test Chamber	15.2 cm (6") Dia. x 10.2 cm (4") High
Temperature Uniformity	± 0.22°C (± 0.4°F)
Nominal Test Temperature	48.9°C (120°F)
Pressure Control	± 690 N/m^2 (± 0.1 psi)
Heater Power	Constant voltage ± 1%. Heater calibration current should not raise heater temperature more than 0.11°C (0.2°F).
Temperature Sensor	12 Sensor Locations 3 Vicinity of each Heater Surface 3 in Bulk Liquid 2 on the Rear of Heater Substrate 1 in surrounding area behind substrate.
Data Requirements	V, I, Time... (19 parameters).
Heater V & I	± 0.1% Meas. Accuracy, but with a sensitivity of ± 0.03% x a full scale.
Temperatures	± 0.06°C (± 0.1°F) Meas. Accuracy
Pressure	± 345 N/m^{2-} (± 0.05 psi) Meas. Accuracy.
Acceleration (3 Axis)	Levels less than 10^{-3}g desired.
Data Requirements	Time correlated to experimental elapsed time Sample Rate - 10 Hz Accuracy - ± 10^{-4} Range - 10^{-2} thru 10^{-4} g Frequency - D.C. thru 2.5 Hz
Photography	100 pps, 10 pps, 0.18 mm (0.007") Resolution
Clock	Nearest 0.01 Sec. Elapsed Time

Appendix B

Coefficients for the Vapor-Pressure Curve for R-113

(From Mastroianni et al, 1978)

$$\ell n\, p = A + \frac{B}{T} + CT + DT^2 + (E)\left[\frac{(F - T)}{T}\right]\left[\ell n\,(F\text{-}T)\right]$$

where:

p = pressure = psia
T = Temperature in °R ≡ °F + 459.67
A = + 23.428348
B = - 9095.6033
C = - 0.012548607
D = $+ 5.3391227 \times 10^{-6}$
E = + 0.14025795
F = + 878.48416
$\ell n\, x$ = Natural logarithm of argument x.

Appendix C. Plots of the X, Y, Z accelerometer measurements for each run of PBE-IA in the STS-47.

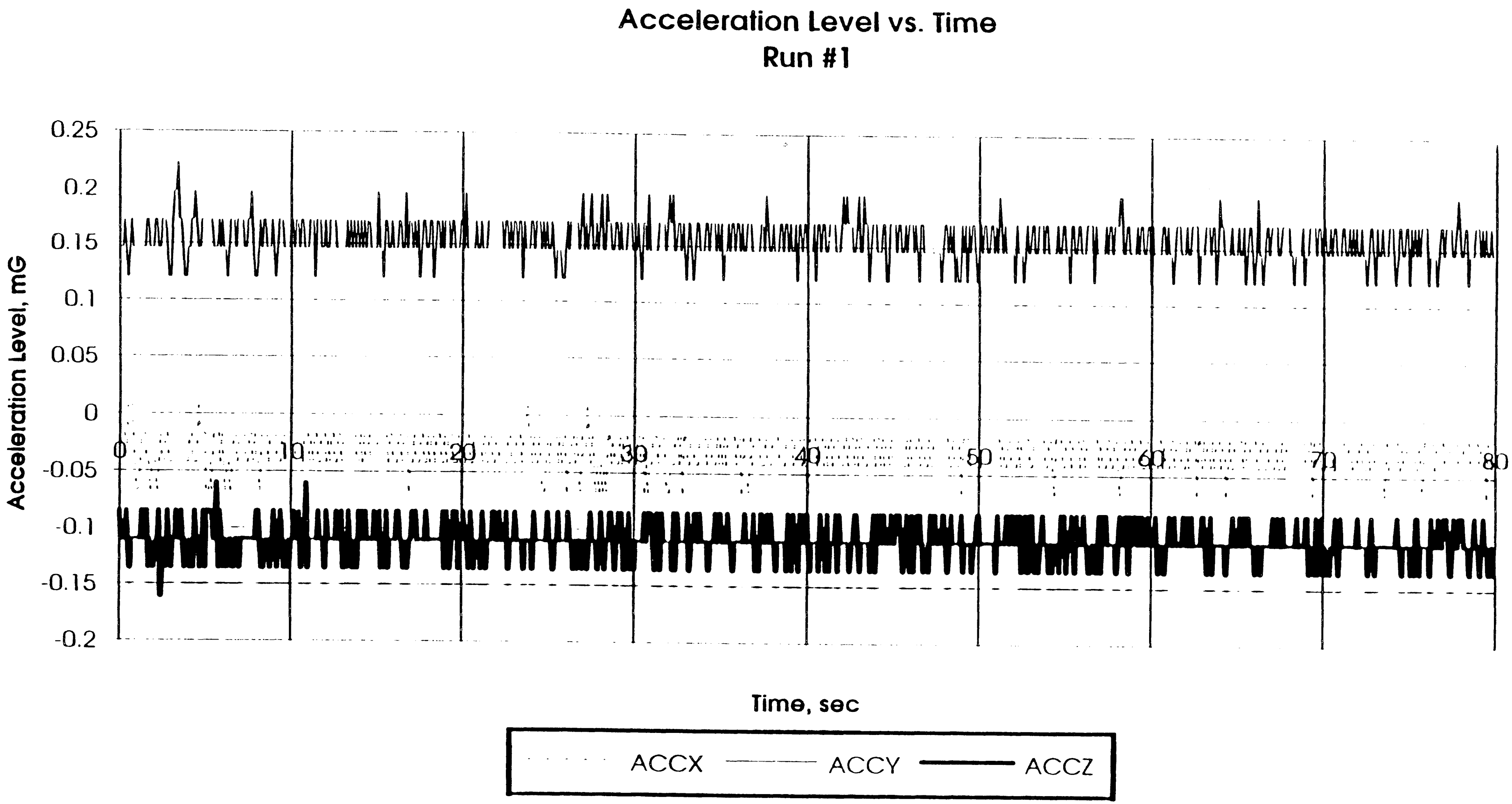

Figure C1. PBE-IA accelerometer measurement. Run No. 1.

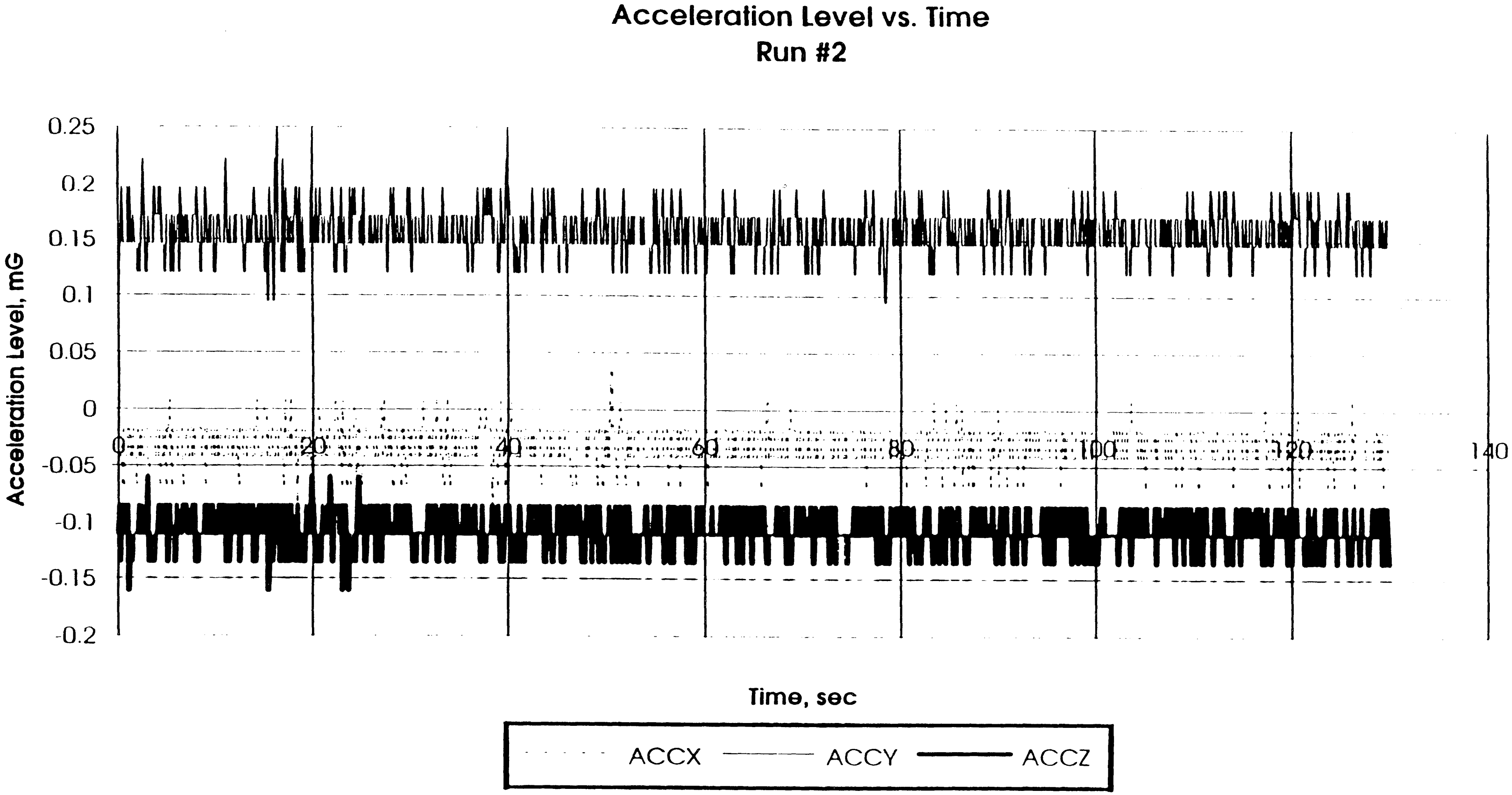

Figure C2. PBE-IA accelerometer measurement. Run No. 2.

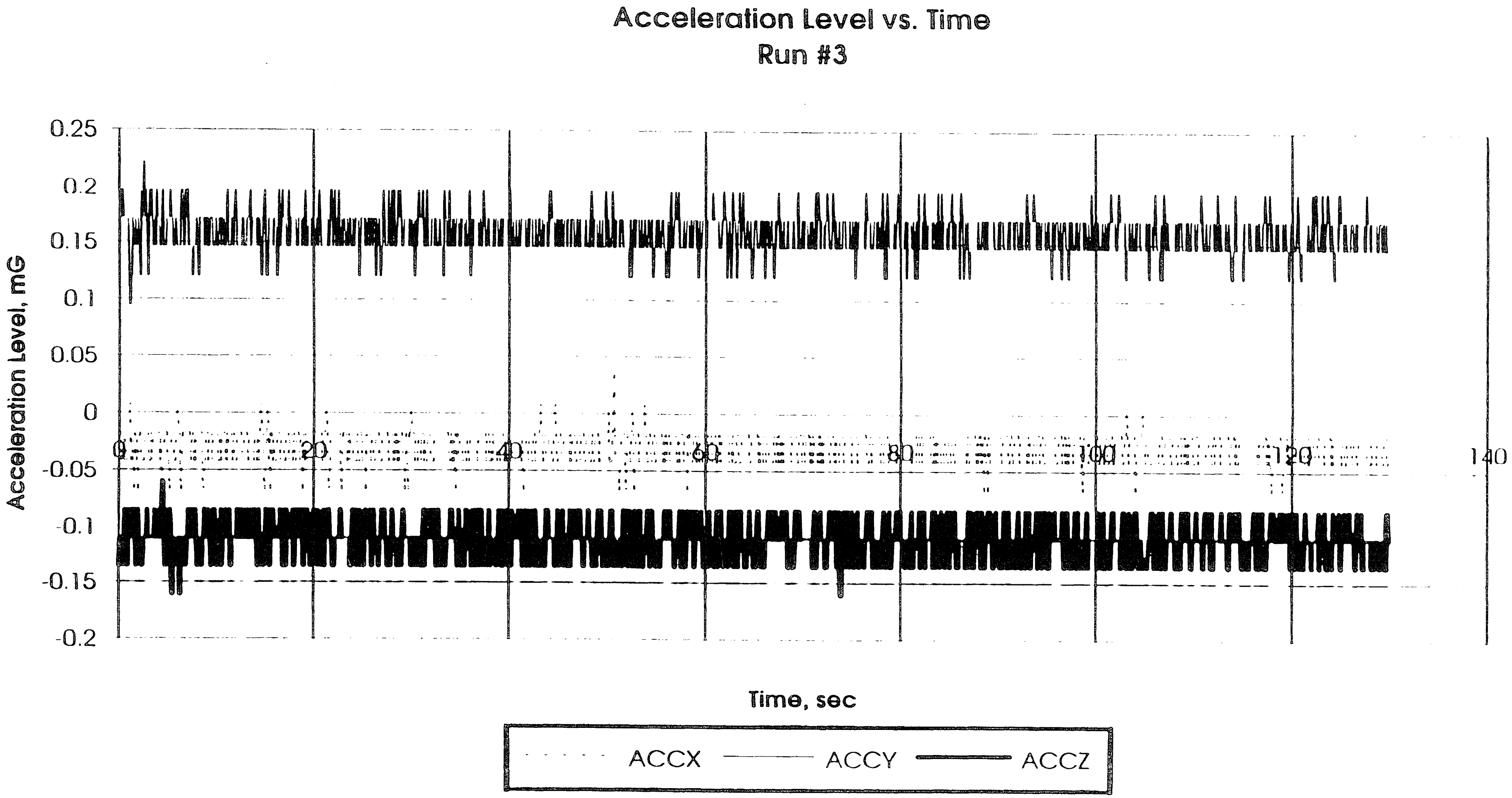

Figure C3. PBE-IA accelerometer measurement. Run No. 3.

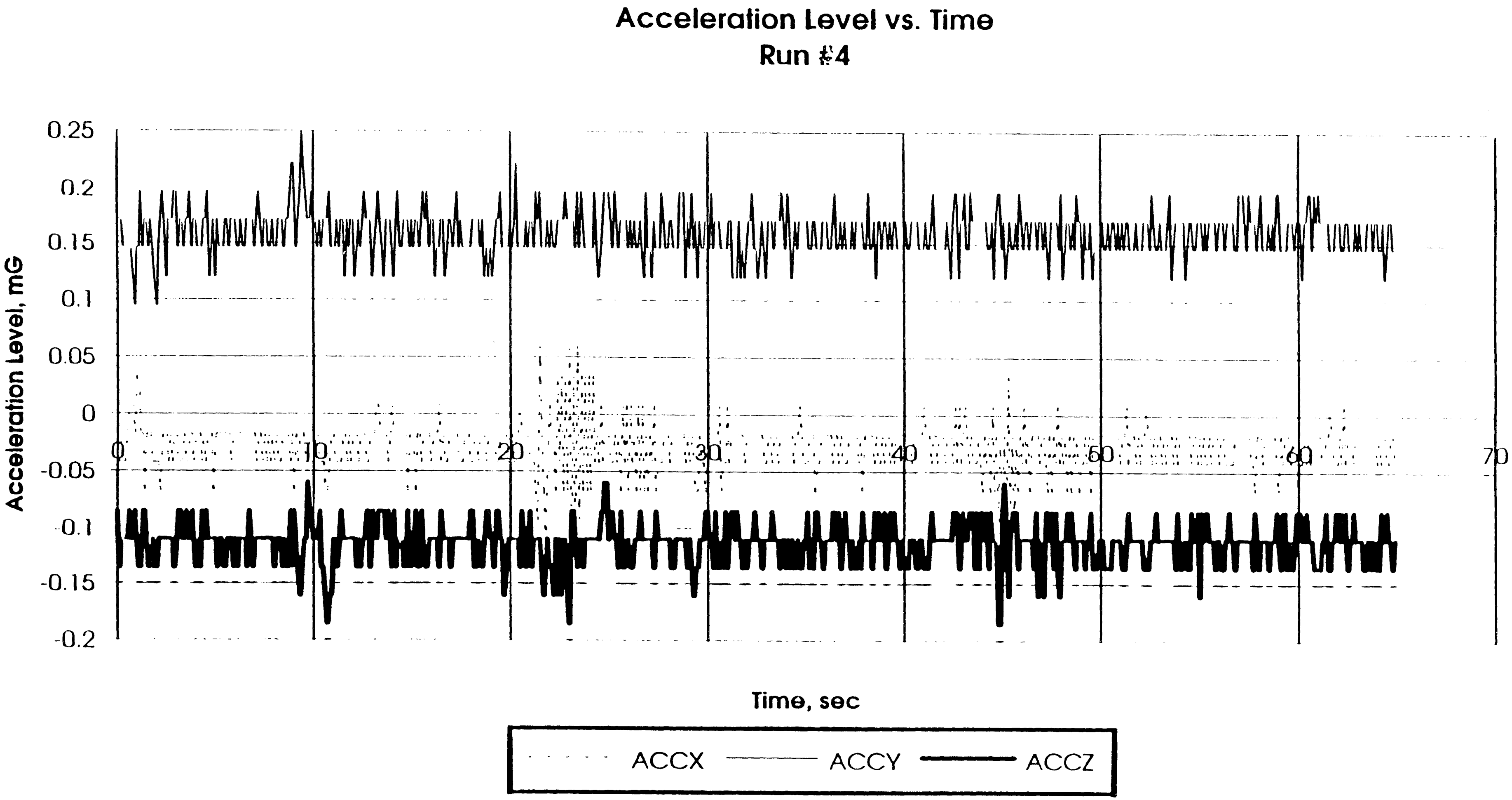

Figure C4. PBE-IA accelerometer measurement. Run No. 4.

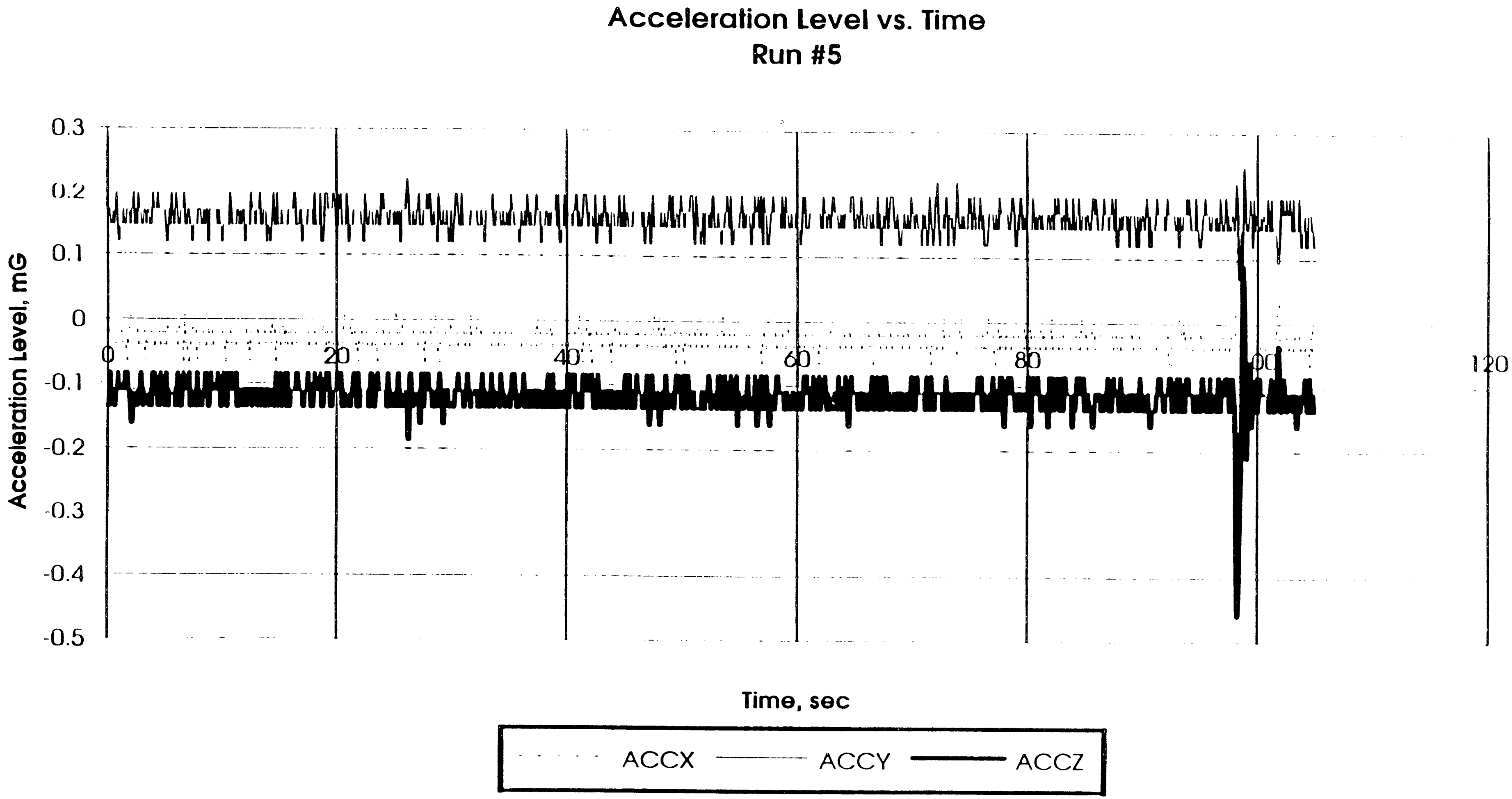

Figure C5. PBE-IA accelerometer measurement. Run No. 5.

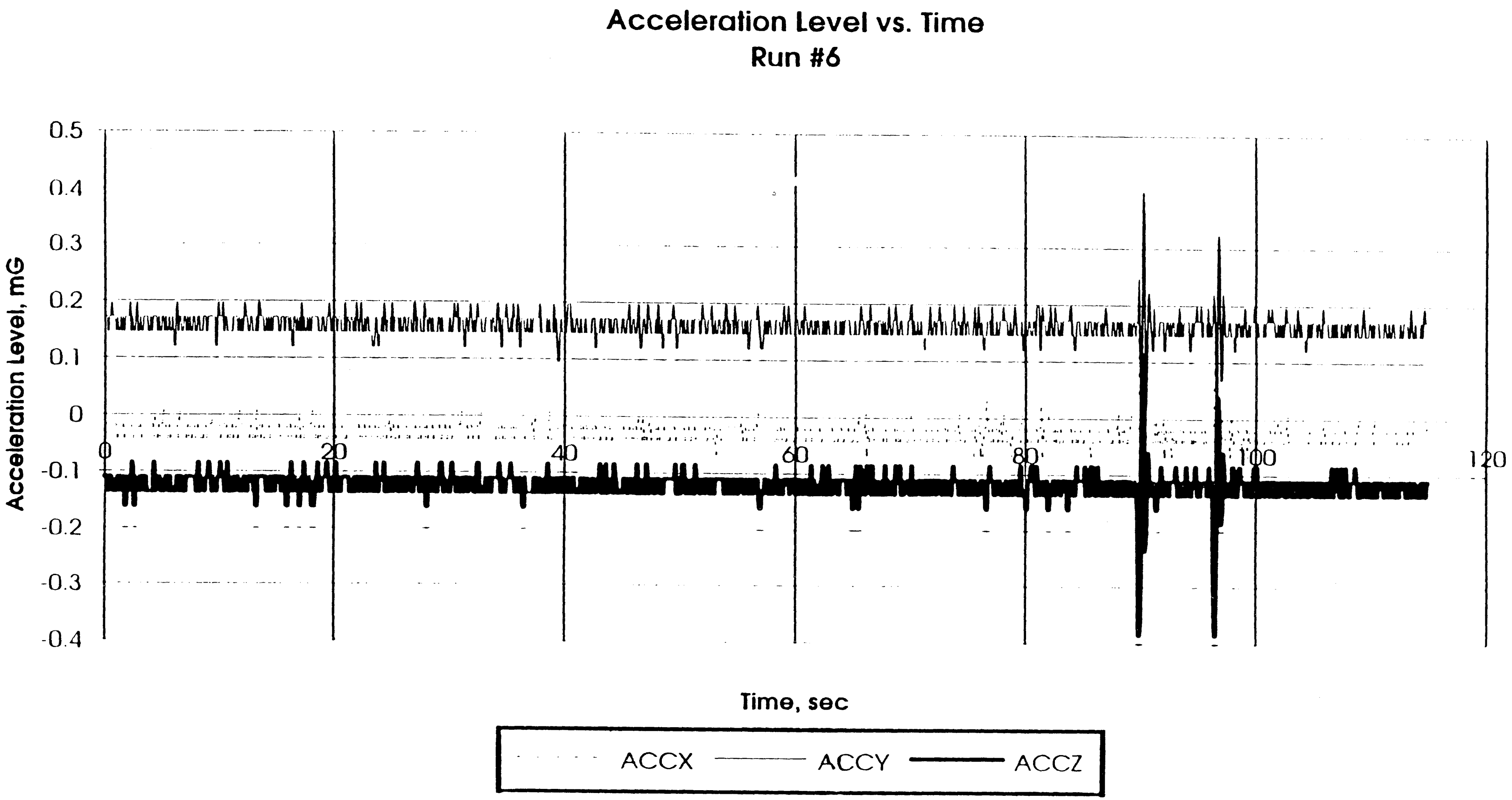

Figure C6. PBE-IA accelerometer measurement. Run No. 6.

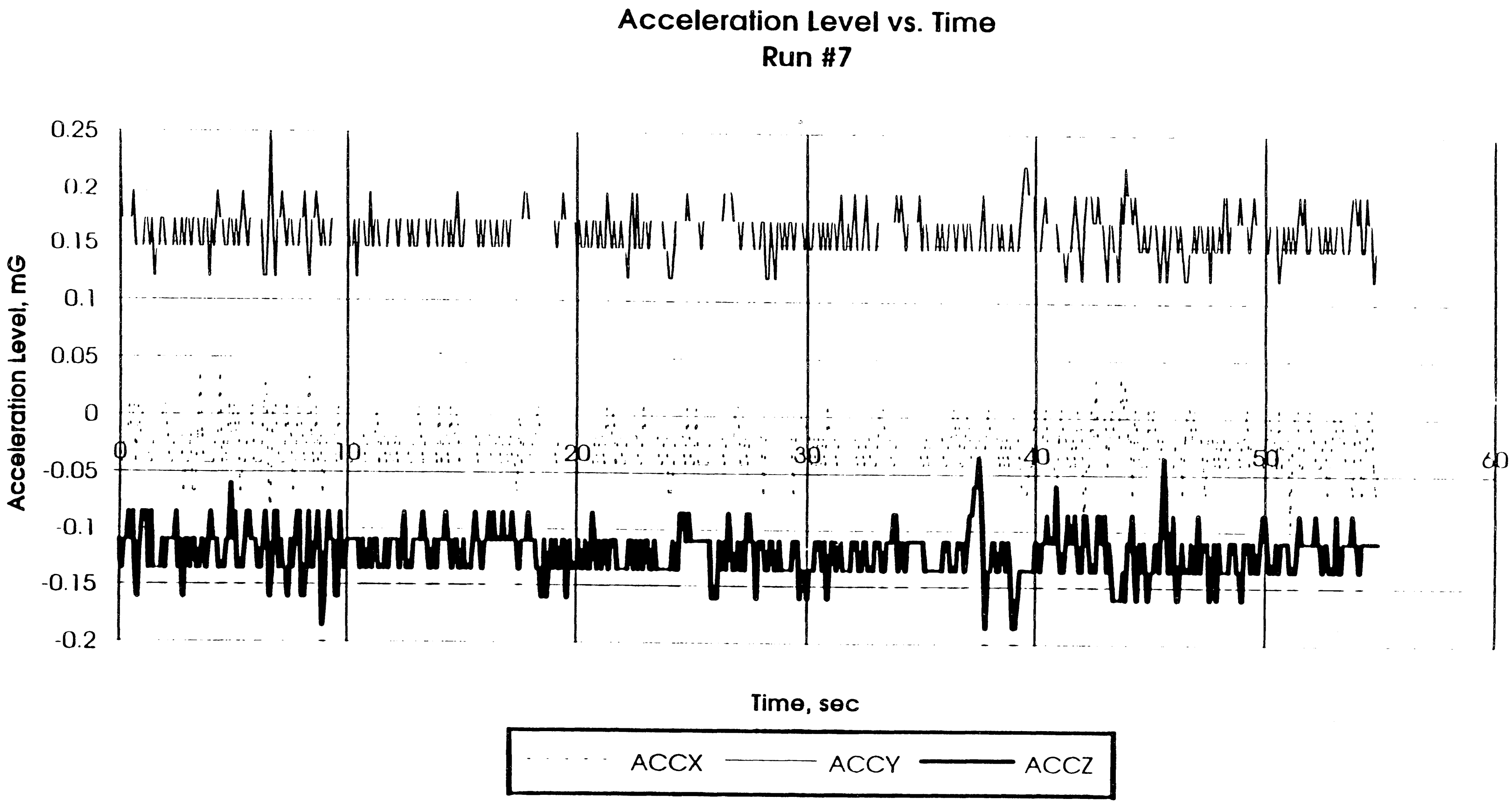
Acceleration Level vs. Time
Run #7

Figure C7. PBE-IA accelerometer measurement. Run No. 7.

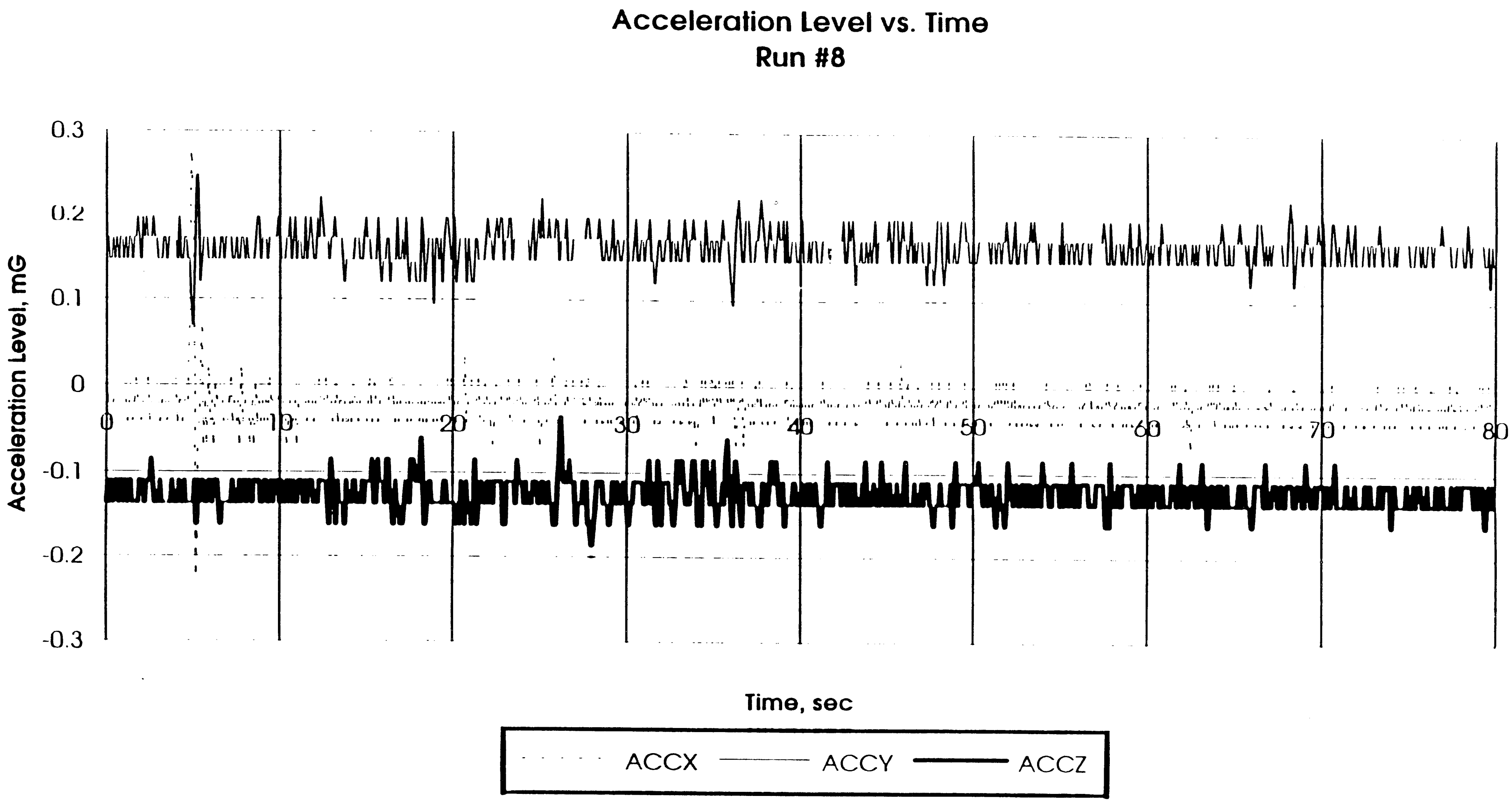

Figure C8. PBE-IA accelerometer measurement. Run No. 8.

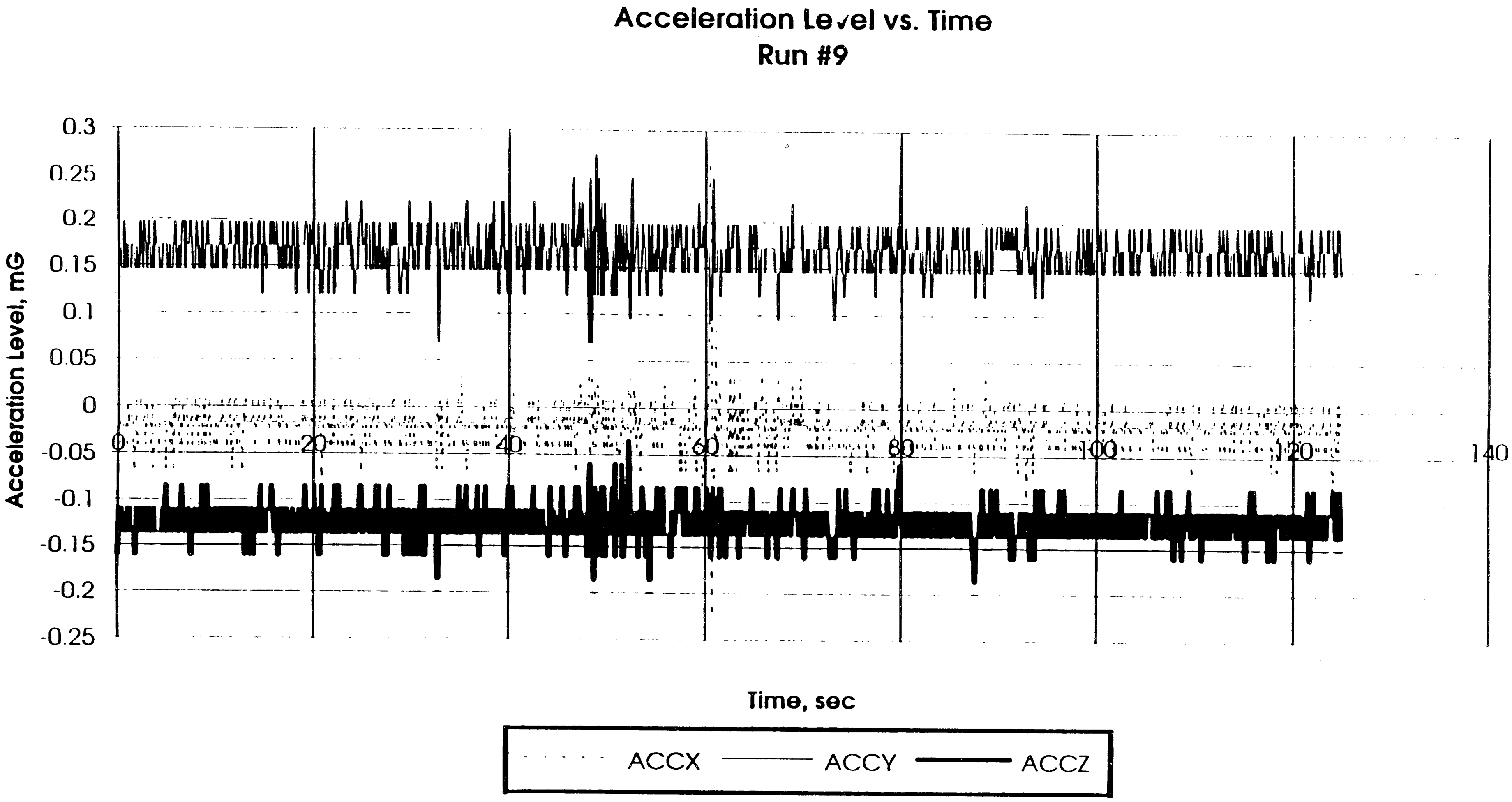

Figure C9. PBE-IA accelerometer measurement. Run No. 9.

Appendix D. Plots of results of Pre-Flight test conducted for PBE-IA at a/g = -1 on 4/28/92.

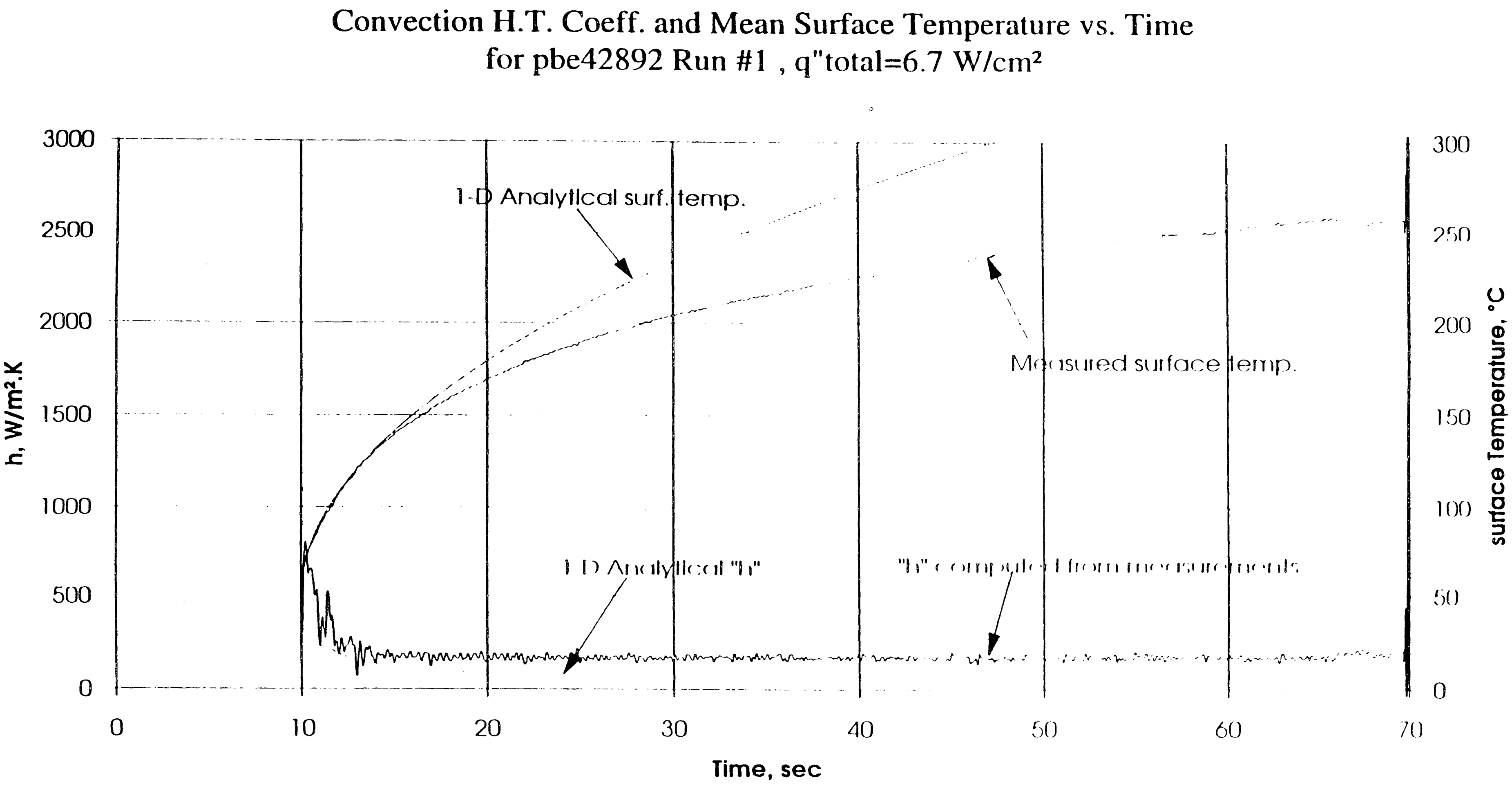

Figure D1a. Mean heater surface temperature and derived heat transfer coefficient. Run No. 1

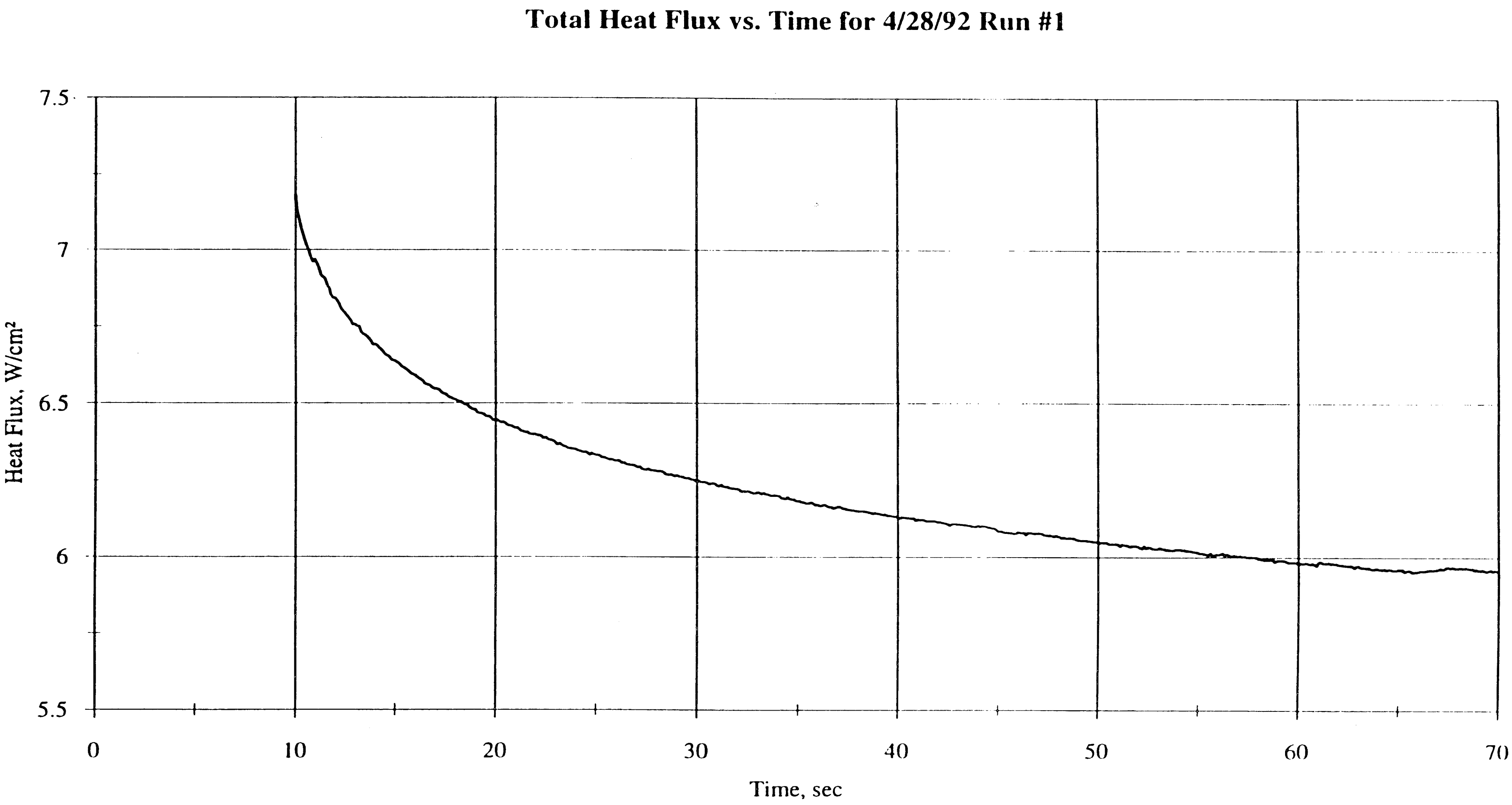

Figure D1b. Heat flux input. Run No. 1

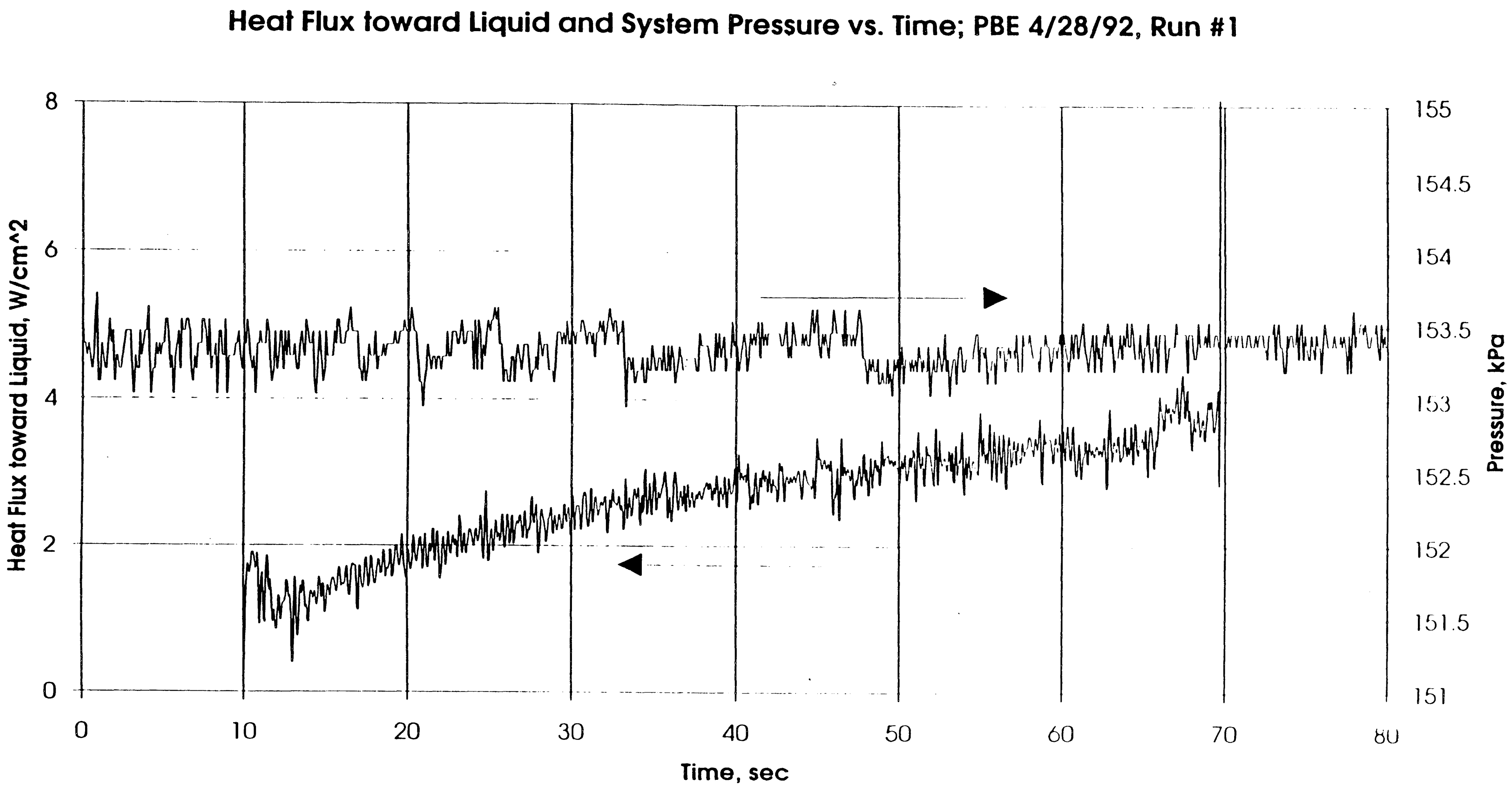

Figure D1c. System pressure and heat flux into fluid. Run No. 1.

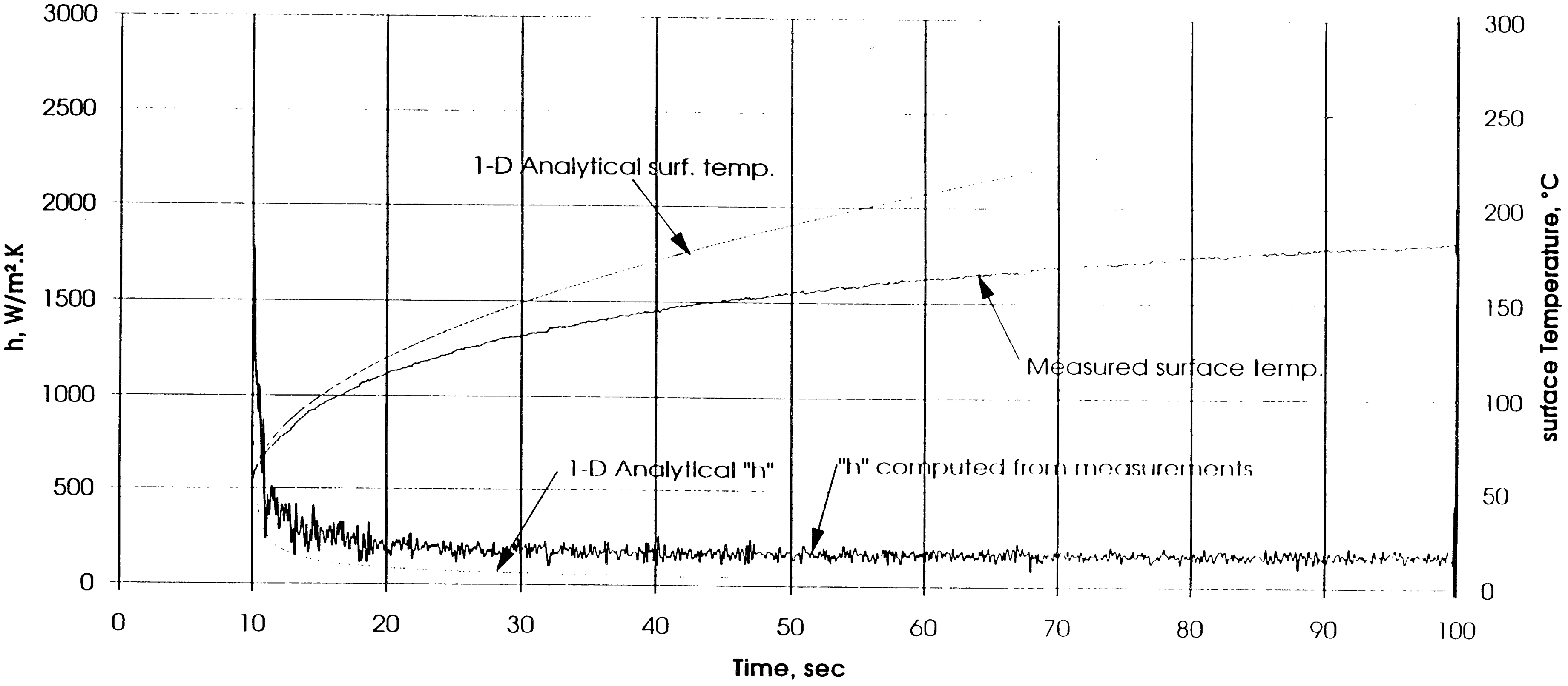

Convection H.T. Coeff. and Mean Surface Temperature vs. Time for pbe42892 Run #2 , q"total=3.65 W/cm²

Figure D2a. Mean heater surface temperature and derived heat transfer coefficient. Run No. 2.

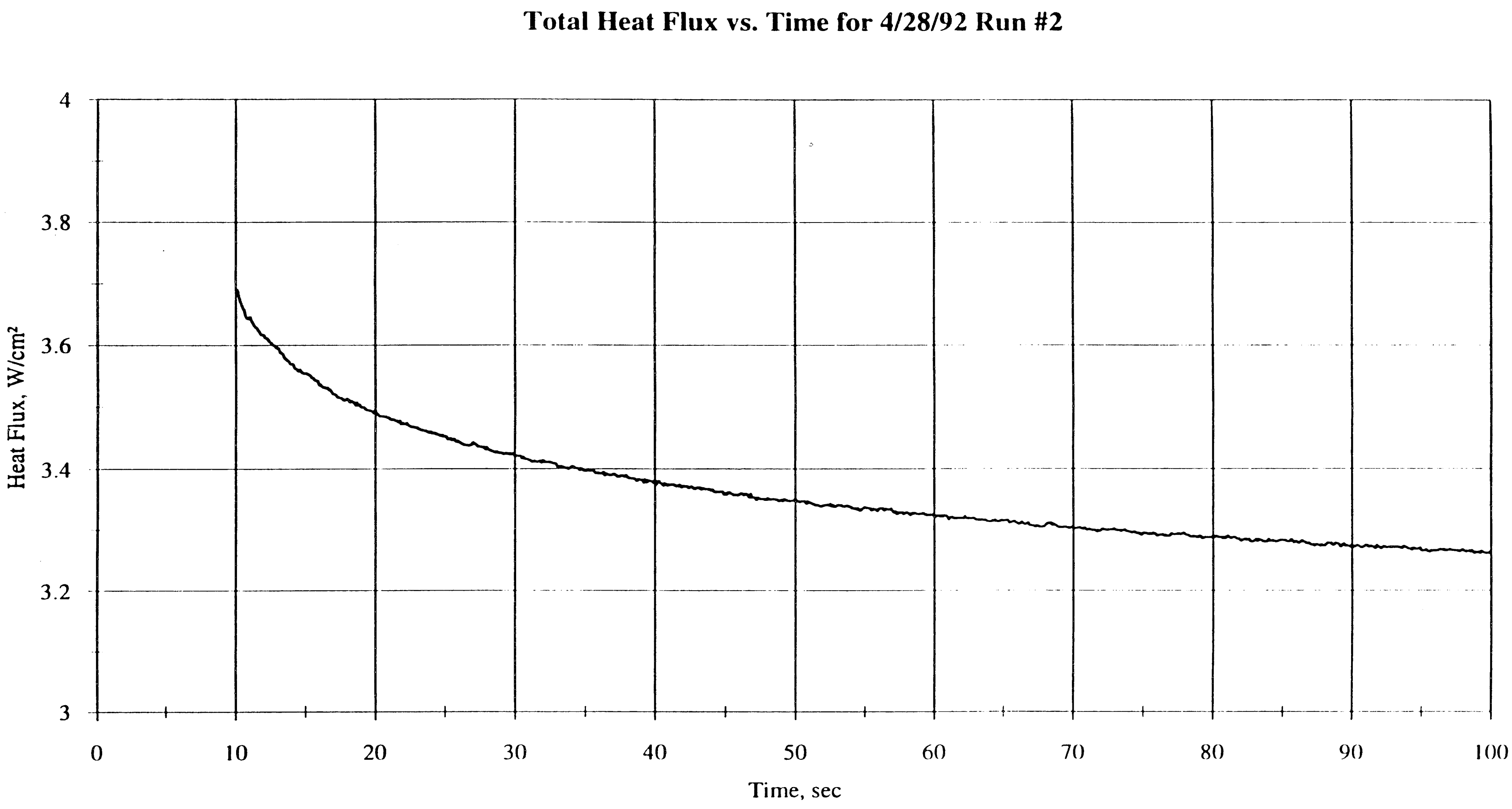

Figure D2b. Heat flux input. Run No. 2.

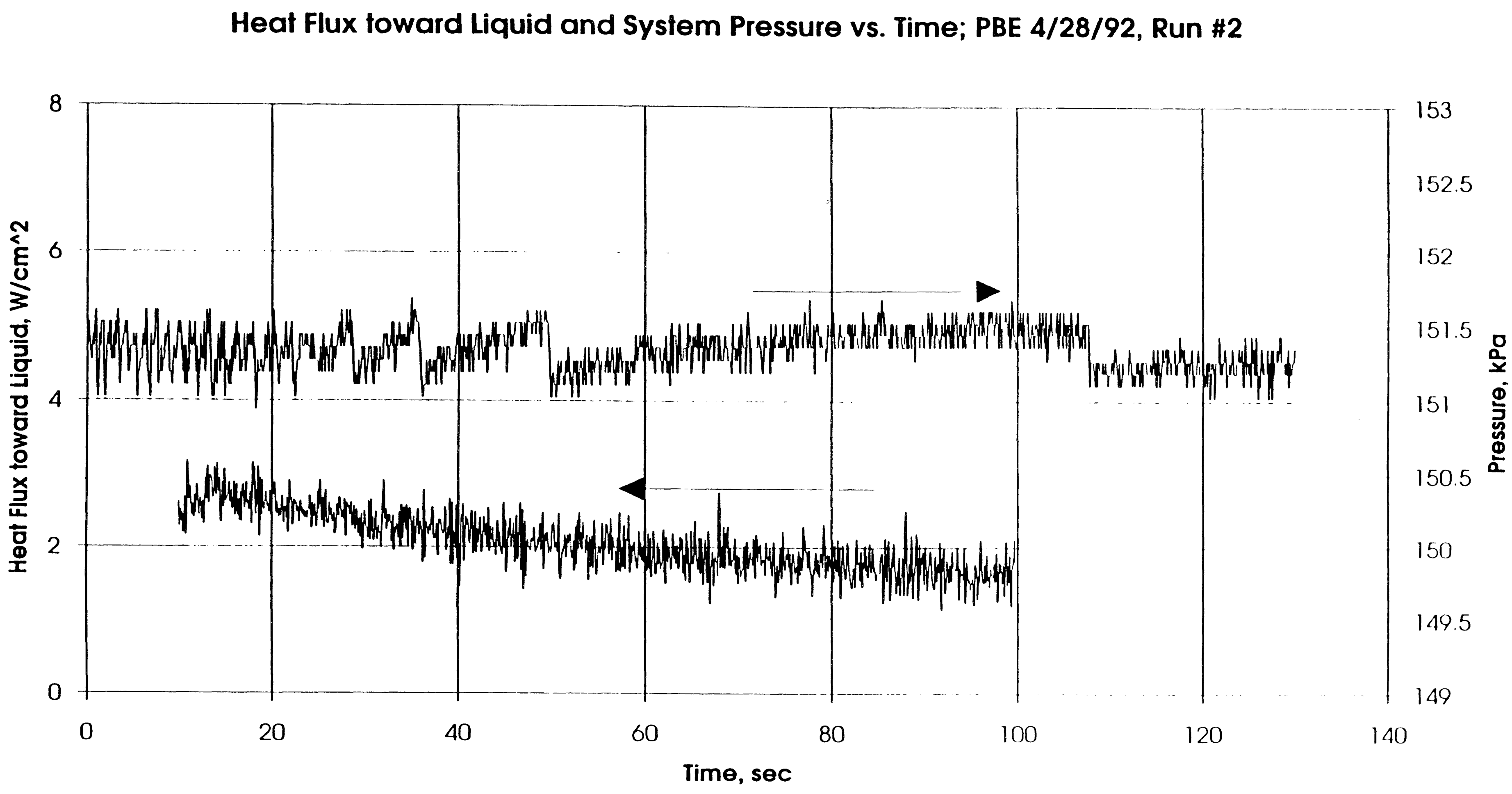

Figure D2c. System pressure and heat flux into fluid. Run No. 2.

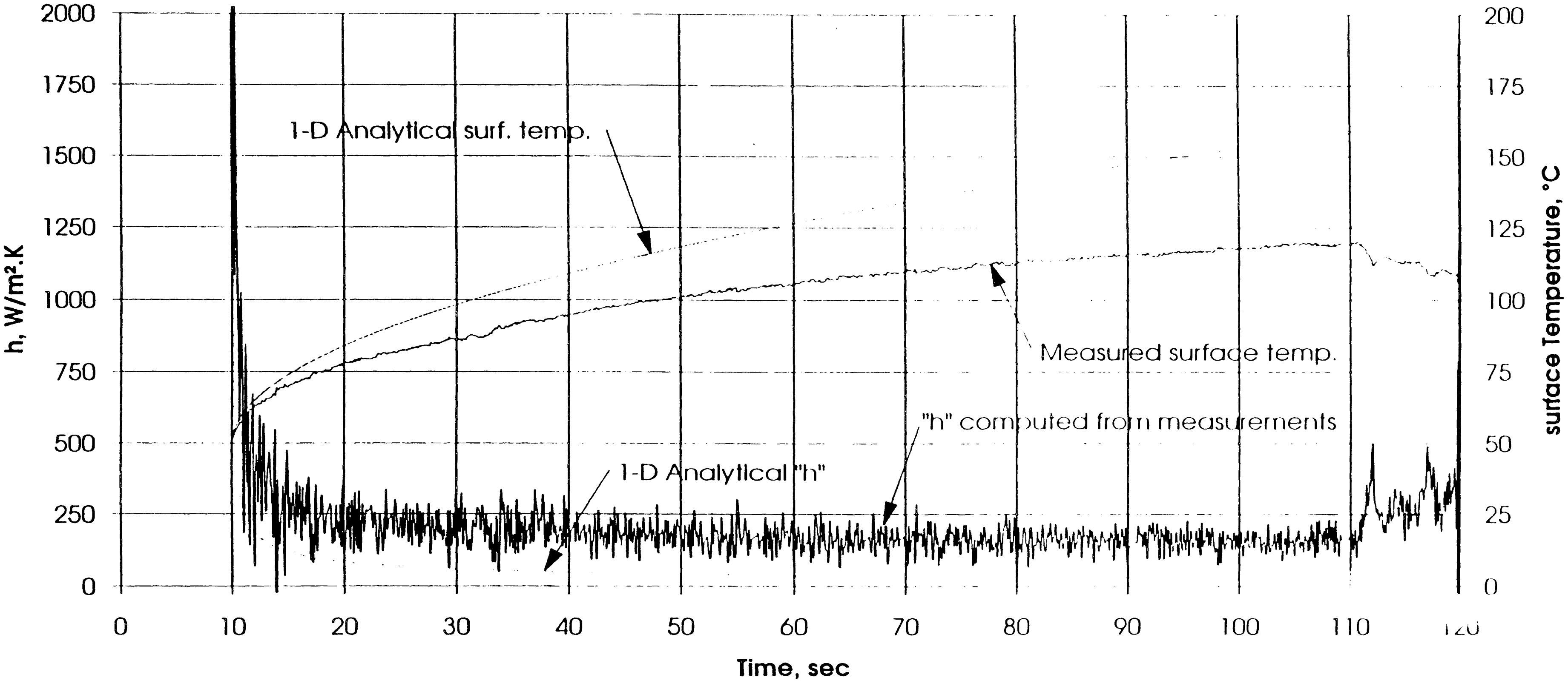

Convection H.T. Coeff. and Mean Surface Temperature vs. Time for pbe42892 Run #3 , q"total=3.65 W/cm²

Figure D3a. Mean heater surface temperature and derived heat transfer coefficient. Run No. 3.

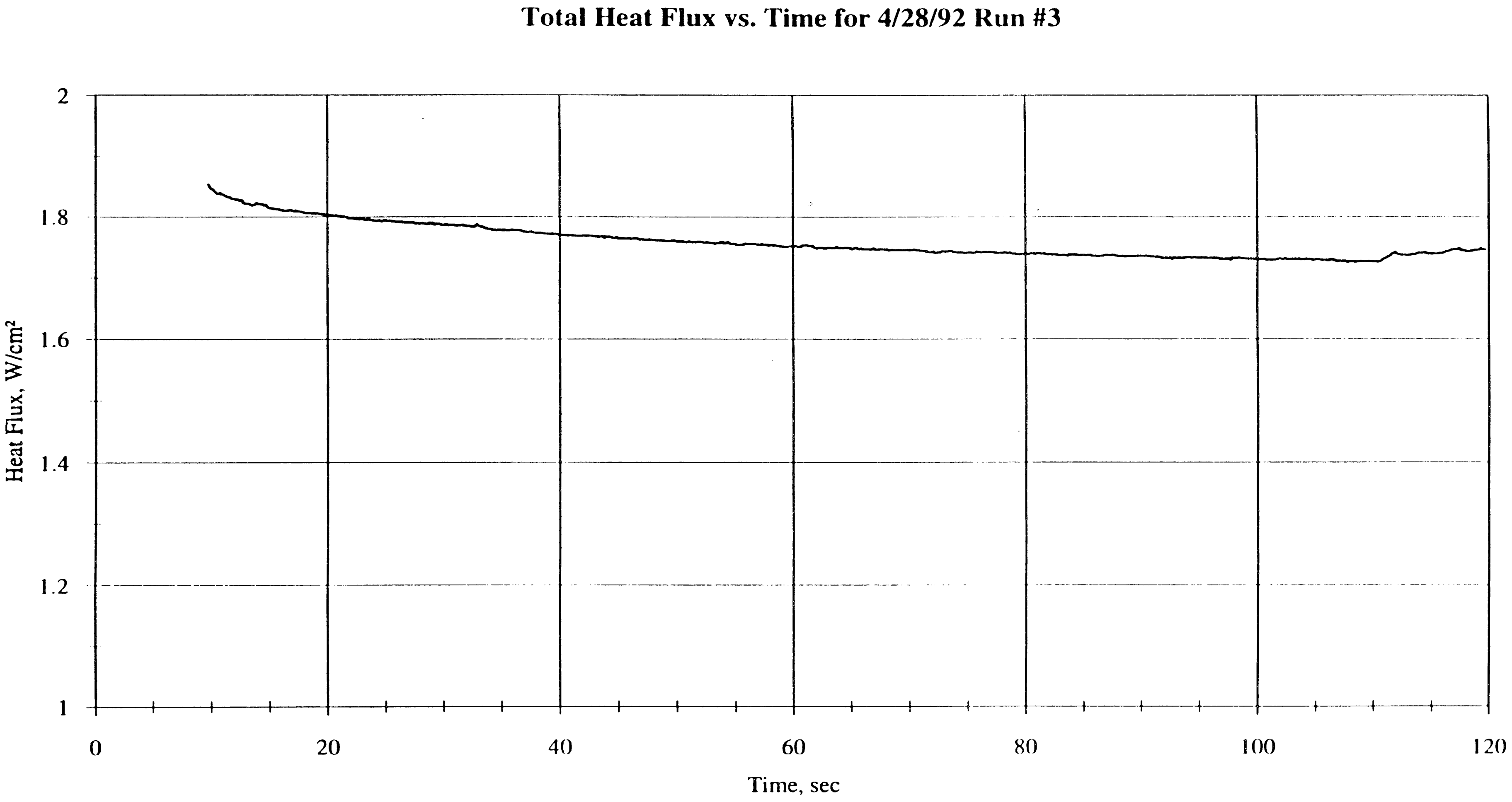

Figure D3b. Heat flux input. Run No. 3.

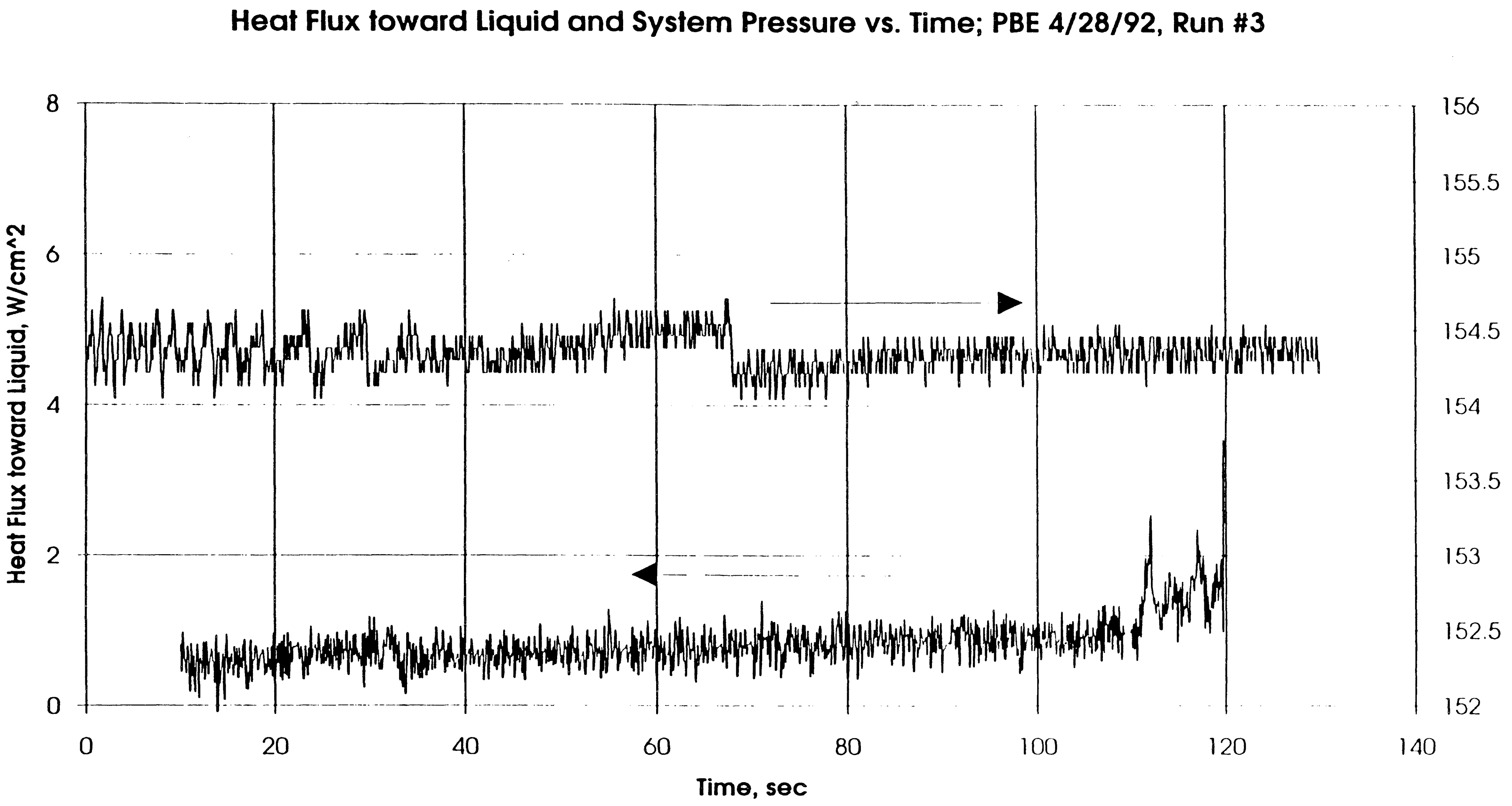

Figure D3c. System pressure and heat flux into fluid. Run No. 3.

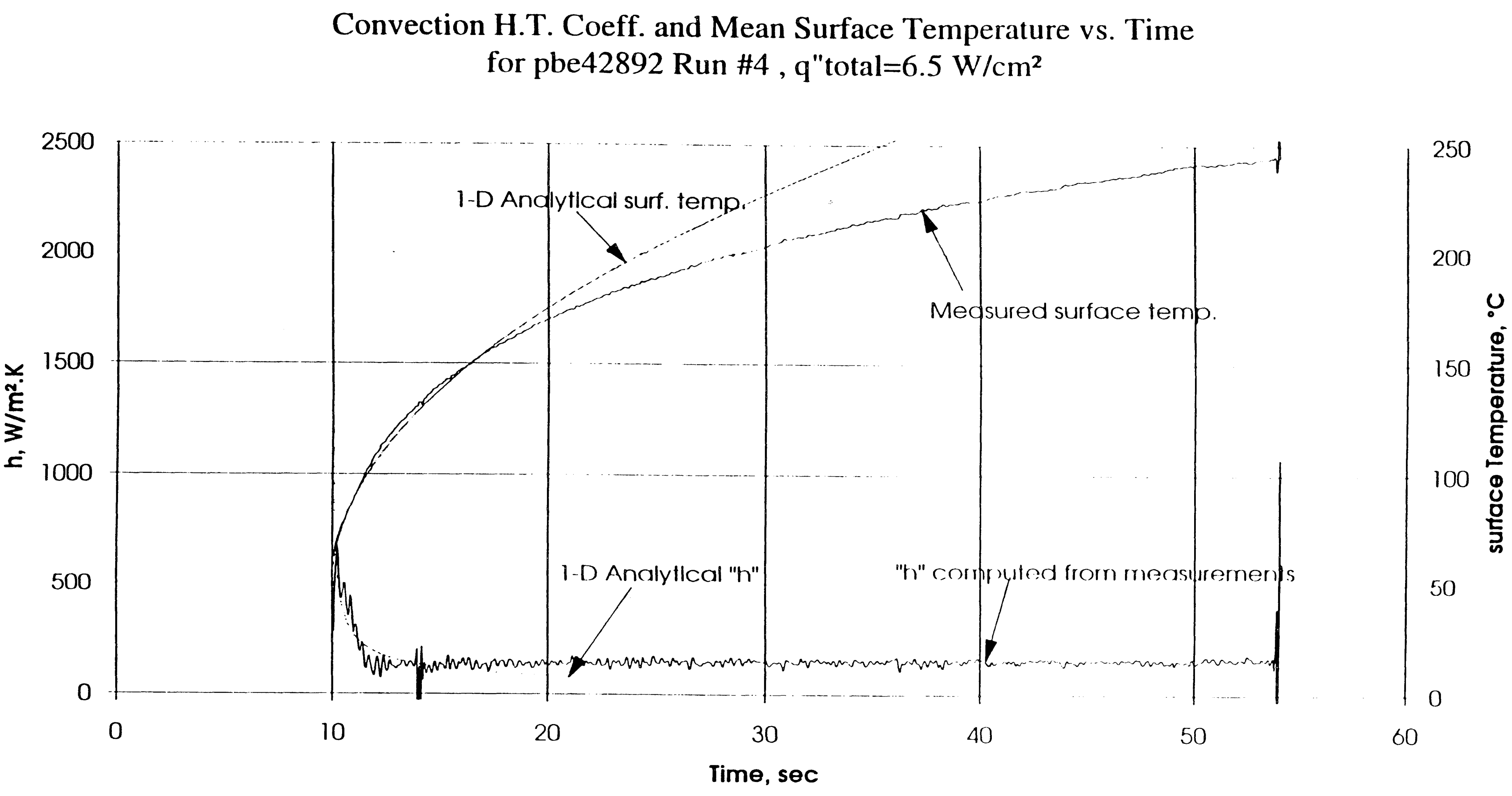

Figure D4a. Mean heater surface temperature and derived heat transfer coefficient. Run No. 4.

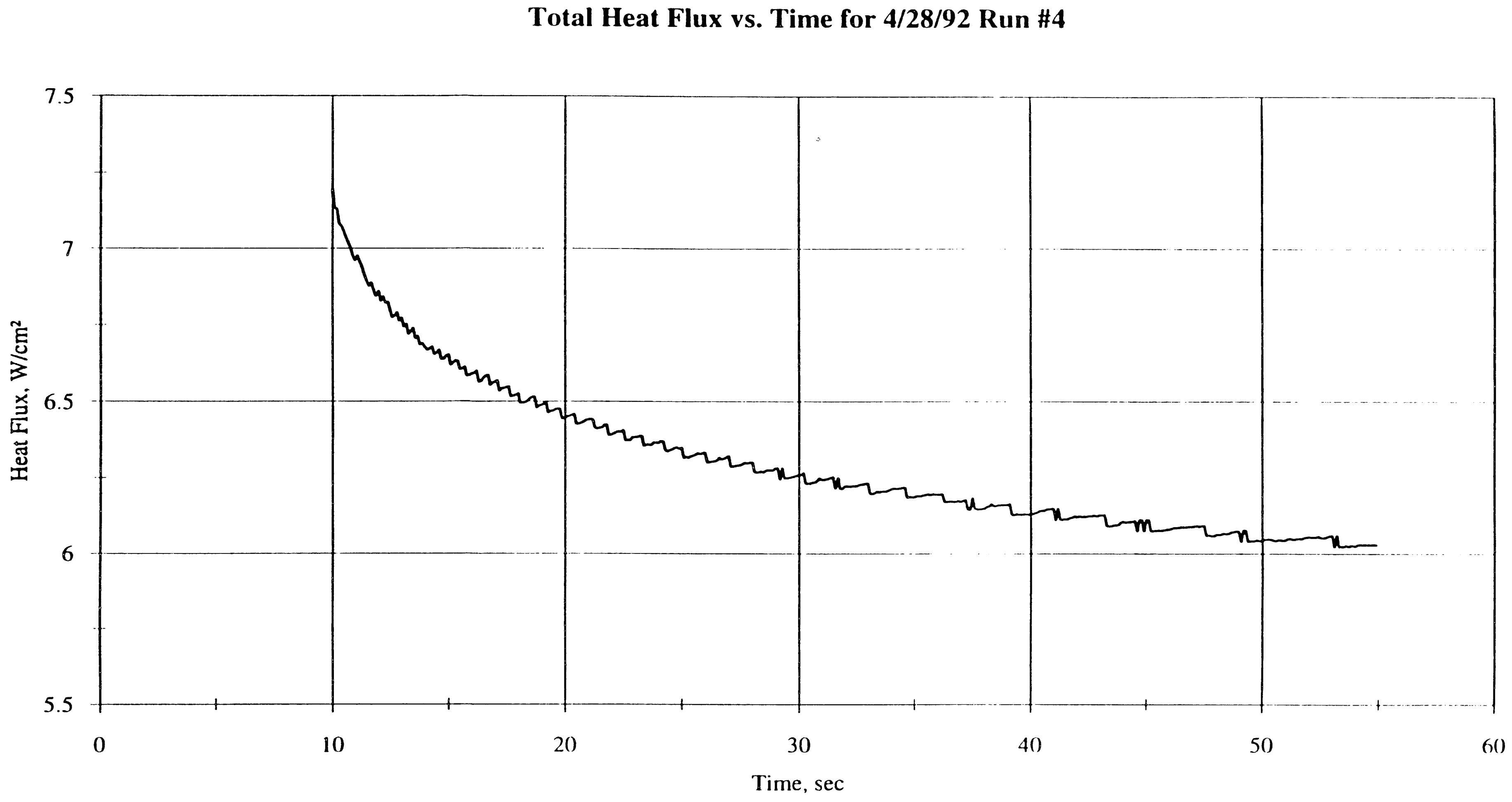

Figure D4b. Heat flux input. Run No. 4.

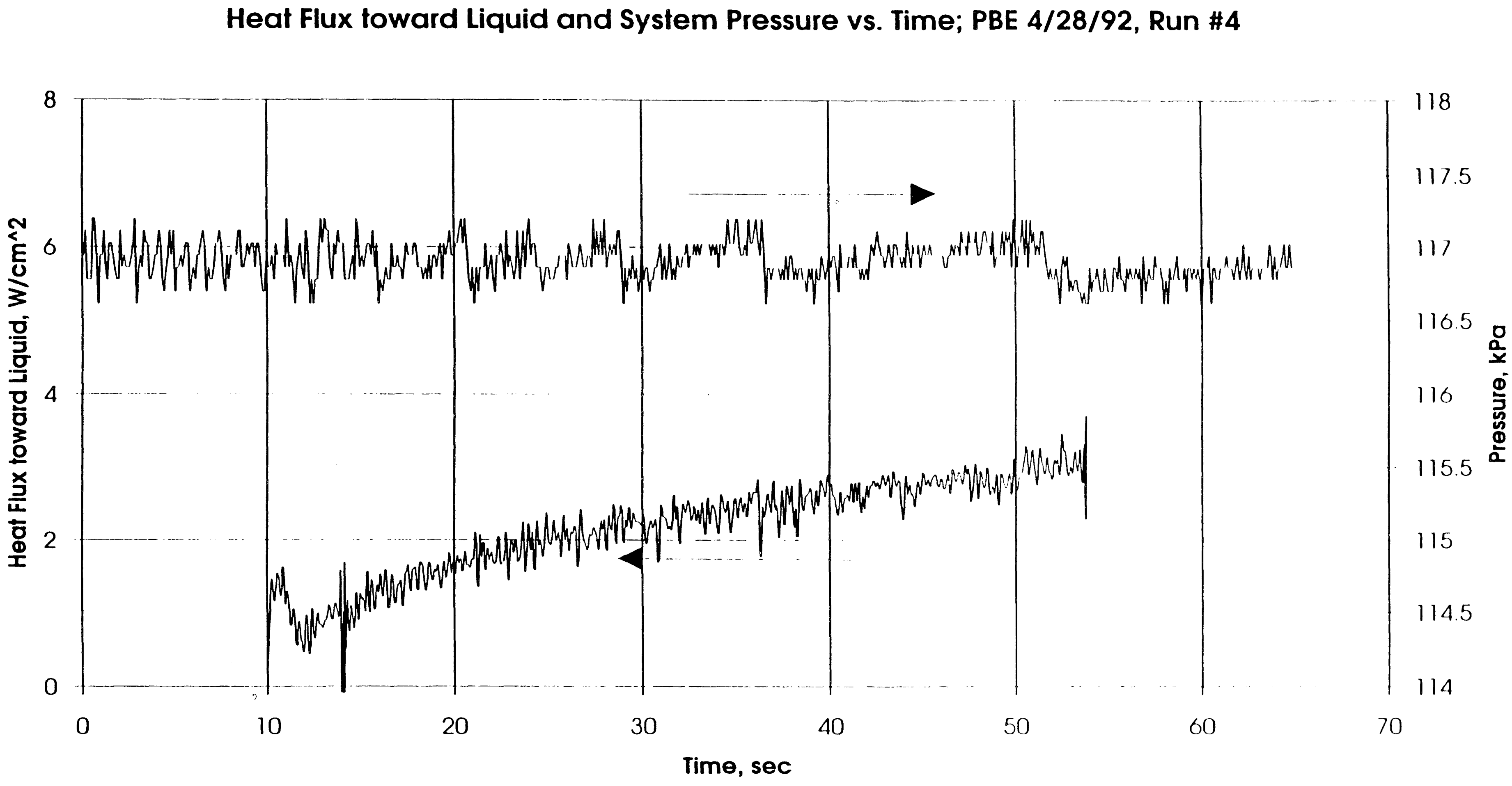

Figure D4c. System pressure and heat flux into fluid. Run No. 4.

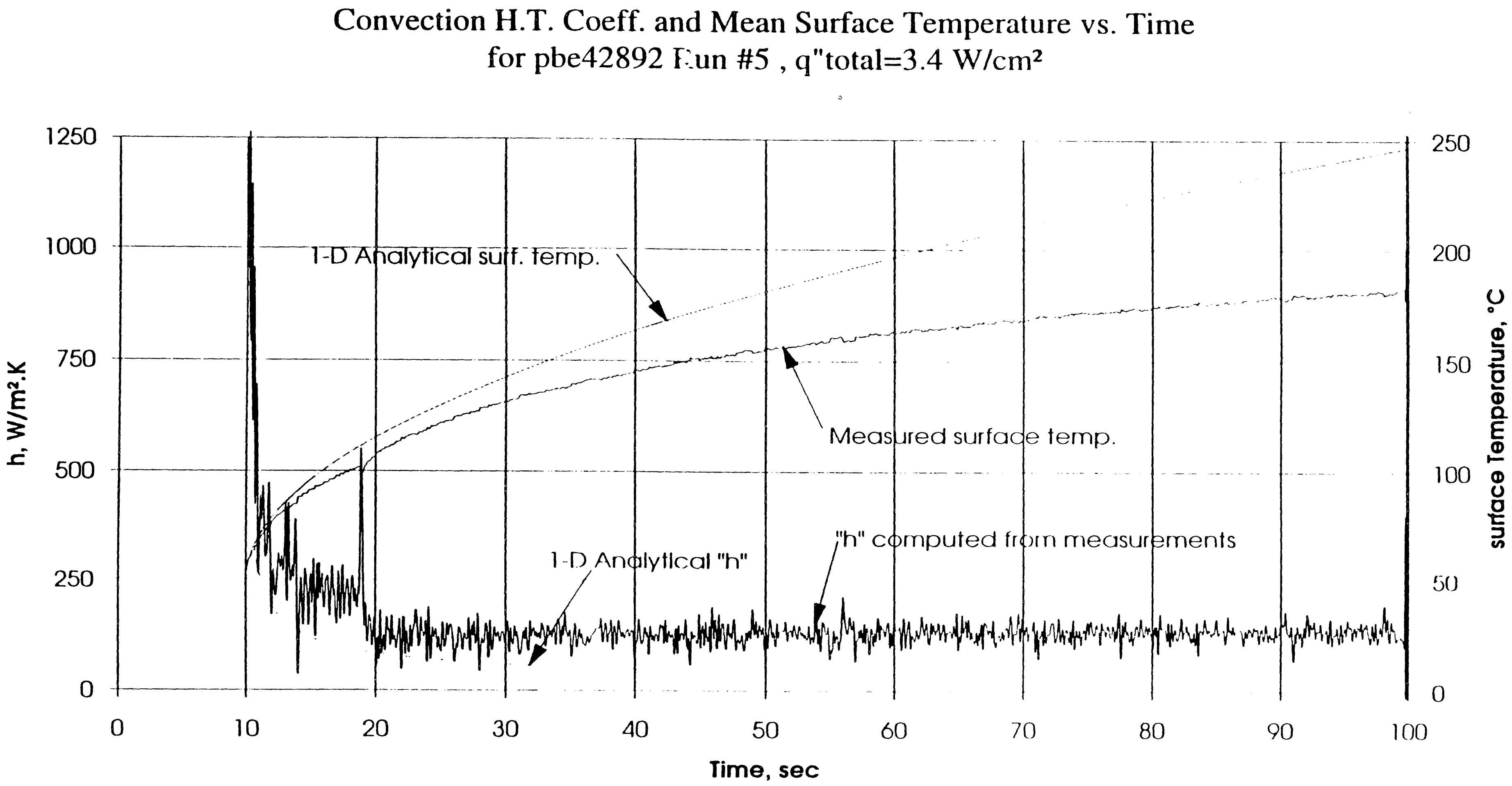

Figure D5a. Mean heater surface temperature and derived heat transfer coefficient. Run No. 5.

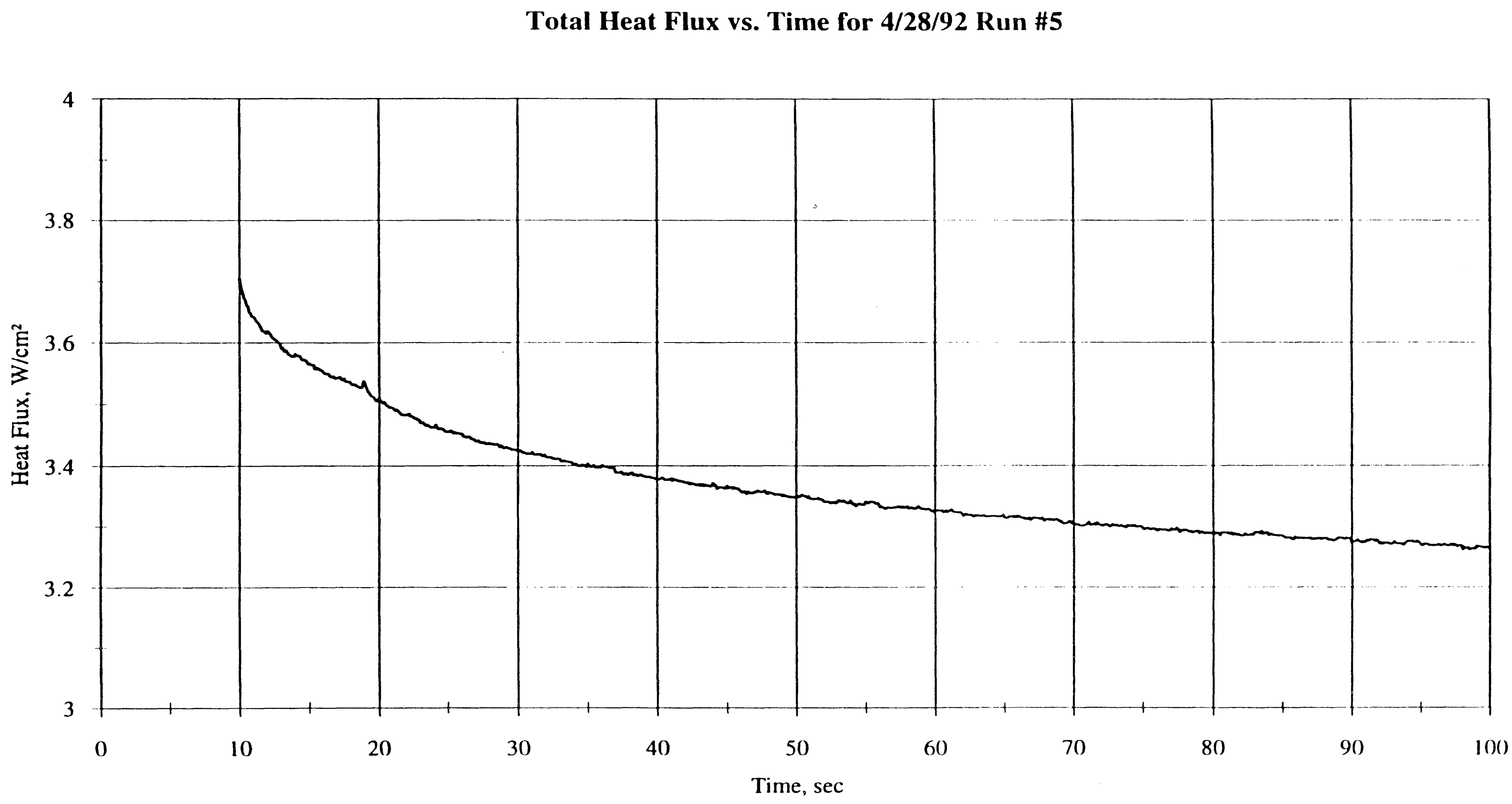

Figure D5b. Heat flux input. Run No. 5.

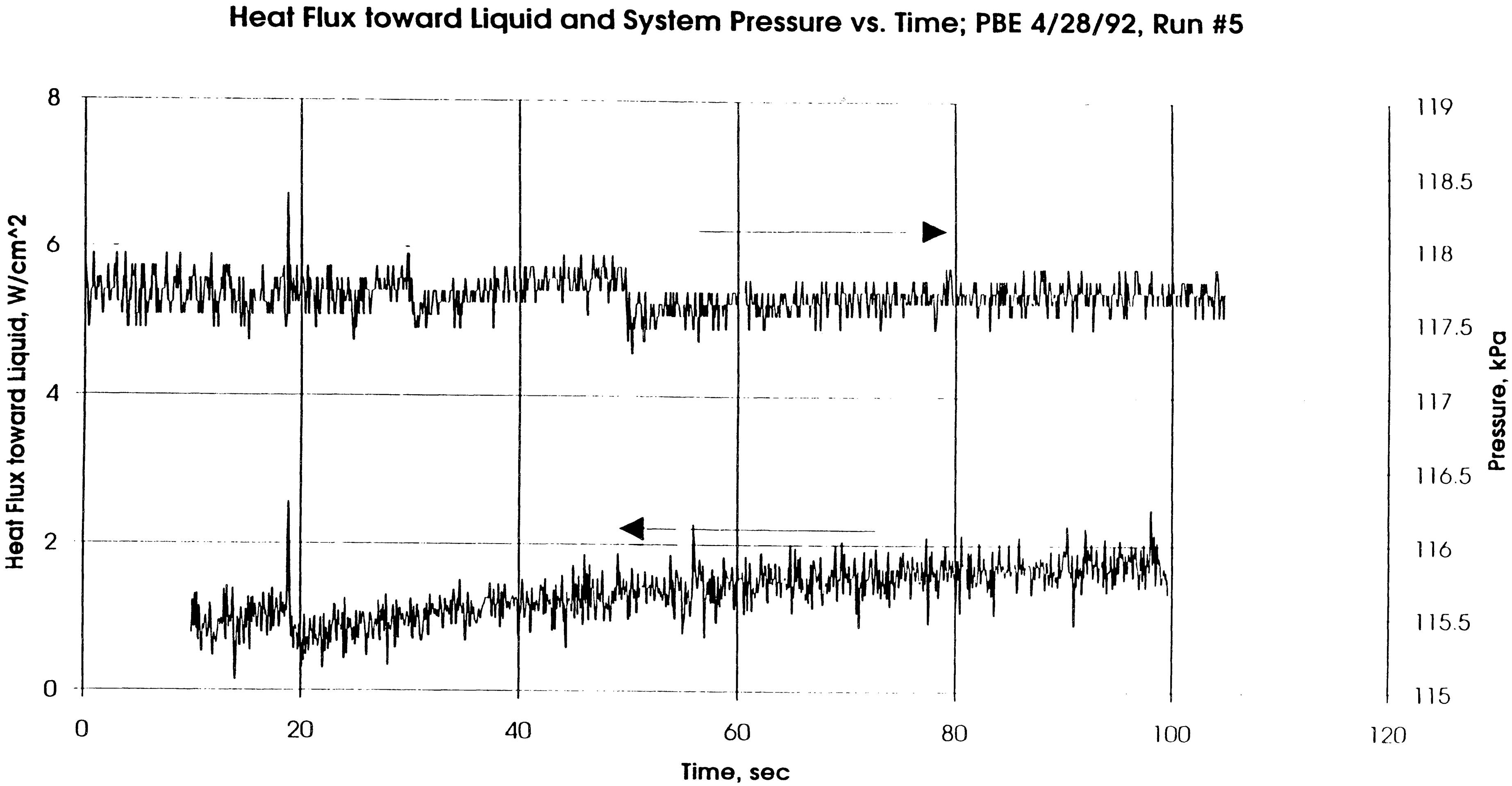

Figure D5c. System pressure and heat flux into fluid. Run No. 5.

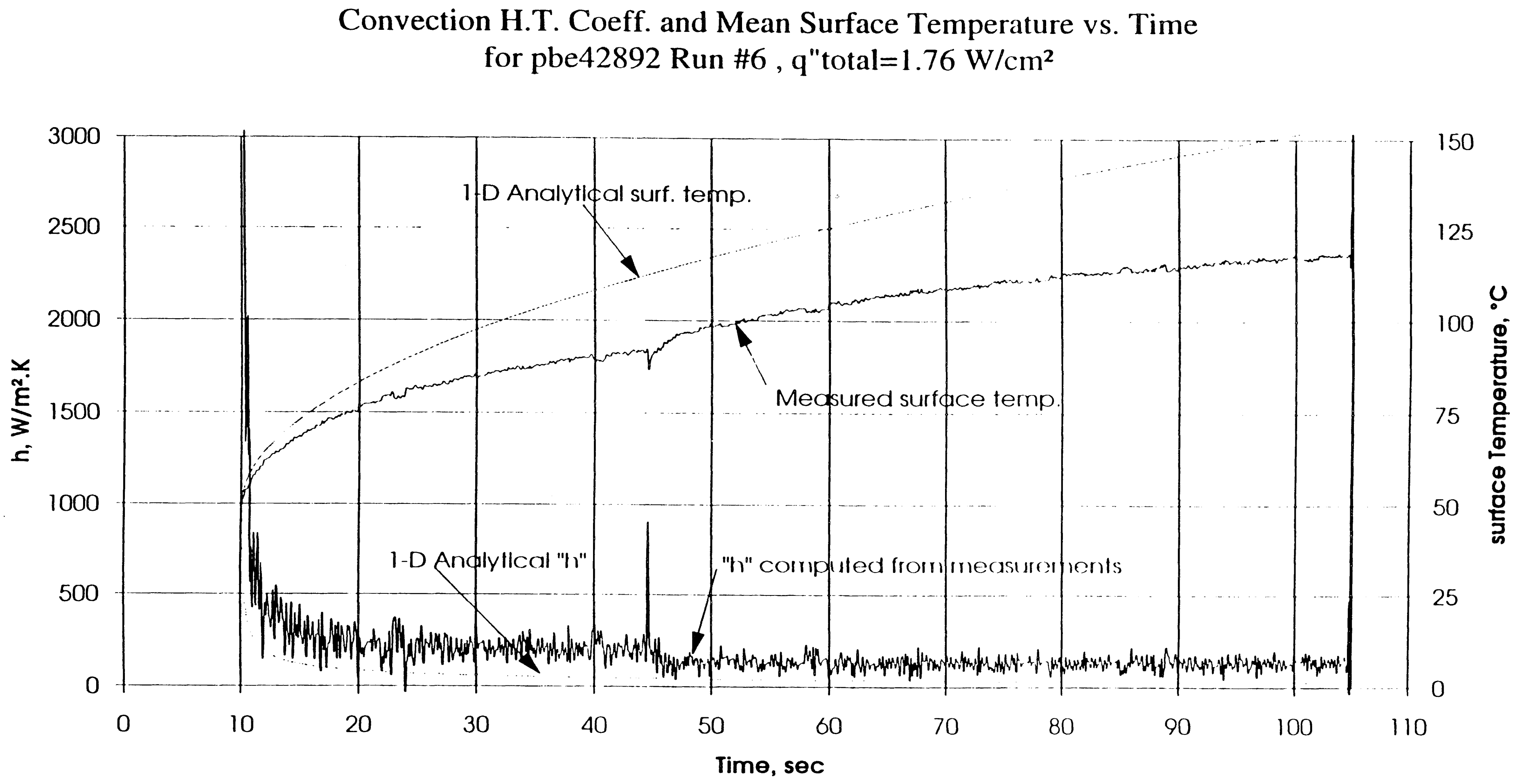

Figure D6a. Mean heater surface temperature and derived heat transfer coefficient. Run No. 6.

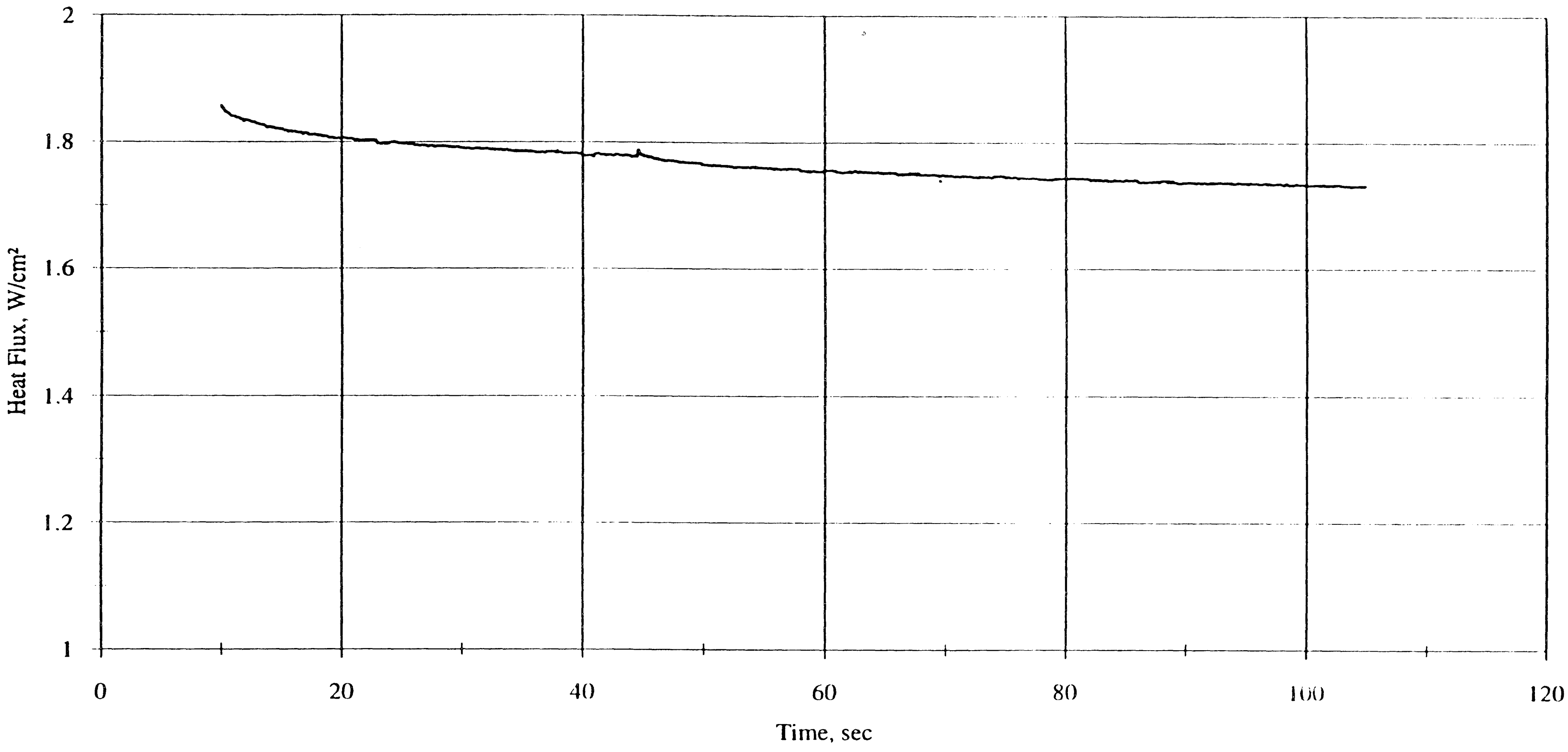
Total Heat Flux vs. Time for 4/28/92 Run #6

Figure D6b. Heat flux input. Run No. 6.

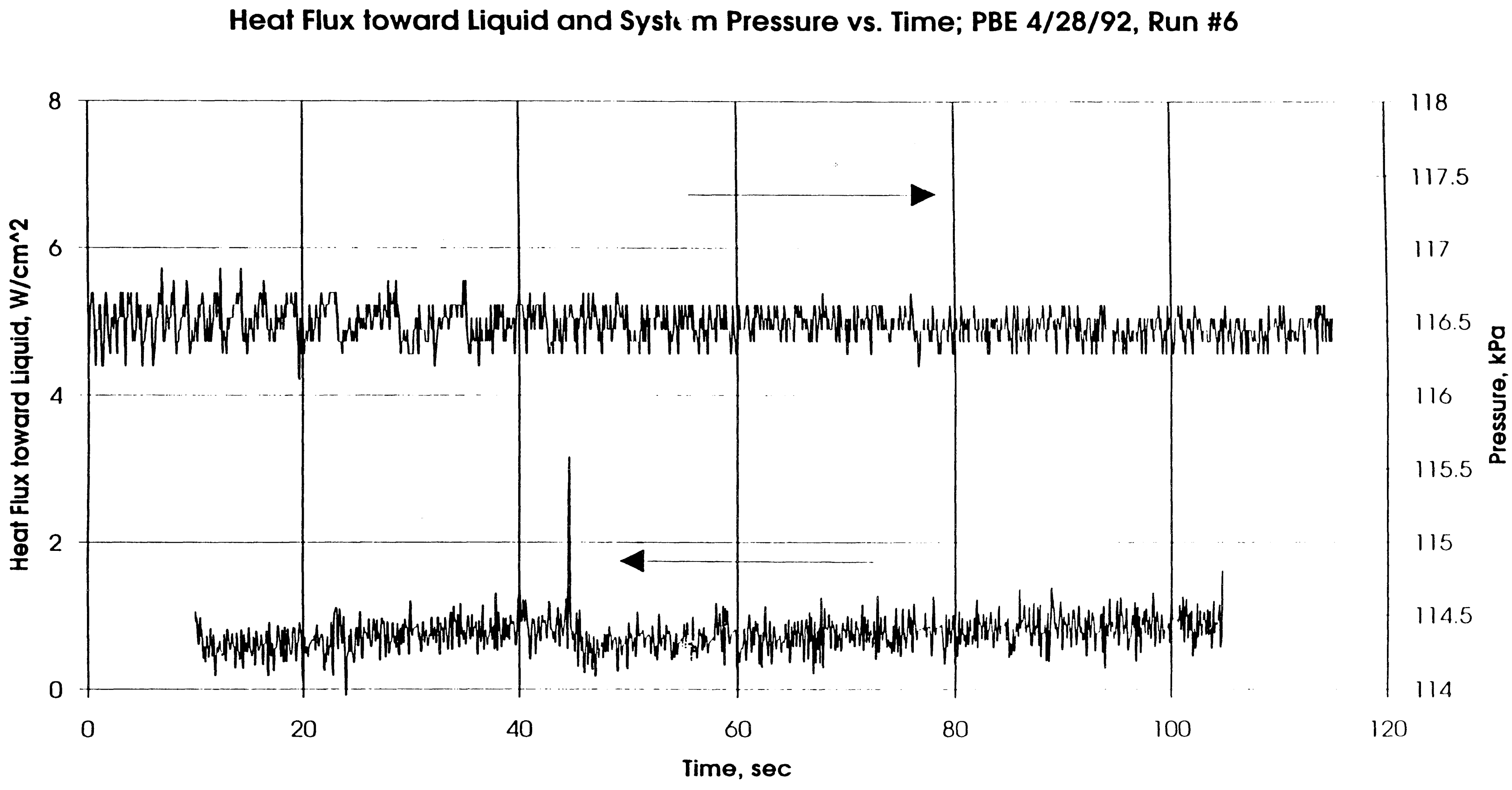

Figure D6c. System pressure and heat flux into fluid. Run No. 6.

Convection H.T. Coeff. and Mean Surface Temperature vs. Time for pbe42892 Run #7 , q"total=6.7 W/cm²

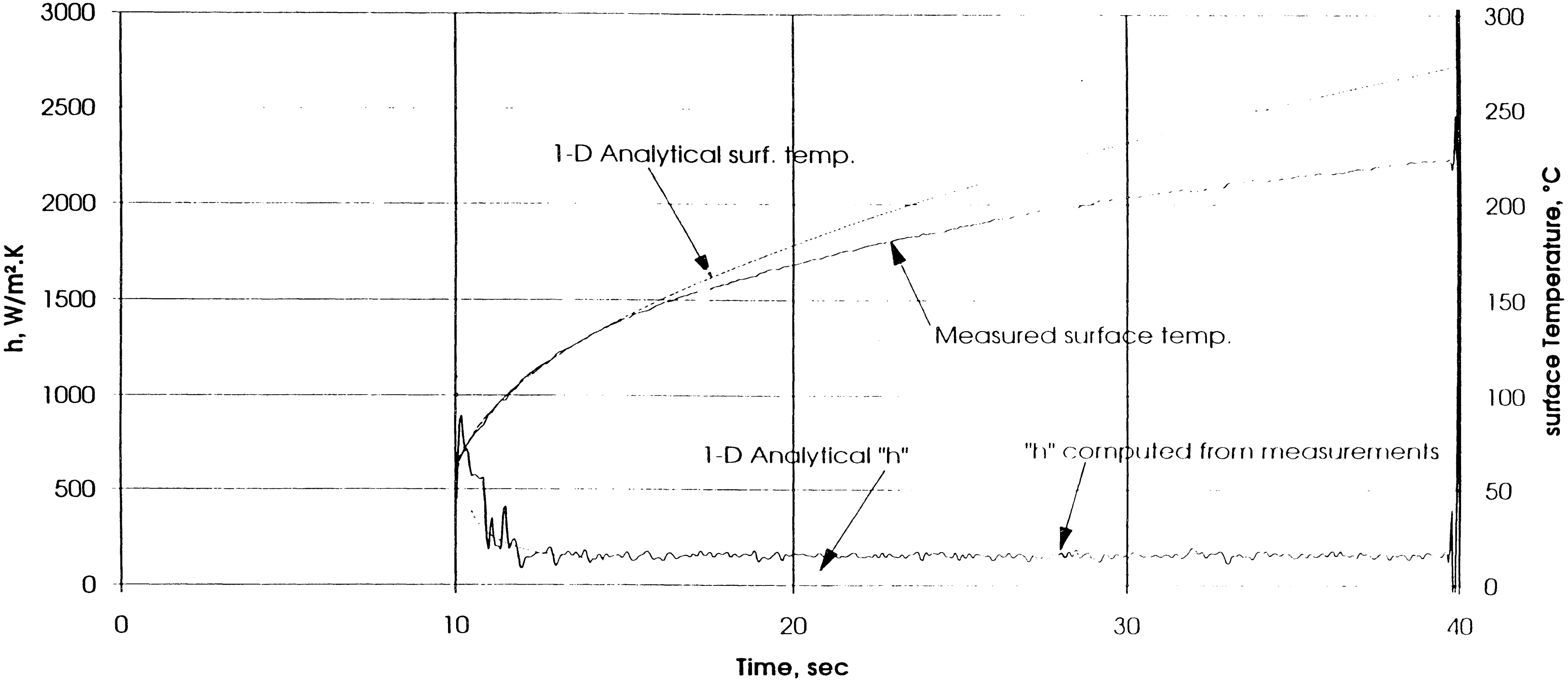

Figure D7a. Mean heater surface temperature and derived heat transfer coefficient. Run No. 7.

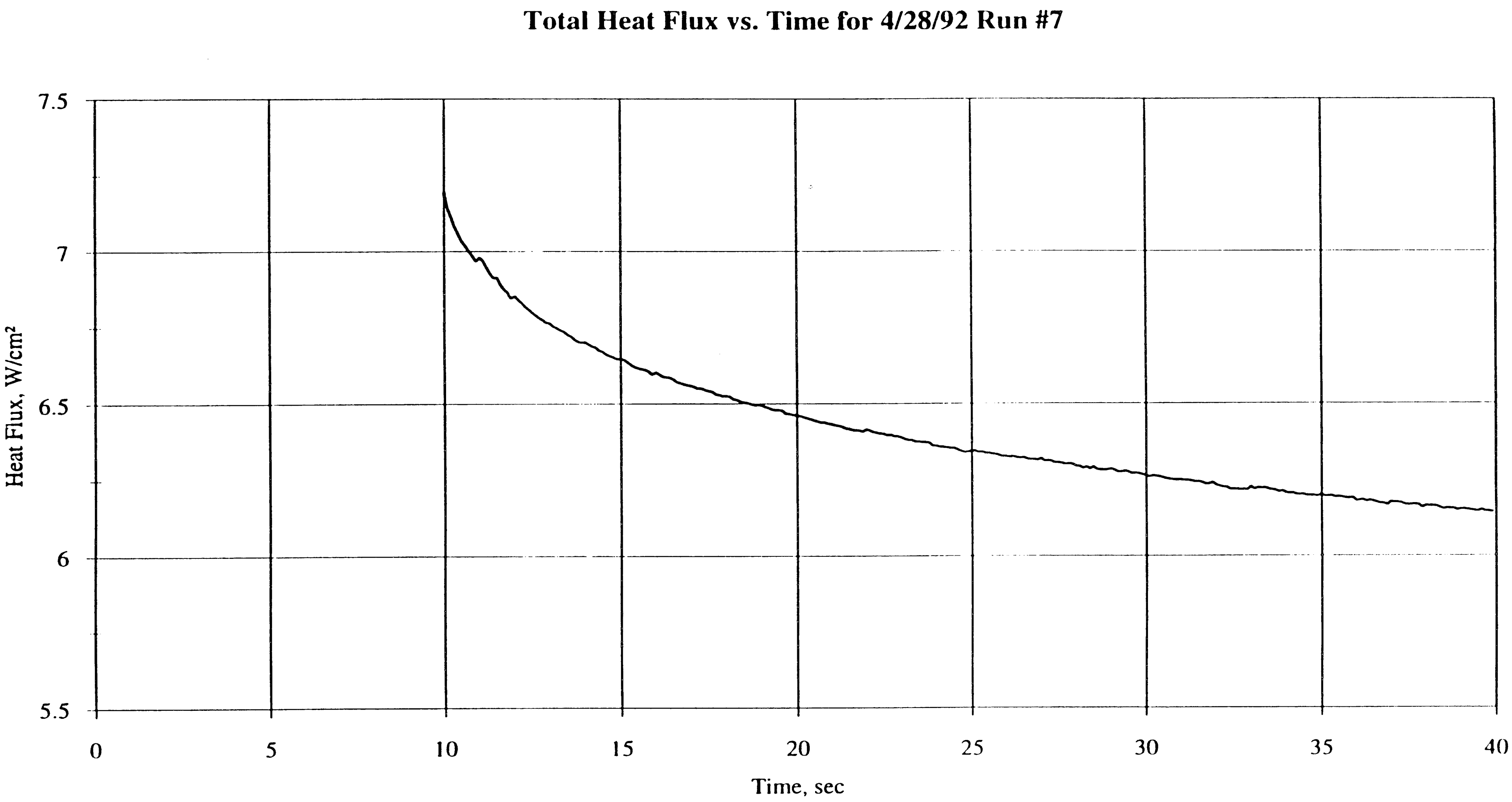

Figure D7b. Heat flux input. Run No. 7.

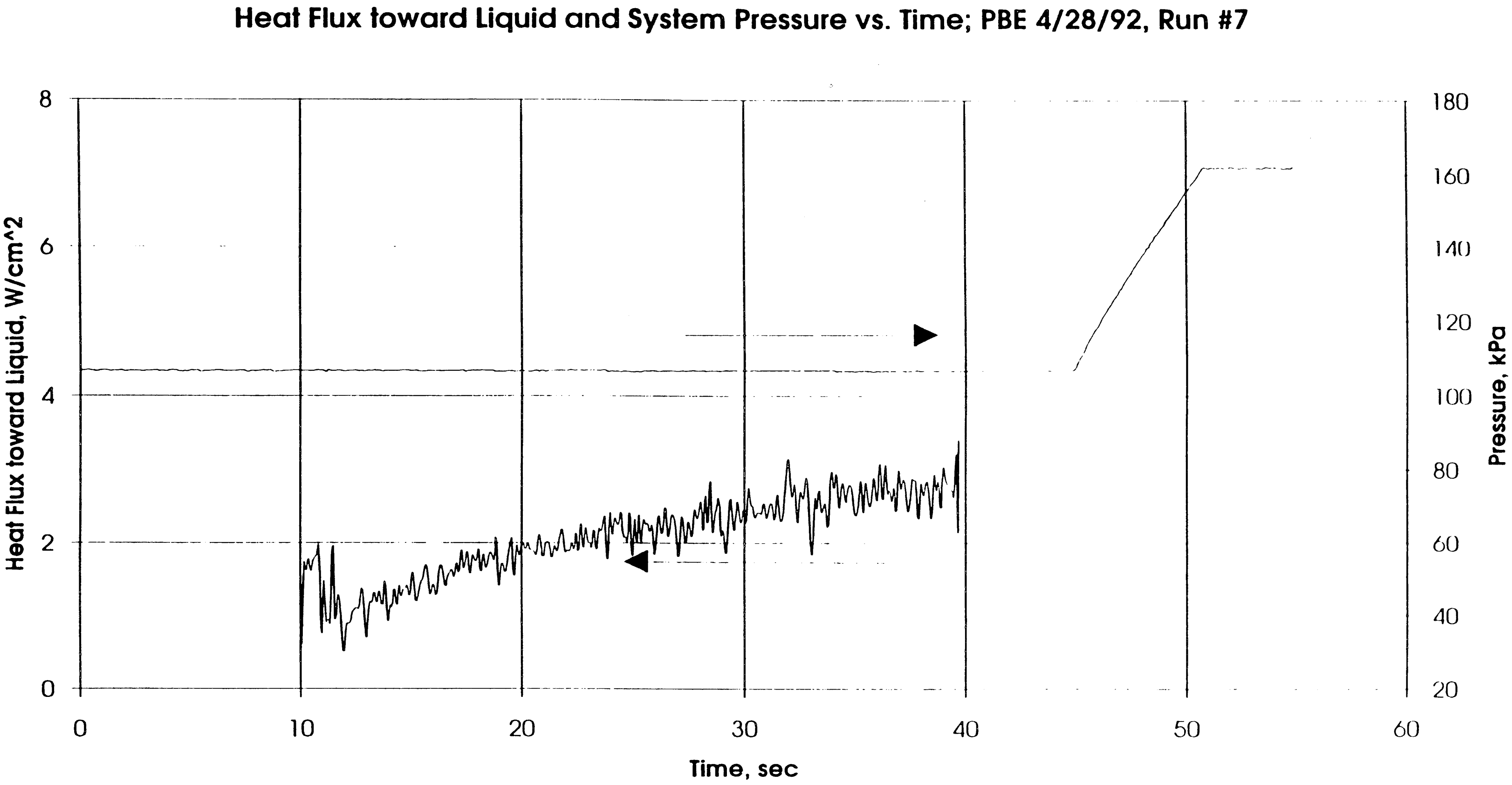

Figure D7c. System pressure and heat flux into fluid. Run No. 7.

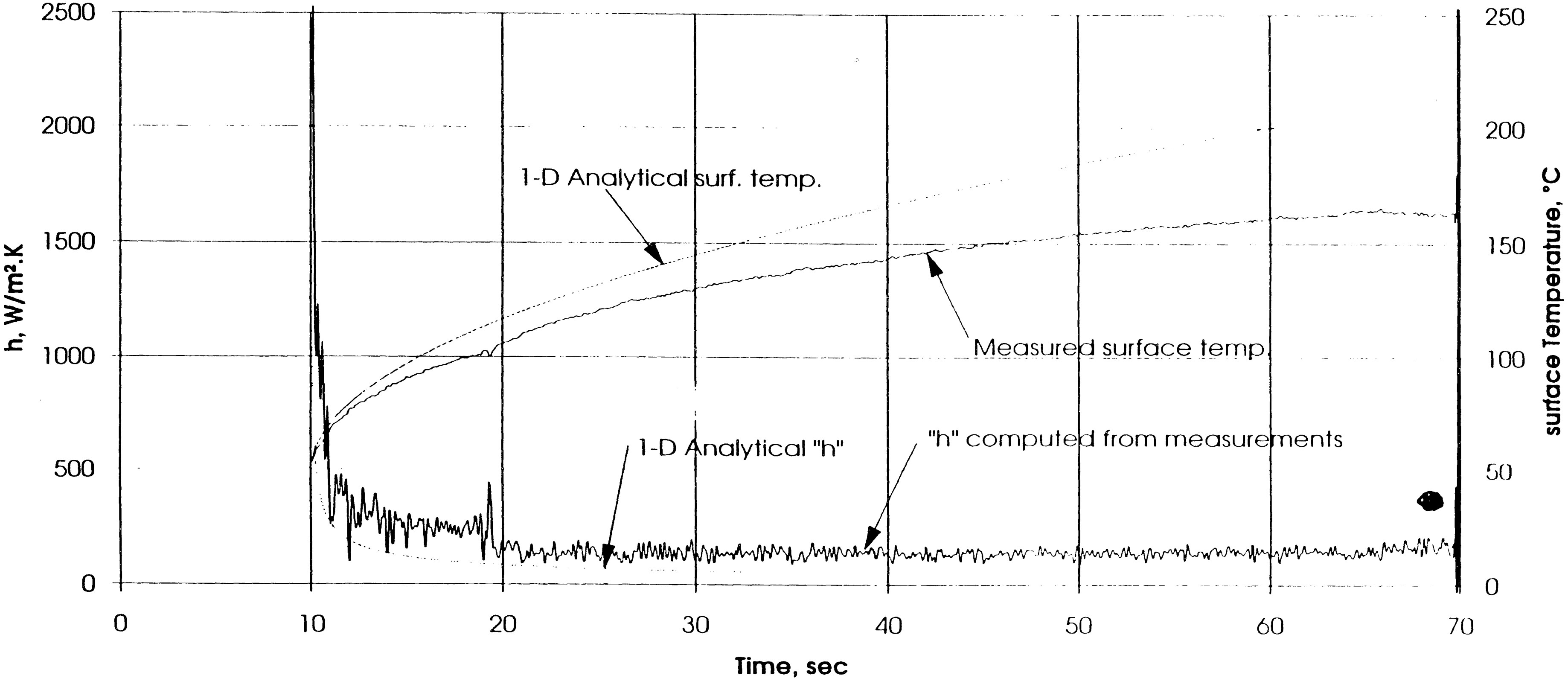
Convection H.T. Coeff. and Mean Surface Temperature vs. Time for pbe42892 Run #8 , q"total=3.5 W/cm²

Figure D8a. Mean heater surface temperature and derived heat transfer coefficient. Run No. 8.

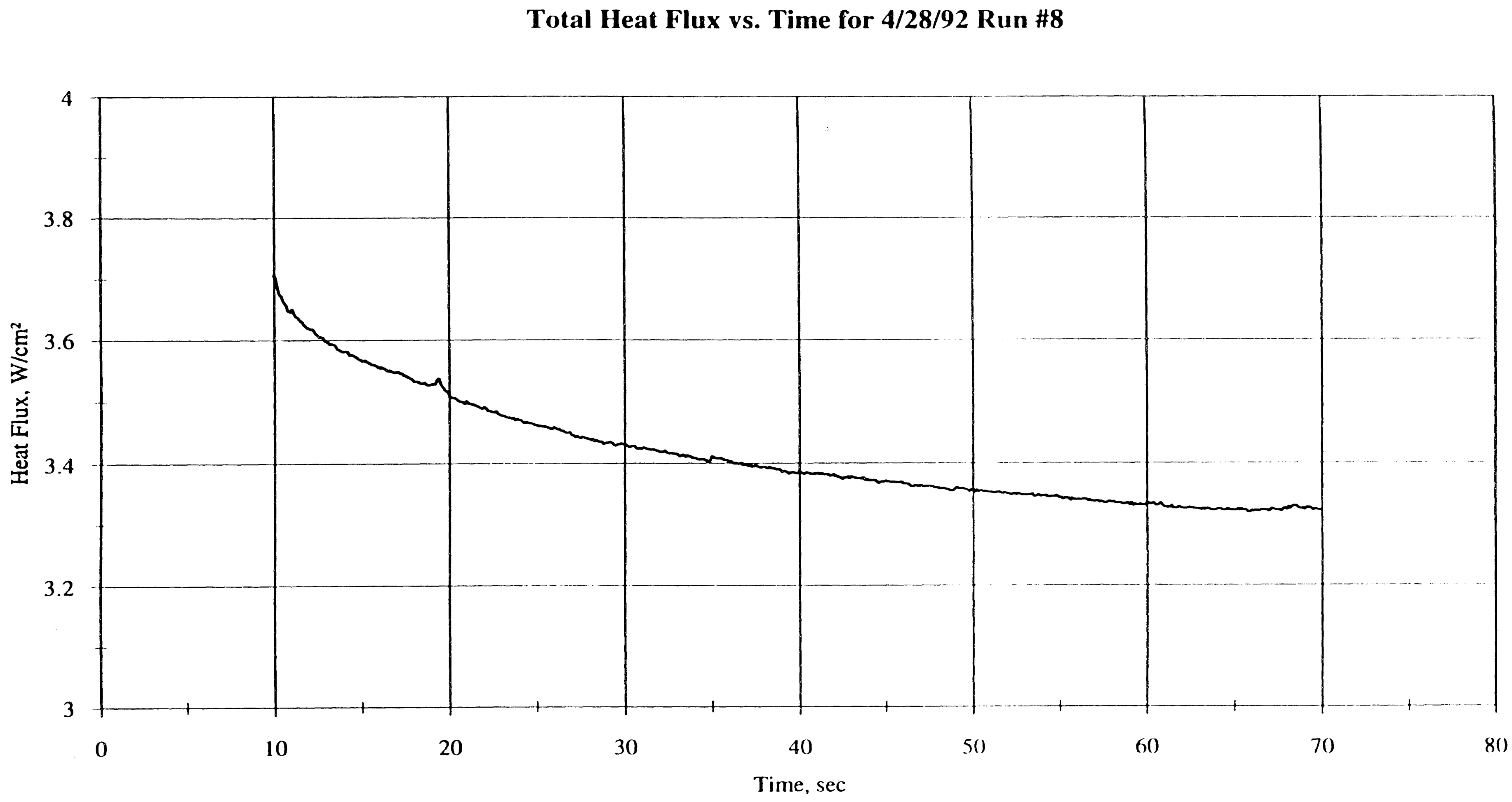

Figure D8b. Heat flux input. Run No. 8.

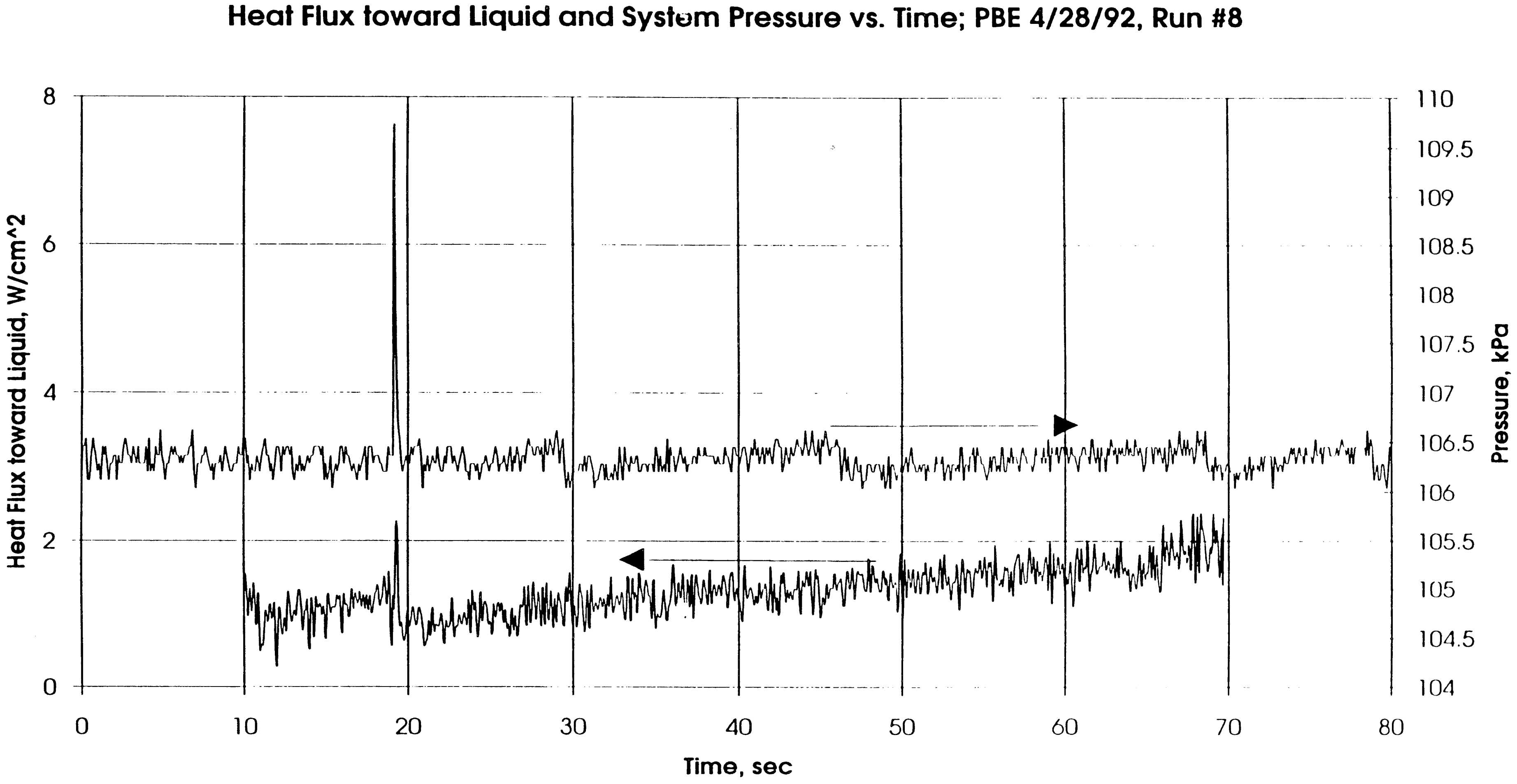

Figure D8c.	System pressure and heat flux into fluid. Run No. 8.

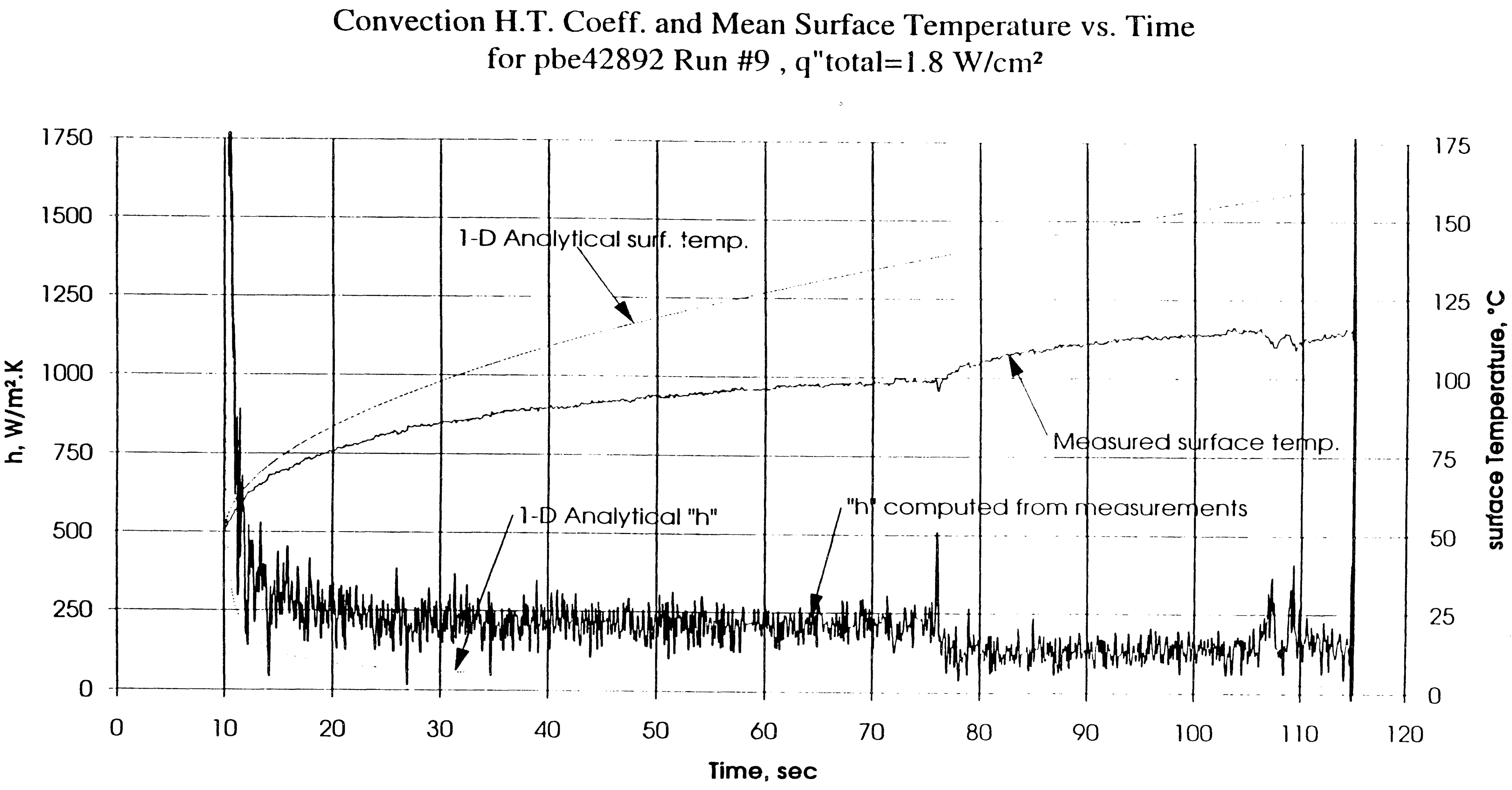

Figure D9a. Mean heater surface temperature and derived heat transfer coefficient. Run No. 9.

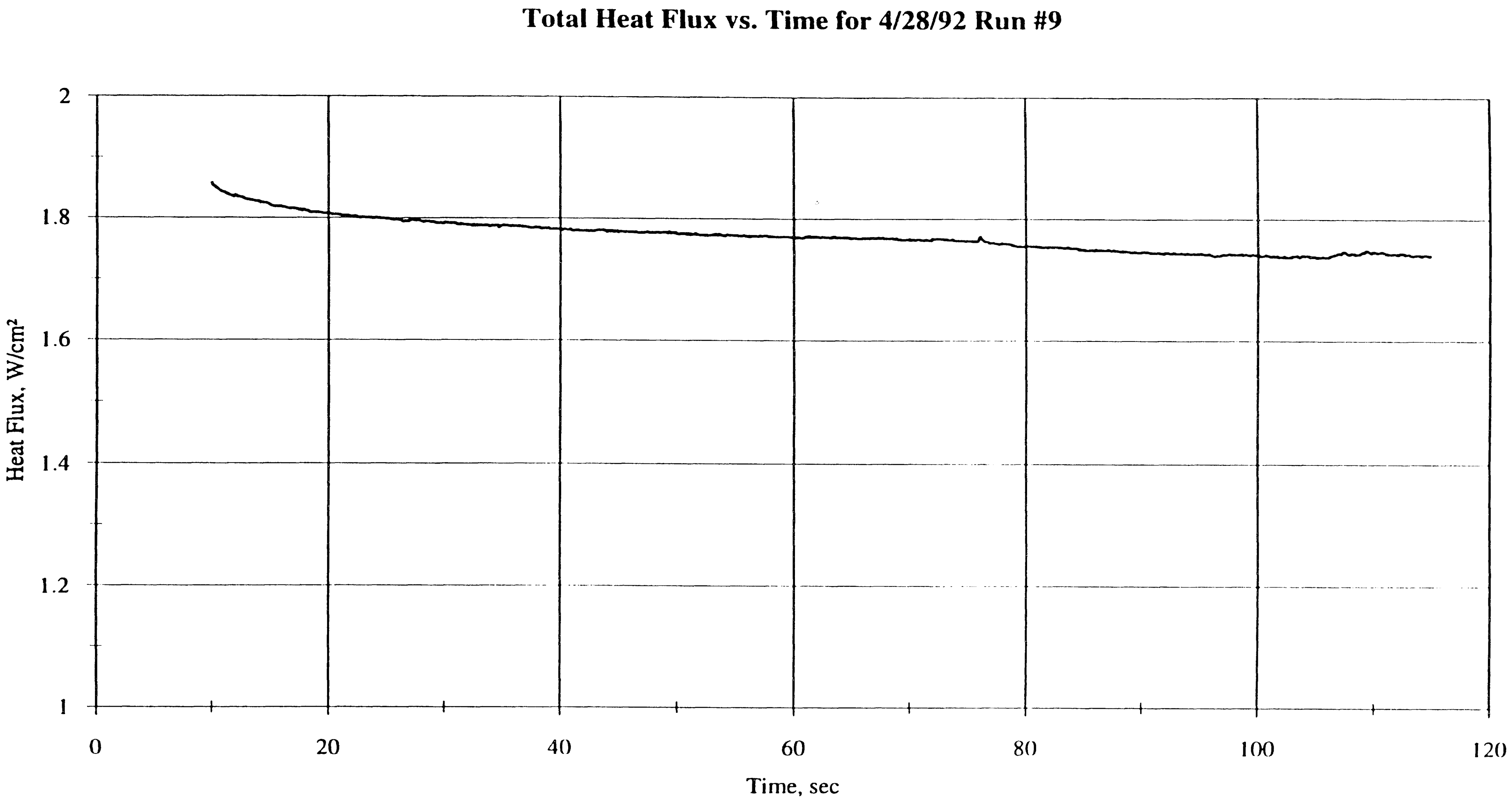

Figure D9b. Heat flux input. Run No. 9.

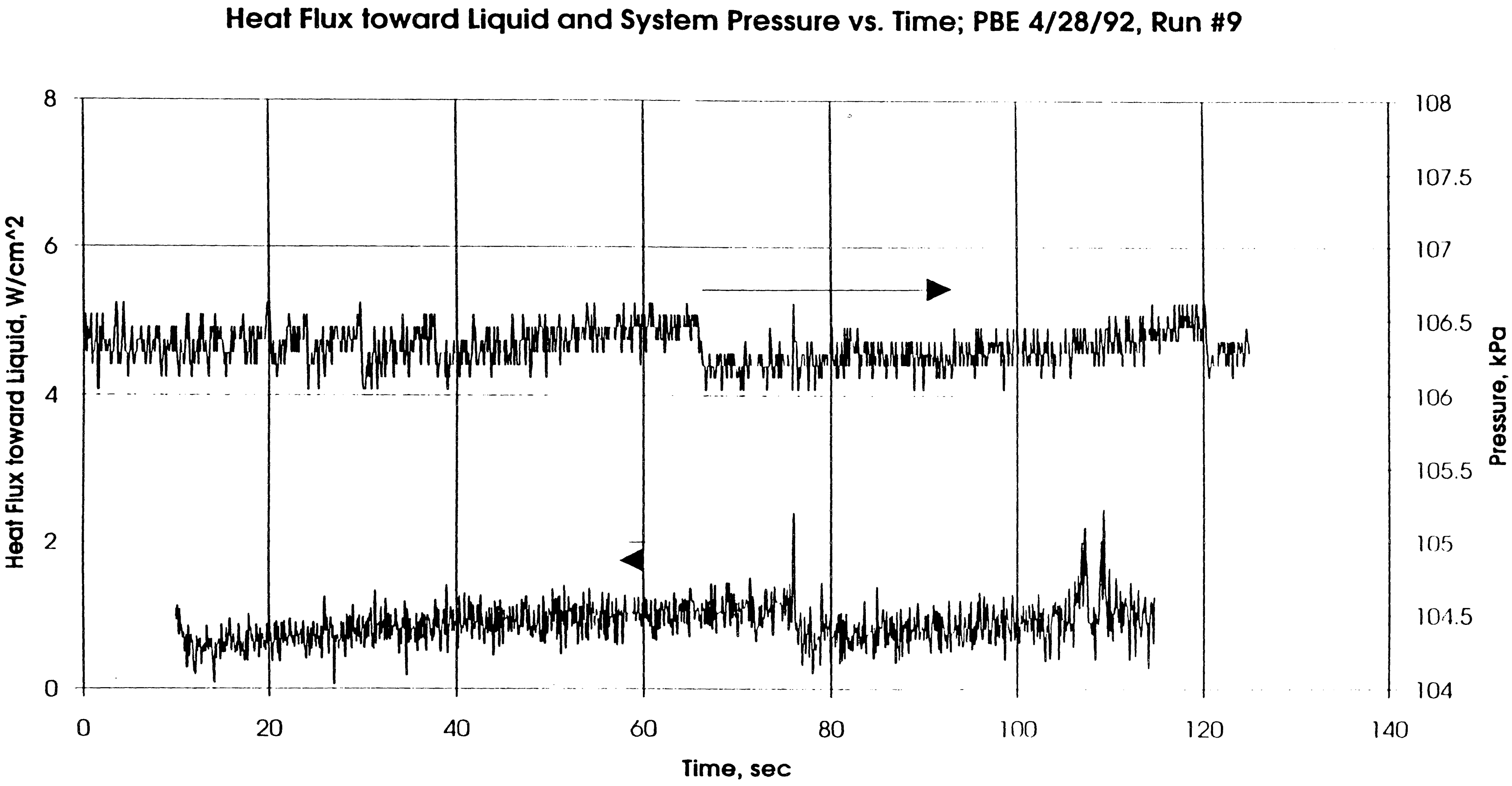

Figure D9c. System pressure and heat flux into fluid. Run No. 9.

Appendix E. Plots of results of Post-Flight test conducted for PBE-IA at a/g = +1 on 11/4/92.

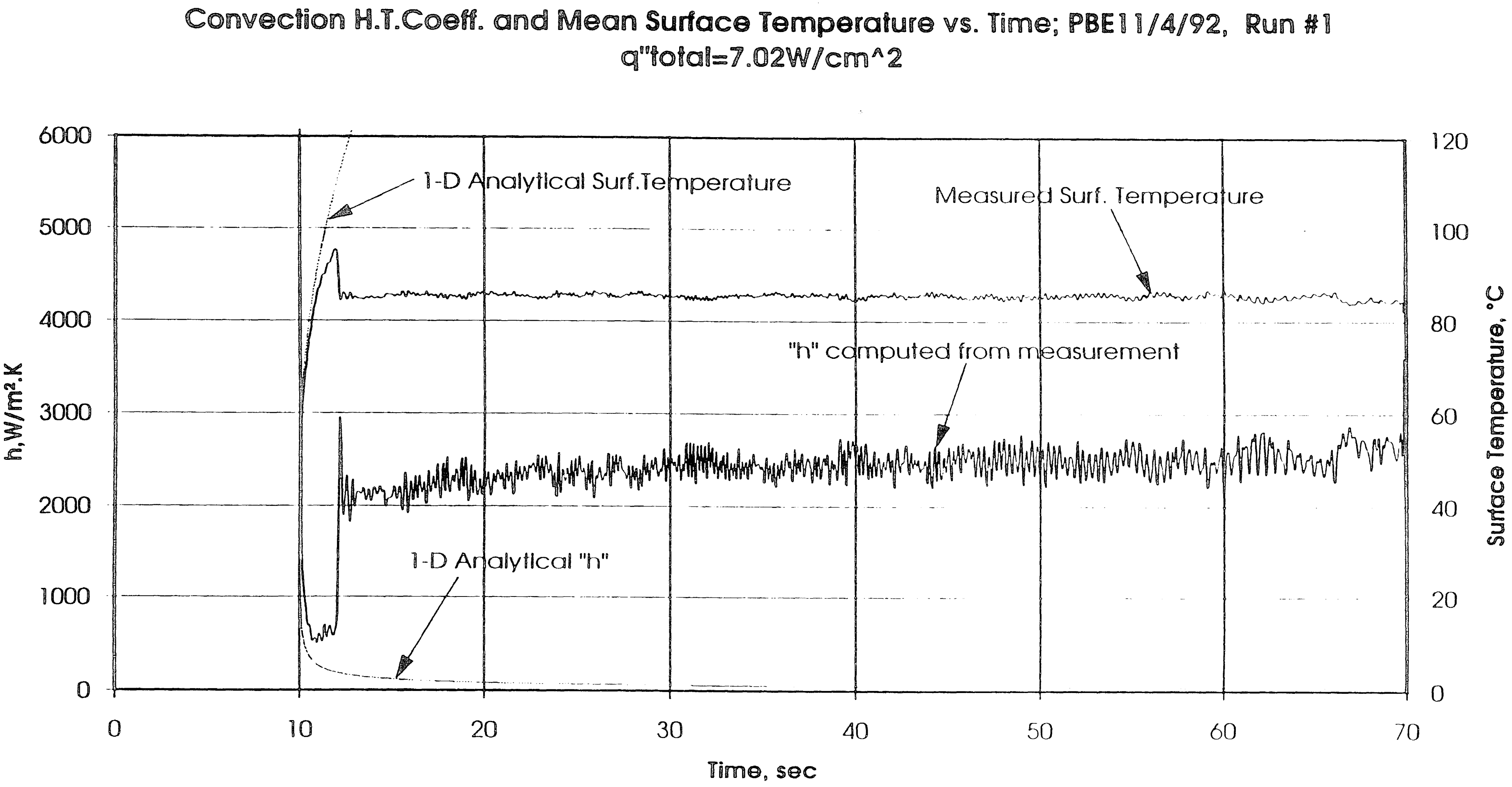

Figure E1a. Mean heater surface temperature and derived heat transfer coefficient. Run No. 1

Total Heat Flux vs. Time for 11/4/92 Run #1

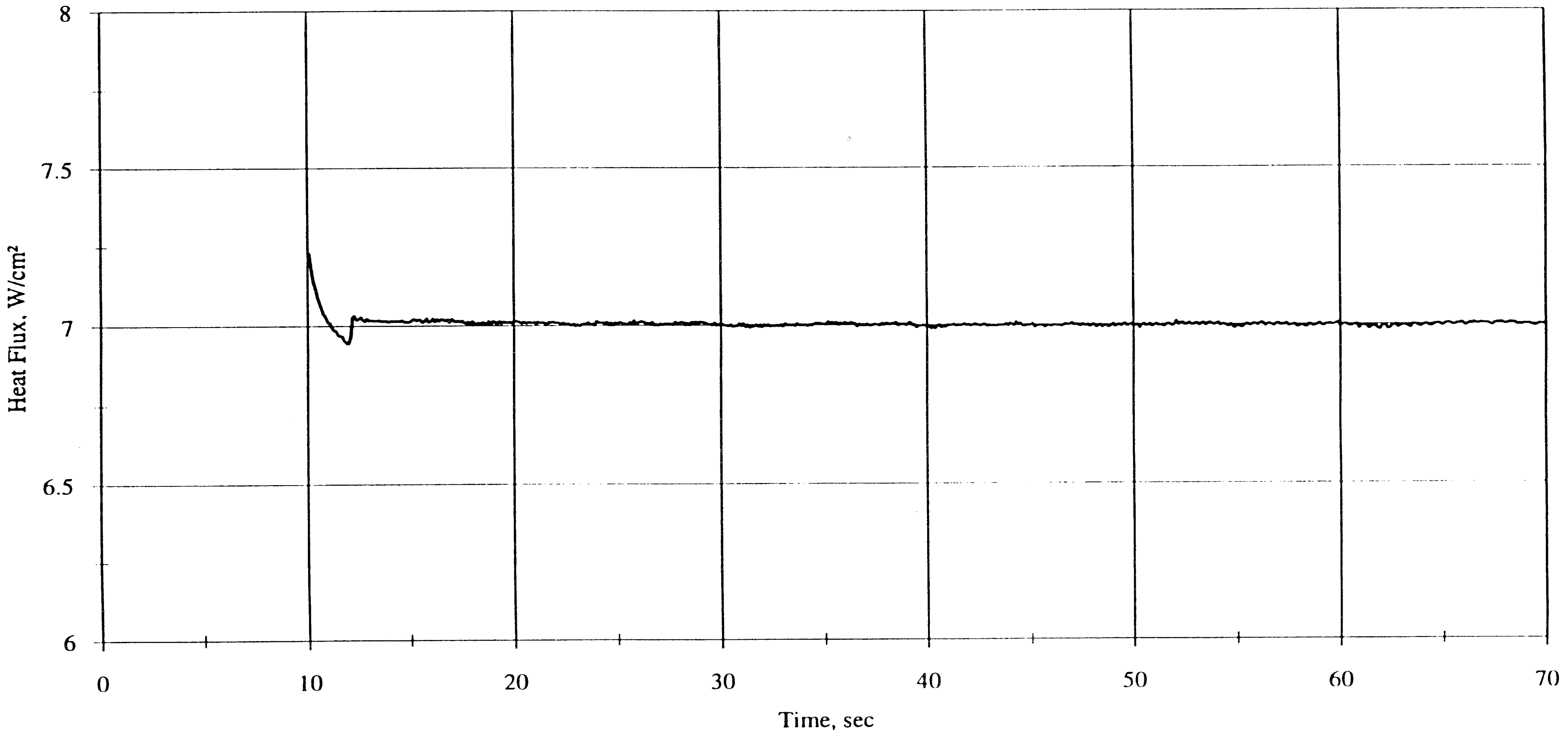

Figure E1b. Heat flux input. Run No. 1

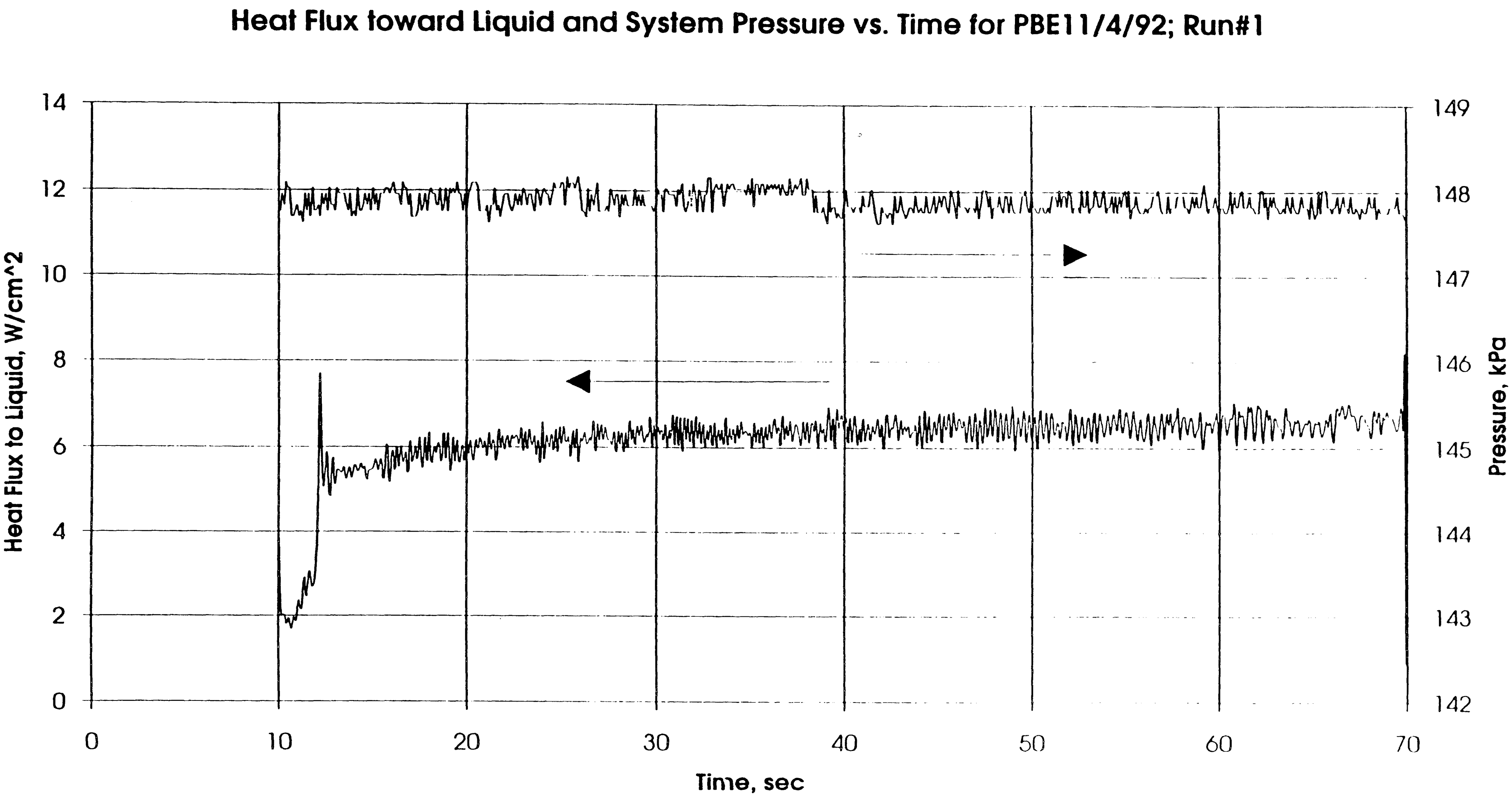

Figure E1c. System pressure and heat flux into fluid. Run No. 1.

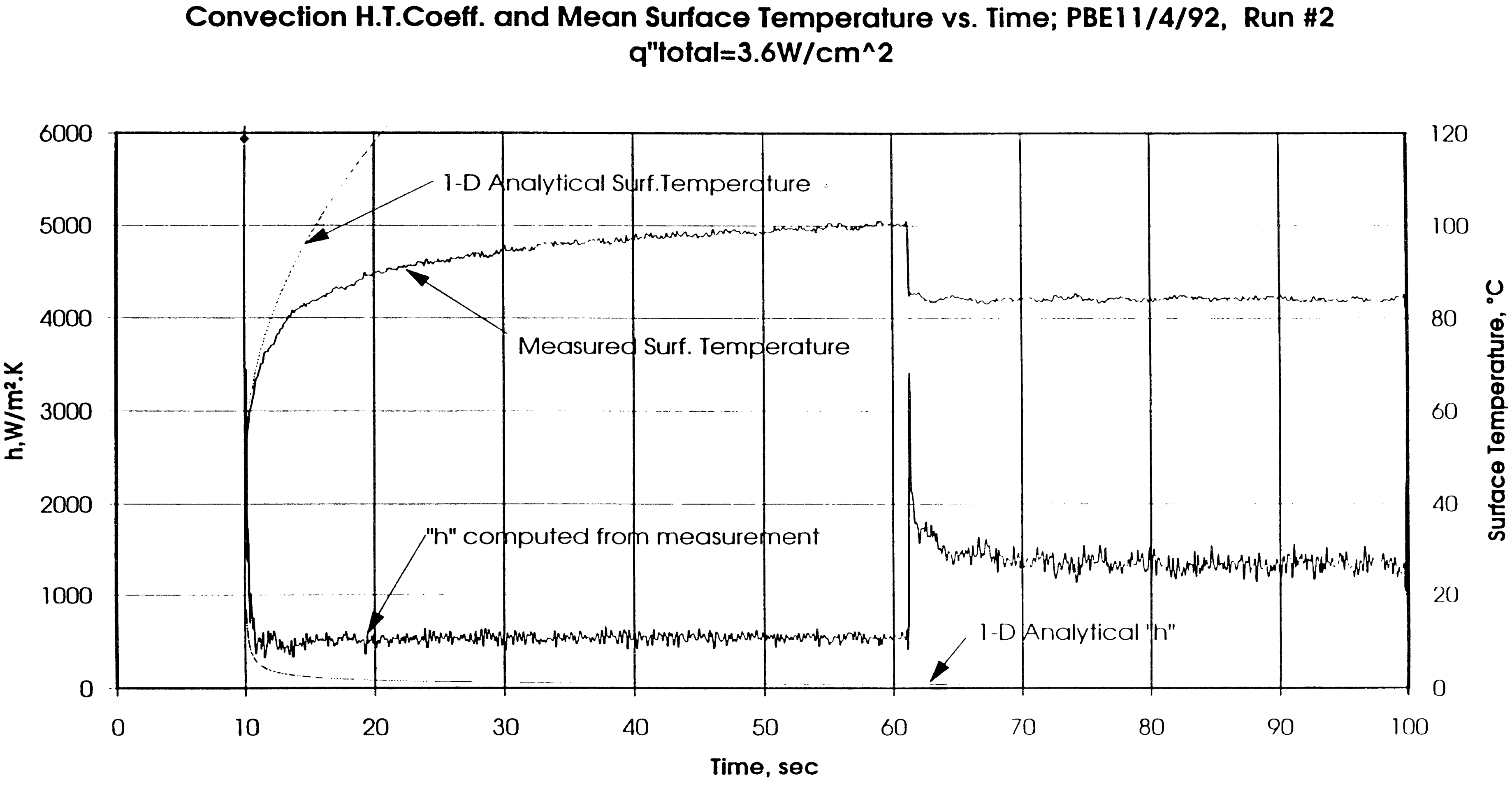
Convection H.T.Coeff. and Mean Surface Temperature vs. Time; PBE11/4/92, Run #2
q"total=3.6W/cm^2

Figure E2a. Mean heater surface temperature and derived heat transfer coefficient. Run No. 2.

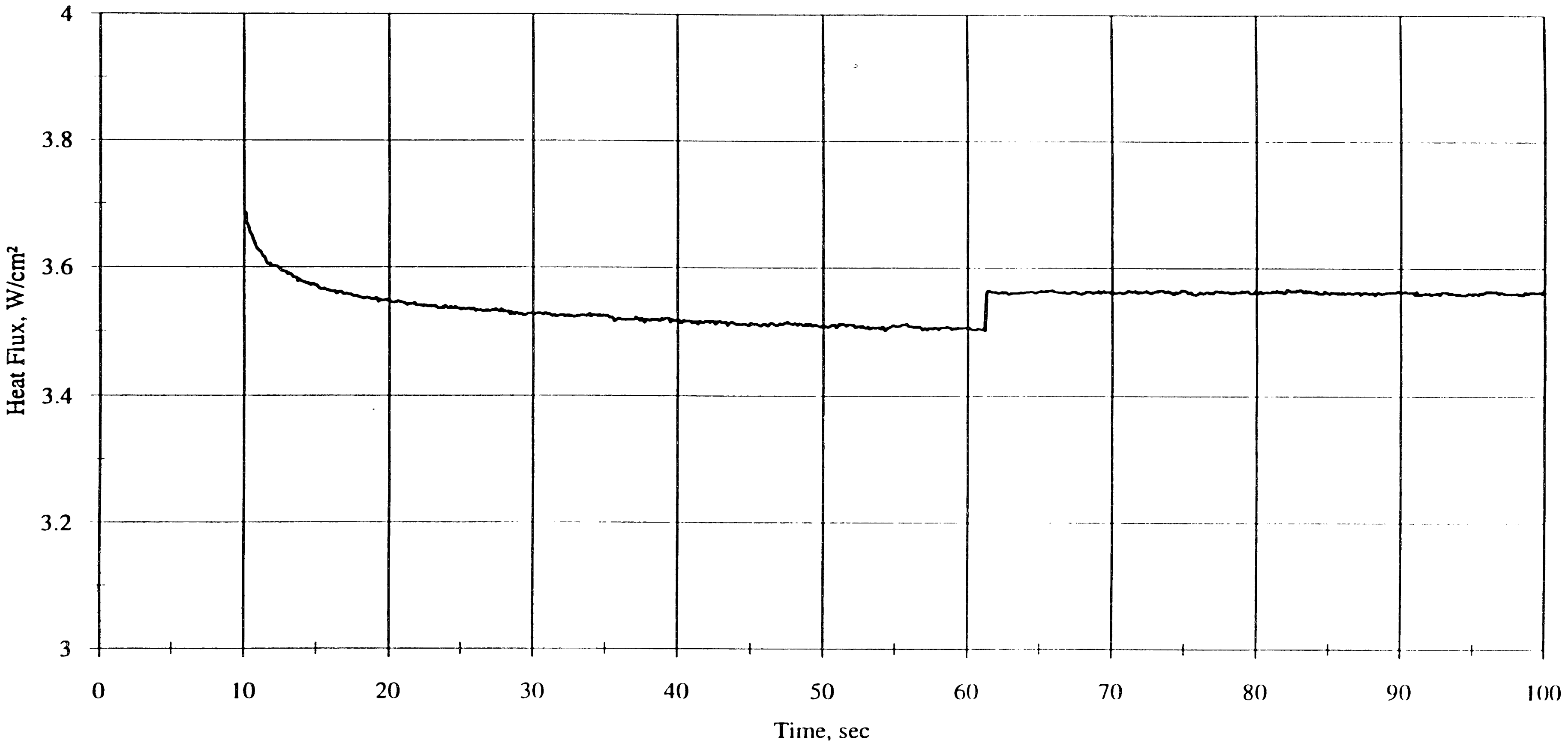
Total Heat Flux vs. Time for 11/4/92 Run #2

Figure E2b. Heat flux input. Run No. 2.

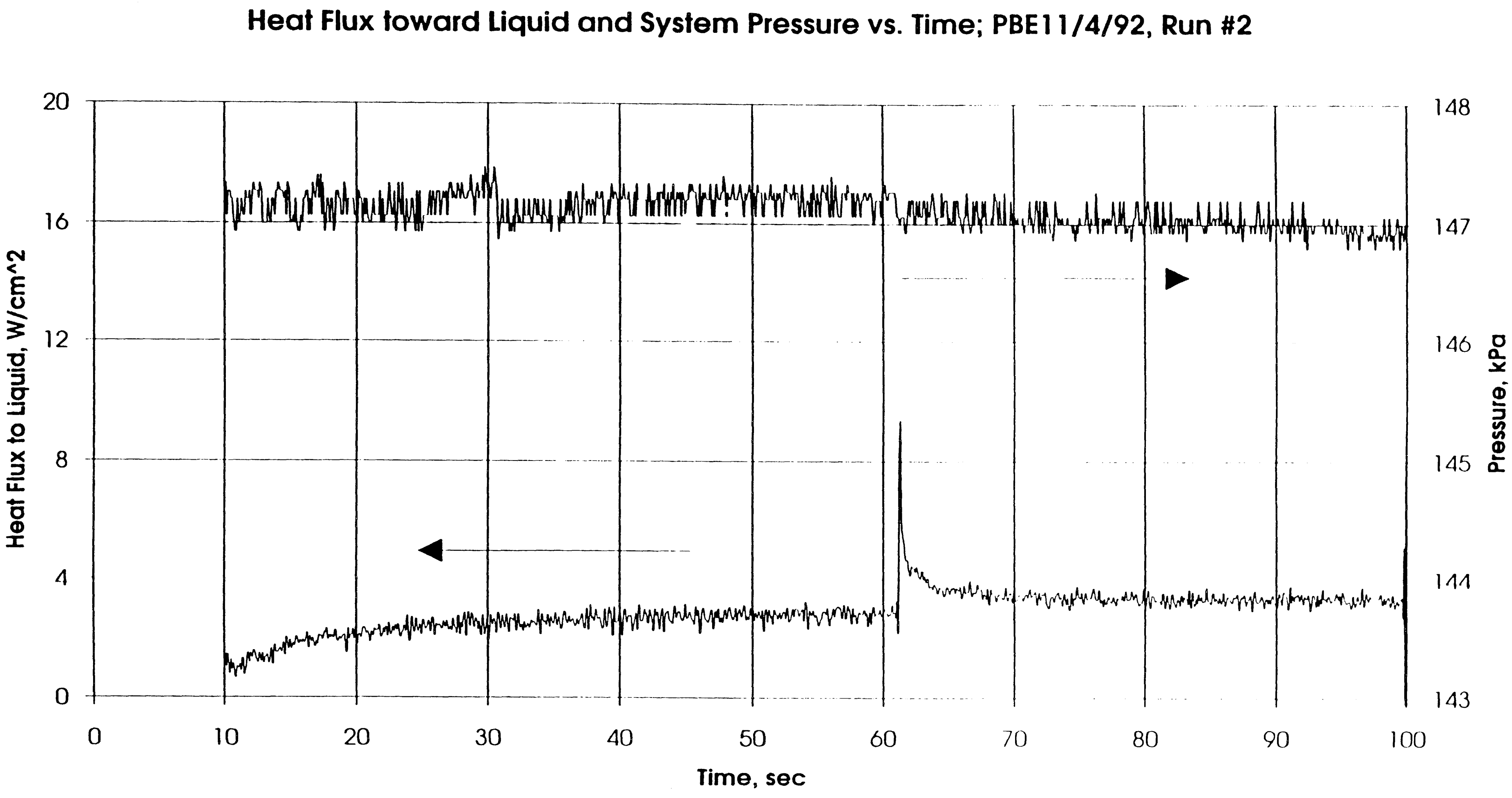

Figure E2c. System pressure and heat flux into fluid. Run No. 2.

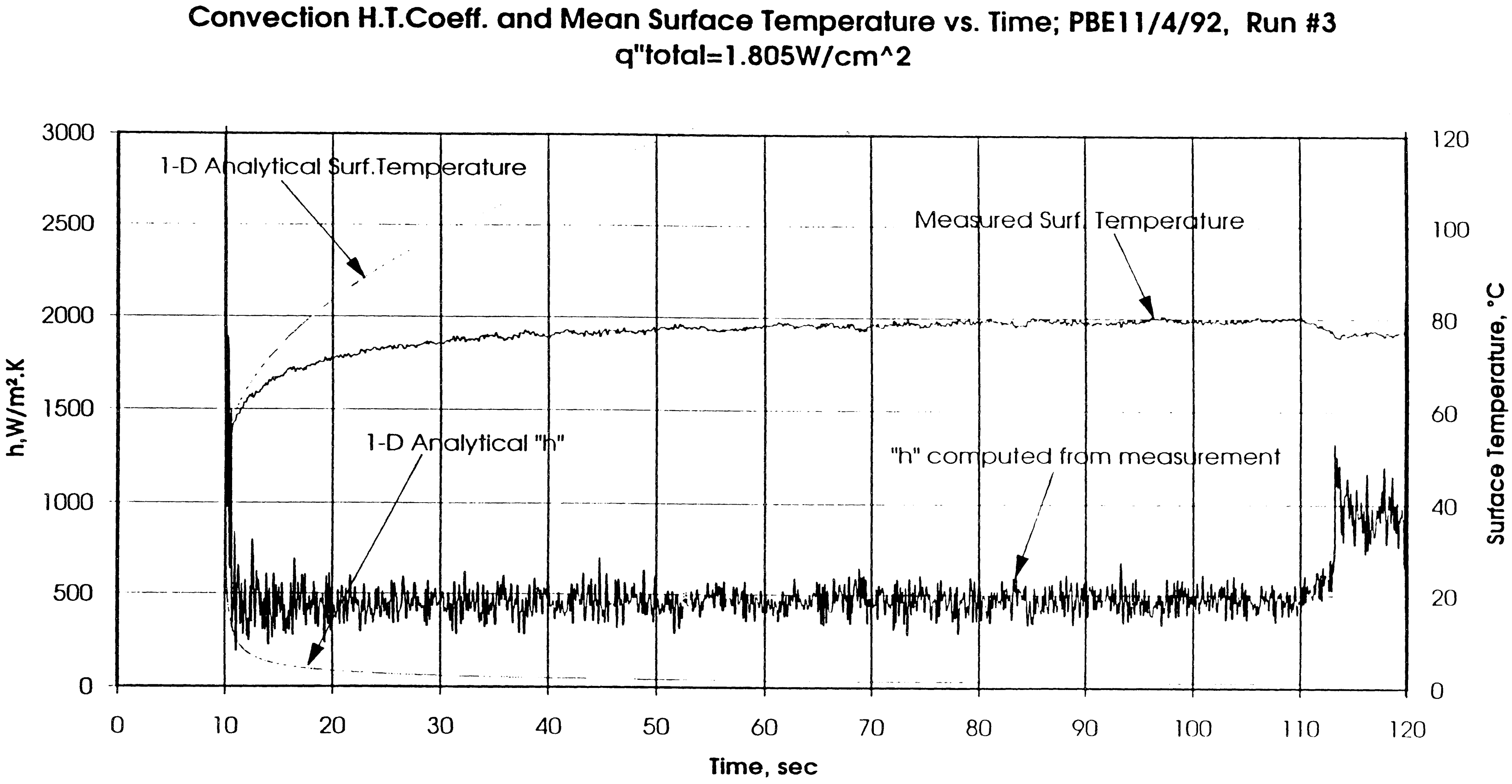

Figure E3a. Mean heater surface temperature and derived heat transfer coefficient. Run No. 3.

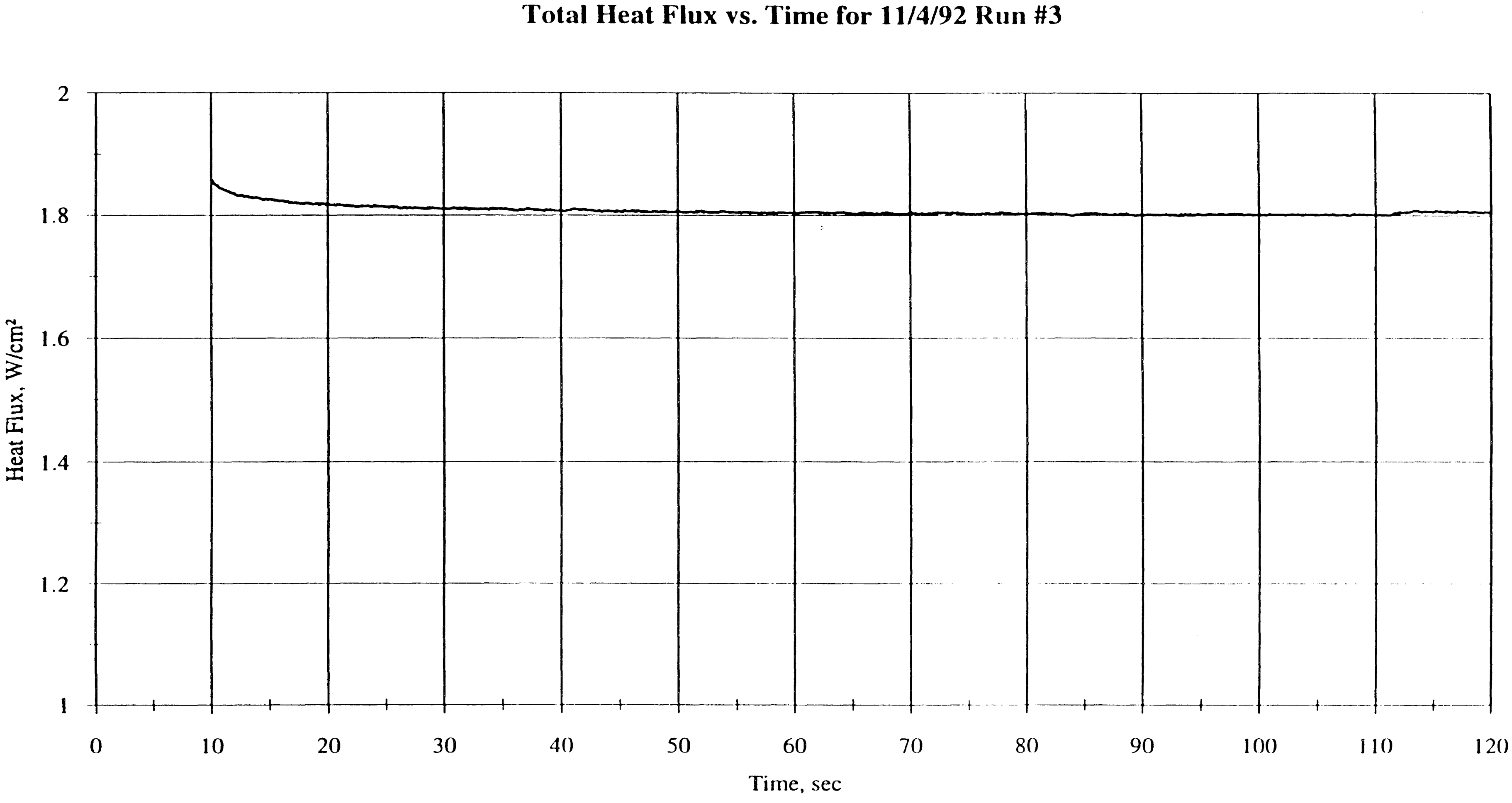

Figure E3b. **Heat flux input.** Run No. 3.

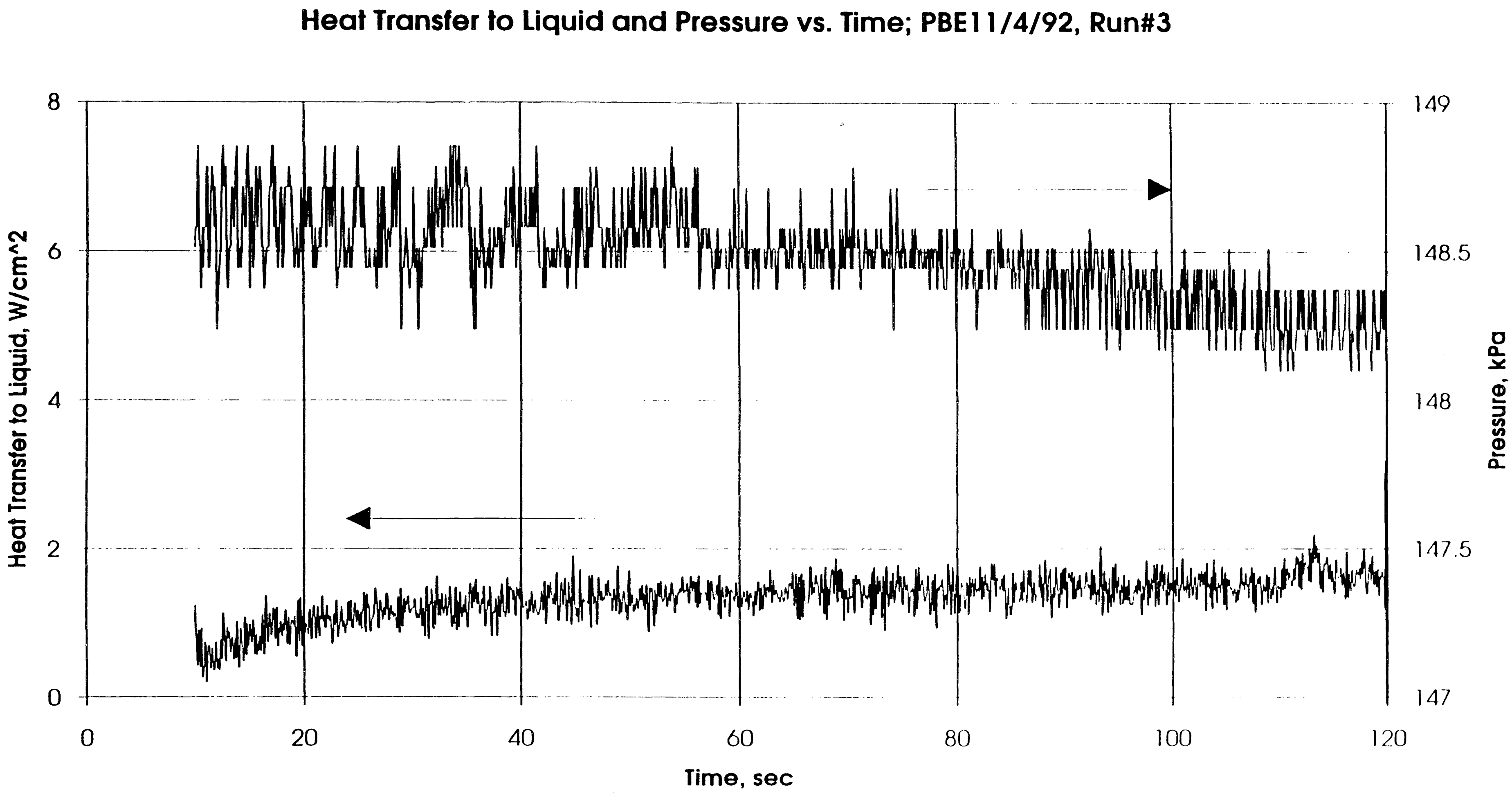

Figure E3c. System pressure and heat flux into fluid. Run No. 3.

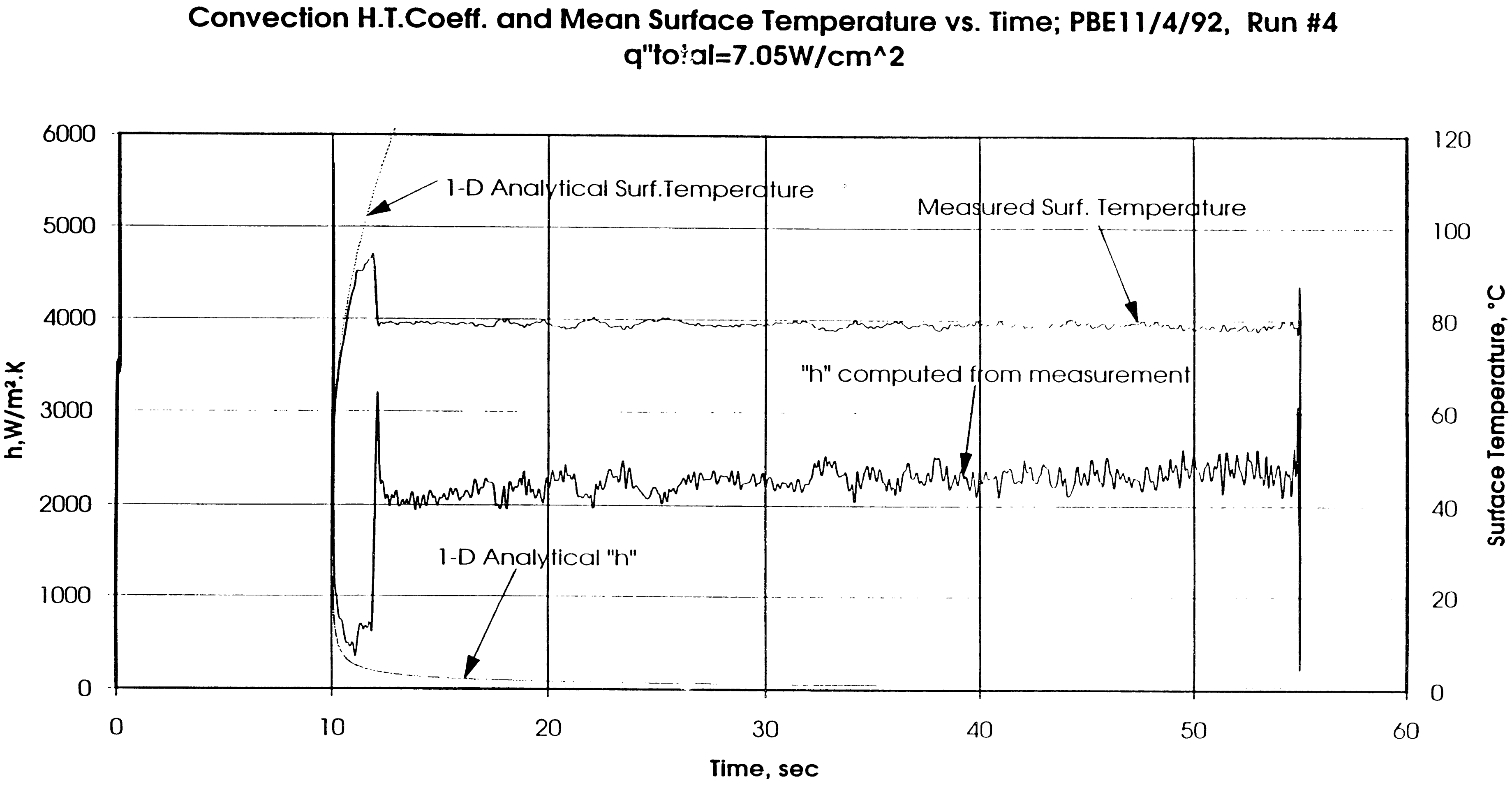

Figure E4a. Mean heater surface temperature and derived heat transfer coefficient. Run No. 4.

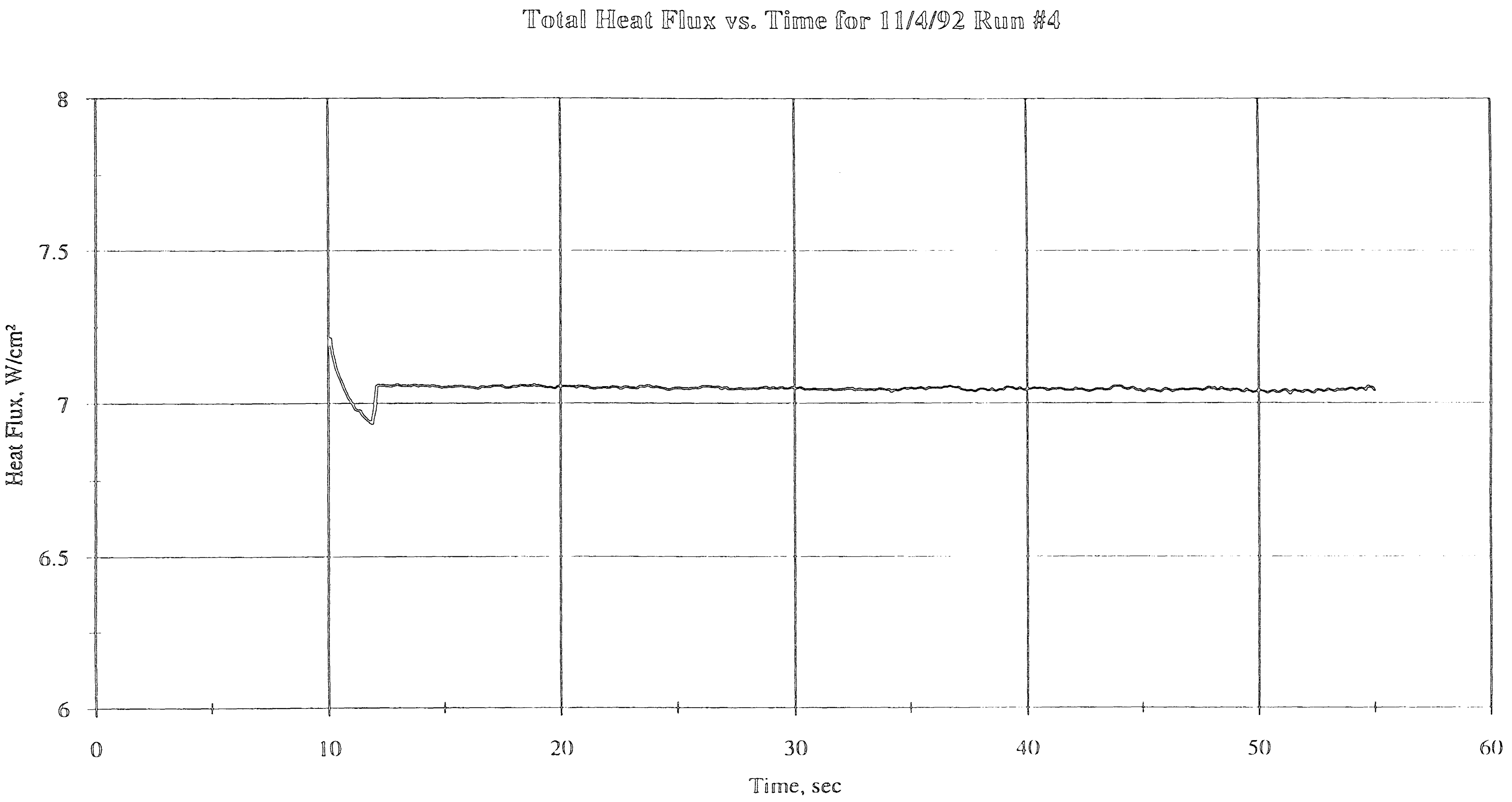

Figure E4b. Heat flux input. Run No. 4.

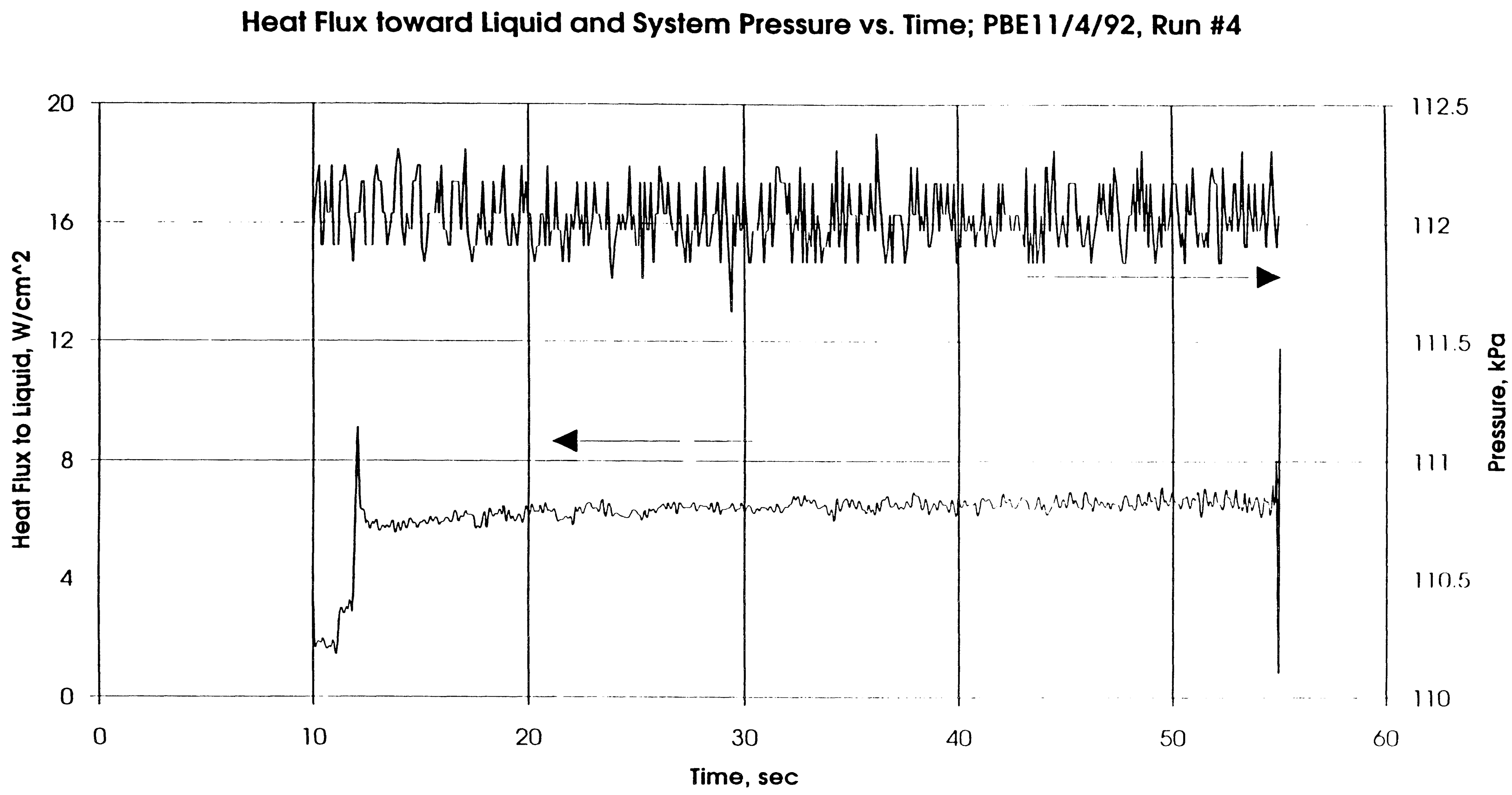

Figure E4c. System pressure and heat flux into fluid. Run No. 4.

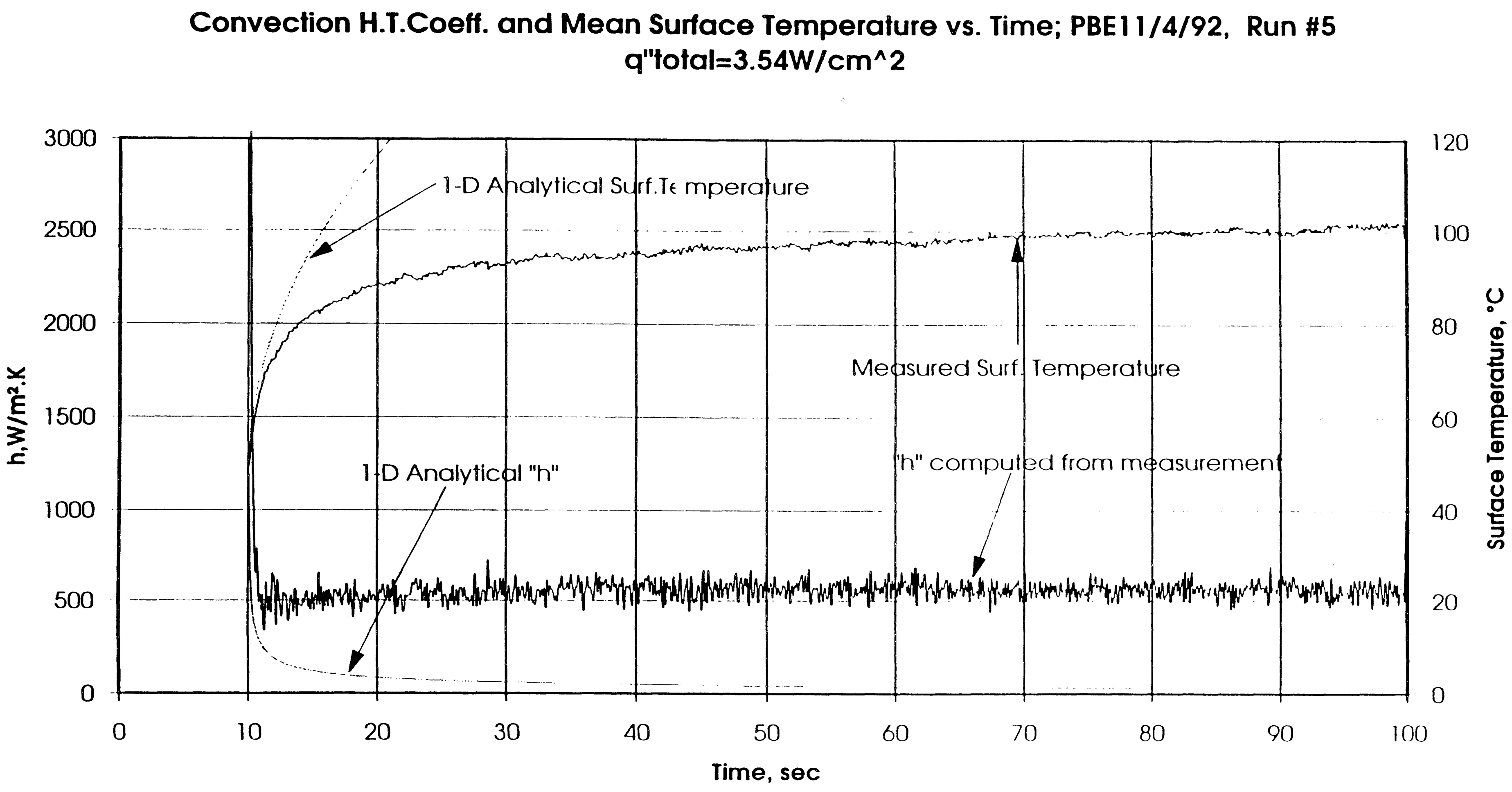

Figure E5a. Mean heater surface temperature and derived heat transfer coefficient. Run No. 5.

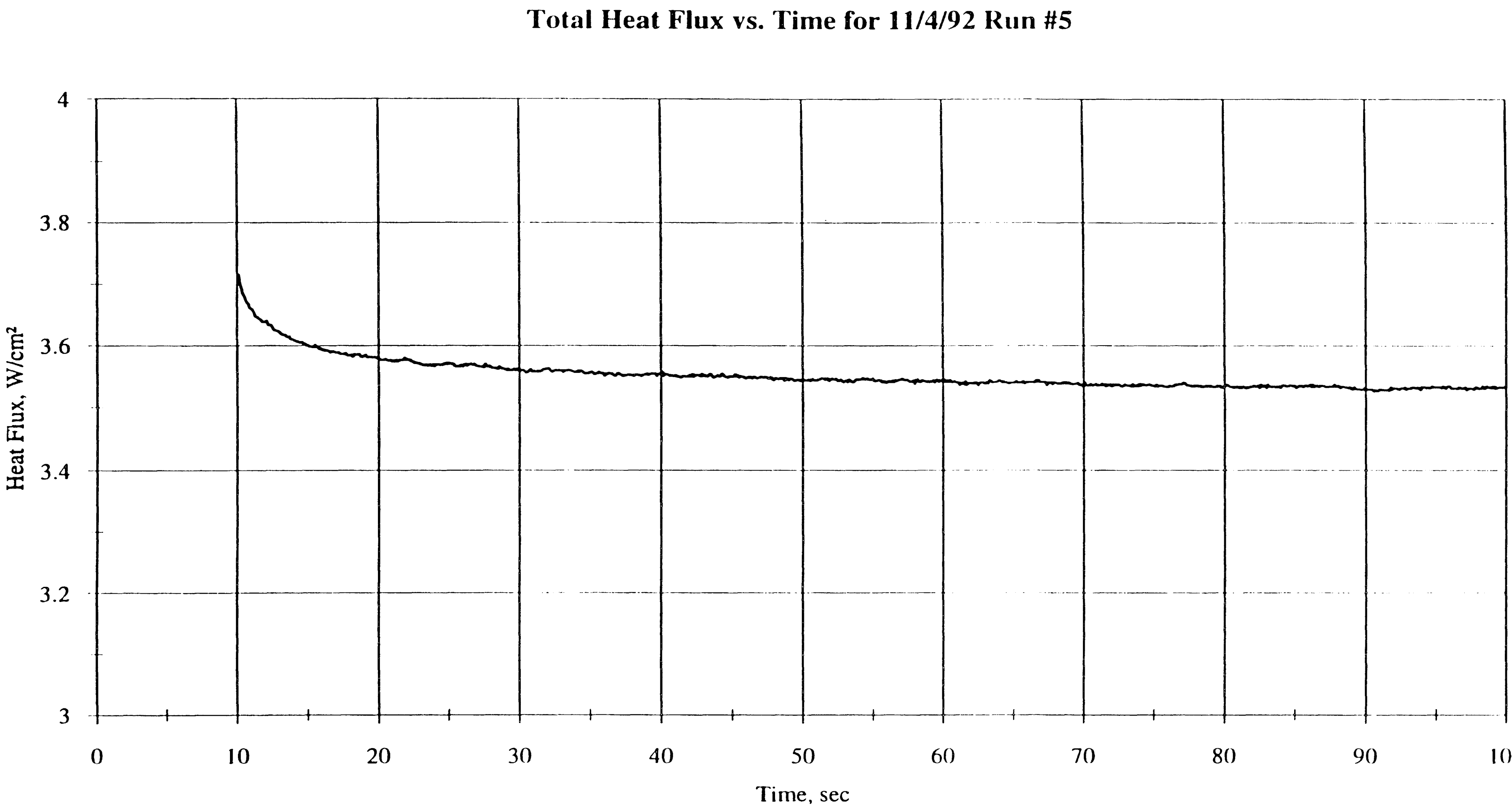

Figure E5b. Heat flux input. Run No. 5.

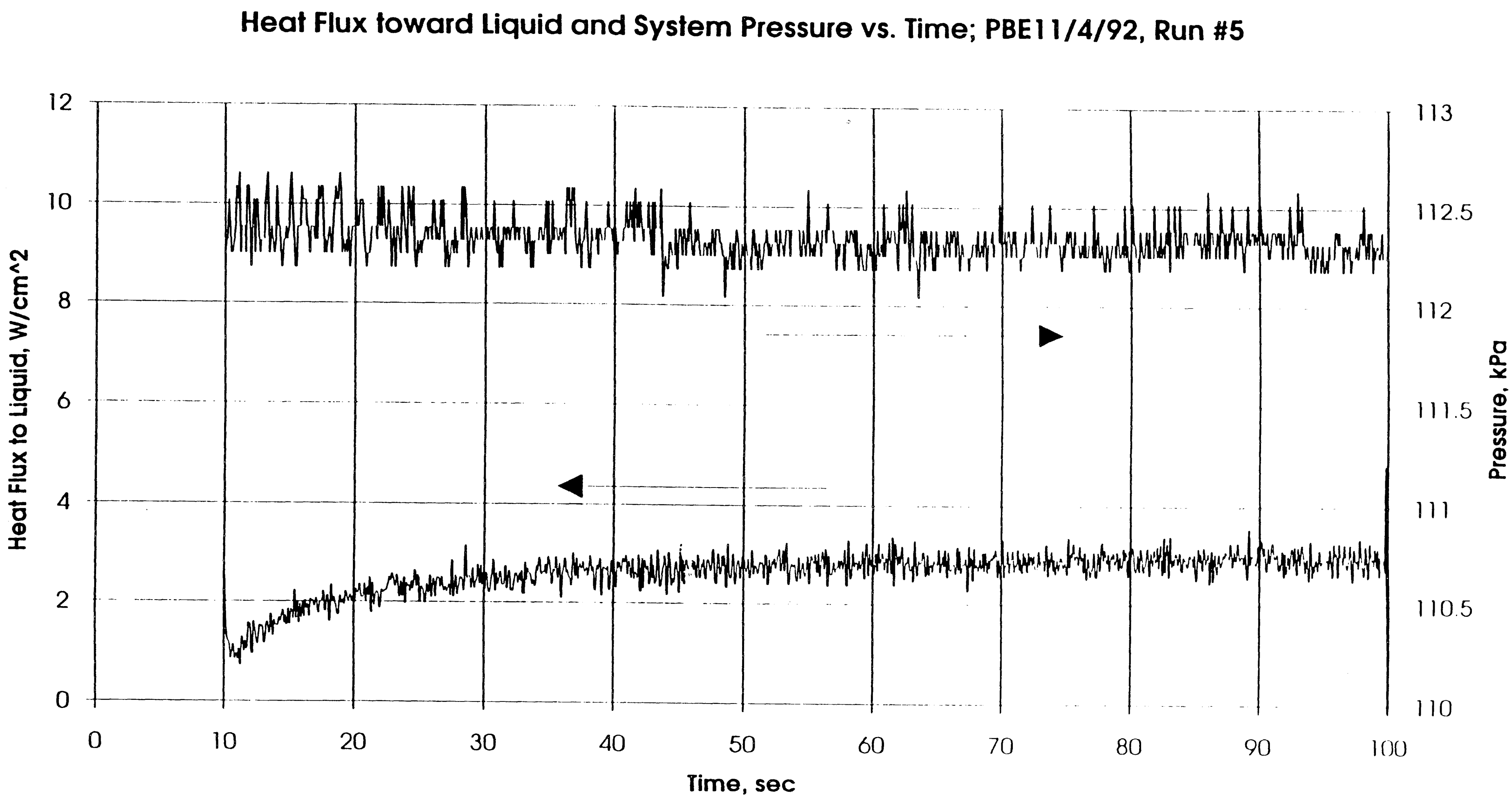

Figure E5c. System pressure and heat flux into fluid. Run No. 5.

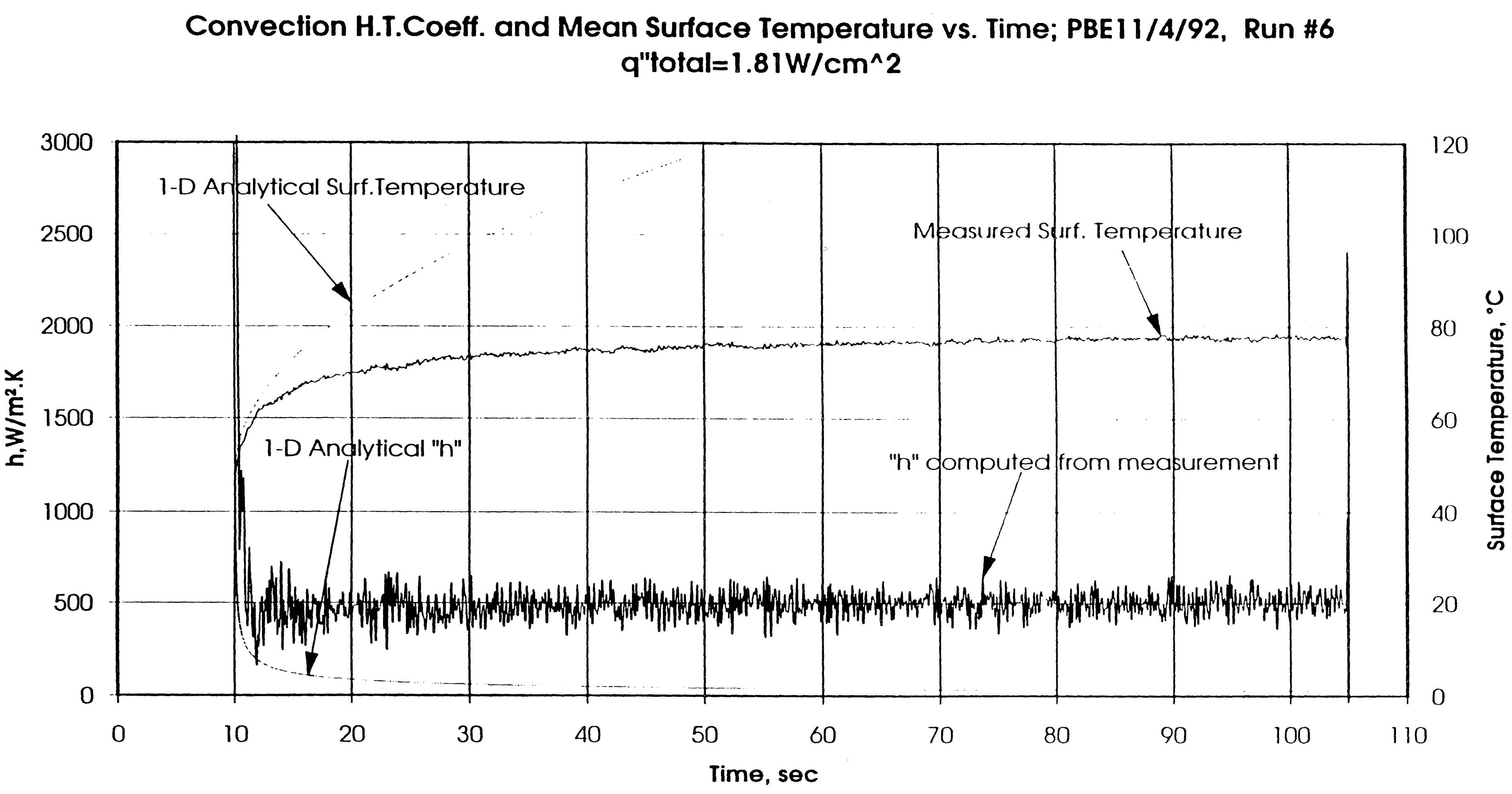

Figure E6a. Mean heater surface temperature and derived heat transfer coefficient. Run No. 6.

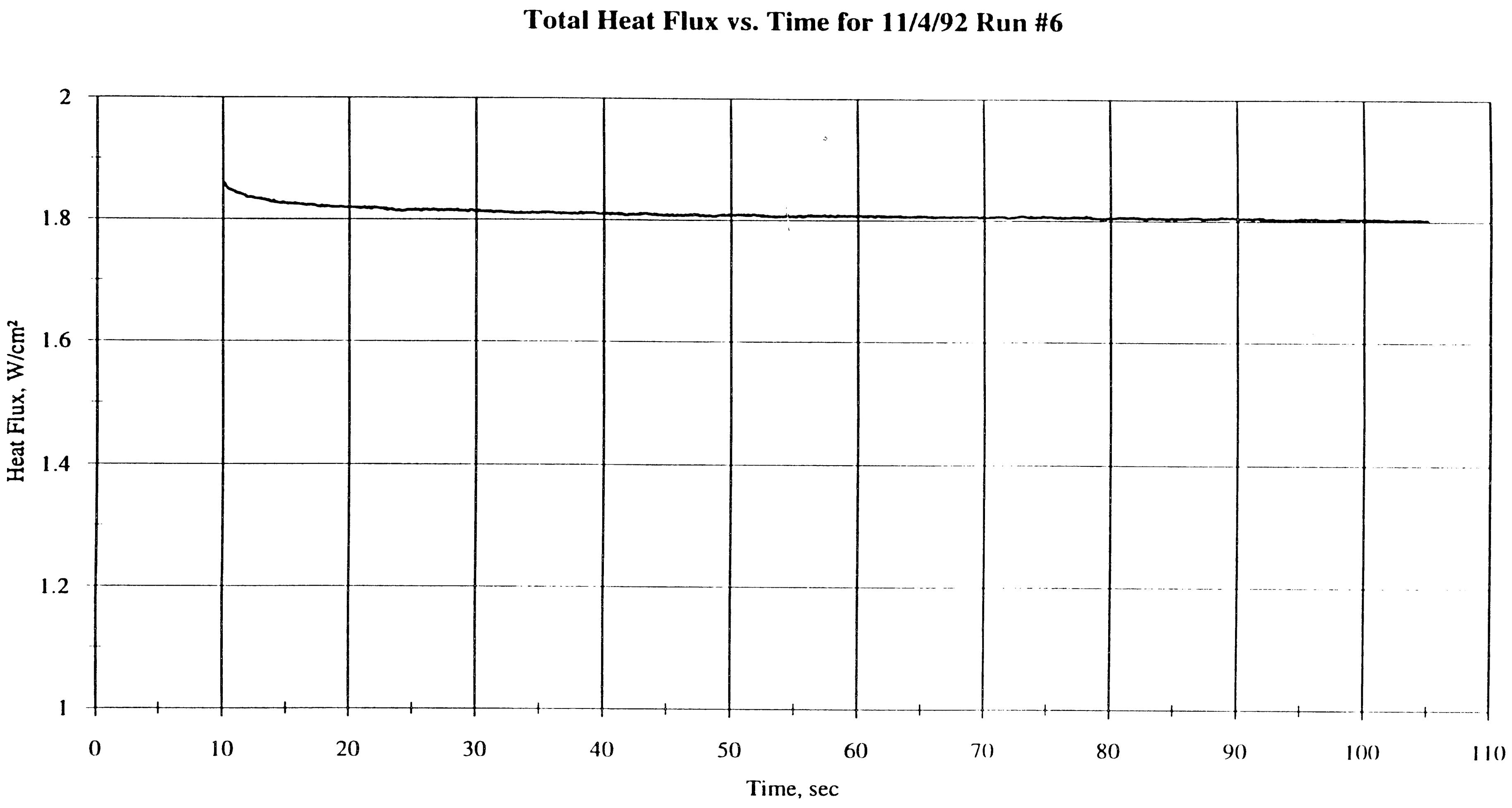
Total Heat Flux vs. Time for 11/4/92 Run #6

Figure E6b. Heat flux input. Run No. 6.

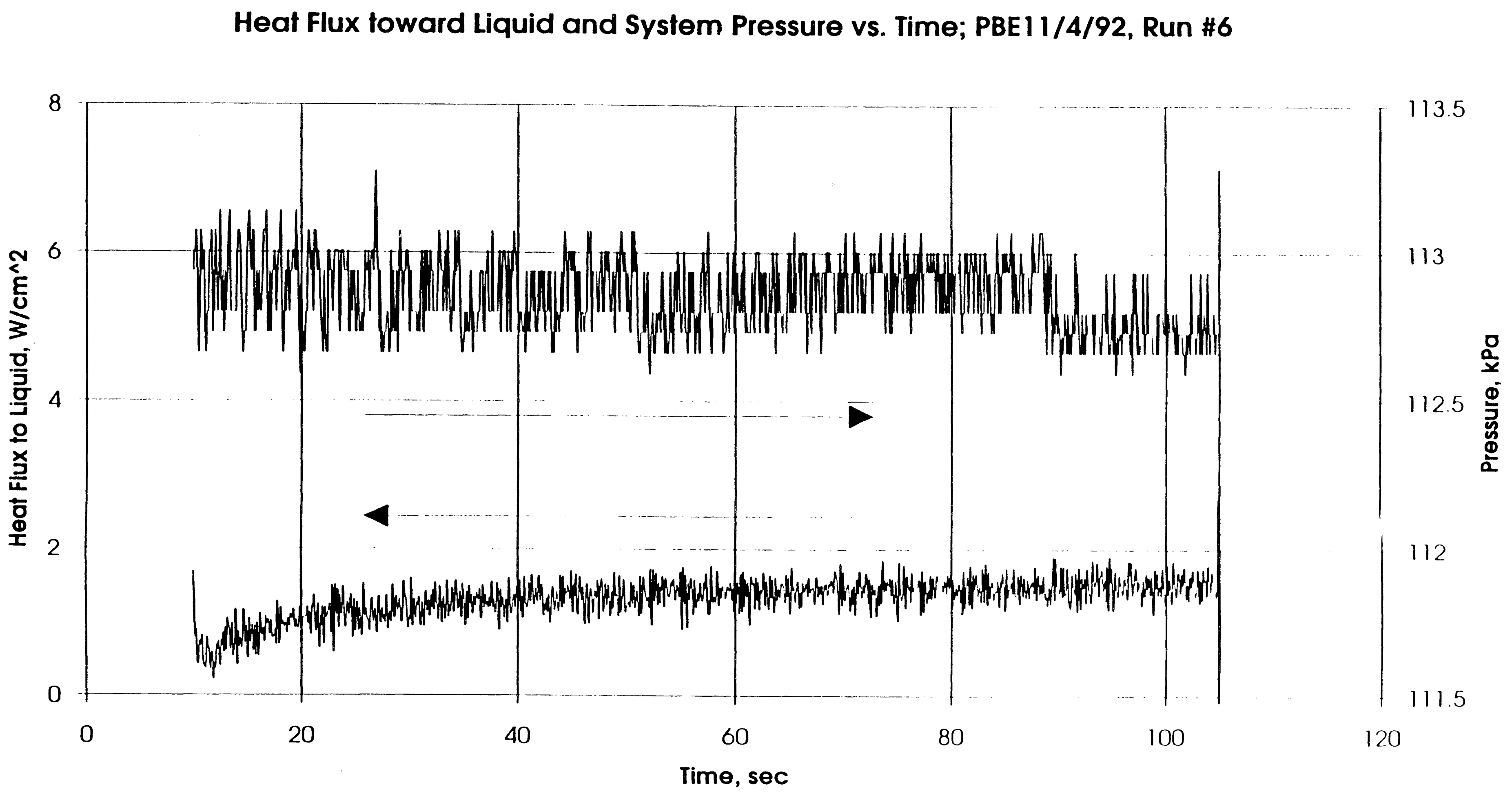

Figure E6c. System pressure and heat flux into fluid. Run No. 6.

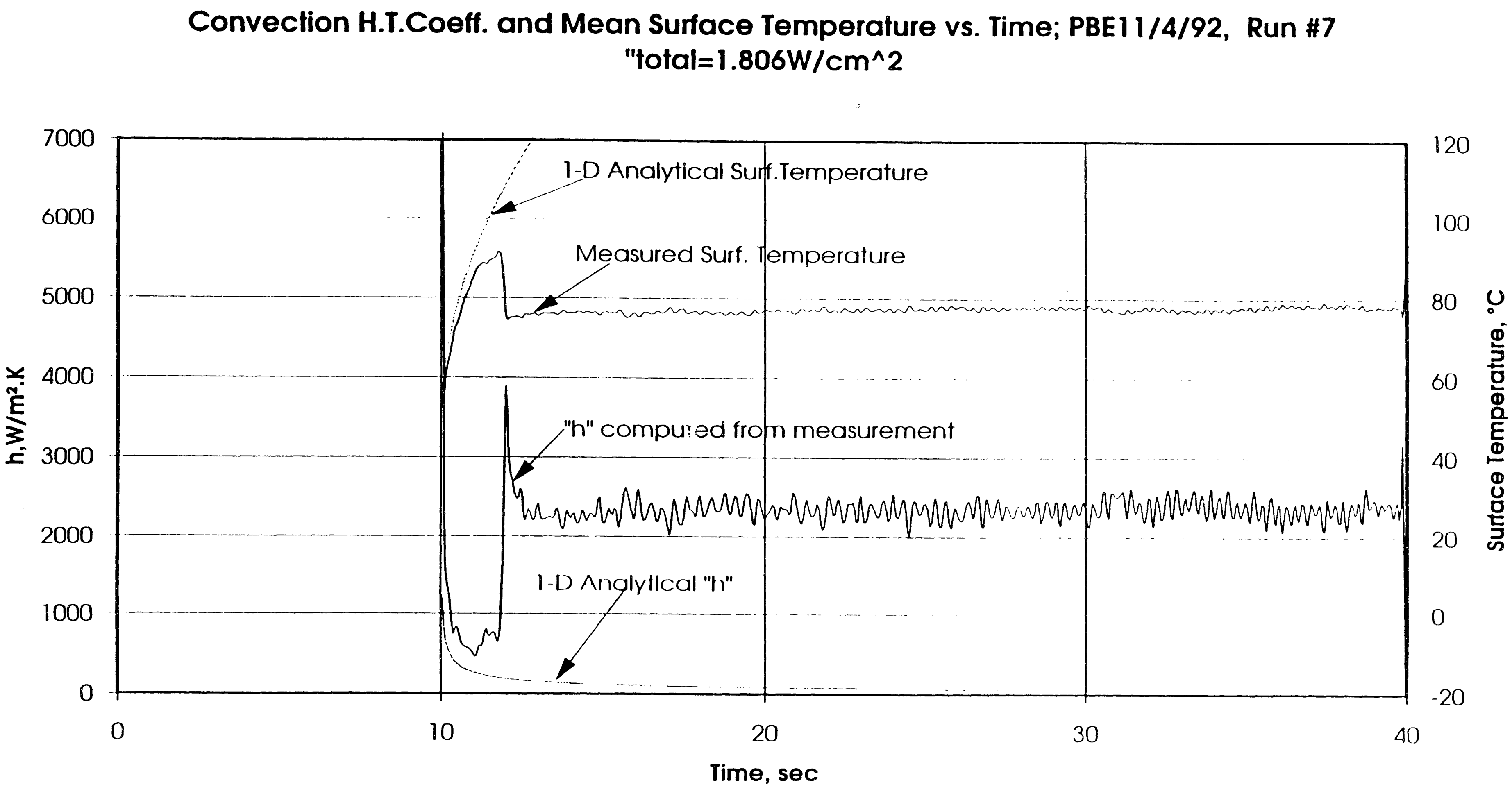

Figure E7a. Mean heater surface temperature and derived heat transfer coefficient. Run No. 7.

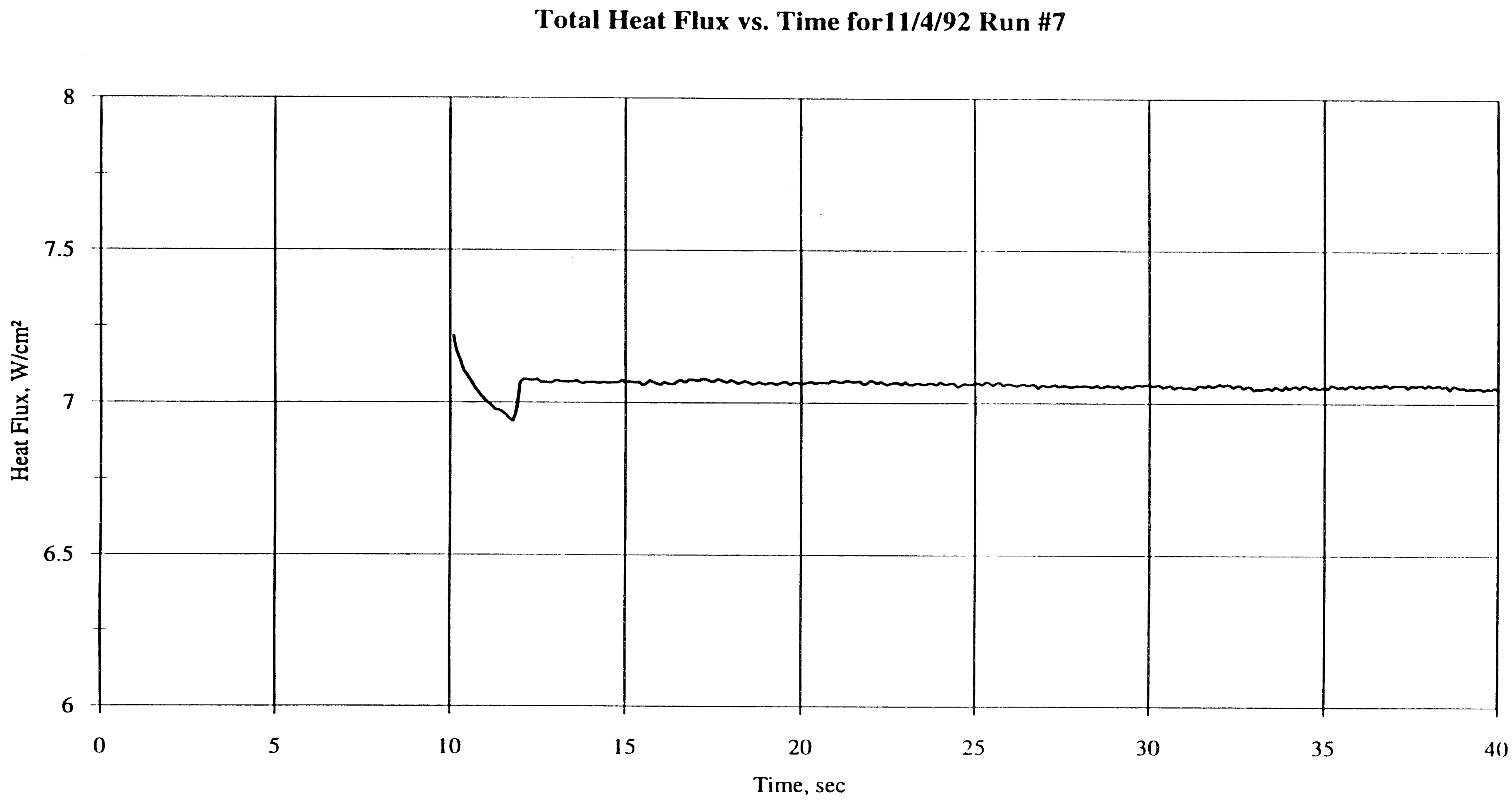

Figure E7b. Heat flux input. Run No. 7.

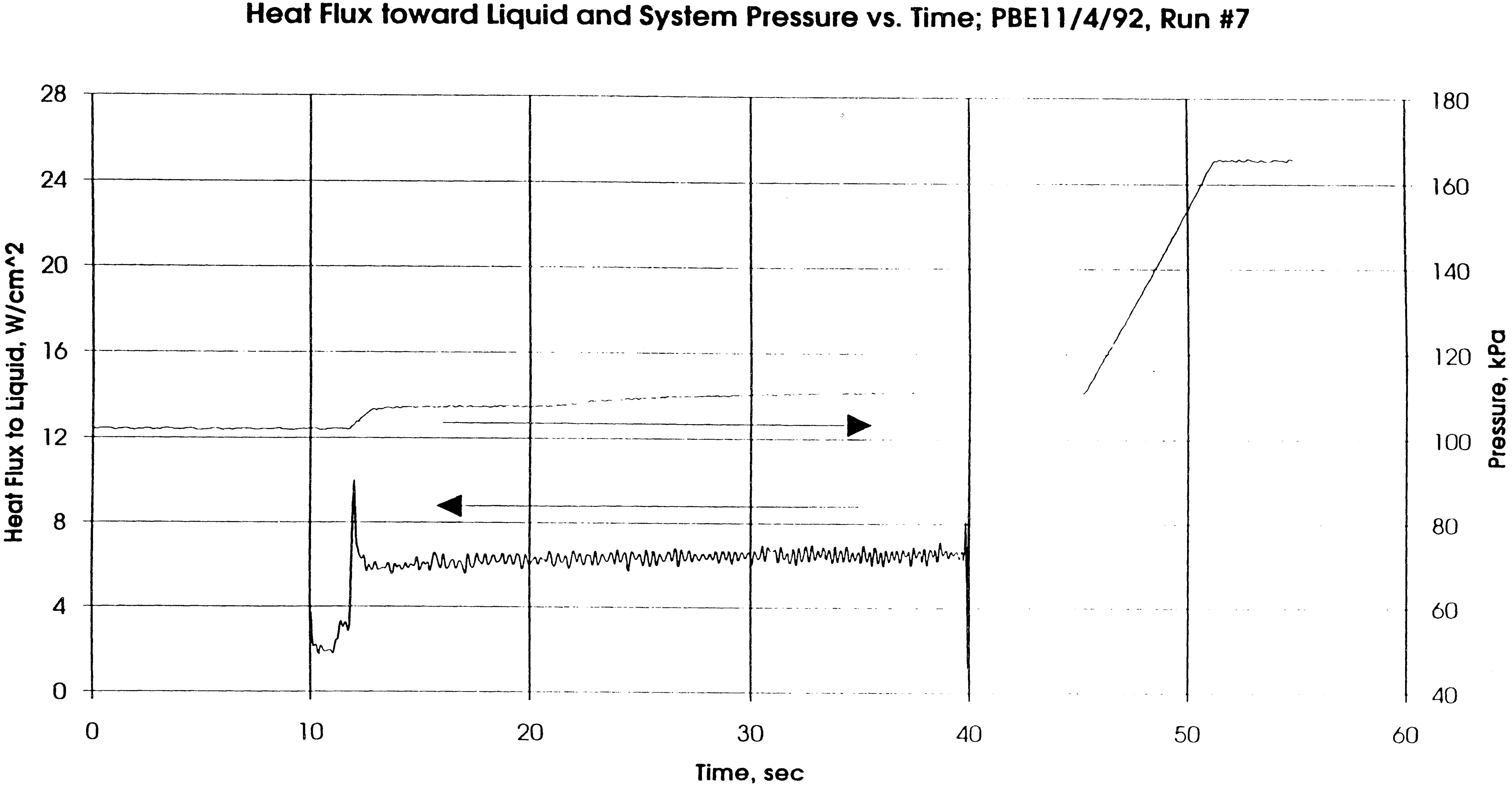

Figure E7c. System pressure and heat flux into fluid. Run No. 7.

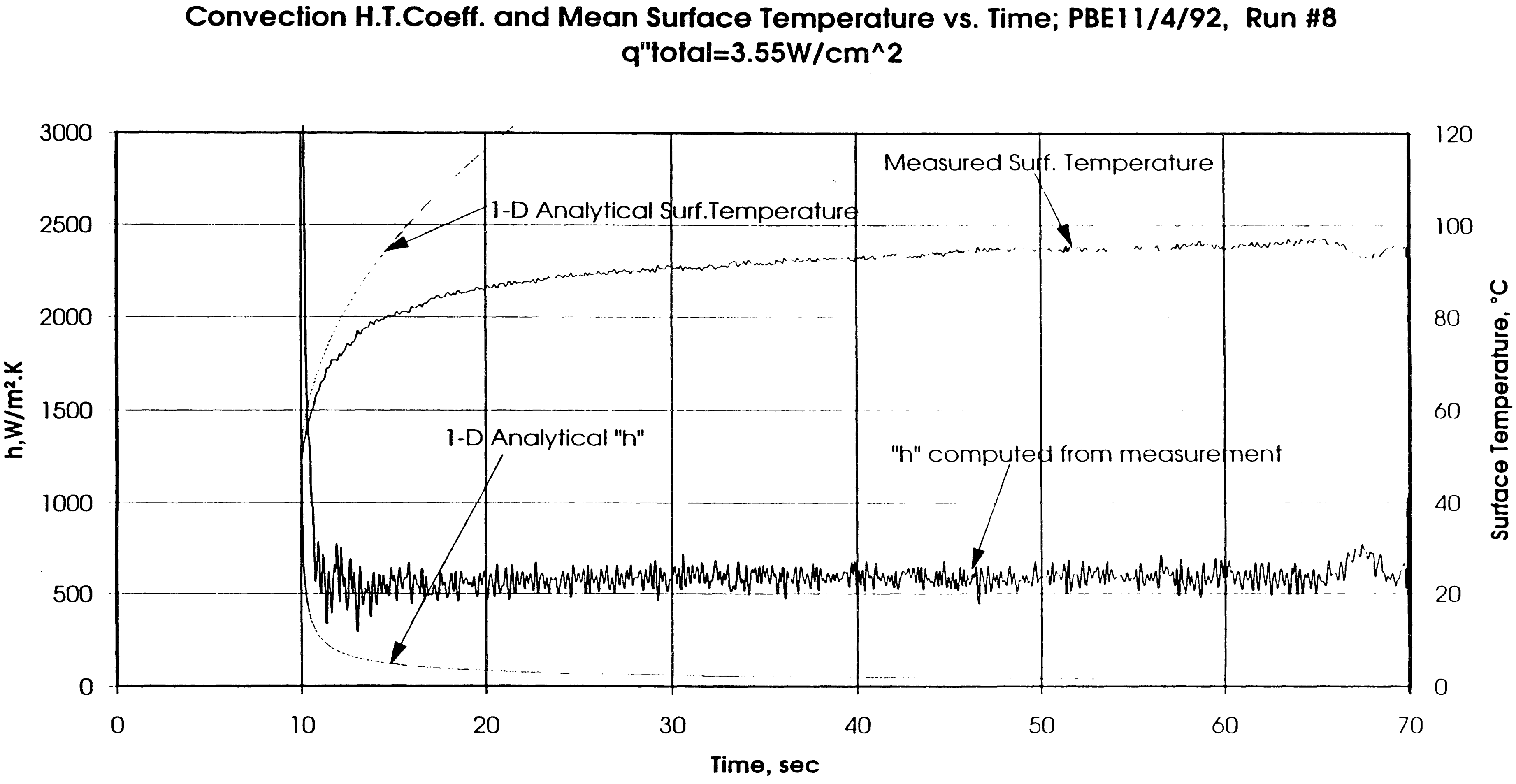

Figure E8a. Mean heater surface temperature and derived heat transfer coefficient. Run No. 8.

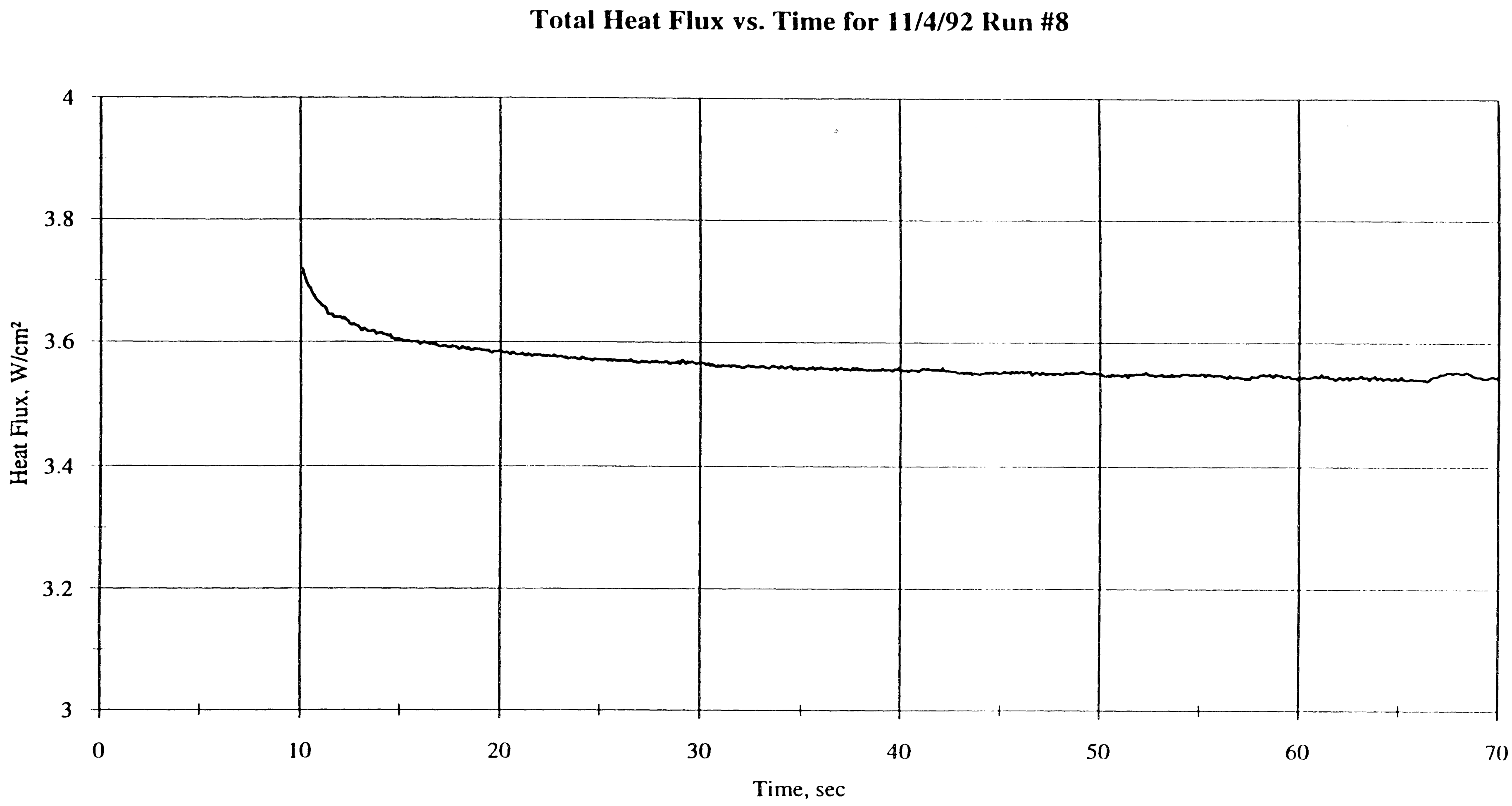

Figure E8b. Heat flux input. Run No. 8.

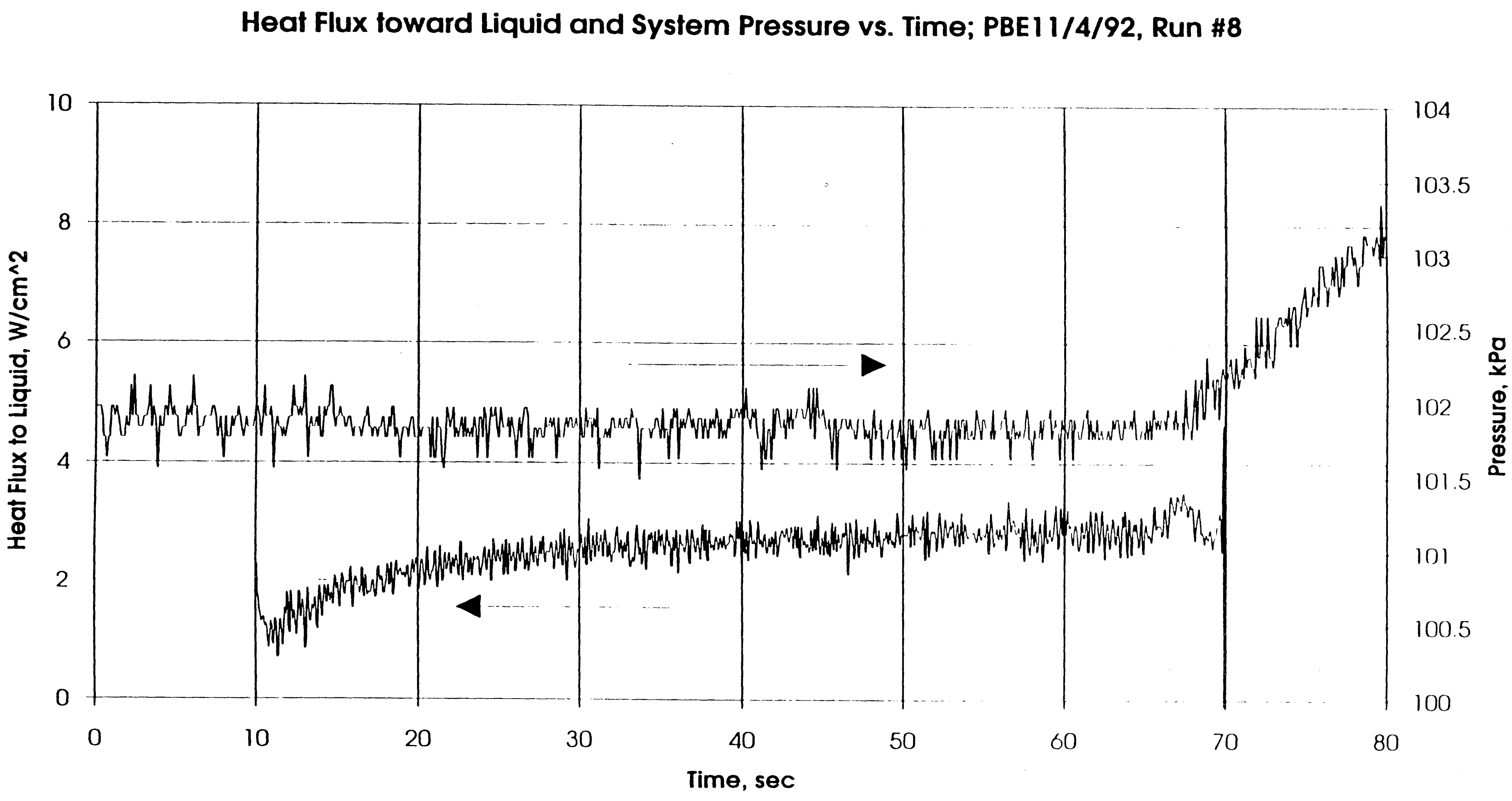

Figure E8c. System pressure and heat flux into fluid. Run No. 8.

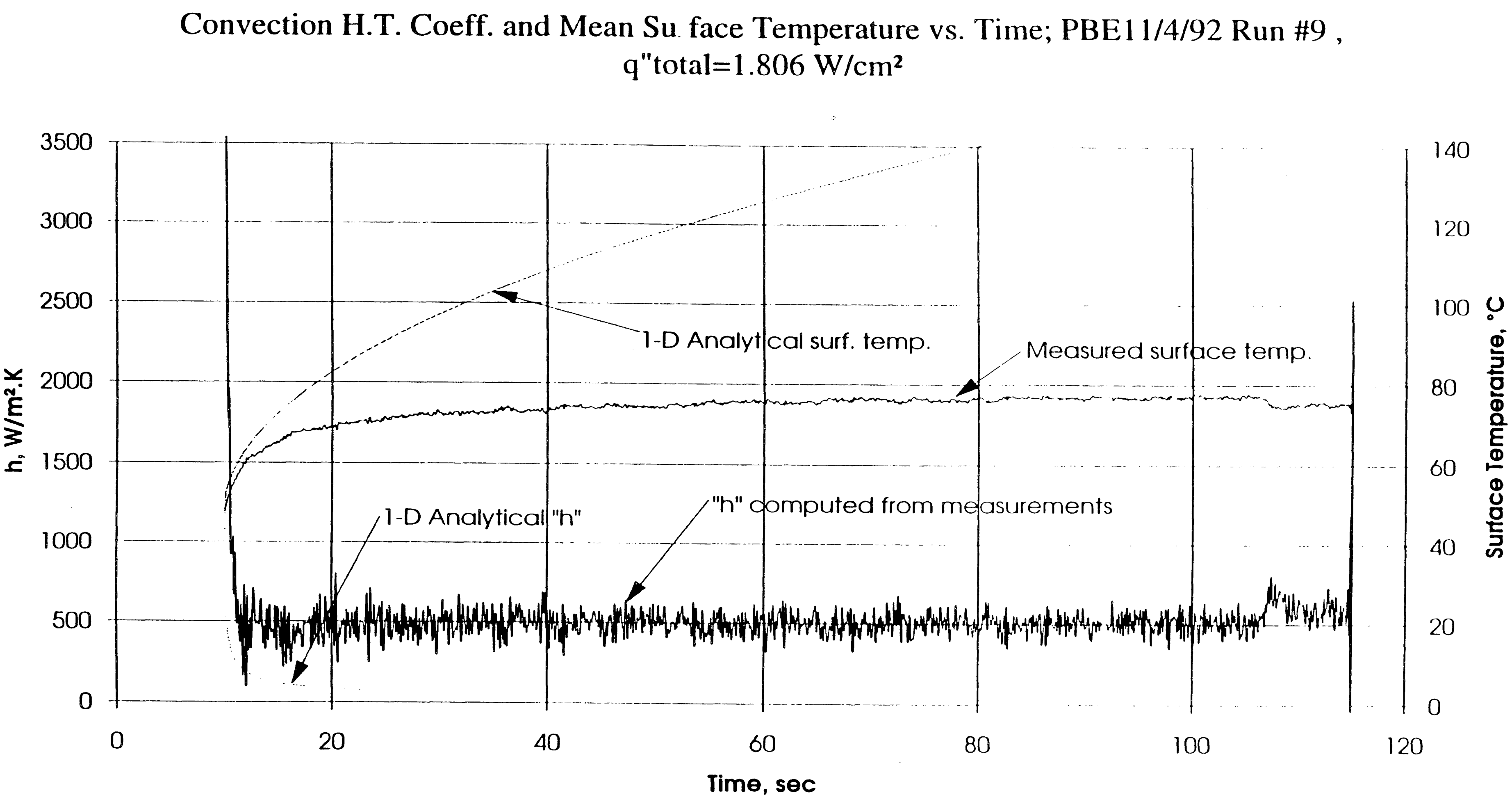
Convection H.T. Coeff. and Mean Su face Temperature vs. Time; PBE11/4/92 Run #9 , q"total=1.806 W/cm²

Figure E9a. Mean heater surface temperature and derived heat transfer coefficient. Run No. 9.

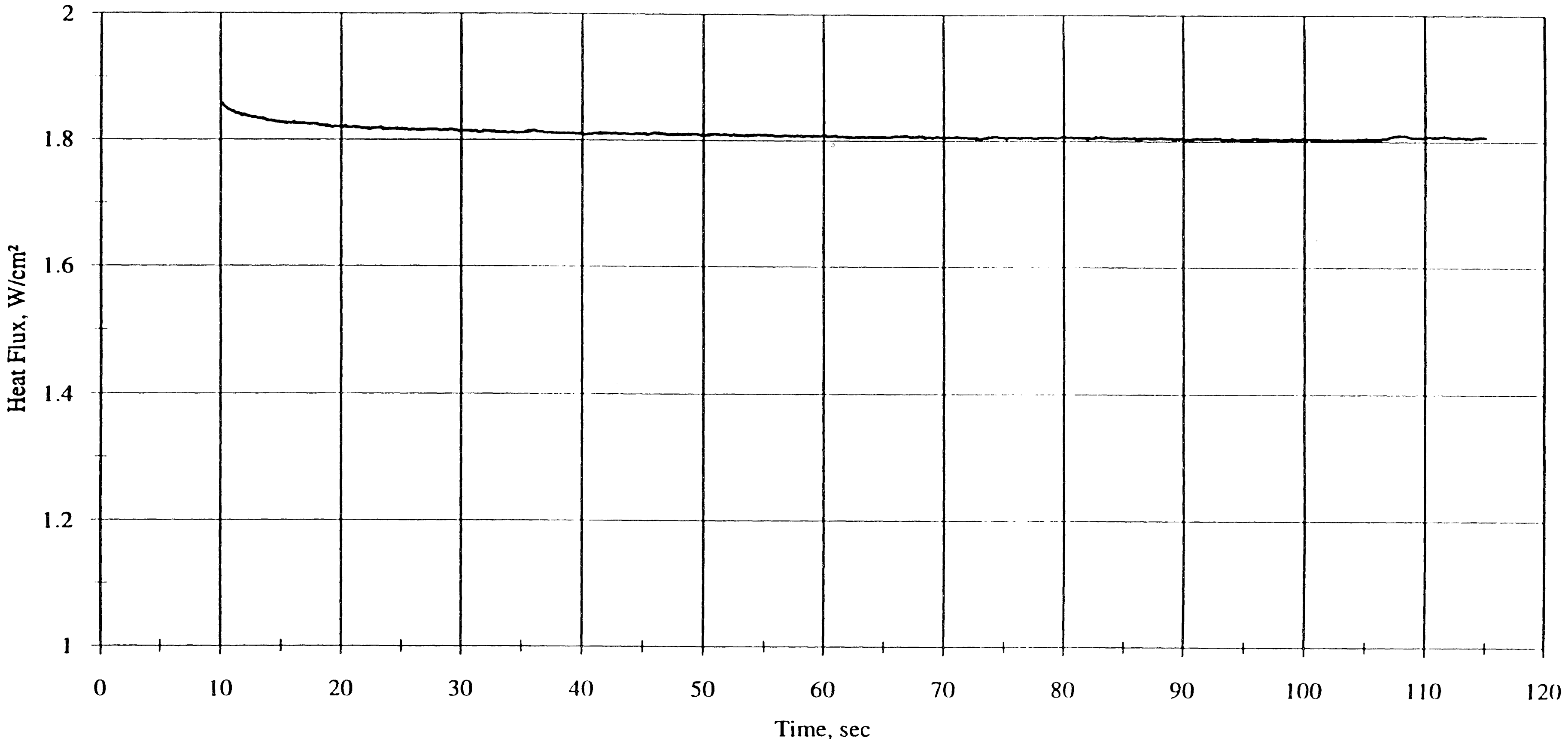

Total Heat Flux vs. Time for 11/4/92 Run #9

Figure E9b. Heat flux input. Run No. 9.

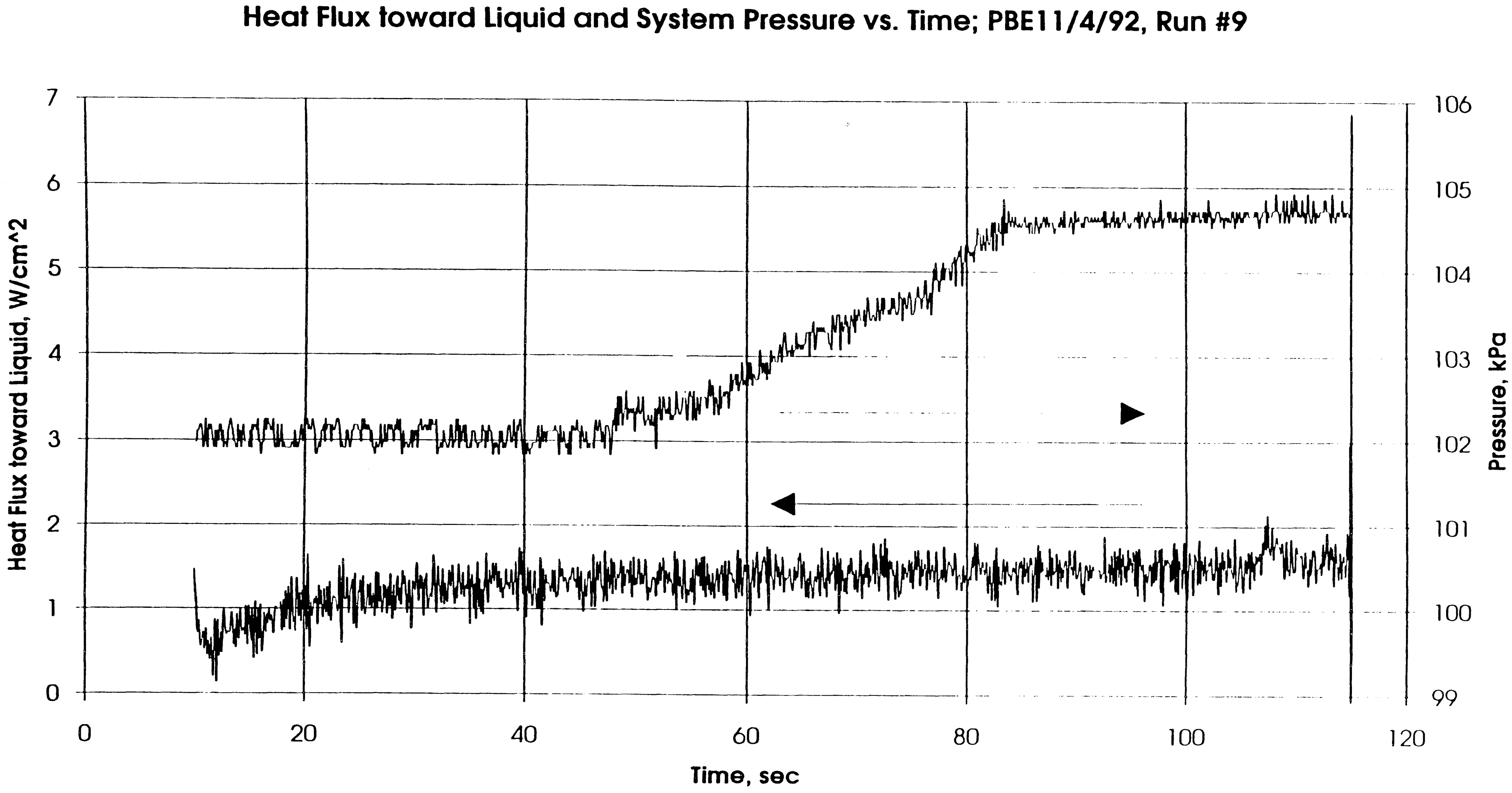

Figure E9c. System pressure and heat flux into fluid. Run No. 9.

Appendix F. Plots of results of Post-Flight test conducted for PBE-IA at a/g = -1 on 12/22/92.

Convection H.T. Coeff. and Mean Surface Temperature vs. Time
for PBE12/22/92 Run #1 , q"total=6.2 W/cm²

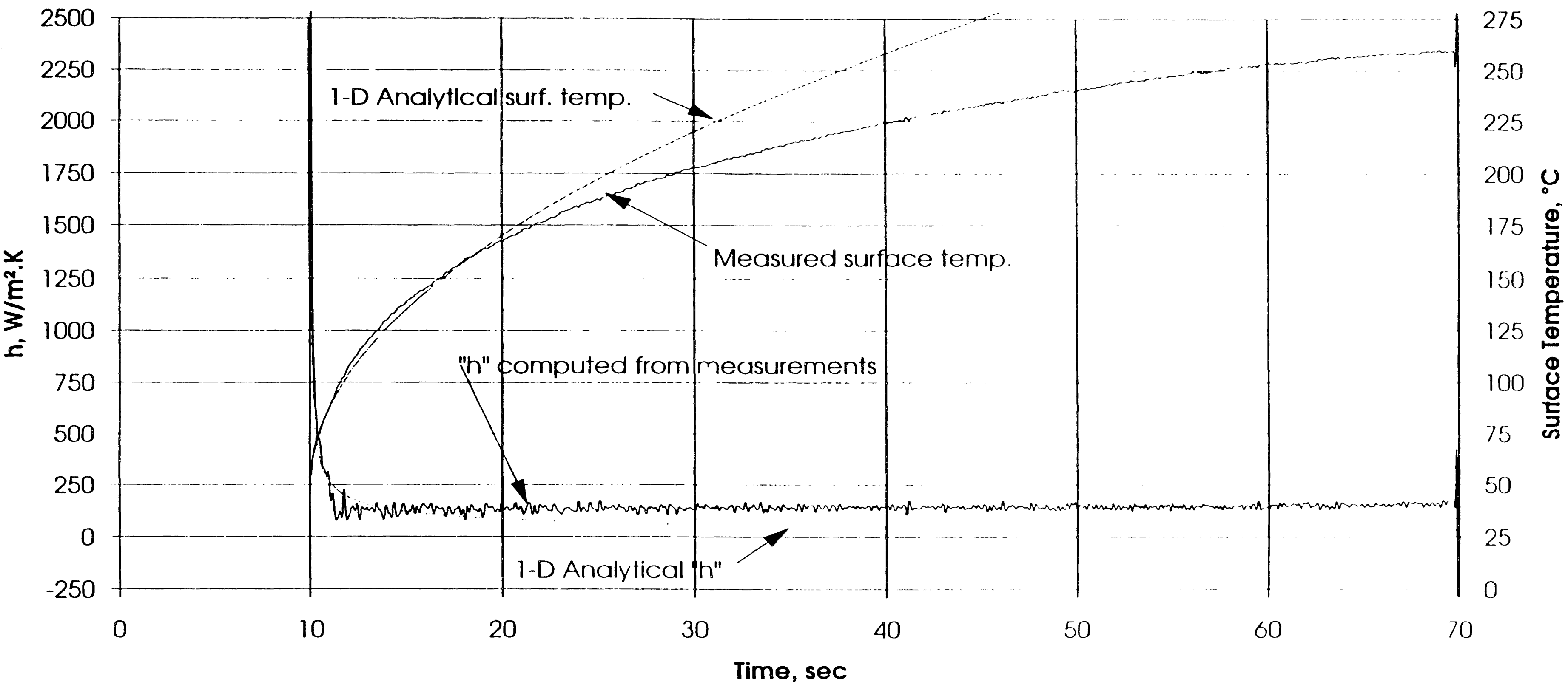

Figure F1a. Mean heater surface temperature and derived heat transfer coefficient. Run No. 1

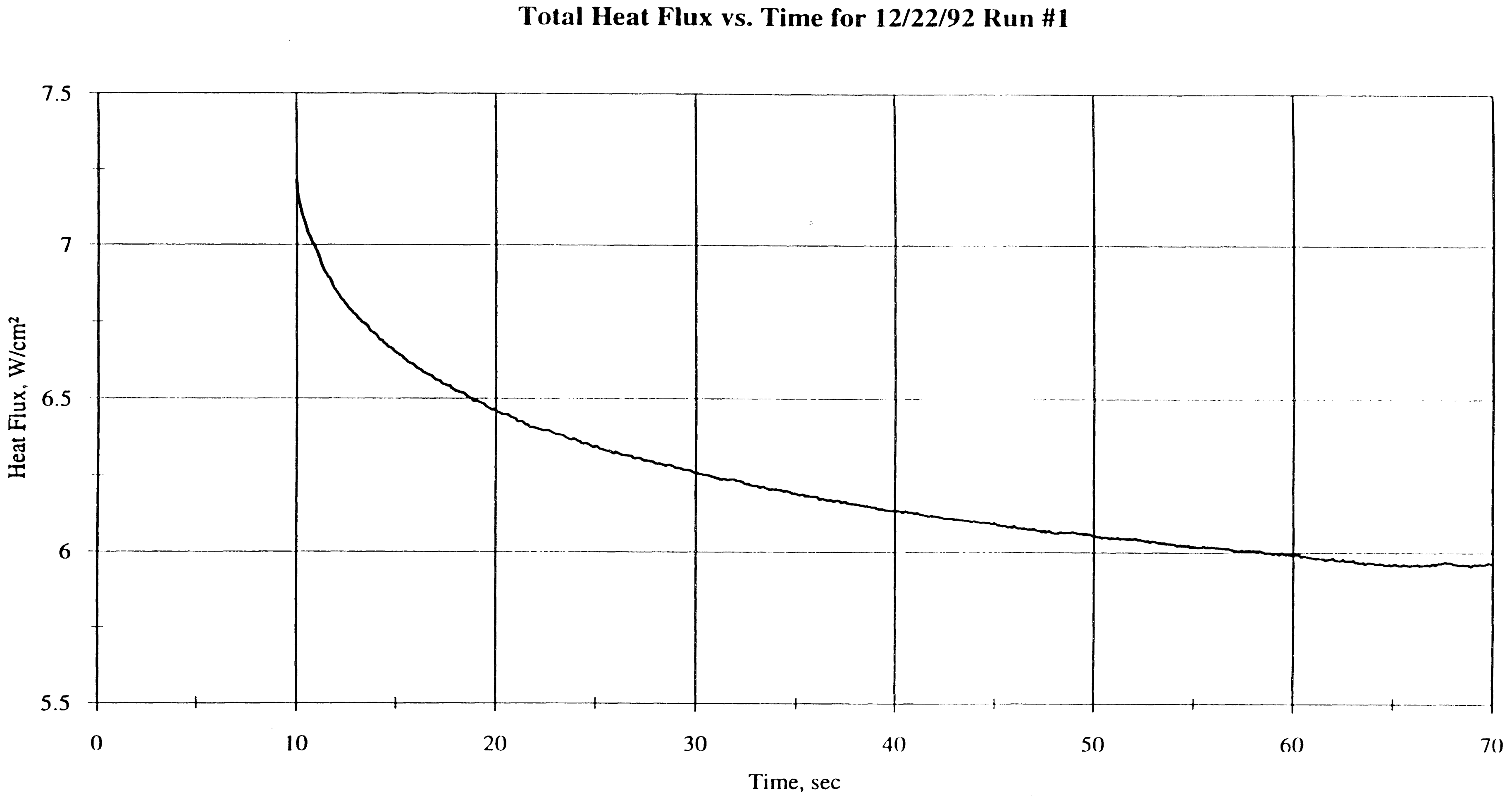

Figure F1b. Heat flux input. Run No. 1

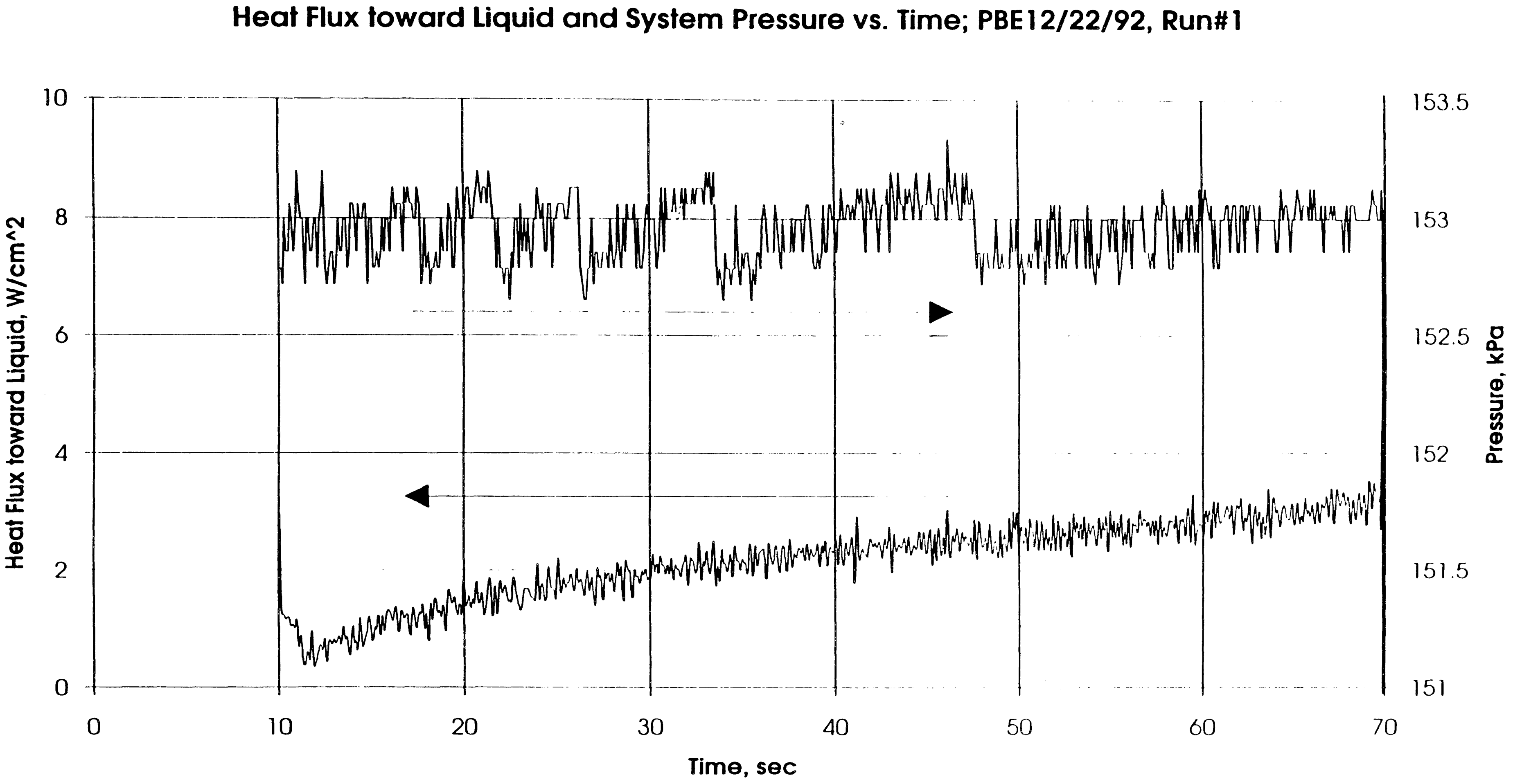

Figure F1c. System pressure and heat flux into fluid. Run No. 1.

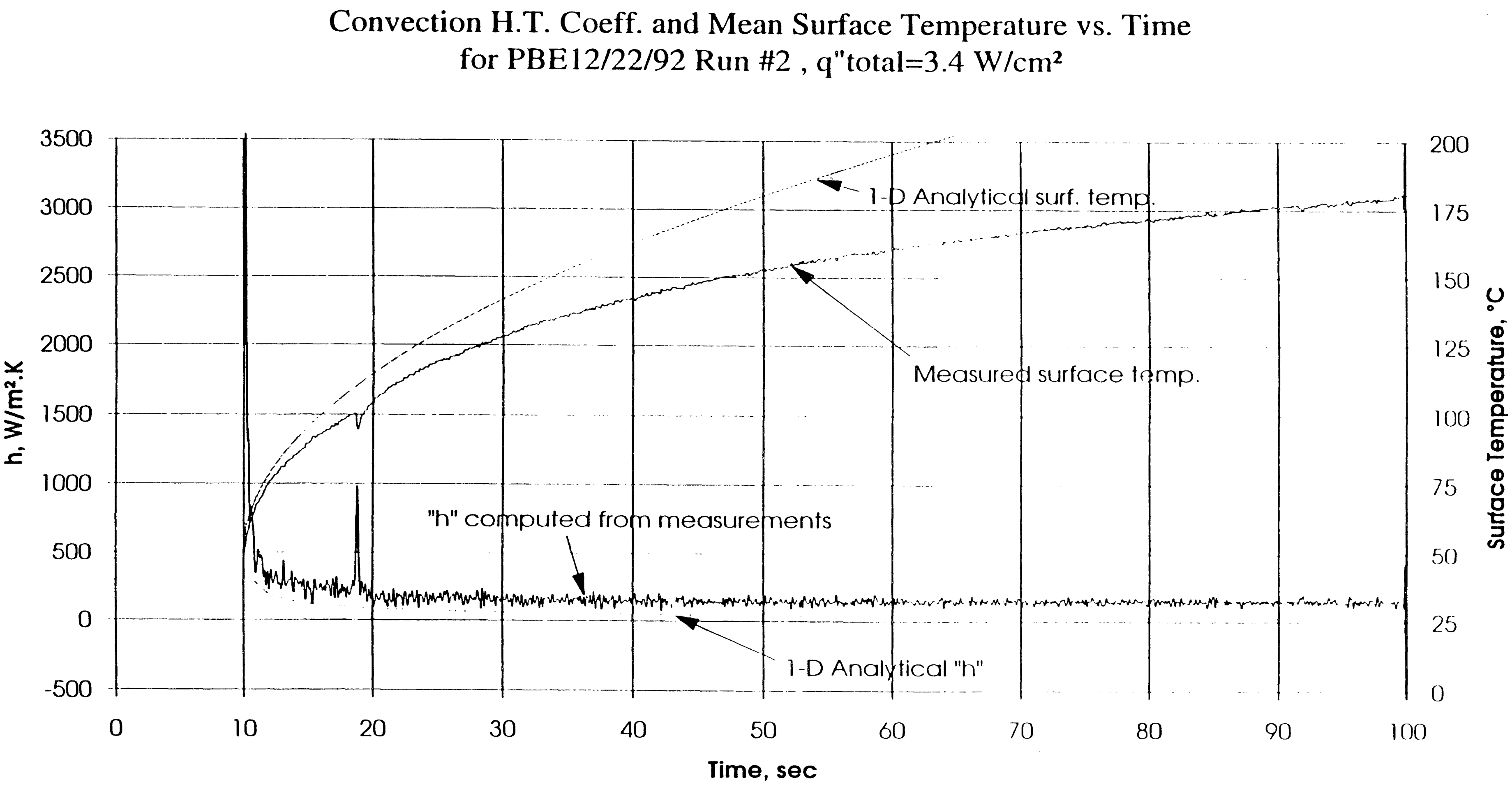

Figure F2a. Mean heater surface temperature and derived heat transfer coefficient. Run No. 2.

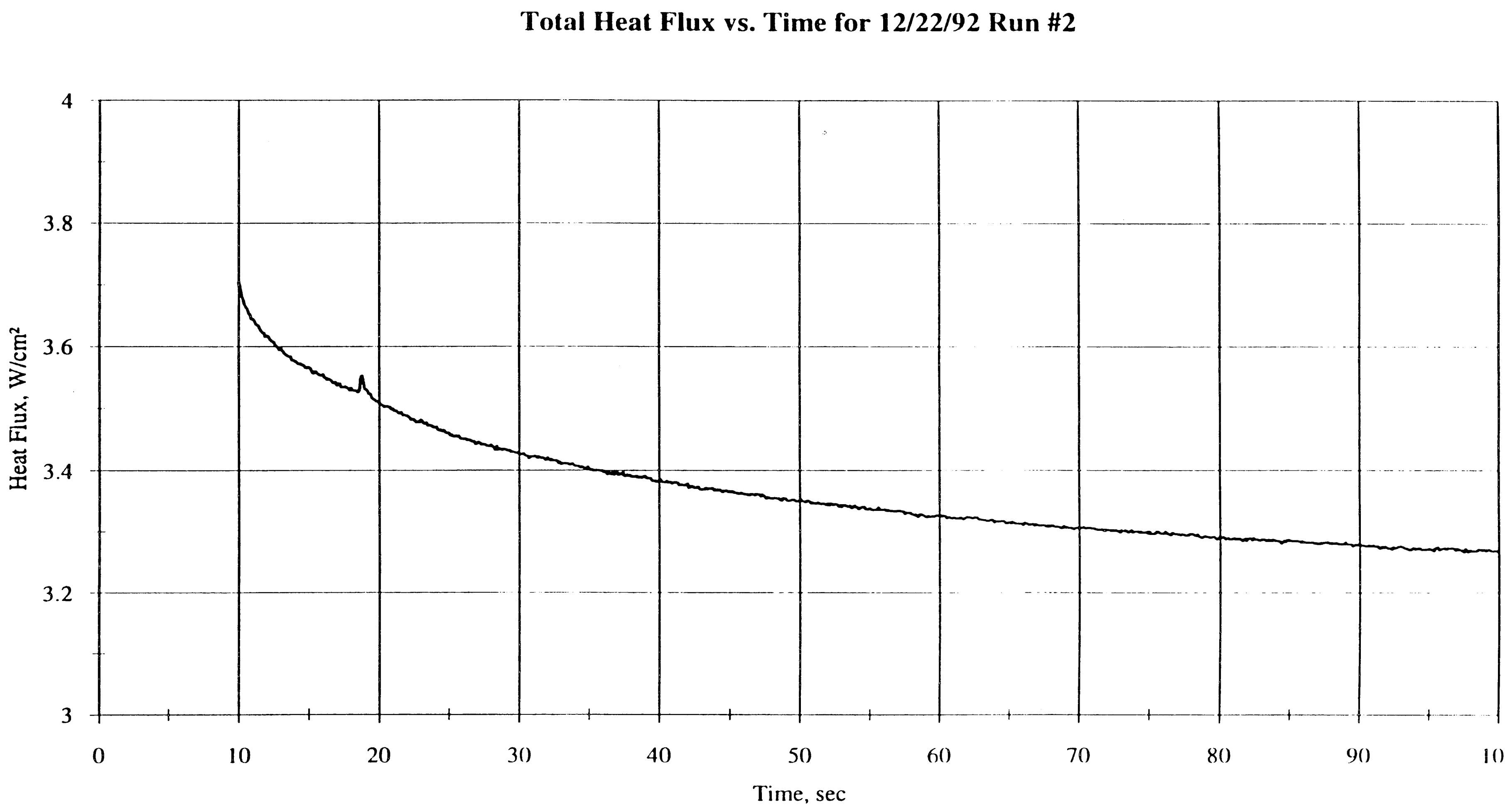

Total Heat Flux vs. Time for 12/22/92 Run #2

Figure F2b. Heat flux input. Run No. 2.

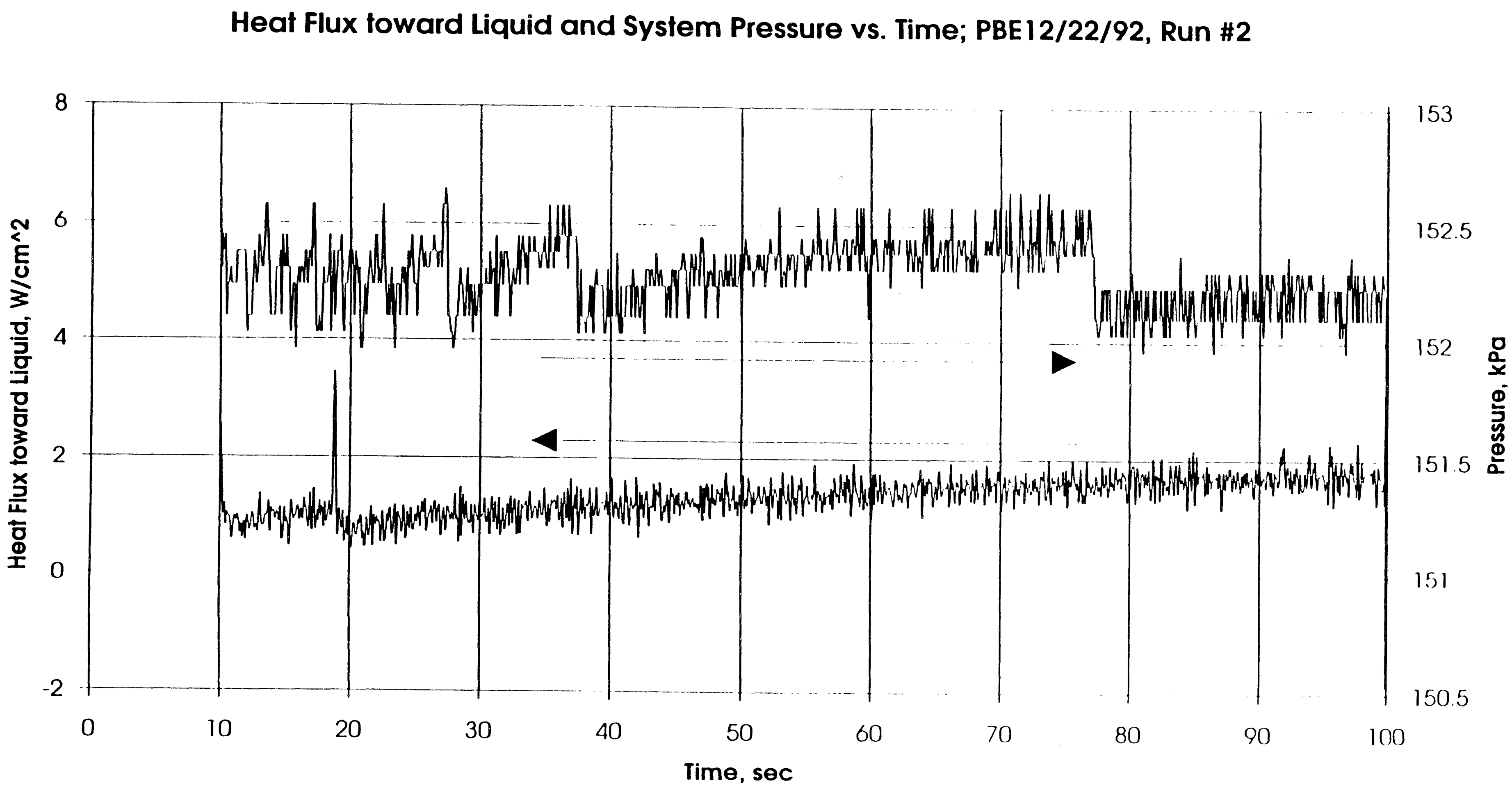

Figure F2c. System pressure and heat flux into fluid. Run No. 2.

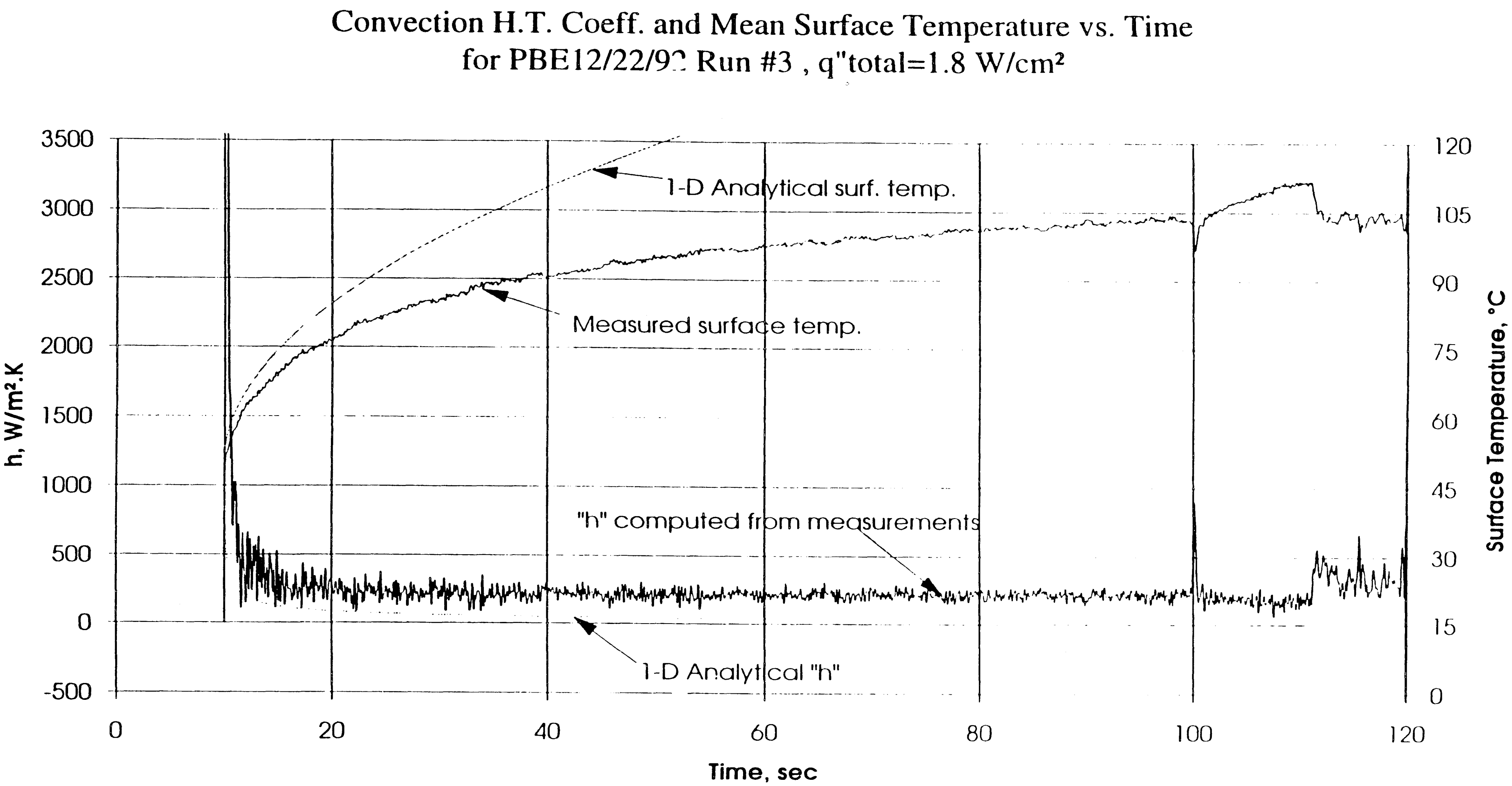

Figure F3a. Mean heater surface temperature and derived heat transfer coefficient. Run No. 3.

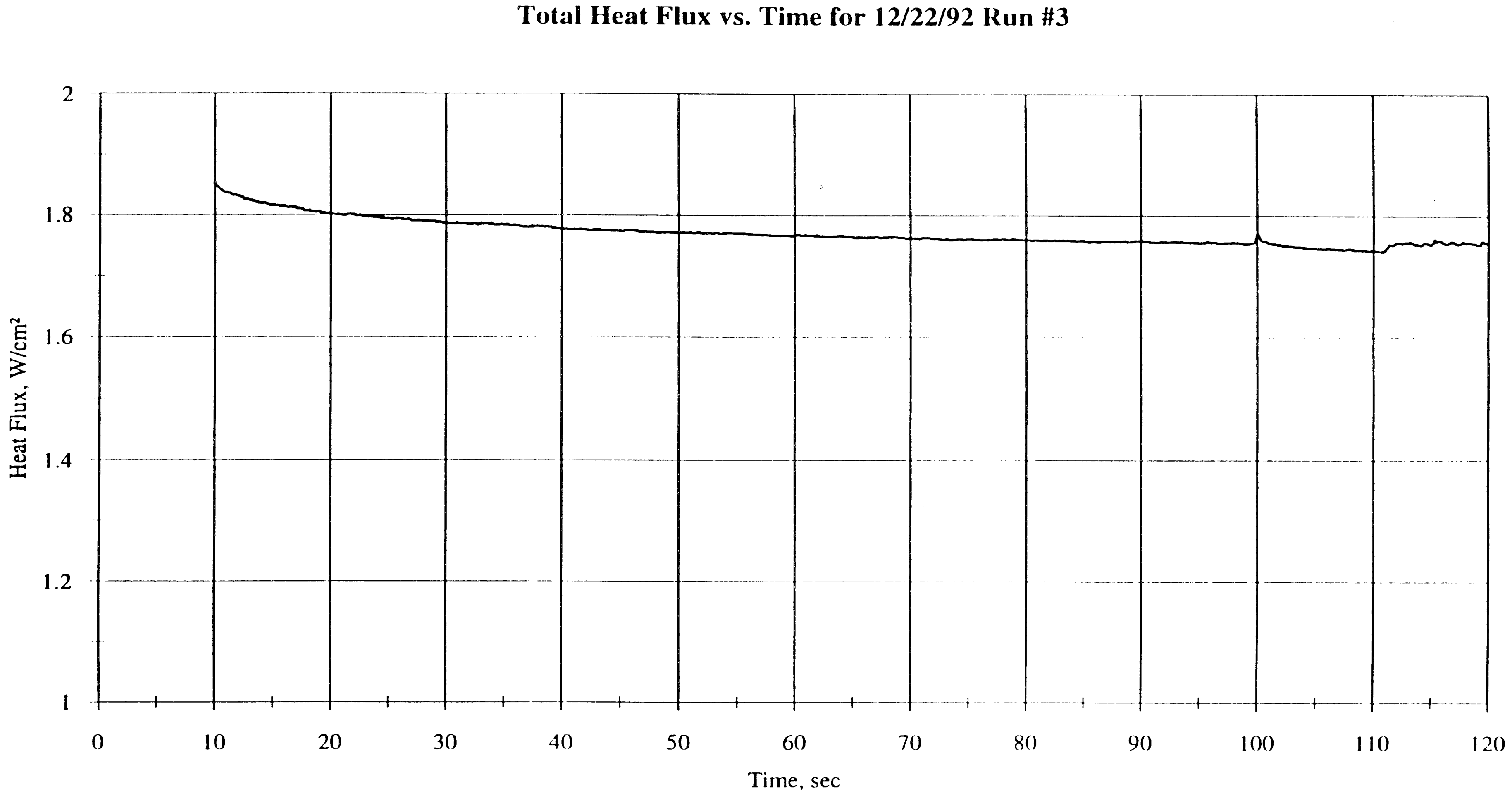

Figure F3b. Heat flux input. Run No. 3.

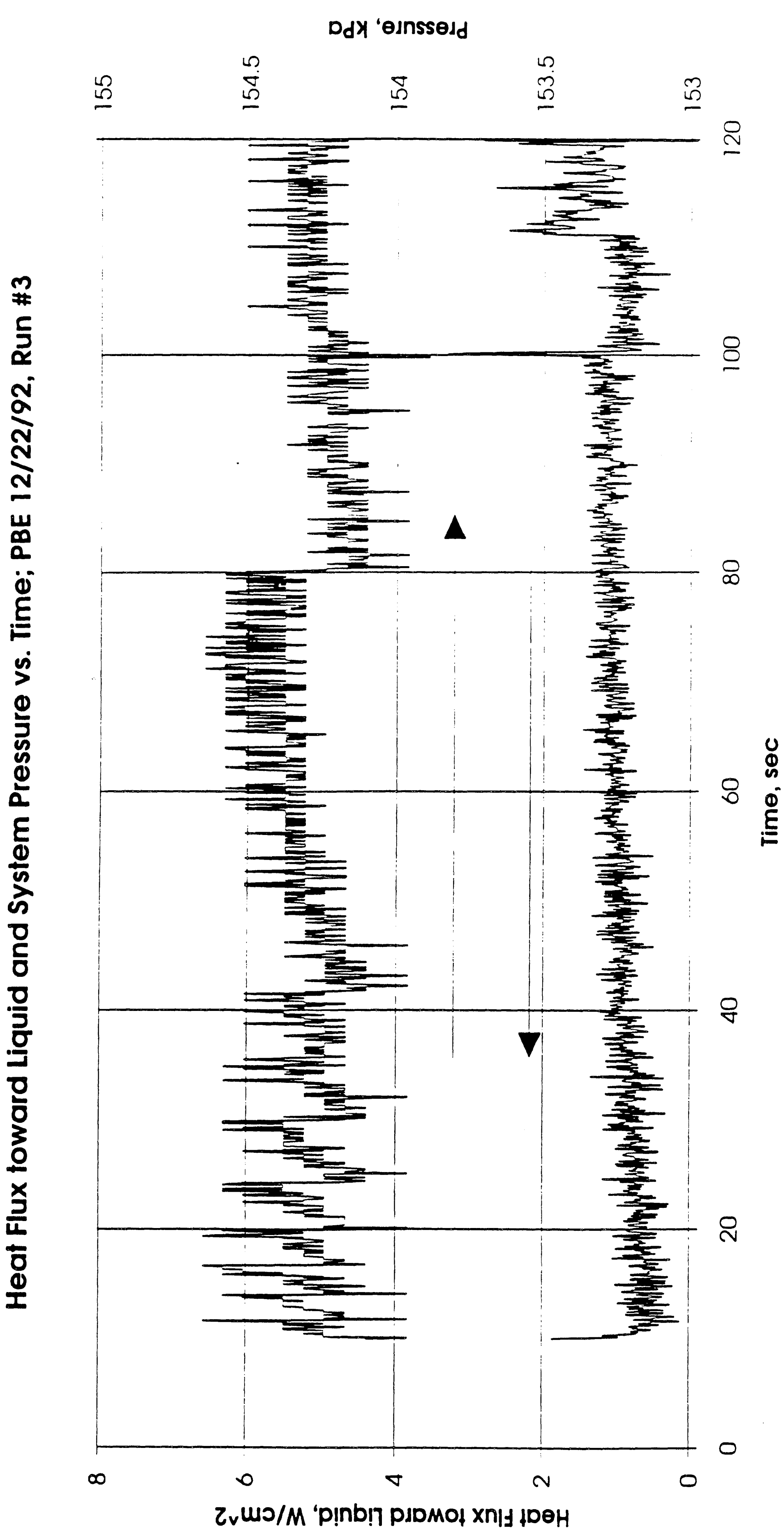

Figure F3c. System pressure and heat flux into fluid. Run No. 3.

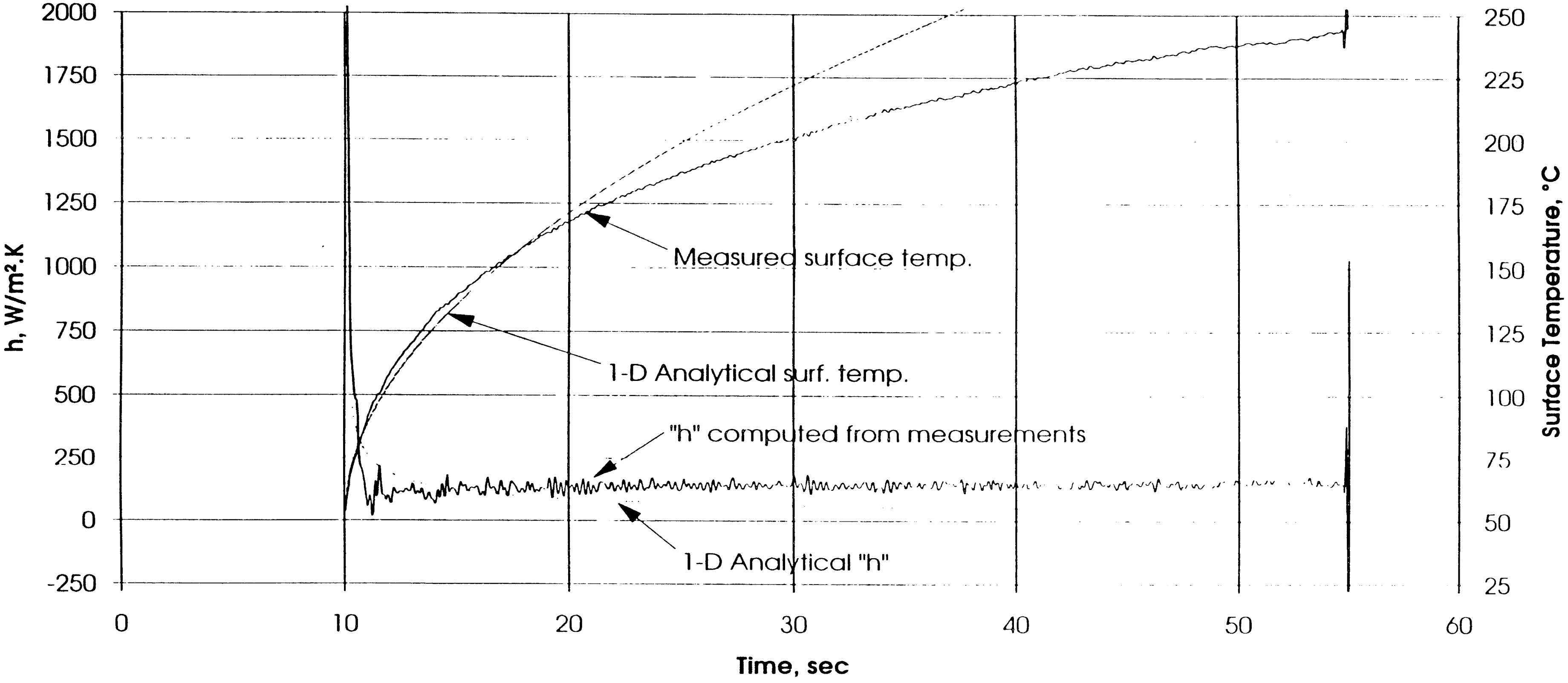

Convection H.T. Coeff. and Mean Surface Temperature vs. Time
for PBE12/22/92 Run #4, q"total=6.3 W/cm²

Figure F4a. Mean heater surface temperature and derived heat transfer coefficient. Run No. 4.

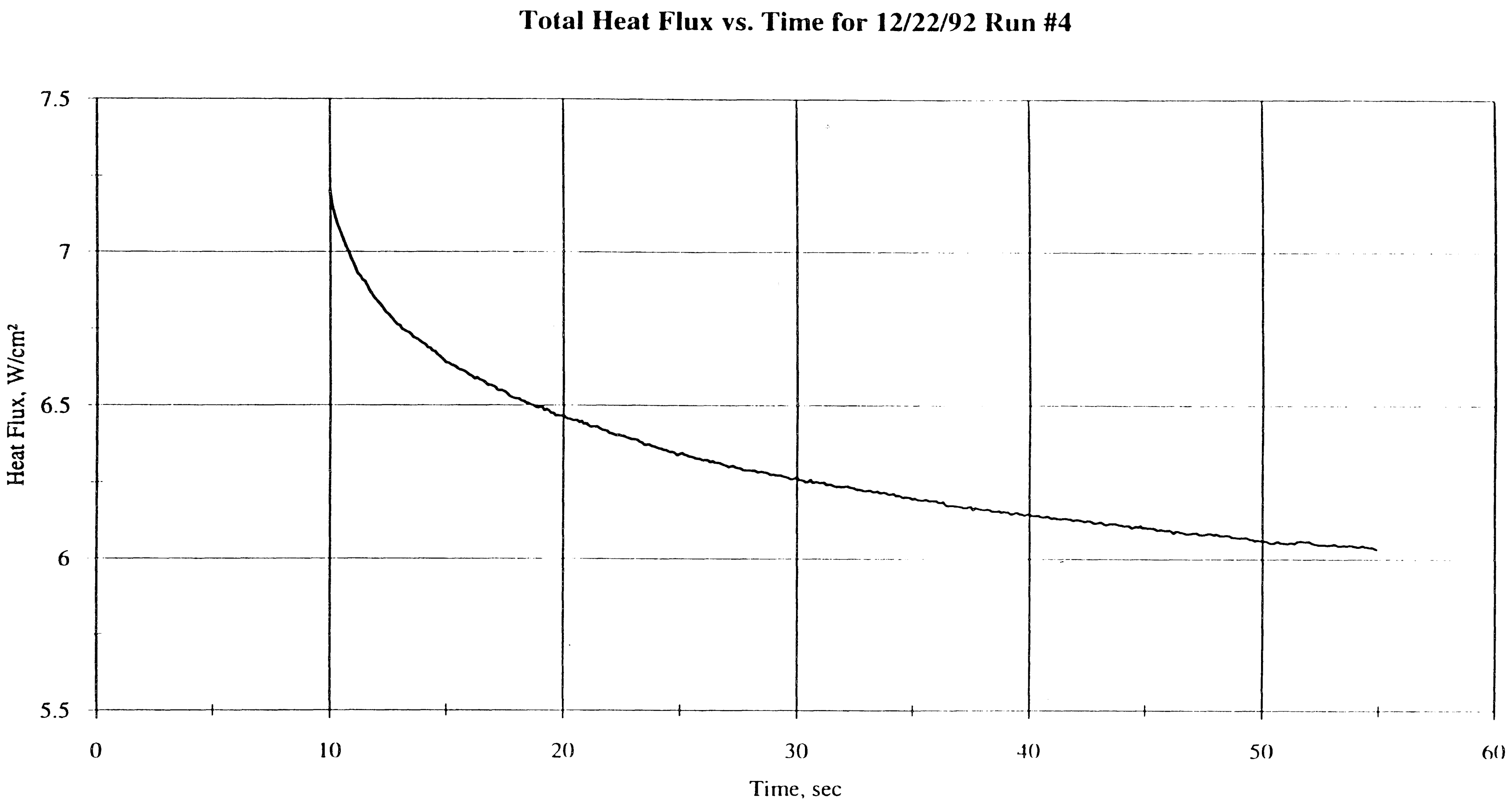

Figure F4b. Heat flux input. Run No. 4.

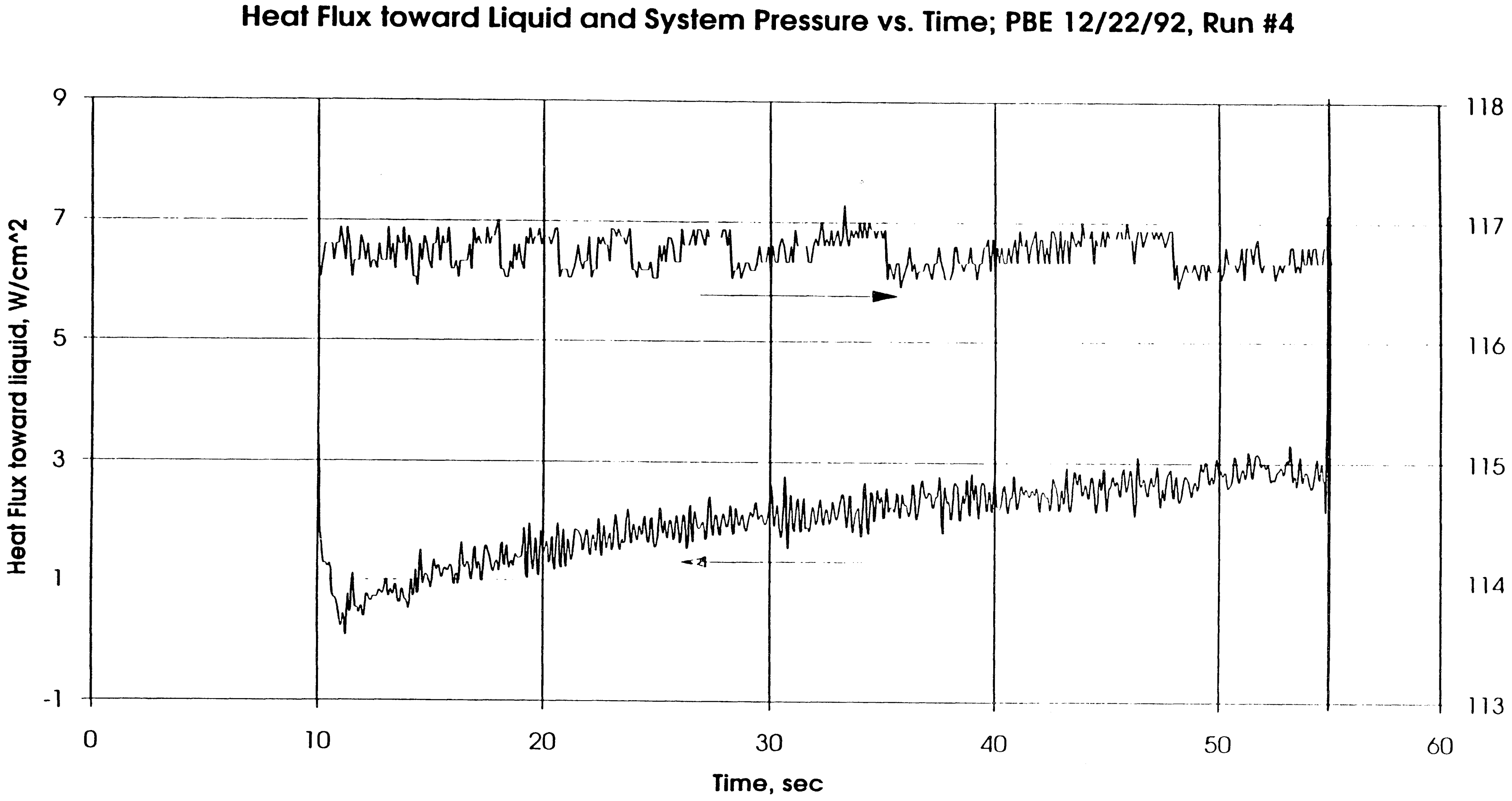

Figure F4c. System pressure and heat flux into fluid. Run No. 4.

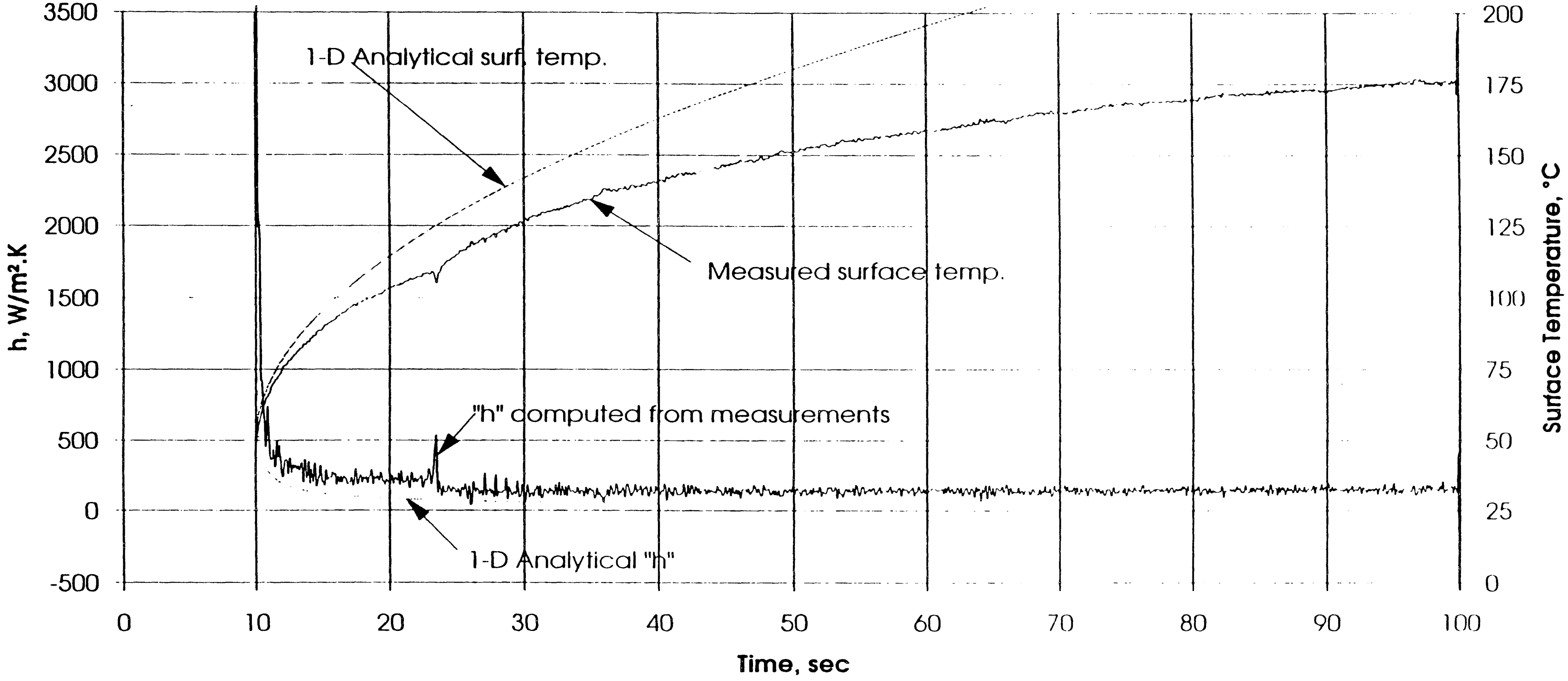

Convection H.T. Coeff. and Mean Surface Temperature vs. Time for PBE 12/22/92 Run #5 , q"total=3.4 W/cm²

Figure F5a. **Mean heater surface temperature and derived heat transfer coefficient. Run No. 5.**

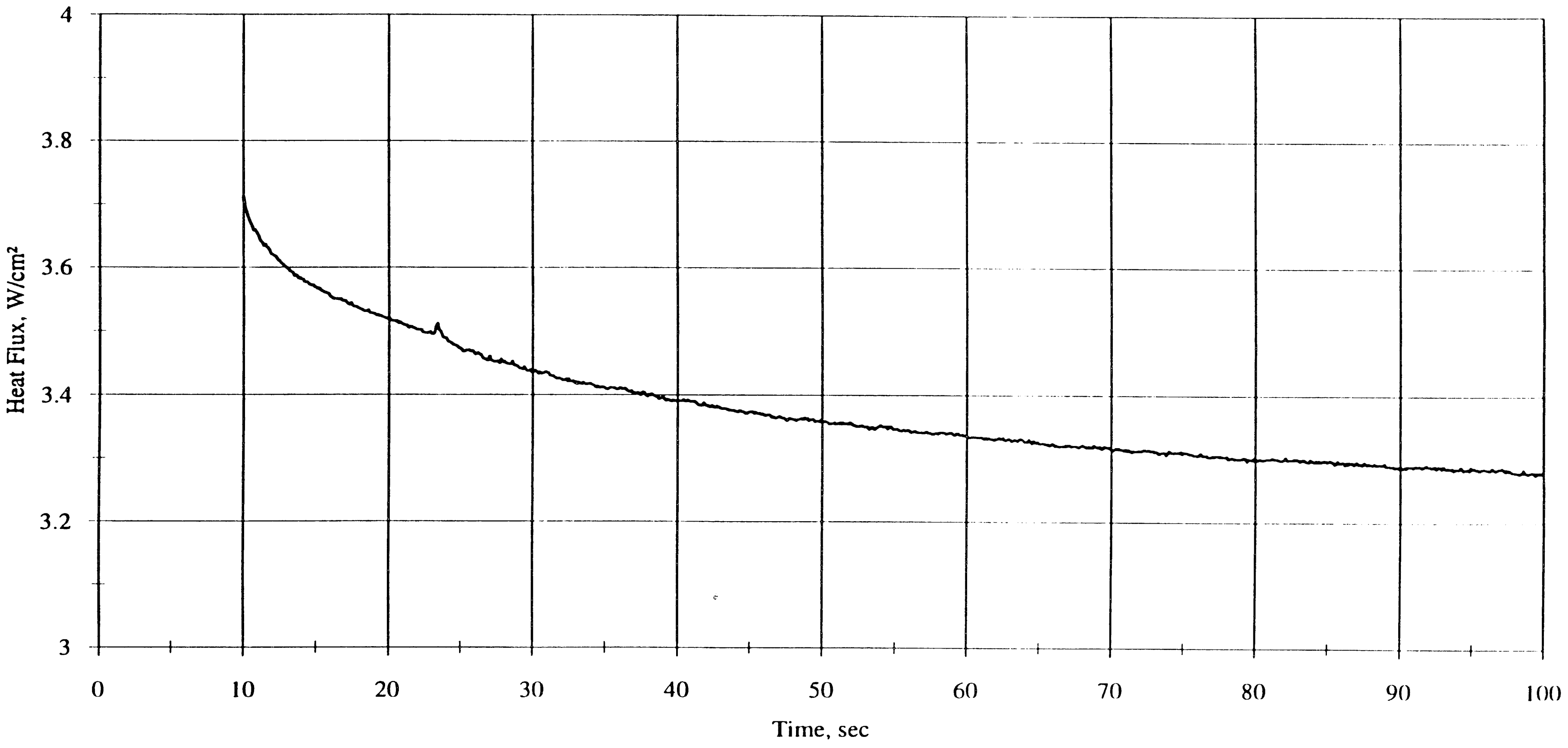
Total Heat Flux vs. Time for 12/22/92 Run #5

Figure F5b. Heat flux input. Run No. 5.

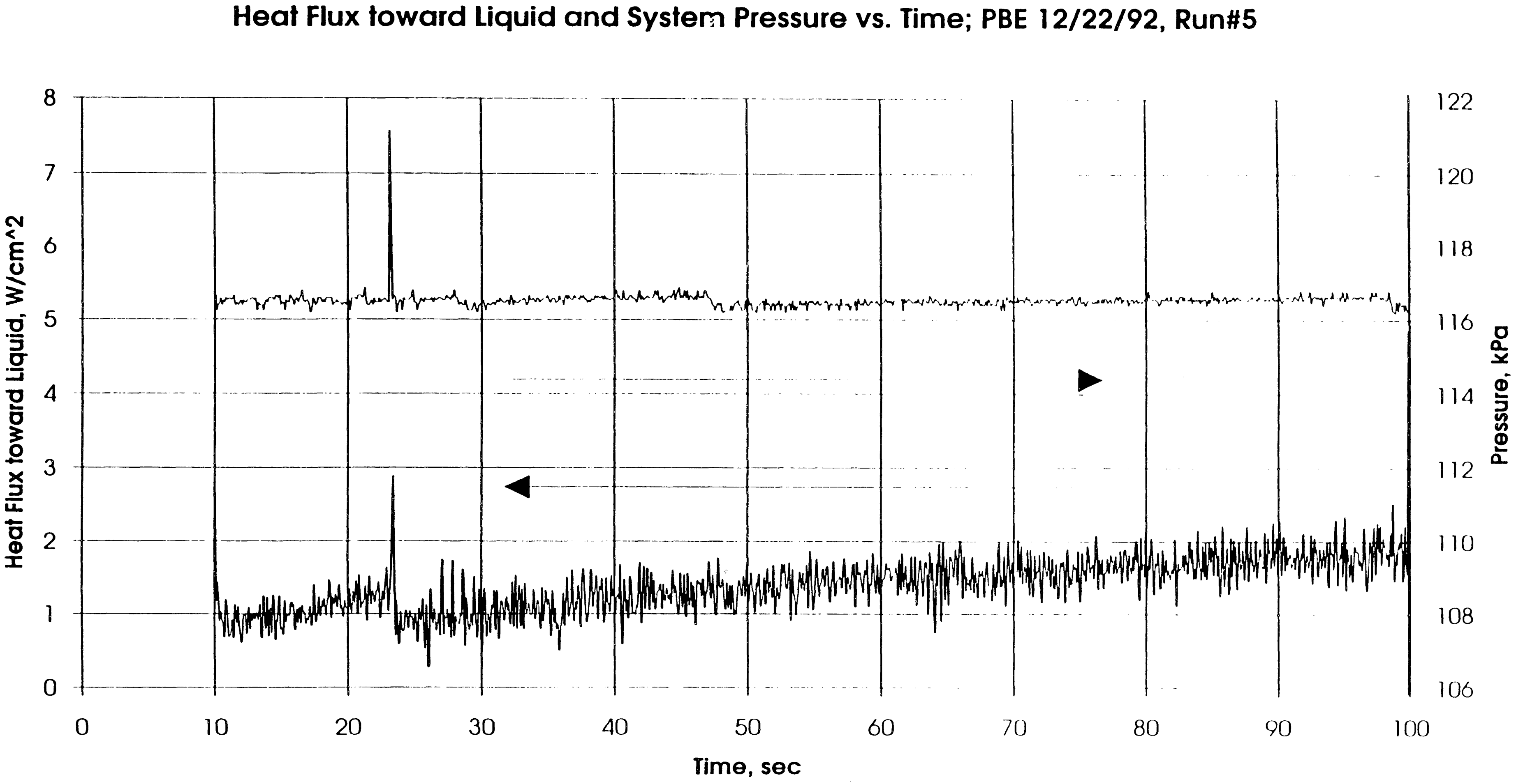

Figure F5c. System pressure and heat flux into fluid. Run No. 5.

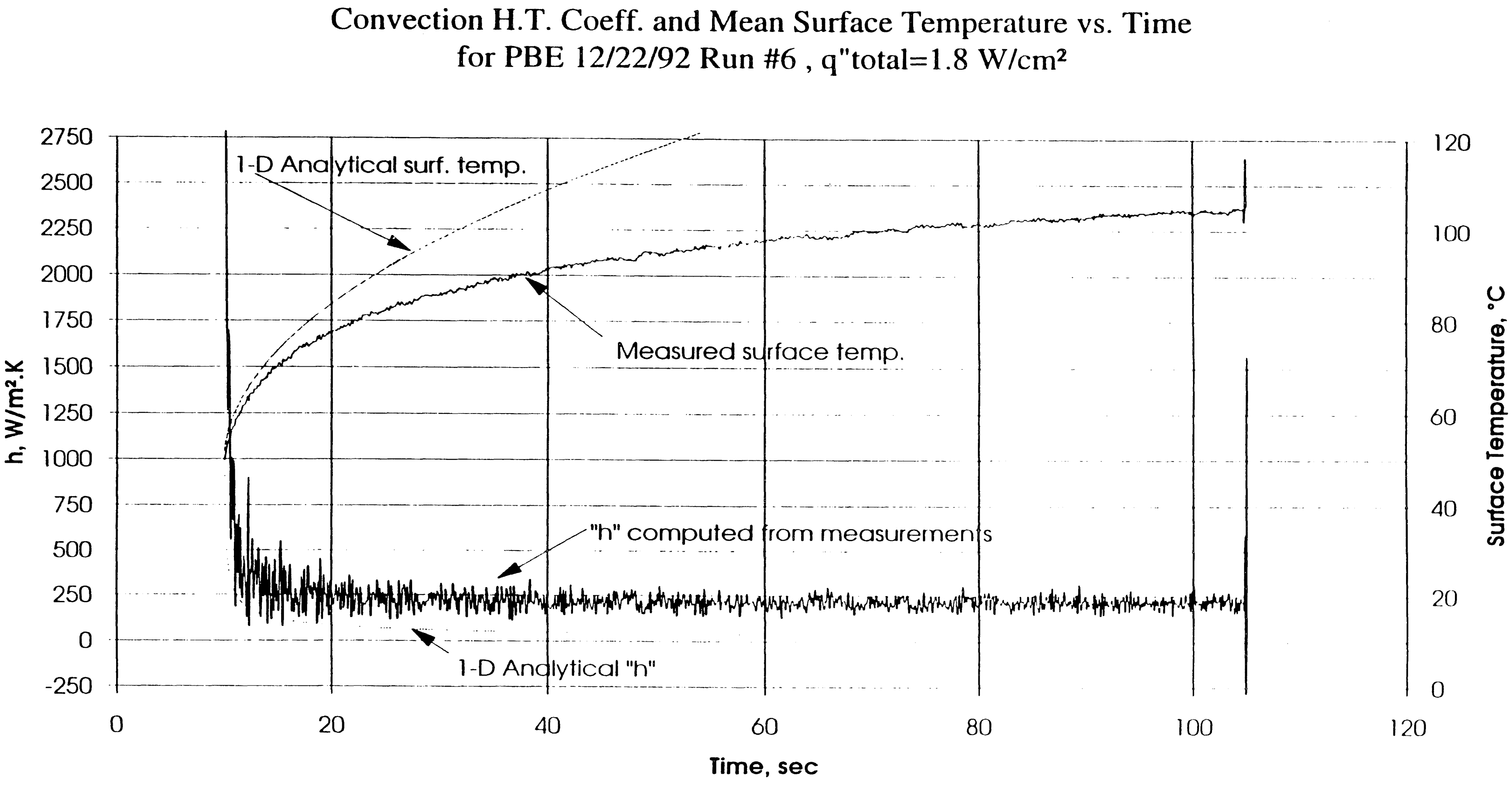

Figure F6a. Mean heater surface temperature and derived heat transfer coefficient. Run No. 6.

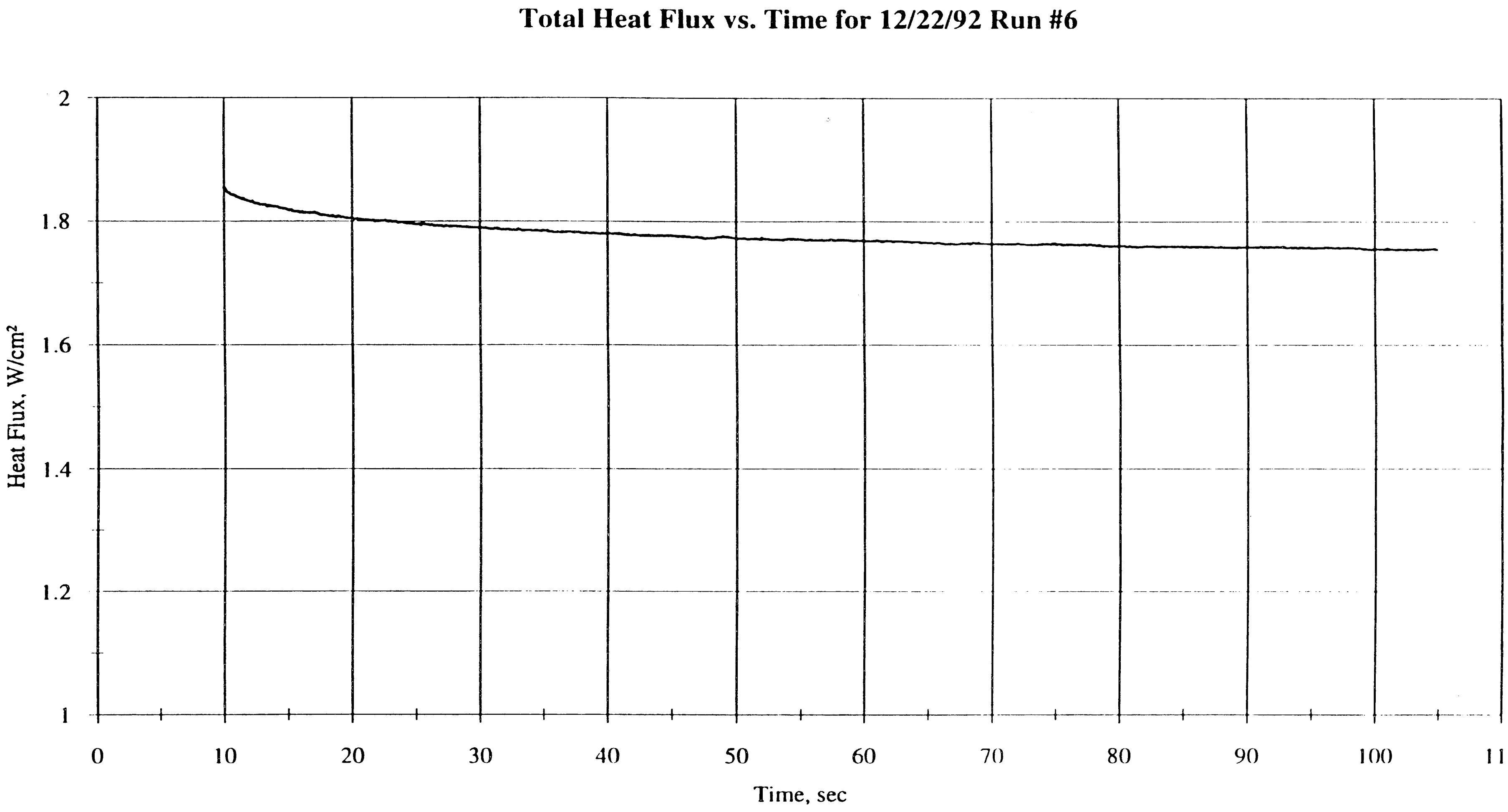

Figure F6b. Heat flux input. Run No. 6.

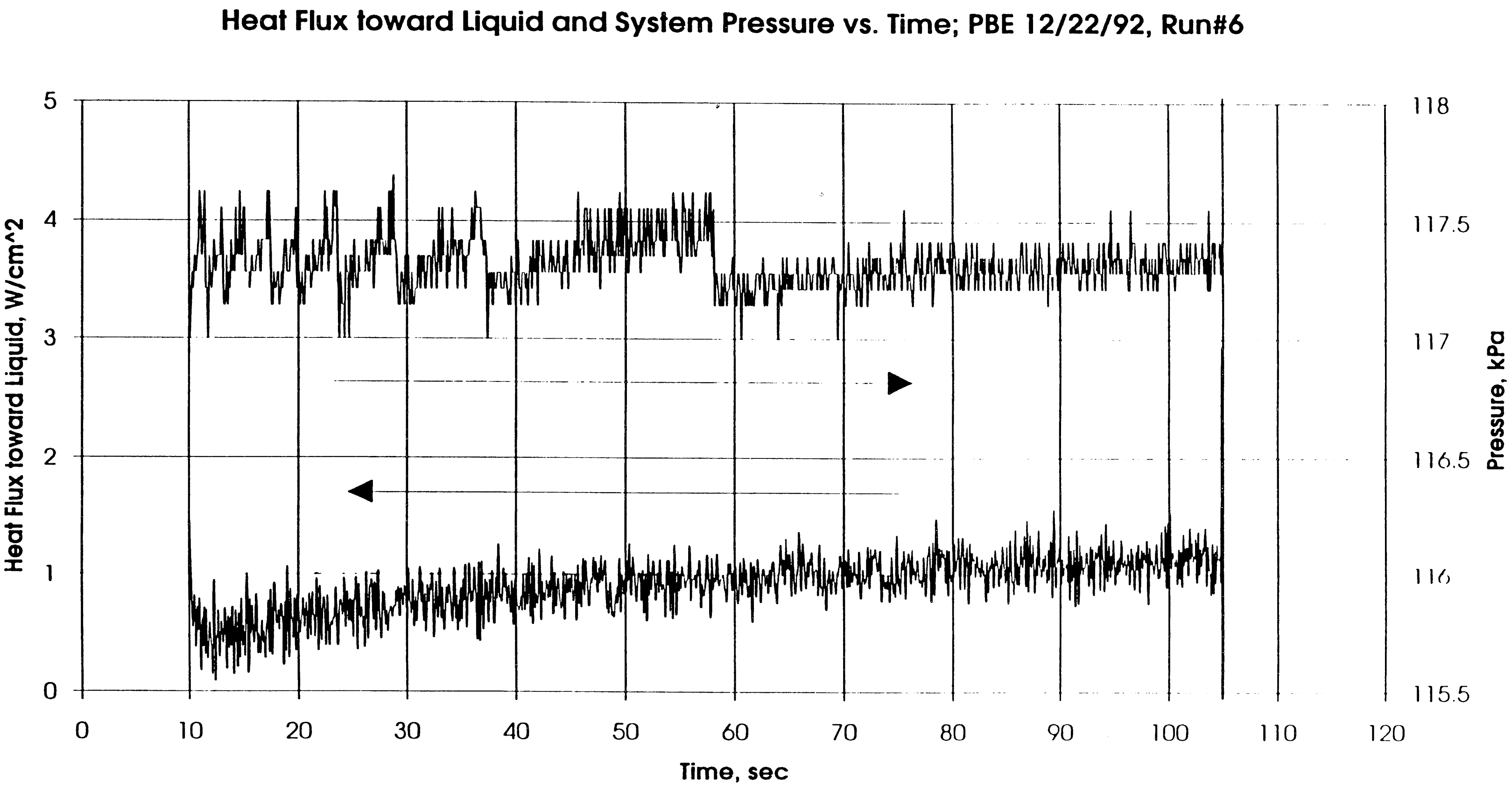

Figure F6c. System pressure and heat flux into fluid. Run No. 6.

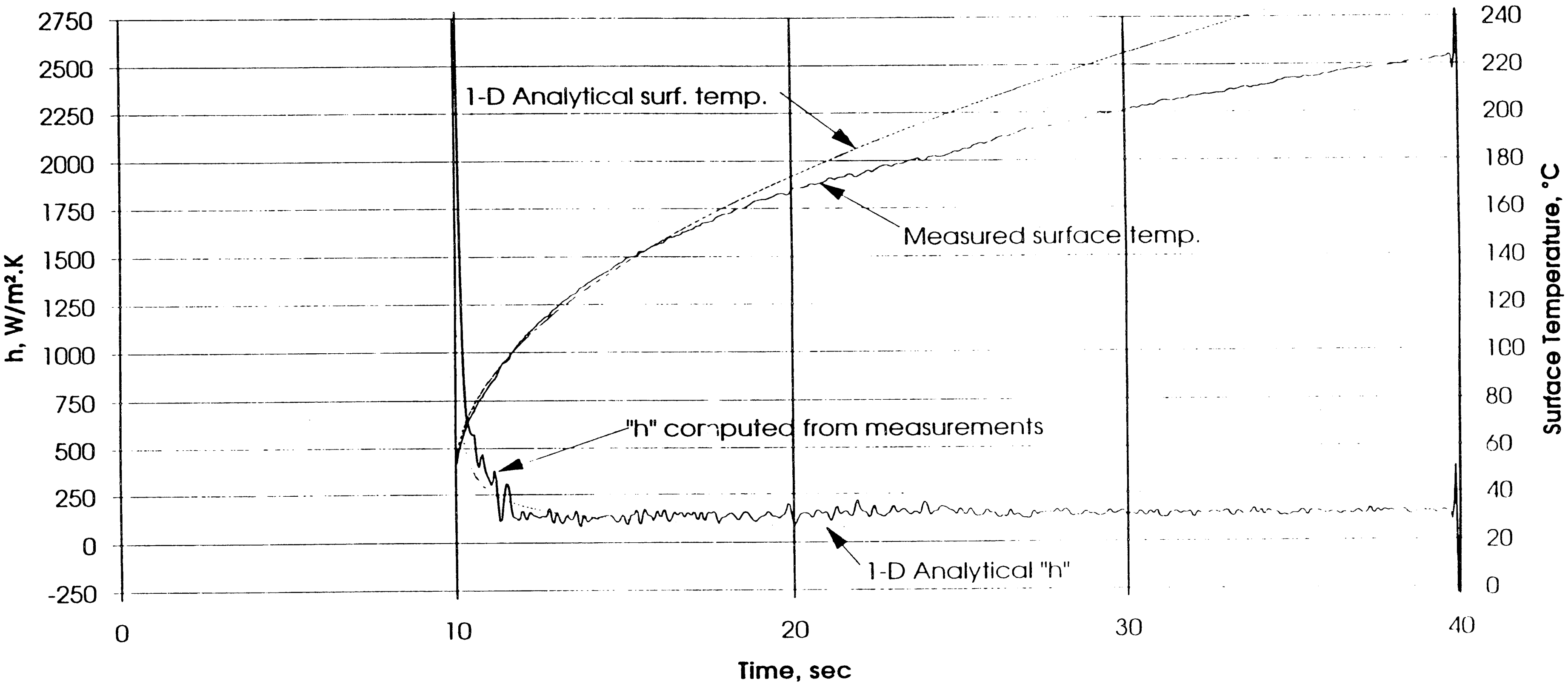

Convection H.T. Coeff. and Mean Surface Temperature vs. Time for PBE 12/22/92 Run #7, q"total=6.4 W/cm²

Figure F7a. Mean heater surface temperature and derived heat transfer coefficient. Run No. 7.

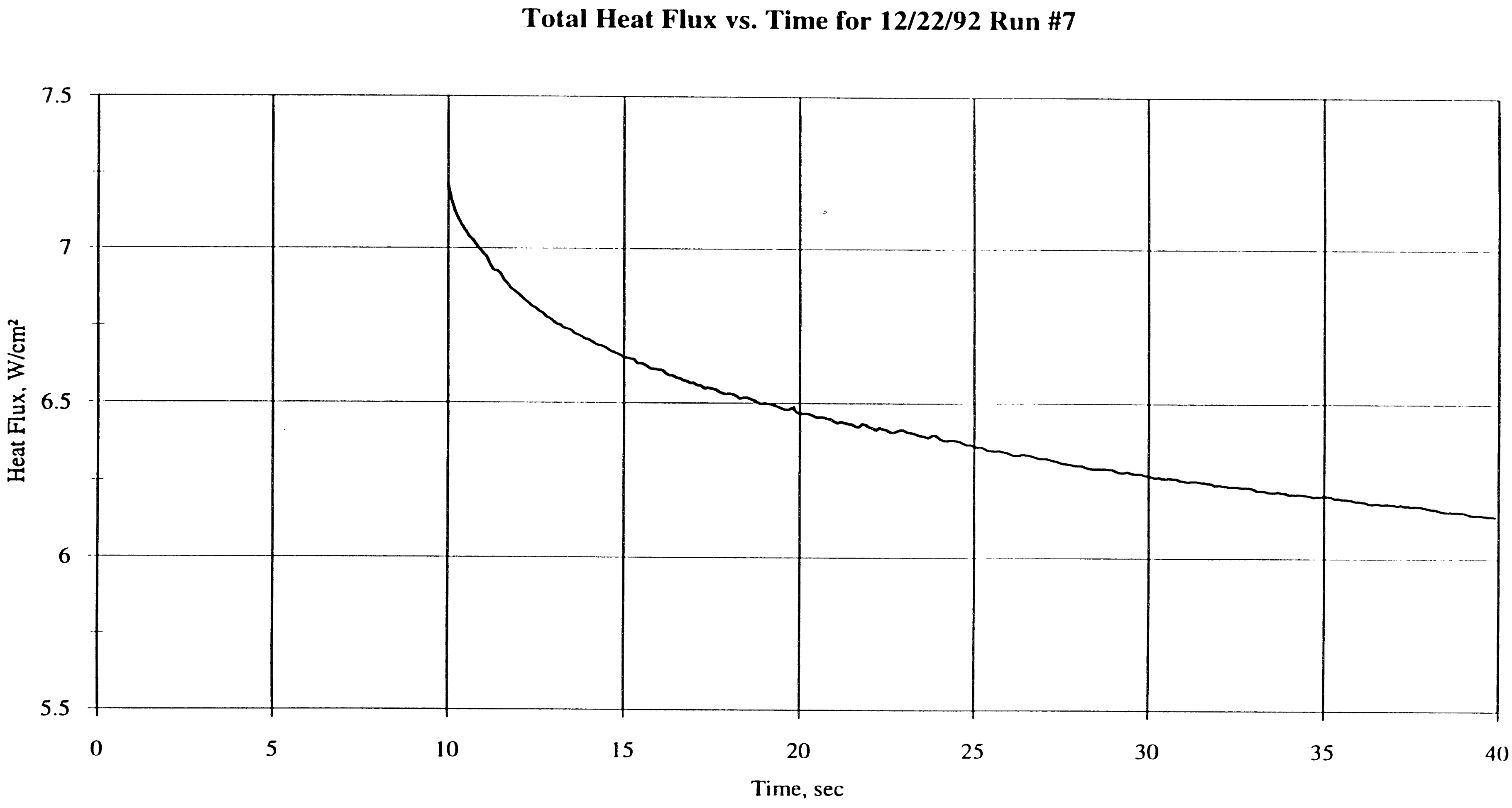
Total Heat Flux vs. Time for 12/22/92 Run #7

Figure F7b. Heat flux input. Run No. 7.

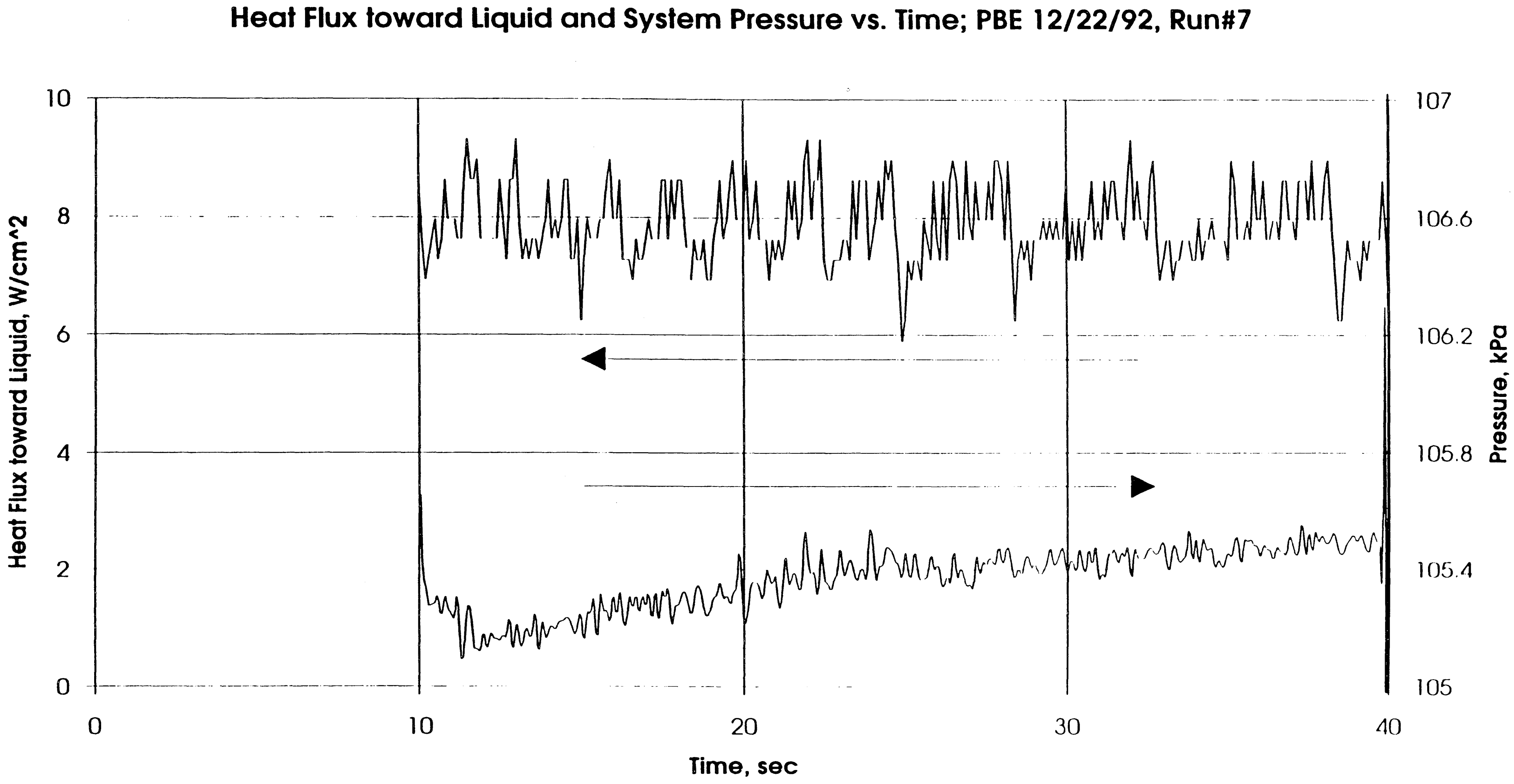

Figure F7c. System pressure and heat flux into fluid. Run No. 7.

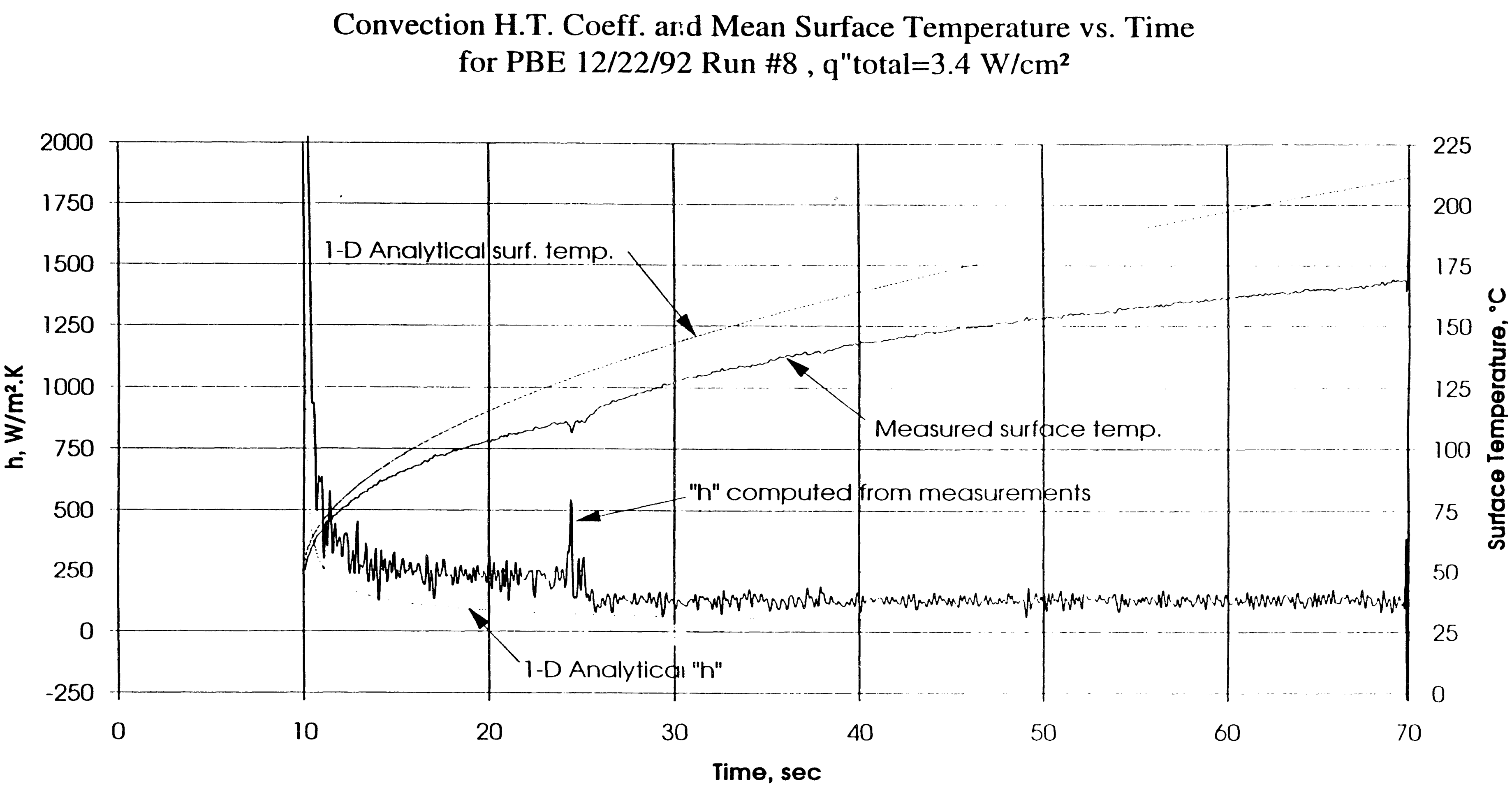

Figure F8a. Mean heater surface temperature and derived heat transfer coefficient. Run No. 8.

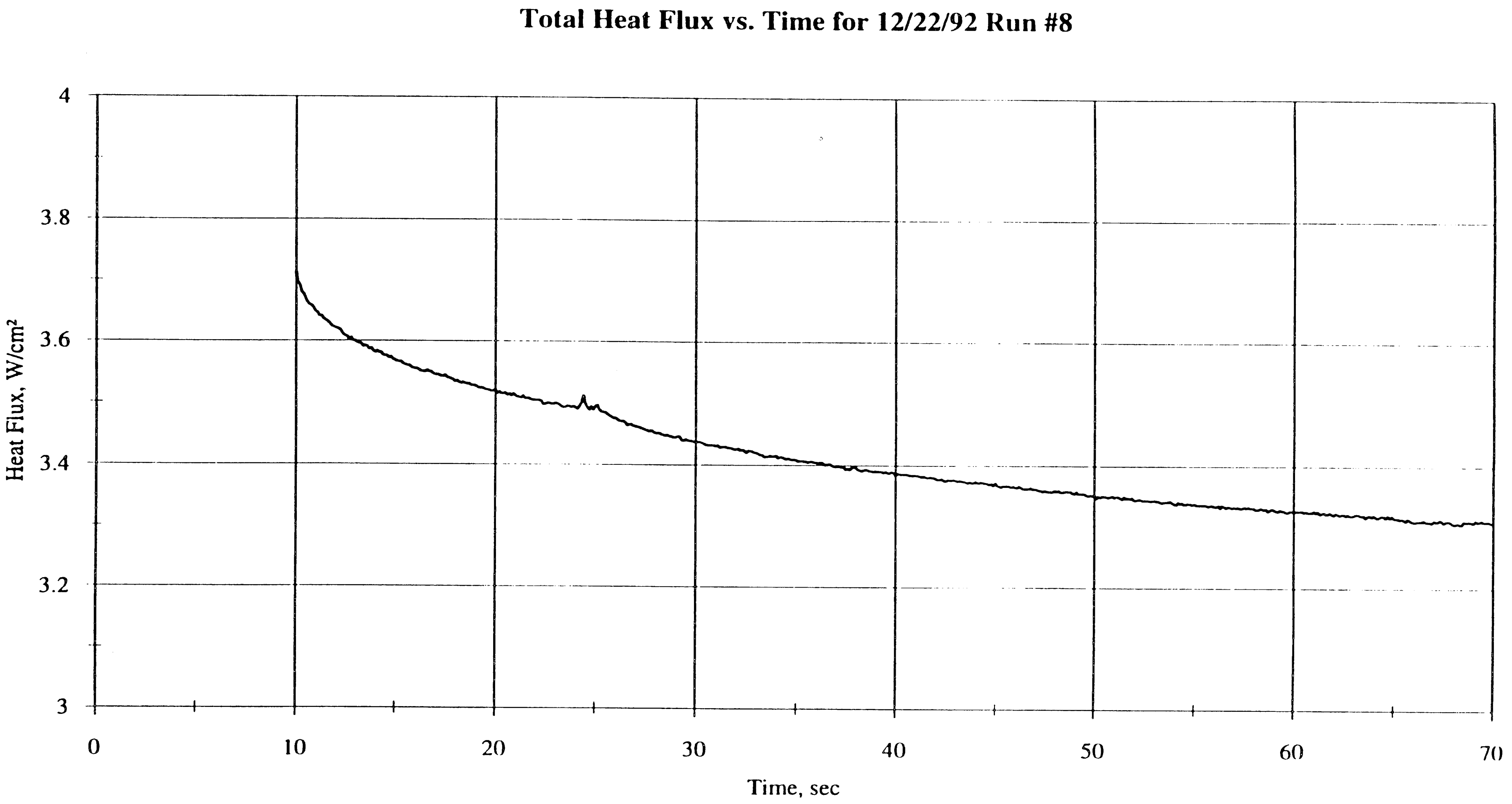

Figure F8b.   Heat flux input. Run No. 8.

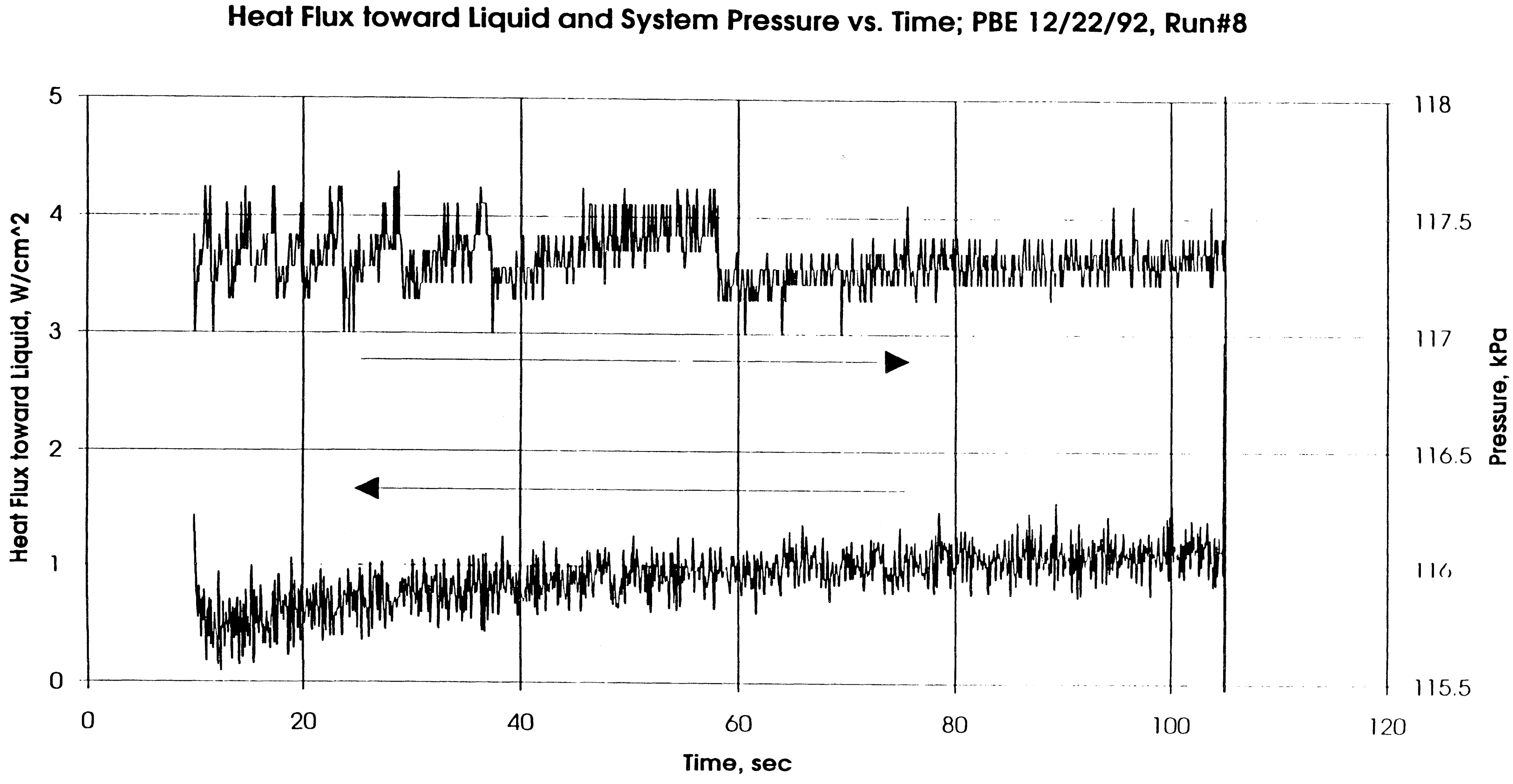

Figure F8c. System pressure and heat flux into fluid. Run No. 8.

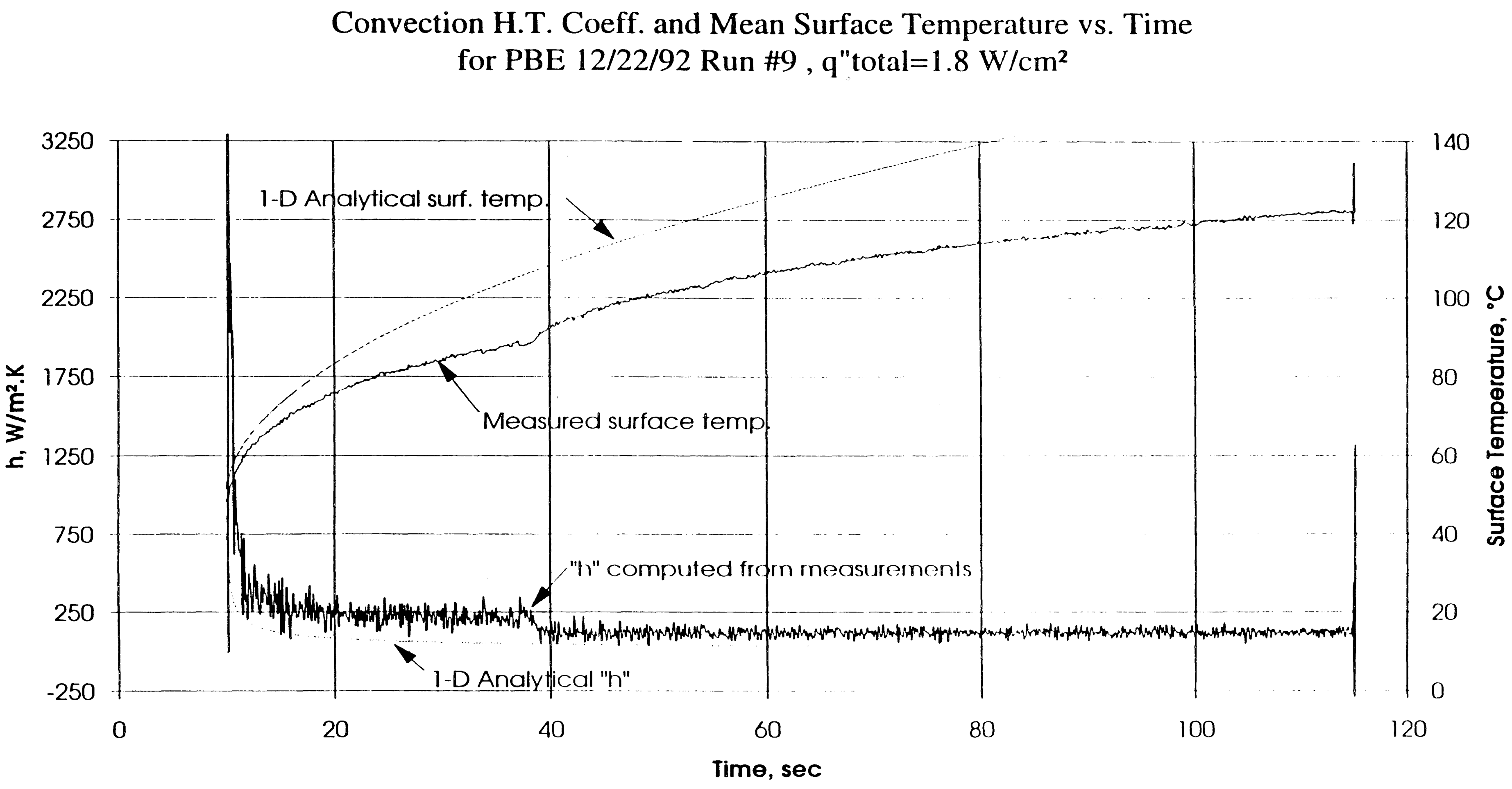

Figure F9a. Mean heater surface temperature and derived heat transfer coefficient. Run No. 9.

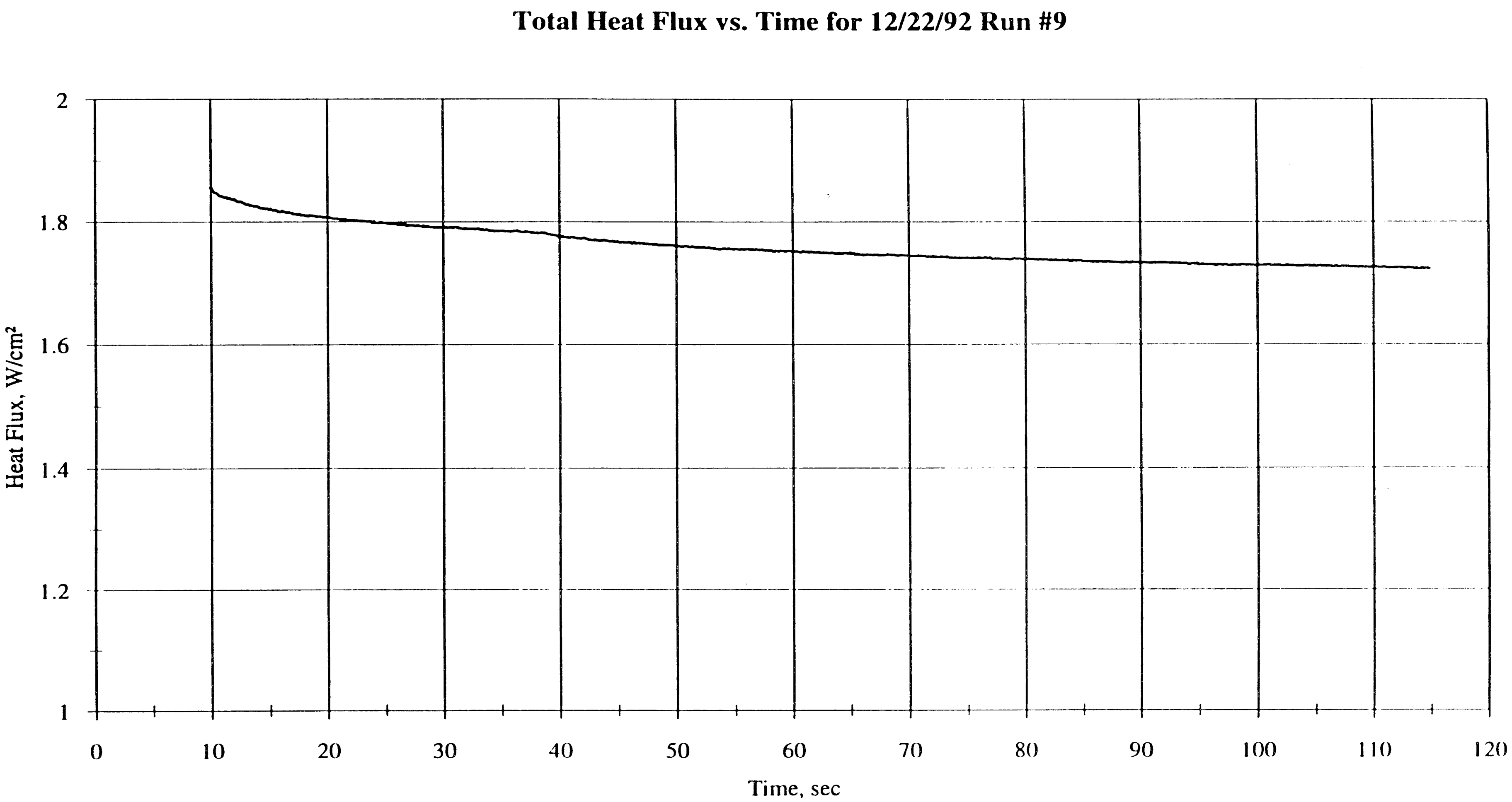

Figure F9b. Heat flux input. Run No. 9.

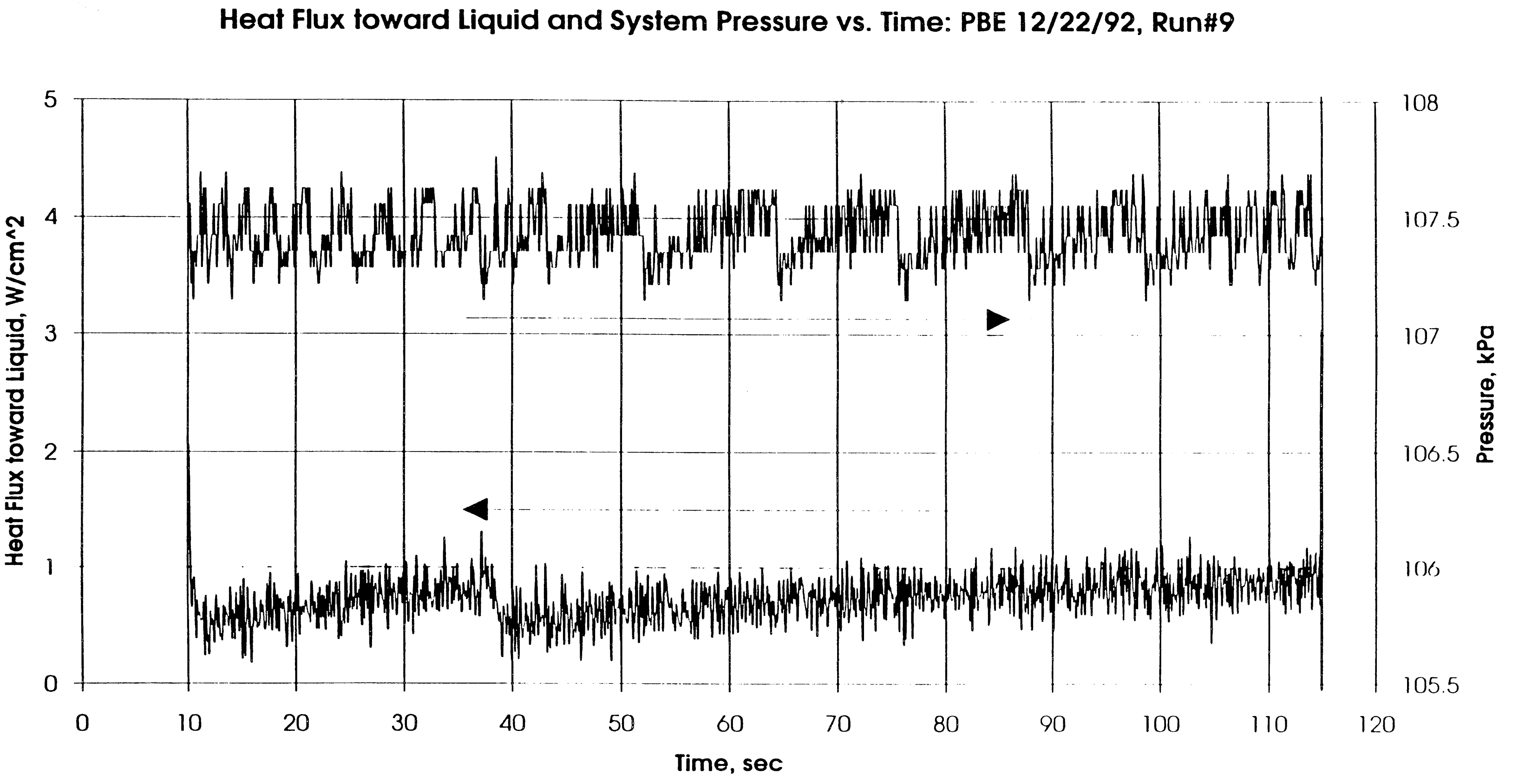

Figure F9c. System pressure and heat flux into fluid. Run No. 9.